Desiccation Cracking: A Weather-driven Deterioration Phenomenon Affecting Infrastructure Slope Resilience

Emma Louise McConnell

BSc (Hons) Earth Science

MSc Civil Engineering

A thesis submitted for the degree of Doctor of Philosophy

School of Engineering

November 2024

Abstract

Weather-driven deterioration of infrastructure embankments is an increasingly severe threat to their stability, longevity, and safe operation. Dry-wet cycles within compacted clay fill instigate shrinking and swelling, forming micro- and macro-scale cracks that drive irrecoverable microstructural changes. This degradation reduces the clay fill's water retention capacity, exacerbating the rate, magnitude, and consequence of these dry-wet cycles. Therefore, understanding the timescales of microstructural degradation and desiccation cracking's role within this is crucial to ensure the long-term serviceability of the transport network.

Laboratory tests, while informative, often fail to capture field scale heterogeneity. To bridge this gap, an intermediate-scale, compacted clay slope was constructed within an outdoor lysimeter. This novel approach provided high-resolution spatial and temporal monitoring, revealing that cracking severity depends on exposure to physical and environmental boundary conditions. Desiccation cracks significantly altered slope hydrology, locally deepening evaporation and infiltration fronts by up to 400 mm and extending weather-driven deterioration to 200 mm. Deep summer crack networks (2021-2022) markedly increased rainfall storage capacity, allowing full infiltration of three simulated 1-in-100-year storm events (each delivering 52 mm of rainfall in one hour, with climate change uplifts applied) and producing no runoff. The resulting soil moisture increase resulted in a sharp decrease in suction, culminating in complete suction loss by the end of the third event. In contrast, shallower crack networks in Spring 2023 generated runoff under the same storm profiles. Seasonal drying patterns were also disrupted, maintaining high moisture contents that suppressed suction generation and inhibited deep cracking observed in prior summers

The lysimeter slope enabled real-time monitoring of desiccation drivers, informing targeted laboratory-scale tests. These experiments provided insight into how altering the physical and environmental boundary conditions through modifying parameters in the Penman-Monteith (1965) equation can influence moisture transfer dynamics and desiccation behaviour within Ampthill Clay fill. Overall, this research qualitatively and quantitatively underscored desiccation as a key accelerator of weather-driven deterioration. Furthermore, it emphasised that all contributing elements to desiccation must be considered to fully assess their risk to infrastructure embankment stability.

Acknowledgments

I would first like to thank the ESPRC-funded ACHILLES grant for enabling this research. It allowed me to work with a team of leading academics and industry professionals who shared the vision of ensuring the future resilience of the UK's key geotechnical infrastructure assets.

To my supervisors – Dr Colin Davie, Dr Ross Stirling, and Professor Stephanie Glendinning – I am incredibly grateful for your continual expertise, wisdom, and support throughout the research and writing process. Working alongside a supervisory team who were as enthusiastic about soil cracking as I had become has been a pleasure. Many thanks are also directed towards the GEST Laboratory Technicians – Richard, Gareth, Mike, Stu, James, Jonathan, Owen, and Frank. Your endless great chat and support have been there since day one – the best technician team out there. I would also like to thank my new team at Mott MacDonald, especially Chris and Verity, who have been nothing but supportive for this final part of the PhD journey.

Special thanks go to the NGIF social club: Alethea, Jess, Narryn, Elena, Helen, Dan, and Ross. You have made the whole PhD experience even more enjoyable, and I will be eternally grateful for that.

To my family – Mum, Dad, Leo, and Daniel – I would be nowhere without your continual support and belief in me. Special thanks go to my Mum for picking up the phone no matter what and being the most supportive sounding board and giver of great advice. I would also like to thank Rich massively. Your continual patience, understanding, support, daily messages, and cute pet content have kept me going through this write-up period.

Finally, I would like to thank my dearest friends. Rachel, you are the best thing to come from Newcastle. Thank you for always reminding me to mini-chunk the thesis, providing snacks, and endlessly supporting me. Finally, to my oldest friends Louise, Holly, Rebekah and Laura, I am extremely grateful for your continual phone check-ins and supportive memes and for providing joy and laughter throughout my life.

Table of Contents

List of Figures

List of Tables

List of Acronyms

Acronym	Full Term
2D	Two-dimensional
3D	Three-dimensional
AEV	Air-entry value
BGS	British Geological Survey
BS	British Standards
CIF	Crack Intensity Factor
CSV	Comma-Separated Values
DDF	Depth Duration Frequency
DE1	Drying Event 1
DE2	Drying Event 2
DIC	Digital Image Correlation
EA	Environment Agency
ERT	Electrical Resistivity Tomography
FEH	Flood Estimation Handbook
FOS	Factor of Safety
GMC	Gravimetric Moisture Content
ISM	Integral Suspension Method
LEFM	Linear Elastic Fracture Mechanics
LIDAR	Light Detection and Ranging
LWIR	Long-wave Infrared
MD	Moisture content density
NETD	Noise Equivalent Temperature Difference
NGIF	National Green Infrastructure Facility
ORR	Office of Rail and Road
PSD	Particle Size Distribution
RACA	Rapid Asset Condition Assessment
RS1	Rainfall Simulation 1
RS2	Rainfall Simulation 2
SCCC	Soil Characteristic Cracking Curve
SEM	Scanning Electron Microscopy
SEM*	Simplified Evaporation Method
SSCC	Soil Shrinkage Characteristic Curve
SWRC	Soil Water Retention Curve
TDR	Time Domain Reflectometry
TS1	Sandy Topsoil
TS2	Clayey Topsoil
UK	United Kingdom
UKCEH	UK Centre for Ecology and Hydrology
UKCP18	United Kingdom Climate Projections 2018
UKCRIC	UK Collaboratorium for Research on Infrastructure and Cities
VWC	Volumetric Water Content
W1	Wind Speed Test 1 (0 m/s)
W2	Wind Speed Test 2 (1.5 m/s)
W3	Wind Speed Test 3 (4.5 m/s)
W4	Wind Speed Test 4 (18 m/s)
X-RAY CT	X-ray Computed Tomography

List of Notations

Notation	Description	Units
A	Activity Index	–
I_P	Plasticity Index	%
W_L	Liquid Limit	%
W_P	Plastic Limit	%
E	Evaporation Rate	mm/day
Δ	Slope of saturation vapour pressure curve at air temperature	kPa/°C
γ	Psychometric constant	kPa/°C
R_n	Net radiation at crop surface	MJ/m²/day
G	Soil heat flux	MJ/m²/day
u	Wind speed at two meters height above the surface	m/s
e_s	Saturation vapour pressure	kPa
e_a	Actual vapour pressure	kPa
ET	Evapotranspiration	mm/day
ρ_a	Mean air density at constant pressure	kg/m³
c_p	Specific heat of air	MJ/kg/°C
r_a	Bulk surface resistance	s/m
r_s	Aerodynamic resistance	s/m
e	Void ration	–
R_{sc}	Surface Crack Ratio	%
w	Water content	%
φ	Suction	kPa
R	Gas Constant	J/(mol·K)
T	Temperature	K or °C
M_w	Molecular mass of water	g/mol
$e_s(T_d)$	Saturation vapour pressure at dew point	kPa
$e_s(T_d)$	Saturation vapour pressure at sample temperature	kPa
θ	Volumetric water content	m³/m³ or %

List of Units

Units	Description
km	Kilometres
mm	Millimetres
µm	Micrometres
m	Metres
m^2/g	Square metres per gram
meg/100g	Milliequivalents per 100 grams
kPa	Kilopascals
kN/m^2	Kilonewtons per square metre
^{O}C	Degrees Celsius
Mg/m^3	Megagrams per cubic metre
J/(mol×K)	Joules per mole per kelvin
ml	Millilitres
MHz	Megahertz
m^3/m^3	Cubic metres per cubic metres
dS/m	Decisiemens per metre
pF	Potential force
cm H_{2O}	Centimetres of water
m/s	Meters per second
W/m^2	Watts per square metre
hPa	Hectopascals
L/hour	Litres per hour
g/mol	Grams per mol
mm/day	Millimetres per day
$MJ/m^2/day$	Megajoules per square metre per day
kg/m^3	Kilograms per cubic metre
$MJ/kg/^{o}C$	Megajoules per kilogram per degree Celsius
s/m	Seconds per metre

Chapter 1. Introduction

1.1 Research Context

In the UK, infrastructure embankments comprise approximately 9660 km of the transport network, largely managed by four primary infrastructure owners: Network Rail (5000 km), London Underground Limited (60 km), National Highways (3500 km), and British Waterways (1100 km). These earthworks assets are critical for physically supporting road, rail, and canal infrastructure across low-lying ground or areas of elevated flood risk. Therefore, maintaining their structural integrity is fundamental to ensure the operational serviceability and safety of the transport network. However, effective asset management is particularly challenging within the ageing network due to the increasing volume of assets requiring maintenance and rising associated costs (Reid & Clark, 2000; Perry et al., 2003; Glendinning et al., 2014a). Network Rail effectively highlights the realistic nature of this task, as only 0.5% to 1% of their asset base receives the necessary maintenance during each five-year control period (Network Rail, 2018).

The likelihood of failure within infrastructure assets is rooted in their inherent vulnerabilities and relative exposure to dynamic threats (Perry et al., 2003; Briggs et al., 2017, 2019). The former relates to the physical properties of embankment fill, which differs greatly across the various transport modes as it is associated closely with construction age. Most rail and canal embankments are over 100 years old, commonly over-steepened and constructed using heterogeneous materials, often in a poorly compacted state. In contrast, road construction began in the 1960s, utilising modern geomechanics principles and incorporating effective drainage systems, significantly improving their overall performance and resilience to environmental stresses (Skempton, 1995; Perry et al., 2003; Mair, 2021). With varying physical properties, embankments across the transport network will exhibit inconsistencies in their responses to dynamic threats. Consequently, this complicates the development of a universal framework for embankment deterioration and failure prediction. Therefore, greater effort is required to relate the relevant failure mechanisms and threats to the range of embankment geologies and geometries across the transport network.

In 2021, Lord Robert Mair and his task force highlighted that the increasing frequency and severity of extreme weather events pose the most significant dynamic threat to the deterioration of earthworks. This insight was documented in their review of Network

Rail's earthwork management practices (Mair, 2021), which was prompted by the fatal train derailment near Carmont, Aberdeenshire, in August 2021. This serious incident underscored the severe impacts of inadequate climate resilience on earthwork and drainage assets. According to the Office of Rail and Road (ORR), the risk of significant failures directly associated with extreme weather events, especially high-intensity summer rainfall, continues to rise. This trend was illustrated using Figure 1.1 (ORR, 2024), which shows that 2023 to 2024 recorded the highest rate of high-consequence failures in Network Rail's earthwork assets since this metric was introduced in 2008.

Figure 1.1: The number of high-consequence earthwork failures occurring within Network Rail's earthworks since the metric began in 2008 (from ORR, 2024)

Mair (2021) identified a critical limitation in current earthwork stability assessments: they largely rely on observations derived from failures under historical climate observations, overlooking how unprecedented climate extremes may exacerbate deterioration processes. Despite their more primitive state, this limitation can be extended to road embankments, where failing to incorporate climate change in stability assessments could grossly underestimate their time-to-failure distributions. This risk posed by climate change to infrastructure embankments stems from the capacity of extreme weather to intensify the shrink-swell behaviour of high-plasticity clay fill (Hughes et al., 2009; Briggs et al., 2017; Spink, 2020; Mair, 2021). Through time this behaviour can deteriorate the fill's microstructural integrity by increasing micro- and macro-porosity through shrinkage-induced crack formation (Basma et al., 1996; Stirling

et al., 2021; Briggs et al., 2023; Dias et al., 2023). Increased intensity and connectivity of desiccation crack networks under more extreme drying will significantly enhance the fill's susceptibility to rapid and voluminous infiltration and suction loss (McBrayer et al., 1997; Greve et al., 2010; Mair, 2021). Therefore, the magnitude of seasonal pore water pressure cycles is set to increase, particularly considering projections of warmer, wetter winters (Davies et al., 2008; Glendinning et al., 2014). Fundamentally, these pore water pressure cycles will lead to irrecoverable strain-softening and progressive downslope movement of fill under a reduced shear strength (Glendinning et al., 2014; Tang et al., 2018; Stirling et al., 2021; Briggs et al., 2023). Therefore, understanding the risks cracks pose to earthwork deformation and how processes like desiccation cracking can amplify these risks is crucial to ensuring long-term asset resilience.

Figure 1.2 (ORR, 2021) presents an example of Network Rail's 11 levers approach to managing the weather resilience of earthworks and drainage on their network. Routed in these levers is the need to fund research (10/11) to raise awareness and fundamentally understand the weather resilience of earthwork assets. Integral to this approach is improved asset knowledge (8/9), reliable forecasting of weather hazards (4), metrics of design resistance (7), and understanding whole system behaviour (2) for intelligent use in high-level decision making (ORR, 2021).

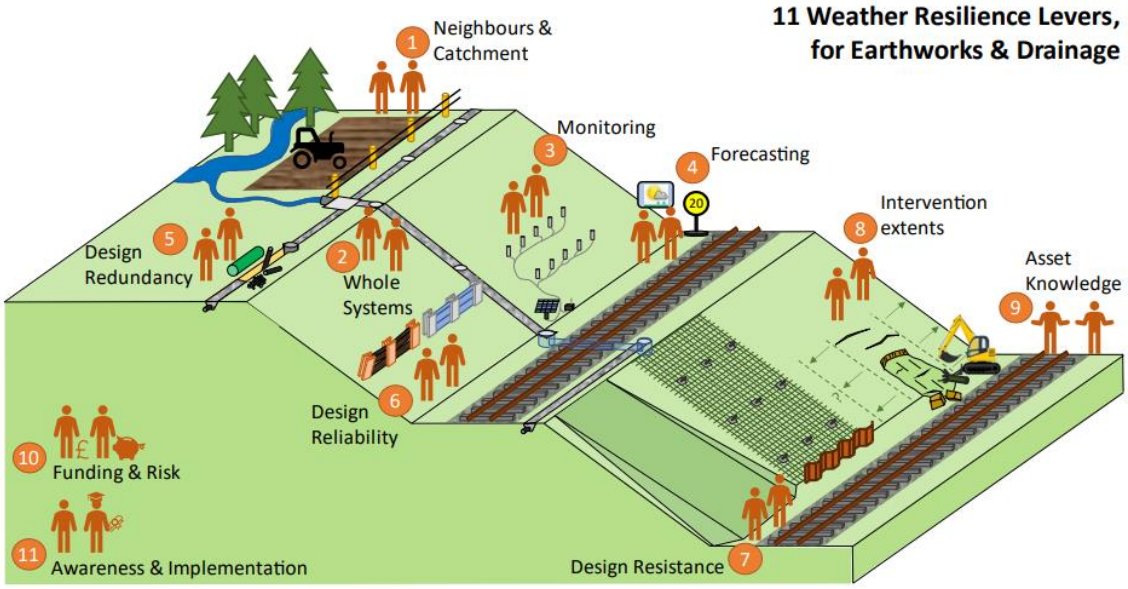

Figure 1.2: Summary of the eleven levers Network Rail has identified to manage the resilience of earthwork and drainage assets to weather-related hazards (from ORR, 2021).

Consequently, a consensus has been reached that a proactive approach to asset management is essential, grounded in empirically established temporal relationships

between embankment characteristics and these weather-driven deterioration mechanisms (Network Rail, 2018; Spink, 2020; Mair, 2021). This approach requires detailed monitoring and measurements which quantify the spatial and temporal evolution of weather-driven embankment deterioration and how it manifests at the field scale. Embedded within this should be evidence-based and realistic assessments of how future climate extremes will alter the nature of key deterioration mechanisms and the frequency and most common mode of embankment failure. Through this, more accurate asset stability categorisation based on time-to-failure distributions can be achieved, facilitating targeted, timely interventions that optimise resource allocation and improve long-term asset serviceability.

1.2 Aims and Objectives

The principal aim of this thesis is to investigate the coupled interaction of desiccation cracking and hydrological processes within an embankment slope across varying temporal and spatial scales. Specifically, this research will examine whether the development and impacts of desiccation-induced deterioration of plastic clay fills can be captured and quantified through changes in their hydromechanical behaviour. A multiscale approach was adopted, with the materials and methods utilised carefully selected to ensure the results are applicable and interpretable within the context of UK infrastructure embankments. To achieve this aim, this research has been structured around the following objectives:

OB1. Determine the differences in moisture flux dynamics between an embankment in a cracked and intact state.

- ***OB1a.*** Develop an experimental methodology that accurately represents and calculates the moisture flux dynamics within cracked and intact soils.
- ***OB1b.*** Determine the differences in moisture flux dynamics across varying temporal scales of drying and wetting.
- ***OB1c.*** Examine whether cracking intensity affects the difference in moisture flux dynamics between desiccated and intact embankment states.

OB2. Determine whether the behaviour of an embankment in its desiccated and intact states changes with cyclic environmental exposure.

- ***OB2a.*** Determine if changes in saturated hydraulic conductivity occur over successive dry-wet cycles and the resultant effect on soil infiltration capacity.

OB2b. Determine if the number of dry-wet cycles, their duration, and intensity influence infiltration capacity over time.

OB2c. Determine whether successive dry-wet cycles impose changes to soil microstructure through desiccation cracking or otherwise.

OB2d. Determine if desiccation cracks significantly impact the infiltration capacity of soil.

OB3. Determine quantitively the controlling factors in desiccation crack formation.

OB3a. Develop a research methodology that identifies and quantifies the range of environmental parameters that affect desiccation crack formation.

OB3b. Develop a research methodology that investigates the role of construction-based parameters in desiccation crack formation.

1.3 Thesis Structure

This section provides a brief overview of the thesis structure, with this chapter (Chapter 1) setting out the context of this research and its relative high importance for ensuring the longevity, stability, and safety of infrastructure embankments, which are key transport assets. Chapter 2 reviews the current relevant literature, firstly understanding threats to the long-term performance of infrastructure embankments. This includes internal threats, such as the inherent properties of embankment fill, and external threats, which dynamically evolve with time, such as physical and environmental loading. Within this review, weather-driven deterioration through desiccation cracking is identified as a critical destabilising mechanism of increasing importance under future climate change projections. An overview of the fundamentals of desiccation crack formation is then given. Finally, a critical assessment of previously employed methods to contextualise weather and desiccation-driven deterioration at the material- or asset scale is conducted, identifying key research gaps.

Chapter 3 details the multi-scale approach implemented to address the research gaps identified in Chapter 2 and the aims and objectives outlined in Section 1.2. The methodology presents the construction of a novel intermediate-scale slope within an outdoor lysimeter. Furthermore, it details a comprehensive laboratory study that allowed further isolation of the parameter space influencing desiccation cracking. In the course of this chapter, there is a persistent emphasis on the significance of the materials and methodologies employed in relation to the replication of processes within

live infrastructure embankments. This focus highlights the critical role that appropriate selection and application of such parameters play in the desiccation crack and weather-driven deterioration processes within these assets.

The results from long-term desiccation cracking and hydrological monitoring of the outdoor lysimeter slope are provided in Chapter 4. This includes adaptations made to the lysimeter design to investigate its behaviour under varying environmental and physical boundary conditions. In Chapter 5, the findings from the laboratory studies are presented, with a detailed analysis that correlates these results with the observations obtained from the lysimeter experiments. This correlation serves to elucidate the broader implications of the laboratory results in the context of monitoring and analysing desiccation cracking within live infrastructure embankments.

Chapter 6 presents a finalised summary of the research findings and key conclusions drawn. It details the significance of these conclusions in relation to the implications of desiccation cracking within infrastructure embankments from a deterioration perspective. Comments on the limitations of this research and recommendations for future development conclude this chapter.

Chapter 2. Literature Review

2.1 Introduction

This chapter offers a comprehensive review of the current understanding regarding the weather-driven deterioration of infrastructure embankments, with a particular emphasis on the processes associated with desiccation cracking. The review starts broadly by explaining the performance of infrastructure embankments and why they are deteriorating, highlighting what is known about the key drivers and mechanisms of failure.

The following section provides a comprehensive review of how environmental processes contribute to the deterioration of infrastructure embankments. It focuses on the weather-driven deterioration framework, examining current knowledge about the key processes that lead to degradation at both the material and asset scales. The pivotal role of desiccation cracking within this theoretical framework is underscored, transitioning into examining the fundamental principles underlying desiccation crack formation. This review encompasses various formation theories, delineates the inherent characteristics of cracks, and identifies the primary driving mechanisms involved. Furthermore, it addresses methodologies for quantifying cracking while contextualising the settings in which this phenomenon has been studied.

The issue of desiccation cracking as a key deteriorating mechanism is then examined. Specifically, this section includes a review of how desiccation cracks affect the hydrological regimes of infrastructure embankments and explores how deterioration caused by desiccation can increase an asset's vulnerability to failure. This includes a critical review of the existing studies on weather- and desiccation-induced deterioration of infrastructure embankments. This study examines three distinct scales of research: laboratory, intermediate, and field studies, each with its respective advantages and limitations. The literature review underscores the importance of thoroughly understanding desiccation processes and their adverse impacts. It advocates for adopting multiscale research methodologies to address and mitigate the risks associated with infrastructure deterioration effectively. Furthermore, this review identifies key research gaps for advancing knowledge regarding embankment deterioration induced by desiccation.

2.2 Performance of Transport Infrastructure Embankments

Infrastructure embankments, composed of natural earth materials, experience performance variations over time due to the inherent tendency of soils to undergo physical, chemical, and mechanical change. Within existing literature, performance rate is related to changes in two primary factors: the hazard posed by the intrinsic properties of their fill material and external dynamic processes that exploit these vulnerabilities and act as triggering events (Glendinning et al., 2009; Briggs et al., 2017, 2019; Spink, 2020). The former category encompasses attributes such as strength, permeability, and compaction, which can render an embankment more vulnerable to several potential threats (Power et al., 2016; Briggs et al., 2019). Conversely, the latter category pertains to environmental (e.g. flooding) and physical loads (e.g. traffic magnitude and frequency) that may exploit the inherent properties of the fill material and disrupt the equilibrium of stabilising forces (Spink, 2020). The literature extensively acknowledges that the inherent soil properties of embankment fill are intrinsically correlated to their age (Skempton, 1995; Perry et al., 2003; Mair, 2021). This correlation results in considerable variability across the transportation network, attributable to the differing construction dates.

2.2.1 Assessing and Projecting Performance

There are different assessment scales, ranging from individual assets to network level and from current to future stability. The current assessment of an individual asset is commonly done using limit equilibrium or numerical analysis (Ullah et al., 2020). Such values are based on engineering parameters alone, computationally exhaustive, and do not account for evolving threats or deterioration states. However, the inherent variability of embankments not only complicates the development of a universally applicable predictive model for deterioration but also means that the threats posed to these assets can be highly specific (Briggs et al., 2019; Spink, 2020; Mair, 2021). Furthermore, the same threat may manifest differently within or across various asset groups, further complicating risk assessment and management strategies.

An example of current procedures in strategic asset risk management involves the ‘bow-tie’ approach in Figure 2.1, which defines the risk of a hazard event based on its likelihood (left side) and consequence (right side) of occurrence (Spink, 2020). Assessments using these methods can be conducted at an individual asset, asset group or network scale. Failure likelihood relies on site-specific assessments of potential hazards and failure triggers (Glendinning et al., 2009). Assessing asset

vulnerability to these failures relies on cyclic visual inspections of earthwork properties, current conditions, and the presence of interventions. A hazardous event's consequence is based on its impact on operational safety. Depending on the relative weighted importance of each condition indicator and impact assessment outcome, a hazard rating from A (low risk) to E (highest risk) can be generated. White et al. (2024) highlighted that 14% of asset failures in 2019 – 2020 were of category A under this assessment framework. Other studies also questioned the applicability of surface observations to assess subsurface deterioration (Mair, 2021; White et al., 2024). White et al. (2024) instead proposed the Rapid Asset Condition Assessment (RACA) framework to combine data sources, assess current asset conditions, and suggest techniques for when further refinement is needed. The toolbox they suggest combines intrusive, non-intrusive and modelling techniques to target remediation. However, the budget must be there to facilitate the use of site-based techniques.

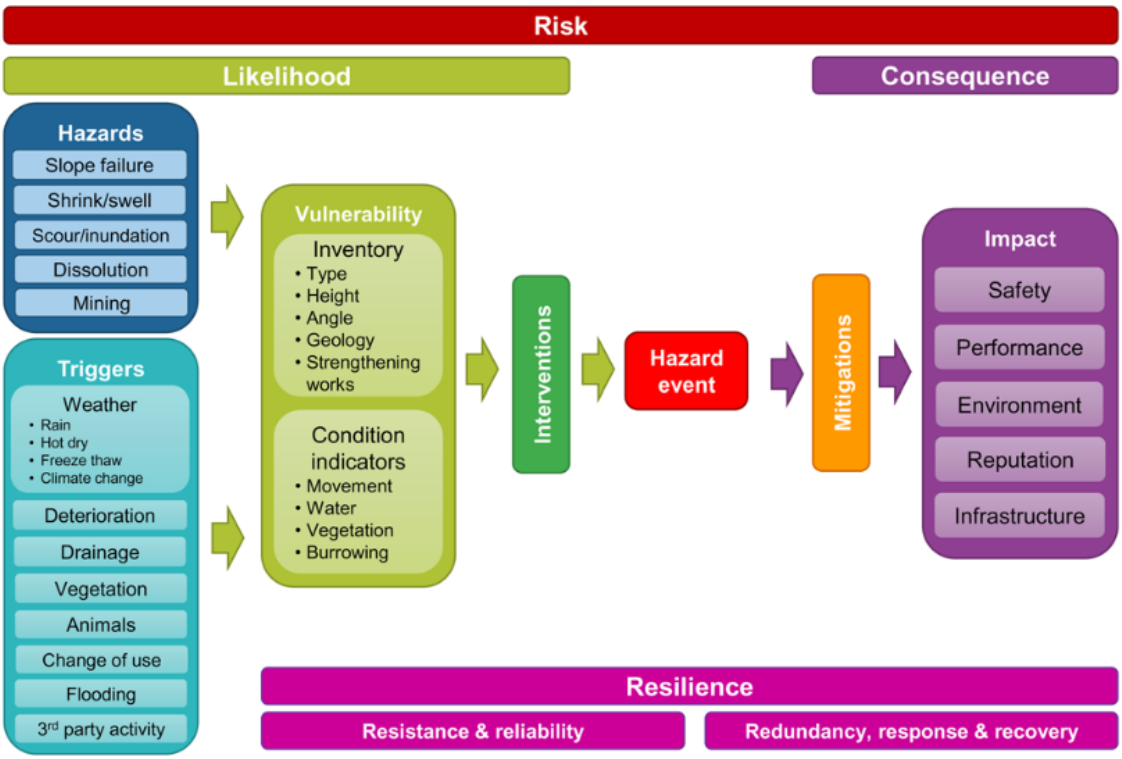

Figure 2.1: Earthworks risk bow-tie diagram from Spink (2020) illustrating how the likelihood and consequence of earthwork failure can be assessed.

More recent developments in this assessment process include the use of the Markov chain modelling to incorporate the dynamic nature of earthwork deterioration into the assessment of stability (Power et al., 2016; Spink, 2020). These models have been projected into the future to predict the condition scores of assets based on their record history of examination data. For example, it demonstrated that soil cuttings in high-

plasticity clays will deteriorate twice as rapidly as those of low plasticity. The primary limitations of such performance assessments are the long intervals between visual inspections, reliance on human observations and not empirical engineering calculations, and challenges in using failures under past climate conditions to evaluate current stability. Furthermore, there is no consideration of climate change, under which fill material properties, hazards, and triggers are likely to evolve (Glendinning et al., 2009; Spink, 2020; Mair, 2021).

Briggs et al. (2019) proposed a conceptual deterioration model, utilising the inverted 'bathtub' curve shown in Figure 2.2 to map embankment performance relative to a preset threshold. The plot can be adapted to analyse the effects of specific performance measures at any asset scale for a particular type of hazard, determining its impact on the curve's trajectory within four distinct phases: i) a post-construction bedding-in period where performance improves, ii) a phase of reliable performance, iii) the onset of deterioration that degrades performance toward a predefined threshold value, and iv) an unreliable stage where the embankment fails to maintain this performance threshold.

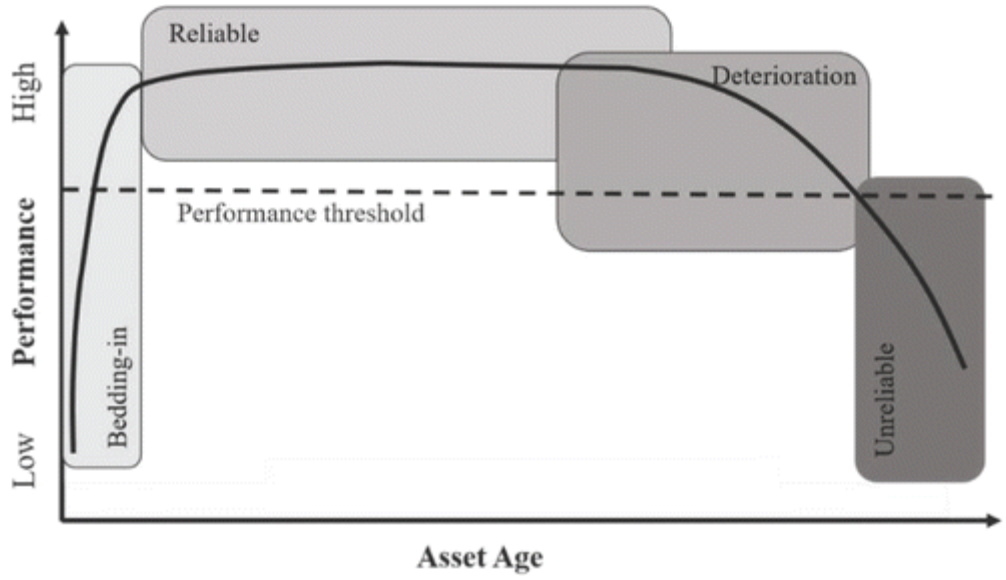

Figure 2.2: Conceptual model from Briggs et al. (2019) for asset deterioration utilising the inverted 'bathtub' curve where an embankment's projected lifecycle can be divided into four performance categories related to a pre-defined threshold: 1) bedding-in period where performance improves, (2) reliable period where performance is sustained, 3) deterioration stage where asset performance is degrading, and 4) an unreliable period where the asset is no longer serviceable.

From a geotechnical perspective, performance thresholds are commonly defined by limit state design– i.e., the exceedance of either serviceability or ultimate limit states

(Perry et al., 2003). Serviceability limit state exceedance is most common and refers to significant deformation, usually through shallow translational slips; however, the embankment can remain functional with repair and maintenance. Conversely, ultimate limit state exceedances are less frequent but more severe and involve the collapse or failure of embankments through deep rotational slips, terminating their operation.

From the methods available, there is yet to emerge a unified approach which can forecast asset performance by considering the response of its current state to varying threats, triggers, deterioration rates and climate change projections. Therefore, there remains a notable gap in the literature requiring improved characterisation of how threats, triggers and inherent material properties will evolve under changing environmental and physical loading.

2.2.2 Challenges with Forecasting Performance

The main uncertainty from these curves in Figure 2.2 and a general challenge in geotechnical asset management comes from predicting the onset and duration of the deterioration portion, i.e., the temporal evolution of change and the time taken to exceed the serviceability or ultimate limit state (Ridley, 2012; Briggs et al., 2019). The absence of such methods in Network Rail and National Highway's current assessment procedure indicates the difficulty in accurately accounting for the non-static nature of both fill properties and imposing triggers/hazards (Power et al., 2016; Spink, 2020). For example, a collective threat receiving increasing attention in the literature is the role of weather, which is the root cause of many common failure mechanisms in infrastructure embankments (Briggs et al., 2017; ORR, 2021; Mair, 2021; Stirling et al., 2021; Briggs et al., 2023). A growing concern is the increasing severity of weather events projected under future climate change scenarios, which is a significant predicted threat to the performance of all transport infrastructure embankments. However, the unpredictability of these extreme weather events and the accompanying uncertainty about how weather-related deterioration processes will evolve within them create significant challenges in predicting future asset stability.

Recent literature has focused on addressing these challenges, emphasising the necessity of site-specific assessments to improve understanding of weather-driven deterioration processes (Mair, 2021). Researchers advocate for better integrating empirical measurements and monitoring programs to characterise infrastructure assets' performance and deterioration trajectories (White et al., 2024). These

approaches aim to improve predictive models by accounting for local variations in material properties, environmental conditions, and operational stresses, thereby reducing uncertainty in asset management and forecasting.

However, the UK has approximately 9,600 km of embankment, along with significant lengths of other geotechnical assets that face similar challenges (Perry et al., 2003; Briggs et al., 2017; Spink, 2020). Due to resource and logistical constraints, it is therefore impractical to implement extensive measurement and monitoring programs across the entire transport asset network (Glendinning et al., 2009). The recognised consensus from academic literature and industry experts is that efforts should shift, focusing instead on detailed analyses of crucial deterioration indicators. Specifically**,** their impact on structural performance and time-to-failure distributions of the asset. By identifying critical metrics – including changes in soil strength, moisture content, deformation, and stress indicators – preliminary assessments of asset vulnerability can improve, informing effective resource allocation and proactive interventions. This approach balances the need for comprehensive understanding with the realities of scalable and efficient asset management.

2.3 Construction Practices and Inherent Problems

The behaviour of infrastructure embankments is broadly generalised into two groups: rail assets and road assets. This categorisation is based on the differences in design principles, material properties, and expected long-term performance each group exhibits (Skempton, 1995; Perry et al., 2003; Glendinning et al., 2009; Spink, 2020). Figure 2.3, adapted from Perry et al. (2003) and Briggs et al. (2017), visualises the percentage of road, rail, and canal embankments constructed yearly from 1800 to 2020. It demonstrates a noteworthy disparity in the relative age of construction, indicating that 99% of rail embankments exceed 100 years of age, whereas the structures within the highway network are considerably more modern.

The age disparity in construction practices yields significant distinctions in the physical and material properties characteristic of that era's methodologies. These differences reflect the technological advancements and material availability that shaped the network’s architecture during that time. Figure 2.4 (Briggs et al., 2017) effectively conveys these critical differences between (A) road and (B) rail embankments.

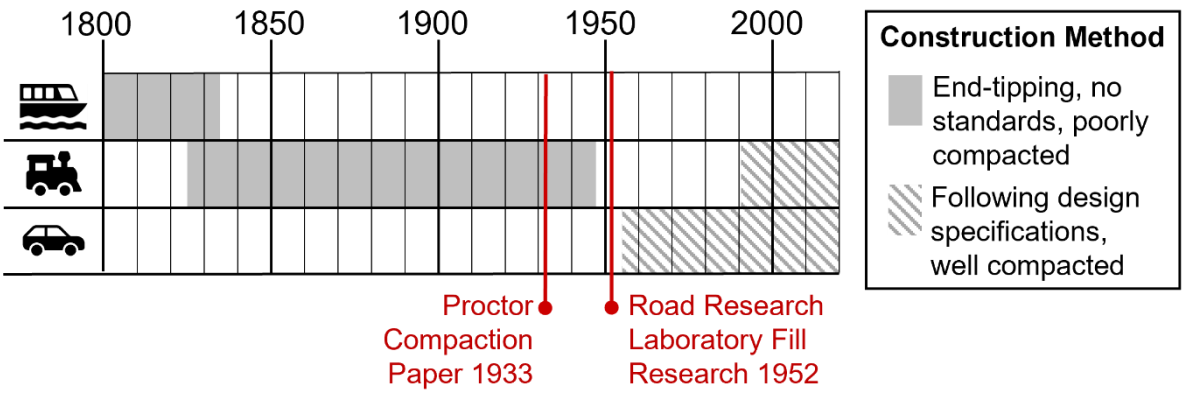

Figure 2.3: Embankment construction history and method for three main transport modes – canal, rail, and road. The construction method used is indicated by the key. Two dates of relevant advances in modern geomechanics principles are annotated – Proctor Compaction Paper 1993 and Road Research Laboratory Fill Research 1952, which helped standardise construction methods. Adapted from Perry et al. (2003) and Briggs et al. (2017).

Rail embankments are characterised by their highly heterogeneous fill, which varies significantly in both geological composition and compaction density. The placement of this fill involved the end-tipping of surplus soil and rock derived from adjacent cutting excavations. Notably, this process was executed with minimal foundation preparation, and without any material pre-processing or the utilisation of compaction machinery. The conditions resulted in over-steepened slope gradients, which is significant given the established correlation between embankment slope angle and the likelihood of failure found through back-analysis of past failures. Overall, assets were highly compressible, losing serviceability through large settlements and failures during and post-construction (Skempton, 1995; Perry et al., 2003). These failures were inadequately documented and often restored by adding ballast or capping materials, which critically left existing shear surfaces intact, where failure could be reactivated.

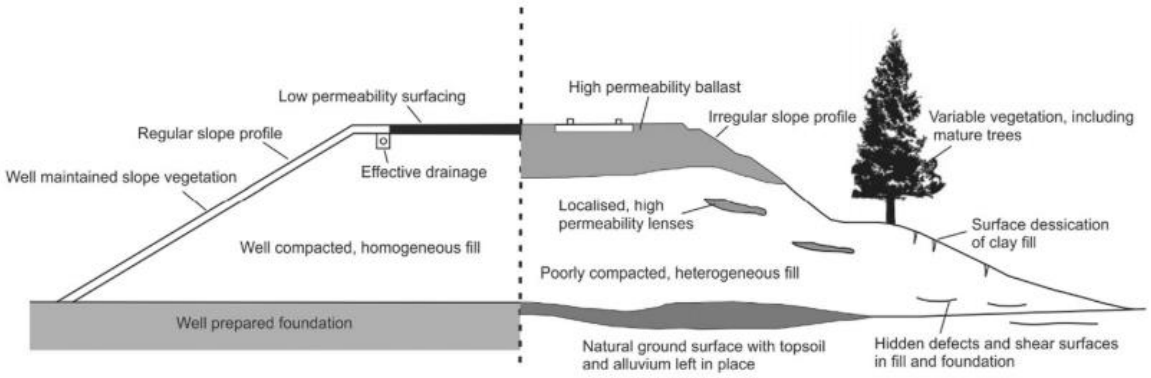

Fig. 1. Embankment profile for a highway embankment (left) a railway embankment (right) (adapted from Perry et al., 2003).

Figure 2.4: Schematic highlighting the key differences in the characteristics of road (left) and rail (right) embankments, from (Briggs et al. 2017).

Conversely, highway embankments illustrate the benefits of two major advances in modern geomechanics principles: (1) soil compaction for reducing instability and settlement (Proctor, 1993), and (2) appropriate compositions and placement methods for embankment fill (Road Research Laboratory, 1952). Consequently, road embankments were constructed on a stable foundation layer using well-compacted, homogeneous fills subject to minimal settlement. The embankment design matured to include adequate drainage, well-maintained slope vegetation, and shallower slope profiles to improve overall asset stability.

Due to these inherent differences, railway embankments have shown a greater susceptibility to failure under both physical and environmental loading. This vulnerability increases, and asset tolerance to stabilising forces decreases, with age due to cyclic exposure to deterioration mechanisms (Glendinning et al., 2014; Briggs et al., 2017; Briggs et al., 2019; Spink, 2020). Such disparity in failure likelihood is evidenced by Table 2.1 (Perry et al., 2003), which categorises common failure causes based on their potential to induce ultimate or serviceability limit state failure in road or rail embankments. Critically, a greater number of mechanisms are associated with the ultimate failure of rail embankments, which are either absent or limited to serviceability issues within road networks.

Table 2.1: Division of common causes of failure within infrastructure embankments into their ability to cause ultimate limit state and serviceability limit state failure within the railway and highway transport modes (after Perry et al, 2003).

	Ultimate Limit State Failure		Serviceability Limit State Failure	
Common causes of failure	**Railways**	**Highways**	**Railways**	**Highways**
Softening of clays				
Positive pore water pressure				
Shrink/swell cycle				
Over-steep slopes				
Defective drainage				
Overstressing				
Piping				
Pre-existing rupture surface				
Culvert collapse				
Internal fire				
Stiffness variations				
Differential settlement				
Wave erosion and scour				
Burrowing animals				

However, Table 2.1 also demonstrates common failure causes, mostly associated with the presence or fluctuation of moisture, which is inherently linked to cyclic changes in weather. These factors include clay softening, positive pore water pressures, shrink-swell cycles, wave erosion, and scour. Furthermore, proper drainage is essential for stability and addresses the inadequate management of excess water ingress. Addressing the forthcoming challenges surrounding water management and resilience to weather extremes was stressed by Mair (2021) as the step-change needed to ensure the future stability of Network Rail's earthwork assets.

2.4 Fill Material and Inherent Problems

Clay soil's engineering behaviour is unique, as their inherent strength depends primarily on water content. The saturation level of the clay matrix influences the interaction between grains, thus affecting the characteristics of plasticity and cohesion (Holtz & Kovacs, 1981). Plasticity refers to the ability of the clay to be moulded or shaped without cracking, while cohesion relates to the attraction between the particles that give them inherent strength and stability. The plasticity of clay can vary depending on the soil's plastic limit and liquid limits. These limits define the range of moisture

contents within which the soil can change its volume. Below the plastic limit, shrinkage ceases, and the soil behaves brittle, exhibiting instability without cohesion. Above the liquid limit, the soil becomes saturated, causing a loss of cohesion and plasticity as the sheer water volume diminishes the attractive forces between clay particles.

The larger the difference in moisture content between the plastic and liquid limit, the greater the plasticity index of the soil, which in turn enhances its capacity for significant volume changes during cyclic wetting and drying. This behaviour, particularly notable in high plasticity clay soils, is known as shrink-swell potential and presents one of the primary engineering challenges and causes of failure for UK infrastructure embankments (see Table 2.1) (Perry et al., 2003; Briggs et al., 2017; Mair, 2021). Shrink-swell is the largest geohazard in the UK, costing an estimated £3 billion in damages between 2010 – 2020 (Jones et al., 2020). Consequently, it is crucial to understand the relationship between water content, particle interactions, plasticity, and cohesion to determine the essential engineering characteristics that influence the strength and stability of these soils.

Clay mineralogy underlies this shrink-swell behaviour and plays a vital role in clay soils' properties. The molecular structure and surface chemistry of clay minerals contribute significantly to their ability to absorb water and become hydrated. This interaction affects the soil's plasticity and strength, highlighting the importance of mineral composition in assessing and managing the engineering challenges associated with clay soils (Jones et al., 2020). Figure 2.5 illustrates the sheet structures of silica and gibbsite, which combine to form distinct layers with either a 1:1 or 2:1 silica to gibbsite ratio, the foundation of all clay minerals (Bowles, 1979). These sheets consist of tetrahedral and octahedral structural units. Tetrahedra comprise a silicon atom bonded to four oxygen atoms. The octahedra comprises a metal atom (aluminium, magnesium, or iron) surrounded by six oxygen or hydroxyl atoms. Both units carry a net negative charge, promoting the sharing of oxygen or hydroxyl atoms, which combine into sheets to resolve valency imbalances.

Figure 2.3 exemplifies the molecular structure of three common clay mineral groups, with their shrink-swell potentials increasing from kaolinite to montmorillonite. Distinct features of these layered mineral structures influence their hydration potentials, displaying a complex interplay between physical interlayer storage capacity, mineral activity, and electrostatic forces.

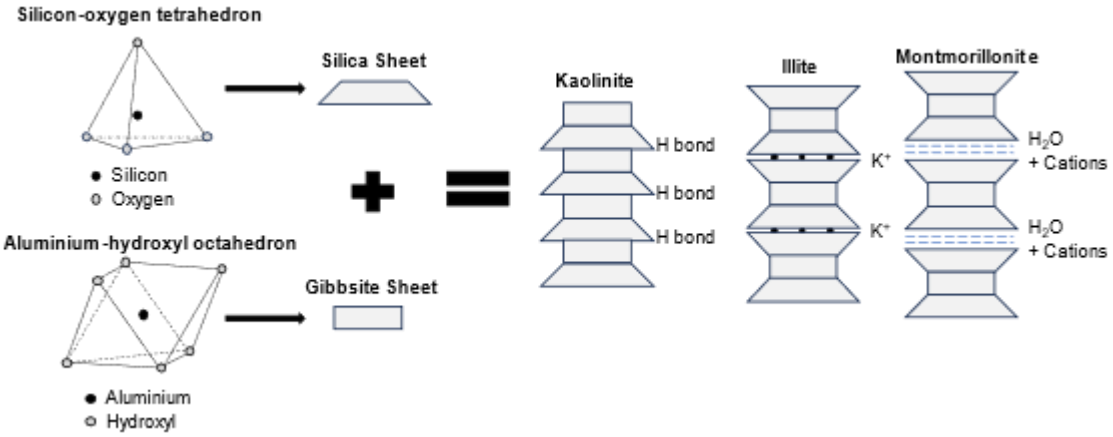

Figure 2.5: The tetrahedral and octahedral structural units which make up silica and gibbsite sheets. These sheets are the foundation of all clay minerals. The molecular makeup of kaolinite, illite and montmorillonite is shown (adapted from Bowles, 1979).

The difference in bonding strength between layers determines the shrink-swell potential (Bowles, 1979). Strong hydrogen bonds between 1:1 layers in kaolinite generate larger crystal structures with lower specific surface area, suppressing swelling. Fixed potassium ions between illite sheets limit moisture intrusion and interlayer expansion, yet comparatively display an elevated swell potential. Conversely, weak van der Waals forces bonding layers in montmorillonite create significant void space with greater expansibility, providing smaller crystals with a higher specific surface for accommodating water absorption.

Specific surface area is the ratio of surface area to volume and is inversely proportional to crystal size. Table 2.2 (Bowles, 1979) compares the crystal sizes of Figure 2.3's minerals, demonstrating that montmorillonite is substantially smaller than illite and kaolinite. With a greater surface area, it takes more water absorption to saturate the soil structure towards its liquid limit, making it more electrochemically active. Activity is inherently linked to the soil plasticity index (PI). as follows:

$$A = \frac{PI}{clay\ fraction} \qquad \textbf{2.1}$$

The $'clay\ fraction'$ refers to the percentage of fine particles that pass the 2 μm sieve, which is the BGS classification for clay-sized particles. Therefore, high-plasticity clay soils often have a more substantial percentage of montmorillonite group minerals.

Table 2.2: Comparison of the specific surface (m^2/g), activity, and cation exchange capacity (meg/100g) of kaolinite, illite and montmorillonite. From Bowles, 1979.

	Kaolinite	Illite	Montmorillonite
Specific Surface (m^2/g)	800	80	15
Activity	0.4 – 0.5	0.5 – 1.0	1.0 – 7.0
Cation Exchange Capacity (meq/100g)	3 – 15	10 – 40	80 – 150

Activity is also a function of the cation exchange capacity of the clay mineral, which is inherently greater for montmorillonite due to its more substantial negative charge, as shown in Table 2.2. This negative charge arises from isomorphic substitution within the mineral structure, where cations in the crystal lattice are replaced by others of similar size but different valence, leading to a net charge imbalance (Holtz & Kovacs, 1981). An increased net negative charge on clay minerals promotes a stronger attraction of water molecules via hydrogen bonding, facilitating additional hydrated cations' attraction. This enhancement leads to greater water bonding at the mineral surface. Furthermore, elevated water content intensifies the electrostatic attraction between dipolar water molecules, further contributing to the hydration dynamics.

Within the UK, more transport embankments are composed of clay than coarser materials. Table 2.3 quantifies this division, with 50% of the road and rail network comprising clays and mudrocks (Spink, 2020). The geographical distribution of clay is concentrated in the younger geologies of southeast England (Jones et al., 2020). These clays are yet to lithify and, therefore, exhibit high plasticity and susceptibilities to the cyclic wetting and drying that drive shrinkage and swelling of the soil structure. Crucially, this concentration of plastic clay soils coincides with the densest concentration of transport infrastructure. Consequently, a disproportionate volume of literature investigates these regions' behaviour and engineering challenges associated with clay fills. However, this means there is an excellent availability of research on attempts to characterise the critical stability issues related to clay fills. On UK infrastructure embankments, shrink-swell is driven by moisture changes from 1) seasonal changes in rainfall and vegetation growth, 2) water demand of trees, 3) deterioration of near-surface soil structure, and 4) large fluctuations in seasonal pore water (Basma et al., 1996; Jones et al., 2020; Mair, 2021).

Table 2.3: Percentage of Network Rail and National Highways' embankments in each broad geological category.

Embankment Geology	% of Network Rail	% of Highways England
Clays & mudrocks	50	54
Sands & gravels	21	15
Rock Fill	29	31

2.5 Environmental Influences of Embankment Behaviour

Embankments extend above the natural ground surface, constituting a component of the unsaturated zone, which exhibits a greater sensitivity to seasonal variations in environmental conditions. These external factors induce cyclic changes in pore-water pressure, which significantly dictate spatial and temporal variations in the water content, shear strength, stability, and deformation characteristics of clay soil (Glendinning et al., 2014). Evaporation reduces soil water content, generating negative pore-water pressures, referred to as suction (Tarantino & Di Donna, 2019).

Suction is crucial in generating apparent cohesion within clay soils through compressive capillary forces. These forces enhance interparticle contact, which increases effective stress and shear strength. The evaporation intensity influences the suction produced and is inversely related to pore diameter (Fredlund et al., 2012; Tarantino & Di Donna, 2019). Consequently, clay soils generate greater suction during drying, significantly enhancing their shear strength in an unsaturated state. However, water infiltration from rainfall or other sources increases water content, which reduces suction and effective stress. This process diminishes the apparent cohesion as water intrusion weakens the capillary forces between soil particles. As a result, the soil's shear strength can decrease significantly, potentially causing slope instability or structural issues in embankments (Ridley et al., 2004; Glendinning et al., 2014).

Cyclic wetting and drying introduce considerable variability in pore-water pressure and shear strength, which is particularly detrimental to the microstructure of clay soils (Zhao et al., 2021). When the soil is wetted, it swells, diminishing suction and the attractive forces among the particles, leading to deflocculation. In contrast, drying decreases pore-water pressure due to evaporation, resulting in shrinkage that pulls the deflocculated particles closer together. However, this often results in incomplete and inconsistent alignment of particles, creating a disorganised and poorly bonded soil structure. More significant fluctuations between these states further drive fatigue of soil microstructure. As these processes accumulate, the microstructure deteriorates,

leading to disaggregated soil with weakened interparticle forces, making it less stable and more prone to failure. Thus, understanding the management of moisture levels in clay soils is crucial for maintaining their structural integrity and preventing rapid deterioration.

2.5.1 Theoretical Models for Bare and Vegetated Soil Evaporation

Understanding the moisture exchange mechanisms at the soil-atmosphere interface is fundamental for assessing environmental impacts on infrastructure embankment behaviour. Moisture exchange is closely linked to processes such as evaporation and transpiration, both of which are critical in regulating soil moisture. Evaporation refers to the transition of water from liquid to vapour at the soil surface, influenced primarily by solar radiation, vapour pressure gradients and aerodynamic factors (Penman, 1948; Monteith, 1965; Allen et al, 1996). Its rate is affected not just by meteorological conditions, but also by the soil's ability to transmit moisture to an asset's evaporative surface. In contrast, transpiration involves water movement through plants and its release via stomata, driven by plant physiology and atmospheric demand (Penman, 1948; Monteith, 1965; Allen et al, 1996). Transpiration rate is primarily influenced by the vapour pressure deficit, energy availability, soil moisture and crop characteristics.

Evaporation and transpiration are integral processes in the soil-atmosphere moisture flux, occurring simultaneously in vegetated soils and often collectively termed evapotranspiration (Allen et al, 1996). By dictating changes in soil water content and pore-water pressure, evapotranspiration underpins the drying-wetting cycles driving microstructural degradation in high-plasticity clay embankments. Therefore, a clear understanding of the contributions and controlling factors of each process is essential for interpreting hydrological behaviour in climate-sensitive geotechnical assets.

Two theoretical models have been foundational in quantifying and conceptualising soil water loss: the Penman equation (Penman, 1948) and its extension, the Penman–Monteith equation (Monteith, 1965). Penman (1948) proposed a new framework for the theoretical estimation of evaporation using meteorological data, which integrates two previously established approaches – the energy balance and aerodynamic methods – into a unified model. The energy balance quantifies the surface energy, mainly net radiation and some sensible heat, available to drive vaporisation by meeting latent heat demands. The aerodynamic component governs vapour removal, driven by the vapour pressure deficit and the aerodynamic conductance or resistance (i.e. turbulence level) of wind, ensuring continued evaporation. By integrating these two

processes, Penman's (1948) formulation captures both the supply of energy and the atmospheric demand, enabling evaporation to be estimated from routine meteorological variables. Equation 2.2 is what was originally proposed by Penman (1948) to calculate the evaporation rate (E) where Δ is the slope of the saturation vapour pressure curve at air temperature, γ is the psychrometric constant, R_n is the net radiation at the crop surface, G is the soil heat flux, u is the wind speed at two metres height, e_s is the saturation vapour pressure and e_a is the actual vapour pressure.

$$E = \frac{\Delta}{\Delta + \gamma}(R_n - G) + \frac{\gamma}{\Delta + \gamma} 6.43(1 + 0.536u)(e_s - e_a)$$

2.2

A recognised limitation of the Penman (1948) equation is the absence of a surface-resistance component, which is crucial for effectively modelling the regulation of transpiration via stomatal conductance and canopy resistance. These elements are vital for the precise calculation of actual evapotranspiration in vegetated soils, as they account for the physiological responses of vegetation to environmental factors such as soil moisture stress, vapour pressure deficit, and temperature (Monteith, 1965; Allen et al, 1996). Therefore, Monteith (1965) proposed an extension to Equation 2.1, referred to as the Penman-Monteith equation (Equation 2.3). This equation calculates evapotranspiration (ET), with the mean air density at constant pressure (ρ_a), the specific heat of the air (c_p), the bulk surface (r_a) and aerodynamic (r_s) resistance parameters added to address this limitation.

$$ET = \frac{\Delta(R_n - G) + \rho_a c_p \dfrac{(e_s - e_a)}{r_a}}{\Delta + \gamma(1 + \dfrac{r_s}{r_a})}$$

2.3

Bulk surface resistance represents the resistance to vapour flow through stomata, leaf surfaces and soil, while aerodynamic resistance accounts for the resistance to vapour transport above the canopy, influenced by air movement and surface roughness.

The Penman-Monteith equation (Monteith, 1965) thereby offers a robust conceptual framework for analysing the influence of environmental variables on moisture flux dynamics within infrastructure embankments. A substantial body of existing literature adopts an approach whereby the parameters of this equation are systematically varied

to assess their impact on key processes contributing to embankment deterioration, such as cyclic dry-wet cycles, shrink-swell and desiccation cracking (e.g., see Estabragh et al, 2015; Tang et al, 2018; Xu et al, 2021; Zeng et al, 2022). These parameters – particularly surface resistance, aerodynamic resistance, and net radiation – can be modulated by altering the physical and environmental boundary conditions (e.g., vegetation cover, atmospheric demand, soil moisture availability). Therefore, this framework serves as a critical starting point for identifying which factors are most influential under field-representative scenarios. This will enable a more predictive understanding of how coupled hydro-meteorological drivers govern the degradation and resilience of infrastructure embankments.

2.5.2 Soil Water Retention Behaviour under Wetting and Drying

While the water absorption capacity of clay is influenced by its mineralogical and molecular processes, the movement and storage of water depend on its soil water retention behaviour. This describes the relationship between suction and volumetric water content and is represented using a Soil Water Retention Curve (SWRC), illustrated in Figure 2.6 (Fredlund & Xing, 1994).

The SWRC comprises a drying and wetting curve, which represent the movement of water in and out of the soil, respectively. A hysteresis is present between the curves due to air entrapment during re-wetting. Each curve's shape reflects the pore size distribution, with key features annotated in Figure 2.6, which include:

1. Air-entry value (AEV): a function of pore size, demonstrates the suction that air enters the pore space and instigates drainage under evaporation. Finer pore sizes in clay delay air entry, generating and maintaining high suctions over a greater moisture content range.
2. The slope of the drying (desorption) curve indicates the rate of change in volumetric water content with suction, i.e., the storage capacity. Steep gradients represent a uniform and coarse pore size distribution, while gradual slopes indicate well-graded soils with higher water retention capacity.
3. The slope of the wetting (adsorption) curve indicates the rate at which suction is lost and moisture is gained under infiltration – steeper curves represent a higher hydraulic conductivity under an interconnected network of coarse pores.

Therefore, SWRC serves as a crucial representation of a clay's microstructure, encompassing the fabric arrangement and size of soil particles and their associated

pores. Consequently, any deterioration of the soil microstructural arrangement under cyclic wetting and drying will be reflected by changes in the AEV and gradient of the SWRC (Stirling et al., 2021). Analysing these dynamic changes is critical to understanding the environmental responses of embankments and their long-term performance.

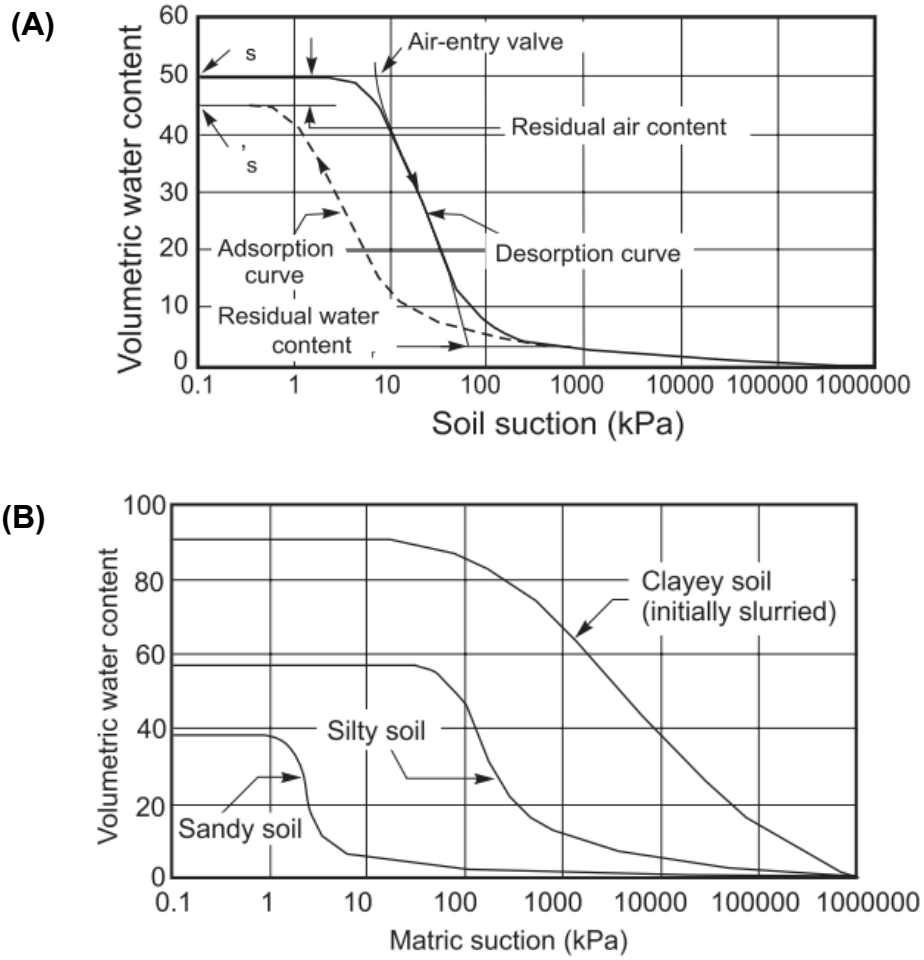

Figure 2.6: (A) Example of drying and wetting portions of the SWRC with air entry (AE) point highlighted and (B) comparison of SWRCs for sandy, silty and clayey soil from Fredlund et al (1994).

2.5.3 Micro-scale Deformation

The repeated cycles of drying and wetting, caused by changes in weather conditions, have been shown to seriously undermine the microstructural integrity of embankments independently, without factoring in other destabilising factors like mechanical loading (Stirling et al., 2021). The methodological approaches within the existing literature on the effects of drying and wetting cycles on clay microstructure exhibit considerable variability. Preliminary investigations often embrace more simplistic methodologies, which, while elucidating fundamental mechanisms of structural changes, lack

application to the context of field embankments. This involves exposing small-scale slurry specimens to cyclic wetting and drying, which demonstrates the progression of desiccation crack formation as a qualitative indicator of soil deterioration (Tang et al., 2010; Tang et al., 2011; Wang et al., 2018; Zeng et al., 2020). Stabilisation of these macro-scale features after three cycles of drying and wetting is commonly reported (Wang et al., 2017; Bordoloi et al., 2020). The main limitation of these studies is the use of slurry specimens, which behave very differently from compacted clay fills used in infrastructure embankments.

Advancing beyond these fundamental studies, a subset of research incorporates key embankment characteristics, notably how microstructural degradation manifests within compacted soils. Such research elucidated the essential differences in behaviour between slurry, loosely compacted and densely compacted specimens under exposure to dry-wet cycling. Most embankments are compacted wet of optimum to reduce porosity, permeability, shrink-swell and therefore, improve long-term strength and stability. However, compaction water content at the onset of drying was shown to impact volume change potential (Albrecht & Benson, 2001; Cheng et al., 2021). The higher the compaction above the optimum moisture content, the greater the clay's shrinkage potential.

Visualising micro-structural degradation at the field scale is notably absent in the literature, as it is difficult to assess the micro and macro contributions to moisture dynamics in situ. However, various laboratory techniques have been utilised to investigate microstructural changes to a wet-of-optimum compacted clay under dry-wet cycling. Scanning Electron Microscopy (SEM) has been used to visualise progressive deterioration (Basma et al., 1996; Louati et al., 2021; Stirling et al., 2021; Zhao et al., 2021), with examples in Figure 2.7A (Stirling et al., 2021) and 2.7B (Zhao et al., 2021) qualitatively evidencing the progressive formation of an interconnected network of microcracks. Louati et al. (2021) specifically demonstrated a condensing effect in loosely compacted clays, contrasting with the disaggregation observed in densely compacted clays. This underscores the significance of the compaction state in assessing the impact of dry-wet cycles on embankment fill. Furthermore, it emphasises the limitations of slurry specimens in accurately representing field-scale behaviours. The notable limitation of SEM is disruption during sampling. However, Stirling et al. (2021) conducted dry-wet cycles in situ, illustrating how this could be overcome.

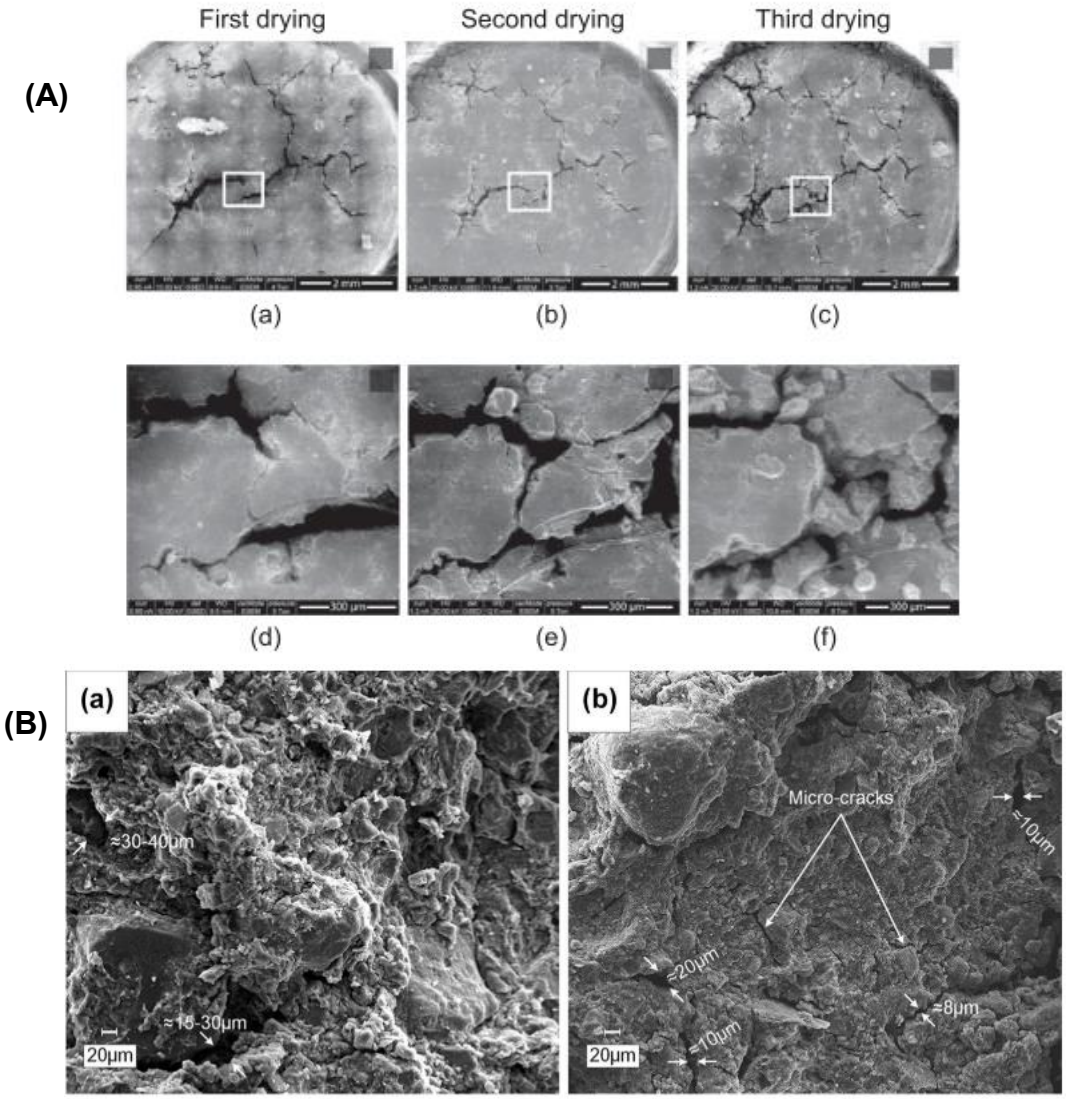

Figure 2.7: (A) Scanning Electron Microscopy (SEM) image showing microstructural degradation due to wet – dry cycles (d – e) with their locations shown by white squares in (a – c) and the larger crack network forming from Stirling et al. (2021), (B) SEM image of (a) original specimen and (b) after 10 dry-wet cycles with microcrack formation shown, from Zhao et al. (2021).

Other informative methods include Mercury Intrusion Porosimetry (MIP), which gave a more detailed analysis that suggested a redistribution of pore-sizes rather than an increase in void ratio during dry-wet cycling (Nowamooz & Masrouri, 2010; Ma et al., 2020; Zhao et al., 2021). These studies elucidate the elimination of macro-porosity formed during compaction due to the disaggregation of clay particles and the accompanying reorganisation of mesopores into smaller dimensions. An example of MIP results is shown in Figure 2.8 (Zhao et al., 2021). The graph compares the initial pore-size distribution (untreated) with that after 10 dry-wet cycles were applied. The formation of a more uniform pore structure, with an enhanced microporosity portion (higher peak) and loss of larger macro-porosity, is evident (Zhao et al., 2021). The right shift of the peak indicates an overall larger diameter of the micropores. This

microstructural rearrangement depends on suction, requiring larger capillary forces to cause deformation in smaller pores, highlighting the potential effects of extreme drying conditions (Nowamooz & Masrouri, 2010).

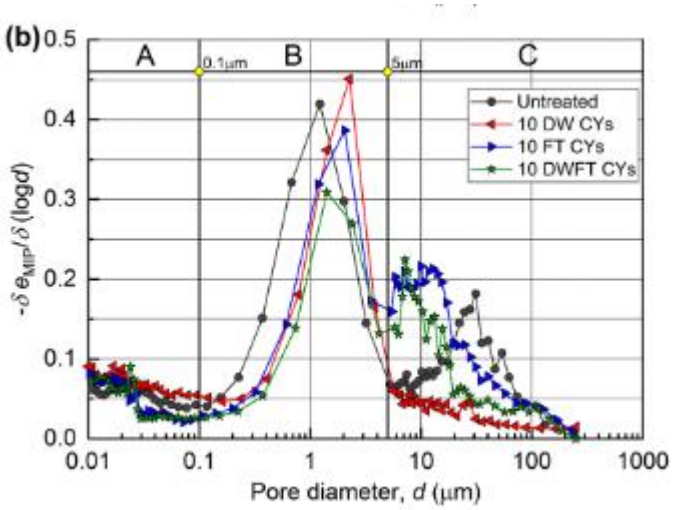

Figure 2.8: Pore size distribution (PSD) curves of specimens untreated (initial) and after 10 dry-wet cycles (10 DW CYs) from Zhao et al. (2021).

In contrast, Pires et al. (2008) recorded a substantial increase in the diameter of pores larger than 500 μm (macro-porosity). This was accompanied by a change in the height of clay samples, suggesting an overall increased pore volume or shrinkage fatigue (Xu et al., 2021). This study utilised resin and image analysis to assess macrometric and micrometric changes in soil structure. The results are shown in Figure 2.9, with an evidential increase in pore areas and connectivity. However, these two-dimensional methods may under- or overestimate pore sizes, contingent on how cross-sectional profiles intersect the resin sample. Micro- and macro-porosity are three-dimensional features that are better assessed using methods that capture their volume and connectivity.

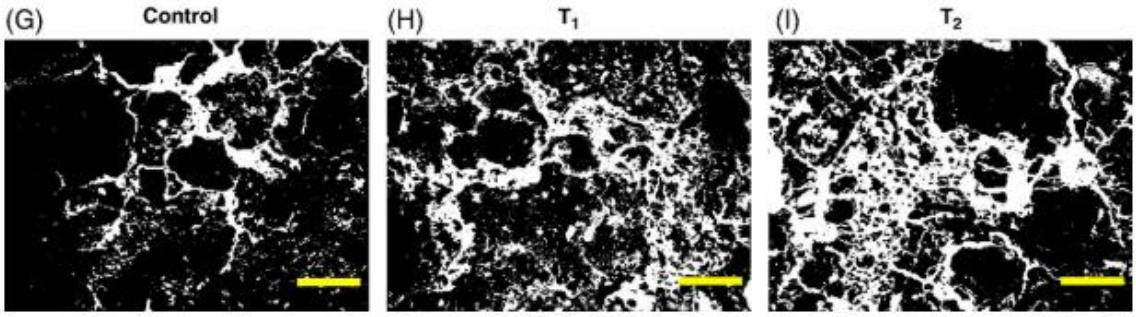

Figure 2.9: Binary image (pores white, soil black) showing structural variation after two dry-wet cycles (T1 and T2) (Scale 1000 μm) from Pires et al. 2008.

Accumulated fatigue in clay's ability to shrink and swell is noted, attributed to irrecoverable microstructural degradation (Basma et al., 1996; Chen & Ng, 2013; Estabragh et al., 2015; Stirling et al., 2021). Such behaviour significantly impacts the clay's ability to regain cohesion and generate high suction during subsequent dry-wet cycles, ultimately degrading soil strength. The stabilisation of microstructural degradation within compacted soils is typically reported after 7 to 10 dry-wet cycles (Nowamooz & Masrouri, 2010; Louati et al., 2021; Zhao et al., 2021a). This phenomenon contrasts sharply with the 3 cycles (Tang, Cui, et al., 2011; Wang et al., 2017; Tang et al., 2021) documented for assessing deterioration at the macro-scale level, such as the evolution of surface visible desiccation cracks. This distinction underscores the notion that microstructural deterioration may persist beyond observations of macro-crack stabilisation. Conversely, these clay soils were cycled under the same magnitude of wetting and drying, not incorporating the role of faster rates or higher magnitudes of drying and subsequent rewetting on structural degradation. Such behaviour is likely to become more significant under future climate change projections and, therefore, fundamental to understand. Consequently, this emphasises the significance of evaluating degradation at the microstructural level under varied environmental conditions to obtain a comprehensive understanding of clay fill integrity.

It is important to note that these studies frequently employed unrealistic environmental boundary conditions, concentrating primarily on extreme scenarios of drying and wetting. Samples are often fully saturated during wetting via techniques such as humidity control (Ma et al., 2020; Stirling et al., 2021), full submergence (Basma et al., 1996; Nowamooz & Masrouri, 2010), capillary rise (Pires et al., 2008; Trabelsi et al., 2018), permeameters (Louati et al., 2021), pressure application (Chen & Ng, 2013), and drip irrigation (Stirling et al., 2021; Zhao et al., 2021b). Similarly, elevated room temperatures or oven drying extremes (Basma et al., 1996; Tang et al., 2010; Wang et al., 2018) are often used for drying events, disregarding other vital variables such as solar radiation and wind and their interactions. Basma et al. (1996) demonstrated how microstructural degradation evolved differently under full desaturation cycles versus partial drying. Such behaviour was attributed to varied microstructural re-arrangement, with partial drying generating a turbulent flocculated system with reduced water absorption and swelling capacity. This process had major implications on re-wetting paths, instigating swell fatigue with a reduced ability to heal microcracks. Such studies'

recognised limitations make it difficult to correlate their findings to field-scale embankment processes, where environmental conditions and their impact on an embankment vary spatially and temporally. Therefore, improved characterisation of microstructural degradation under realistic environmental boundary conditions is required.

2.5.4 Changes in Soil Water Retention Behaviour

The control of microstructure on soil water retention behaviour is paramount, as a particle and pore space arrangement directly influence how water is held and transmitted within the clay matrix (Fredlund & Xing, 1994; Fredlund et al., 2012; Tarantino & Di Donna, 2019). Changes in microstructure can alter porosity, void ratios, and the connectivity of pores, which in turn affect the soil's ability to retain water. Researchers have sought to incorporate quantitative measures into the observations of microstructural degradation discussed in the previous section. This approach aims to enhance understanding of the overall impacts of dry-wet cycles on soil hydrological processes. Specifically, changes in permeability, hydraulic conductivity, and soil water retention behaviour have been widely investigated at both laboratory and field scale.

Many laboratory studies have shown that with repetitive exposure to cyclic drying and wetting, a measured increase in hydraulic conductivity occurs, visible after 1-2 cycles (McBrayer et al., 1997; Albrecht & Benson, 2001; Muddle & Briggs, 2019; Louati et al., 2021). The magnitude of this increase was correlated to the compaction state, plasticity and shrink-swell potential of the soil being analysed (Albrecht & Benson, 2001; Louati et al., 2021). Albrecht and Benson (2001) illustrated hydraulic conductivity increases of 5 to 500 times the original value depending on the soil type. This has been associated with both a disaggregation of the compacted structure and an increasing influence of flow through micro-cracks (Albrecht & Benson, 2001; Louati et al., 2021). Features such as greater pore uniformity (McBrayer et al., 1997) and macropore length (Muddle & Briggs, 2019) have been shown to have a more significant impact on infiltration capacity.

When saturated, a permanent change in hydraulic conductivity was also observed, attributed to microstructural degradation and the lasting alteration of permeability in the zones of micro- and macro-cracks (McBrayer et al., 1997; Albrecht & Benson, 2001). Cheng et al. (2021) recorded an increase in infiltration capacity with a heightened number of dry-wet cycles, visualised in Figure 2.10. This was accompanied by an increase in the magnitude and equilibrium time of the steady state infiltration rate,

related to the greater porosity and storage capacity introduced by microstructural degradation.

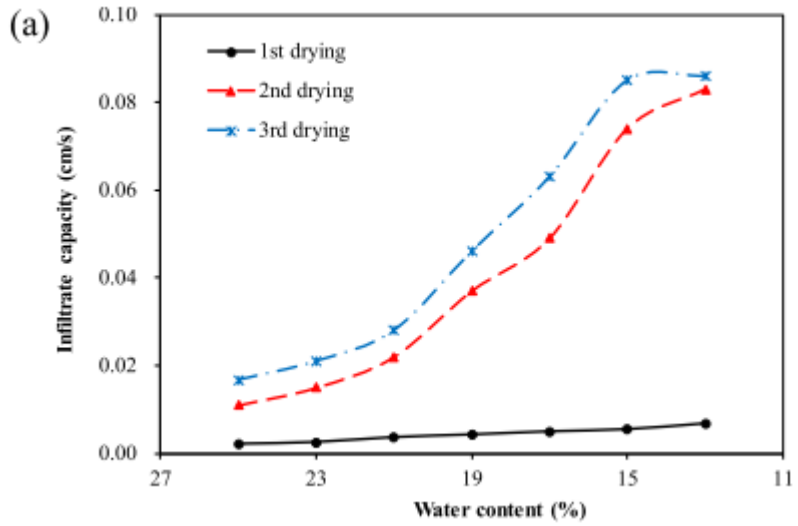

Figure 2.10: Changes in infiltration capacity across dry-wet cycles with varying initial moisture content from Cheng et al. (2021).

These fundamental changes in permeability and hydraulic conductivity illustrate how microstructural degradation can influence water movement through the soil profile. Enhanced permeability has critical implications for rapid fluctuations in pore-water pressure, which are a fundamental driver of greater deterioration. However, laboratory investigations on hydrological processes are limited in their scope, with much greater variability present in field-scale assets due to macro-cracking, animal burrowing, and vegetation roots. Muddle and Briggs (2019) conducted triaxial cell constant head permeability tests on samples taken within the core of an embankment. The results demonstrated no clear relationship between macropore distribution and hydraulic conductivity with depth. These results stress the highly heterogeneous nature of field-scale assets that cannot be accurately replicated within small-scale laboratory investigations. Further efforts have been made to test in-situ permeabilities of a field-scale test embankment using double-ring infiltrometers (Dixon et al., 2019) and Guelph permeameters (Glendinning et al., 2014; Dixon et al., 2019). Both analysis (Glendinning et al., 2014; Dixon et al., 2019) demonstrated a significant variation in permeability in the near-surface zone (upper 1 m) of the embankment, which decreased with depth.

Disparities in behaviour between the north and south aspects, as well as across poorly and well-compacted panels, of the BIONICS embankment were observed (Glendinning et al., 2014). This was attributed to greater solar and wind exposure on the south slope,

driving larger fluctuations in pore water pressure. This enhanced variability in shrink-swell and macro-scale desiccation, particularly in poorly compacted panels, due to their more transient state of permeability. However, these differences were masked under future testing (Dixon et al., 2019). This highlights the important role of prolonged environmental exposure, with disparities decreasing as the sheltered or well-compacted slope sections reach a more advanced stage of deterioration. These in-situ measurements do not incorporate the role of micro- and macro-desiccation cracking, with tests deliberately situated within intact soil peds. Additional permeability from desiccation cracking has been shown to have a significant impact on near-surface fluctuations in moisture and pore-water pressure (Stirling et al., 2021; Yu et al., 2021). Consequently, failure to consider such features may grossly underestimate the permeability of an infrastructure embankment.

Approaches have been taken to visualise how these changes in microstructural behaviour, as well as quantifiable changes in hydraulic conductivity, can be captured by the deterioration of clay soils' water retention behaviour. This has been illustrated in both the laboratory (Liu et al., 2020; Stirling et al., 2021)and field (Glendinning et al., 2014; Stirling et al., 2021) which unanimously show key shifts in the soil-water retention behaviour with time and environmental exposure. Within the same embankment, Glendinning et al. (2014) illustrated soil water retention deterioration occurring within two years post-construction, with Stirling et al. (2021) evidencing its continuation across the following 5 years of monitoring. This was measured using in-situ suction and volumetric water content sensors to form SWRCs presented in Figure 2.11A (Stirling et al., 2021). Key observable features are: 1) a shift in the AEV to lower suctions, 2) reduced ability to generate high suction at full saturation and for a given stage of drying, 3) changes occurring in the upper (Figure 2.11A(a/b) and lower (Figure 2.11B(c/d) regions, 4) greater deterioration in the upper slope.

Within the SWRCs of Figure 2.11A and better highlighted in Figure 2.11B from Glendinning et al. (2014), is the biphasic trajectory of desaturation, which becomes more enhanced with increased microstructural degradation. Such trends in the SWRC indicate an increasing influence of macro-porosity, such as desiccation cracks, on the water retention behaviour on the clay fill at low suctions. The importance of incorporating an evolving, dual-porosity model of water retention behaviour in future stability assessments of embankments is becoming increasingly stressed within the literature (Louati et al., 2021). This underscores the substantial impact of both micro-

and macro-desiccation on soil hydrology, which must not be overlooked. It necessitates comprehensive field-scale assessments that accurately evaluate the effects of non-static factors on water movement within embankments. This includes volume and microstructure, as well as crack intensity and connectivity. Such investigations are crucial for enhancing our understanding of hydrological processes in these assets.

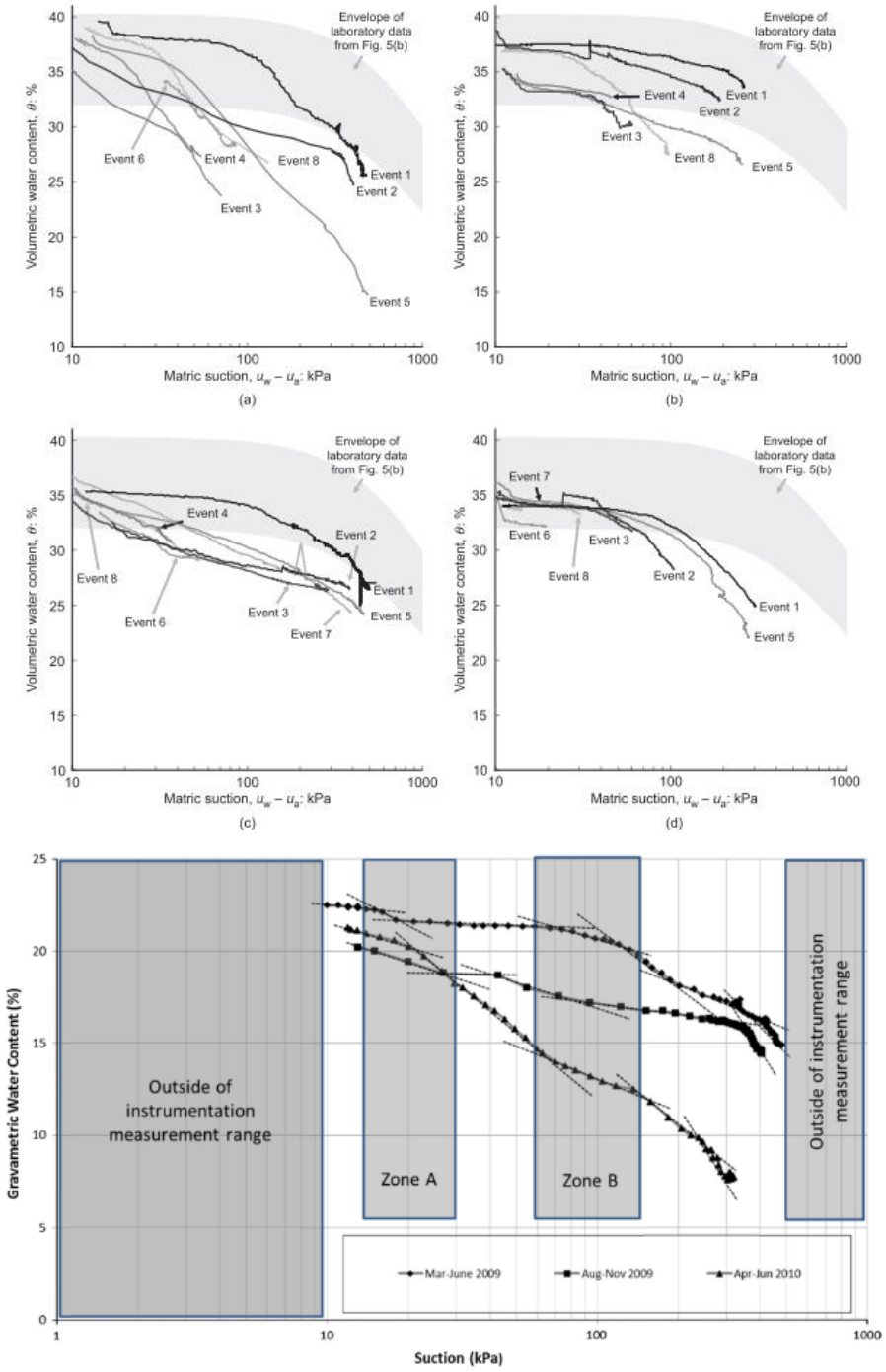

Figure 2.11: (A) SWRCs for the BIONICS field embankment between 2009 and 2015 (a) upper slope 0.5m (b) upper slope 1.0 m (d) lower slope 0.5 m and (e) lower slope 1.0 m from Stirling et al., (2021), (B) SWRCs for the same embankment for 2009 – 2010 showing biphasic desaturation from Glendinning et al., (2014).

2.5.5 Loss of Strength and Macro-scale Deformations

Shifts in the particle arrangement and water retention behaviour of clay fill will have critical implications for effective stress and an embankment's mechanical strength. Increasing micro- and macro-porosity will change the rate and magnitude of moisture content change, influencing the cyclic fluctuations in pore water pressures that ultimately control soil strength. Stirling et al. (2021) measured both changes in shear and tensile strength over dry-wet cycling, the former being significant for asset-scale ability to resist failure while the latter is significant for resilience to desiccation crack formation.

Figure 2.12A demonstrates the 60-80% reduction in shear strength that occurred over the first three dry-wet cycles before stabilising. Tensile strength (Figure 2.12B) also exhibited a decrease after one dry-wet cycle. Similar results have been found by other researchers using comparable methods (Khan et al., 2017; Charkley et al., 2019; Xu et al., 2021; Zhao et al., 2021). Due to its lower water retention capacity, clay will exhibit a greater tendency to undergo shrinkage and swelling. As soil tensile strength decreases, it creates less opposing stress, making it easier for desiccation cracks to form. These cracks can lead to a quicker loss of suction when water infiltrates the soil. A recognised limitation of these experiments is the absence of macro-crack features within the tested samples. Cracks are weakened zones of poor cohesion which disturb fill integrity and would implicate embankment resilience to external loading. Khan et al. (2017) conducted a slope stability analysis that incorporated the degradation of shear strength due to dry-wet cycle exposure. The results indicated a clear shift of failure planes into the shallow subsurface of embankments, where weather-driven deterioration is most active.

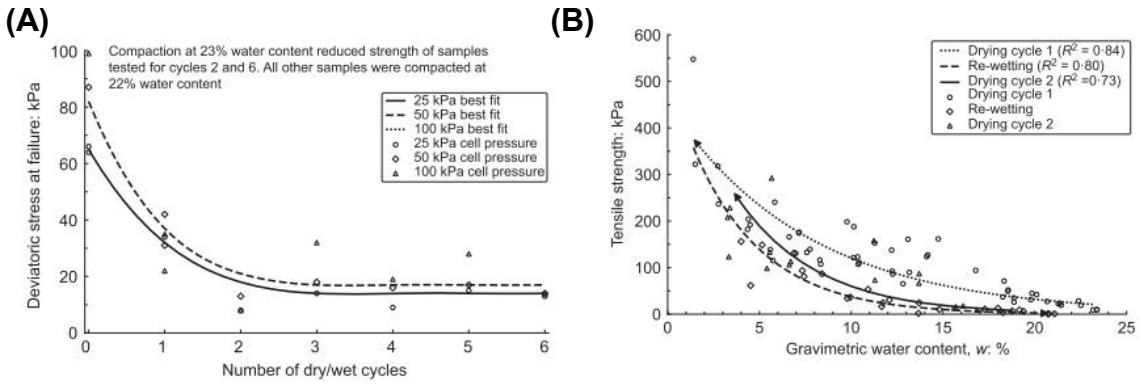

Figure 2.12: Change in (A) shear strength and (B) tensile strength across dry-wet cycles from Stirling et al. (2021).

Stirling et al. (2021) developed a conceptual model for weather-driven deterioration that integrates findings on microstructural changes, soil water retention, and mechanical strength deterioration. The model is shown in Figure 2.13 and demonstrates how these material-scale factors accumulate to contribute to macro-scale deformation at the asset scale.

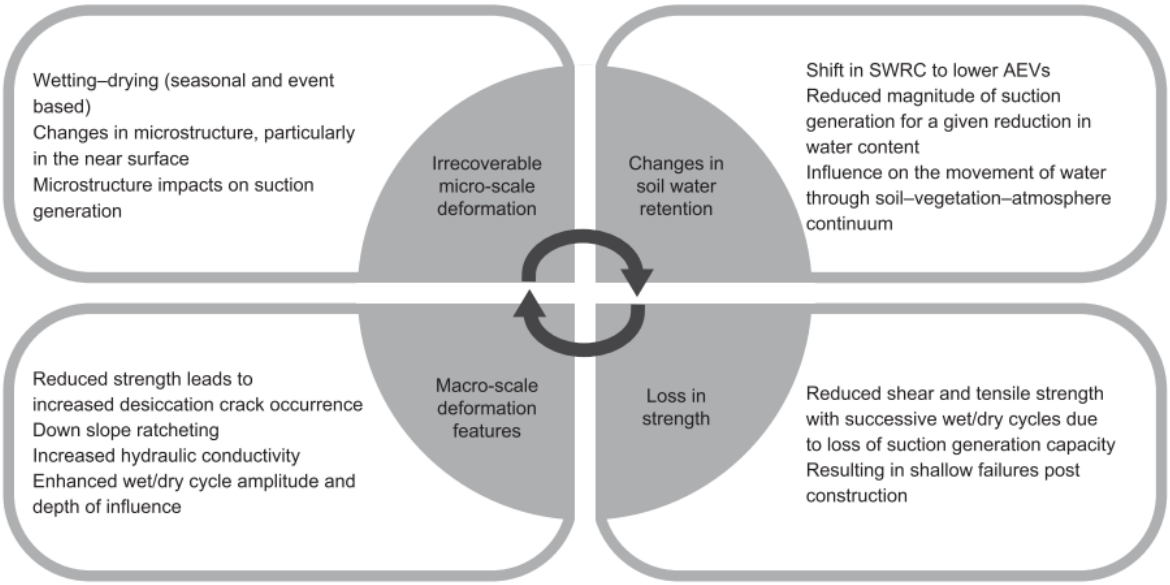

Figure 2.13: Conceptual model for weather-driven deterioration of clay fill proposed by Stirling et al. (2021).

Fundamentally, these macro-scale deformation features are rooted in the formation and associated implications of macro-desiccation. This includes an increase in mass permeability and the extension of the active weathered zone into the embankment core over time (Stirling et al., 2013, 2018; Glendinning et al., 2014; Briggs et al., 2023). As a result, the depth of influence of cyclic wetting and drying, along with weather-driven deterioration, can significantly impact the stability of embankments. By organising these elements within a comprehensive framework, the model underscores their interrelatedness and collective influence on the stability and performance of embankments. Essentially, it describes weather-driven deterioration as a continuous, self-perpetuating cycle that occurs independently of external loading factors (Stirling et al., 2021; Briggs et al., 2023). These environmental changes can jeopardise structural integrity, making monitoring and managing these influences crucial to upholding the long-term resilience of embankment systems. Given its pivotal role, desiccation cracking will be the primary focus of this study herein, addressing the mechanisms by which it amplifies weather-driven deterioration.

2.5.6 Changes in Behaviour under Climate Change Projections

According to the Met Office UKCP18 climate change projections, hotter and drier summer conditions are anticipated (Met Office, 2022). Additionally, there is an expectation of increased frequency and intensity of hot spells and heavy rainfall events. Theoretically, the interplay of these conditions is likely to intensify soil shrinkage and desiccation, thereby elevating the embankment's susceptibility to rapid infiltration and suction loss during summer convective storms (Dijkstra & Dixon, 2010; Loveridge et al., 2010; Baninajarian et al., 2019; Robert Mair, 2021; Sun et al., 2024). Dijkstra & Dixon (2010) conceptually illustrated the impact of more frequent extreme events on an asset's future vulnerability to failure using Figure 2.14.

If there is sufficient time between recovery events, (Figure 2.14A), system vulnerability will remain static. However, insufficient recovery between events (Figure 2.14B) will drive an asset toward failure at a considerably elevated rate. These conceptual models inadequately account for the system's increasing failure vulnerability from pore water pressure fluctuations occurring across extreme weather events, irrespective of the intervening recovery duration. However, this model introduces the importance of shorter-duration environmental cycles, which have been insufficiently examined in existing literature. These cycles provide a more accurate representation of daily natural weather patterns, the significance of which may increase as seasonality becomes obscured under the predicted highly variable weather.

Winters are expected to be warmer and wetter under prolonged rainfall, likely leading to more significant fluctuations in seasonal pore water pressure regimes, which can exacerbate weather-driven microstructural degradation (Loveridge et al., 2010; Ridley, 2012; Huang et al., 2024). Lord Robert Mair's technical review of Network Rail's earthwork management procedures emphasised that enhancing water management within their assets was integral to their future resilience. Particular attention must be given to the implications of desiccation cracking on the hydrological dynamics associated with transport earthworks constructed from high-plasticity clay. The report evidenced the need for more substantial empirical evidence that quantifies desiccation's potential impact on water retention, permeability, and overall stability of earthworks under climate change projections (Mair, 2021).

Addressing these effects of climate change on asset stability is becoming an essential focus of academic literature (Davies et al., 2008; Kilsby et al., 2009; Loveridge et al., 2010; Toll et al., 2012; Tang et al., 2018; Kandalai et al., 2023; Ighil, 2023; Huang et

al., 2024) and is being integrated into the asset management strategies of Network Rail (Power et al., 2016; Spink, 2020; Mair, 2021; ORR, 2021) and National Highways (National Highways, 2022). The existing literature has taken varied approaches to addressing the uncertainties surrounding future asset performance under climate change, broadly divided into monitoring, retrospective analysis, and prospective modelling (Huang et al., 2024).

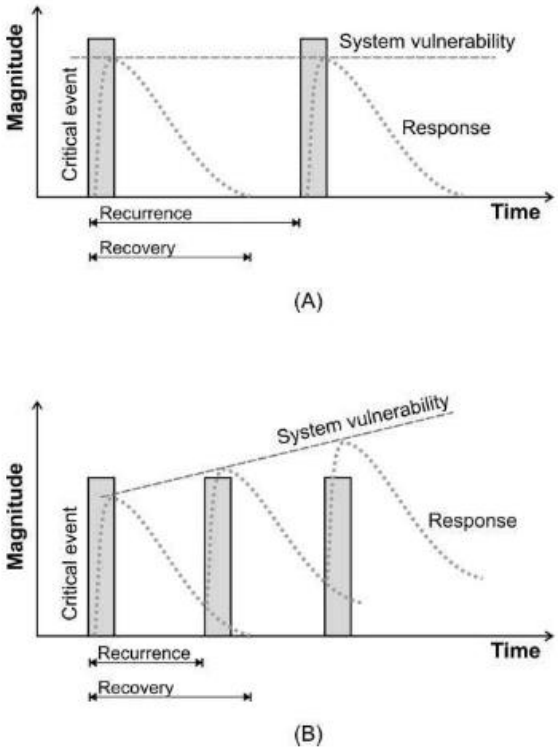

Figure 2.14: Projected vulnerability of infrastructure assets to extreme weather events when (A) recovery time exceeds event recurrence and (B) recovery time is interrupted by an event occurrence. From Dijkstra & Dixon, (2010).

Monitoring Approaches

Geotechnical monitoring approaches have included real-time or periodic condition assessments to identify changes in an embankment's physical, structural, or hydrological behaviour (Hughes et al., 2016; Smethurst et al., 2017; White et al., 2024). Instrumentation that measures pore water pressure, displacement and strain accumulations is employed within individual assets to capture site-specific responses to antecedent and extreme weather. However, these are commonly only employed on problematic assets, with the associated costs of system-wide geotechnical monitoring systems being implausible (Network Rail, 2018). The challenges associated with the vast scale and intrinsic variability of assets significantly impede the standardisation of monitoring methodologies. This lack of uniformity subsequently limits the

generalisability of findings, ultimately hindering their capacity to inform the behaviours of other assets.

System-wide condition monitoring approaches increasingly rely on non-intrusive geophysical and remote sensing technology. This includes fibre optic sensing, satellite imagery, and LiDAR, which can detect surface movements, deformations, and strain accumulations (Hughes et al, 2016; Smethurst et al., 2017; White et al, 2024). However, the scope of such techniques is still developing, and their resolution is currently restricted by the cost and time available for data processing (Hughes et al., 2016). Furthermore, whether these techniques provide a high enough subsurface resolution to capture spatial and temporal changes in material-scale deterioration is questioned. To maximise the utility of monitoring, it is essential to integrate the data with either retrospective or prospective methodologies. This approach facilitates a comprehensive analysis of the implications for embankment stability, ensuring a thorough understanding of the results.

Retrospective Analysis

Retrospective approaches primarily involve diagnostic analysis of earthwork failures to identify the causes, identify correlations with climate and use this information to predict future performance (Huang et al., 2024). Emerging evidence collated from retrospective approaches suggests that the impacts of climate change are already affecting the stability of infrastructure earthworks. For example, from 2019 to 2024, Network Rail has recorded an increase in high-consequence earthwork failures inherently linked to more frequent extreme weather events, particularly drought followed by high-intensity rainfall (Network Rail, 2018; Mair, 2021; ORR, 2024). However, such correlations can only be conducted after failure events, relying on historical datasets where high-resolution climate data is often unattainable and frequently fails to capture the complex progression of deterioration.

In contrast, Loveridge et al. (2010) stated that understanding future climate impacts on earthwork stability requires first investigating current climate and embankment interactions. Using historical data, they demonstrated that the minutes of delay and incidents on the rail network correlated most strongly with the shrink-swell-associated geohazards. The results are shown in Figure 2.15, with shrink-swell geohazard categories A to E indicating increasing hazard, while Z indicates no hazard. Plastic clays characterised by high shrink-swell potential (D) represent the most significant

contributors to incidents and delays in construction projects. Nevertheless, it is crucial to acknowledge a substantial and non-linear impact from lower-risk categories as well. This observation underscores that inherent material vulnerability alone cannot account for all instances of failure. Moreover, the escalating threats posed by extreme weather events may further heighten the risk of failure even within these lower-risk categories.

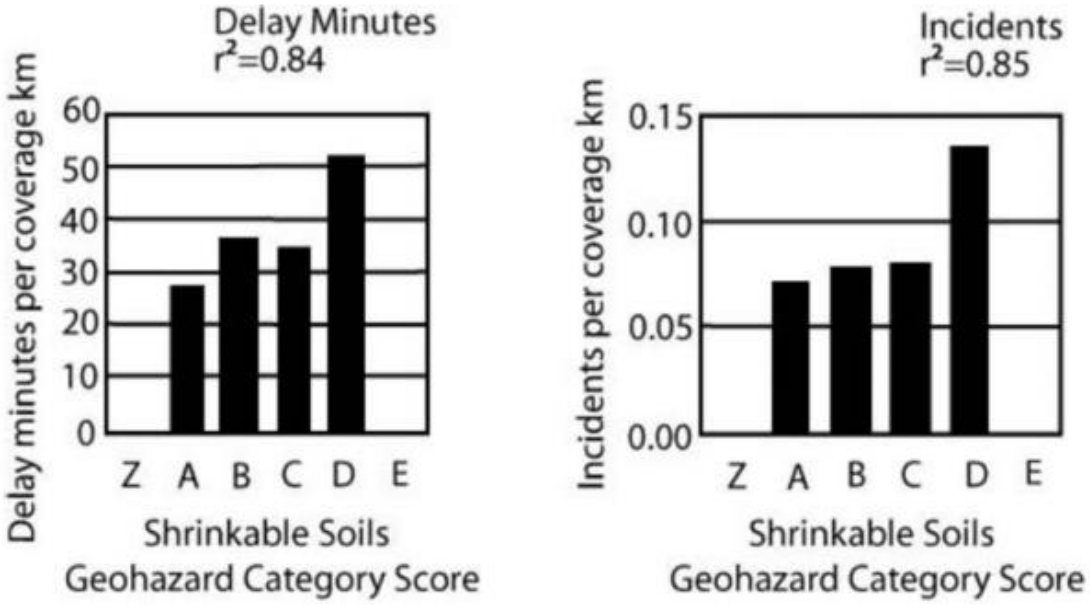

Figure 2.15: Delay minutes and incidents incurred by each shrinkable soils geohazard category (increasing hazard A – E, no hazard Z). From Loveridge et al., (2010).

Field studies by Ighil (2023) relied on observations of soil desiccation under present-day drought conditions to help inform climate change risks. The study demonstrated a 2 m extension of the desiccation zone under severe summer drying with respect to average conditions. However, retrospective approaches fundamentally assume the modes, mechanisms and drivers of failure are static under a shifting climate. Such assumptions are problematic and may lead to a considerable underestimation of climate change's impacts, with the mechanisms and modes of failure likely to evolve as weather patterns change over time (Dijkstra & Dixon, 2010; Huang et al., 2024).

Prospective Modelling

Experimental-based prospective methodologies may encompass both controlled laboratory and field-based studies that subject soil to various weather conditions, incorporating an applied climate change uplift. Ng et al. (2024) and Zhong et al. (2024) utilised laboratory-based centrifuge modelling to analyse the thermo-hydro-mechanical response of an embankment to heating-cooling and extreme drought-rainfall cycles on stability. Thermal cycles induced irrecoverable net settlement in the crest and upper

slope regions that exceeded allowable serviceability limits within 10 years of exposure. With extreme drought-rainfall cycles, desiccation cracking proved fundamental in dictating the rate and mode of failure. Figure 2.16 (Ng et al., 2024) shows surface displacement by shallow-slip failure originating from a large desiccation crack, which facilitated rapid preferential flow and loss of strength.

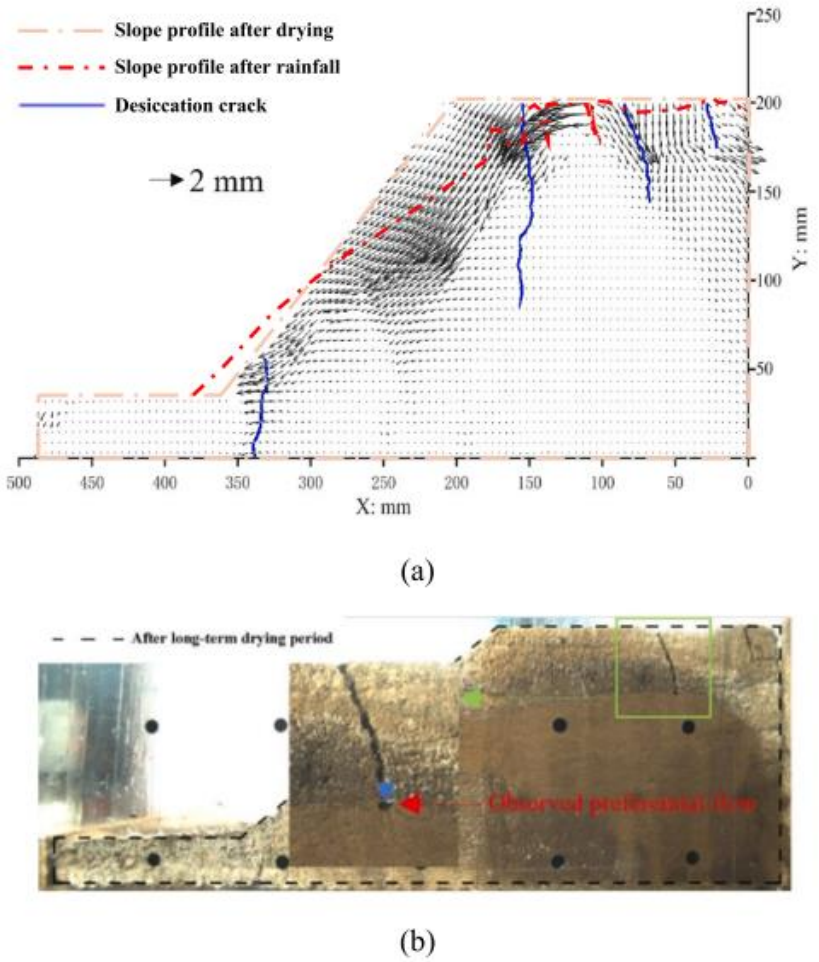

Figure 2.16: (a) displacement vectors on a cracked slope during high-intensity rainfall events showing shallow slip occurrence, (b) evidence of preferential flow through large cracks. From Ng et al. (2024).

Applying climate extremes to live infrastructure embankments is not feasible due to the risk of damaging these assets. However, the field-scale BIONICS test embankment provided an opportunity to observe behaviour under simulated extreme weather events by installing a climate control system (Toll et al., 2012). The results indicated substantial increases in positive pore water pressures to depth, generating substantial swelling and heave within the embankment. The rainfall was applied during a wetter-than-average summer, and therefore, the full extent of its effect on a dry slope could not be analysed. Except for small-scale laboratory studies that illustrate the role of high

temperatures in soil deterioration through desiccation (Vallejo, 2009; Tang et al., 2010; Liu et al., 2020), few studies are available that apply extreme wetting or drying events at a specimen scale comparable to real-field embankments.

Most prospective approaches involve predicting changes in pore water pressure, material strength and deformation using numerical simulations which integrate the UKCP18 climate scenario projections. Huang et al. (2024) utilised a one-dimensional finite element seepage model to analyse climate-induced changes in pore-water pressure for the 1981 – 2000, 2021 – 2040 and 2061 – 2080 projection periods. The model considered vegetation, compaction (road versus rail embankment) and desiccation effects, incorporating a high permeability surface layer to represent a microstructurally degraded zone. From this, a conceptual model was constructed, shown in Figure 2.17. Fundamentally, the persistent summer drying regimes will provide a greater infiltration capacity for wetter winters. This will delay the onset of critical positive porewater pressures in winter yet increase the magnitude of dry-wet cycles by up to 42%. The resultant effect is enhanced microstructural and strength degradation, increasing the likelihood of failure.

These results agreed with the soil water balance model produced by Clarke & Smethurst (2010), which utilised synthetic climate data. Further insights included the extension of the summer drying cycle, leading to a severe soil-moisture deficit and desiccated state. This study also stressed the importance of regional variations in climate change projections, which will generate local variations in the hazard and threats to embankment stability. Numerical approaches which do not include the impacts of summer desiccation cracks suggest an improvement in asset performance due to overall higher evapotranspiration (Manning et al., 2008; Rouainia et al., 2009). This stresses the importance of considering transient permeability through desiccation cracking and microstructural degradation. Furthermore, bypass flow through cracks may affect vegetation health, decreasing evapotranspiration and increasing embankment vulnerability to shallow erosional and washout failures during intense summer rainfall events (Clarke & Smethurst, 2010).

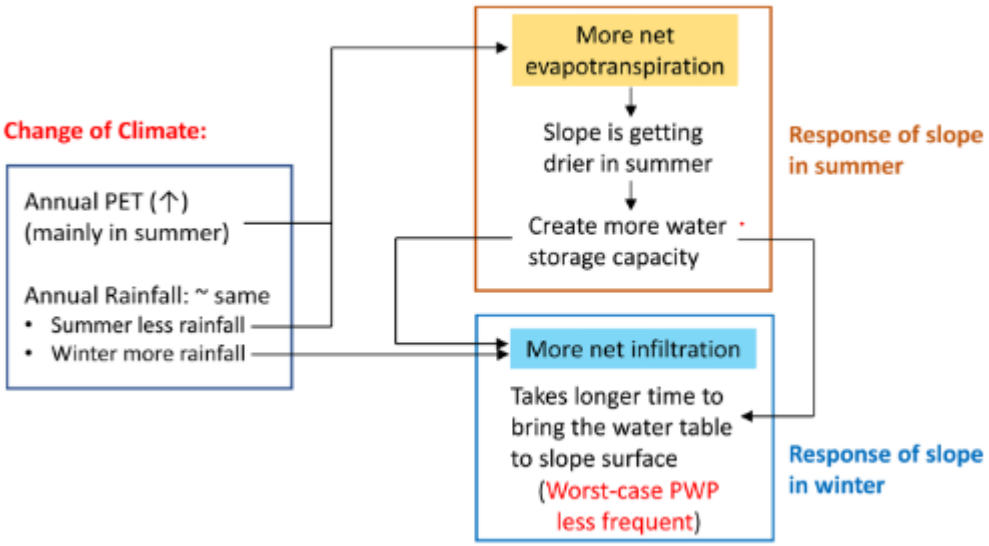

Figure 2.17: Conceptual model for the impact of climate change on embankment stability from Huang et al. (2024).

These simulations are powerful tools for predicting embankment performance under shifting climate conditions and are evolving to incorporate more detailed two-dimensional seepage analysis methods (e.g., see Booth, 2014; Baninajarian et al., 2019; Rouainia et al., 2020). However, their computational expense currently limits their capabilities, often compromising by focusing solely on limited climate scenarios, a singular asset type and geology, specific critical weather events or one aspect of embankment behaviour, e.g. hydrological or deformation changes only (Huang et al., 2024). Furthermore, the reliability and accuracy of these models fundamentally depend on the availability of high-quality field monitoring and material characterisation data. For example, accurate asset-level predictions require high-resolution climate data. Whilst the spatial resolution of climate models is improving, they still display significantly localised variability, which is difficult to account for in numerical models (Slingo et al., 2021).

Numerical models that simplify their inputs or focus solely on hydrological processes without integrating stability analysis fail to capture the full complexity of embankment behaviour. Moreover, their reliability becomes increasingly questionable if these models do not account for the temporal variability in material properties. This includes changes due to microstructural degradation, which is projected to accelerate under climate change (Tang et al., 2018). There is a need for models that incorporate coupled thermo-hydro-mechanical processes and the progressive weakening of geomaterials under repeated exposure to extreme weather conditions. To achieve this holistic

approach, employing a multifaceted methodology that integrates real-time monitoring, retrospective analyses, and prospective modelling is required (Dijkstra & Dixon, 2010; Tang et al., 2018; Mair, 2021). This triadic framework will facilitate predictions based on empirical quantification of the temporal and spatial dynamics associated with the degradation processes inherent to clay embankments.

As emphasised in this review, desiccation cracking is critical in amplifying the severity of extreme weather impacts through its formation and the additional vulnerabilities it introduces by exacerbating infiltration. The interaction between these cracks and hydrological processes must be fully integrated into assessments of future earthwork performance. Long-term studies subjecting desiccated soils to prolonged antecedent conditions and extreme weather events are essential to improve predictive models. This is particularly urgent as the current literature lacks empirical field data on the combined effects of desiccation and extreme climatic variability.

2.6 Fundamentals of Crack Formation

Multiple theories focusing on different material contexts have been proposed to explain the formation of desiccation cracks during drying-induced shrinkage in soils. Table 2.4 presents an overview of these theories (Shin & Santamarina, 2011). At their core, they revolve around the dynamics of the air-water interface and the resultant changes in the stress state this creates within the soil. As the soil dries, the movement and behaviour of this interface significantly influence the development of tensile stresses, leading to crack propagation and, ultimately, desiccation cracking.

The irregular drying front theory is based on the spatial variability in evaporation due to heterogenous soil properties, which leads to non-uniform shrinkage and crack initiation (Zarzycki et al., 1982). This method includes a realistic assumption that natural soils are not homogeneous mediums. Scherer (1990) proposed the circumferential tension theory, which suggests that boundary constraints during drying induce circumferential tensile stresses due to radial shrinkage. Cracks form when these circumferential tensile stresses exceed the material's tensile strength.

Table 2.4: Theories of desiccation crack initiation based on the movement of the air-water interface during drying. Adapted from Shin and Santamarina (2011).

Theory	Mechanism	References
Tensile Failure *** Most commonly adopted**	Tensile stress generated during shrinkage exceeds soil tensile strength. 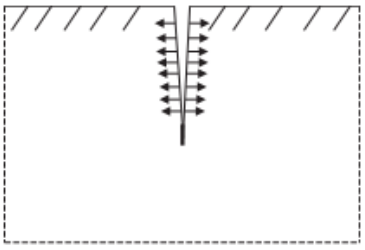	(Morris et al., 1992; Konrad & Ayad, 1997; Hallett & Newson, 2005) Modified concept - (Shin & Santamarina, 2011)
Irregular drying front *** Conceptual without verification**	Difference in capillary pressures and subsequent failure of pore walls. 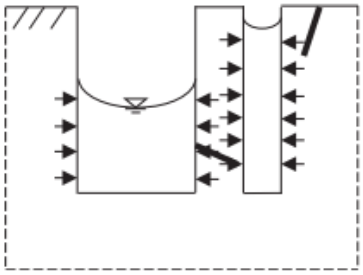	(Zarzycki et al., 1982)
Circumferential tension ***Conceptual without verification**	Growth of radial crack due to hoop tension. 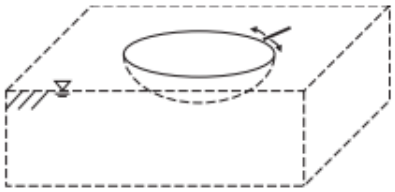	(Scherer, 1990)
Air entry ***Conceptual without verification**	Menisci invasion due to increasing capillary tension 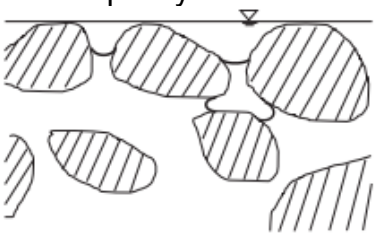	(Brinker & Scherer; 1990; Herrera et al., 2007)
Packing Collapse	Collapse of particle layers by capillary suction. Use to explain desiccation cracks in a drying strip. 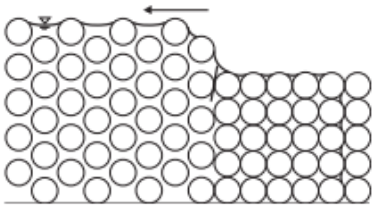	(Holmes et al., 2006)

However, real-life boundary conditions often exert more complex constraints on soil, questioning the validity of a simplistic circular tension field developing. The air-entry theory focuses on the interplay between pore structure, water retention characteristics and air-entry behaviour. Menisci invasion ultimately controls the tensile stress distribution and points of crack initiation (Brinker & Scherer; 1990; Herrera et al., 2007). This theory neglects other forms of tensile stress, mainly shrinkage-induced or the role of heterogeneity. Fundamentally, these three mechanisms have not been verified experimentally and are conceptual only. The packing collapse theory encompasses differential settlement at the microscopic level, driven by uneven drying-induced capillary forces and tensile stress accumulation (Holmes et al., 2006). However, such methods are focused on the behaviour of loosely compacted soils.

The tensile failure mechanism is the most adopted and experimentally verified theory for desiccation cracking within cohesive, fine-grained soils (Morris et al., 1992; Konrad & Ayad, 1997; Hallett & Newson, 2005). Numerous experimental and analytical modelling approaches in the existing literature provide validation. For example, Konrad & Ayad (1997) developed a theoretical model using linear elastic fracture mechanics (LEFM). This model demonstrated how tensile stresses resulting from moisture loss led to cracking when the material's tensile strength exceeds it. The model aligned closely with field observations, predicting stable crack spacing due to stress redistribution and effectively describing the transition from shrinkage to cracking in sensitive clays.

Such correlations of crack initiation with tensile stress accumulation have been demonstrated experimentally. A similar approach using LEFM analysis was conducted by Miller et al. (2015), where predicted crack depths agreed with those modelled. This research also incorporated experimental measures of uniaxial tensile strength using load cells during a desiccation test. Maximum tensile stresses coincided with the soil’s intact condition immediately before desiccation. Sawada et al. (2021) used a similar setup, with the temporal history of tensile stress and a corresponding record of surface desiccation provided in Figure 2.18. The results demonstrate the initiation of cracking 15 minutes after the peak value of tensile stress, quantifying the soil stress state that leads to desiccation. Methods thoroughly considering sequential crack initiation and complex stress distributions arising from significant material heterogeneity are still being developed in the literature.

(A)

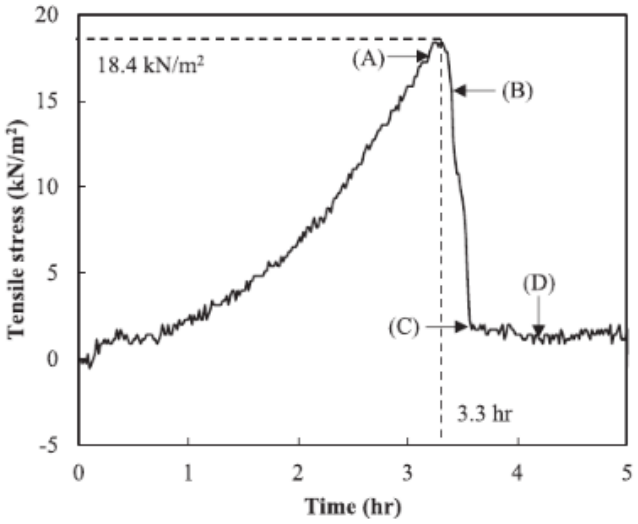

Fig. 12. Time history of tensile stress in cracking process.

(B)

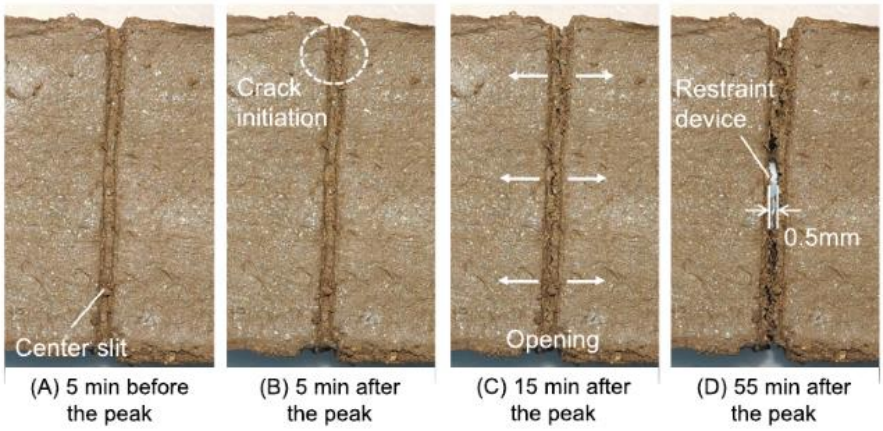

Figure 2.18: (A) Temporal history of tensile stress (kN/m^2) obtained experimentally showing the occurrence of photographs (A) - (D), (B) Temporal history of crack pattern annotated in (A). From Sawada et al. (2021).

2.6.1 Controlling Factors in Crack Initiation

Tang et al. (2011) provided the schematic in Figure 2.19 to illustrate the desiccation crack initiation process within a saturated and homogeneous clay layer under the tensile stress criterion. Upon exposure to drying, the water-air interface reaches the surface of the fully saturated clay layer (a). With continued drying, a water-air meniscus forms between clay particles instigating vertical consolidation (b) due to the formation of capillary suction (c). With continued air intrusion, the menisci's curvature increases, intensifying the capillary suction and effective stress acting between clay particles, generating a tensile pull (d). A crack is initiated (e) when the stress generated by this tensile pull exceeds the overall soil tensile strength.

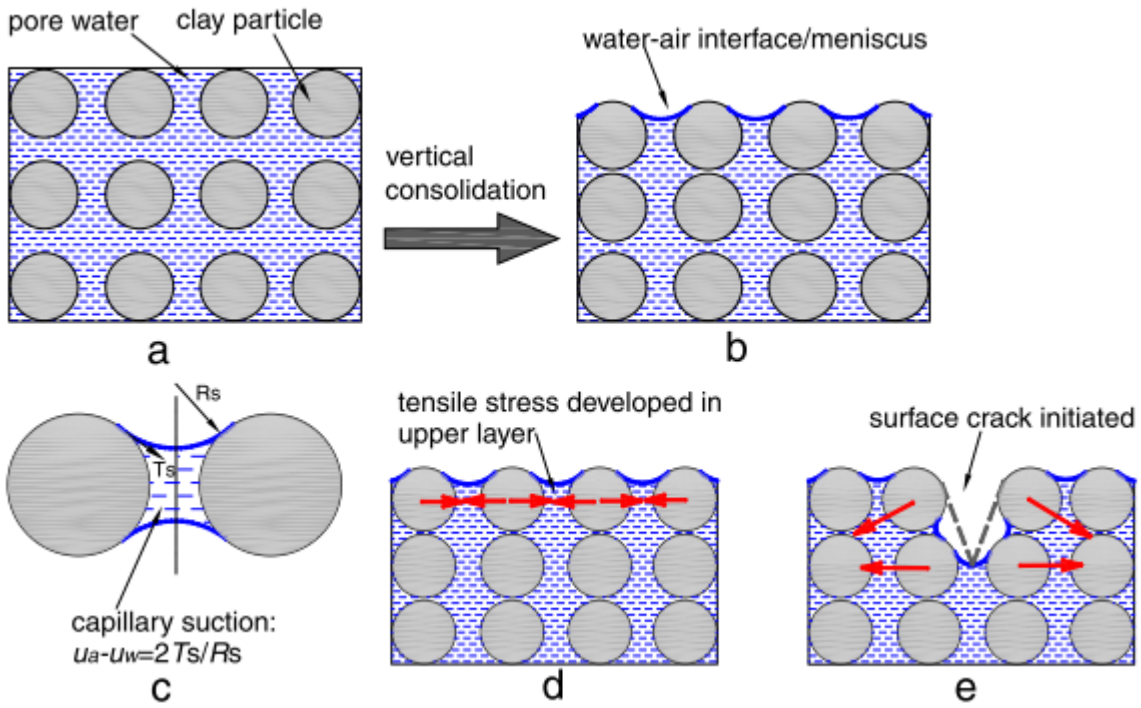

Figure 2.19: Schematic of the crack initiation process under the tensile failure criteria for an initially homogeneous and saturated clay layer: (a) initially fully saturated soil, (b) water-air meniscus develops and vertical consolidation occurs, (c) capillary suction forms, (d) tensile stress develops in the upper layer, and (e) crack initiated. From Tang et al. (2011).

However, crack initiation in heterogeneous clay fill is considerably more complex than the case presented in Figure 2.19. Crack initiation in heterogeneous clays is unpredictable due to the influence of defects and inconsistencies within the material. This is particularly true for older railway embankments, where material heterogeneity has intensified through time due to localised repairs and cyclic environmental deterioration (Perry et al., 2003; Briggs et al., 2017; Stirling et al., 2021). Localised tensile stress at these inconsistencies tends to dominate over the primary stress fields, further complicating the prediction of crack locations (Weinberger, 1999; Wang et al., 2018). The cyclical wetting and drying process induces microstructural degradation, resulting in bimodal water retention behaviour. This phenomenon arises from developing micro- and macro-cracks that alter drainage patterns. Consequently, tensile stress concentrations migrate toward regions with increased porosity due to accelerated drainage in these areas. Costa et al. (2013) demonstrated such an effect using Figure 2.20 for the case of a hoop stress distribution in a circular sample laboratory test. The sample restraint controls the overall tensile stress distribution in the clay sample due to the frictional force it exerts (indicated by the dashed line). However, flaws on the clay's surface can cause local tensile stress to exceed the overall tensile strength, leading to the initiation of cracks. This process is highly

random, depending on the distribution and nature of heterogeneities within the soil (Wang et al., 2017). It is important to note that in real infrastructure embankments, the stress distribution is likely to be significantly more complex than a simple hoop distribution. This complexity arises from various boundary restraints, including inter- and intra-layer contacts, vegetation roots, and interactions with other utilities.

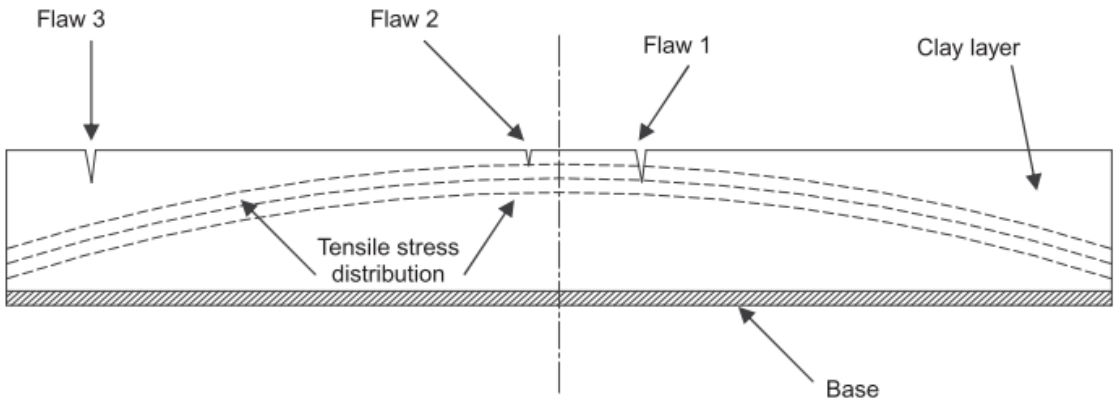

Figure 2.20: Effect of flaws on crack initiation using hoop stress distribution in a circular test. Location of flaws controlled by surface defects, where tensile stress locally exceeds soil tensile strength. From Costa et al. (2013).

The existing literature has reported a range of defects and inconsistencies that control crack initiation. Figure 2.21A illustrates the initiation of a desiccation crack at the base of an air bubble, where desaturation is concentrated due to its higher relative void ratio (Shin & Santamarina, 2011). A similar effect is recorded where pore size is locally coarser. The inverse relationship between capillary forces and pore size in clay soils can explain the phenomenon. Coarser pores exhibit lower capillary suction, which reduces effective stress and water retention capacity (Tarantino & Di Donna, 2019). As a result, coarser pores tend to drain more rapidly than finer pores. This drainage rate disparity between varying pore sizes generates uneven moisture distribution and differential shrinkage, locally amplifying the risk of tensile failure. The differences in water retention behaviour are amplified by the inclusion of contrasting compositions, which can lead to concentrated drying and stress accumulation.

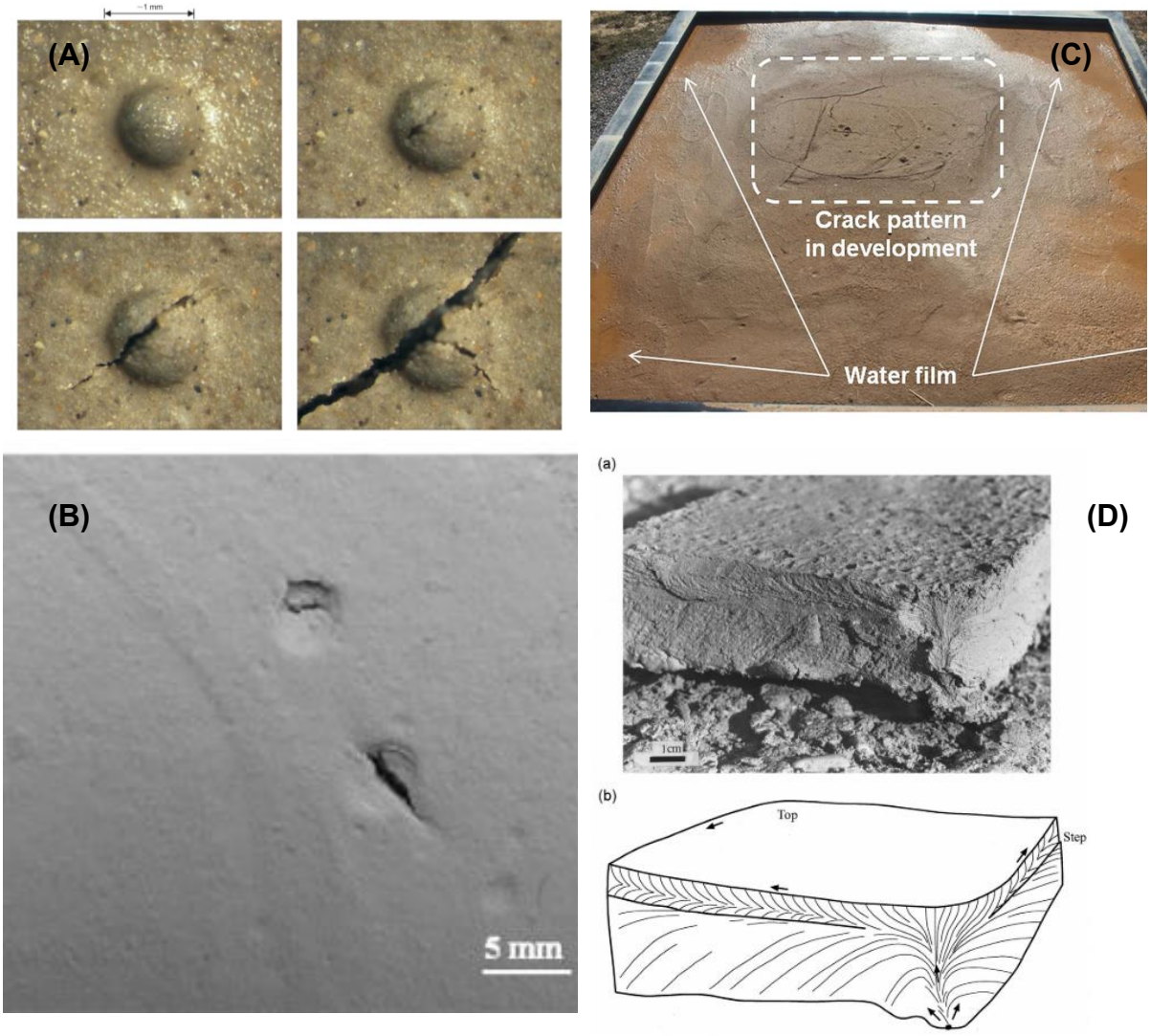

Figure 2.21: Crack initiation at surface defects, including (A) an air bubble (From Shin and Santamarina, 2011), (B) at surface indentations (From Tang et al., 2011), (C) locally more pronounced and desaturated regions (From Cordero et al., 2021), (D) boundaries between layers where the dot marks the initiation site (From Yesiller et al., 2000).

Inconsistencies in the soil matrix between components of varying characteristics are also an essential control of crack initiation. Variations in particle size and compaction density disrupt the continuity and cohesion of the clay matrix, generating weakened zones of tensile strength more readily exceeded by drying-induced tensile stresses. Figure 2.21B illustrates crack initiation at surface indentations, which distort the shrinkage and stress concentration (Tang et al., 2011). Weakened zones of strength at the soil-specimen container interface in laboratory experiments have commonly produced desiccation cracks at these boundaries (Tang et al., 2008; Tang et al., 2011). Similar behaviour has been observed at the field scale, albeit in a different context. Specifically, boundaries between compacted or stratified soil layers of the same material create zones of weaker cohesion in the soil matrix (Yesiller et al., 2000). These

are exploitable by tensile stress to form cracks, as shown in Figure 2.21D, where initiation occurred at the base of a stratified mud layer (Weinberger, 1999, 2001). However, if these boundaries pose frictional resistance, this can also focus tensile stress as the soil opposes homogeneous shrinkage. The subsurface initiation of cracks is commonly discounted in thin and slurry laboratory specimens yet is fundamental to the permeability and stability of infrastructure embankments formed of compacted layers.

Localisation of evaporation due to varying degrees of environmental exposure has been observed to control crack initiation in larger-scale lysimeter experiments (Cordero et al., 2021) and field embankments (Yu et al., 2021). More topographically pronounced regions of the clay's surface exhibited greater exposure to environmental conditions, while localised depressions remain beneath ponded surface water. This results in heterogeneous drying and shrinkage, ultimately becoming the primary sites for crack initiation, as shown in Figure 2.21C (Cordero et al., 2021).

In laboratory investigations of soil desiccation, standard sample preparation protocols often involve segregating finer soil fractions and creating homogeneous slurries to mitigate the influence of heterogeneities (Tang et al., 2021). However, it is essential to recognise that natural soil is inherently heterogeneous, and such preprocessing techniques are not employed when constructing actual transport embankments (Perry et al., 2003). This discrepancy raises significant questions regarding the applicability of laboratory-derived observations of desiccation behaviour to in situ conditions, particularly given the critical role that heterogeneities play in crack initiation.

There is a notable gap in the literature concerning the examination of desiccation crack initiation at the scale of heterogeneities typically observed in infrastructure embankments. This encompasses a variety of factors, including differential moisture distributions, variations in soil composition, pore-size distributions, and diverse environmental exposures. While attempts have been made to isolate these factors in the laboratory, they are an inherently coupled problem, coexisting to dictate embankment desiccation behaviour. Addressing this gap is imperative for enhancing understanding of the desiccation phenomena and its implications for the structural integrity of embankments in real-world applications.

2.6.2 Crack Propagation and Network Stabilisation

Although surface defects control the initiation of desiccation cracks, the subsequent growth and propagation are dictated by the emerging moisture and mechanical stress gradients within the clay soil. Once initiated, open discontinuities cannot support interparticle stress, redistributing and concentrating tensile stress within the intact material ahead of the crack tip. With this redistribution, Shin & Santamarina (2011) anticipated a dilatation ahead of the crack tip as the tensile stress exceeds the soil tensile strength. This dilation increases the void ratio while decreasing the air-entry value and frictional resistance to tensile failure to sustain crack growth. Supporting this is observations of depressions ahead of crack tips during propagation, as the tensile pull condenses and separates particles (Tang et al., 2010; Lakshmikantha et al., 2013; Tollenaar et al., 2017; Zeng et al., 2022). An example is provided in Figure 2.22 from Tang et al. (2010), with the white arrows highlighting depressions which reveal the intended direction of crack propagation.

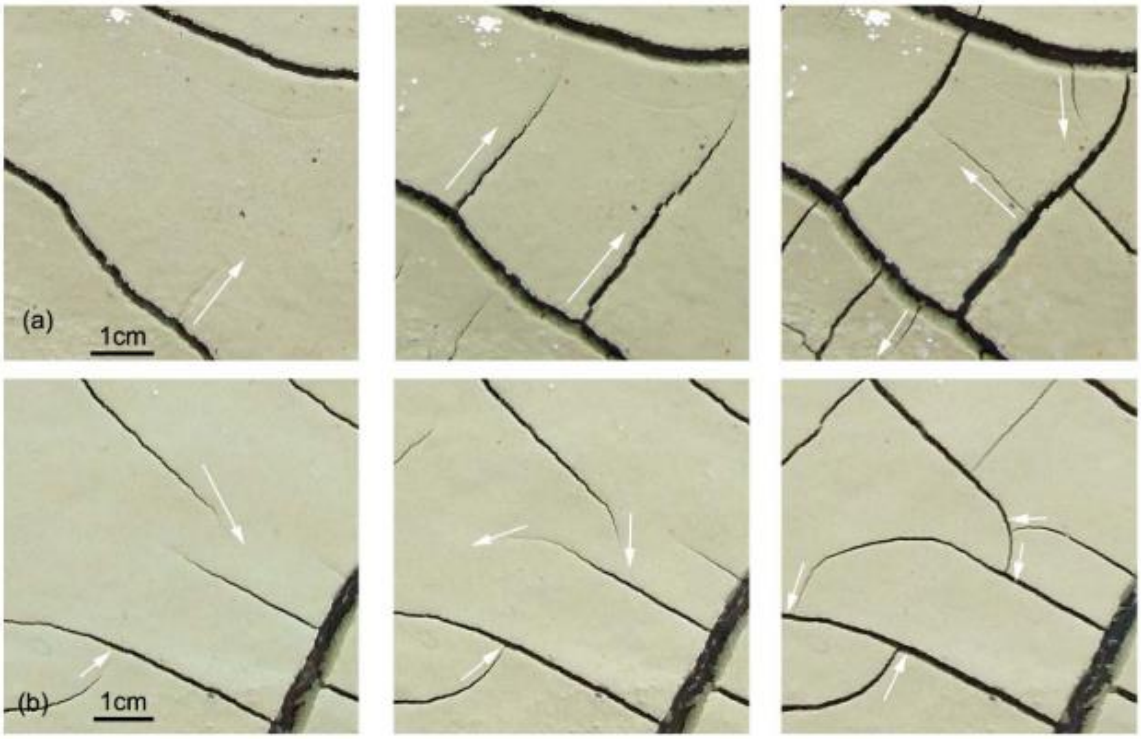

Figure 2.22: Depressions in clay ahead of the propagating crack tip as indicated by white arrows. From Tang et al. (2010).

Other theories for crack propagation are centred on Griffith's Theory (Griffith, 1924), which focuses on the energetics of crack propagation. This theory states that the magnitude of energy released from crack initiation dictates the relative propagation. Larger cracks propagate further than smaller cracks as the energy release rate usually

exceeds the surface energy required to create new crack surfaces. Both tensile and energy-based mechanisms have been validated in the literature, some of which have used the theories in combination (Levatti, 2023). However, this literature review will focus solely on tensile stress mechanics.

Moisture gradients and stress distribution significantly influence the direction of crack propagation during drying by generating areas of lower tensile strength. Crack propagation typically follows the path of least resistance, advancing perpendicular to the direction of maximum tensile stress, thereby minimizing the energy required for crack initiation and growth (Lakshmikantha et al., 2008; Miller et al., 2015; Stirling et al., 2015; Sawada et al., 2021). However, weakened areas caused by material inconsistencies or previous failure planes can also influence the propagation path. This process leads to the formation of primary cracks, often the largest discontinuities to develop under the tensile stress regime (Tang et al., 2011).

Secondary cracks, on the other hand, arise sequentially from the stress redistribution caused by primary cracks. When primary cracks form, they relieve tensile stress perpendicular to its plane, realigning the maximum stress normal to its orientation. Consequently, secondary cracks initiate from or terminate at orthogonal angles to form the characteristic polygonal patterns observed in the laboratory, as shown in Figure 2.22 (Tang et al., 2010), and in unvegetated bare slopes (Li & Zhang, 2011). Digital image correlation (DIC) has been widely utilised to map the development of stress and strain fields during soil drying and desiccation (Wang et al., 2018). Figure 2.23 (Wang et al., 2018) exemplifies typical DIC results, with the strain contours illustrating i) the initial randomly distributed stress field pre-crack formation (Step 6), ii) ordered distribution into a tensile regime ahead of the opening secondary crack (Step 7), iii) compression around the opened cracks as they widen (Step 8). A clear deviation of the crack path is also evident to ensure an orthogonal intersection with the primary crack.

Under differential shrinkage, shear forces can modify the crack opening mode, forcing non-orthogonal intersections between 60 – 180 degrees (Tang et al., 2011; Tollenaar et al. 2017), both of which are observed simultaneously in existing research (Wei et al., 2016). This indicates the evolution of a complex, non-uniform stress field, the prevalence of which would increase with greater soil heterogeneity. This stress field can be influenced by the simultaneous widening of cracks in different orientations, exerting compressive forces in multiple directions. This was measured by Wei et al.

(2016), where the differential compression caused traversal displacement of a crack during growth, as shown by the white strain vectors in Figure 2.23.

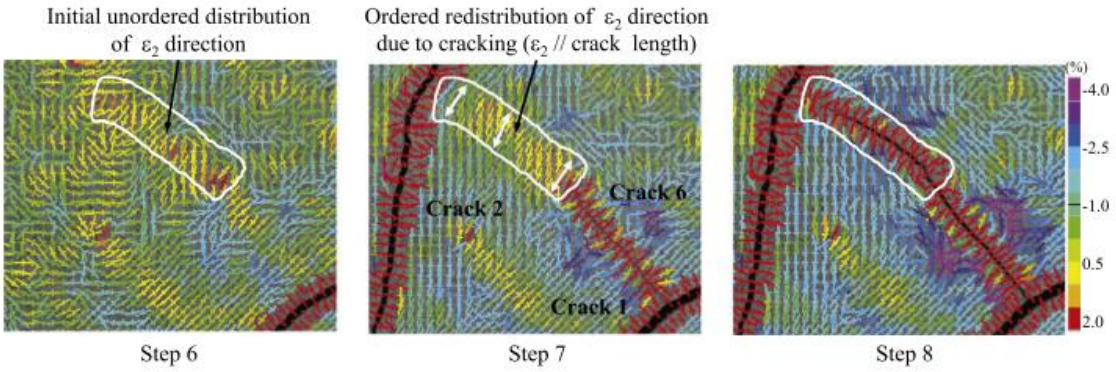

Figure 2.23: Deviation of crack propagation towards an adjacent crack to form an orthogonal intersection based on the organisation of the tensile strain field. Positive values show compression, whilst negative values indicate tensile strain. From Wang et al. (2018).

The subsurface propagation rate and drying fronts' intensity determine how deeply surface desiccation penetrates within a soil profile (Tang et al., 2008; Tang et al., 2010; Costa et al., 2013). The same tensile stress mechanisms govern subsurface propagation. However, it is usually less effective due to the increasing confining stress experienced with depth because of the soil overburden pressure (Sivakumar et al., 2015). In field embankments, crack depth is normally dictated by the depth of a surface-weathered zone, which is more exposed to cyclic environmental loading. Consequently, it exhibits a lower tensile strength and greater permeability, allowing more efficient propagation of drying fronts and crack initiation. Due to the limited scale of laboratory experiments, the depth of cracks is rarely studied. However, it has been recorded that cracks can extend more than 3 meters in infrastructure embankments (Alexsander et al., 2017), playing a crucial role in the slope's hydrological behaviour. Field studies emphasise the significance of desiccation cracks in the processes of evaporation and crack propagation, where open cracks have been shown to accelerate the subsurface extension of drying fronts and desiccation growth. This synergistic relationship between cracking and evaporation warrants further larger-scale investigation, as it cannot be adequately addressed through small-scale laboratory studies that fail to capture the scale and connectivity of desiccation observed in the field.

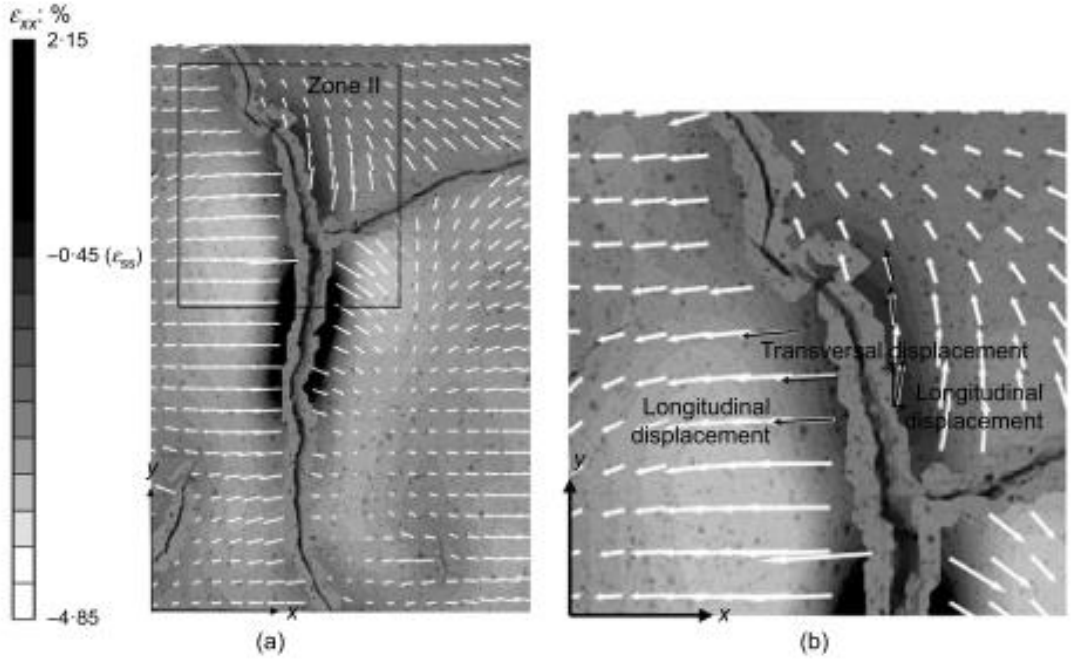

Figure 2.24: Traversal displacement of a crack section due to the differential compression field from simultaneously widening cracks. Positive strain values are compression, and negative values are extension. Arrows show displacement vectors. From Wei et al. (2016).

2.6.3 Physical Factors Controlling Desiccation

Numerous sensitivity analyses have been conducted in the laboratory to isolate specific physical specimen parameters and to examine how the experimental setup influences desiccation processes. The findings from these investigations indicate that the formation and propagation of desiccation cracks are fundamentally linked to the material properties of soil, as well as both internal and external shrinkage constraints (Tollenaar et al., 2017). Thus, it is imperative to interpret these results cautiously and critically assess their applicability to real infrastructure embankments. Below are some of the vital physical controls identified through these studies.

Moisture Content, Composition and Particle Size

The initial moisture content and subsequent mass loss rate impact the desiccation crack formation process (Tollenaar et al., 2017). The amount of water held in a clay soil is subject to both the predominant clay minerals present and its percentage fine fraction (Bowles, 1979; Yesiller et al., 2000; Albrecht & Benson, 2001). Soils rich in smectite minerals exhibit high plasticity and shrink-swell potential, allowing greater moisture absorption between sheet layers. In contrast, low-plasticity clay soils dominated by less active minerals (e.g., kaolinite) exhibit reduced cracking potential due to their limited shrink-swell capacity (Römkens & Prasad, 2006; Jones et al., 2020;

El-Zein et al., 2021). An increased fine content in clay soil significantly enhances its water-holding capacity and elevates its shrink-swell potential. This dynamic contributes to more significant desiccation and amplifies the likelihood of crack formation during the drying process.

The interplay between desiccation cracking and shrinkage is effectively represented through the Soil Shrinkage Characteristic Curve (SSCC), which delineates the relationship between changes in void ratio and moisture content. An example SSCC is illustrated in Figure 2.25 (red line), with the black line representing desiccation crack evolution (SCCC) (Tang et al., 2021). The moisture content at which crack initiation occurs is commonly called 'cracking water content'. Observations suggest that this phenomenon takes place prior to the soil reaching its air-entry value, while the soil remains saturated. The higher the air-entry value, the finer the pore size of the soil and the greater the suction-induced stress that can be generated before a significant loss in moisture content (Fredlund et al., 2012; Tarantino & Di Donna, 2019). Therefore, for fine-grained, plastic clay soils, approximately 80% of the total crack growth can occur during the normal shrinkage phase under high suction (Tang et al., 2011), slowing as shrinkage approaches the residual phase. The transition between the normal and residual shrinkage phases commonly represents the air-entry point, beyond which crack growth slows. Upon reaching the soil's shrinkage limit, cracking stabilises as tensile stresses due to differential shrinkage are relieved. The air-entry value and shrinkage limit are unique to each soil, defining a different shrinkage relationship during drying. Furthermore, an increase in the initial moisture content of the clay at the onset of drying is associated with a shift further right on the SSCC, which signifies a greater shrinkage potential.

The correlation between the cracking process and the overall air-entry value, coupled with the assertion that cracking occurs at saturation, can be substantiated in thin laboratory samples where drying conditions are relatively uniform. However, in thicker soil bodies characterised by more heterogeneous drying patterns, the effects of local desaturation past air-entry may represent a more accurate depiction of the mechanisms governing desiccation cracking.

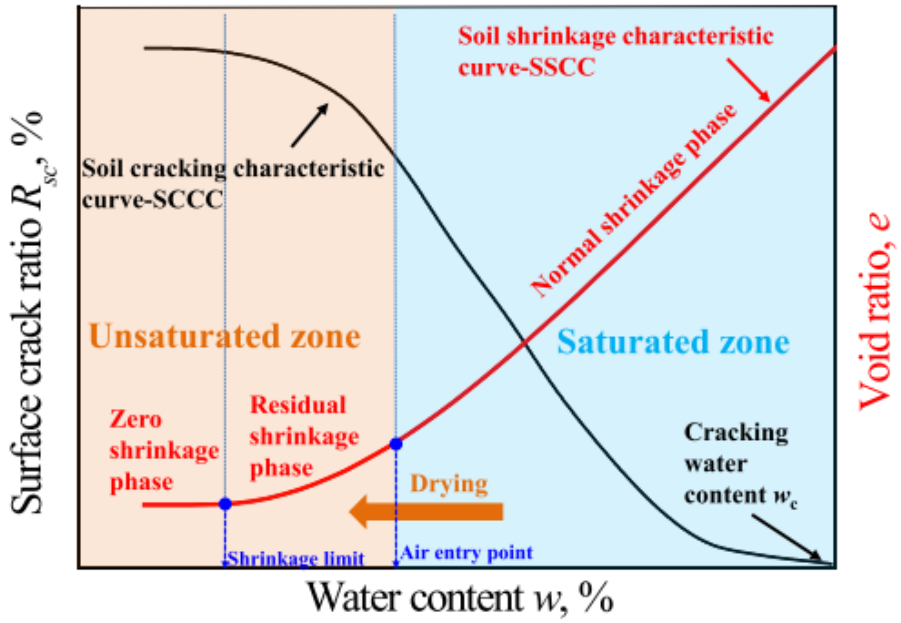

Figure 2.25: Relationship between the soil cracking characteristic curve (SCCC) and the soil shrinkage characteristic curve (SSCC). From Tang et al. (2021).

Specimen Setup and Boundary Effects

There are several aspects of the experimental setup which have been shown to control the resultant desiccation pattern (Costa et al., 2013; Tollenaar et al., 2017; Zeng et al., 2020). Container materials which exert a greater frictional or adhesive force on the soil body can generate higher differential stress at the soil-container interface, increasing the cracking intensity. This is compared to low friction or adhesive materials that allow free and uniform shrinkage, which generates lower tensile stress and crack formation. Although container effects are not present in the field, differential shrinkage along layer boundaries and contacts with other buried infrastructure have shown a similar effect (Weinberger, 1999, 2001).

The dimensions of the specimen in terms of thickness, aspect ratio and surface area have also recorded an impact on desiccation. Tollenaar et al. (2017) observed an increase in surface desiccation in samples with a greater surface area. This was attributed to the greater frictional force with the sample base under its higher overburden pressure. Thicker clay layers display fewer, wider cracks of greater spacing compared to smaller, tightly spaced cracks in thinner samples (Nahlawi & Kodikara, 2006; Peron et al., 2009; Costa et al., 2013; Tollenaar et al., 2017). Furthermore, thicker layers of soil generally exhibit higher moisture content at the onset of cracking, allowing a greater range of moisture content for crack growth (Z. Luo et al., 2023).

These differences in crack networks are shown in Figure 2.26 for 20 mm, 50 mm, and 100 mm thick specimens (Tollenaar et al., 2017).

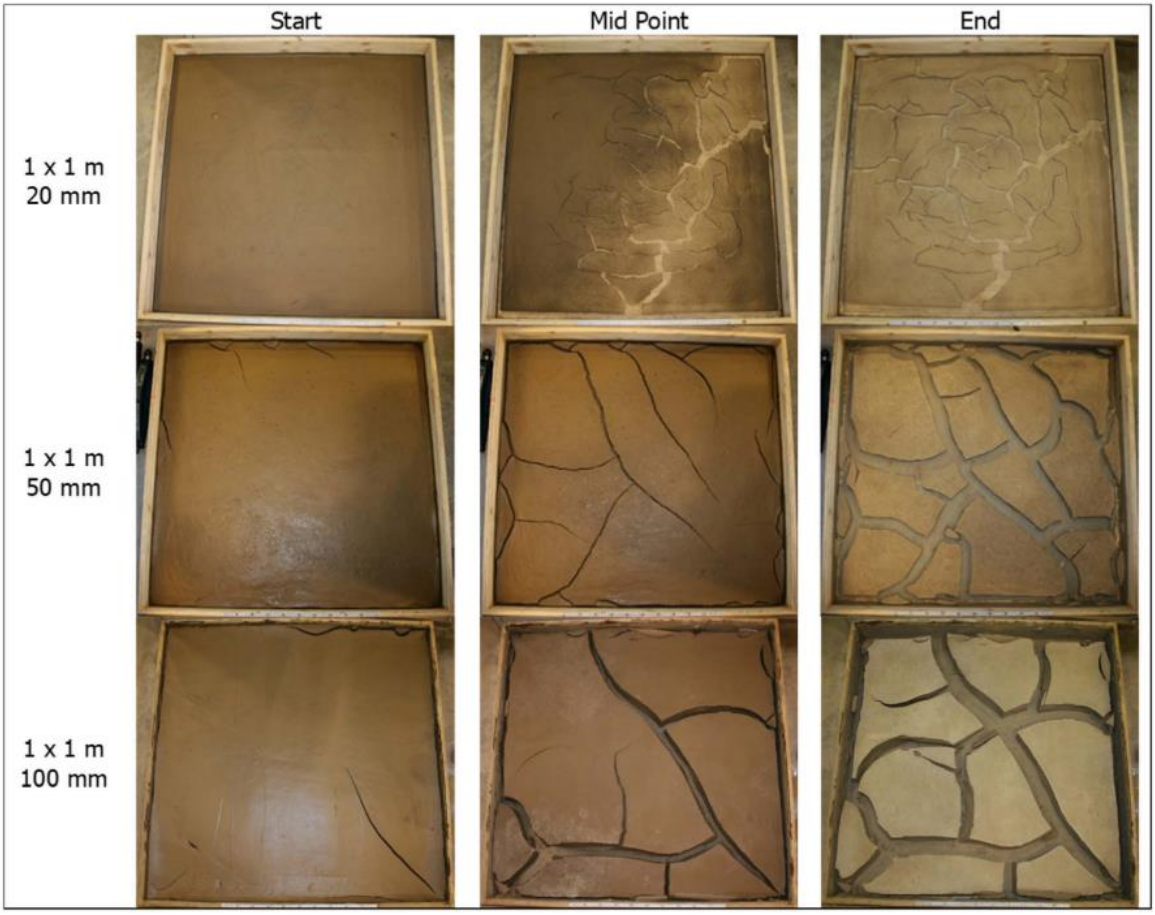

Figure 2.26: Increase in crack spacing and width with an increase in soil thickness from 20 mm to 100 mm. From Tollenaar et al. (2017).

The observed disparity in desiccation behaviour is primarily attributed to variations in soil water retention characteristics and specific environmental boundary conditions. The interactions between layers exhibiting differing moisture contents can initiate cracking at lower moisture levels. This phenomenon may be evident and requires further investigation within compacted soil layers within embankments, which are subjected to differential drying processes. Accelerated and finer desiccation typically correlates with more irregular drying patterns, thereby amplifying the heterogeneity of stress distribution and leading to an increased density of cracks (Tollenaar et al., 2017). Consequently, the rapidity of the drying process contributes to a more heterogeneous stress distribution, resulting in the formation of thinner and more frequent cracks. The cracking variations observed under varying specimen setups further emphasise the need to study desiccation at scales comparable to real field embankments.

Density and Compaction

The hydromechanical properties of desiccated clays differ significantly from those of intact soil, particularly due to moisture driven changes in porosity, void ratio, hydraulic conductivity, and density during drying (Trabelsi et al., 2018; Louati et al., 2021). The initial hydromechanical properties of the soil play a crucial role in the subsequent development of cracking (Trabelsi et al., 2018). During dry-wet cycles, loosely compacted soils quickly develop cracks to a peak, after which further shrinkage densifies the structure, leading to a decrease in crack apertures and soil porosity. Conversely, initially compacted soils gradually form more cracks, resulting in increased soil porosity (Trabelsi et al., 2018; Cordero et al., 2020; Louati et al., 2021). These differences are particularly relevant for infrastructure embankments, which are compacted to various specifications based on transport mode and construction age.

While embankments are primarily composed of compacted clay soil, laboratory experiments often utilise slurry specimens to ensure homogeneity and prevent crack formation from soil imperfections (Tang et al., 2021). However, when compared to compacted soils, slurry specimens tend to form simultaneous, orthogonal crack networks of higher cracking intensity rather than sequential, non-orthogonal patterns in compacted clay (Weinberger, 1999; Kodikara et al, 2000; Dyer et al, 2009; Lakshmikantha et al, 2009; Lakshmikantha et al, 2012; Zeng et al, 2020). This raises questions about the reliability of using slurry specimens to study cracking in infrastructure embankments, where heterogeneity is introduced during construction and with time due to microstructural degradation under cyclic environmental loading (Lakshmikantha et al., 2009; Stirling et al., 2021). Consequently, there is a pressing need for more field-scale investigations that incorporate this inherent heterogeneity.

Vegetation

Available studies on the role of vegetation on desiccation cracking are limited compared to bare soil investigations due to the difficulty in uncoupling soil-atmosphere-vegetation interactions and their synergistic effects. Consequently, the consensus on vegetation remains unclear in existing literature, with its effects on desiccation cracking being presented from both preventative and enabling perspectives.

From a preventative standpoint, transpiration-induced soil suction manages soil moisture levels, inducing high suctions and increasing shear strength. However, there is a maximum suction-induced stress that vegetation can withstand, beyond which

desiccation is initiated (Bordoloi et al., 2019). Furthermore, physical roots add a reinforcing strength effect, increasing the apparent cohesion of soil and resisting opposing tensile stress (Morris et al., 1992; Bordoloi et al., 2018). Similarly, natural fibres in clay can reduce cracking intensity by 50%, shown to increase the water retention capacity yet not the desorption rate (Bordoloi et al., 2019). Scanning Electron Microscopy (SEM) utilised by Tang et al. (2007) illustrated enhanced bond strength and frictional characteristics of fibres in soil facilitated such reinforcement, as visualised in Figure 2.27. However, Bordoloi et al. (2018) demonstrated that vegetation's ability to reduce desiccation is species-dependent, with some grasses decreasing intensity by 20% relative to bare soil. Effectiveness was also enhanced further under a greater vegetation density.

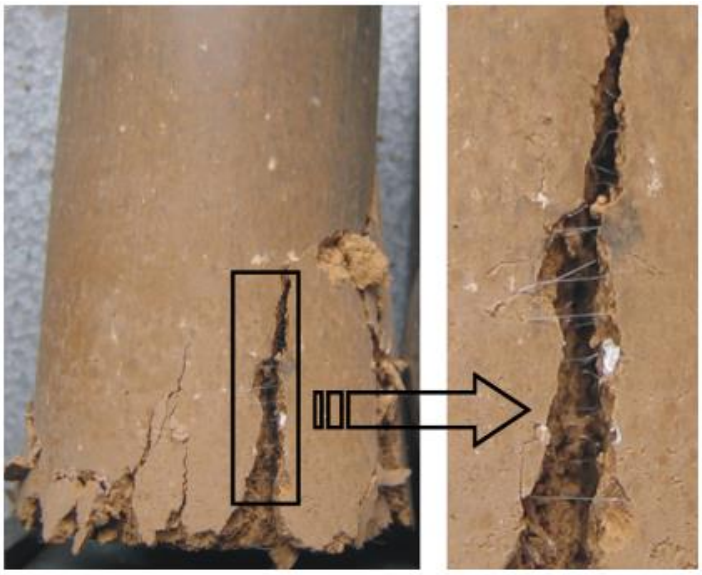

Figure 2.27: Soil fibres provide a reinforcing effect across the crack aperture. From Bordoloi et al. (2018).

Other studies noted that the beneficial effects are localised around desaturated root zones. Agricultural research has demonstrated how this causes cracking to exploit the more saturated soil regions between dense vegetation (Morris et al., 1992). Furthermore, added tensile strength can resist crack closure during clay swelling, leaving the desiccated slope more vulnerable to infiltration-induced stability for longer. Problematic tree and plant species with a high water demand have also been shown to exacerbate shrink-swell in the shallow surface of infrastructure embankments, increasing the likelihood of desiccation cracking (Jones et al., 2020; Huang et al., 2024). Additionally, evidence suggests that subsurface root growth can exacerbate the width and depth of desiccation cracks (Bordoloi et al., 2020).

Yu et al. (2021) recorded discrete, linear desiccation cracks on the BIONICS test embankment, attributing this disparity from laboratory polygonal networks to the constraining role of dense vegetation. The study hypothesised that dense vegetation limited surface crack propagation, encouraging growth to depth rather than in surface length. The literature widely recognises that the role of vegetation in the formation of desiccation cracks requires further investigation, especially considering that most infrastructure earthworks are vegetated.

2.6.4 Environmental Factors Impacting Desiccation Cracking

It is recognised that the prevailing environmental conditions are integral to the desiccation crack formation process, as these influence moisture movement, volume change, and, consequently, crack initiation. The existing literature has focused significantly on analysing crack formation under varied temperatures. This is primarily due to its ease of application and replication within laboratory environments. Furthermore, the process of desiccation crack formation under dry-wet cycling has been extensively analysed, as wetting and drying cycles can be easily replicated with control of temperature and water volume inundation. However, a much wider range of environmental variables and interactions fundamentally regulate soil moisture (Sun et al., 2024), which is crucially underrepresented in the existing literature. Considerations of how spatially and temporally varying the degree of environmental exposure is also notably absent. Below, an examination of the existing knowledge regarding the impacts of environmental variables, exposure, and dry-wet cycling is presented.

Environmental Variables

Multiple aspects of desiccation crack formation are influenced by temperature. High temperatures increased the evaporation and crack initiation rate, cracking water content, and crack intensity (Tang et al., 2008; Tang et al., 2010; Xiao et al., 2021). The difference in surface crack ratio evolution with water content for samples exposed to 22^{o}C, 60^{o}C and 105^{o}C was measured by Tang et al. (2020), the results of which are shown in Figure 2.28. The graph illustrates a cracking water content of 40% for 22^{o}C which increases to 90% upon exposure to 105^{o}C. This phenomenon is attributed to the higher tensile stress and lower tensile strength that occur in the soil at elevated temperatures. Additionally, at higher temperatures, the interfacial tension of water decreases, causing water molecules in the soil to become more kinetically active and evaporate more easily (Tang et al., 2008; Tang et al., 2010; Xiao et al., 2021). Laboratory scale analysis of temperature effects does not advance beyond this,

despite these extreme temperature ranges not representing more temperate climates under which cracking variation still occurs (Yu et al., 2021). The impacts of temperature have also been inferred at the field scale, with higher temperatures sustained from spring to summer facilitating the surface and subsurface propagation of desiccation cracks (Eminue et al., 2018; Stirling et al., 2018; Yu et al., 2021). However, it is difficult to fully uncouple the influence of environmental variables in field settings to calculate their individual effects on desiccation.

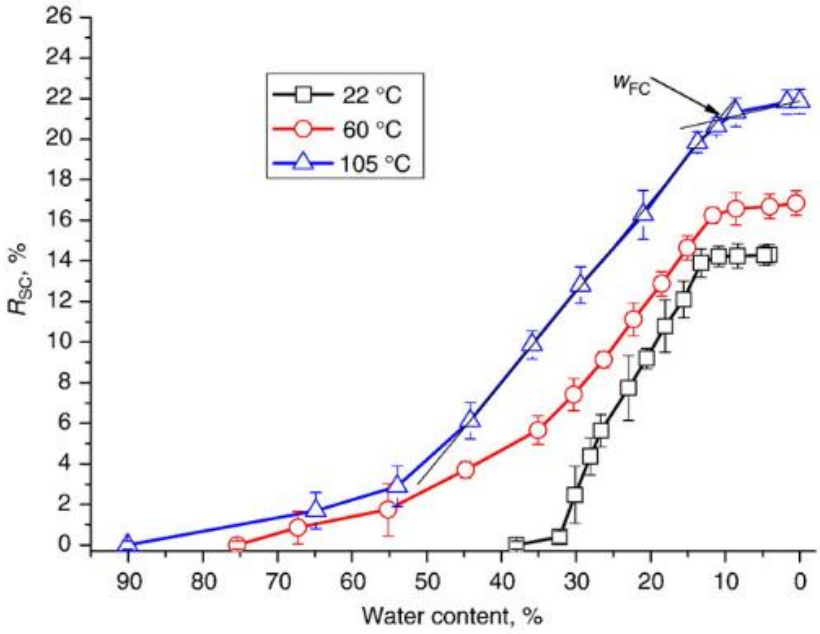

Figure 2.28: Increasing surface crack ratio (R_{sc}) and moisture loss (%) with increasing temperature. From Tang et al. (2020).

Relative humidity is inherently linked to temperature, as warmer air can hold more moisture than cooler air, making its influence on desiccation cracking difficult to isolate. Most laboratory tests subject samples to high temperatures and low relative humidities, not observing the full possible range. Consequently, limited studies observe the role of relative humidity in desiccation cracking. However, Zeng et al. (2022) exposed clay samples to different relative humidities between 15.0 and 93.7%. The evaporation rate decreased with increasing relative humidity, instigating crack initiation at higher moisture contents, and facilitating a more gradual and sequential propagation of bimodal crack networks. In contrast, lowering humidity accelerated evaporation, causing the simultaneous formation of a unimodal crack network. The transition from a unimodal to a bimodal crack network is observed as relative humidity is increased from 15.0% to 93.7% as shown in Figure 2.29 (Zeng et al., 2022). This illustrates the potential for deeper and wider crack networks to form under higher relative humidities,

which is more significant for associated deterioration mechanisms. Other researchers confirmed this effect of relative humidity (Nahlawi & Kodikara, 2006; Chen et al., 2023).

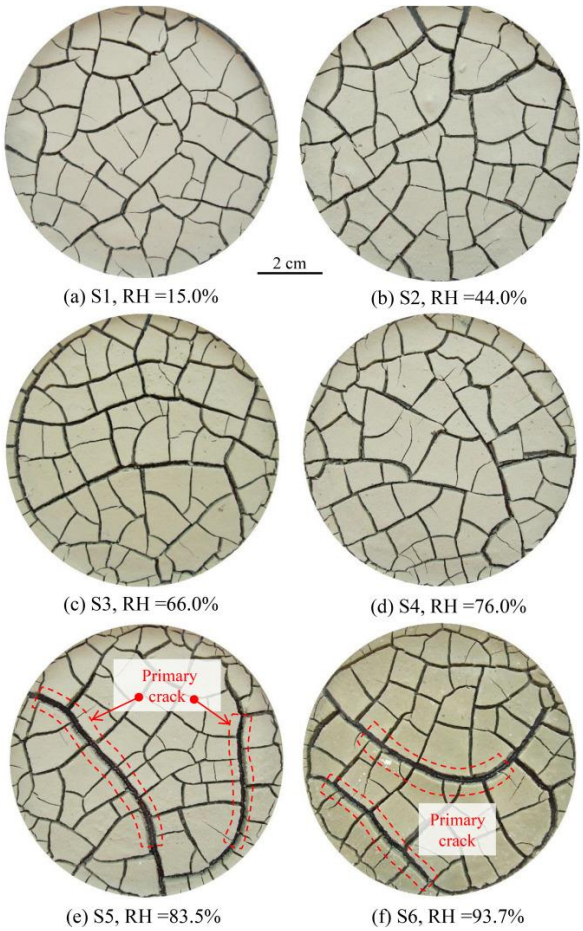

Figure 2.29: Formation of an increasingly bimodal (primary and secondary) crack network as relative humidity is increased from 15.0 % to 93.7 %. From Zeng et al. (2022).

Solar radiation is a fundamental source of energy for evaporation (Sun et al., 2024). However, the scarcity of laboratory techniques that can effectively simulate solar radiation often leads to its oversight in desiccation studies. This limitation hinders the comprehensive understanding of evaporation dynamics under natural conditions. The proposed effects of solar radiation on desiccation cracking come from indirect measurements. Yu et al. (2024) recorded greater desiccation cracking on the southern slope aspect, which received greater sunlight. Furthermore, Bordoloi et al. (2018) also observed the role of vegetated canopies in intercepting solar radiation, limiting evapotranspiration, suction generation, and desiccation crack formation. These results highlight the important role of varying environmental exposure in generating heterogeneous responses to cracking. Such mechanisms are notably absent from existing literature, except where they have been observed as an ancillary result of a wider study. However, there are many natural and man-made features surrounding

infrastructure embankments that could vary exposure. Therefore, a more detailed investigation into the role of heterogeneous environmental exposure is crucial to understanding the temporal and spatial distribution of desiccation cracking in infrastructure embankments.

While wind constitutes an essential variable in the dynamics of soil-water interactions, there is a notable scarcity of studies integrating its effects into experimental investigations of desiccation cracking. Nevertheless, existing research emphasises the significance of incorporating wind considerations to understand the desiccation process comprehensively. These studies have elucidated a soil saturation dependency on the effectiveness of wind-driven evaporation (Zeng et al., 2024). The wind is most effective when the soil remains saturated, sustaining a continual replenishment of soil-atmosphere moisture gradients and the microclimate's capacity to store water vapour.

This important role of wind in improving evaporation efficiency was demonstrated by Song et al. (2016) through their analysis of microclimate changes. In this study, an air compressor system was used within an environmental chamber to adjust the supply rate of hot air. The researchers measured the temperature and humidity of the incoming air and compared it to the conditions at the outlet. The results showed a decrease in temperature, indicative of air-soil heat exchange, and an increase in humidity reflecting the displacement of humid air by dry air. This exchange significantly enhances the vapour pressure gradient across the soil-atmosphere interface, increasing the air's ability to absorb additional moisture evaporating from the soil. As a result, this process facilitates a higher evaporation rate, which can improve drying regimes in infrastructure embankments. Although desiccation cracks occurred in this study, their response under varying wind speeds is not addressed. These results stress the highly coupled behaviour of wind and relative humidity.

Poulsen et al. (2020) conducted experiments in a wind tunnel and determined that elevated wind speeds enhanced evaporation rates. Notably, they identified a synergetic relationship between wind dynamics and desiccation cracking, emphasising that a comprehensive analysis of soil evaporation must account for the interplay of both factors. Cracks that are oriented parallel to the prevailing wind direction extend the wind speed profiles into the subsurface, leading to a substantial increase in the overall soil evaporation. Other researchers found a similar linear correlation between crack depth and wind ventilation depth (Nachshon et al., 2012). The cracks in this study were

manmade, and notably simplified relative to the complex connectivity seen in field conditions.

While establishing informative relationships, laboratory studies have limitations due to their inability to realistically replicate the complex and variable nature of natural winds. In the field, it is impossible to isolate wind for analysis, with its effect on desiccation inferred based on observations. These field observations have hypothesised a dependency of cracking intensity on wind speed, also seen in intermediate-scale lysimeter tests (Ritchie & Adams, 1974). An embankment's aspect relative to wind direction suggests a heterogeneous cracking response can occur within a singular asset relative to the degree of exposure (Yu et al., 2021). Furthermore, during the winter months, the prevalence of desiccation suggested that wind effects are more pronounced in the absence of high temperatures (Cordero et al., 2021). Directly observing and quantifying how cracks evolve spatially and temporally under varying wind remains a notable gap in this research area.

Dry-wet cycling

Cyclic exposure to wetting and drying has been shown to profoundly impact the nature of desiccation cracking. As illustrated by Stirling et al. (2021) the cyclic action of environmental loading facilitated the growth of an interconnected network of micro-cracks. These micro-cracks initiated irrecoverable deterioration of soil microstructure (Pires et al., 2008), lower water retention capacity, a cyclic reduction in soil-tensile strength, and an increased likelihood of macro-scale crack formation. Laboratory studies of clays subject to dry-wet cycling record a notable increase in crack segments, forming a highly fragmented surface across the initial three cycles (Tang et al., 2011; Wang et al., 2018; Tang et al., 2020; Tian et al., 2022).

Furthermore, associated increases in the measured cracking water content, surface crack ratio, and layer thickness have also been recorded under the formation of a coarser pore network (Tang et al., 2011). These changes in desiccation behaviour commonly stabilised in the subsequent cycles, as shown in Figure 2.30 (Tang et al., 2011). Such behaviour was also observed in intermediate-scale experiments conducted outdoors, where crack irregularity increased with environmental exposure as crack walls destabilised and collapsed (Cordero et al., 2021). This behaviour has been attributed to reduced unconfined compressive stress, soil stiffness and increased ductility that the cracks facilitated (Tang et al., 2020). Cracks exhibit high repeatability,

reopening in permanently damaged zones created by desiccation during previous cycles (Tang et al., 2008; Li & Zhang, 2011). However, most of these cyclic investigations were 1) conducted on homogeneous slurry specimens, and 2) cycled over the same range of moisture contents. Other researchers have evidenced that exposing the soil to more significant drying than previously experienced can reactivate microstructural degradation (Stirling et al., 2021). This is facilitated by more significant fluctuations in pore water pressure between wet and dry states, inducing irrecoverable fatigue to the soil fabric and structure.

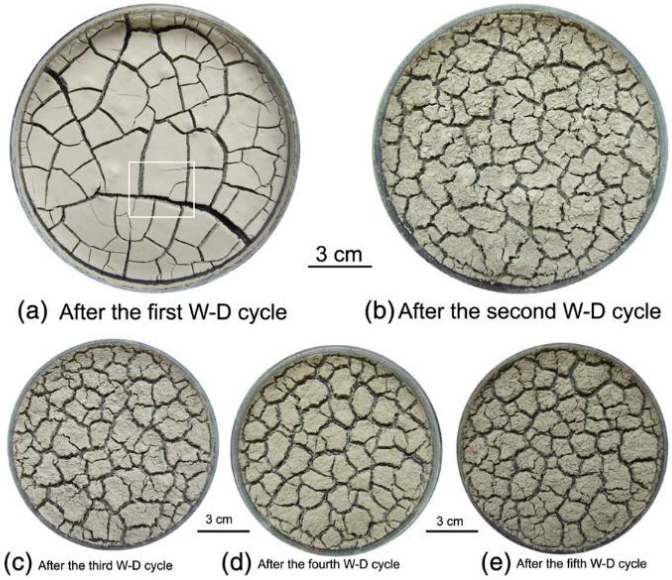

Figure 2.30: Increasingly fractured clay surface as exposure to numerous dry-wet cycles. The surface desiccation stabilises after three dry-wet cycles. From Tang et al. (2011).

Furthermore, these cycle magnitudes are not realistic of natural climate variability, which induces seasonal and intra-seasonal changes in cracking intensity in the field. This can be observed in the BIONICS test embankment where Stirling et al. (2021) installed linear transducers across an active crack site on a field-scale, vegetated test embankment (BIONICS), capturing its behaviour through an entire annual rhythm of seasons (June 2015 – December 2016). Crack opening and closure were influenced by seasonal variations in suction, opening during the transition from spring to summer and closing from late autumn into winter as suction initiated and dissipated, respectively. Correlating cracking to measured suction is rarely considered in small-scale laboratory tests. A summer period of crack expansion and progressive autumn contraction were also noted. The relative aperture of cracks was shown to be a function of evapotranspiration and rainfall, widening under net drying regimes, fluctuating under periodic high-intensity summer rainfall, and closing under prolonged wetting. This

demonstrates the highly dynamic nature of field cracks under dry-wet cycles of varying intensity, magnitude, and duration. Therefore, cracking in the field is considerably more complex than what laboratory testing indicates.

Greater detail of the crack characteristics on the BIONICS embankment was given within Yu et al. (2021). Figure 2.31 illustrates the crack locations and paths recorded, emphasising discrete linear features that reached a maximum recorded depth of 1.0 m. The network showed repeatability across the monitoring years, with new cracks also initiating over time (Eminue et al., 2018). This field network markedly differs from the surface-extensive, highly connected, polygonal patterns observed in laboratory settings (e.g. see Yesiller et al., 2000; Tang et al., 2010; Shin & Santamarina, 2011; Cui et al., 2014). This variation in crack patterns and behaviour underscores the critical importance of analysing field-scale desiccation under conditions that closely simulate those encountered by real infrastructure embankments. This is a notable research gap within the existing literature that critically requires further investigation.

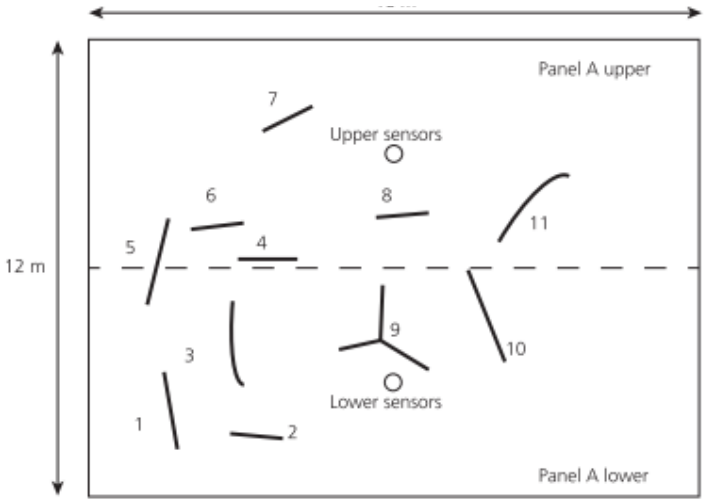

Figure 2.31: Locations of discrete linear cracks recorded on the BIONICS test embankment. From Yu et al. (2021).

2.6.5 Quantification of Desiccation Cracking

Several methodologies have emerged within the literature to quantify the severity of desiccation cracking in clay soils. These approaches can be categorised into two-dimensional (2D) and three-dimensional (3D) methods, with each successive approach enhancing the ability to capture the key features of the desiccation pattern. Below, examples of these methodologies, along with their respective benefits and limitations, are discussed.

Two-dimensional methods

Digital image processing is one of the most widely utilised 2D techniques in the literature (Lakshmikantha et al., 2009; Liu et al., 2013; Auvray et al., 2014; Wang et al., 2018), and the standard procedure is visually outlined in Figure 2.32 (Wang et al, 2018). The initial phase (a) entails the acquisition of high-resolution images that track temporal changes in surface desiccation across a fixed field of view. These images are subsequently analysed using advanced software tools such as ImageJ or MATLAB. Following a comprehensive pre-processing stage designed to eliminate noise – particularly that arising from uneven lighting – and to enhance contrast, the images undergo segmentation (b). This process involves the establishment of an intensity threshold that effectively differentiates cracked areas from intact soil, thereby producing a binary image. The Crack Intensity Factor (CIF) is derived from this binary representation. Initially introduced by Miller et al. (1998), the CIF quantifies the percentage of the total surface area that exhibits cracks in relation to the overall surface area of the specimen.

The CIF is the most used quantitative parameter for categorising cracking severity in existing literature. Recent advancements in image processing techniques have added techniques such as skeletonisation (c), which facilitates the quantitative assessment of additional geometric, shape, dynamic, and topological parameters throughout the desiccation process (d). These enhancements significantly contribute to the understanding of surface desiccation phenomena. However, using the CIF to track temporal crack evolution is limited to surface desiccation. For subsurface cracking, the CIF can only be applied after the test is concluded, requiring extraction of cross-sectional samples and subsequent image processing (Yesiller et al., 2000; Leonard et al., 2003).

The digital image processing technique is predominantly utilised for small-scale laboratory samples, where it facilitates the acquisition of high-quality images. However, applying these methods in field quantification is often impractical due to several challenges, including variable natural lighting conditions, deteriorated surface features, obstruction by vegetation, and the extensive spatial coverage required. Utilising the CIF as a comprehensive measure of crack severity is subject to scrutiny, as it neglects the crucial dimensions of depth and volume. Subsurface cracking, including its magnitude, volume, and connectivity, plays a fundamental role in facilitating infiltration, storing water, and increasing the vulnerability of an asset to potential failure.

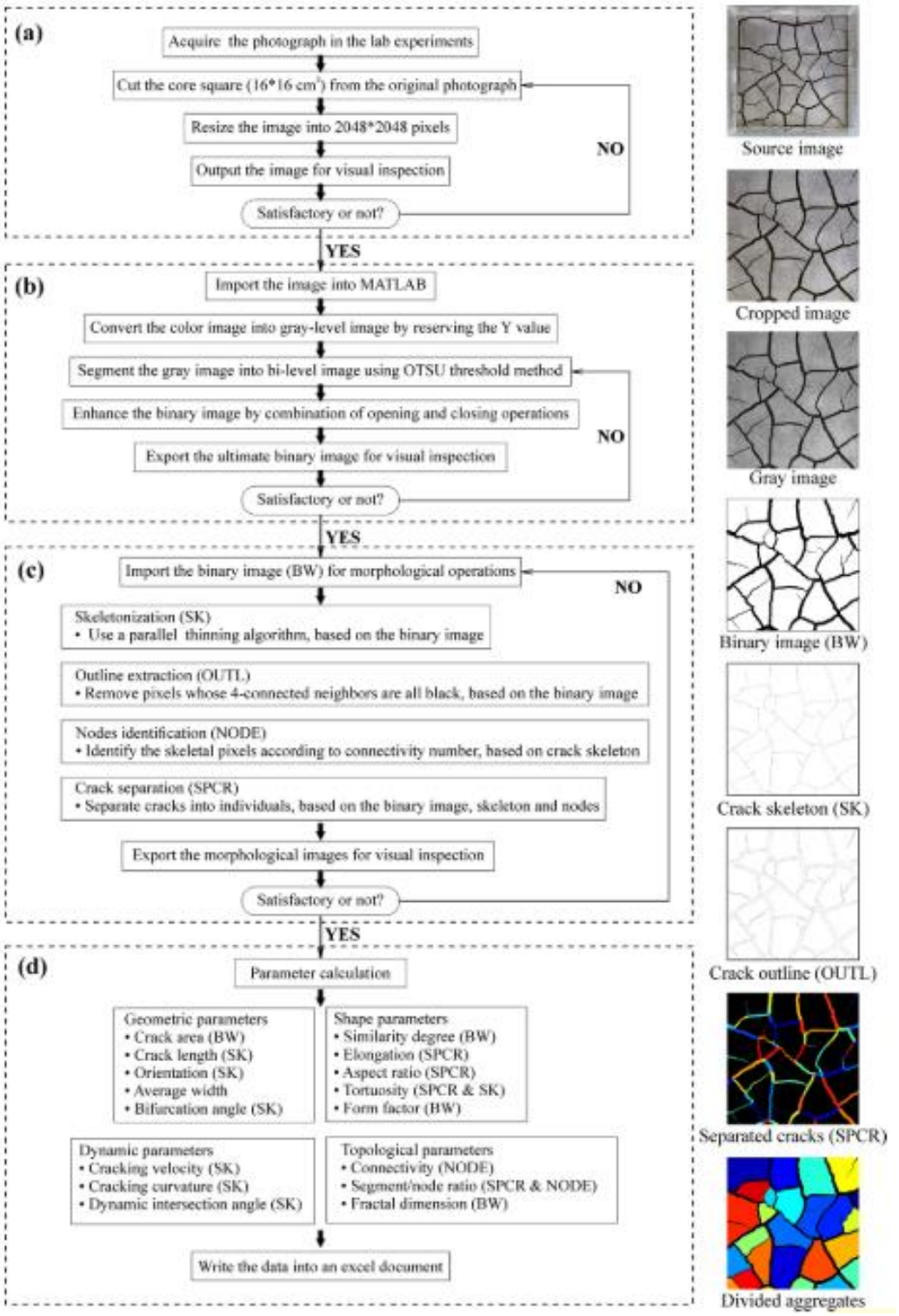

Figure 2.32: Flow chart of digital image processing technique commonly used to quantify cracks with (a) image acquisition and pre-processing, (b) image segmentation, (c) further skeletonisation and quantification, and (d) parameter calculation. From Wang et al. (2018).

At the field scale, desiccation cracks are typically assessed qualitatively by noting their presence or absence. The severity of their impact is usually evaluated instead by analysing changes in the hydrological behaviour of the slope when cracks are open versus when they are closed. This analysis enables the formulation of an additional permeability value and infiltration depth that these cracks provide. Some destructive techniques have been utilised by the excavation of trenches in the field (Dyer et al., 2009; Konrad & Alanazi, 2011; Li & Zhang, 2011).Such methods help gain insight into field desiccation, yet they are not practical for use on live assets, where excavation would destabilise the embankment. Non-destructive 2D techniques have also been used. Stirling et al. (2018) utilised electrical resistivity tomography (ERT) on a field-scale test embankment to visualise developing crack features and the moisture content changes they induced. Laser devices have also been used to obtain a 2D topographic profile of desiccation cracks, as shown in Figure 2.33 (Sanchez et al., 2013). However, such techniques are limited to small-scale laboratory tests and are not yet employed in field-scale applications.

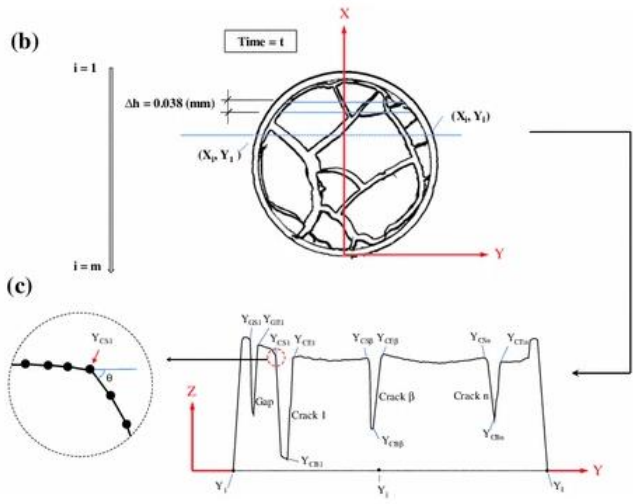

Figure 2.33: Laser profile for 2D crack analysis with cross-section location shown in (b) and change in elevation with depth (z) across the specimen length (y) is shown in (c). From Sanchez et al. (2013).

Three-dimensional methods

Non-destructive techniques that allow 3D characterisation include Ground Penetrating Radar (GPR) (Levatti et al., 2017), X-ray computed tomography (X-ray CT) (Julina & Thyagaraj, 2019; Tang et al., 2019), structured light scanning (Zhuo et al., 2022) and 3D laser scanning (Hirmas et al., 2016). While these techniques have provided valuable insights into subsurface desiccation processes, their application to samples representative of infrastructure embankments is not yet available. Typically, these

methods are applied to smaller-scale, homogeneous slurry specimens (Leonard et al., 2003; Sanchez et al., 2013; Levatti et al., 2017; Tang et al., 2019) which exhibit inherently different behaviour to heterogeneous embankment fill.

On field-scale embankments, 3D subsurface desiccation has been estimated using an empirically derived geometric relationship, where the length, depth, and width of cracks are measured between two representative points (Yu et al., 2021). This assumes that the three-dimensional subsurface crack geometry resembles a triangular pyramid, as shown in Figure 2.34 (Yu et al., 2021). This method effectively correlated changes in crack volume with the embankment's hydrologic response. However, it oversimplifies the complexities associated with the variable trajectories and connectivity of subsurface cracks.

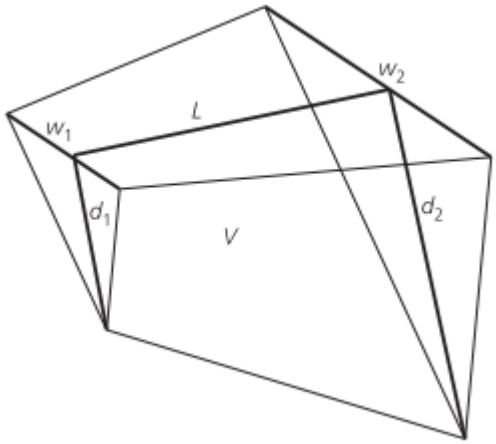

$$V = \frac{1}{3}L\left[\left(\frac{1}{2}w_1 d_1\right) + \left(\frac{1}{2}w_2 d_2\right) + \sqrt{\left(\frac{1}{2}w_1 d_1\right)\left(\frac{1}{2}w_2 d_2\right)}\right]$$

Figure 2.34: Process used to quantify the volume of a field crack where width (W), length (L) and depth (d) measurements are taken to calculate the volume (V). From Yu et al. (2021).

This review underscores the critical need for enhanced three-dimensional quantification of desiccation cracking at a field scale. An accurate assessment of the subsurface depth and volume dimensions is essential for a comprehensive analysis of the total risk that desiccation presents to embankments.

2.6.6 Preferential Flow as a Deterioration Mechanism

UK transport infrastructure owners have reported an inherent link between high-intensity rainfall events and embankment failures (Network Rail, 2018; Mair, 2021; ORR, 2021, 2024). Such relationships are particularly evident when convective summer storms occur following a protracted period of drought. During this transition, Mair (2021) highlighted the important role of desiccation cracks in facilitating deeper and faster propagation of wetting fronts and dissipation of stabilising negative pore water pressures. Under projected climate change scenarios, the anticipated rise in both the frequency and intensity of desiccation cracking, in conjunction with an increase in summer storm occurrences, places preferential flow-induced stability as a critical contributor to the high-risk deterioration mechanisms affecting infrastructure embankments (Stirling et al., 2021; Briggs et al., 2023; Huang et al., 2024).

A substantial body of literature has investigated the impacts of desiccation cracks on the storage and distribution of moisture within clay soils. In the laboratory, mapping of wetting fronts has illustrated their highly irregular nature, controlled by the location and depth of desiccation cracks (Bouma, 1980; Wells et al., 2003; Römkens & Prasad, 2006; Cheng et al., 2021). An example demonstrating the relationship between crack location and the deeper propagation of the wetting fronts is presented in Figure 2.35. In this figure, the solid line indicates the depth of the crack, the upper dotted line represents the wetting front prior to desiccation, and the lower dotted line shows the wetting front that forms after the slope has desiccated (Wells et al., 2003). In comparison to intact soil, desiccation cracking in soil has been observed to enhance the penetration depth of the wetting front by a factor of six (Bouma, 1980) and the infiltration capacity by double (Novák et al., 2000).

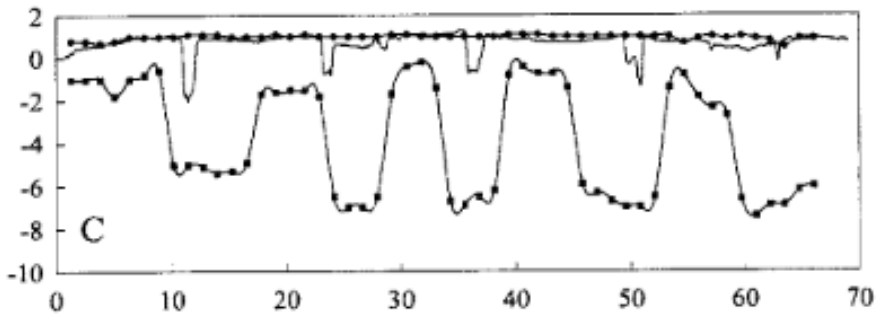

Figure 2.35: Plot of depth (y-axis) against length (x-axis) showing the surface elevation with cracks (solid line), the initial wetting front position at the soil surface after saturation (upper dotted line) and the propagation of wetting fronts around surface cracks (lower dotted line). From Wells et al. (2003).

The mechanism of preferential flow has also been observed within intermediate-scale specimens (Cordero et al., 2021) and model test slopes (Luo et al., 2021) using well-distributed suction and water content sensors. Cordero et al. (2021) investigated a large slurry specimen's desiccation and hydrological behaviour within an outdoor lysimeter. The results gave evidence of preferential flow, with mid-layers increasing in moisture content over surface layers, corresponding to the depth of cracks and illustrating by-pass flow. The relative dissipation rate of pore-water pressures was considerably faster than the rate of gain, suggesting infiltration was faster than evaporation. The mechanism of preferential flow has been shown to be further exacerbated by the development of an impermeable crust over intact soil peds (Wells et al., 2003; Römkens & Prasad, 2006). This phenomenon results from the cumulative kinetic compaction induced by raindrop impact, along with the clogging of soil pores by deposited fines. Consequently, this process directs runoff into the existing cracks within the soil structure, with a doubling in the infiltration rate recorded (Wells et al., 2003). Developing an impermeable crust may increase the risk of washout or erosional failure on embankments, especially during short-duration, high-intensity rainfall events that are expected to occur more frequently due to climate change.

Luo et al. (2021) constructed a full-scale model test slope, where an increase in rainfall infiltration was measured even when cracks appeared healed. Numerous laboratory studies have reported that cracks heal during the complete re-saturation of samples (Wang et al., 2017). However, these findings are often not corroborated by subsurface, mechanical, or hydraulic analysis that confirm the self-repair of the cracks (El-Zein et al., 2021). Investigations into the hydrological behaviour of desiccated soils in their healed state have indicated an increase in saturated hydraulic conductivity following each wetting cycle (McBrayer et al., 1997; Albrecht & Benson, 2001; Trabelsi et al., 2018; Morsy et al., 2023). Coupled with the tendency for cracks to reform in the exact locations, these results suggest the presence of permanently weakened zones, characterised by irrecoverable microstructural degradation, irreversible loss of strength and a consistently heightened water storage capacity (Greve et al., 2010; Stirling et al., 2021; Xu et al., 2021). Increasing dry-wet cycles form more micro- and macro-cracks, which leads to extended re-saturation periods, thereby delaying or inhibiting the apparent self-healing process. (Römkens & Prasad, 2006; Cheng et al., 2021; Luo et al., 2023). Such behaviour is expected to be exacerbated under climate change

projections, with embankments reaching a critical saturated state less frequently due to this microstructural degradation (Huang et al., 2024).

Stirling et al. (2021) evidenced a clear relationship between cracking, near-surface saturation, and runoff within the BIONICS field-scale test embankment, recorded in Figure 2.36. Crack aperture was measured using displacement transducers (A), and the movement was compared with subsurface suction and volumetric water content (B), environmental variables (C), and slope runoff (D). Figure 2.36 reveals that runoff was generated only after the closure of cracks, despite similar rainfall magnitudes across both its desiccated and intact states. In response to rainfall, the width and depth of cracks showed a more dynamic response than the surface length (Yu et al., 2021). The reduction in volume was largely due to crack closure at depth, highlighting how cracks can divert rainfall and runoff from the shallow subsurface. This underscored the critical role of crack dynamics in regulating water movement within the embankment profile. Furthermore, it effectively demonstrates the increased storage capacity of desiccated soils, which can be detrimental for stability. Similar measurements were made by Greve et al. (2010), where desiccated soil stored the entire water volume from three irrigation events without generating drainage. There exists a pressing necessity for more comprehensive analyses, such as the BIONICS test embankment, which evaluates desiccation-induced deterioration at a scale comparable to that of live assets. This approach underscores the importance of integrating holistic methodologies in assessing structural integrity and performance over time.

Shifting crack patterns are rarely recorded within existing literature, with the exception of a few studies (Wells et al., 2003; Greve et al., 2010; Qi et al., 2020). For Greve et al. (2010) and Qi et al. (2020), the shift occurred when irrigation methods that facilitated flooding occurred. For Wells et al. (2003), the shift was attributed to the crack-controlled moisture re-distribution, with drier intact peds becoming the focal point of crack initiation in the following cycle. These studies highlight the importance of more significant changes in particle arrangement during flooding, which may become increasingly relevant under future climate change extremes. Furthermore, the results stress the importance of heterogeneous moisture distribution in the subsequent cracking patterns, which could enhance weak zones in the soil through time.

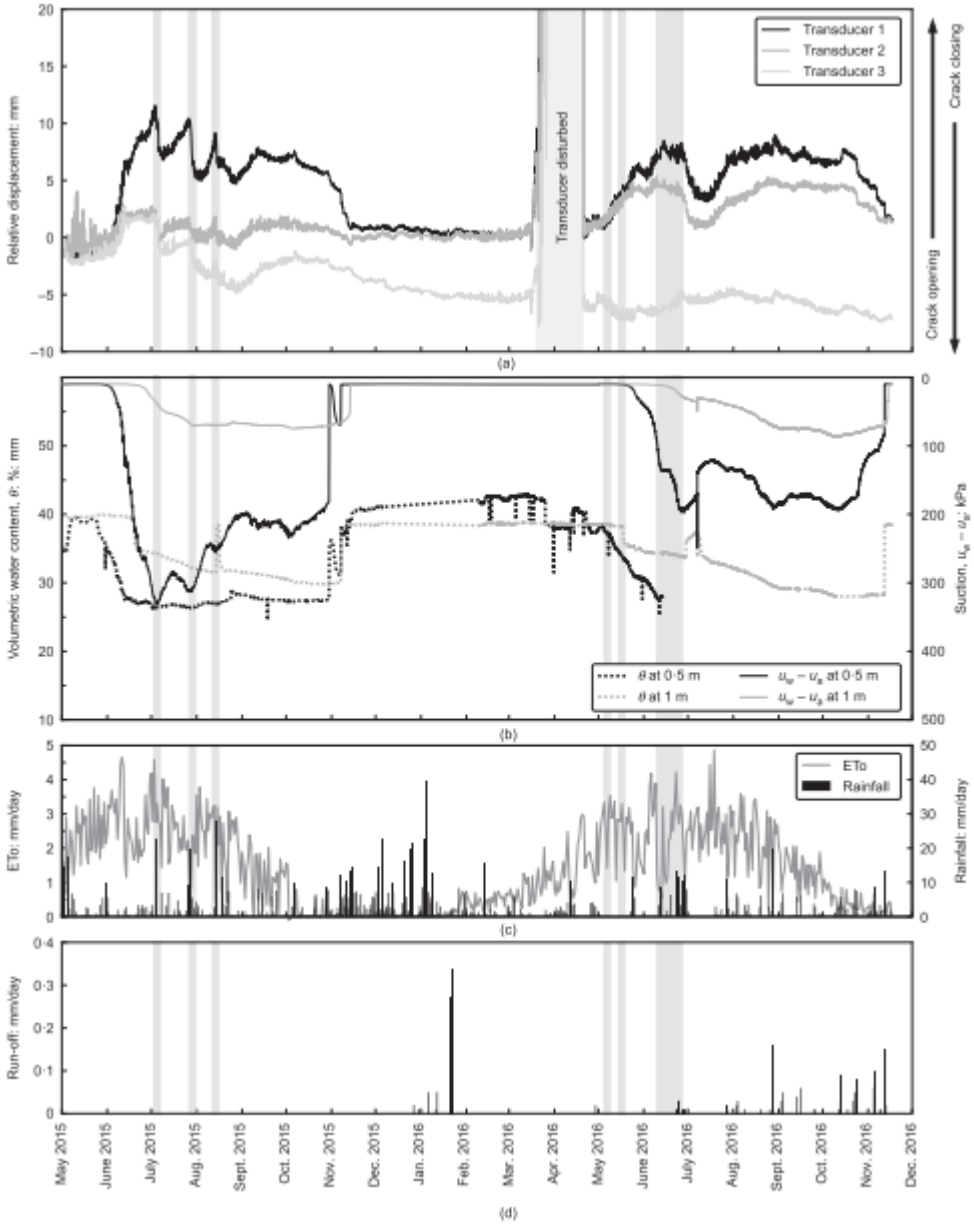

Figure 2.36: (a) Crack displacement with (b) water content and suction, (c) Evapotranspiration (ETo) and rainfall, and (d) runoff for the BIONICS test embankment. From Stirling et al. (2021).

Various seepage modelling approaches have been carried out to relate cracking geometries to infiltration capacity. For example, Zeng et al. (2018) used a modelling approach to analyse the effects of crack depth and density on infiltration patterns. As the crack depth increased, the pore-water pressure within the crack heightened, and the infiltration depth was extended. Increased crack density facilitated the connectivity of positive pore water pressure plumes around cracks, increasing their zone of influence. Multiphase, hydromechanical numerical simulations used by Morsy et al. (2023) demonstrated that crack contributions to water content fluctuations would convert the BIONICS test embankment into a fully softened state by 20 years of cyclic environmental exposure.

To relate these observed changes in infiltration behaviour to failure vulnerability, slope stability analyses incorporating cracking permeability have been conducted (Alexsander et al., 2017; Mukhlisin & Khiyon, 2018; Zhang et al., 2020). Alexsander et al. (2017) conducted a forensic analysis of a slip failure within a compacted embankment, using tomographic resistivity and induced polarisation to reveal an extensive network (max 10 m) of desiccation cracks and trapped water in the embankment profile. Integrating these measured features into a slope stability analysis revealed a significant reduction in the factor of safety (FOS). This decrease was due to the inundation of heavy rainfall into the deep crack network, which led to rapid increases in porewater pressure. As a result, the embankment became destabilised and ultimately failed. Mukhlisin & Khiyon (2018) demonstrated that the FOS decreased more rapidly with increased crack depth, longer rainfall durations, and when cracks were located in the crest compared to the upper slope. Similarly, Zhang et al. (2020) recorded a continual decline in the FOS towards instability as the cracking intensity increased.

The literature review presented in this section offers compelling evidence regarding the potential detrimental effects that cracks can have on infiltration. Nonetheless, there are notable gaps in the current analysis. First, it is crucial to investigate hydrological and crack behaviour over extended time periods and under various natural environmental cycles. Second, studying the behaviour of cracks in the context of extreme climate change conditions is vital. Addressing these gaps would significantly enhance our understanding of the timescales over which deterioration from preferential crack flow can develop and evolve. Furthermore, it would inform how desiccation cracks influence embankment stability within an evolving climate.

2.7 Concluding Remarks

A research gap has been identified through a thorough analysis of the existing literature on desiccation cracking and its associated deteriorating mechanisms. The research area has benefited from a magnitude of small-scale laboratory tests, which have been integral to advancing the understanding of the fundamental mechanisms of desiccation cracking. However, the methods available for conducting field-scale analyses of desiccation cracking are notably limited compared to the diverse techniques employed in small-scale laboratory experiments. However, field-scale studies are arguably more informative, fundamentally depicting how desiccation cracking manifests in a real-world context.

The interplay between slope hydrology and prevailing weather patterns on a spatial and temporal scale is essential for understanding the dynamics of desiccation patterns. However, these complex relationships are seldom accurately replicated or addressed in controlled laboratory settings. Furthermore, observations of desiccation cracking within infrastructure embankments differ significantly from those commonly reported in a laboratory setting, underscoring the importance of understanding these processes within their natural context. To effectively address the identified research gaps, a multi-scale methodological approach is proposed and presented in the following chapters of this thesis. This approach will enable the monitoring of spatial and temporal changes in hydrological conditions and desiccation cracking regimes, crucially in contexts relevant to real infrastructure embankments. Furthermore, this methodology will allow for a realistic evaluation of how desiccation-induced deterioration evolves in the field over time with antecedent and extreme cycles of environmental exposure.

Chapter 3. Methodology

3.1 Introduction

In Section 1.2, research gaps were identified, which required a methodology that investigated the hydraulic and mechanical impacts of desiccation cracking at a scale spatially and temporally comparable to live infrastructure embankments. This chapter introduces the methodologies used to address these research gaps, which can be divided into intermediate-scale lysimeter experiments and field-informed laboratory investigations.

The design, construction, and monitoring of an intermediate-scale, compacted clay slope located outdoors and subject to natural and simulated environmental conditions are discussed. This translates to a novel, multi-parameter investigation where long-term monitoring of relationships between environmental conditions, crack formation, soil hydrology, and mechanical properties could be conducted simultaneously. Later adaptations to the lysimeter included applying simulated storm events that analysed the behaviour of desiccated slopes to 1 in 100-year high-intensity rainfall events, uplifted to account for climate change projections. The role of vegetation canopies in moderating environmental exposure was also considered, installing a faux grass canopy over one-half of the lysimeter slope. A comprehensive justification of the materials and monitoring methods used for each investigation is also given.

This chapter also presents a comprehensive overview of a series of laboratory investigations developed in response to active observations conducted on the lysimeter slope during monitoring. These investigations isolated construction and environmental-based parameters underrepresented in the existing literature to aid understanding of their individual contributions to the desiccation cracking process. Furthermore, the design of these investigations incorporated processes encountered within live infrastructure embankments, enhancing the relevance and applicability of their findings in real-world contexts.

The closing section of this chapter summarises all the methods utilised in this research methodology to address the overarching aims and objectives of this thesis.

3.2 The Ampthill Clay

To investigate desiccation cracking, soil which exhibits considerable shrink-swell and desiccation behaviour was required. Figure 3.1A identifies the rock formations most susceptible to shrink-swell behaviour in the UK, concentrated in the southeast region. These rock formations are the youngest in the UK and comprise shallow clay deposits that are yet to lithify and, therefore, remain highly susceptible to the cyclic changes in moisture content that drive volume change. The British Geological Society (BGS) GeoSure dataset (BGS, 2020) has been used to categorise the shrink-swell susceptibility of UK rock formations, with Figure 3.1B demonstrating moderate to significant potentials primarily focused on these young, southeast clay deposits.

Considering the objectives set within Section 1.2, an understanding of the development of desiccation-induced deterioration of infrastructure slopes and its temporal evolution under increased environmental stress from weather extremes is sought. Therefore, Figure 3.1C and 3.1D place these deposits within that context, identifying which strata will exhibit the greatest susceptibility to shrink-swell-induced subsidence by (a) 2030 and (b) 2070 under the UKCP18 climate change projections. As expected, 2030's highest probability areas overlap areas of significant shrink-swell potential (Figure 3.1B), with subsidence most imminent within the Ampthill, Kellaways, and London Clay Formations. With greater time, the probable and possible likelihoods in 2070 expand further within these deposits, indicating their higher risk relative to other formations. For this research, using soil suitable for constructing a real-life infrastructure slope was equally important. Figures 3.1C and 3.1D contain an overlay of the rail and major road networks within the UK, illustrating a high density of transport links traversing these high-risk Ampthill, Kellaway, and London Clay Formations.

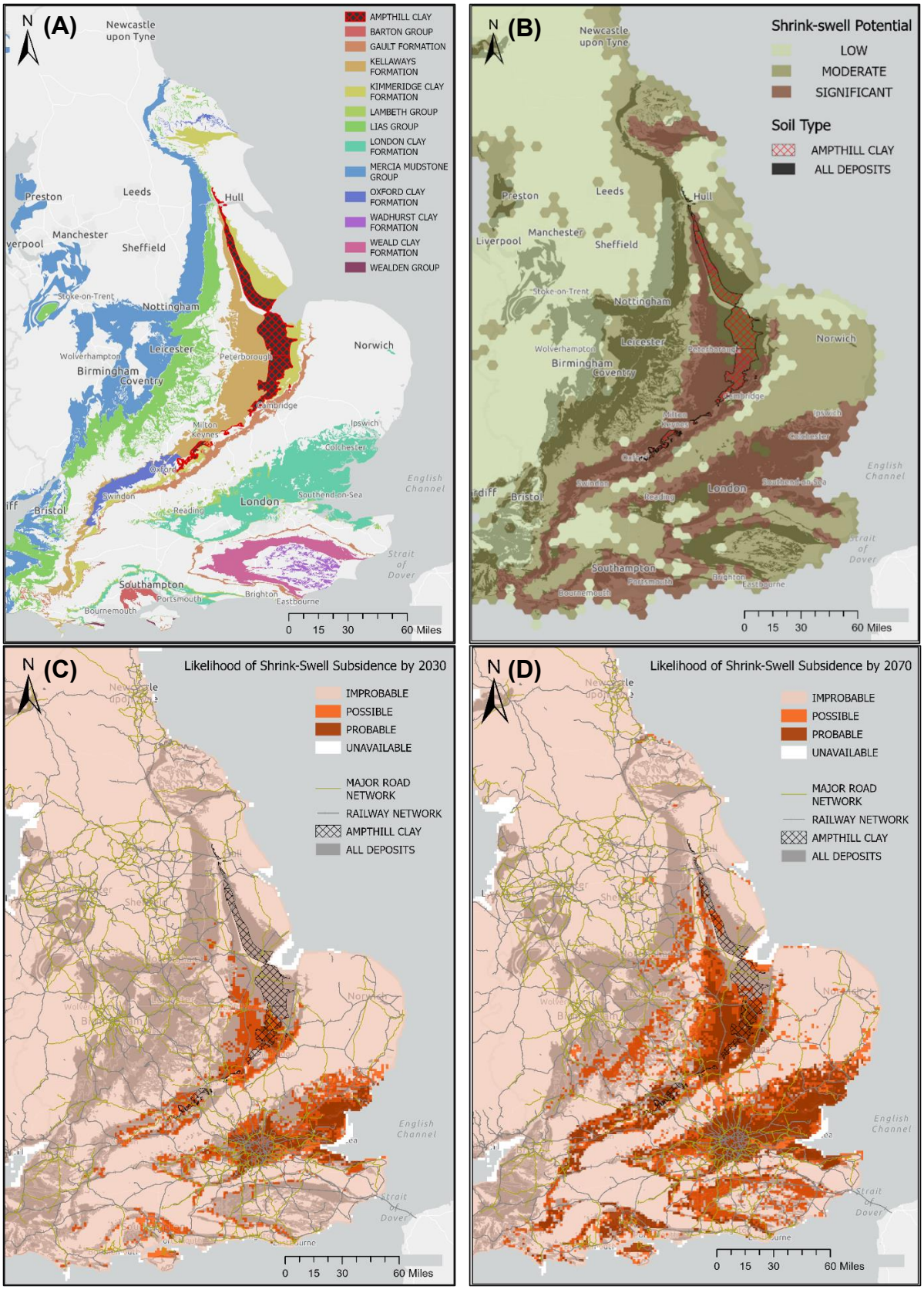

Figure 3.1: Informative maps of southeast England showing rock formations with (A) highest susceptibility to shrink-swell and B) low, moderate and significant potential for shrink-swell. Impossible, possible, and probable areas of shrink-swell subsidence under the UKCP18 Projections by (C) 2030 and (D) 2070 are also shown. Created using BGS GeoSure Layers (BGS, 2020).

Within existing literature, the London Clay Formation members have been investigated comparatively more in this research context than the former two formations. However, the Ampthill Clay knowingly constitutes sections of the Great Western Main Line from Bristol to London and the M4 and M40 road corridors, indicating its use in real-life applications (Nicholls, 1994). Consequently, given its high coverage in areas of significant shrink-swell potential and most probable subsidence, gaining an improved understanding of its behaviour in response to cyclic variations in moisture is critical for managing subsidence risk within these key transport assets. Therefore, for this research, Ampthill Clay from Needingworth Quarry in Cambridgeshire was utilised to address the knowledge gap and enhance the analysis of these high-risk materials.

3.2.1 Classification Testing

The Ampthill Clay is a slightly silty, dark grey mudstone with calcareous concretions and shell fragments. A series of laboratory classification tests were conducted to further classify its baseline hydrological and mechanical properties with experimental data. The particle size distribution (PSD) curve for the Ampthill Clay is given in Figure 3.2. For the coarser fraction of the PSD curve, the wet sieving method given by BS1377-2 Section 9.2 (British Standards, 1990) was conducted to give the relative proportions of sand, gravel, and cobbles.

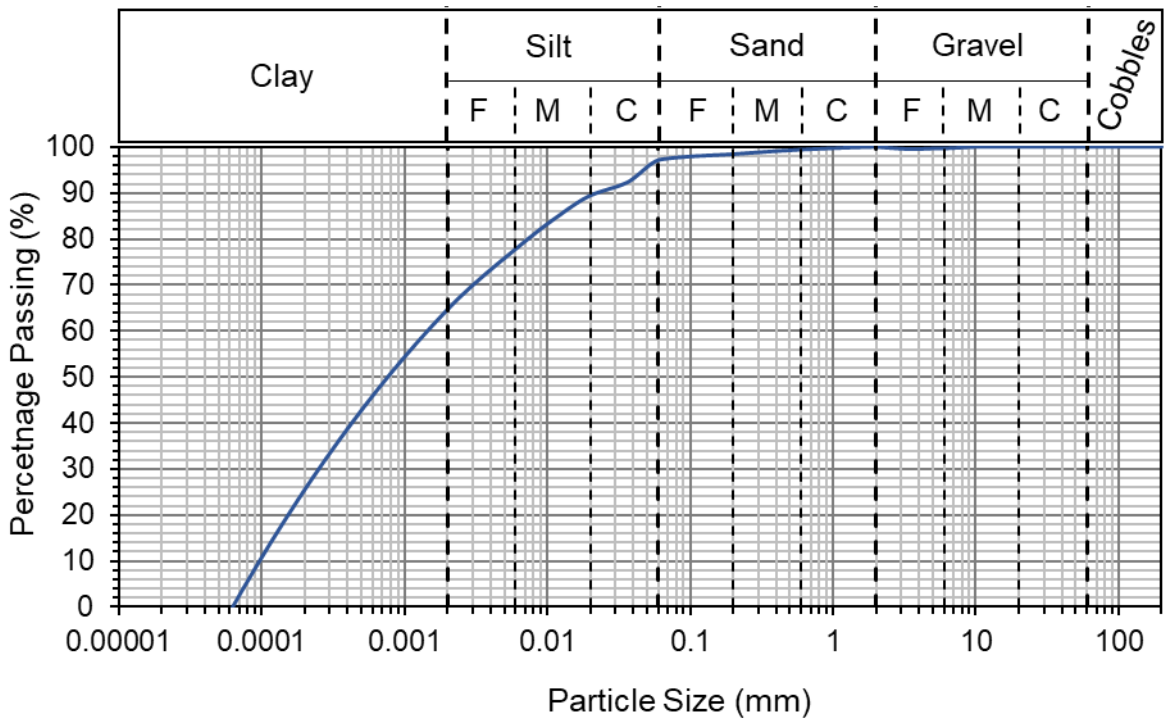

Figure 3.2: Particle size distribution (PSD) curve for the Ampthill Clay obtained via the wet sieving method (BS1377-2) and PARIO Automated Soil Particle Size Analysis.

The PARIO Automated Soil Particle Analysis was used to obtain the PSD curve's finer silt and clay fractions. Sample preparation followed the procedure outlined in BS1377-2 Section 9.4.5.1 to 9.4.6.2, creating a homogeneous suspension within a PARIO settling column. The PARIO device measures the sedimentation of soil particles in water over time, following the principles of the Integral Suspension Method (ISM) and Stokes' Law (Durner & Iden, 2021). A high-precision pressure sensor, positioned at a fixed depth within the suspension column, continuously measures the total pressure exerted by the soil-water mixture (Meter Group, 2021). This total pressure comprises the hydrostatic pressure from the water and the pressure contribution from suspended solids. As particles settle past the sensor, the concentration of suspended solids above it decreases, while the hydrostatic pressure remains constant. This results in a measurable drop in total pressure over time. Since total pressure is directly proportional to the suspension's effective density, PARIO interprets these changes to determine settling velocities and applies Stokes' Law to calculate equivalent particle diameters (Durner & Iden, 2021). This fully automated method produces a high-resolution, continuous PSD curve based on the calculated particle diameter ranges. The relative percentage of each grain size for Ampthill Clay is 65% clay, 31% silt, 3.2% sand and 0.8% gravel, with no cobbles or boulders recorded. The particle density was determined via BS1377-2 (British Standards, 1990) and yielded a value of 2.73 Mg/m^3.

Figure 3.3 presents the compaction curve for Ampthill Clay, achieved by following the Standard Proctor method using the 2.5 kg rammer as outlined in BS1377-4 (British Standards, 1990). The graph demonstrates an optimum moisture content of 26% and a maximum dry density of 1.52 Mg/m^3 for the Ampthill Clay. The measured curve has been interpolated from 35% to 50% gravimetric moisture content to predict dry density, as this is the as-compacted moisture content range of the Ampthill Clay used in the lysimeter experiments.

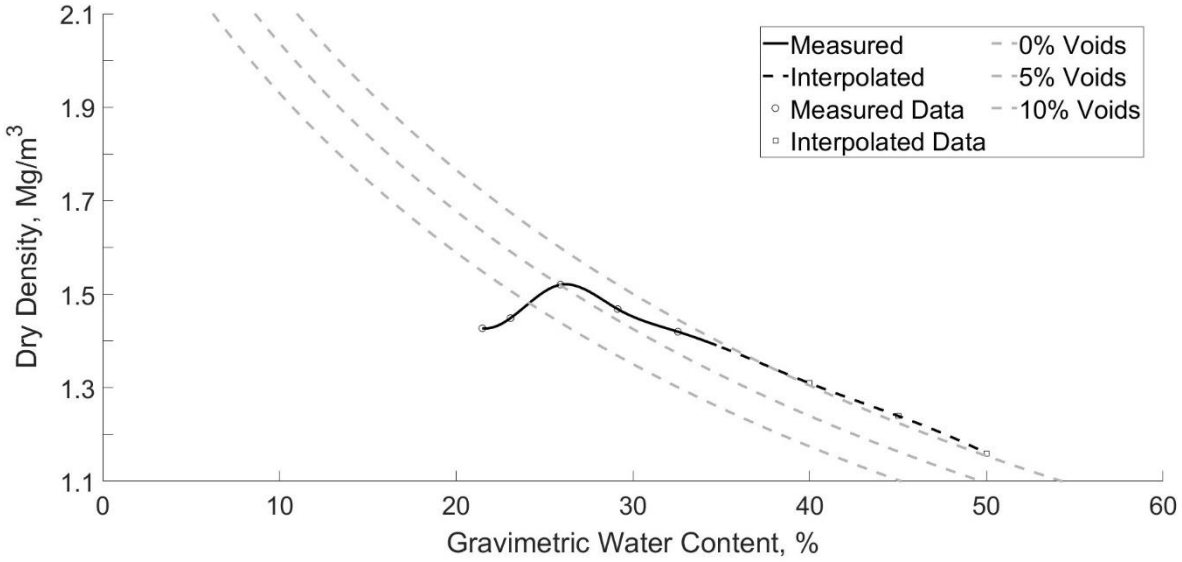

Figure 3.3: Compaction curve illustrating the relationship between dry density (Mg/m^3) and water content (%) for the Ampthill Clay following BS1377-4 (British Standards, 1990). The circle markers/solid line shows measured data, and interpolations are represented by the square markers/dashed line.

The plasticity of the Ampthill Clay was determined using the cone penetrometer method within BS1377-2 (British Standards, 1990). Liquid (w_L) and plastic (w_P) limits of 71% and 27% were calculated in this test, giving a plasticity index (I_P) of 44% for Ampthill Clay. These values define a clay of very high plasticity (CIV), according to the Casagrande Chart in Figure 3.4. Classifying the plasticity of the Ampthill Clay is important to determine the range of moisture contents over which the soil can change in volume without desiccation. This is related to the percentage and mineralogy of the clay minerals present in the soil. The higher the percentage of expansive clay minerals, the greater the plasticity index and degree of volume change that will occur.

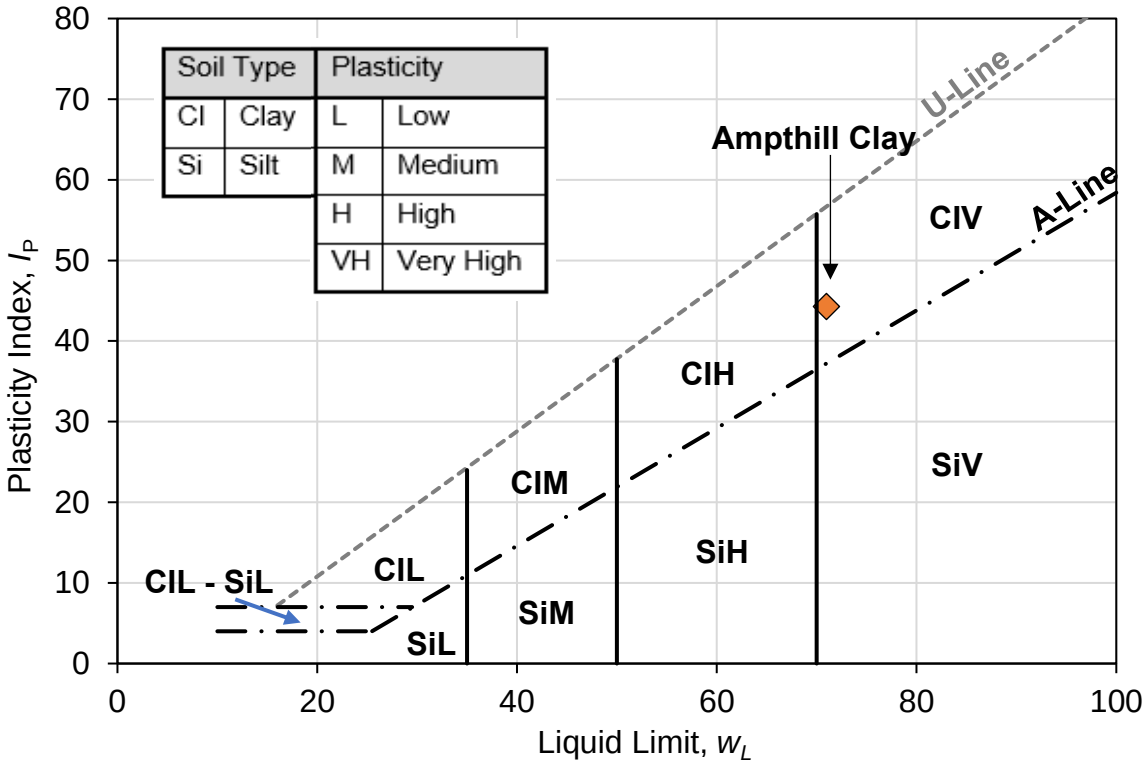

Figure 3.4: Casagrande Chart for the Ampthill Clay to classify the soil type and plasticity level, calculated using the procedure outlined in BS1377-2 (British Standards, 1990). The Ampthill Clay plots on the chart as a clay of very high plasticity.

To estimate the volume change potential of the Ampthill Clay, a linear shrinkage test was conducted following BS1377-2 (British Standards, 1990). A 16% and 9% average reduction in volume was recorded when placed within grease- and non-grease-lined moulds, respectively. This difference in volume change is attributed to the difference in frictional boundary conditions imposed between the mould and the clay sample. As discussed in Section 2.6.4, the influence of non-environmental boundary conditions should be considered in the experiment design as it could affect the rate and total shrinkage volume.

3.2.2 Laboratory Soil-Water Retention Curves

A soil-water retention curve (SWRC) defines the relationship between volumetric water content and suction for a particular soil. The SWRC is unique to each soil and reflects the permeability, storage potential and drainage characteristics for a pore network of a particular size, distribution, and connectivity. Therefore, the shape of the SWRC reflects the soil's hydro-mechanical properties, including hydraulic conductivity and shear strength. Consequently, changes in the curve's behaviour can represent improvement or deterioration to these hydro-mechanical properties, which govern the stability of an infrastructure embankment.

To develop a complete SWRC for the Ampthill Clay, a combination of two instruments from Meter Group was used – the HYPROP 2 and WP4C Dewpoint PotentiaMeter – for the wet and dry ends of the SWRC, respectively. The HYPROP 2 and WP4C have measurement ranges of -0.3 – 300 kPa ± 0.25 kPa and -5 – 300 MPa ± 1 %, respectively. Therefore, combining these two methods allowed the full range of water retention behaviour to be captured for the Ampthill Clay. It is noted, however, that a limitation of both of these methods is that they assume constant volume of the samples during drying. This may be appreciable for high-plasticity clays, where volume change (shrinkage) can occur even in the saturated to near-saturated range (i.e., at suctions below air-entry point). Reductions in the void ratio within this range alter the pore structure, influencing suction generation and initiating tensile stresses that lead to desiccation crack formation. Once air-entry is exceeded, the void ratio rapidly tends towards stabilisation, and volume change becomes less significant. The implications of this assumption will be discussed and examined throughout the thesis.

This test intends to obtain the preliminary soil water retention behaviour of the Ampthill Clay in a primitive state before placement within the lysimeter (Section 3.3) and cyclic environmental exposure. To enable comparison between laboratory and in-situ field SWRCs generated from the lysimeter slope (see Section 3.3.5), while acknowledging the limitations of the tests in the saturated range, Ampthill Clay was compacted within a proctor mould at 40% moisture content (average lysimeter slope moisture content) using the 2.5kg rammer method outlined in BS1377-4 (British Standards, 1990) and then extruded for sample preparation.

The HYPROP-2 uses the Simplified Evaporation Method (SEM*), shown in Figure 3.5. A sensor unit connected to a soil sample is placed on a balance to measure mass loss under exposure to atmospheric conditions at designated time intervals. Within the sensor unit are two tensio-shafts of different lengths that compute an average suction based on the pressure at the capillary contact between the water in the shafts and the soil. The moisture content at each time interval is then calculated by subtracting the mass of the equipment and dry soil from the total sample mass.

For the HYPROP-2 test, a 250 ml sample was taken from the prepared proctor compacted sample at 40% moisture content using a HYPROP ring with a cutting edge and sealed with plastic lids to inhibit evaporation. For measurement of a full drying cycle, the sample was firstly fully saturated under a vacuum with degassed water. Prior to conducting the test, the sensor unit and tension-shafts need to saturate under a

vacuum. This is to degas the water and prevent air from interfering with suction measurements. Once the sample and equipment are saturated, a tensio-shaft adapter is used to guide the coring of small holes into the sample, allowing the tensiometers and sensor unit to be attached. The complete unit is placed on and connected to an automated balance to take measurements and generate the SWRC's wet end.

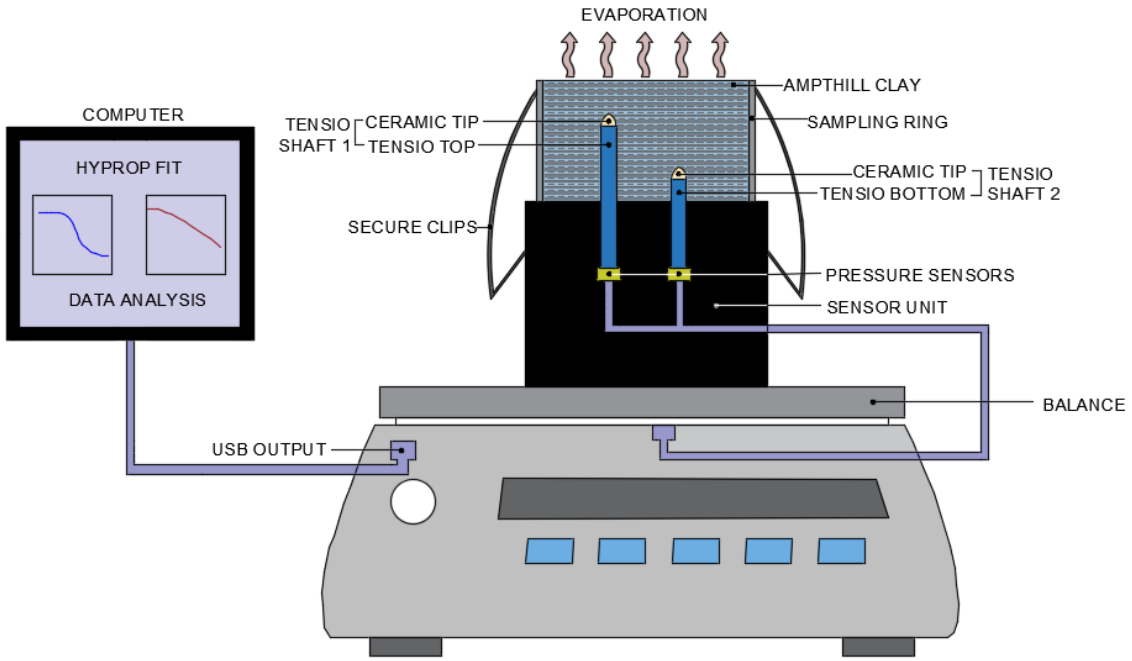

Figure 3.5: Schematic diagram of the HYPROP-2 components and setup for monitoring and data analysis.

For the dry end of the curve, a WP4C Dewpoint PotentiaMeter was used. A cylindrical core (37 mm diameter) was taken from the prepared proctor compacted sample at 40% moisture content and cut into 5 mm specimens for four stainless steel sample cups with lids to reduce pre-test moisture loss. To measure suction at various stages of a drying cycle, the lids were removed, and samples were dried to a pre-determined moisture content, which was calculated via sample mass. When the desired moisture content was reached, samples were sealed and allowed to equilibrate for 24 hours before being placed within the sealed chamber of the WP4C Dewpoint PotentiaMeter shown in Figure 3.6. A suction measurement for each moisture content was taken, and the process was repeated for lower moisture contents until the samples were air dry. The average suction of two samples was taken for each moisture content to improve measurement accuracy.

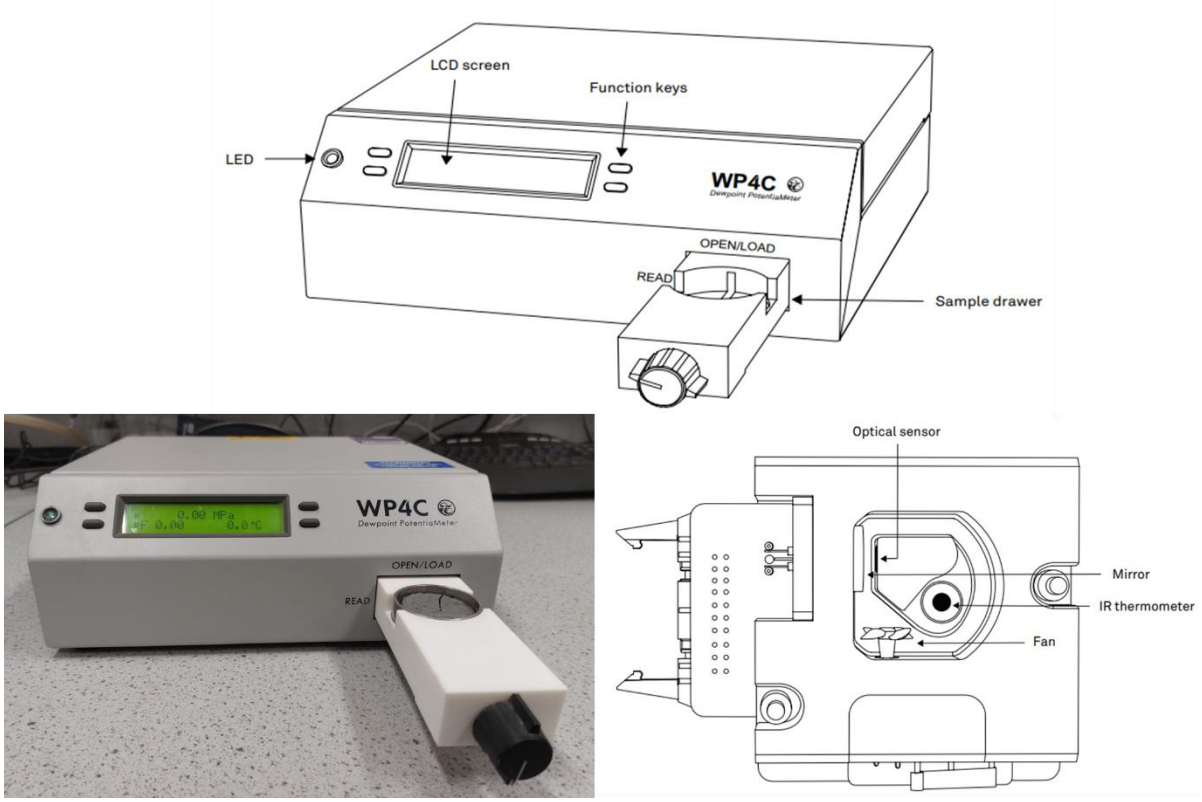

Figure 3.6: Labelled schematics taken from Meter Group (2024) showing the main components of the WP4C equipment are provided in (A) externally and (B) internally, with (C) demonstrating the loading of an Ampthill Clay sample into the sample drawer.

Within the sealed chamber, the WP4C Dewpoint PotentiaMeter uses the chilled-mirror dew point technique to measure the saturation vapour pressure of the air once in equilibrium with the soil sample at dew point temperature. For this, a photodetector uses light emittance to associate changes in the reflectance of a mirror with the first appearance of condensation. When equilibrium is reached, the suction of the sample (φ) and chamber air are the same, and can be calculated for the soil using Equation 3.1:

$$\varphi = \frac{RT}{M_w} \ln \frac{e_s(T_d)}{e_s(T_s)} \quad \textbf{3.1}$$

Where $e_s(T_d)$ and $e_s(T_s)$ are the saturation vapour pressure at dew point and sample temperature, respectively, as given by the WP4C measurement; R is the gas constant of 8.31 J/(mol×K); T is the temperature of the sample in Kelvin; M_w is the molecular mass of water.

To generate a SWRC across the full moisture content range for the Ampthill Clay, the results from the WP4C and HYPROP 2 tests were combined within the HYPROP-FIT

software. This software allows measured data to be fitted with hydraulic functions and the best fit for this data was the Fredlund-Xing method (Fredlund and Xing, 1994). The results are shown in Figure 3.7, and the contributions of each method are distinguished. As this study is mainly concerned with the suction generation capabilities of desiccated soil during drying, only the drying and not the wetting SWRC was determined. Given the methods used, the SWRC presented has been drawn without consideration of volume change in the soil. Therefore, fitting with the Fredlund-Xing model has been limited to beyond the air-entry value, where soil behaviour closely aligns with the HYPROP and WP4C method assumptions of minimal volume change.

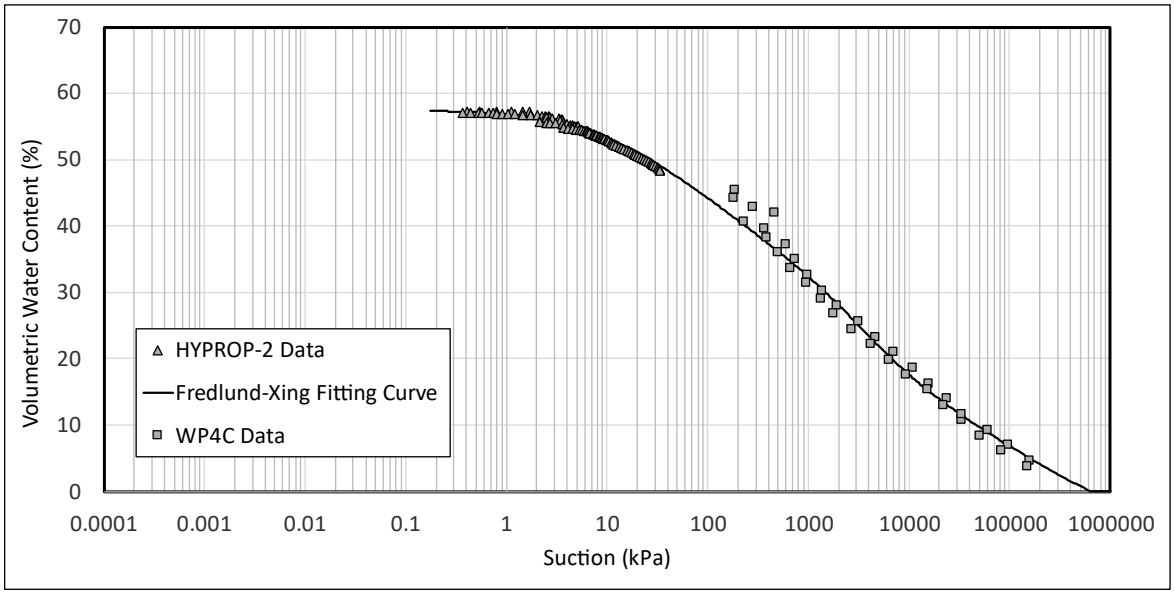

Figure 3.7: Soil water retention curve (SWRC) for the Ampthill Clay using the HYPROP-2 Data (triangle markers) and WP4C data (square markers). The curve was fitted using the Fredlund and Xing (1994) equation.

3.3 Lysimeter Study

As identified within the literature review (Section 2.6.6), a limited number of studies are available investigating desiccation-induced deterioration of infrastructure slopes at scales comparable to real-life assets. Small-scale laboratory tests cannot accurately replicate the environmental conditions and slope-scale hydrological processes that control desiccation and enhance slope deterioration. Additionally, the durations of these laboratory tests are usually too short for deterioration to be measurable. However, research methodologies on live assets are often restrictive due to the risk of disturbing transportation networks. Furthermore, isolating and controlling the parameter space affecting desiccation is difficult. To address these research gaps, an intermediate-scale infrastructure slope was designed to allow the rigour of laboratory-scale monitoring to be applied to a field-scale challenge. The following sections will

discuss the slope's design, construction, and instrumentation and detail the experimental methodologies applied over a 26-month monitoring period.

3.3.1 Slope Design and Construction

Figure 3.8 gives an as-built plan and side view of the intermediate-scale slope's setup, which was constructed within a 4.5 x 2 x 1.2 m outdoor lysimeter at the UKCRIC National Green Infrastructure Facility (NGIF), Newcastle University, United Kingdom. A lysimeter is a large-scale and self-contained measurement device used in this study to research and quantify the hydrological and desiccation crack properties of a large body of compacted clay. As shown in Figure 3.8 , the lysimeter slope was sectioned along its length axis into Side A, which remains the baseline control throughout the study, and Side B, which becomes the variant. Referred to throughout the thesis are the upper, lower and crest slope regions, the locations of which are also shown.

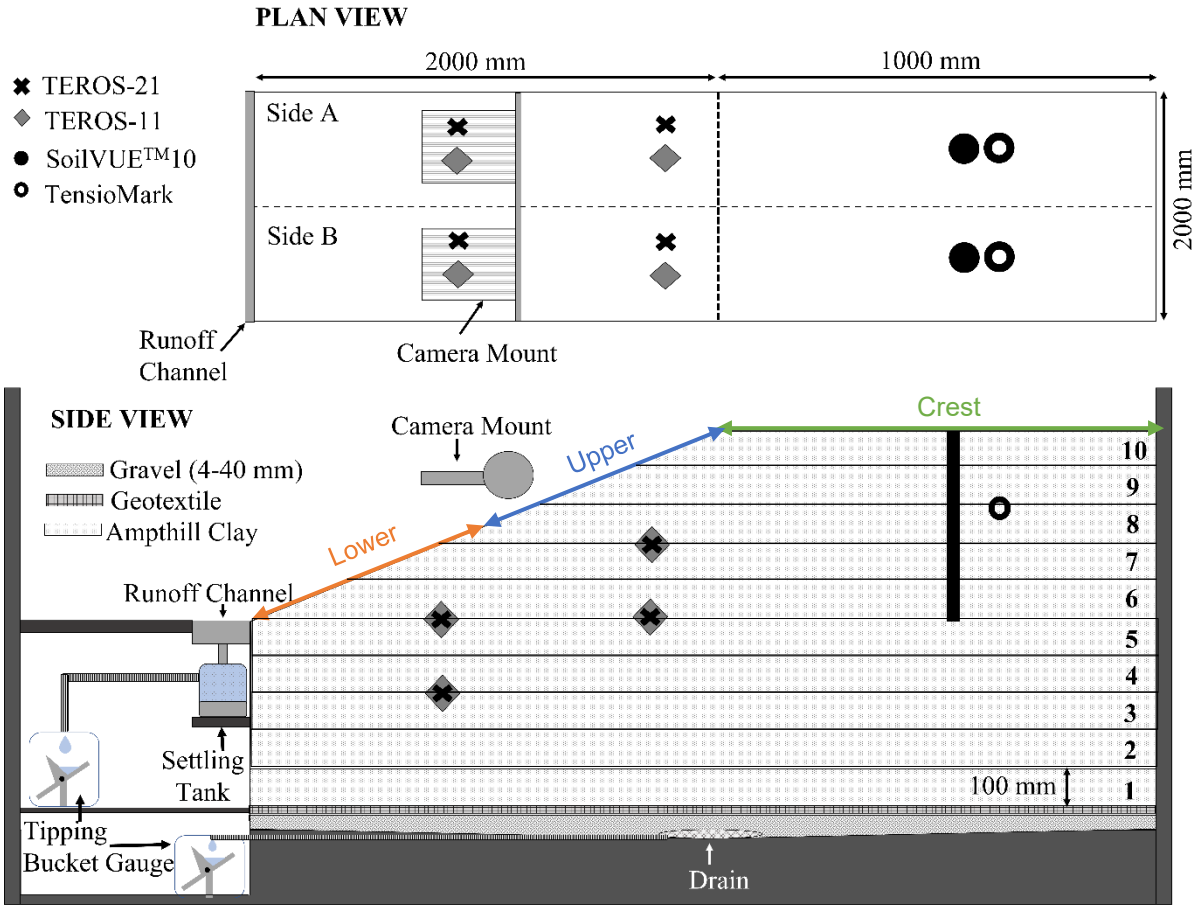

Figure 3.8: Plan view (upper) and side view (lower) of the lysimeter slope constructed of ten 100 mm compacted layers of Ampthill Clay fill, which lay above a geotextile and drainage layer. The locations of suction (TEROS-21 & TensioMark) and volumetric water content (TEROS-11 & SoilVUE™10) sensors are shown, and the camera mount for surface crack imaging. A runoff channel at the slope toe collected surface water and measured it using a tipping bucket gauge. The basal drain collected drainage flow; however, the connected tipping bucket malfunctioned during monitoring.

The slope body was constructed by compacting ten layers of Ampthill Clay, each 100 mm thick. All compaction of soil layers was done manually using earth rammers to minimise inclusion of large air voids. Post-compaction of each layer, moisture content-density (MD) ring samples were taken to determine their average dry density (Mg/m^3) and gravimetric moisture content (GMC) (%); the results are given in Figure 3.9. Compacting slightly wet of optimum moisture content is common practice in slope construction, to allow most of the clay swelling to occur prior to placement. However, due to the outdoor storage of Ampthill Clay in large bulk bags, the material was near saturation before its use in constructing the lysimeter slope.

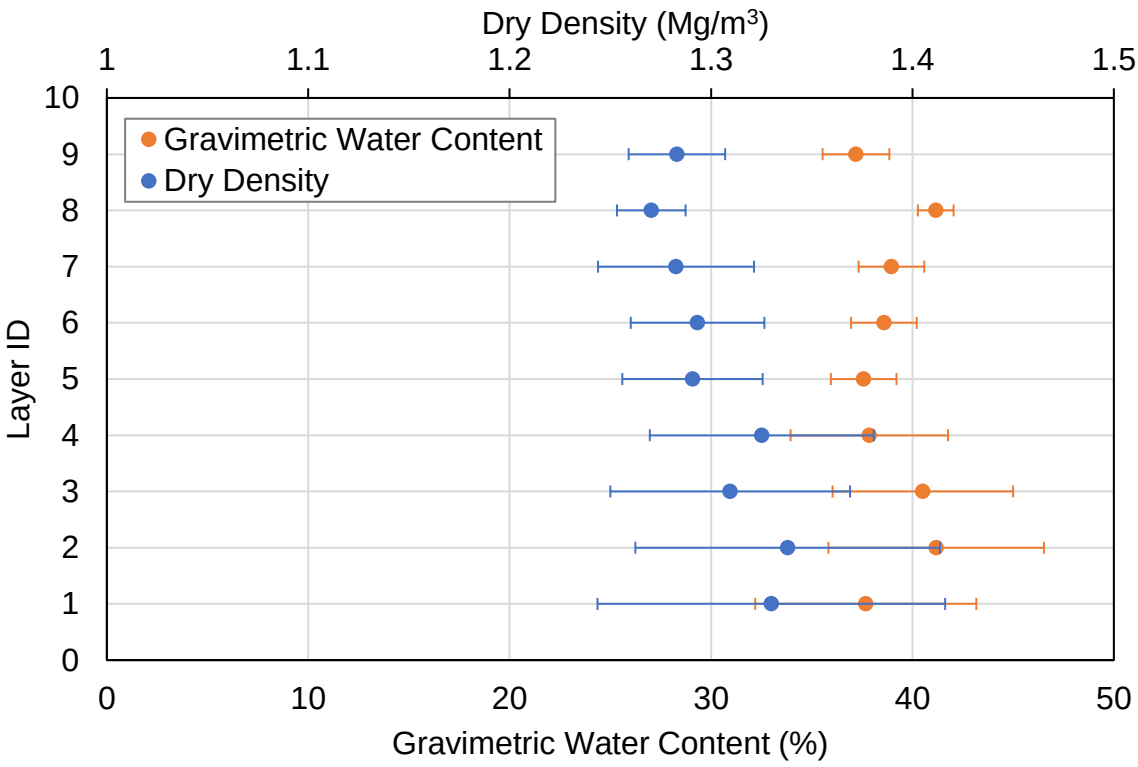

Figure 3.9: Plot of dry density (Mg/m3) and gravimetric moisture content (%) for each layer within the lysimeter slope given by moisture content-density (MD) ring samples. Refer to Figure 3.8 of layer ID references.

Given the substantial volume of clay required, pre-processing measures aimed at reducing particle size heterogeneity and achieving the desired moisture content and dry density were deemed impractical. Consequently, the Ampthill Clay was compacted to the maximum allowable extent, achieving an average GMC and dry density of 38% and 1.284 Mg/m^3, respectively. Comparing these values to the results in Figure 3.3, the Ampthill Clay was near saturation when compacted, achieving a dry density significantly below the optimum. These conditions, together with inherent soil heterogeneity, likely exacerbated the Ampthill Clay's high volumetric shrinkage and

desiccation crack potential during the initial drying phase. This observation presents a notable limitation to the experimental setup and warrants consideration when interpreting results.

The geometry of the slope consisted of a 1000 mm flat crest, which transitions into a 2000 mm slope with a 1:4 profile to facilitate runoff. From the crest to the toe of the slope, the thickness of Ampthill Clay tapers from 1000 mm to 500 mm. A photograph of the lysimeter slope immediately post-construction is provided in Figure 3.10.

Figure 3.10: Photograph of the lysimeter slope immediately post-construction, illustrating the slope geometry.

3.3.2 Sensor and Monitoring Equipment

To facilitate drainage from the slope, a permeable layer of 4 – 40 mm-sized gravel was placed at the lysimeter base, which reached a maximum depth of 100 mm above a centrally located drain. The lysimeter base was gently sloped to assist in channelling outflow through the central drain and into a 100 ml tipping bucket gauge where the number of 100 ml tips quantifies the outflow volume. However, this drain malfunctioned and was inaccessible to repair, and therefore, drainage outflow could not be quantified during these experiments. Figure 3.8 demonstrates a layer of permeable, needle-

punched, non-woven geotextile was installed above and below the gravel to prevent blockage of the drainage system by washout of fines from the slope above.

Two collector channels were installed at the toe of the slope to collect surface runoff for Sides A and B. The opening of the channels was level with the slope toe and hydrologically separated below the surface by a steel insert to capture surface flow only. From each channel, the runoff entered settling tanks to separate out any suspended solids washed out from the clay. The runoff was then routed into 100 ml tipping bucket gauges through an overflow pipe to quantify the volume.

Figure 3.8 shows sensor installation was identical for both sides of the lysimeter to allow comparison of measurements between the baseline control (Side A) and any applied variance (Side B). The choice of volumetric water content (VWC) and suction sensors reflected the research objectives, which were focused on identifying changes in slope hydrology resulting from desiccation cracking processes. Two different types of VWC and suction sensors were installed in the slope to compare and provide validation of the results they produced. TEROS-21 and TEROS-11 sensors, manufactured by Meter Group were centrally installed and spaced 200-mm apart at depths of 200- and 400-mm within both sides of the slope. Sensor installation in the was conducted concurrently with soil layer construction rather than emplacement post-construction to avoid introducing loosely compacted zones of lower strength where crack initiation could exploit. For the same reasons, no sensors were installed at the surface. The only exception was the SoilVUE^{TM} probe, which was augured into the crest region post-construction. While the grooved structure of the SoilVUE^{TM} sensors promotes improved contact with the surrounding soil, the installation increased the risk of air gaps forming compared to other slope sensors. This may compromise sensor-soil interface integrity as the soil changes in volume during drying.

The TEROS-21 sensor measures the soil suction using porous ceramic disks, which calculate water content via dielectric permittivity once equilibrium is reached with the surrounding solid matrix. As the SWRC of the ceramic disk can be pre-determined, suction can be calculated via the measured water content. The measurement range of the TEROS 21 for suction is 0 to 100,000 kPa, with a resolution of 0.kPa and measurement accuracy of 10% ± 2 kPa. Positive pressure cannot be recorded as the air entry point limits sensor performance. This was not seen as a limitation to this study as the deterioration mechanisms being investigated are driven by suction, not positive

pressures. Temperature in the range of -40°C to +60°C (0.1°C resolution, ±1°C accuracy) is also measured using a surface-mounted thermistor within the sensor.

To obtain volumetric water content (θ), the TEROS-11 generates an electromagnetic field to charge the sensor points by supplying a 70-MHz oscillating wave. The time taken to charge the sensor points to a certain value is directly proportional to the dielectric permittivity. This relationship outputs a raw (RAW) value, which can then be input into Equation 3.2 to calculate θ of the surrounding soil matrix:

$$\theta\left(\frac{m^3}{m^3}\right) = 3.879 \times 10^{-4} \times RAW - 0.6956 \quad \textbf{3.2}$$

The measurement range for the TEROS-11 is 0.00 – 0.70 m^3/m^3 with a resolution of 0.001 m^3/m^3 and accuracy of 0.03 m^3/m^3. Measurements of temperature (range -40°C to +60°C; resolution 0.1°; accuracy, ±1°C), using a thermistor, and electrical conductivity (range 0 – 20 dS/m (bulk); resolution 0.001 dS/m; accuracy ±5% + 0.01 dS/m from 0 – 10 dS/m & ± 8% from 10 20 dS/m) using two electrodes, were also taken by the TEROS-11.

A SoilVUE™10 sensor from Campbell Scientific was installed centrally on both sides of the slope crest following construction by augering a hole and inserting the probe to surface level. The augered hole was intentionally smaller than the outer diameter of the sensor, allowing the probe to be carefully threaded into place. This installation approach was designed to promote firm contact between the sensor and the surrounding soil matrix, thereby minimising the potential for air gaps that could compromise data accuracy. Despite this, disturbing the particle cohesion within Ampthill Clay fill post-construction made this sensor area more vulnerable to desiccation crack initiation. However, soil was also hand-compacted around the sensor post-installation to minimise this risk and prevent sensor damage. The SoilVUE™10 is a multiparameter probe which measures θ using the time-domain reflectometry (TDR) method across sensors located within six helical waveguides at 50-, 100-, 200-, 300-, 400-, and 500-mm depth. The TDR method relates the transmission velocity of an electromagnetic signal across a helical waveguide to the dielectric permittivity of the solid matrix, from which θ is calculated. The measurement range is 0 to 100% with a ± 1.5% accuracy. Electrical conductivity (range 0 to 10 dS/m, ± 5% accuracy) and soil temperature (range -30°C and +40°C, ± 0.15°C accuracy) are also measured by the SoilVUE™10.

To measure soil suction in the crest, a Tensiomark was installed at 200 mm depth in both Side A and B and separated from the SoilVUE^{TM}10 by 200 mm. A porous ceramic tip within the Tensiomark equilibrates with the water in the soil matrix to measure its heat capacitance. The Tensiomark measures soil suction based on the thermal storage properties of the soil, with units of pF, which is the logarithmic measure of soil suction in centimetres of water column (cm H_2O). Conversion of units to kPa can then be carried out using Equation 3.3:

$$kPa = \frac{10^{pF}}{10} \qquad \textbf{3.3}$$

The measurement range is pF 0 to pF 7.0 or 0.1 to 1,000,000 kPa. Temperature is also measured between -40^{o}C and +80^{o}C.

To collectively record all lysimeter slope data, the GP2 Data Logger and Controller from Delta-T services were chosen. Simultaneous logging of several SDI-12 sensors was required, and the GP2 Data Logger provided this with twelve compatible channels. The logger was set to take hourly measurements for all sensors within the lysimeter slope.

To track changes in surface desiccation, two fixed camera mounts were installed mid-slope onto a structural pole over Sides A and B. Photographs were taken daily and qualitatively assessed to establish key changes in cracking in response to different temporal and severity scales of environmental cycling. The slope was also instrumented with the Mobotix S16 DualFlex thermal imaging camera which allowed the surface temperature of the lysimeter slope to be captured every hour. This camera had a Noise Equivalent Temperature Difference (NETD) of 50 mK and a maximum of 79 mK, operating within the long-wave infrared (LWIR) range of 7.5 to 13.5 μm. Such specifications allowed temperature differences of 0.05^{o}C or greater to be detected. A raw CSV file is produced, which was then processed using Python in Spyder. This runs the following steps to produce a measurement of surface temperature within a defined region of interest:

1. Loads the CSV file.
2. Identifies coordinates of selected non-cracked surfaces on Side A (bare) and Side B (vegetated) regions of the lysimeter slope.
3. Isolation of pixels within defined coordinates.
4. Extraction of thermal data from CSV file for isolated coordinates.

5. Average temperature for all isolated pixels calculated.
6. Export to CSV file.

This methodology was utilised to measure differences in the temporal evolution of surface temperature between Sides A and B after installation of the faux grass canopy (see Section 3.3.7).

Finally, a Weather Transmitter (WXT530 Series) from Vaisala was installed onsite within an adjacent lysimeter and gave hourly readings of rainfall (mm), wind speed (m/s) and direction (°), air temperature (°C), relative humidity (%), solar radiation (W/m^2) and air pressure (hPa).

3.3.3 Introduction to Experimental Programme

Within this section, the experimental programme carried out using the setup described in Section 3.3.1 and 3.3.2 is outlined and spans a monitoring period of 26 months. A continuous catalogue of hydrological and extensive surface desiccation crack data was collated within this time frame. From this, relationships between the two datasets were explored to address the overarching aim of this research. The procedures followed to attain this data will be outlined below.

A series of modifications were applied to the lysimeter slope during the monitoring period. Firstly, simulated storm events which applied high-intensity rainfall with an uplift incorporated for climate change projections were applied in 2022 and again in 2023 to a progressively deteriorated slope. The procedures adopted for investigating the role of depth, duration, intensity, and frequency of rainfall events, as well as antecedent moisture content and cracking conditions at the onset of a storm, are detailed below. These experiments are aimed at addressing the primary objectives set by OB1B and OB2B. Secondly, active monitoring of the lysimeter highlighted that varying parameters within the Penman-Monteith framework (Equation 2.3) by altering the physical and environmental boundary conditions can instigate heterogeneity in crack formation. Therefore, a methodology was devised to investigate these effects more thoroughly by installing a faux grass canopy over half the lysimeter slope. The impacts of the structural aspects of a canopy only on slope hydrology and desiccation were subsequently analysed.

This section also provides justifications for designing a supplementary laboratory study. The primary purpose of this study is to investigate lysimeter observations in finer detail. This includes isolating the effects of a range of construction- and environmental-

based parameters which influence evaporation and desiccation through the Penman-Monteith (1965) framework to address OB3.

3.3.4 Hydrological Monitoring

As desiccation cracking is a dynamic, weather-dependent process, it can facilitate temporary and highly variable increases in infiltration. For an inherently impermeable clay, this means changes to soil hydromechanical properties to allow faster and deeper propagation of wetting fronts and positive pore water pressures. Section 2.6.6 highlighted the limited knowledge available on quantifying the evolution of these hydrological changes due to their complexity. Therefore, OB2 was set to address this research gap and focus on whether the lysimeter slope's short- and long-term hydrological monitoring could detect desiccation-induced changes in soil hydro-mechanical properties. The characteristics of these changes and whether they were cautionary precursors to desiccation-induced deterioration were also investigated.

Hydrological monitoring was carried out for the lysimeter slope using the volumetric water content and suction sensors described in Section 3.3.2 as cyclic drying and wetting can be identified through variation in these parameters. Real-time, data collection from these sensors at 1-hour intervals over a 26-month monitoring period was carried out. This allowed a realistic range of environmental conditions to be analysed, with the hydrological response under antecedent weather conditions and natural extremes of wetting and drying captured. The collated data was compared at many temporal scales – daily, over one or numerous dry-wet cycles, monthly, seasonally, and annually. Quantification of daily weather conditions, as well as the dry-wet and seasonal scale cycles applied to the slope, was carried out using the continuous dataset of meteorological data provided by the on-site weather station.

Soil hydro-mechanical properties – which control slope stability – can be estimated from the magnitude and rate of change of volumetric water content and suction readings, given by the SWRC. As shown in Figure 3.8, volumetric water content and suction sensors were co-located at the same depths throughout the slope to track temporal and spatial changes in soil water retention behaviour. Results were annually collated using data from the summer season scale to specifically establish whether the initial stages of hydro-mechanical deterioration were occurring. More details on the process to obtain these in-situ SWRCs are given in Section 3.3.5. Continuous monitoring of moisture changes, rainfall, and runoff provided insight into potential variation in the lysimeter slope’s storage capacity with changes in its desiccated state.

Soil temperature was utilised as a proxy for evaporation front propagation, as were substantial changes in moisture content and gain of suction.

Desiccation cracks occur predominantly within the shallow subsurface “active zone” of a slope, as illustrated in Figure 3.11 (Tang et al., 2018a). The shallow active zone exhibits greater cyclic variations in moisture content and volume change, forming a weathered zone of higher porosity and weakened mechanical strength through time (Stirling et al., 2021; Briggs et al., 2023). Figure 3.11 attributes this behaviour to soil-atmosphere-vegetation interactions, where the soil is directly exposed to the prevailing environmental conditions, as well as the water demands of the vegetation it typically supports. As a result, greater evapotranspiration in the shallow active zone occurs, making it inherently more prone to high suction gradients and desiccation crack formation. The effects of this are likely to be observed in changes in shallow subsurface hydrological regimes, which are indicative of microstructural deterioration.

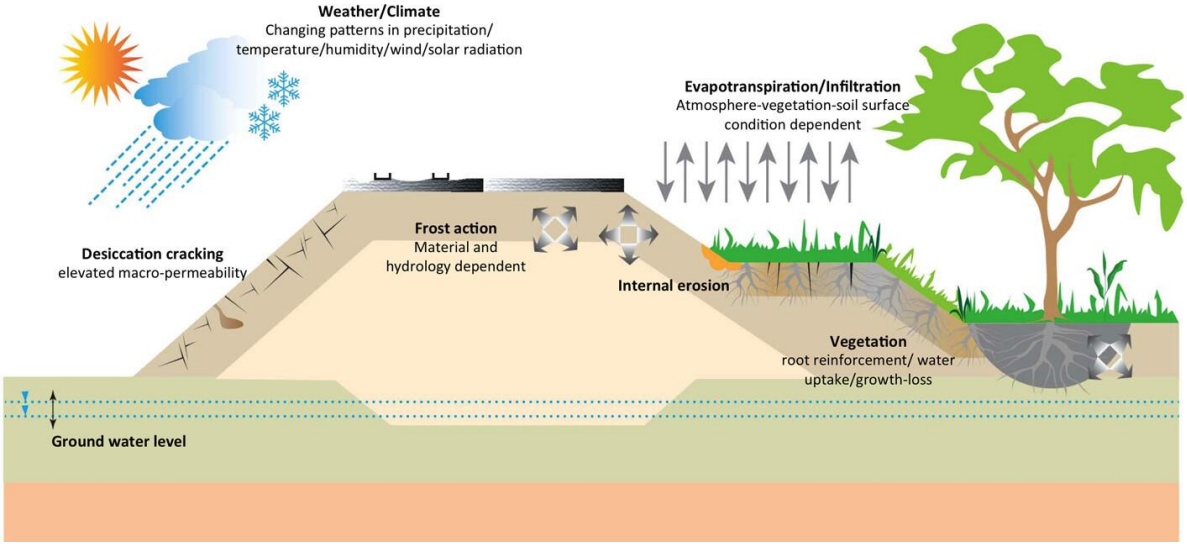

Figure 3.11: Schematic from Tang et al (2018) demonstrating the soil-atmosphere-vegetation interactions which place the shallow active zone (dark brown) at greater risk of cyclic changes in moisture content, volume and desiccation crack formation,

Therefore, VWC and suction sensors were installed at regular intervals through the active zone (upper 500 mm), to allow tracking of the temporal and spatial progression of this weathered region through the slope. Additionally, the movement of water fluxes during rainfall events of different durations, magnitudes and intensities was visualised by recording the reaction time at each sensor depth. Similarly, the intensity of drying events was determined using the same process. Reaction depth during drying and wetting was also used as a proxy for the depth and intensity of surface desiccation cracks.

To map infiltration and drainage patterns across the slope, VWC and suction sensors were distributed across the crest, upper, and lower regions (see Figure 3.8). This allowed results to be compared, and any relationships between slope locality and wetting and drying gradients, environmental exposure, and rate of deterioration were determined. This information may indicate that the slope regions are at a greater risk of desiccation-induced instability.

3.3.5 Determination of In-situ SWRCs from Lysimeter Data

As discussed in Section 3.3.4 changes in soil-water retention behaviour over successive dry-wet and crack formation cycles can be indicative of deterioration in soil hydro-mechanical properties (Stirling et al., 2021; Briggs et al., 2023). This deterioration is irreversible, making it crucial to quantify for assessing the short-term and projecting the long-term stability of infrastructure slopes.

To establish a set of in-situ SWRCs for the lysimeter slope, suction and VWC sensors were co-located at the same depth, 200 mm apart (see Figure 3.8). Across the 26-month monitoring period, two major drying cycles, in which significant suction was generated, were identified. Drying Cycle 1 (DC1) was established post-construction in July 2021, and ended at the onset of a series of intense, natural rainfall events in September 2021. The second drying cycle (DC2) was initiated in April 2022 and ended in August 2022 at the onset of simulated storm events. No drying cycle was established in 2023, the reasons and implications for this will be discussed in Chapter 4. To reduce noise in the dataset, the suction and VWC measurements were filtered to extract every fourth value from a set of 20. This process was carried out for the upper and lower slope at 200- and 400-mm depth as well as at 200-mm within the slope crest. The filtered dataset was then input into the HYPROP-FIT software discussed in Section 3.2.2 where the Fredlund-Xing (1994) hydraulic function was fitted to the observations.

All field SWRCs generated were then compared with those obtained using laboratory methods (Section 3.2.2). Specifically, any changes in the soil air entry value, saturated water content, and gradient of the de-saturation curve were noted.

3.3.6 Storm Design and Implementation

Sections 3.3.3 and 3.3.4 detailed the daily hydrological and desiccation crack monitoring of the lysimeter slope under natural climatic conditions. However, understanding the long-term hydrological evolution of a desiccated slope, particularly under weather extremes introduced by climate change, is also sought in the objectives

of this research. The UKCP18 (discussed in Section 2.5.5), suggests more frequent, high-intensity summer rainfall events will enable greater shrink-swell subsidence on infrastructure slopes by exploiting the increased crack prevalence and intensity formed under hotter, drier conditions. This is highlighted in the UKCP18 shrink-swell risk maps previously presented in Figure 3.1C and 3.1D. The severity and consequences of the slope's hydrological response during summer convective storms will depend on crack intensity, as well as the depth, duration, intensity, and frequency of rainfall these extreme events impose. After one or more events, deterioration may be visible through (1) swelling clay and loss of strength (Stirling et al., 2021; Briggs et al., 2023); (2) deeper and faster propagation of wetting fronts and sustained positive pore-water pressures (Hughes et al., 2009; Powrie & Smethurst, 2019; Kandalai et al., 2023); (3) erosional deterioration from fine washout, scour and detachment of desiccated blocks (Perry et al., 2003; Mair, 2021).

A requirement for any development consent order submitted for infrastructure projects, including road and rail embankments, is a flood risk assessment (EA, 2014). This assessment must demonstrate that runoff generated by a 1% annual exceedance (1 in 100 year) storm event can be effectively managed on-site without compromising environmental and structural integrity (EA, 2016). To help with the site-specific design of a 1% annual exceedance storm, the UK Centre for Ecology and Hydrology (UKCEH) provide the FEH Web Service, which is based on the guidance published within the Flood Estimation Handbook (FEH). The FEH Web Service generates depth-duration-frequency (DDF) curves at a 1km resolution, which specify the rainfall depth for a design storm depending on its duration and return period. The DDF model projections are based on the duration and frequency of historic rainfall data spanning 1881 to 2020. DDF curves can be generated for design storms with durations between 1 and 192 hours and return periods of 1 to 100,000 years, depending on the design life of the infrastructure project. The DDF curves formulated for a site located at the NGIF are presented in Figure 3.12, and rainfall depths for 0 to 24-hour storm durations for return periods between 2 and 200 years are detailed. Overall, the greater the event duration and return period, the higher the rainfall total that must be applied for a design storm.

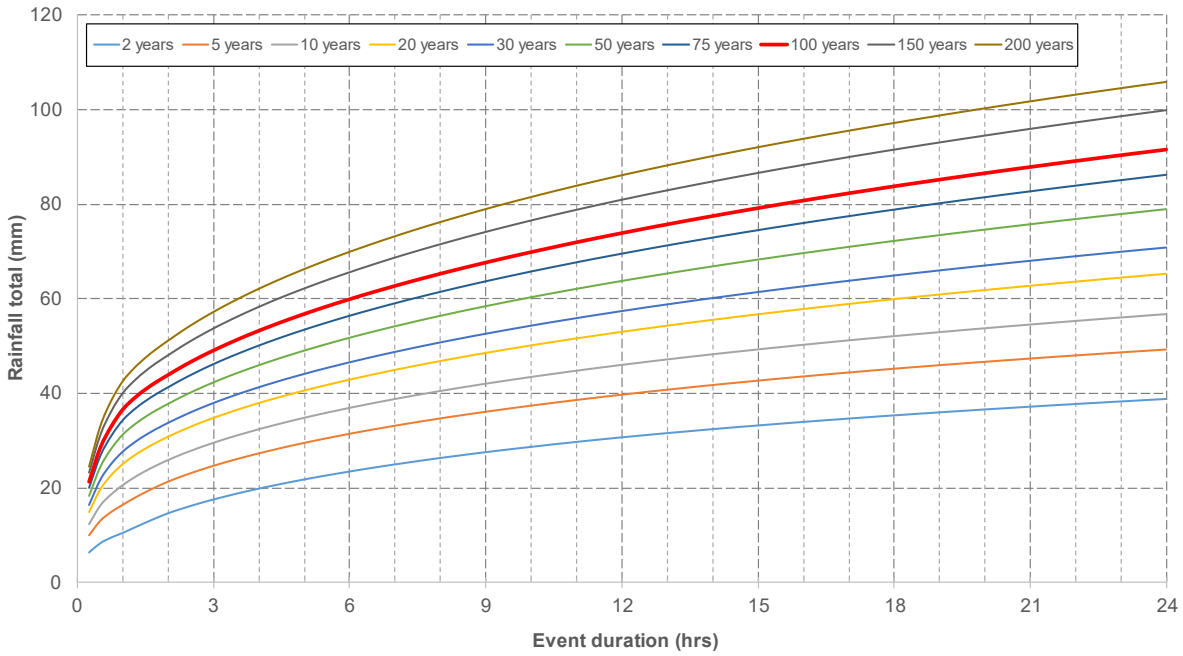

Figure 3.12: DDF (depth-duration-frequency) curves for a site located at the National Green Infrastructure Facility (NGIF). The range spans storm durations from 0 to 24 hours and return periods of 2 to 200 years.

The DDF curves in Figure 3.12 have no allowance for uplift in rainfall contributed by climate change, which the EA requires to be included in flood risk assessments. The EA guidance on the percentage uplift to be applied to peak rainfall allowances for a 1% annual exceedance rainfall event is provided in Table 3.1. Allowances for two epochs– 2050s and 2070s – are given depending on the expected lifetime of a development. Infrastructure slopes are designed to operate in excess of 40 years; therefore, the 2070s epoch was chosen for the lysimeter slope. The uplift value at the time of application was 40%; however, this has since been increased to 45% (Met Office, 2024). This change was not incorporated into the rainfall simulations conducted after this change to ensure consistency. The DDF curves were then updated by adding this 40% uplift to the rainfall totals, as illustrated in Figure 3.13.

Table 3.1: Tyne Management Catchment peak rainfall allowances for a 1% annual exceedance rainfall event (adapted from Met Office, 2024). Allowances for two Epochs—2050s and 2070s—are given and depend on the expected lifecycle of the proposed development. The upper-end allowance for the 2070s epoch, which was 40% at the time of experiment design, was chosen for this study.

Epoch	Central allowance	Upper-end allowance
2050s	25%	40%
2070s	35%	40% (now 45%)
*Use '2050s' for development with a lifetime up to 2060 and use the '2070s' epoch for development with a lifetime between 2061 and 2125.		

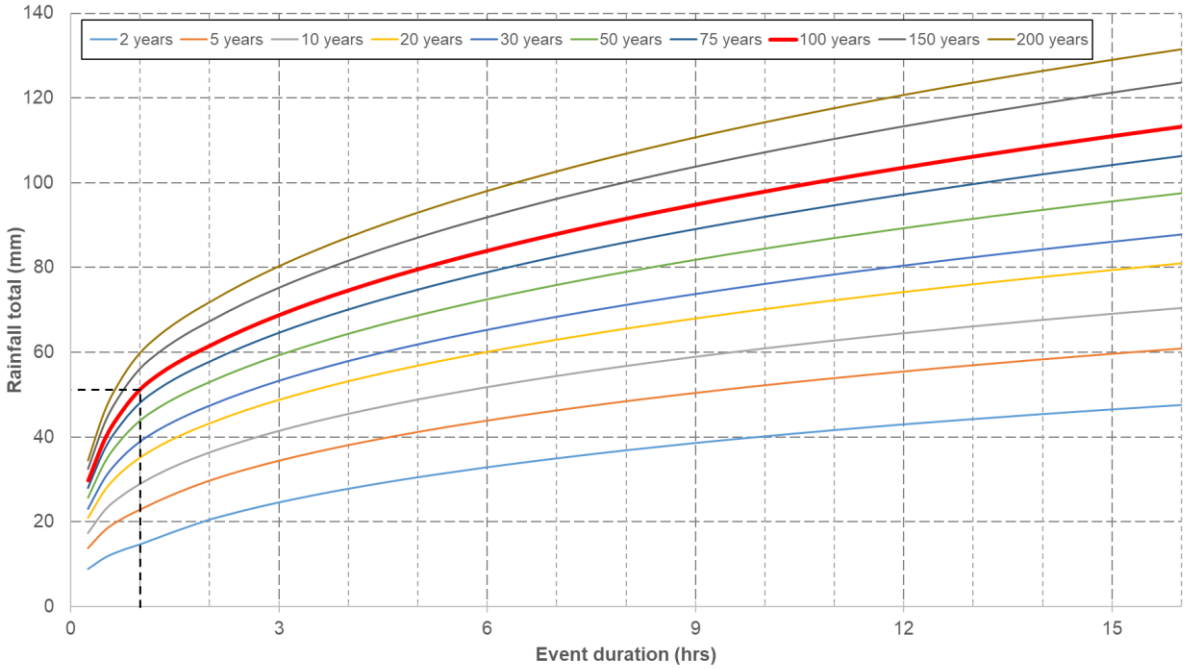

Figure 3.13: DDF (depth-duration-frequency) curves for a site located at the National Green Infrastructure Facility (NGIF) with an added 40% climate change uplift. The storm range spans 0-to-24-hour durations and return periods of 2 to 200 years. The black dashed line indicates the rainfall total (mm) for the chosen 1-hour storm during a 1% annual exceedance event, equalling 52 mm.

A 100-year return period plus a 40% uplift for climate change was chosen for the design storms applied to the lysimeter slope as suggested by the EA guidance. An event duration of 1 hour was selected based on the logistical limitations of water supply to the rainfall simulator. From Figure 3.13, this is equivalent to 52 mm of total rainfall, which was supplied to the slope via 102, evenly spaced, drip nozzles, each with an outflow rate of 2L/hour. As illustrated in Figure 3.14A, the nozzles were attached to a pipe network secured to a 2 x 2 m steel frame. Pre-deployment tests of the setup,

(A)

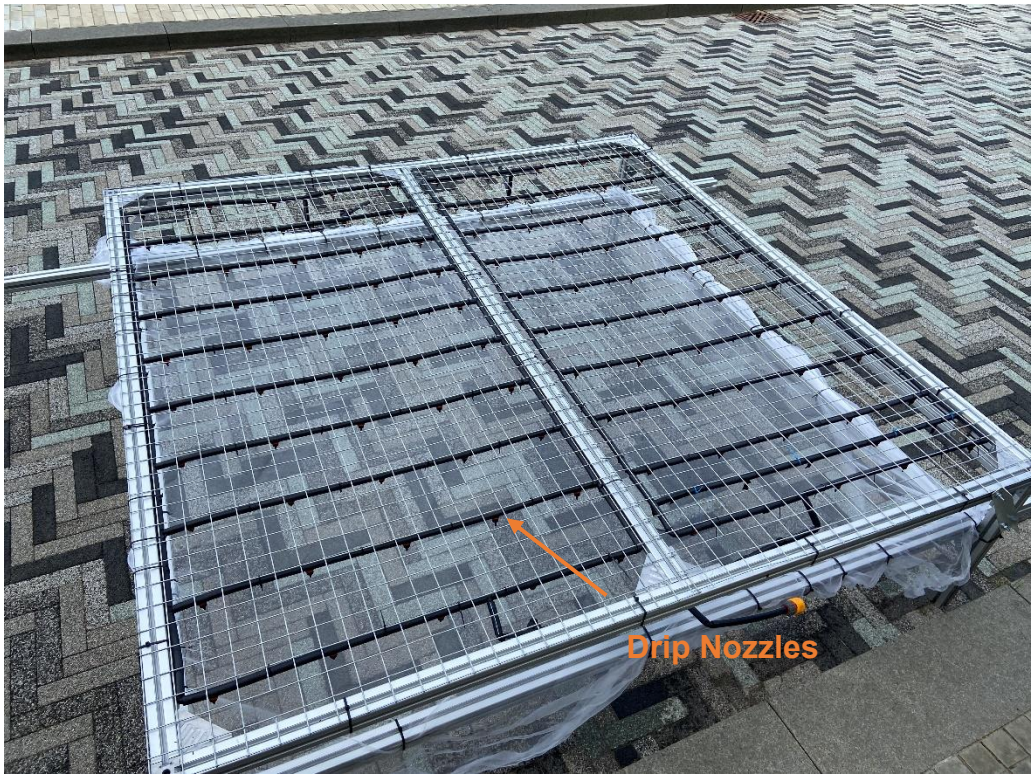

(B)

Figure 3.14: (A) Photograph of the rainfall simulator demonstrating the 102 drip nozzles fed by a pipe network and secured to a 2 x 2 m steel frame, and (B) Photograph illustrating the rainfall simulator deployed over the crest and top region of the upper slope.

which captured and measured the outflow volume generated in one hour, confirmed the design storm specifications were met. The rainfall simulator covered the crest and upper 1-metre of the slope to prevent direct filling of the runoff channels, shown in Figure 3.14B.

It should be noted that the FEH specifies that the geometry of storm profiles should be symmetric, single-peaked, and bell-shaped, which reflects reaching the maximum intensity in the middle of the storm, as illustrated by the 50% summer hyetograph in Figure 3.15. Adopting this storm profile involves varying the flow rate over the storm duration, which was beyond the capabilities of the rainfall simulator used in this experiment. Therefore, a constant intensity of 2L/h was applied, removing the peak from the hyetograph in Figure 3.15 yet still allowing a significant volume of rainfall to be applied over a short duration.

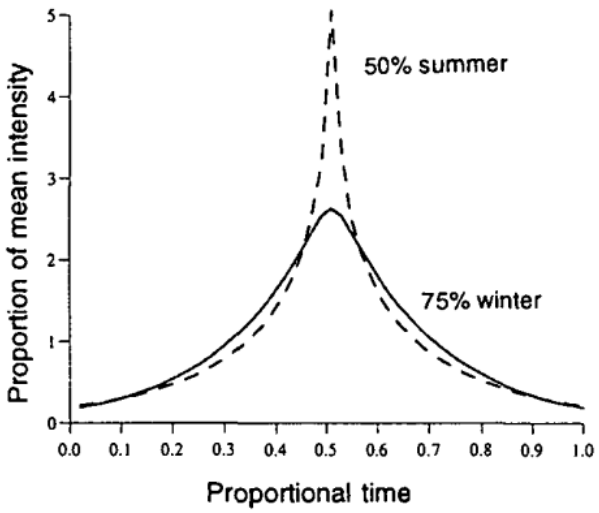

Figure 3.15: A hyetograph illustrating the recommended design storm profiles for a summer and winter event extracted from the Flood Estimation Handbook (FEH) (Faulkner, 1999).

In total six design storms with the above specifications were applied to the lysimeter slope using the rainfall simulator. Three storms, each one week apart, were applied from 23/08/2022 until 09/09/2022 and were repeated the following year between 26/05/2023 and 09/06/2023. Photographs of a fixed frame were taken at 1-minute intervals to capture the change in crack intensity through the storm application. Applying three successive simulated storms allowed the impacts of storm frequency on desiccated slopes to be assessed. The phase of primary drying, suction and crack generation within infrastructure slopes has been observed to begin in the spring (April/May) and end at the transition into Autumn (August/September) (Yu et al., 2021).

Therefore, applying the rainfall simulations at these key seasonal boundaries allowed the impact of extreme storm events on these transitions to be investigated. Additionally, as there was no isolation from the natural climatic conditions during the simulations, each storm was applied to different antecedent soil conditions. This allowed the role of initial moisture content and desiccated state at the onset of extreme storms to be explored. Furthermore, repeating these storms in 2023 allowed the response of a progressively more deteriorated slope to storm events to be analysed.

3.3.7 Faux Grass Canopy

Daily monitoring of the lysimeter slope yielded real-time data that informed subsequent phases of experimental design. Desiccation crack monitoring demonstrated the important influence of localised variations in environmental exposure. For example, the interaction between the sun's daily migration and surrounding buildings led to variable solar exposure in certain slope regions, resulting in spatially variable desiccation cracking. These observations highlighted the need for further investigation into how environmental shading influences soil temperature gradients, moisture distribution, and suction within slopes, as these factors critically affect crack development.

In real infrastructure slopes, vegetation canopies, particularly grass, often provide shading, which moderates the energy and moisture exchange at the soil-atmosphere interface. However, modelling the interactions between vegetation and desiccation processes is inherently complex and remains poorly understood. Introducing live vegetation into the lysimeter would have added dynamic processes like root water uptake, transpiration, mechanical reinforcement, and variable effects on energy balance and airflow. While this is more realistic, it would significantly increase system variability and require advanced modelling to interpret results reliably. Instead, a faux grass canopy was implemented over Side B of the lysimeter slope. The objective was not to replicate the full physiological processes of a real grass canopy (e.g., transpiration and root uptake), but to approximate key structural modifications to soil boundary conditions typically imposed by vegetation, such as radiative shading, wind sheltering, and rainfall attenuation.

Although the Penman-Monteith (1965) equation (Equation 2.3) applies similarly to both bare soil and vegetated surfaces, treating evaporation and transpiration as energy- and aerodynamic-driven processes, the location and nature of water loss differ. Evaporation occurs directly from the soil surface, whereas transpiration involves water loss through plant leaves. Therefore, when dividing the model slope into Side A (bare)

and Side B (faux grass), the former more accurately represents the natural evaporation conditions of vegetated slopes by allowing direct soil surface evaporation. Conversely, the faux grass serves only as a simplified tool to reduce two key drivers of evaporation as per Equation 2.3 from Penman-Monteith (1965): incoming solar radiation and near-surface air turbulence (aerodynamic resistance and conductance). Additionally, it provides rainfall attenuation, playing a critical role in controlling the rate of dry-wet cycling, which drives crack development. To summarise, the goal of the faux canopy experiment was to simply isolate and study these boundary condition effects, not to fully simulate the hydrological behaviour of a live vegetative canopy.

The faux grass canopy installed over Side B on April 20th 2023 is illustrated in Figure 3.16. A wooden frame was constructed to suspend the faux grass canopy 30 mm above the slope's surface. This was to ensure the investigation was isolated to the structural effects of a vegetation canopy on the imposing boundary conditions. The wooden frame was built in two halves – one which matched the dimensions of the flat crest (1000 mm x 500 mm) and the other for the sloped (2200 mm x 500 mm) section. Each half consisted of ten, 25- by 40-mm wooden slats, each spaced 75 mm apart and supported every 500 mm by a metal rod. The two halves were joined together at the change in slope using a metal rod, which enabled the frame to pivot to approximately 26^{o} – i.e., the angle of the slope surface.

For the vegetation, bundles of artificial grass, similar to natural grass geometry but whose canopy structure was notably more simplistic, were obtained. A bundle of faux grass was secured using sealant into holes that were drilled every 100 mm along the length of the wooden slats. To give the full coverage appearance of natural grass, the faux grass on every second wooden slat was offset by 50 mm to facilitate sufficient canopy coverage . The wooden frame was attached to two structural beams to secure it within the lysimeter – one above the crest and the other beyond the toe. The hydrological and desiccation crack monitoring continued post-installation of the faux grass canopy. Side A became the control to which the results from the changes implemented on Side B were compared. A photograph which visualises the faux grass canopy's final placement on Side B of the lysimeter slope is given in Figure 3.17.

.

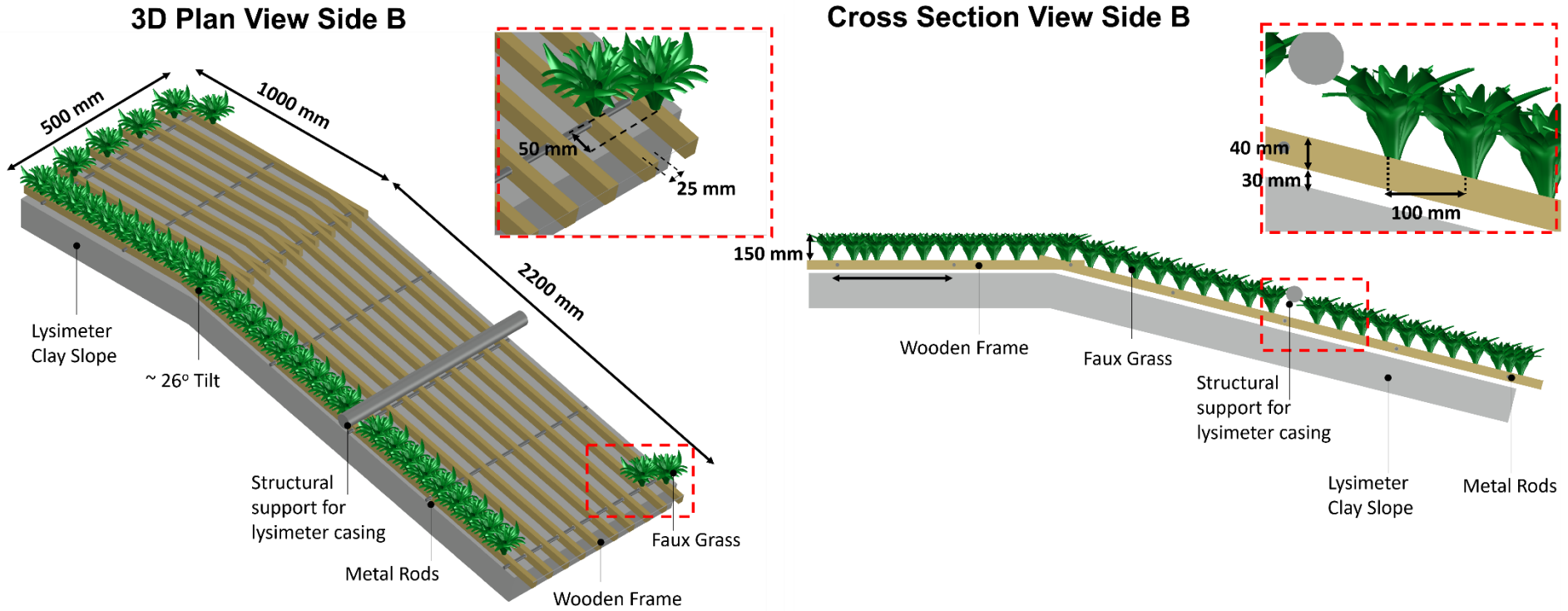

Figure 3.16: (A) 3D plan view of the method of faux grass installation on the wooden frame that was installed over Side B of the lysimeter slope. The location of the metal rods is indicated on the figure and the zoomed insert illustrating the 50 mm offset between faux grass bundles on adjacent slats to avoid gaps in the canopy, and (B) Cross-sectional view of the faux grass canopy suspended 30 mm above the lysimeter slope's surface, showing a 500 mm spacing between metal rods and a 150 mm canopy height. The zoomed insert demonstrates the 100 mm vertical spacing between faux grass bundles.

Figure 3.17: Photograph illustrating the final installation of the faux grass canopy over Side B of the lysimeter slope on April 20th 2023.

3.4 Laboratory Study

Long-term and continuous monitoring of the lysimeter slope allowed the emergence of potential controls on desiccation to be observed in real-time. Such observations informed the design of supplementary laboratory investigations, whose objectives were either to expand on conditions more conducive to live infrastructure assets or to isolate the effect of specific controlling parameters on desiccation cracking.

The former objective is investigated using the methodology of Section 3.4.1, where the role of topsoil composition and thickness on evaporation and desiccation within the Ampthill Clay was investigated. Topsoiling of infrastructure embankments is routinely undertaken to promote vegetation growth. However, it also plays a key role as an environmental buffer by moderating moisture and energy exchanges at the soil-atmosphere interface. These processes, as described by Penman (1948), govern the evaporation dynamics that critically influence desiccation and shrinkage in clay fills. Therefore, adding some real-world practices to desiccation crack analysis will further aid the understanding of their formation within field environments.

Section 3.4.2 outlines the methods used to address the latter objective, focusing on the effects of wind speed on evaporation and desiccation cracking. Wind speed is a

key factor in the Penman (1948) equation's aerodynamic resistance component, governing the evaporative loss rate. However, the variation of this component under differing wind speeds – and its influence on moisture fluxes, suction gradients, and the intensity of desiccation cracking – remains less well quantified within compacted clay fills. This study aimed to investigate these relationships, prompted by observations of desiccation cracking on the lysimeter slope during winter, when low temperatures confirmed wind-driven evaporation as a significant driver of soil drying and crack formation. To ensure consistency with the lysimeter slope, all laboratory experiments utilised Ampthill Clay, compacted at the same moisture content and initial dry density. This experiment set provided a further opportunity to improve the sub-surface characterisation of desiccation crack networks within the Ampthill Clay. Such analysis is fundamental to fully assess the hydrological response of desiccated slopes to drying and wetting. Therefore, the severity and connectivity of subsurface crack networks were investigated by pouring resin into the wind speed samples and taking cross-sections for image analysis, the methods of which are detailed in Section 3.4.3.

3.4.1 Topsoil Experiments

It is common practice to topsoil and vegetate real-life infrastructure assets in the final stages of construction to assist in stabilising the slope surface. The topsoil used varies depending on its source; however, it is usually dissimilar to the underlying plastic clay and, therefore, will exhibit a different water retention behaviour. Within the existing literature, little research surrounding how topsoiling infrastructure slopes impacts the process of desiccation crack formation can be found. In particular, how the thickness and composition of topsoil affect the rate and magnitude of evaporation and desiccation within the slope. Therefore, a laboratory study investigating the effects of two different topsoil thicknesses – 20 and 40 mm – and compositions – sandy (TS1) and clayey (TS2) – on evaporation from Ampthill Clay was conducted under controlled environmental conditions.

Adding topsoil above the Ampthill Clay fill introduced an additional material interface, reflecting standard embankment construction practices. The intention of these topsoil layers was not to accurately replicate the structural, biological, and compositional characteristics of naturally matured topsoil. Instead, they were simplified materials chosen to simulate contrasting hydraulic behaviour at the clay-topsoil interface, effectively imposing a boundary condition for investigating the resultant evaporation dynamics and moisture redistribution within the Ampthill Clay.

The experimental setup for these experiments is provided in Figure 3.18. For both tests, 90 mm of Ampthill Clay was compacted at 40% moisture content into four plastic boxes (368 x 260 x 168.5 mm) – labelled A, B, C and D. The clay was compacted in four 22.5 mm layers using an earth rammer to ensure a consistent density with minimal void space was achieved. These conditions were chosen to replicate and draw comparisons with the conditions of the lysimeter slope outlined in Section 3.3.1.

Box A acted as a control sample to which no topsoil was added. For Boxes B and C, the Ampthill Clay was overlain by 20 mm and 40 mm layers of TS1 at 2% moisture content, respectively. Finally, a 40 mm layer of TS2, at 2% moisture content, was added to Box D. For Test 2, the experimental setup was identical to Figure 3.18, except an increase in TS1 and TS2's initial water content to 20.4% and 18.6%, respectively. This was to investigate whether the initial topsoil moisture content affected moisture migration and, therefore, the rate and magnitude of evaporation from the underlying Ampthill Clay.

In each test, the surface state of the topsoil was photographed, and the initial mass of each box was recorded before they were placed inside an environmental chamber. The temperature and relative humidity inside the chamber were set to 14^{o}C and 80%, respectively, to represent average Newcastle upon Tyne summer conditions. Summer conditions were chosen to represent the maximum period of expected evaporation. The temperature and humidity choices were determined by calculating the average values of northeast England for June to August from 1883 until 2023 using the HadUK-Grid 1km gridded dataset from the Centre of Environmental Data Analysis (Met Office et al, 2018).

Each week, the boxes were temporarily removed from the chamber to photograph the surface and measure mass. The end of the test was defined as the point at which no further mass loss was recorded with time. Once this was achieved, the surface of the Ampthill Clay and topsoil was photographed, and the mass of the topsoil and Ampthill Clay was recorded separately. The clay and topsoil were sampled to determine the final moisture content at the end of the test. To determine the shrinkage volume of the Ampthill Clay layer, the end dimensions of the soil block were taken and compared to the initial readings. No desiccation cracking occurred in any sample; therefore, image analysis was not carried out.

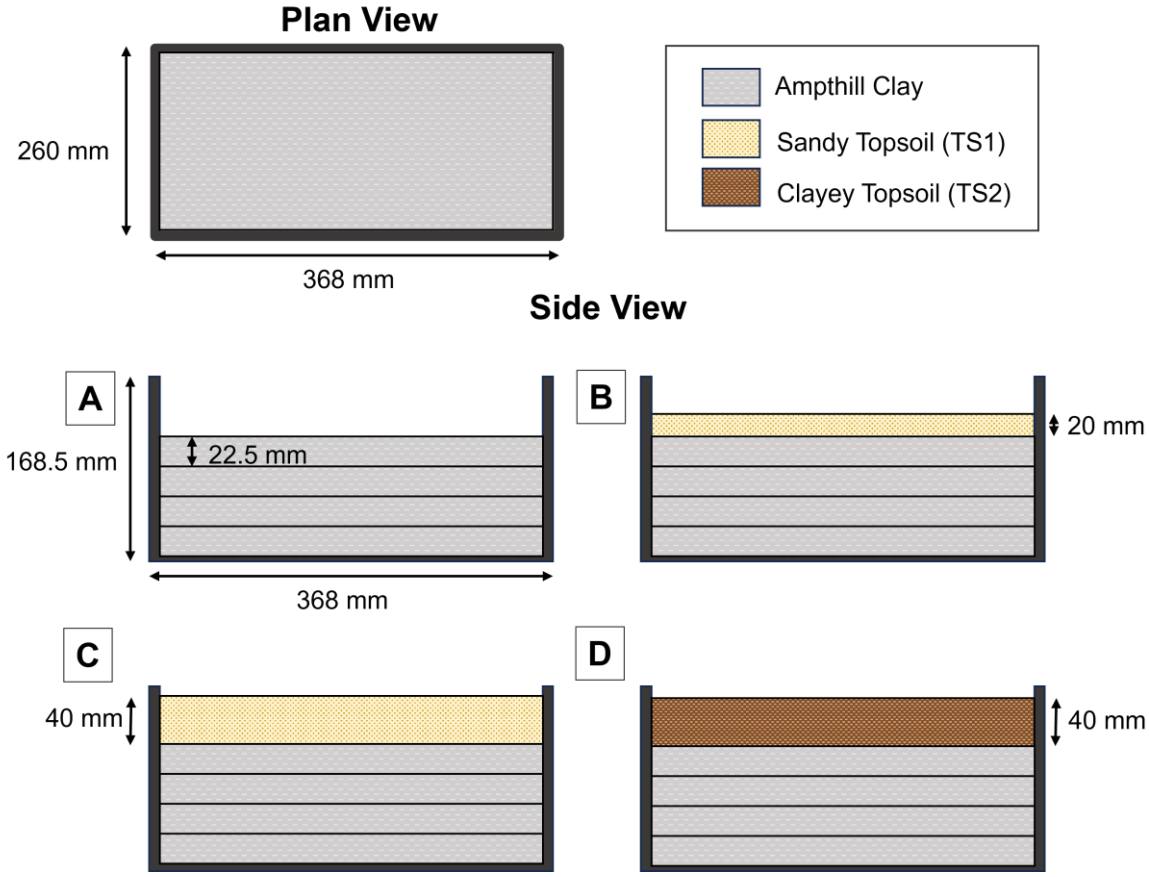

Figure 3.18: Experimental setup to investigate the role of topsoil composition and thickness on evaporation and desiccation crack formation within the Ampthill Clay. A plan view of the boxes (368 x 260 x 168.5 mm) used in these tests is given. The following variations were tested: (A) no topsoil, (B) 20 mm of sandy (TS1) topsoil, (C) 40 mm of sandy (TS1) topsoil, and (D) 40 mm of clayey (TS2) topsoil.

3.4.2 Wind Speed Experiments

Within existing literature, drying cycles to initiate desiccation cracking are mostly applied to a soil sample using fast application of extreme temperatures. For the UK, applying temperatures using this method would be an unrealistic representation of its climate, even during heatwave conditions. Furthermore, it neglects other important contributors to drying as per the Penman (1948) and Monteith (1965) equations for evaporation – primarily solar radiation and wind. Investigation into the role of varying solar exposure in desiccation crack formation was carried out using the faux grass canopy discussed in Section 3.3.7. However, to isolate and understand the effects of wind speed on desiccation crack formation, a controlled laboratory methodology was designed and is outlined below.

Figure 3.19 illustrates the components of the experimental setup. A plastic box (368 x 260 x 168.5 mm) was filled with 90 mm of Ampthill Clay, compacted in four 22.5 mm layers using an earth rammer. The box was placed on a balance and covered with a

custom-made Perspex chamber with dimensions 464 mm x 335 mm x 400 mm. The chamber was designed with the following features: (1) sealed interlocking edges to channel airflow across the soil surface and minimise loss through equipment, (2) an air inflow pipe that was connected to an electric fan using flexible pipe (150 mm diameter), (3) an air outflow pipe to provide an escape outlet for the added wind; (4) an inbuilt camera dock to take photographs of the soil surface using a fixed frame of view; (5) a temperature-humidity sensor attached to the inside wall to closely monitor environmental conditions during the tests.

The source of airflow was an electric fan that was fitted with a vari-ac to control the speed of airflow across the soil surface. Four tests were carried out using this setup at different wind speeds to vary the aerodynamic component of Penman-Monteith's (1965) equation, and capture the range of wind conditions experienced in Newcastle upon Tyne: (1) 0 m/s representing calm conditions with no wind; (2) 1.5 m/s representing a gentle breeze; (3) 4.5 m/s representing a moderate breeze; (4) 18 m/s high winds and storm conditions. The wind speeds were held constant, which is a recognised limitation of the methodology, yet provides a worst-case exposure for analysis. Prior to conducting the tests, a sensitivity analysis was carried out to relate the power positions on the vari-ac to the resultant wind speed experienced inside the chamber, which was measured using an anemometer.

To record changes in soil mass, the plastic box and Perspex chamber were placed onto a balance, and measurements were taken at 5-minute intervals. Recording mass was a fully automated process conducted by connecting the balance to a computer with the recording software provided by RS Communications. The test was terminated when there was no longer a change in soil mass, with time indicating that no more evaporation was taking place.

The camera dock was used to capture changes in surface desiccation state within a consistent frame at 1-minute intervals across the duration of each test. To measure the surface crack characteristics, the photographs were processed using the MATLAB, which is detailed in Section 3.4.4.

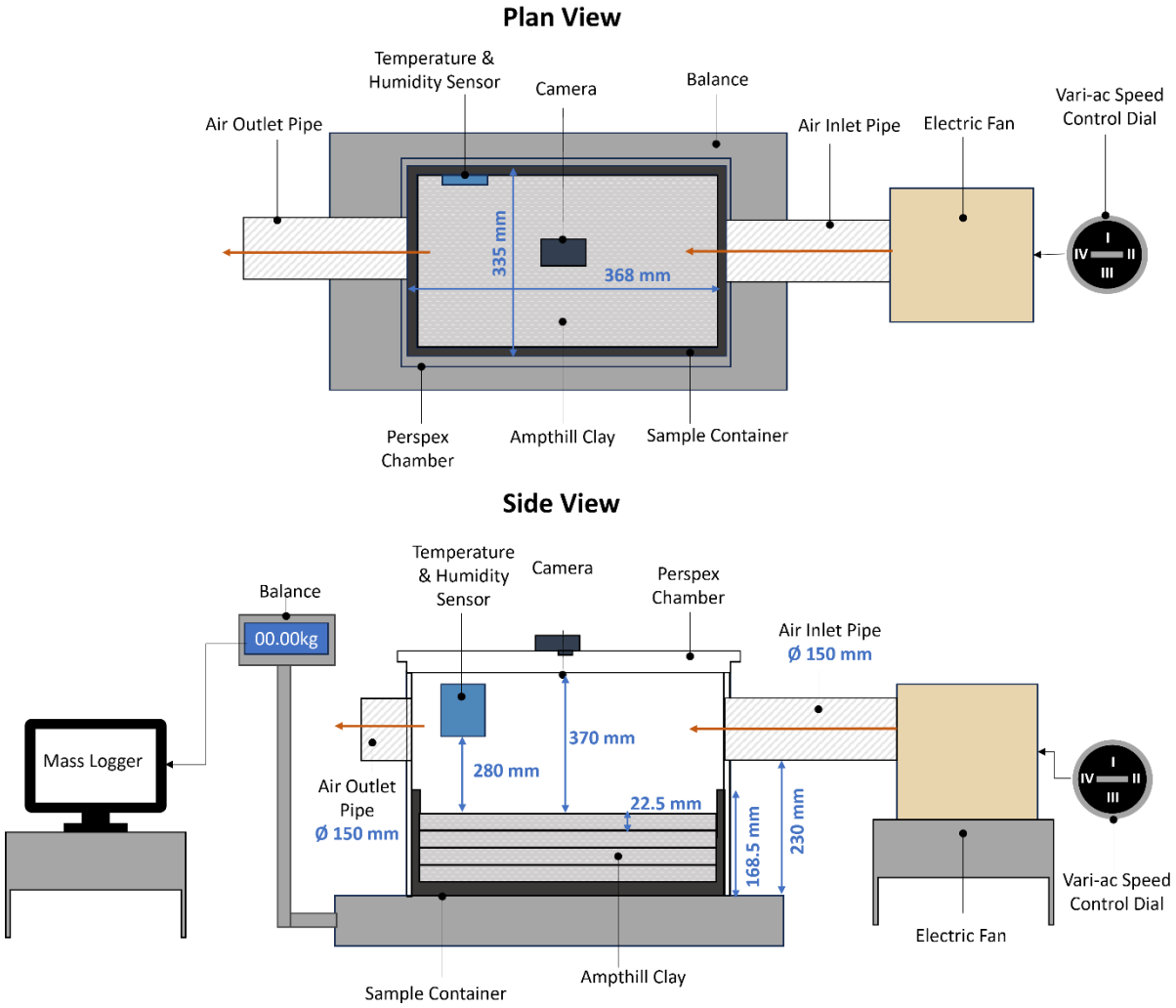

Figure 3.19: Plan and side views of the experimental setup for the wind speed investigations. A plastic box (368 x 260 x 168.5 mm) was filled with 90 mm of compacted clay and sealed within a Perspex chamber. Air was supplied via an electric fan (speed controlled by a vari-ac) and was channelled across the sample using an inlet and outlet pipe. The sample was placed on a balance to record mass loss during drying, and a camera monitored surface desiccation.

3.4.3 Subsurface Crack Analysis with Resin

Due to the intrusive nature of sub-surface crack analysis, quantification of cracking is heavily weighted in existing literature to surface examination only. Section 2.6.5 highlighted some non-intrusive, geophysical-based techniques that researchers are developing; however, they do not yet cover materials and conditions conducive to infrastructure embankments. Therefore, to visualise sub-surface development of the crack network, the wind speed samples (Section 3.4.2) were sealed at the end of the test to prevent moisture ingress, and resin was poured until it encapsulated the soil surface. This approach is novel in its application, as no existing studies have utilised resin injection as a method to explore sub-surface desiccation crack patterns. The

successful implementation of this technique demonstrates its potential as a crack quantification method, marking this work as an original contribution to the field.

The type of resin used was Polytek EasyFlo 60 Polyurethane Liquid Plastic Casting Resin and came in two parts (A and B) which were mixed at a 1A:1B ratio. This resin was chosen for its super low viscosity to increase the likelihood of penetrating through the soil sample and highlighting sub-surface crack discontinuities. Polycraft Poly Colour Polyurethane Dye/Pigment in yellow was added to the resin mix at 0.5% the resin weight to increase contrast with the surrounding soil. Once mixed, the resin was quickly poured into the soil sample due to the 2-2.5-minute working time (Figure 3.20A). The sample was sealed and allowed to cure for 1 week to minimise breakage during further analysis.

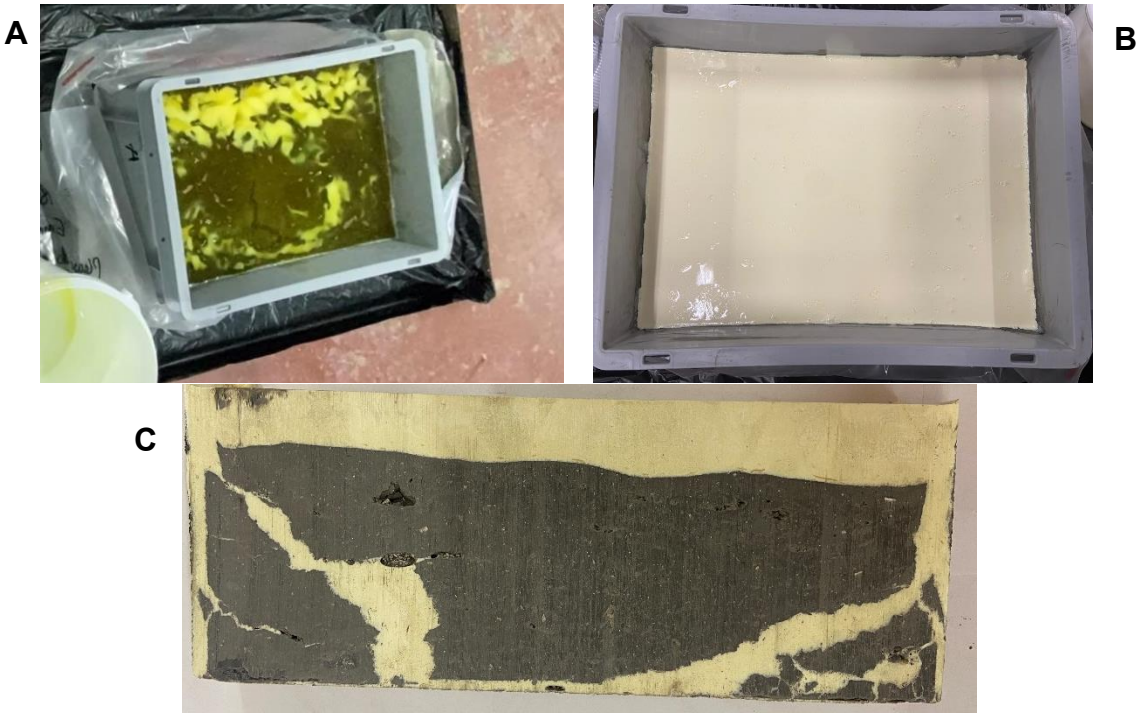

Figure 3.20: Photographs illustrating (A) the resin immediately after pouring into the sample, (B) the cured state of the resin, and (C) an example ross-section taken through the sample post-resin cure.

Once curing was complete (Figure 3.20B), the resin blocks were removed from the container and cut into 40 mm cross-sections using a mechanical saw (Figure 3.20C). The internal surfaces were photographed and processed using the crack analysis technique outlined in Section 3.4.5. From this, attention was given to investigate how subsurface desiccation cracks interact with compacted soil layers, in particular at layer boundaries, and vary under different wind speeds.

3.4.4 Crack Image Analysis of Wind Speed Experiments

Digital image analysis was conducted to analyse the surface and subsurface intensities of desiccation cracking within the wind speed specimens. This process used MATLAB to calculate the percentage surface area occupied by cracks, known as the Crack Intensity Factor (CIF). The methods adopted varied slightly between surface and subsurface desiccation analysis, the reasoning of which is outlined below.

During the wind speed experiments, the temporal evolution of surface desiccation was captured at a high resolution, with images of the Ampthill Clay's surface taken every minute. Therefore, a curve of CIF variation through time could be produced. The process followed within MATLAB is summarised in Figure 3.21, with visual aids for each stage. An extract of the MATAB code used to process the crack images and calculate a CIF value is provided within Appendix A. Firstly, the original RGB image was converted to grayscale using MATLAB's inbuilt "*im2gray"* function, which transforms the colour JPG image to a single-channel intensity image. This was conducted to 1) remove colour variation by reducing image complexity to one colour channel, 2) focus on intensity differences within this colour space, and 3) ensure compatibility with thresholding techniques used later for binarisation.

Next, the grayscale image was segmented through binarisation to distinguish cracked areas from intact soil and produce a binary mask. An adaptive threshold was applied, calculating each pixel's threshold based on the intensity values of its nearest neighbours. This dynamic thresholding method was essential due to significant spatial and temporal variations in grayscale intensity caused by changing lighting conditions and colour variations in the drying Ampthill Clay. To implement this, MATLAB's built-in *"adaptthresh" and "imbinarise"* functions were utilised sequentially. A sensitivity parameter, which ranges from 0 to 1, must be selected to determine the aggressiveness of the applied adaptive threshold. In this study, a value of 0.9 was identified as optimal, based on a thorough visual inspection of a subset of representative images from the dataset. Tables A.1 for W3 (4.5 m/s) and A.4 for W4 (18 m/s) in Appendix A illustrate the effects of 0.4, 0.9, and 1.0 sensitivity thresholds on the computed CIF for four sample images from each of these crack datasets. The 0.4 sensitivity threshold included excessive non-cracked regions in the CIF summation, while the 1.0 threshold underestimated the cracked area by eroding the crack width. Thus, the 0.9 sensitivity threshold was uniformly applied throughout the analysis to

ensure consistent detection of crack regions and accurate representation of relative CIF changes over time.

Morphological operators were then applied to the threshold image to refine the binary output further and remove noise. MATLAB provides built-in functions *"imopen"* and *"imclose"* for this process, which were applied sequentially to the binarised masks. These morphological operations require defining a structuring element – a small, shape and width defined matrix that determines whether a pixel should be removed or retained based on its local neighbourhood of pixels. For *"imopen"*, the structuring element removes slight foreground noise and smooths the boundaries of larger objects, such as cracks, by eroding and then dilating the foreground. Conversely, during *"imclose",* slight gaps or breaks within foreground regions are filled by applying dilation followed by erosion.

For this study, a square structuring element with a width of four pixels was determined as the optimal choice. This conclusion was reached through a detailed visual inspection of a representative sample of images, while also considering the characteristics of crack features being segmented. Examples of how different shapes of structuring elements (disk, diamond and square of constant 4x4 pixel width) impacted the CIF are provided in Tables A.2 (W3) and A.5 (W4) within Appendix A. Comparatively, the square element resulted in minimised erosion of the finer crack segments, giving a more accurate CIF value. A CIF sensitivity analysis of different structuring element widths (square elements with 1x1, 4x4 and 8x8 pixel grids) is also provided in Tables A.3 (W3) and A.6 (W4) within Appendix A. The 4x4 pixel grid effectively balanced background noise reduction with crack width preservation.

After this refinement stage, the final binary mask of the grayscale image was produced, with black pixels representing cracked areas and white pixels intact clay. The binary mask was then queried to output the relative numbers of black (cracked) and white (intact clay) pixels to an excel file, from which the CIF was calculated using Equation 3.4:

$$CIF\ (\%) = \frac{(Cracked\ Pixels)}{(Cracked + Intact\ Clay\ Pixels)} \times 100 \qquad 3.4$$

This process was conducted for wind speed tests W3 and W4, which exhibited desiccation cracking, producing a curve of CIF evolution through time for each.

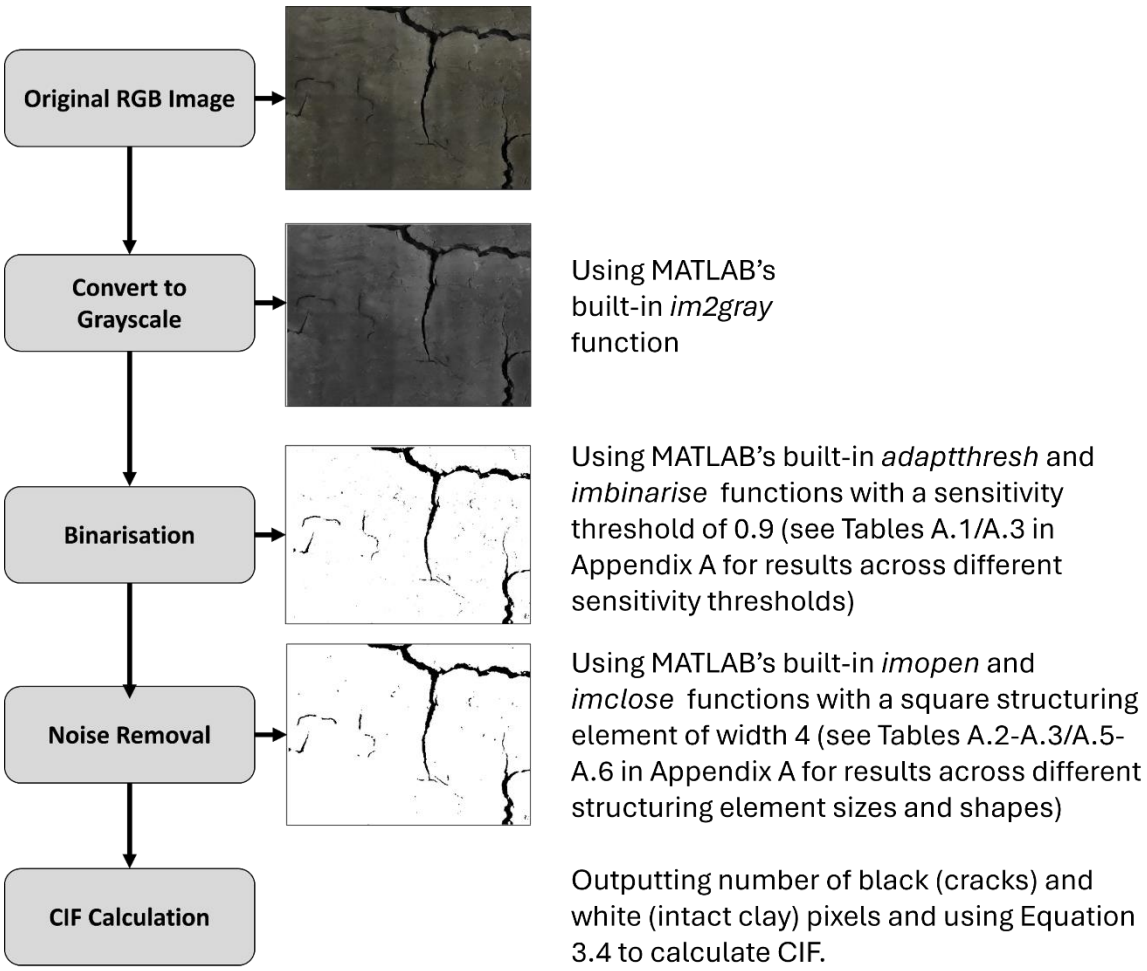

Figure 3.21: The digital image processing procedure conducted in MATLAB to calculate the Crack Intensity Factor (CIF) of the surface images of wind speed samples W3 and W4. Refer to Appendix A for extracts of the MATLAB code and sensitivity analysis results.

For subsurface analysis, images represent an end-of-desiccation cracking state, taken from the cross sections through W1 – W4 after the resin was added to the samples. Therefore, a curve of CIF evolution over time could not be attained. However, insight was provided into the subsurface desiccation pattern, and CIF values were compared between different wind speed intensities to understand their impact. The digital image processing method adopted in MATLAB for these images is summarised with visual aids in Figure 3.22. An extract of the MATAB code used to process the crack images and calculate a CIF value is provided within Appendix A.

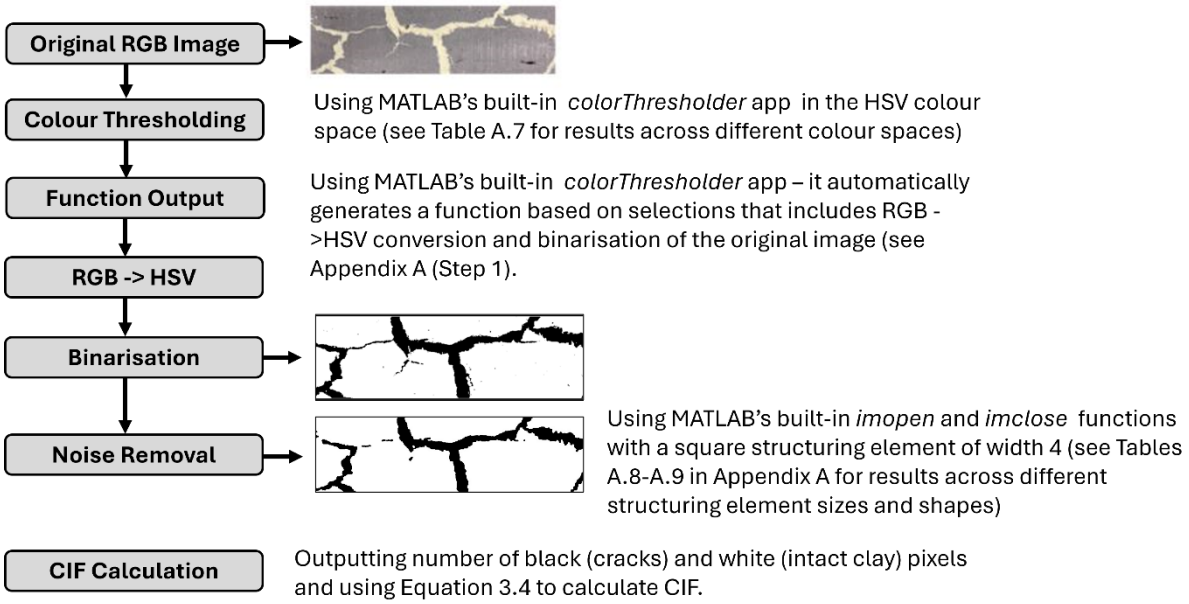

Figure 3.22: The digital image processing procedure conducted in MATLAB to calculate the Crack Intensity Factor (CIF) of the subsurface images taken of wind speed samples W1 – W4 after the resin was poured. Refer to Appendix A for an extract of the MATLAB Code and sensitivity analysis results.

In contrast to surface cracks, subsurface cracks were clearly delineated by yellow resin, which exhibited minimal infiltration into the adjacent intact soil. This characteristic rendered colour thresholding a more suitable and accurate segmentation method for quantitative crack analysis. The first step involved using MATLAB's in-built "colorThresholder" app. This interactive tool allows images to be segmented by defining colour thresholds within the various colour spaces (RGB, HSV, Lab* and YCbCr). Each colour space was trialled, and its suitability for segmenting the cracked regions was assessed in real-time. The HSV colour space yielded the most effective segmentation results. Suitable thresholds for Hue (H), Saturation (S), and Value (V) were determined through an iterative adjustment process and visual inspection within the app. This approach aimed to accurately isolate all crack regions that display the specific shade of yellow characteristic of the resin. The chosen threshold ranges for the H, S and V components were as follows:

- H: 0.086 – 0.208
- S: 0.000 – 1.000
- V: 0.000 – 1.000

Illustrative and quantitative examples of the sensitivity of the CIF to the different colour spaces (RGB, HSV, Lab, Lab* and YCbCr) are given in Table A.7 in Appendix A. Except for the RGB option, the colour spaces showed minimal CIF difference, with the HSV

colour space yielding marginally better segmentation across the four sample images. The app then auto-generates a function (see Step 1 in Appendix A) which was used to convert all RGB images in the subsurface crack dataset into the HSV colour space, applies the pre-defined thresholds and creates a binary mask. MATLAB's built-in *"imopen"* and *"imclosed"* morphological operations were also added to this function to refine these binary masks. A disk-shaped structuring element with a 10x10 pixel grid width was determined to be most appropriate for this analysis. This selection was influenced by the pronounced curvature of the subsurface cracks and the need to manage fewer, yet larger, clusters of noise effectively. The effect of the shape and size of the structuring element on the outputted CIF value is shown in Tables A.8 and A.9 within Appendix A. After this refinement stage, the final binary masks of the RGB images were produced, and the count of black (cracked) and white (intact clay) pixels was exported to an excel file for calculating the CIF using Equation 3.4.

3.5 Summary of Research Methodology

The methodological approach taken to address the aims and objectives of this thesis have been presented within this chapter. These aims and objectives are centred around observing, quantifying, and assessing the impact of weather- and desiccation crack-driven deterioration within infrastructure embankments. Integral to this approach is conducting these methodologies using techniques representative of the complexity observed within live infrastructure embankments. Addressing the implications of desiccation cracking at this key scale was identified as a notable gap within the existing literature. An outline of which research objectives each methodology section aims to address is provided within Figure 3.23. The long-term hydrological and desiccation crack monitoring of the lysimeter slope and its added modifications are shown to target all three primary objectives (OB1 – OB3). Objective 3 (OB3) also relies on detailed laboratory studies to isolate and better understand the parameter space controlling the severity of desiccation cracks.

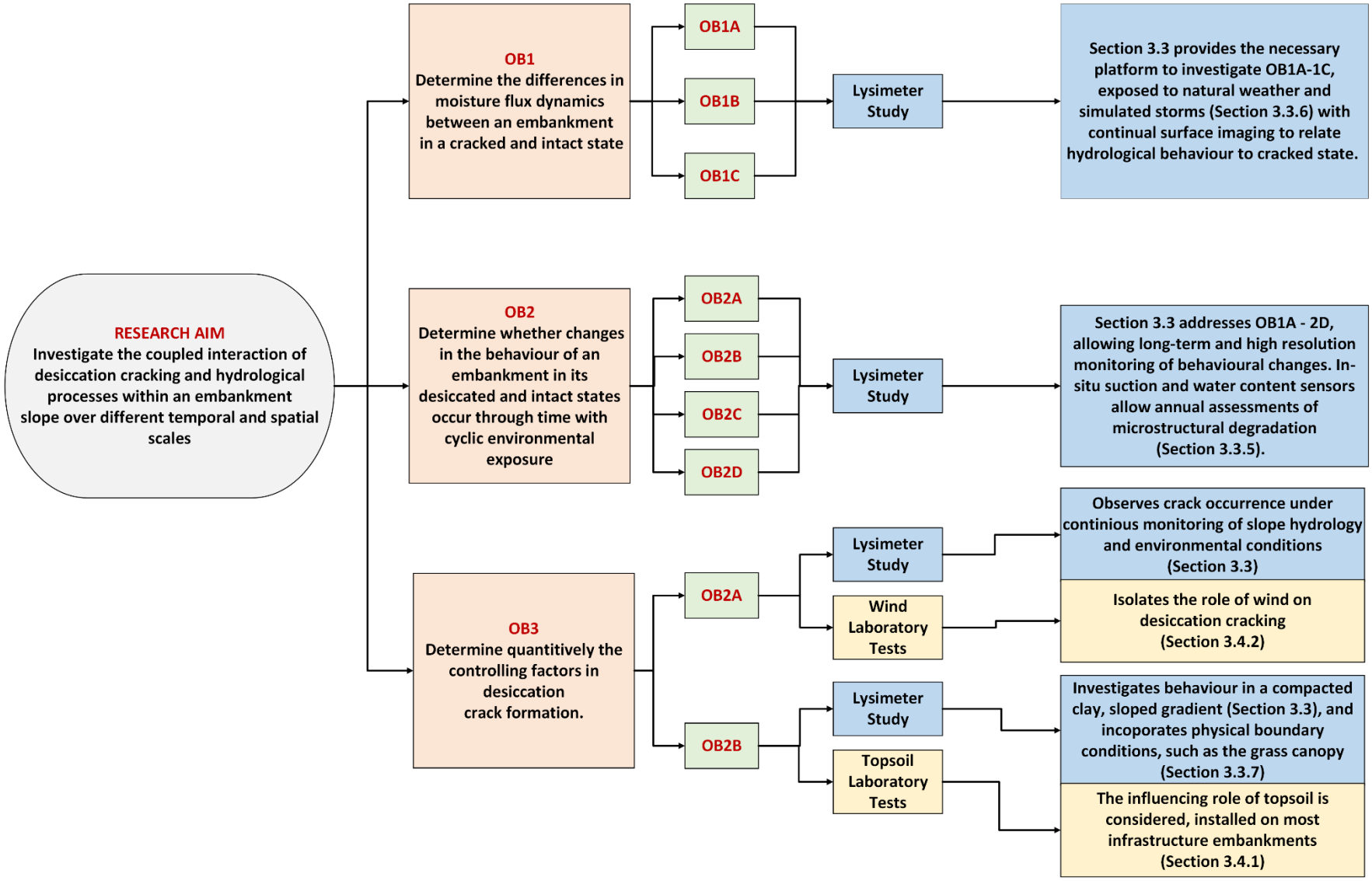

Figure 3.23: Schematic illustrating how the adopted methodologies address each of the aims and objectives (Section 1.2).

Chapter 4. Long-term Desiccation and Hydrological Behaviour of a Compacted Clay Slope

4.1 Introduction

Conceptualising and quantifying weather-driven deterioration within infrastructure embankments is fundamental to maintain the stability, longevity, and safety of the transport network. The cyclic exposure to wetting and drying, associated volume change, and desiccation crack formation are heightening threats to embankment stability under the weather-driven deterioration framework (Glendinning et al., 2014; Stirling et al., 2021; Briggs et al., 2023; ORR, 2024). Furthermore, the occurrence, severity, and consequence of these threats are set to increase under the weather extremes predicted under future climate change projections (Kilsby et al., 2009; Loveridge et al., 2010; Toll et al., 2012; Mair, 2021). Therefore, to ensure effective long-term management of these key assets, an improved understanding of how these highlighted threats manifest within infrastructure embankments is critical.

Knowledge on the fundamentals of desiccation crack formation under dry-wet cycling has benefited greatly from extensive laboratory-scale studies. However, rarely do their findings address the field-scale complexities encountered within desiccated infrastructure embankments. These factors are integral to the advancement of weather-driven deterioration within an infrastructure embankment, highlighting a critical gap in knowledge. Conversely, conducting investigations on field-scale assets can be restrictive from the perspectives of accessibility, parameter control, and installing detailed monitoring. However, the limited studies that are available commonly express the complex and highly evolving nature of these assets under dry-wet cycling and weather-driven deterioration (Stirling et al., 2018, 2021; Powrie & Smethurst, 2019; Briggs et al., 2023). A few examples of intermediate-scale investigations on desiccation cracking have been presented in the literature (Greve et al., 2010; Song et al., 2013; Cordero et al., 2021). Although their findings addressed scale effects, these studies were not posed in an infrastructure embankment context, in terms of geometry, material composition, wider hydrological processes, and the longer-term development of deterioration.

Therefore, to bridge this identified gap between small-scale laboratory experiments and field-scale investigations, an intermediate scale, compacted clay slope was constructed within an outdoor lysimeter. This setup allowed detailed monitoring of the

hydrological and desiccation crack behaviour of a compacted clay slope under a naturally varying climate, with key observations discussed in Section 4.2. Potential evidence for the development of microstructural deterioration within the lysimeter slope was also investigated, the findings and implications of which are assessed in Section 4.5.

Modifications to the lysimeter slope were also conducted to observe its response under simulated storm events, which is crucial to understanding future assessments of weather-driven deterioration. Section 4.3 reviews the results and determines the impact of these events on the short- and long-term behaviour of embankment slopes subject to desiccation. Within field infrastructure embankments, vegetation canopies can alter environmental exposure, by acting as physical interceptors of rainfall, solar radiation and wind. These interactions are often overlooked in small-scale laboratory testing. Therefore, they were incorporated into the modifications made to the lysimeter methodology, with a faux grass canopy installed over Side B of the lysimeter slope. The findings of this study are discussed in detail in Section 4.4.

Throughout the design and review of these experiments, their relevance to processes observed within live infrastructure embankments was continually considered and critically assessed. This allowed the key findings to help inform how desiccation cracking manifests within real infrastructure embankments, its nature, and controlling parameters (physical and environmental). How the desiccation process itself can escalate deterioration within embankments is also fundamental to determining future asset stability and resilience to increasing environmental stressors.

4.2 Pattern of Desiccation Crack Evolution

Understanding the spatial and temporal patterns of desiccation cracking within an infrastructure embankment is crucial for assessing its structural health. Desiccation cracks can compromise soil strength and stability by facilitating deeper and faster infiltration, rapid suction loss, and microstructural degradation (Stirling et al., 2021; Briggs et al., 2023). Therefore, analysing crack evolution may help identify areas of vulnerability within an embankment, allowing targeted interventions to manage deterioration. Detailed desiccation crack and hydrological monitoring within the lysimeter slope commenced on the 2nd of July 2021 and was completed on the 31st of August 2023.

This experiment allowed a major observational study of desiccation evolution within a compacted clay slope, producing an almost complete 2-year sequence of daily crack images. A video tracking surface crack development across the monitoring period was generated. The video is provided as supplementary material and is available to view at the following location https://figshare.com/s/ac973e5473fb402d3c5e. Combining this desiccation dataset with measured changes in slope hydrology and weather trends, a holistic view of the conditions under which cracking behaviour evolved could be developed. Interactions between desiccation cracking and slope hydrology could also be examined, enabling assessment of how various networks may impact moisture dynamics within an infrastructure embankment.

Systematic documentation of surface desiccation cracking over a fixed frame of view began on the 22nd of September 2021, after two camera mounts were installed over Side A and B (see Figure 3.8 for locations). Importantly, Side A served as the control throughout the lysimeter's monitoring, while Side B was later modified in April 2023 for further investigations. To this date, cracking exhibited comparable behaviour in both localities. Therefore, for simplicity, Side A's image dataset alone was utilised for this section's analysis, taken as representative of the whole slope behaviour under natural environmental conditions.

Similarly, the long-term datasets of suction and volumetric water content were examined, with a comparison of the raw data from Sides A and B provided in Appendix B. Discernible from this dataset was that these parameters behaved broadly the same within Sides A and B, following consistent wetting and drying trends until the experiment was changed in April 2023. Minor differences in the magnitude of these changes likely stem from sensor noise, cracks developing close to a sensor, or inherent heterogeneity in porosity due to manual soil compaction; however, these variations do not significantly alter the overall hydrological patterns observed over the two-year monitoring period. Therefore, again, for simplicity and for consistency with the crack images, the discussion will focus on Side A's hydrological monitoring results, with confidence that its data reliably represents whole-slope behaviour. Deviations in behaviour between Sides A and B after April 2023 are detailed within Section 4.4.

4.2.1 Observations of Crack Morphology Evolution

Important major shifts in surface desiccation cracking behaviour between 2021 and 2023 are visually documented within the timeline of Figure 4.1. Significant changes have been classified as an "Event" (red dots), while supplementary visual information

appears as purple dots. Figure 4.1 illustrates Event 1 (E1) on the 2nd of July 2021, where desiccation cracks had formed within the first 24 hours after the lysimeter slope was constructed. At E1, the crack network was primitive, featuring fine superficial cracks with limited connectivity, focused in the more prominent central slope regions. By Event 2 (E2) on the 4th of August 2021, this developing network had significantly expanded (Figure 4.1), having reached maturity by Event 3 (E3) on the 22nd of September 2021, where systematic imaging over a fixed frame was introduced. This crack network will henceforth be referred to as the "Summer 2021" crack network, with its key characteristics as follows: 1) a deep (300 – 400 mm) set of wide (max 40 mm) and distantly spaced primary cracks, which encased, 2) a shallower (max 50 mm), narrow (max 10 mm) yet surface extensive and closely spaced network of secondary cracks. During development, the spacing of the secondary crack network increased to generate a highly fragmented and friable slope surface, as shown by E3. Throughout its prevalence, the Summer 2021 crack network exhibited temporary aperture reductions. However, the desiccation cracks exhibited no shifts in location.

The Summer 2021 crack network closed fully on October 6th, 2021, designated as Event 4 (E4) in Figure 4.1. Within 24 hours of closure, cracking had regenerated, maturing into a distinctly different network by the 11th of October 2021, labelled as Event 5 (E5) in Figure 4.1. This shift in crack pattern is significant and displays the following key contrasting features to the Summer 2021 network: 1) no deep primary crack network enclosing secondary cracks, 2) shallower network (max 50 mm) of greater uniform size, 3) moderate aperture (max 20 mm) and spacing, 4) less friable slope surface, 5) larger initial surface area of intact soil peds. This pattern will herein be referred to as the "Winter 2021" crack network.

Despite opening and closing throughout the winter period, the Winter 2021 crack pattern remained relatively consistent through to the 19th of May 2022. Small shifts in the crack paths occurred after full or partial healing, which led to minor changes in the relative shape and size of the soil peds through time. An example to illustrate these small changes is provided by (A) in Figure 4.1, taken on February 8th, 2022. Further desiccation of the intact soil peds was visible over time due to the initiation of secondary cracks. Once matured, the secondary network exhibited a similar aperture to the older established cracks. Moreover, with continued cyclic environmental exposure, the surface extensivity of this network intensified, dissecting the previously intact soil peds and gradually reducing their average surface area.

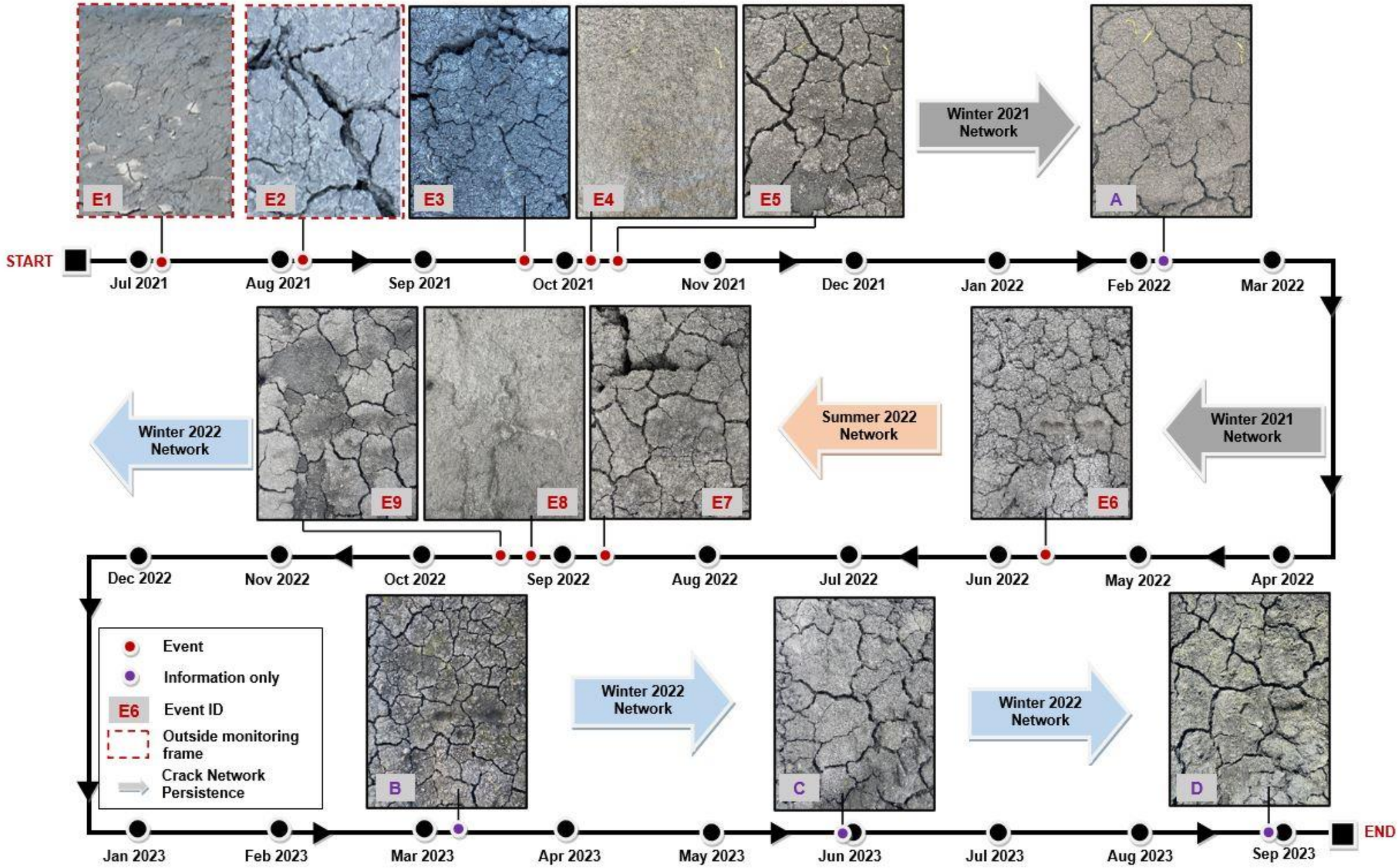

Figure 4.1: Timeline of major changes in desiccation cracking behaviour within the lysimeter slope between July 2021 and August 2023. Key changes in behaviour are marked as Events (red dots), while images providing additional information only are represented as purple dots. The large arrows indicate the persistence of a particular crack network across the timeline.

Birds disturbed the area on April 22nd, 2022, generating local disparities in behaviour. The affected areas appeared more friable and finely desiccated than the undisturbed regions, whose crack locations did not shift.

From the 20th of May 2022, cracking behaviour once again shifted with the seasonal transition into Summer, annotated as Event 6 (E6) within Figure 4.1. This is referred to as the "Summer 2022" crack network, whose structure is consistent with that of Summer 2021. However, although the sizes and depths are similar, the locations of the primary and secondary cracks vary, influenced by the existing expression of the Winter 2021 network. The aperture of the primary network was initially unstable between May 20th and June 14th, while the secondary crack network remained relatively stable. From June 14th, the primary cracks substantially widen, remaining a notable feature through to the 8th of September 2022. Conversely, the locations of the secondary crack network visually shift throughout the Summer of 2022, specifically when re-opening after fully healing. An example of the Summer 2022 crack network after rapid primary crack widening and a shift in the secondary crack locations is shown as Event 7 (E7) in Figure 4.1.

The Summer 2022 crack network does not fully heal until the 8th of September 2022, referred to as Event 8 (E8) in Figure 4.1. A new crack pattern, identified as "Winter 2022" crack network, is then established within the lysimeter slope by the 13th of September 2022. This significant change in the network is noted as Event 9 (E9), as shown on Figure 4.1's timeline. The Winter 2022 crack network is structurally and geometrically comparable to the features of the Winter 2021 crack network. However, the locations of the cracks within the lysimeter slope have changed.

The characteristics of the Winter 2022 crack network prevailed until the end of monitoring on August 31st, 2023, exhibiting no seasonal transition into a deeper primary and secondary network. Opening and closure of the network occurred throughout this period, with some cracks appearing memoryless, whilst others continued to exploit the previous discontinuity path. This can be seen by visually comparing the Winter 2022 network across images (B) to (D) in Figure 4.1. The slope surface was substantially disturbed by birds on the 26th of April 2023, not visibly resetting until simulated storms were applied between May 26th and June 9th, 2023. With this reset, the crack network shifts (see (C) Figure 4.1). Subsequent small changes in the pattern prevailed through to June 2023. New cracks formed to reshape the geometry and surface area of the previously intact soil peds, forming a more intensive and closely spaced network. From

June 2021, the crack localities remained stable until the 31st of August 2023, when monitoring concluded.

The existing literature presents contradictory findings regarding whether desiccation cracks shift in location across dry-wet cycles. Reasons for repetitive patterns have been attributed to restraining conditions from sample containers in the laboratory (Tang et al., 2008; Lakshmikantha et al., 2012; Wang et al., 2018) and vegetation in the field (Eminue et al., 2018; Yu et al., 2021). However, cracks have also illustrated a higher re-occurrence in intermediate-scale slurry specimens with a lack of inherent heterogeneity (Cordero et al., 2021), while other studies have highlighted how such inconsistencies in density fundamentally generate differing patterns (Tian et al., 2022).

Important contrasting features of the lysimeter slope study presented here include the exposure of compacted clay, which has inherent heterogeneity, to naturally varying environmental conditions. Under these conditions, the state of compaction and, therefore, density temporally evolved under dry-wet cycling driven volumetric change. Therefore, inconsistencies in desiccation behaviour across the slope emerged depending on the magnitude and rate of change of these parameters. The shifting effect of desiccation may have been mitigated had the slope been vegetated, suggesting that the findings presented herein exemplify a worst-case scenario regarding the poor predictability of desiccation crack initiation in heterogeneous compacted clays with no inherent restraints. These results significantly underscore the potential for dynamic shifts in the primary sites of material degradation under such conditions. Furthermore, it emphasises the impact of seasonal and intra-seasonal climate variations on both the location and intensity of cracks, which may temporarily exacerbate the risks associated with desiccation cracks and their implications for the structural integrity of embankments.

This qualitative analysis of desiccation crack evolution within the slope shows a clear seasonally dependent behaviour between 2021 and 2022, with distinct transition events noted. Cracking behaviour during 2023 deviates from this trend, exhibiting no seasonality yet a considerably more dynamic superficial network. The following subsections provide a more detailed analysis of the key events documented in Figure 4.1, comparing the timing of these events with the slope's hydrological behaviour and prevailing weather conditions. A thorough review of desiccation cracking in relation to these two parameters is fundamental to understanding the observed desiccation behaviour and assessing its impact on the slope.

4.2.2 Seasonality in Crack Patterns – 2021

Figure 4.2 documents the changes in, (A) volumetric water content (%), (B) suction and (C) runoff recorded in the lysimeter slope from July to December 2021. Daily trends of relative humidity (%) (C), total rainfall (mm) and air temperature (°C) (D), as well as wind speed (m/s) and solar radiation (W/m^2) (E) for this monitoring period are also given. The volumetric water content and suction records cover three zones within the slope – the crest (C), upper slope (U) and lower slope (L) – the locations of which are shown in Figure 3.8. During monitoring, a zone of data loss occurred, the timings of which are shown on Figure 4.2A – B. The volumetric water content data was plotted using a moving average to eliminate the sensor noise at high saturations (see Appendix B for raw data). The temporal occurrence of events E1 – E5 from Figure 4.1 have also been annotated within Figure 4.2.

Formation of the Summer 2021 Crack Network (E1 – E3)

Events E1 – E3 from Figure 4.1 marked the initiation of desiccation cracking within the lysimeter slope, and the maturation of the Summer 2021 crack network. At E1 in early July, the onset of desiccation cracking occurred within 24 hours of the construction of the lysimeter slope, despite the Ampthill Clay retaining a high saturation. This behaviour is frequently documented in the literature, which attributes it to localised desaturation generating elevation suction gradients and zones of shear and tensile stress, ultimately leading to the initiation of cracking (Peron et al., 2009; Li & Zhang, 2011; Tollenaar et al., 2017; Wang et al., 2018; Cordero et al., 2021). The poorly connected and sporadic network of cracks recorded at E1 within Figure 4.1 supports such behaviour. Following E1, rapid desaturation in the upper 100 mm of the slope crest is recorded, with open cracks likely enhancing aerodynamic conductance (i.e. lowering resistance) as per Penman-Monteith's (1965) equation. Therefore, this increased moisture loss suggests a synergistic relationship between crack initiation and the propagation of drying fronts, whereby drying gradients facilitated the initiation of cracks, which then accelerated subsurface progression and depth of evaporation.

In mid-July, the seasonal peaks in temperature (23°C) and solar radiation (250 W/m²), accompanied by minimal rainfall, accelerated and deepened soil drying by increasing net radiation and the latent heat flux through evaporation (Penman, 1948). This increased energy flux led to significant desaturation and suction generation to a depth of 200 mm. Changes in void ratio induced by increased suction at 200 mm likely heightened shear and tensile forces at depth, resulting in strain development that

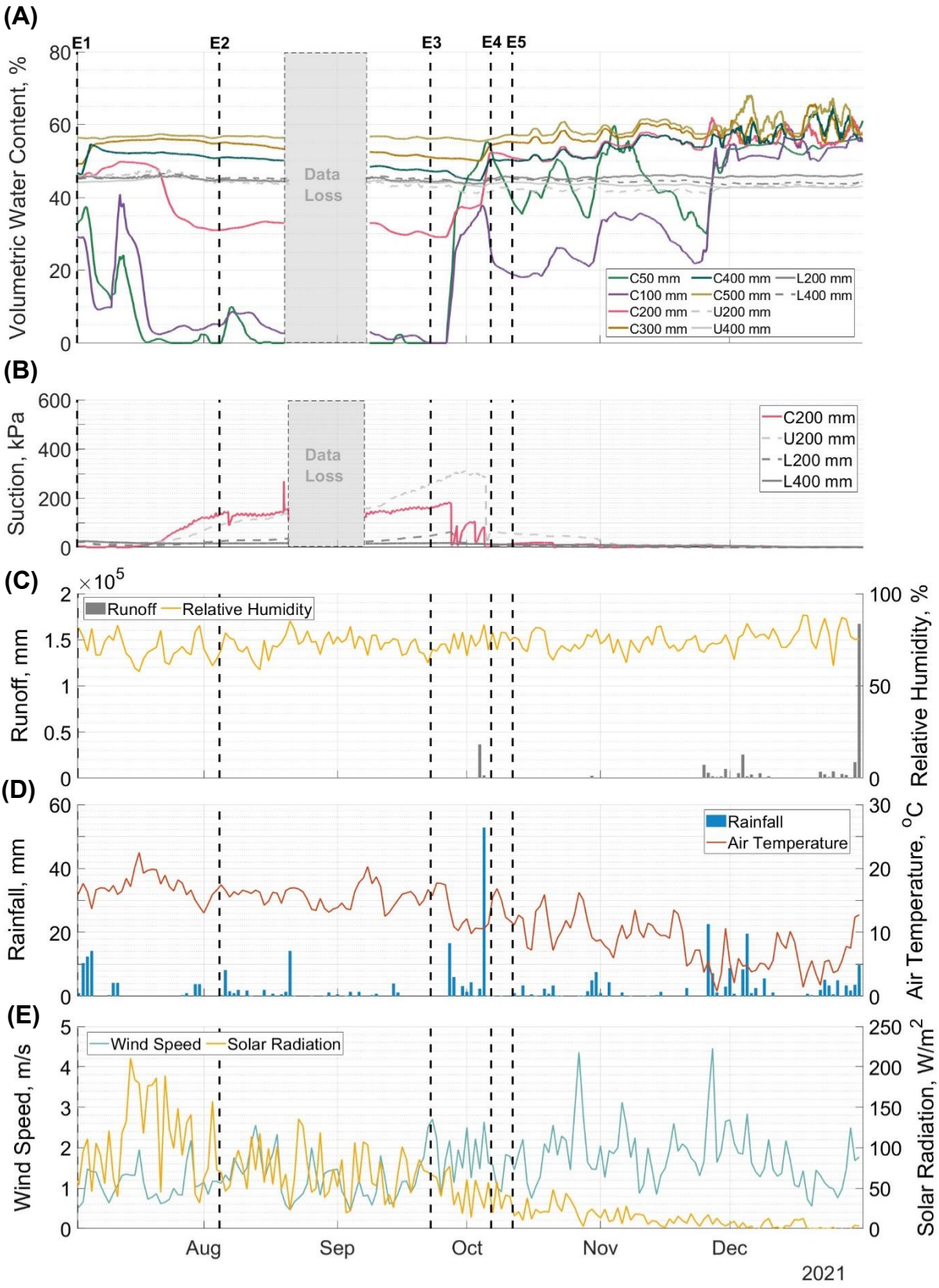

Figure 4.2: Plots demonstrating the temporal evolution of (A) volumetric water content (%) and (B) suction (kPa) through the upper (U), lower (L) and crest (C) regions of the lysimeter slope from July to December 2021. Time series data for (C) slope runoff (mm) and relative humidity (%), (D) rainfall (mm) and air temperature (°C), and (E) wind speed (m/s) and solar radiation (W/m^2) are also given. Events E1 – E5 are also annotated on all plots.

exceeded the soil's tensile strength and promoted the subsurface growth of desiccation cracks. An absence of rainfall lowered moisture ingress, allowing suction, evaporation, and tensile stress to persist. This further expanded the width and depth of desiccation cracks, culminating in the Summer 2022 crack captured by E2 in Figure 4.1.

After reaching a peak in mid-July, the ambient air temperature and relative humidity gradually declined. By E3 in late September, a markedly desiccated and friable surface had developed. Sporadic rainfall occurs across this period, as illustrated in Figure 4.2D. However, this rainfall does not significantly affect the primary crack network, produces no substantial change in soil moisture content, and does not generate surface runoff. In contrast, the secondary crack network rapidly absorbed the incoming moisture fluxes, which exhibited a pattern of partial healing followed by subsequent reopening during the drying intervals. This cyclic behaviour occurred within an overarching seasonal drying regime, allowing quick secondary crack network recovery. Moreover, the ongoing cycling resulted in a progressively more friable and finely desiccated surface, as recorded by E3 in Figure 4.1. This overall process allowed the deep primary cracks to persist into late September, despite the seasonal change in weather.

Formation of the Winter 2021 Crack Network (E4 – E5)

The Summer 2021 crack network heals fully in early October after sustained and intense natural rainfall, documented as E4. With the closure of the Summer 2021 crack network, the first instance of runoff is recorded, illustrated in Figure 4.2C. This critically demonstrates the additional water storage capacity the Summer 2021 network gave to the lysimeter slope, which could significantly affect overall stability. In the 24 hours preceding E4, 52 mm of rainfall was measured (Figure 4.2D), which generated an increase in volumetric water content down to 400 mm (Figure 4.2B), coinciding with the maximum depth of subsurface desiccation. The magnitude of this increase reduces with depth, with shallow layers exhibiting a near-instantaneous return to saturated conditions. With increased rainfall and moisture, there is a rapid loss of all summer-generated suction, which does not recover for the remainder of the year, importantly terminating the seasonal drying cycle. The corresponding responses observed in the suction and water content sensors at 200 mm during this event demonstrate their reliability in accurately capturing soil moisture dynamics.

Figure 4.2A illustrates a prompt reduction in moisture content within the upper 100 mm of the lysimeter slope following the cessation of heavy rainfall. This initial rapid desaturation is followed by stabilisation at a consistently elevated moisture level, indicating sustained water retention provided by the desiccated and likely deteriorated slope. Event E5 occurs at this inflection point, which marks the formation of the Winter 2021 crack network. As discussed in Section 4.2.1, this network prevailed through to May 2023, gaining no further depth or width past its extent in Figure 4.1 (E5). By analysing the hydrologic regime of the lysimeter slope and the variations in weather patterns during this period, a framework can be established for understanding the observed seasonal transition changes in cracking behaviour.

At the onset of the Winter 2021 network, autumnal air temperatures had dropped to approximately 10 °C, and solar radiation had weakened to an average of 50 W/m². As winter progressed, Figures 4.2D and 4.2E show a continued decline in both parameters, alongside increased rainfall frequency. According to the Penman-Monteith (1965) equation, net radiation and temperature reduction substantially lowers evaporative demand. Consequently, the lysimeter slope experienced a marked shift in its hydrological regime. Without significant evaporative energy, moisture content fluctuated near saturation in the upper 100 mm or remained saturated at greater depths throughout the winter. A lack of moisture content and suction gradients reduced stress accumulation, providing less energy for desiccation. This led to the development of thinner and shallower networks that are more sensitive to changes in moisture. The reduced intensity of these desiccation cracks is visible through the increasing magnitude and frequency of surface runoff as they tend towards their late-December closure.

From E5 to late November, the Winter 2021 network persisted, driven by the cyclic wetting and drying restricted to the upper 100 mm, limiting crack propagation depth. The expedited re-opening of the Winter 2021 network following wetting events may reflect the altered hydrological dynamics and structural integrity of the Ampthill Clay under desiccation-induced deterioration. The accelerated crack opening and closure rate observed here would possibly enhance such structural degradation. However, these findings may also highlight the significance of alternative drying mechanisms in environments where elevated temperatures are not prevalent. Notably, Figure 4.2E indicates that considerably windier conditions were observed during the autumn and winter seasons of 2021. These findings support Penman’s (1948) assertion that wind

speed is a critical factor in enhancing evaporation. Therefore, during the colder winter, wind is responsible for sustaining soil evaporation and desiccation. These isolated effects of wind speed on desiccation cracking will be explored in greater detail using targeted experiments within Section 5.3. However, other researchers have highlighted it as an important factor in drying slopes and similar scale experiments (Eminue et al., 2018; Cordero et al., 2021; Yu et al., 2021).

In December, saturated conditions were attained through continuous incoming moisture fluxes, resulting in the Winter 2021 network largely remaining closed. It subsequently reopened and re-established itself as a consistent feature beginning in mid-January. The findings presented herein contrast with the prevailing literature, which predominantly indicates that desiccation cracking remains closed from mid-November through May (Yu et al., 2021). However, the lysimeter study on a bare slope exemplifies a worst-case scenario for environmental exposure without beneficial vegetation effects. This underscores the necessity of considering a complex array of parameters to comprehensively evaluate the processes of desiccation crack formation and subsequent deterioration in infrastructure embankments.

4.2.3 Seasonality in 2022 and Impact of Temperature Extremes

In 2022, a full calendar year of monitoring allowed for observing seasonal transitions from spring to summer and from summer to autumn into winter. This monitoring facilitated the study of desiccation crack evolution at these critical environmental boundaries. These transitions offered valuable insights into how deviations from seasonal norms can significantly affect desiccation and its influence on slope hydrology. Figure 4.3 displays the same suction, volumetric water content, runoff, and environmental variables as Figure 4.2 for the monitoring period of April 2022 to December 2022. This monitoring period encapsulates a series of simulated storm events applied to the lysimeter slope in August and September 2022. The effect of these will be discussed broadly, with a detailed assessment provided within Section 4.3.

Formation of the Summer 2022 Crack Networks (E6 – E7)

Figure 4.3A shows the initiation of substantial drying within the shallow subsurface (upper 100 mm) from April 2022. The upper 200 mm of the crest experienced desaturation in early May, albeit at a reduced rate. The generation of slight suction closely accompanied this desaturation at the same depth and location (Figure 4.3B).

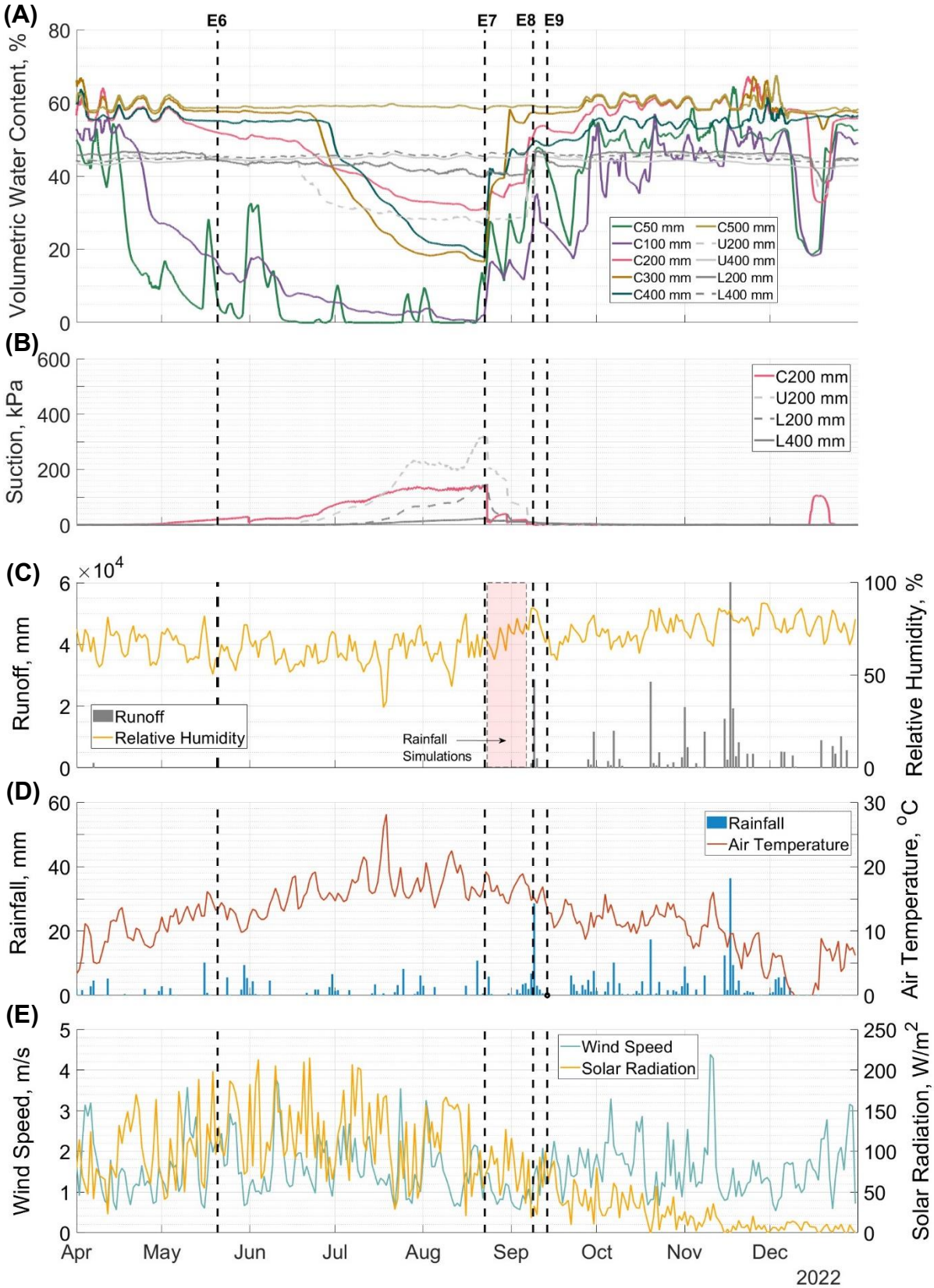

Figure 4.3: Plots demonstrating the temporal evolution of (A) volumetric water content (%) and (B) suction (kPa) through the upper (U), lower (L) and crest (C) regions of the lysimeter slope from April to December 2022. Time series data for (C) slope runoff (mm) and relative humidity (%), (D) rainfall (mm) and air temperature (°C), and (E) wind speed (m/s) and solar radiation (W/m^2) are also given. Events E6 – E9 are also annotated on all plots, as well as the occurrence of rainfall simulations applied to the slope.

In April and May, the air temperature and solar radiation showed an upward trend, which is commonly associated with the progression of Spring toward Summer.

As indicated by E6, the first appearance of the Summer 2022 crack network was observed in late May during the Spring season as suction accumulation began. However, the stability of this network into a permanent feature did not occur until mid-June. Notably, the larger primary cracks that formed exhibited increased sensitivity to fluctuations in moisture during Spring compared to their resilience observed in Summer 2021. This is likely associated with more transient behaviour in weather and, subsequently, soil moisture and suction observed across Figure 4.3A – E, which facilitated an equally dynamic response of crack apertures. An illustration of how the primary crack's aperture fluctuated during this period is given in Figure 4.4.

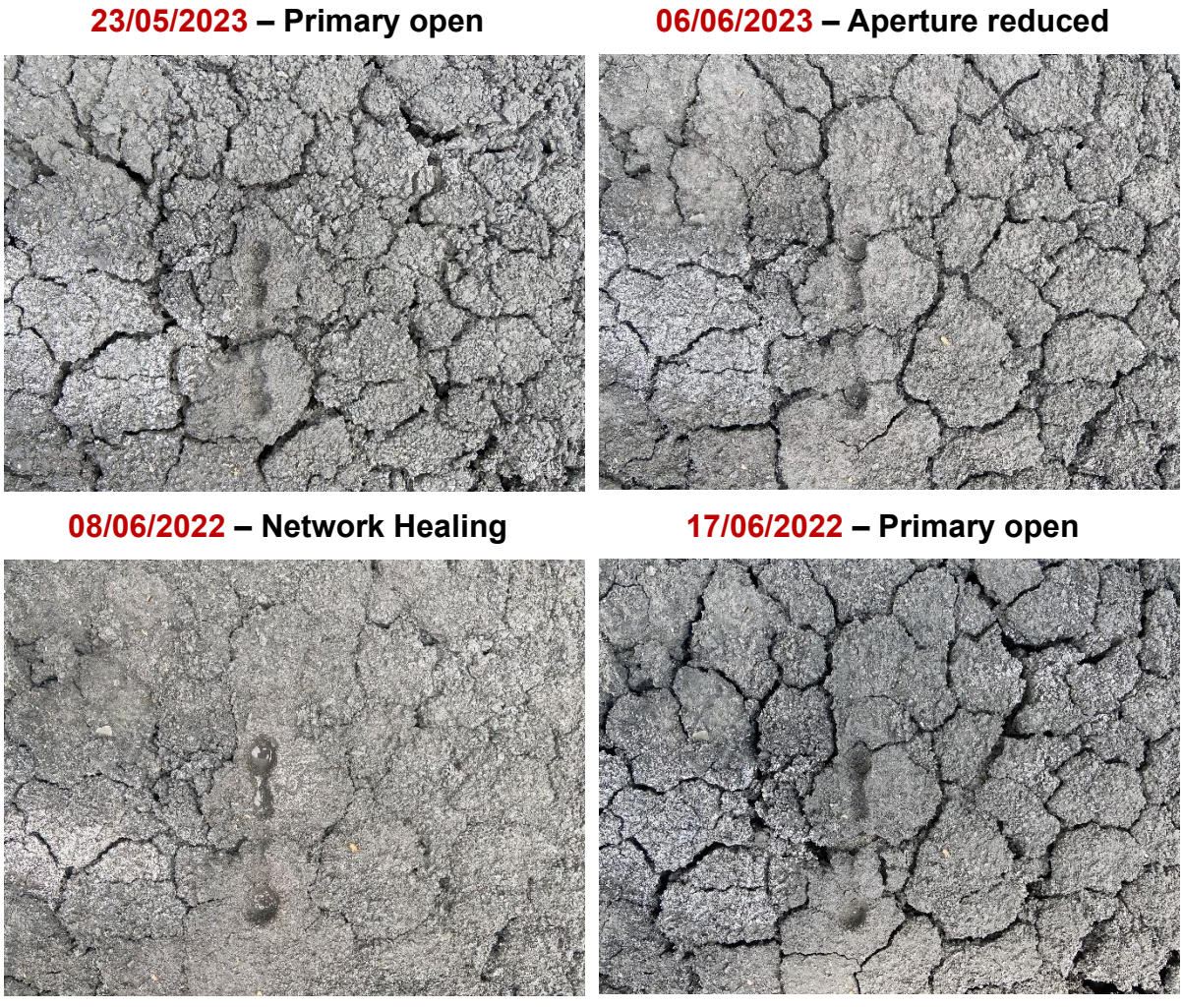

Figure 4.4: Time series of desiccation crack images showing the unstable aperture of the deep primary cracks within the Summer 2022 network after they first emerged in late May before later stabilising in mid-June.

The timing of this emergence in late May, coupled with the network's more pronounced sensitivity to spring conditions, presents significant implications. Firstly, it underscores the potential onset of substantial desiccation within infrastructure embankments before more intensive summer drying. Secondly, it highlights the critical nature of environmental conditions in this transitional period, which may influence the onset of deep desiccation in embankments. Given projections of future climate change that suggest warmer conditions than those typically experienced in Spring, there exists a heightened risk that these detrimental crack networks may persist for extended durations on embankment slopes (Met Office, 2019; Mair, 2021; ORR, 2021). Consequently, such prolonged presence would increase vulnerability to enhanced infiltration and rapid suction loss, potentially posing a greater threat to the structural integrity of these key assets.

Progressing through June and July, the Summer 2022 crack network exhibited considerable expansion in width and depth in response to rising air temperatures, increased solar radiation, and variable wind speeds – all key components that enhance evaporative demand according to the Penman-Monteith (1965) equation. A primary difference between Summer 2022 and Summer 2021 is the occurrence of two significant heatwaves, defined by the Met Office as events when maximum air temperatures exceed 25°C for three or more consecutive days. The first heatwave was observed in mid-July, as indicated by the notable peak in average air temperature in Figure 4.3D. This heatwave persisted for three days and occurred amidst already elevated summer temperatures. The maximum air temperature recorded during this heatwave reached 37.7°C, representing an increase of 10 degrees compared to the peak summer temperature of 27.9°C observed in 2021.

Heat wave conditions increase net radiation and air temperature, raising the energy available for evaporation. According to the Penman-Monteith (1965) equation, higher temperatures increase the vapour pressure deficit, intensifying evaporative demand and accelerating soil moisture loss. Such effects are observed in the slope hydrology, as shown in Figures 4.3A and 4.3B. Moisture loss extended to depths of 400 mm within the crest, with significant reductions also recorded in the upper slope region for the first time. All 200 mm sensors indicated an increase in suction, albeit with a lag in response to soil moisture, with a secondary peak aligning with the mid-August heat wave that spanned four days. The accelerated rate and depth of moisture loss, suction generation, and stress accumulation were concurrent with the widening and deepening

of Summer 2022's primary crack network, annotated as E7 in Figures 4.1 and 4.3. Importantly, the severity of the networks in Summer 2021 and 2022 is comparable. However, such deep crack networks proved fundamentally more critical for slope hydrology under heatwave conditions in 2022, with the response limited to the upper 200 mm in Summer 2021 (see Figure 4.2). These observations further suggest a synergetic relationship between the two parameters, which combine to exacerbate weather-driven deterioration within infrastructure embankments. Such results are fundamental to understanding the potential risk posed by desiccation-driven deterioration under heatwave conditions, which are predicted to increase in severity and frequency under future climate change projections (Met Office, 2018).

Formation of the Winter 2022 Crack Network

The Summer 2022 crack network persisted within the slope until September 8th, 2022, after which it healed. In Figures 4.1 and 4.3, this period is referred to as E8. Between August 23rd and September 6th, 2022, three simulated storms were applied to the lysimeter slope. Figure 4.3C demonstrates the temporal occurrence of these events within the monitoring timeline. In response, a substantial increase in moisture content throughout the slope profile is observed, accompanied by a rapid loss of suction, with their agreeable behaviour confirming sensor reliability. This hydrological response of the slope to simulated storms is discussed in greater detail within Section 4.3. However, for this analysis only, the fundamental observation from these intense rainfall events is that the primary crack network remained partially open and did not close until a high-intensity natural rainfall event occurred two days after the last simulated storm. This also marks the first record of runoff of 2022 (Figure 4.3C), demonstrating the lysimeter slope's substantial additional storage capacity in a highly desiccated state.

Another crucial observation is that following E8, volumetric water content remains close to saturation and suction at zero until a temporary relative decrease and increase in late December. These moisture content and suction changes occur in the upper 200 mm and coincide with freezing temperature conditions (see Figure 4.3D). Other studies have attributed such behaviour to frost heave, where water migrates toward the freezing front in soil, causing local desaturation and stress accumulation (Seto & Konrad, 1994; Boley & Herzog, 2015). However, further analysis would be needed to confirm such a hypothesis. Nevertheless, Summer 2022's crack development and suction generation terminated a month earlier than Summer 2021. This observation

suggests that the intensity of autumn rainfall is critical in influencing the duration of seasonal-scale drying cycles.

After the closure of the Summer 2022 crack network, a new pattern was established within five days, displaying characteristics consistent with those of the Winter 2021 crack network. This is named the Winter 2022 crack network, and E9 represents its formation point in Figures 4.1 and 4.3. Through late autumn, the Winter 2022 network opens and closes in response to small fluctuations in shallow surface (upper 100 mm) moisture content as rainfall events increased in frequency. However, the slope remains near saturation, with the network remaining largely closed through December and re-establishing in late January. Compared to 2021, this autumn and winter period is associated with a significantly higher runoff volume. This is likely associated with the slope's higher saturated state gained after the rainfall simulations and the more frequent closure of the winter network under smaller moisture influxes. The generated runoff volume would significantly impact surface erosion and fines washout, adding additional risks to overall embankment stability. Although these shallow winter networks do not significantly impact slope behaviour beyond 100 mm, their prevalence is still significant from a deterioration perspective. For example, an increased likelihood of shallow or washout failures may occur, with cyclic desiccation continuing to degrade and loosen the soil structure (Mair, 2021).

The behaviour of desiccation cracking in the Summer of 2021 and 2022 indicates a clear seasonal dependence, where interactions between weather and slope hydrology dictate its relative severity. Observing these interactions across seasonal transitions indicates the importance of weather in these boundary zones for dictating the initiation and cessation of summer desiccation. Any deviations from seasonal norms, particularly under future climate change projections, may amplify the severity and increase the duration of the desiccation cracking window within infrastructure embankments. Winter desiccation is evaluated here in the context of a bare, non-vegetated slope, which represents a worst-case scenario for environmental degradation. Nonetheless, given projections of increasingly warmer and wetter winters (Met Office, 2018), the prevalence of desiccation cracks and the associated cyclic volumetric changes will likely become increasingly critical issues warranting further attention and investigation.

4.2.4 Deviation for Seasonal Behaviour in Summer 2022

A fundamental change in desiccation cracking behaviour occurs in 2023, where no seasonal change in the crack network occurs. As previously illustrated in Figure 4.1,

the shallow Winter 2022 crack network prevails within the lysimeter slope until monitoring cessation on August 31st, 2023. Figure 4.5 plots the hydrological (suction, runoff, and volumetric water content) and weather data from April to August 2023. Significant differences in hydrological behaviour are observed in Figures 4.5A and 4.5B, with no desaturation occurring beyond 100 mm and suction remaining zero throughout the monitoring period. A continuous cyclic pattern of shorter wetting and drying cycles is also noted within the upper 100 mm. This behaviour shows greater similarity to the slope's hydrological response during the autumn and winter seasons of 2021 (Figure 4.2) and 2022 (Figure 4.2), suggesting it is an influence of a shallower crack network.

To understand this deviation from seasonal patterns of desiccation crack behaviour in 2023, a detailed comparison of weather trends across the 2021 – 2023 monitoring period was conducted. Figure 4.6A compares the total monthly rainfall of each calendar month for 2021 – 2023 against the 1991 – 2020 Climate Period average for Northeast (NE) England, provided by the Met Office. In 2023, six months exceeded this average, a marked increase from two months in 2022 and five months in 2021. A significant exceedance occurred in July 2023, which was nearly double the NE England average. In contrast, rainfall from 2021 to 2023 between April and August was significantly below this threshold, with higher rainfall volumes primarily occurring in the late autumn and winter.

The same comparison for average air temperature is provided in Figure 4.6B. In May and June 2023, the average temperature reached the NE England average. However, in March, July and August 2023, average temperatures were substantially lower than this threshold. For 2021, the threshold was exceeded in July yet lower in August, and 2022 exhibited above-average temperatures for most of the year. Moreover, Summer 2023's peak temperature was 26°C, 1°C and 11°C lower than 2021 and 2022, respectively. With little difference in peak summer temperatures, the disparity in behaviour with Summer 2021 was driven by an absence of prolonged drying periods in Summer 2023 due to higher rainfall.

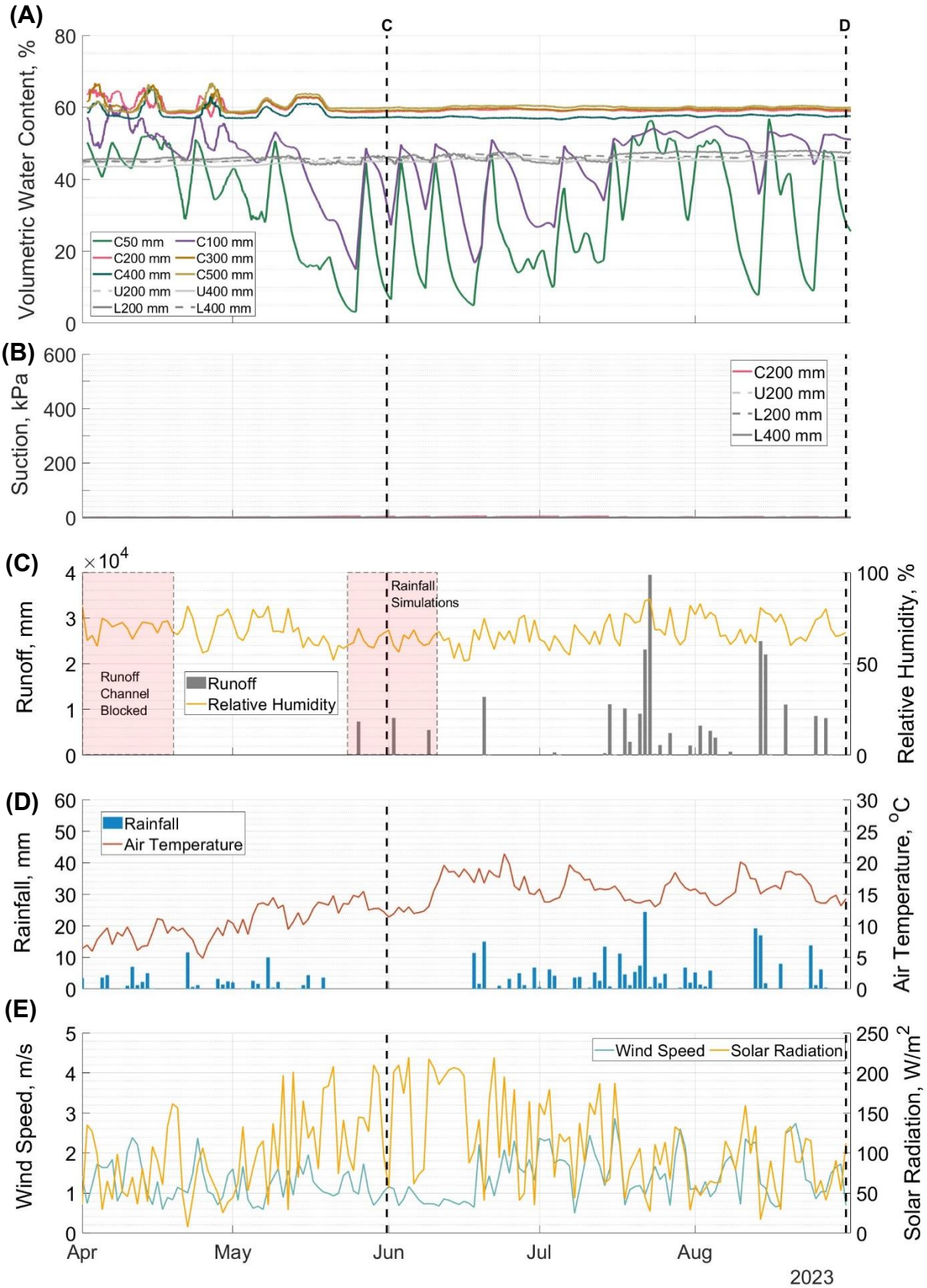

Figure 4.5: Plots demonstrating the temporal evolution of (A) volumetric water content (%) and (B) suction (kPa) through the upper (U), lower (L) and crest (C) regions of the lysimeter slope from April to August 2021. Time series data for (C) slope runoff (mm) and relative humidity (%), (D) rainfall (mm) and air temperature (°C), and (E) wind speed (m/s) and solar radiation (W/m^2) are also given. Events E1 – E5 are also annotated on all plots, as well as the zone rainfall simulations were applied and a period where the runoff channel was blocked.

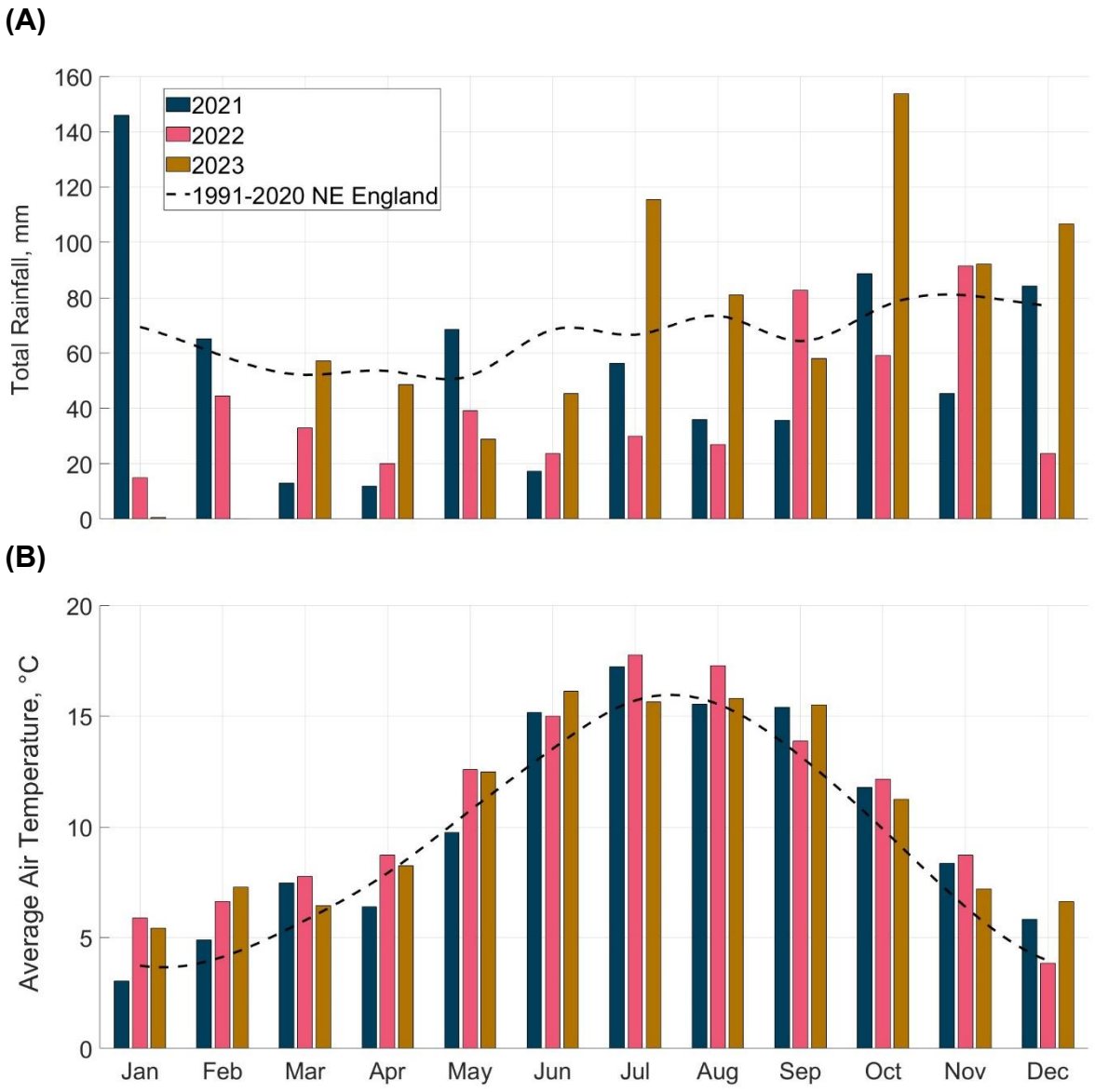

Figure 4.6: Comparison of (A) total monthly rainfall (mm) and (B) monthly air temperature averages (°C) for 2021, 2022, and 2023 with the 1991 – 2020 climate period averages recorded by the Met Office.

Crack network development in Summer 2022 revealed the critical role of elevated net radiation and vapour pressure deficits in controlling evaporative demand and triggering deep desiccation in the transition from late spring to early summer. Figures 4.6A and 4.6B support sustained periods of drying prevailing through these critical months, with shorter periods of greater rainfall counterbalanced by hot and dry spells which followed. In contrast, rainfall and air temperature were above and below average for March and April of 2023, with conditions appearing drier in May and June. However, this graph does not consider the simulated storm events applied to the lysimeter slope in late May and early June, which would have significantly elevated the total rainfall

within these months to above the 1991 – 2020 climate period average. The temporal occurrences of these events are demonstrated in Figure 4.5A, all of which generated substantial runoff and closed the crack network during application. With advancement into July and August 2023, unseasonably high rainfall intensified this effect, while reduced net radiation and lower vapour pressure deficits did little to offset it. Figure 4.5E demonstrates comparatively lower solar radiation during Summer 2023, likely associated with cloudier and wetter conditions. This starkly contrasts the drier and warmer conditions that drove deep desiccation in the Summer of 2021 and 2022. Consequently, these results evidence that the persistence and timing of intense rainfall events are critical controls of desiccation crack severity.

Comparable magnitude storm events were applied to Summer 2022's deep desiccation network in August and September 2022. The associated implications of this are discussed in greater detail within Section 4.3. However, the lysimeter slope exhibited no suction and high saturation for the remaining months of 2022, particularly in the absence of conditions described by Penman (1948) conducive to sustained and extensive drying. Under naturally intense rainfall, the lysimeter slope's hydrologic behaviour in 2021 exhibited similar behaviour during the summer-to-autumn transition. These simulated and natural storms had a distinct termination effect on the Summer 2021 and 2022 crack networks and suction generation. Therefore, the early application of these storms in spring before unseasonably high summer rainfall did not allow the lysimeter slope to desaturate, generate substantial suction and facilitate deep desiccation. Consequently, summer desiccation shifted to shallower depths where drying fronts could penetrate to, exhibiting increased cyclic behaviour in the shallow subsurface.

Figure 4.5C illustrates that runoff remains substantially higher and more frequent in Summer 2023 compared to zero recorded during Summer 2021 and 2022. This is attributable to the high cyclicity of crack aperture under a heightened sensitivity to small variations in moisture. This behaviour is illustrated in Figure 4.7, where desiccation cracks can be observed opening, closing, and regenerating within 48 hours. Although desiccation cracking exhibited a shallower influence on slope hydrology during Summer 2021, these more frequent crack opening and closure cycles could still have detrimental impacts. Repeated cycling could accelerate microstructural degradation in the upper 100 m, potentially initiating a shift of instability into the shallow subsurface. With this shift and increased summer runoff, a change in failure mechanisms to shallow

surface slips or washout failures could occur. This is particularly relevant if fill material becomes progressively more disaggregated under repeated cycles.

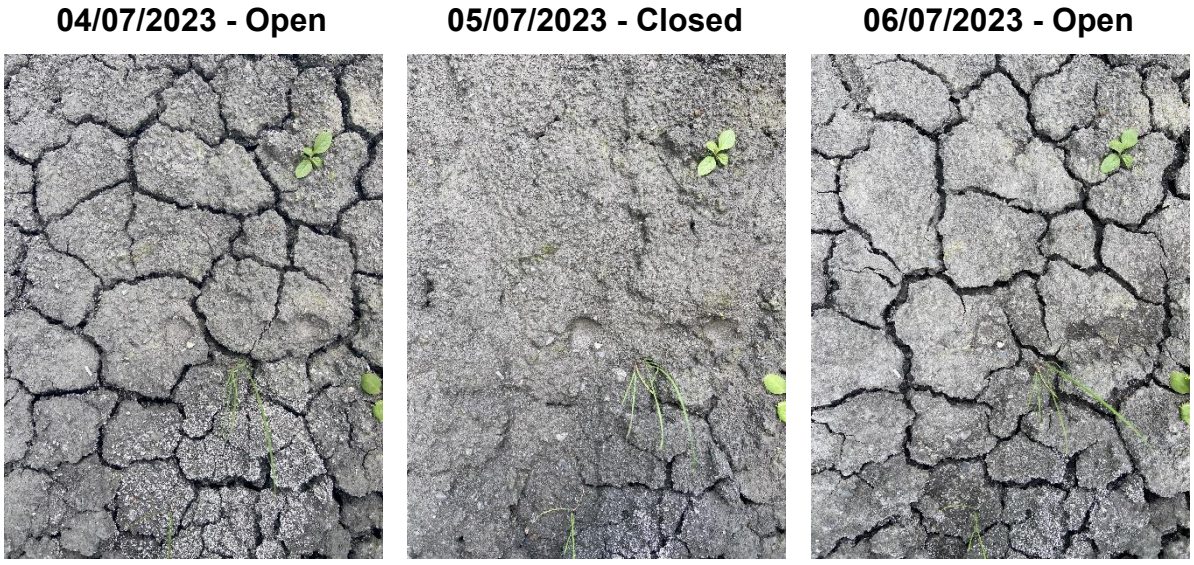

Figure 4.7: Example of the short cyclic behaviour of the crack network during Summer 2023, where shallow cracks exhibited a high sensitivity to small changes in moisture content.

The findings presented here fundamentally highlight the dynamic nature of desiccation cracking, illustrating that the interactions between seasonal weather patterns and slope hydrology are crucial in determining its severity. In the context of climate change, this relationship is particularly significant, as the increasingly indistinct transitions between seasons complicate the predictability of drying regimes and, therefore, desiccation cracking (Met Office, 2018). Therefore, such insights are vital steps toward understanding the complexities associated with desiccation-driven deterioration under a variable climate.

4.2.5 Additional Effects of Shading in Desiccation Crack Distribution

The sections above have demonstrated the high sensitivity of desiccation cracking to changes in environmental conditions. However, spatial variation in the impact of these environmental conditions across the slope was observed. Such variation was formed through the interaction of diurnal, intra-seasonal and seasonal weather cycles with physical boundary conditions. The resultant effect was spatial and temporal heterogeneity in the duration and magnitude of environmental exposure across the lysimeter slope. Such effects generated heterogeneous evaporation by spatially modifying the inputs to Penman-Monteith's (1965) equation, an effect which is associated with more localised crack initiation in the existing literature (Stirling et al., 2021; Yu et al., 2021). For the lysimeter slope, the physical boundary conditions which

appeared to influence environmental exposure were slope prominence and the natural and urban fabric of the surrounding environment.

Slope prominence is related to static morphological features such as slope height gradient and aspect, which can locally enhance environmental exposure. More pronounced regions of the lysimeter slope were predisposed to faster evaporation and crack formation. Figure 4.8 illustrates this effect, showing desiccation cracks initiating first across the lysimeter slope's central upper slope region at the onset of drying. This region is geometrically more elevated, limiting its interactions with other physical boundary conditions. The increased net radiation enhanced available energy for evaporation, which, according to the Penman-Monteith (1965) equation, intensified soil drying and accelerated desiccation crack formation

Similarly, the surrounding environment's natural and urban features influenced net radiation by altering the duration of environmental shading across the lysimeter slope. Figure 4.9 documents the temporary shade cast by the lysimeter casing across the lower slope region, present only during the low winter sun. Cracking forming outside this shade band was observed to terminate at its upper boundary, as illustrated by Figure 4.9. Such cracking behaviour suggests that this seasonal reduction in net radiation reduced the energy for evaporation. However, the reduced cracking in the lower slope region may also be attributed to decreased air circulation, as the walls of the lysimeter container act as wind deflectors, further impacting evaporation through the aerodynamic component of the Penman-Monteith (1965) equation. With reduced solar radiation and wind circulation, the evaporation-driven cause-chain effect of water loss, suction generation, soil shrinkage, tensile stress accumulation, and crack initiation is critically absent (Tang et al., 2021; Zeng et al., 2024).

The sun’s diurnal migration and traversal around the surrounding high-rise buildings had a similar, albeit more temporary, shading effect. This caused Side A to remain shaded for longer than Side B. The thermal image in Figure 4.10 quantifies the potential difference in surface temperature that could develop between the two sides during the diurnal migration process as a reduced of reduced net radiation. In this example, the shaded region on Side A (dark blue) is 5 – 12^{o}C colder than the non-shaded Side B. This capture also emphasises the preferential heating of the central upper slope area. Therefore, evaporation and desiccation cracking were often initiated foremost in Side B before propagating towards Side A as exposure to solar radiation occurred and the soil heat flux increased.

Figure 4.8: Photograph illustrating the emergence of desiccation cracks on the central upper region of the lysimeter slope (red box) due to its prominence relative to surrounding slope regions and minimal interference from the physical bounds of the lysimeter container.

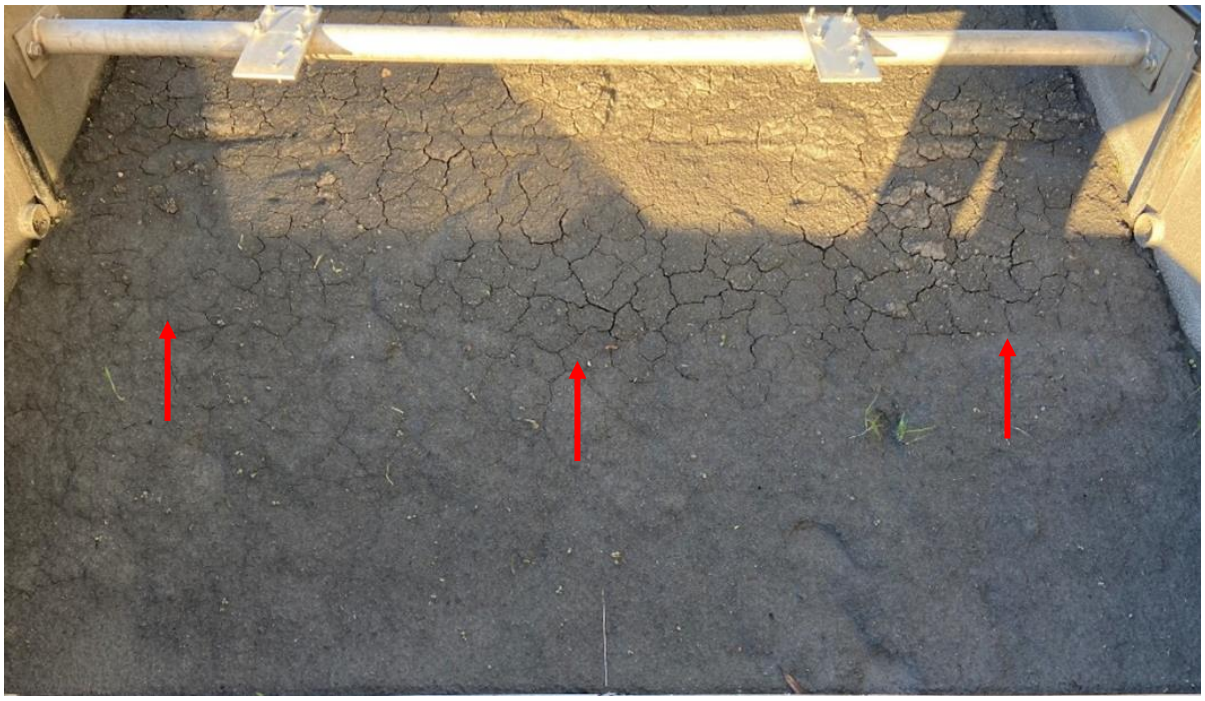

Figure 4.9: Photograph which illustrates a temporary band of shade cast by the lysimeter casing over the lower slope only during winter when the sun was lower in the sky. The red arrows point toward the termination of desiccation cracks at the upper boundary of the shade band.

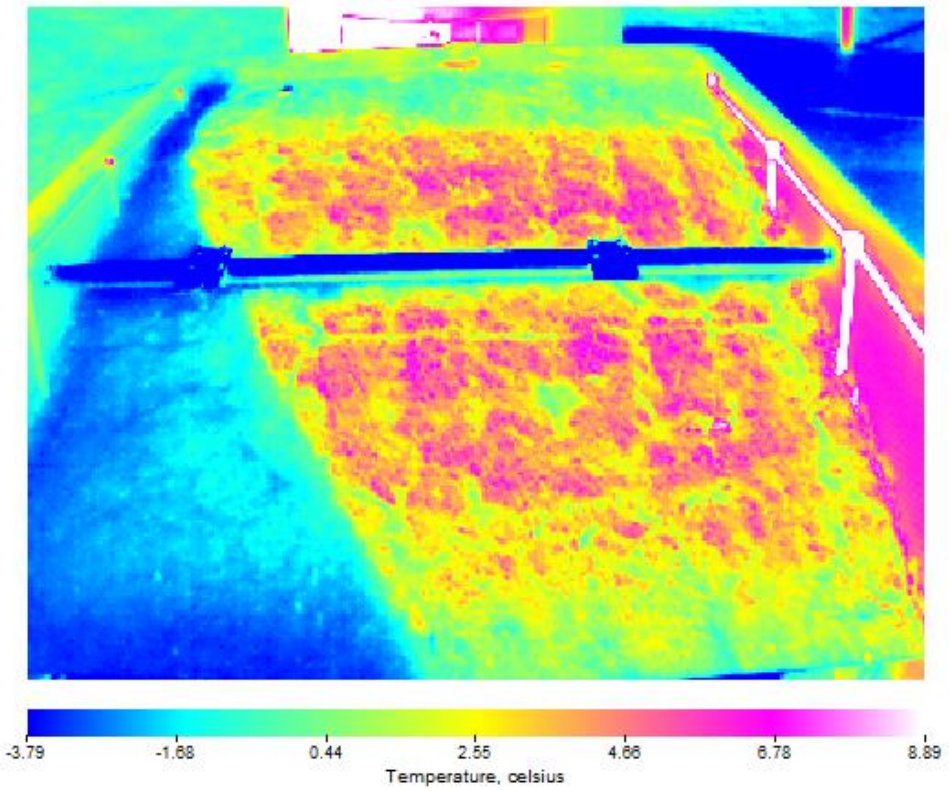

Figure 4.10: Thermal capture of the effects of a temporary shade band cast due to the diurnal migration of the sun around the surrounding high-rise building. The difference in surface temperature between Side A (left) and Side B (right) is shown in this example to be between 5 and 12°C.

Although real field embankments are morphologically similar and experience comparable physical boundary conditions to the lysimeter slope, they are not encased within a lysimeter. Consequently, infrastructure embankments are subject to a broader range of physical and environmental influences that the lysimeter does not model, adding further complexity to the pattern of evaporation and desiccation. These results suggest that solely monitoring weather patterns cannot predict an embankment's desiccation behaviour. A full appreciation of site conditions is needed, particularly investigating changes in evaporative and energy fluxes under varying environmental exposure, as these parameters are critical controls on desiccation rate and severity.

4.3 Slope Response to Simulated Storms

Currently, the most reliable knowledge on infrastructure embankment deterioration is derived from forensic analysis of past failures or field monitoring conducted under past or present environmental conditions. While these approaches offer valuable insights into weather-driven deterioration mechanisms and their potential to cause failure, they do not provide definitive predictions for future asset behaviour. As a result, there

remains a critical gap in our ability to forecast the future stability and resilience of embankments under shifting climate conditions. This limitation is especially significant in light of climate change, where these assets are set to experience unprecedented weather extremes while already in an advanced state of deterioration (Perry et al., 2003; Kilsby et al., 2009; Loveridge et al., 2010; Mair, 2021).

Future UK climate change projections are predicting warmer, drier summers with an increased frequency of hot spells and convective storms (Met Office, 2022). Such drying extremes are likely to exacerbate the severity and prevalence of desiccation cracking in high-plasticity clay embankments. This, in turn, increases their susceptibility to preferential flow and rapid loss of stabilising suction, heightening the assets' vulnerability to failure at the onset of the intense summer rainfall events (Loveridge et al., 2010; Huang et al., 2023; Kandalai et al., 2023). As discussed in Section 4.2.3, soil drying under natural heatwave conditions in Summer 2022 appeared enhanced in the presence of desiccation cracks. Warmer and wetter winters are also forecasted (Met Office, 2022), amplifying the seasonal differences in pore water pressure and further driving the development of irreversible microstructural degradation within infrastructure slopes (Stirling et al., 2021; Briggs et al., 2023).

Limited high-resolution monitoring and the inability to conduct controlled experiments make performing such research on live infrastructure embankments significantly challenging and labour-intensive. In Section 4.2, heavy natural rainfall significantly influenced slope hydrology and the timing of seasonal-scale patterns of crack initiation and propagation. However, the potential impact of rainfall events of the magnitude projected under climate change models remains unexplored. Therefore, the lysimeter methodology was adapted using the setup described in Section 3.3.6, which applied two rainfall simulations (RS1 and RS2), each consisting of three high-intensity rainfall events spaced one week apart, to the lysimeter slope. Each rainfall event equated in magnitude to a 1 in 100-year storm, with a 45% climate change uplift applied, which totalled 52 mm of rainfall per hour.

Keeping the lysimeter slope continuously exposed to natural conditions enabled a comparative analysis of the changes in runoff and infiltration characteristics within a desiccated slope under different rainfall intensities. The rate and magnitude of water ingress control the severity of suction loss via the SWRC, which is a key mode of destabilisation and failure in infrastructure embankments, particularly for highly unsaturated and desiccated assets (Novák et al., 2000; Powrie & Smethurst, 2019;

Zhang et al., 2020; Stirling et al., 2021). Furthermore, understanding how the evolving nature of the Ampthill Clay fill's hydromechanical properties can enhance or deter the severity of these convective storm events is crucial for assessing their potential impacts on asset deterioration and stability. Therefore, each simulation series was applied one year apart and within different seasons, capturing the response of the slope under transient crack morphologies, antecedent saturations, and hydromechanical properties.

It should be noted that interpreting suction and volumetric water content data presents well-established challenges, particularly at the finer temporal and spatial scale being analysed in this section. A primary source of uncertainty in the measurement data arises when sensors lose contact with the surrounding soil. In this study, extensive desiccation within the lysimeter added complexity, as cracking may have intersected sensor measurement zones, distorting local hydraulic conditions. Determining the precise cause of such deviations is not feasible without disturbing the slope, which would compromise its natural behaviour. Sensor installation was carefully executed (Section 3.3.2) to ensure optimal soil-sensor contact; however, the shrink-swell and cracking dynamics of the highly plastic clayey soil may degrade this contact over time.

Although suction and water content sensors were positioned in close proximity, a separation remained over which material properties could vary due to local compaction, contact inconsistencies, or intersecting cracks. Consequently, while readings may be accurate for their specific locations, discrepancies between co-located sensors are expected due to micro-scale heterogeneity. This inherent limitation is acknowledged as an unavoidable caveat in the dataset. Nonetheless, the measurements exhibited consistent and interpretable responses to controlled wetting and drying events, supporting their reliability in capturing the slope's broader hydromechanical behaviour. Consequently, the interpretation focuses on relative changes and general trends, rather than the reliability of exact measurement values.

4.3.1 Implications of Summer Convective Rainfall on a Desiccated Slope

The first set of rainfall simulations (RS1) was applied during the late summer months as three events (E1 – E3) one-week apart between August 23rd and September 6th, 2022. This period was chosen as 2022's summer season had resulted in a desaturated and vulnerable slope condition. Before RS1, the lysimeter slope had generated significant suction and a deep network of desiccation cracks, which could considerably enhance its susceptibility to infiltration induced failure. An extensive and interconnected crack network can advance wetting fronts, causing a rapid loss of stabilising suction. This process can markedly reduce shear strength and an embankment's resistance to failure.

Figure 4.11 and Figure 4.12 plot time series data for Side A and B, including (A) volumetric water content at 50-, 100-, 200-, 300-, 400-, and 500 mm, (B) suction (kPa) at 200 mm (C) runoff (mm). The natural and simulated rainfall (mm) (E1 – E3) applied, and air temperature (°C) are also provided in Figures 4.11D and 4.12D, and solar radiation and relative humidity are given in Figure 4.11E and 4.12E. This data has also been generated for the upper and lower slope regions of Side A (Figure 4.13) and B (Figure 4.14). Annotated in Figures 4.11 and 4.3 is the temporal occurrence of A1 – A15 from Figure 4.15, which visualises crack evolution in Side A during RS1's application. For Side B, desiccation crack evolution is illustrated by B1 – B15 in Figure 4.16, with timings annotated in Figure 4.12 and 4.14. Side B was included in this analysis to gain insights into whether spatial heterogeneity in short-term infiltration patterns occurs and if the vegetated canopy varied its response to these storm events.

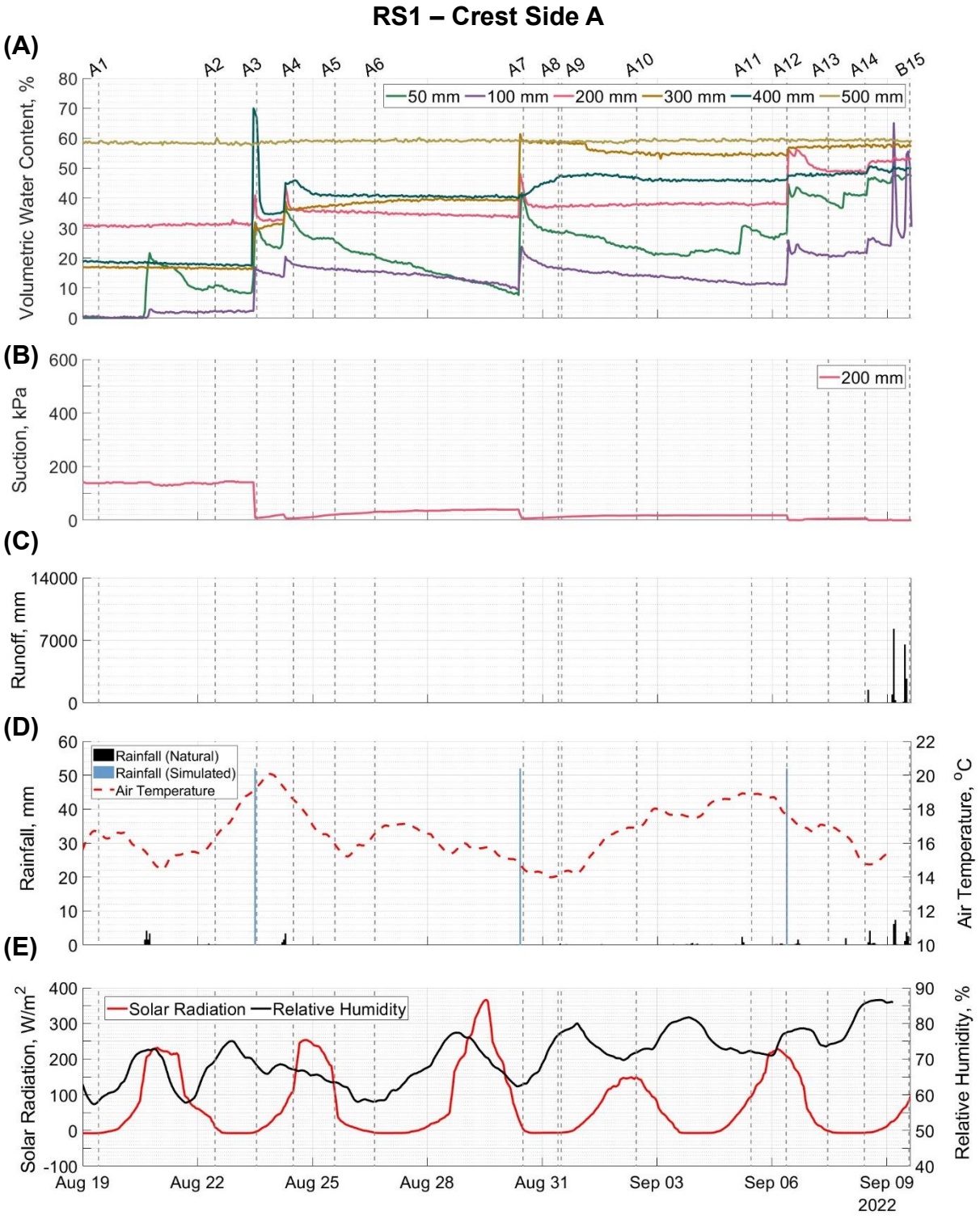

Figure 4.11: Time series data for Side A's crest region during the application of the first rainfall simulation (RS1) with graphs demonstrating (A) volumetric water content (%) at 50-, 100-, 200-, 300-, 400-, and 500 mm depths, (B) suction (kPa) at 200 mm, (C) runoff (mm) captured by Side A's channel, (D) simulated storm (blue) and natural (black) rainfall (mm) during RS1 and the ambient air temperature (°C), (E) relative humidity (%) and solar radiation (W/m^2) recorded during RS1. The annotated grey dashed lines mark the temporal occurrence of crack images A1 – A15 for Side A, provided in Figure 4.15.

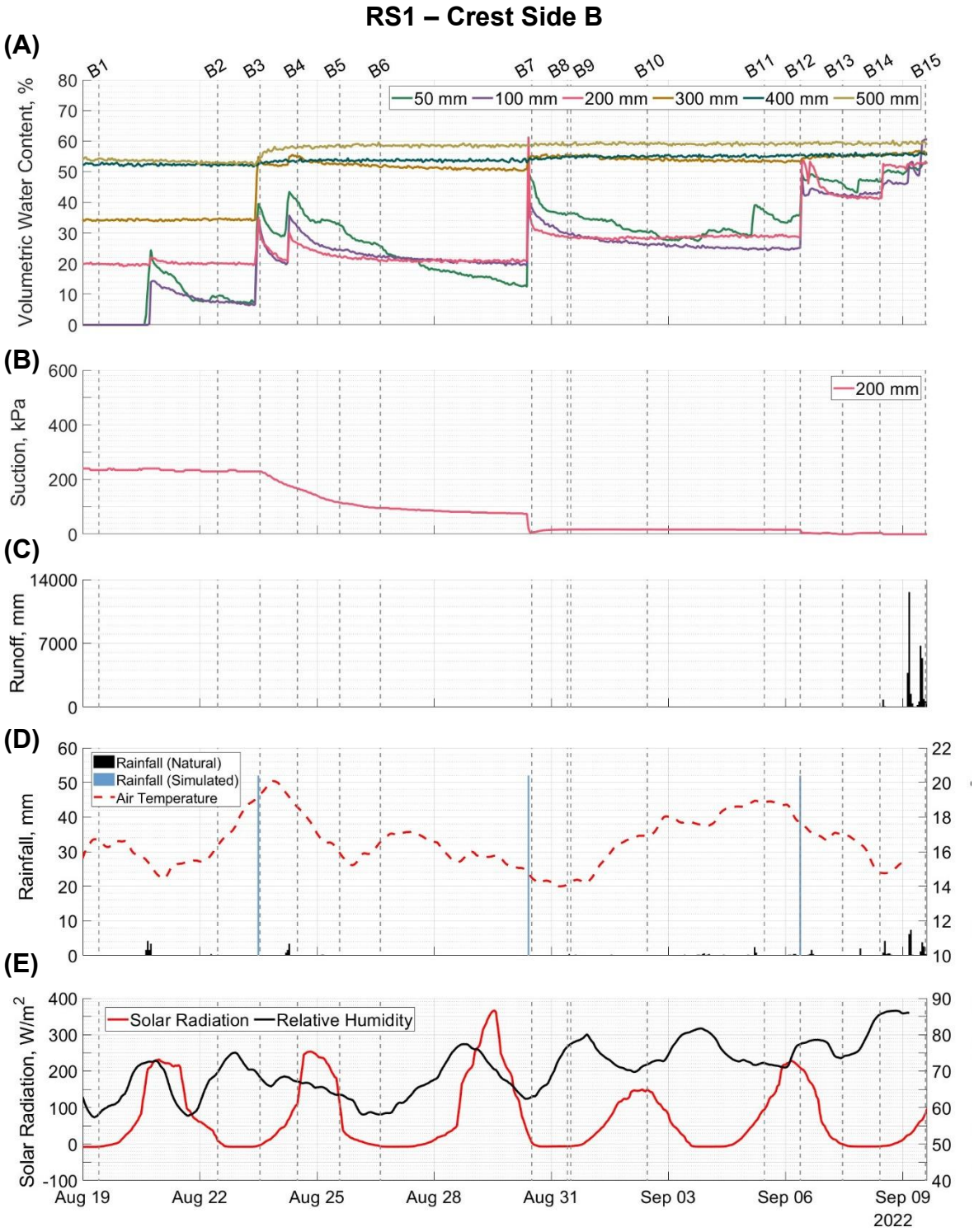

Figure 4.12: Time series data for Side B's crest region during the application of the first rainfall simulation (RS1) with graphs demonstrating (A) volumetric water content (%) at 50-, 100-, 200-, 300-, 400-, and 500 mmm depths, (B) suction (kPa) at 200 mm, (C) runoff (mm) captured by Side B's channel, (D) simulated storm (blue) and natural (black) rainfall (mm) during RS1 and the ambient air temperature (°C), (E) relative humidity (%) and solar radiation (W/m^2) recorded during RS1. The annotated grey dashed lines mark the temporal occurrence of crack images B1 – B15 for Side B, provided in Figure 4.16.

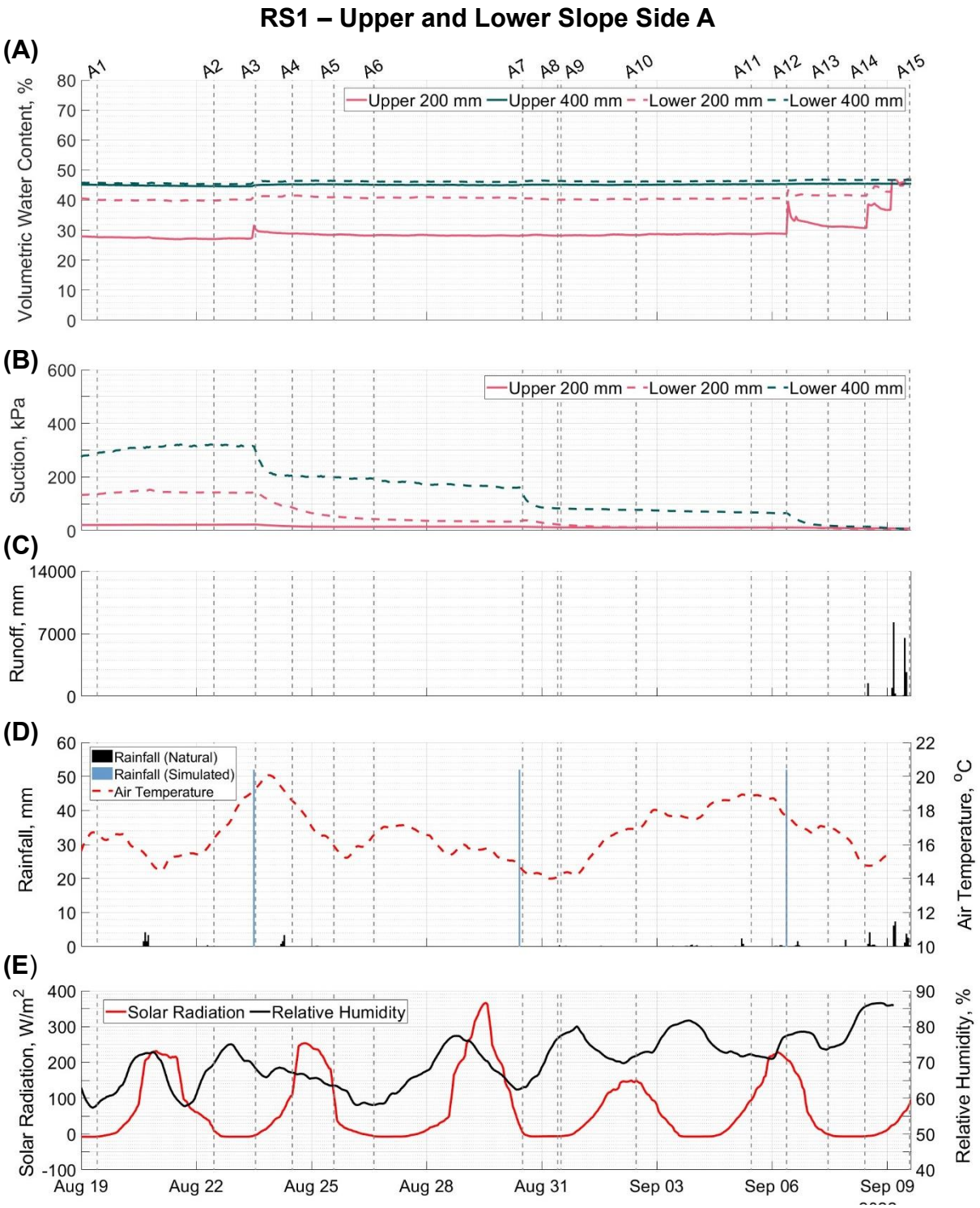

Figure 4.13: Time series data for Side A's upper and lower slope regions during the application of the first rainfall simulation (RS1) with graphs demonstrating (A) volumetric water content (%) 200- and 400 mm depths, (B) suction (kPa) at 200 mm and 400 mm (lower slope only due to upper slope sensor malfunction), (C) runoff (mm) captured by Side A's channel, (D) simulated storm (blue) and natural (black) rainfall (mm) during RS1 and the ambient air temperature (°C), (E) relative humidity (%) and solar radiation (W/m^2) recorded during RS1. The annotated grey dashed lines mark the temporal occurrence of crack images A1 – A15 for Side A, provided in Figure 4.15.

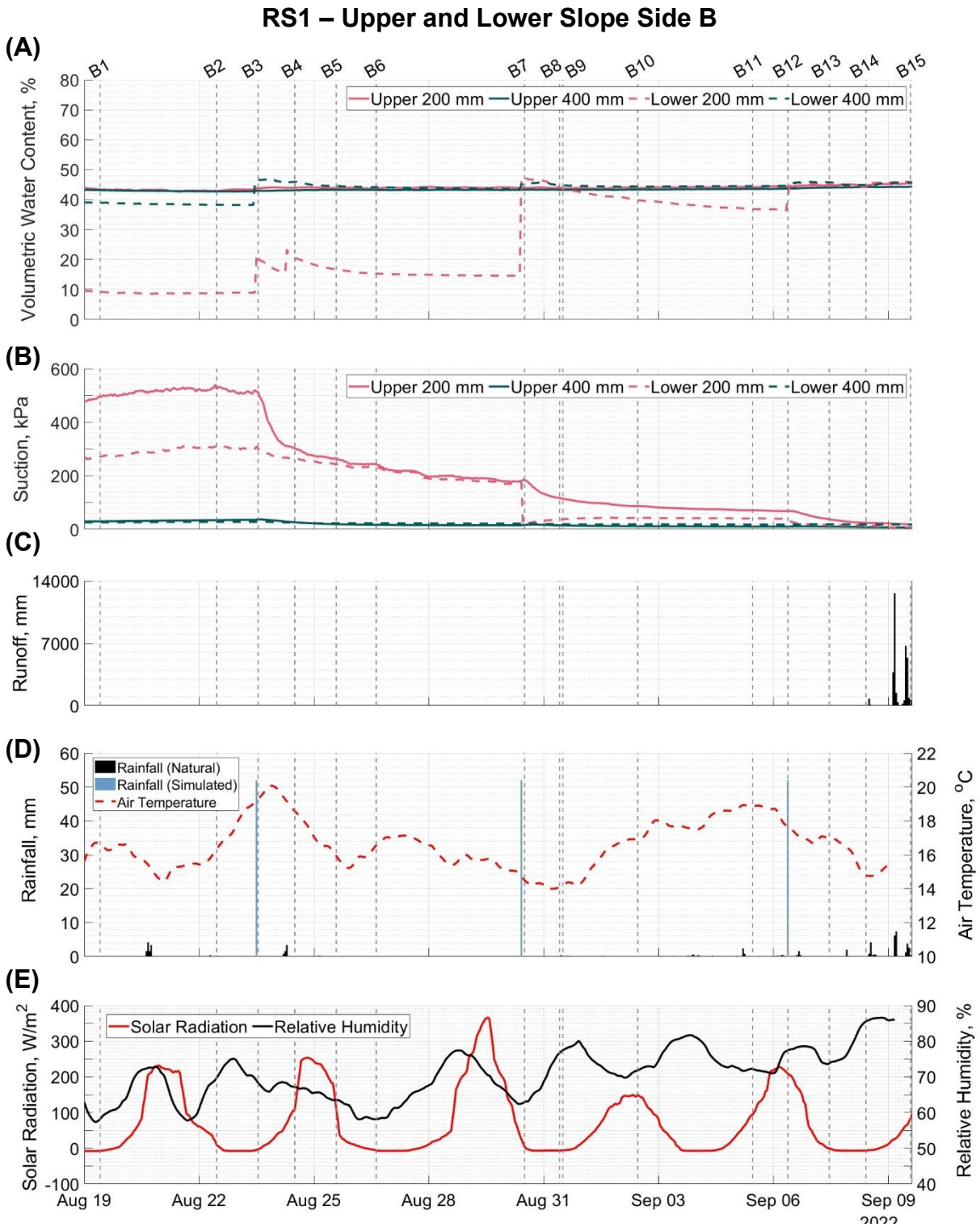

Figure 4.14: Time series data for Side B's upper and lower slope regions during the application of the first rainfall simulation (RS1) with graphs demonstrating (A) volumetric water content (%) 200- and 400 mm depths, (B) suction (kPa) at 200- and 400 mm, (C) runoff (mm) captured by Side B's channel, (D) simulated storm (blue) and natural (black) rainfall (mm) during RS1 and the ambient air temperature (°C), (E) relative humidity (%) and solar radiation (W/m^2) recorded during RS1. The annotated grey dashed lines mark the temporal occurrence of crack images B1 – B15 for Side B, provided in Figure 4.16.

RS1 – Side A Crack Evolution

A1 – 19/08/2022	A2 – 22/08/2022	A3 – 23/08/2022 (POST E1)	A4 – 24/05/2022	A5 – 25/08/2022
				
A6 – 26/08/2022	**A7 – 30/08/2022 (PRE E2)**	**A8 – 30/08/2022 (POST E2)**	**A9 – 31/08/2022**	**A10 – 02/09/2022**
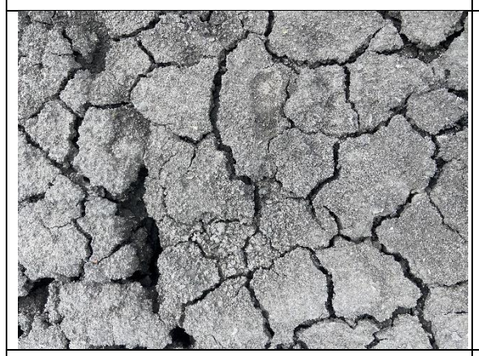				
A11 – 05/09/2022	**A12 – 06/09/2024 (PRE E3)**	**A13 – 07/09/2022**	**A14 – 08/09/2022**	**A15 – 09/09/2022**
				

Figure 4.15: Visualisation of the temporal evolution of the desiccation crack network on Side A of the lysimeter slope across the period RS1 was applied. The field of view covers the midpoint between the upper and lower slope regions. The temporal occurrence of these crack patterns is annotated in Figures 4.11 (Side A crest) and Figure 4.13 (Side A upper and lower slope).

RS1 – Side B Crack Evolution

B1 – 19/08/2022	B2 – 22/08/2022	B3 – 23/08/2022 (POST E1)	B4 – 24/05/2022	B5 – 25/08/2022
				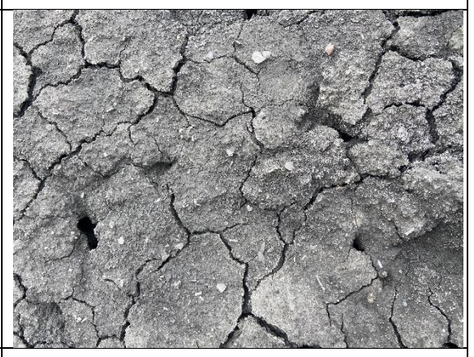
B6 – 26/08/2022	**B7 – 30/08/2022 (PRE E2)**	**B8 – 30/08/2022 (POST E2)**	**B9 – 31/08/2022**	**B10 – 02/09/2022**
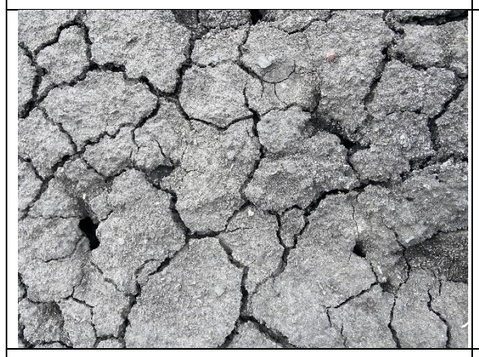			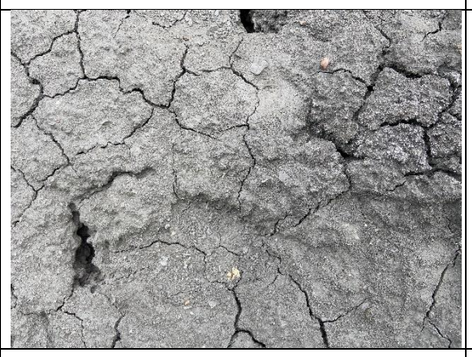	
B11 – 05/09/2022	**B12 – 06/09/2024 (PRE E3)**	**B13 – 07/09/2022**	**B14 – 08/09/2022**	**B15 – 09/09/2022**
			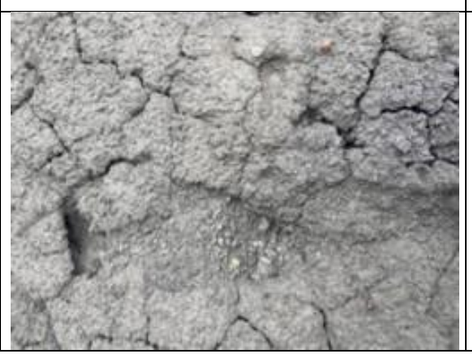	

Figure 4.16: Visualisation of the temporal evolution of the desiccation crack network on Side B of the lysimeter slope across the period RS1 was applied. The field of view covers the midpoint between the upper and lower slope regions. The temporal occurrence of these crack patterns is annotated in Figures 4.12 (Side B crest) and Figure 4.14 (Side B upper and lower slope).

Pre-application of E1

From August 19th to 22nd, the lysimeter slope demonstrated significant spatial variability in saturation levels with depth and across different regions. This theme remained prevalent throughout the application of RS1 and RS2, elucidating the complexity of the hydrological processes within infrastructure embankments under desiccated conditions. For Sides A and B, the upper 100 mm within the crest was largely desaturated, as shown in Figure 4.11A and 4.12A, respectively. During this period, Side B exhibits the typical increase of moisture content with depth as shallower layers function as environmental buffers to deeper layers. Saturation is reached in Side B by 400 mm, achieving a volumetric moisture content of 55%. Conversely, Side A diverges from this conventional pattern, potentially demonstrating the aforementioned caveat of soil-sensor contact issues. Given the installation post-compaction of the slope, the SOILVUE^{TM} sensor used in the crest was at greater risk of this.

However, Images A1 and B1 within Figure 4.15 and Figure 4.16 display the surface desiccation pattern observed between August 19th and 22nd, characterised by deep (300 – 400 mm) primary cracks encasing a shallower (max 50 mm) network of secondary cracks. Therefore, it is highly likely that the lower moisture content recorded at deeper (300 and 400 mm) compared to shallower regions (200 mm) could be an artefact of the controlling influence of the crack network in the sensor's effective measurement area, as discussed in Section 4.3. Saturation is only achieved at 500 mm in Side A's crest, with the remaining sensors recording volumetric water contents below 35%. The absence of this effect on Side B's crest underscores the crucial role of cracks in locally extending drying fronts and depleting moisture reserves at depth. However, accurately predicting these effects is challenging without detailed knowledge of the extent of subsurface desiccation. Such behaviour remains likely in Side B given the identical desiccation characteristics, with differences driven by sensor locations relative to subsurface crack paths. Furthermore, as microstructural deterioration progresses, greater heterogeneity will develop within the fill. Desiccation will take advantage of these heterogeneities, resulting in more irregular and unpredictable crack networks that further complicate drying and wetting patterns.

Entering August 19th, substantial suction had already accumulated at 200 mm within Sides A and B's crest under exposure to warmer and drier summer conditions. Figure 4.11E demonstrates high solar radiation and low relative humidity, which supply greater net radiation and evaporative energy as per Penman-Monteith (1965). This is

sustained until August 22nd under moderate air temperatures and low natural rainfall (Figure 4.11E). A comparison of Figure 4.11B and 4.12B reveals suction is higher within Side B than Side A for the crest region, recording 240 kPa and 140 kPa, respectively. This is likely due to the lower volumetric water content recorded at 200 mm within Side B, and possible local differences in sensor contact, compaction and crack influence. However, it also may result from greater environmental exposure or variation in the hydromechanical properties between localities, which is common in compacted soils. Due to the diurnal migration of the sun, Side B was first exposed to direct solar radiation whilst Side A remained shaded by the lysimeter casing. Therefore, this may have generated differential hydrological responses to changing net radiation, with a slight lag occurring in Side A.

The resolution of volumetric water content monitoring is limited to the 200- and 400 mm depths within the upper and lower slope regions. Consequently, the fluctuations in moisture content observed in the upper 100 mm of the crest – due to greater proximity to environmental exposure – are not represented in the data. In contrast, more stable trends are discernible in RS1 for the upper and lower slope regions, as illustrated in Figure 4.13A (Side A) and 4.14A (Side B). From August 19th to 22nd, the moisture distribution in the upper and lower slope regions varies greatly between Sides A and B. Within Side B, the lower slope exhibits a lower moisture content and greater sensitivity to rainfall events, particularly at 200 mm, initially recording 10% moisture content. Conversely, both depths within the upper slope in Side B remain saturated at 45% moisture content for the entire duration of RS1. The difference in saturated moisture content between the crest and other slope regions is likely due to the different sensors installed. In contrast, the upper slope at a depth of 200 mm exhibits the highest responsiveness to environmental change within Side A. As illustrated in Figure 4.13A, saturated conditions are maintained at the remaining depths, which consistently ranged between 40% and 45% during the RS1 monitoring period.

This disparity in behaviour is likely attributable to variation in the soil water retention behaviour introduced by heterogeneous distributions of compaction, environmental exposure, deep desiccation and deterioration across the lysimeter slope. The distribution of suction within the upper and lower slope regions of Sides A and B supports this suggested hypothesis. At 400 mm within Side A's lower slope region, suction is highest at 300 kPa, followed by the lower slope at 200 mm, which records 140 kPa. A malfunction of the suction sensor at 400 mm in the upper slope prevented

data collection. The volumetric water content at these depths does not deviate from saturated levels, which contrasts with the upper slope at 200 mm, where moisture content is 20% less, yet suction is only 20 kPa. As previously noted, discrepancies between suction and water content readings from co-located sensors are possible, as spatial heterogeneity in hydromechanical properties can occur across the 200 mm separation between them. However, these may also indicate a lesser ability of the upper slope at 200 mm within Side A to generate high suction, pointing toward a less compacted or more deteriorated microstructure than the other localities. A greater concentration of micro- or macro-cracking in the sensor regions may also contribute to these observed disparities, influencing the maximum producible suction.

Similarly, suction is at 520 kPa at 200 mm within Side B's upper slope, while volumetric water content is near saturation at 45%. Caveat aside, this may allude to enhanced capillary action under a less deteriorated or finer pore network, allowing higher suctions to be generated and sustained before any significant desaturation occurs. However, the upper and lower slopes at 400 mm within Side B produce only 20 kPa of suction despite having a similar moisture content of around 45%. Such disparity in behaviour is likely due to lower evaporation at these deeper depths, resulting from reduced exposure and influence of surface-level environmental conditions. Conversely, the lower slope of Side B at 200 mm generates substantial suction when desaturated at a moisture content of 10%. Such conditions suggest the presence of a fine pore network, with a locally lower crack influence, which is likely further along the drying curve due to enhanced environmental exposure. Fundamentally, these varying evaporation behaviours are likely to be observed during re-wetting, with the rate and magnitude of saturation being dictated by soil structure and enhanced locally depending on environmental exposure. Within ageing UK transport infrastructure embankments, temporal and spatial heterogeneity in soil water retention behaviour is likely to be exacerbated through time by more advanced deterioration. This may introduce greater differential stress between regions of contrasting behaviour and further amplify desiccation cracking.

Event 1 (E1) Application and Subsequent Recovery Period

On August 23rd, the first event (E1) of RS1 was applied to the lysimeter slope, with the surface desiccation state at onset presented in A1 and A2 of Figure 4.15 and 4.16. Within Side A's crest, Figure 4.11A shows a sharp and near-instantaneous increase in volumetric water content toward peak values occurring at all depths except 500 m,

which remained static. This peak coincides with the endpoint of the E1's one-hour storm event. As illustrated in Figure 4.12A, the same increase occurs in Side B's crest. However, no response is recorded at 400- and 500 mm, documenting a lower susceptibility to environmental change with depth in the sensor vicinity, likely attributable to a locally lower crack influence.

Importantly, a comparative analysis of Figure 4.11A and 4.12A reveals the distribution and magnitude of these peak volumetric water contents, which vary greatly with depth and between Sides A and B. For Side A's crest, the most notable relative increase occurs at 400 mm, which reaches 70%, followed by 300 mm and 50 mm. A considerable increase is also documented at 100 mm, with the most muted response observed at 200 mm. This significant rise in moisture at depths could be attributed to soil-sensor gaps. However, they also coincide with the subsurface extent of primary (300 – 400 mm) and secondary (50 mm) cracks, and given the extensivity of desiccation across the slope, it is likely evidence of preferential flow. The secondary crack network seems to have enhanced the near-surface response at 50 mm. However, a larger rainfall volume has been redirected to deeper layers (300 – 400 mm), captured in Side A's crest and suggesting a greater crack influence in its monitoring region. A lower response at 100 – 200 mm also supports this suggested hypothesis, with the primary crack network enabling infiltrating water to bypass these intermediate depths, reducing the magnitude of their response. An illustrative example of this preferential flow is given in Figure 4.17, where a clear dry-wet divide in the fill is visible as a large primary crack intercepts the downward flow of surface water.

Figure 4.2A for Side B's crest similarly evidences the occurrence of preferential flow. However, greater relative changes occurred at shallower depths, with the most significant magnitude increase occurring in the upper 100 mm. This was followed closely by the 300 mm depth, while the 200 mm depth showed a muted response similar to Side A. This disparity in behaviour may be attributed to a local reduction in microstructural degradation or crack depth in the region monitored by Side B's crest sensors. The subsequent decrease in volumetric water content from all peak values suggests the dispersion of this moisture away from the sensor locations. However, moisture content remains elevated after this decrease, indicating rainwater storage within the lysimeter slope.

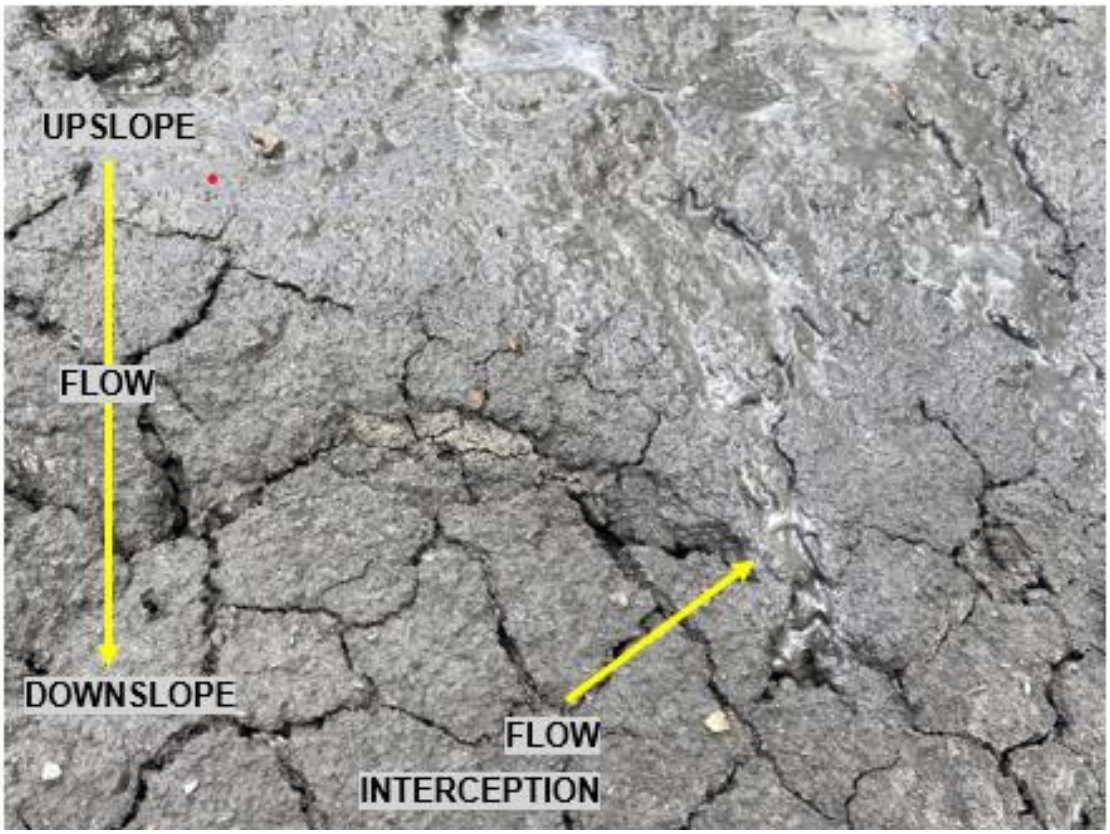

Figure 4.17: Illustrative example of a large primary crack intercepting the downward flow of surface water, with a clear wet-dry divide of the slope visible at either side of the crack.

Upon comparing the response of the upper and lower slope regions to that of the crest, these fundamental differences in soil structure and their impact on soil water retention behaviour become more evident. Within the hour post-E1, Figure 4.11B and 4.12B document suction at 200 mm within the crest of Sides A and B rapidly decreasing to 0 kPa. This demonstrates the limited ability of these regions to sustain high suctions and resist water influx, which will be closely linked to a coarser, interconnected network of micro- and macro-pores formed under deterioration processes or poorer compaction. Additionally, the flat crest region of an embankment is frequently the most vulnerable due to its relative positioning and the absence of physical boundary conditions that provide shelter. Consequently, this heightened natural exposure exacerbates the effects of drying and wetting cycles within the crest. However, the rainfall simulator covered a 2 m zone of the lysimeter slope, straddling the crest and uppermost slope regions, subjecting them to more severe impacts associated with the simulated high-intensity rainfall.

Suction loss after E1's application gradually declines for the upper and lower slope regions, as demonstrated in Figures 4.3B and 4.4B. Within Sides A and B, the lower slope at 200 mm suction is reduced slowly across the recovery period between E1 and E2. Similar behaviour is observed at 400 mm within the lower slope of Side A, as shown

in Figure 4.3B. This slower response can be related to the lack of direct exposure of the lower slope region to the simulated rainfall event. Figure 4.18A was taken one hour post-E1 on August 23rd, demonstrating a largely desaturated lower slope region with an intact crack network. However, gravitational moisture redistribution and assistance from a small natural rainfall event in the following 24 hours gradually increased lower slope saturation and reduced the secondary crack network, as visualised by Figure 4.18B. Although the degree of exposure may delay an immediate response, the redistribution of excess moisture due to gravity is an essential secondary effect to consider post-storm. This redistribution can lead to this gradual suction loss, which increases the risk of slope instability for an extended period after storm events.

Throughout the entire monitoring period of the lysimeter slope, the lower region exhibited a consistently higher level of saturation. Such behaviour is common within embankments, as the lower slope's geospatial positioning provides shading from environmental conditions, and due to gravitational forces, it operates as an accumulation zone for both runoff and subsurface flow. As a result of these processes, the lower slope displays a lower magnitude response to drying and wetting cycles, maintaining greater structural integrity, which elevates suction and resists rapid saturation. Consequently, the gradual reduction in suction within the lower slope may indicate a reduced rate of water influx, either due to exposure, as discussed above, or associated with slower infiltration through a finer pore network over time. Both these hypotheses would be supported by the volumetric water response documented in Figure 4.13A and 4.14B.

Conversely, Side B's upper slope at 200 mm exhibits a larger magnitude fall in suction in the 12 hours following E1 from 500 kPa to 300 kPa. Since this depth produced the highest suction after E1, the significant decrease is instead likely due to increased rainfall exposure in this area or the concentration of subsurface flow toward it. Downslope drainage of the crest region likely contributed, with the upper slope's closer proximity relative to the lower slope accelerating its response. Such processes would facilitate greater advancement of this region along the wetting curve for as long as moisture is supplied. The variability in moisture distribution displayed during E1's application underscores the importance of heterogeneity within desiccated embankments in influencing infiltration patterns. This variability can lead to

unpredictability regarding where the focal points of rapid moisture gain and suction loss are located and, therefore, the areas at a heightened risk of instability.

(A)

(B)

Figure 4.18: Photographs illustrating (A) the unsaturated and desiccated nature of the lower slope region one hour post-E1 and (B) the closure of secondary cracks and increased surface saturation in the lower slope after gravitational moisture redistribution and assistance from a small natural rainfall event.

Images A3 and A3 within Figure 4.15 and 4.16 were taken after the application of E1. These images visualise almost complete closure of the secondary crack network, while

the larger primary cracks have retained substantial surface aperture. Notably, the secondary crack network located immediately down-slope of the large primary cracks (on the left side of A3 and B3) remains partially open. The inconsistent closure of this network may be connected to the interception of surface flow by the large primary cracks, a more detailed example of which is provided in Figure 4.19. This interception channelled water through the cracks to greater depths, altering sub-surface flow patterns and forming isolated zones of lower saturation where secondary cracks remained open.

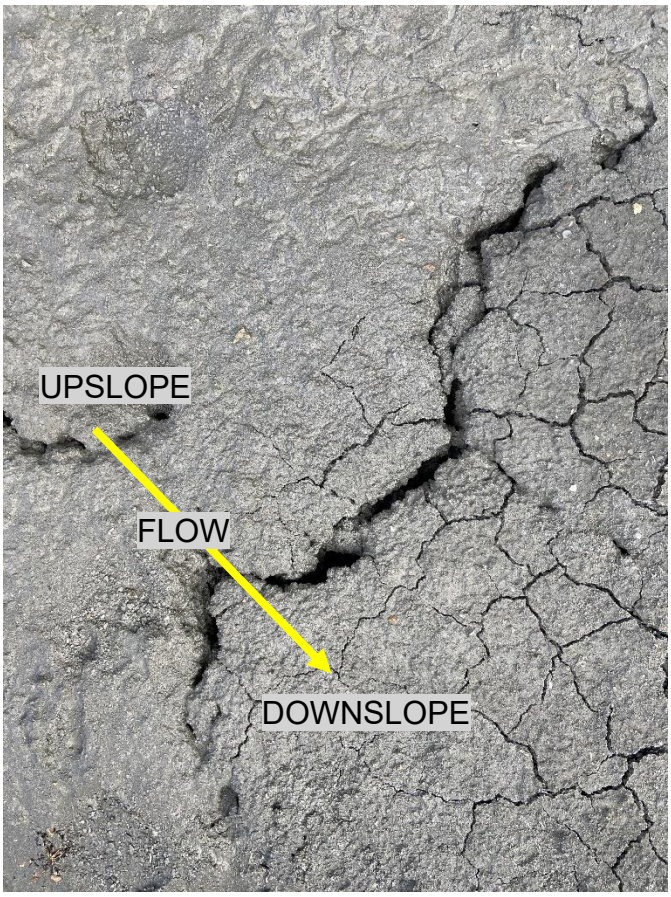

Figure 4.19: Demonstration of primary crack interception of surface flow allowing cracks downslope to remain open post application of E1.

Furthermore, rainwater redirection into the primary and secondary crack networks fundamentally enhanced infiltration and the storage potential of inherently impermeable clay. The absence of surface runoff within Sides A (Figure 4.11/ 4.13C) and B (Figure 4.12/4.14C), and the sustained higher volumetric water contents at all depths and regions post-E1 support this hypothesis. Critically, these results demonstrate that all 52 mm of rainfall applied during E1 entered the lysimeter slope, with a significant volume of this stored to generate substantial moisture gain and suction loss. This emphasises the detrimental effects that an open crack network may

impose on the rate and magnitude of water infiltration into an embankment during severe summer storm events. Moreover, with the primary cracks remaining open post-E1, the slope maintains an advanced state of vulnerability for any sequential rainfall events.

During the one-week recovery period between E1 and E2, a natural rainfall event occurred on August 24th. Smaller secondary peaks in volumetric water content are observed in response to this event through to 400 mm in the crest (Figures 4.11A and 4.12A) and at 200 mm in Side B's lower slope (Figure 4.14A). This event interrupts the suction gain within the crest regions and restricts the re-opening of the secondary crack network. A similar-sized natural rainfall event was recorded pre-E1 on the 20th of August, with its magnitude not sufficient to generate a considerable increase in volumetric moisture content beyond 100 mm or suppress suction generation. However, it is important to note that the response to these natural rainfall events was incomparable to the significant changes induced by E1. Firstly, this demonstrates the higher consequence of high-intensity storm events over low-intensity antecedent rainfall on the integrity of desiccated embankments. Secondly, the higher saturated hydraulic conductivity supplied by the slope's now saturated state post-E1 eases moisture influx. This contrasts with soil's greater resistance to infiltration in an unsaturated state due to high suction. Therefore, greater saturation facilitated the deeper response to natural rainfall post-E1, stressing how the antecedent conditions at the onset of rainfall can further a slope's vulnerability and control its hydrological response under subsequent wetting events.

After this natural rainfall event, sustained moderate air temperatures, high solar radiation and dry conditions facilitate partial recovery of, 1) suction within the crest to 40 kPa, 2) lower moisture contents in the upper 100 of the crest, 3) a slowing of suction loss in the upper and lower slope regions. Under shallow subsurface desaturation, the secondary crack network reopens on August 25th, expanding alongside the primary cracks until the application of E2 on August 30th. The rapid formation of the secondary crack network indicates significant deterioration in the shallow subsurface, where moisture retention and resistance to tensile stress have been lowered under long-term deterioration. Furthermore, the lower suction present for the onset of E2 will reduce the slope's ability to resist rapid infiltration. These behaviours have important implications for how quickly the vulnerability of an embankment can increase,

especially if intense storm events occur in quick succession or are followed by a hot spell that intensifies desiccation.

Event 2 (E2) Application and Subsequent Recovery Period

On August 30th, Event 2 (E2) of RS1 was applied to the lysimeter slope, with a notable shift in the depths where the hydrological response is most visible within Figures 4.11 – 4.14. For Side A's crest, the shallow subsurface at 50 mm records the greatest increase in moisture, followed by 300 mm, which increases toward and subsequently remains at saturation, equal to 58% volumetric water content. Notable increases also occur at 100- and 200 mm, slightly greater than during E1. At 400 mm, the sharp rise in moisture observed in E1 has transitioned to a gradual and lower gain in moisture across the following 24 hours post-E2, suggesting a switch to matrix rather than crack flow. Conversely, rapid increases in moisture within Side B's crest are restricted to the upper 200 mm, with the lower slope exhibiting similar behaviour at the same depth. No other localities in the upper and lower slope regions responded to E2 as they had reached a steady-state saturation. This unanimous shift in the focal depths of moisture increase may evidence a shallowing of the subsurface crack network, importantly not captured by surface imaging. The increase in saturation at 300- and 400 mm from E1 to E2 would facilitate swelling of the Ampthill Clay, driving the healing of primary cracks at depth. The absence of moisture loss at these depths between E1 and E2 is also conducive to crack closure, elucidating to a reduced evaporative surface area. However, it is possible that the short- and less-intensive drying regime during this recovery period only penetrated the shallow subsurface, limiting crack growth to the shallow depths.

After E2, suction decreased at all depths, exhibiting a more rapid reduction in the crest regions due to greater direct rainfall exposure. By the onset of E3, suction only remained within Side B's upper slope at 200 mm and Side A's lower slope at 400 mm, both recording 60 kPa. Images A7 and B7 illustrate a significant finding post-application of E2 in Figures 4.15 and 4.16, which reveals sections of the primary crack network remaining open. Coupling this finding with the absence of surface runoff and the sustained higher soil saturations, the lysimeter slope accepted an additional 52 mm of rainfall, despite a reduced crack depth. Images A7 and B7 also demonstrate the formation of scour channels, illustrating the erosive power of these heavy rainfall events. With micro- and macro-cracking forming an increasingly loose, fractured, and

disaggregated structure, this erosivity can lead to the washout of fines and further exacerbate microstructural degradation.

Within the 48 hours following E2, A8 – A9 and B8 – B9 document the growth of secondary cracks under elevated air temperatures. However, their aperture significantly reduces in the days following due to a series of natural rainfall events, demonstrated by images A10 and B10. Therefore, the crack pattern at the onset of E3 is shown by A11 and B11 in Figures 4.15 and 4.16, with small sections of primary cracks and the finest network of secondary cracks present. Although air temperature is higher, the average relative humidity has also substantially increased, and solar radiation decreased, which would suppress evaporation by reducing net radiation (Penman, 1948; Monteith, 1965) and subsequently lower crack formation. These findings indicate that exposure to prevailing weather conditions directly impacts the severity of desiccation cracking. Furthermore, a feedback loop is present in which the crack network itself influences environmental exposure, thereby affecting the depth, distribution, and intensity of the drying and wetting fronts observed within the embankment.

Event 3 (*E3) Application and Subsequent Recovery Period*

The final event (E3) of RS1 was applied to the lysimeter slope on September 6th. A further shallowing of the subsurface crack network during E3 is suggested in Figures 4.11A – 4.14A, with volumetric water increases now limited to the upper 200 mm. After E3, all remaining suction within the slope is lost, with no further increases evident during this monitoring period. Significantly, small sections of primary and secondary cracks remain open, and like E1 and E2, no surface runoff is generated by this event. Despite its less desiccated state, the lysimeter slope accepted and stored E3's 52 mm of rainfall, illustrating that substantial crack networks are not required to impact slope hydrology significantly. The sustaining of higher saturations post-E3 also evidences some capacity for increased water storage within the lysimeter slope.

Figure 4.11C – 4.14C does not record substantial surface runoff in Sides A and B until 3 days after E3 when heavy natural rainfall occurs, and desiccation cracks completely heal (see A15 and B15 in Figure 4.15 and 4.16). The volumetric water content response to the natural rainfall displays two distinct peaks at 100 mm. This indicates some influence from the remaining open yet greatly shallowed primary cracks. However, the near-saturated slope cannot absorb a significant volume of water from

these natural rainfall events, as evidenced by the sharp decline in water content and the generation of substantial surface runoff. No further opening of desiccation cracks occurs for the remainder of the monitoring period. Rainfall continues, and air temperature reduces, lowering the available energy available for evaporation, suction (stress) accumulation and crack initiation within the shallow subsurface of the Ampthill Clay fill.

The results produced during RS1 clearly show the severe vulnerability of a desiccated slope to infiltration and suction loss during high-intensity storm events. The extensive surface and subsurface crack networks produced under intense summer drying significantly increase the volume of infiltrating water an embankment can accept and subsequently store. With wider consideration of long-term weather-driven microstructural degradation establishing within the lysimeter slope, if a hot spell follows these intense summer storms, the slope's ability to retain this moisture and resist substantial desaturation is reducing with time. Therefore, fluctuations between intense summer storms and heavy convective storms could exacerbate the rate of change between and magnitude of dry-wet and suction cycles, accelerating weather-driven deterioration and advancing the slope toward instability at a faster rate. Following the commencement of RS1, no further suction was generated in the lysimeter slope for the remainder of the year.

The findings from RS1 stress the pronounced vulnerability of desiccated slopes to infiltration and loss of stabilising suction during high-intensity storm events. The development of extensive surface and subsurface crack networks, which occurs under intense summer drying, markedly increases the volume of infiltrating water that an embankment can accept and subsequently store. Moreover, when evaluating the long-term effects of weather-induced microstructural degradation occurring within the slope of the lysimeter, it becomes evident that its ability to retain moisture and withstand substantial desaturation will progressively decline over time. This effect will be particularly detrimental when a prolonged hot spell follows these intense summer storms, where desiccation cracking will exploit the lower tensile strength and quickly re-establish within the embankment. Therefore, the interplay between these intense summer storms and subsequent heavy convective rainfall events may exacerbate the frequency and magnitude of dry-wet cycles, thereby accelerating weather-driven deterioration and advancing the slope toward instability at an increasingly rapid pace.

4.3.2 Heavy Spring Rainfall and Implications for Summer Stability

The second set of rainfall simulations (RS2) was applied during late Spring in three consecutive events (E4 – E6), each one week apart between May 26th and June 9th, 2023. The antecedent conditions at the onset of RS2 were intentionally different to RS1. This allowed the lysimeter slope's hydrological response to high-intensity rainfall to be analysed during late Spring, where desiccation cracking was less intense, and the Ampthill Clay fill exhibited a higher initial saturation. In 2022, the environmental conditions during this transition from late Spring to early Summer played a critical role in establishing a seasonal drying regime within the lysimeter slope and initiating suction accumulation. Therefore, it is essential to investigate how significant interruptions to this transition period may affect the long-term behaviour of an embankment during the summer season, as this analysis is crucial for assessing asset stability. Additionally, a deeper understanding of how desiccation cracking contributes to these behavioural changes is necessary to fully evaluate the impact of high-intensity rainfall events.

In contrast to the bare slope when RS1 was applied, a faux grass canopy had since been installed over Side B and was present during RS2. This installation was integral to an investigation aimed at elucidating the influence of physical boundary conditions, such as a structural canopy, on the resultant environmental boundary conditions imposed on an embankment. The findings of this investigation are elaborated upon in Section 4.5. A brief examination of effects is covered in this section, focusing solely on how the vegetative canopy moderated the behaviour of Side B during the applied simulated storm events.

Figures 4.20 and 4.21 plot time series data for the crest regions of Sides A and B, respectively, including (A) volumetric water content at 50-, 100-, 200-, 300-, 400-, and 500 mm, (B) Suction (kPa) at 200 mm (C) Runoff (mm). The natural and simulated rainfall (mm) (E4 – E6) applied, and air temperature (^{o}C) are also provided in Figure 4.20D and 4.21D. Solar radiation and relative humidity are given in Figure 4.20E and 4.21E. This data has also been generated for the upper and lower slope regions of Side A (Figure 4.22) and B (Figure 4.23). Annotated in Figure 4.20 and 4.22 is the temporal occurrence of A16 – A30 from Figure 4.24, which visualises crack evolution in Side A during RS2's application. For Side B, desiccation crack evolution is illustrated by B16 – B30 in Figure 4.25, and their temporal occurrence is annotated in Figure 4.21 and 4.23.

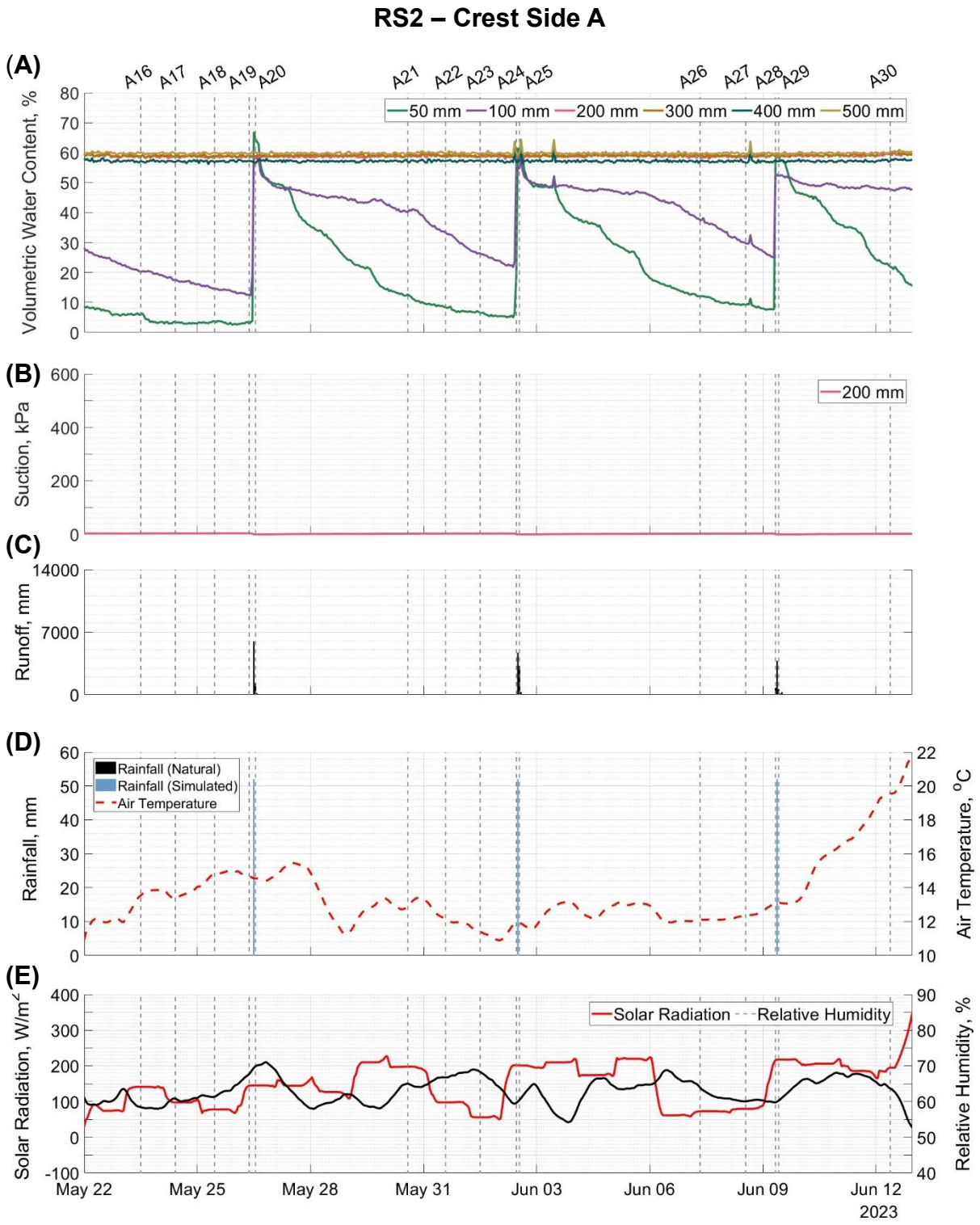

Figure 4.20: Time series data for Side A's crest region during the application of the second rainfall simulation (RS2) with graphs demonstrating (A) volumetric water content (%) at 50-, 100-, 200-, 300-, 400-, and 500 mm depths, (B) suction (kPa) at 200 mm, (C) runoff (mm) captured by Side A's channel, (D) simulated storm (blue) and natural (black) rainfall (mm) during RS2 and the ambient air temperature (°C), (E) relative humidity (%) and solar radiation (W/m^2) recorded during RS2. The annotated grey dashed lines mark the temporal occurrence of crack images A16 – A30 for Side A, provided in Figure 4.24.

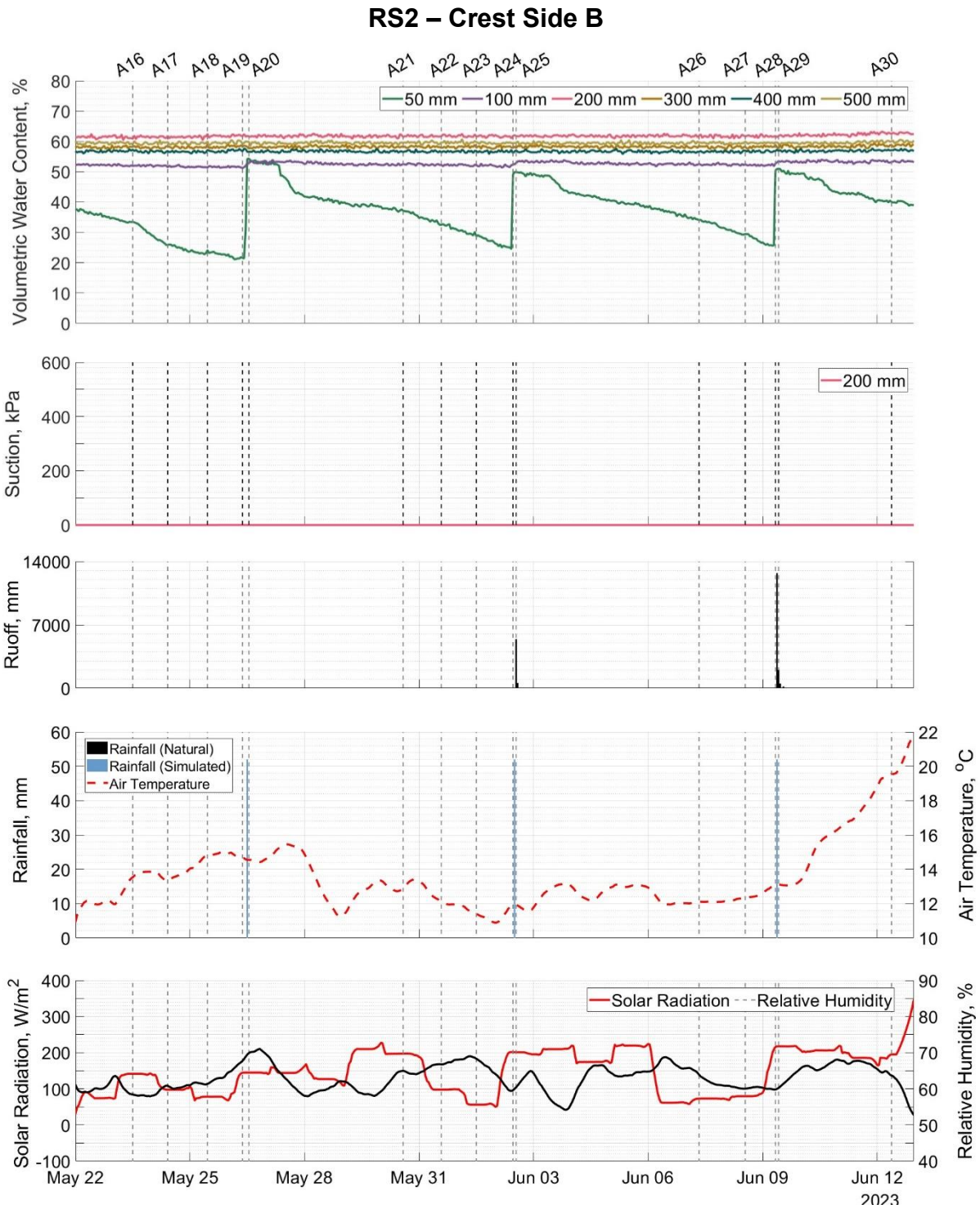

Figure 4.21: Time series data for Side B's crest region during the application of the second rainfall simulation (RS2) with graphs demonstrating (A) volumetric water content (%) at 50-, 100-, 200-, 300-, 400-, and 500 mm depths, (B) suction (kPa) at 200 mm, (C) runoff (mm) captured by Side B's channel, (D) simulated storm (blue) and natural (black) rainfall (mm) during RS2 and the ambient air temperature (°C), (E) relative humidity (%) and solar radiation (W/m^2) recorded during RS2. The annotated grey dashed lines mark the temporal occurrence of crack images B16 – B30 for Side B, provided in Figure 4.25.

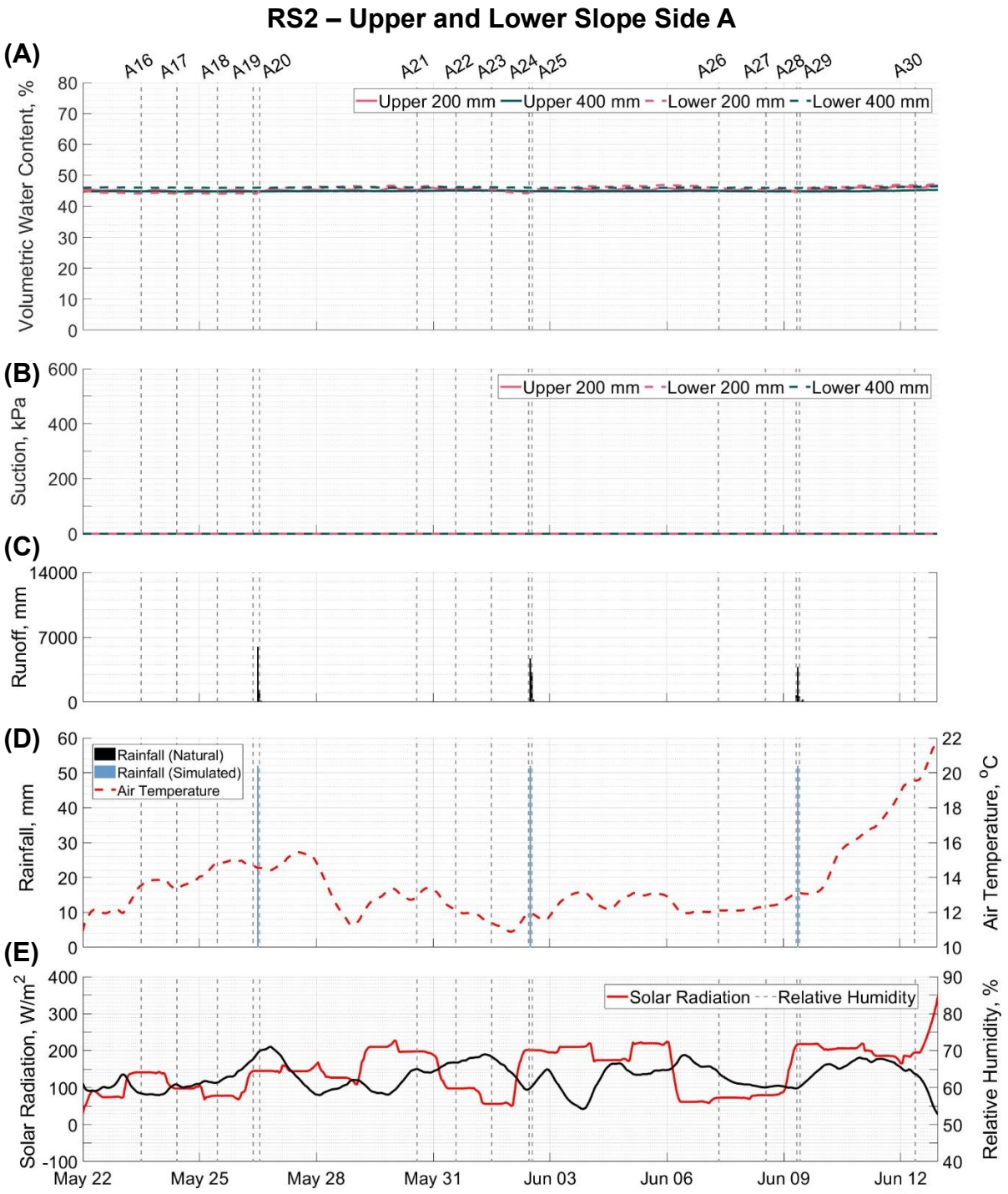

Figure 4.22: Time series data for Side A's upper and lower slope regions during the application of the second rainfall simulation (RS2) with graphs demonstrating (A) volumetric water content (%) at 200- and 400 mm, (B) suction (kPa) at 200- and 400 mm (Side B only due to sensor malfunction in Side A), (C) runoff (mm) captured by Side A's channel, (D) simulated storm (blue) and natural (black) rainfall (mm) during RS2 and the ambient air temperature (°C), (E) relative humidity (%) and solar radiation (W/m^2) recorded during RS2. The annotated grey dashed lines mark the temporal occurrence of crack images A16 – A30 for Side A, provided in Figure 4.24.

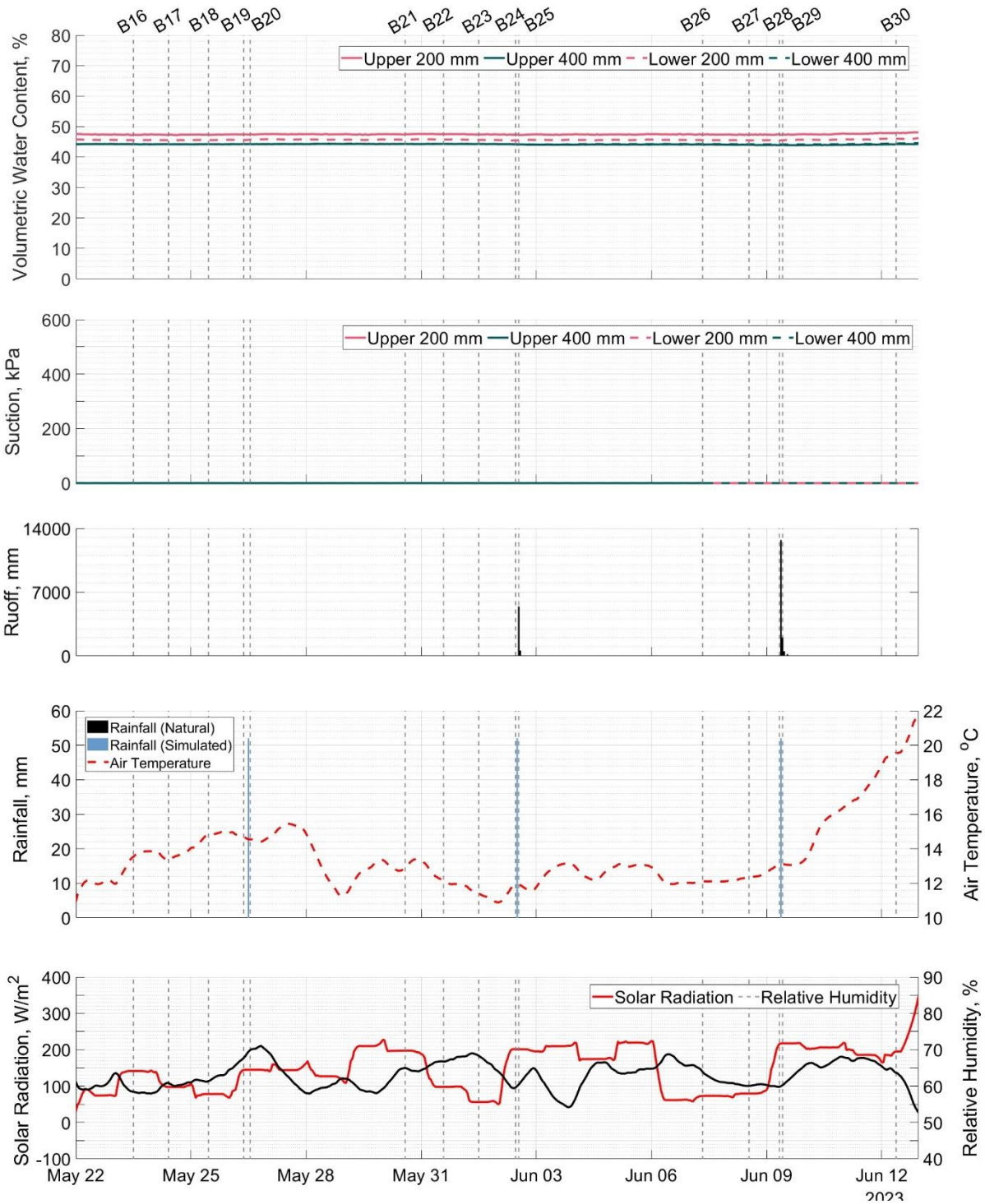

Figure 4.23: Time series data for Side B's upper and lower slope regions during the application of the second rainfall simulation (RS2) with graphs demonstrating (A) volumetric water content (%) at 50-, 100-, 200-, 300-, 400-, and 500 mm depths, (B) suction (kPa) at 200 mm, (C) runoff (mm) captured by Side B's channel, (D) simulated storm (blue) and natural (black) rainfall (mm) during RS2 and the ambient air temperature (°C), (E) relative humidity (%) and solar radiation (W/m^2) recorded during RS2. The annotated grey dashed lines mark the temporal occurrence of crack images B16 – B30 for Side B, provided in Figure 4.25.

RS2 – Side A Crack Evolution

A16 – 23/05/2023	A17 – 24/05/2023	A18 – 25/05/2023	A19 – 26/05/2023 (PRE E4)	A20 – 26/05/2023 (POST E4)
				
A21 – 30/05/2023	**A22 – 31/05/2023**	**A23 – 01/06/2023**	**A24 – 02/06/2023 (PRE E5)**	**A25 – 02/06/2023 (POST E5)**
				
A26 – 07/06/2023	**A27 – 08/06/2023**	**A28 – 09/06/2023 (PRE E6)**	**A29 – 09/06/2023 (POST E6)**	**A30 – 12/06/2023**
				

Figure 4.24: Visualisation of the temporal evolution of the desiccation crack network on Side A of the lysimeter slope across the period RS2 was applied. The field of view covers the midpoint between the upper and lower slope regions. The temporal occurrence of these crack patterns is annotated in Figures 4.20 (Side A crest) and Figure 4.22 (Side A upper and lower slope).

RS2 – Side B Crack Evolution

B16 – 23/05/2023	B17 – 24/05/2023	B18 – 25/05/2023	B19 – 26/05/2023 (PRE E4)	B20 – 26/05/2023 (POST E4)
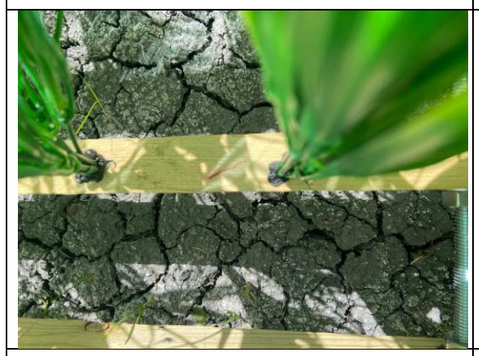				
B21 – 30/05/2023	**B22 – 31/05/2023**	**B23 – 01/06/2023**	**B24 – 02/06/2023 (PRE E5)**	**B25 – 02/06/2023 (POST E5)**
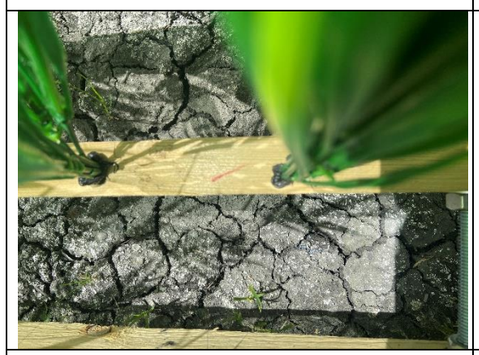			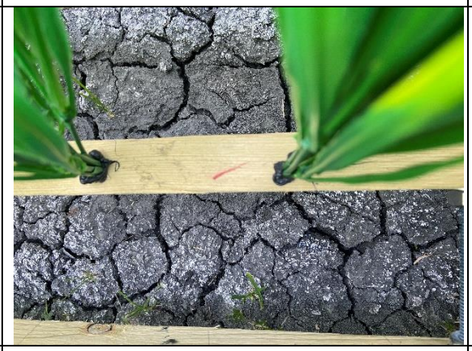	
B26 – 07/06/2023	**B27 – 08/06/2023**	**B28 – 09/06/2023 (PRE E6)**	**B29 – 09/06/2023 (POST E6)**	**B30 – 12/06/2023**
				

Figure 4.25: Visualisation of the temporal evolution of the desiccation crack network on Side B of the lysimeter slope across the period RS2 was applied. The field of view covers the midpoint between the upper and lower slope regions. The temporal occurrence of these crack patterns is annotated in Figures 4.21 (Side B crest) and Figure 4.23 (Side B upper and lower slope).

Pre-Application of Event 4 (E4)

Between May 22nd and 26th, Figures 4.20 – 4.24 unanimously show that the lysimeter slope was saturated below 200 mm in all regions and that no suction was present. For the crest, this was around 60%, and the upper and lower regions were static at approximately 46%, the disparity attributable to the caveats previously discussed in Section 4.3. Side A's crest recorded evaporation within the shallow subsurface at 50 mm and 100 mm. This was likely facilitated by the increase in air temperature, as presented in Figures 4.20 – 4.24, which is still comparatively low compared to that recorded during RS1 in the summer. Moderate solar radiation, low relative humidity, and minimal natural rainfall would have helped sustain this low magnitude of shallow subsurface drying.

However, it is also probable that the shallow network of desiccation cracks still enhanced evaporation by continuing to expose a greater evaporative surface area to atmospheric drying than intact soil. The crack network between May 22nd and 26th is presented by images A16 – A19 (Side A) and B16 – B19 (Side B) in Figures 4.24 and 4.25, respectively. The subsurface distribution of this network was constrained by the propagation depth of evaporation fronts, extending to a maximum depth of 50 mm. Therefore, a fundamentally different crack network formed without intense summer drying and suction generation. The primary cracks formed are markedly narrower and shallower than those recorded during RS2, suggesting their overall influence on slope hydrology will be comparatively diminished.

In contrast to Side A, evaporation is limited to the upper 50 mm in Side B within the crest and is of much lower magnitude. Given the deteriorated microstructural state of the shallow subsurface, its capacity to retain moisture during drying and resist ingress during wetting is compromised. Consequently, even minor environmental changes can lead to significant moisture content fluctuations. This deterioration was established by the Summer of 2022 (see Section 4.5 for more detail) and has likely advanced under a further 11 months of dry-wet cycling. Therefore, considering this deterioration, the buffer effect the canopy is providing must significantly suppress the drying magnitude and propagation rate for no moisture loss to be recorded at 100 mm in Side B.

With respect to microstructural degradation, the higher saturated water content at 200 mm within all Side B's slope regions compared to deeper sensors is especially noteworthy. Prior to the installation of the grass canopy, Side B experienced greater

exposure to environmental conditions, while Side A benefited from the protective enclosure of the lysimeter casing. Consequently, the intensified environmental loading on Side B may have advanced microstructural degradation in the shallow subsurface, thereby enhancing its porosity and possibly explaining its increased capacity for water storage.

Event 4 (E4) Application and Subsequent Recovery Period

The first event (E4) of RS2 was applied to the lysimeter slope on May 26th, 2023. The predominantly saturated conditions pre-E3 and shallow cracking contrasted sharply with the conditions during RS1, where severe desiccation left the slope significantly more vulnerable to infiltration-induced instability. In RS1, the extensive drying created deeper, more pronounced cracks, which prevailed across simulated rainfall events, providing a heightened risk of rapid infiltration and destabilisation during each successive storm. Conversely, the surface expression of this shallower network had entirely closed by the cessation of E4, as shown in A20 (Side A) and B20 (Side B) within Figures 4.24 and 4.25. Rapid crack closure was in response to fast saturation in the upper 50 mm (Side A and B) and 100 mm (Side A only) of the crest, likely aided by the open status of cracks at E4's onset. No response is recorded deeper than 100 mm across all slope regions, which remains a consistent observation throughout all events in RS2. Crack closure, coupled with a limited capacity to accept rainwater in its saturated state, expedited the generation of voluminous surface runoff during E4, as documented in Figures 4.20/4.22 for Side A. Runoff also occurred in Side B, with a blockage in the runoff channel preventing its quantification in Figures 4.21/4.23. This was subsequently cleared for future simulated rainfall events.

Following E4, the crest's upper 50 mm and 100 mm (Side A only) promptly desaturated as the shallow crack network reopened. This occurred within 24 hours of E4, with images A21 – A24 (Side A) and B21 – B24 (Side B) documenting its re-growth before E5 was applied on June 2nd. Importantly, although natural rainfall was low during this transition period, air temperature declined significantly, and the slope did not benefit from high solar radiation (e.g., see Figure 4.20D/E). This observation suggests a diminished resistance to tensile stress within the shallow subsurface, thereby increasing the likelihood that the tensile strength will be exceeded. Consequently, these conditions facilitated the rapid initiation and propagation of desiccation cracks, even under moderate environmental conditions, where typical drivers of rapid drying –

such as elevated temperatures and intense solar radiation as per penman-Monteith (1965) – were absent.

Event 5 (E5) and Event 6 (E6) Application

The second (E5) and third (E6) rainfall events of RS2 were applied to the lysimeter slope on June 2nd and June 9th, respectively. The hydrological and desiccation crack response of the lysimeter slope and the following recovery periods were identical to that recorded during E4. Substantial runoff was generated after each event as the shallow subsurface reached saturation and the desiccation crack network healed, as shown by A25/A29 for E5 and B25/B29 for E6 within Figures 4.24 and 4.25. Comparatively, runoff was consistently higher from Side B (Figures 4.21/4.23C) than from Side A (Figures 4.20/4.22C). This may be associated with evaporation suppression by the canopy, which slightly lowered the crack intensity and further limited the shallow sub-surface's capacity for rainwater storage. However, additional features such as runoff from the wooden frame and faux vegetation also would have impacted Side B's records. By the application of E6, significant ponding within the crest region was noted, illustrated in Figure 4.26, stressing the saturated state of the slope. Within field embankments, ponding of rainwater within the crest is considered a destabilising threat. The additional surcharge can increase the stress exerted on the embankment and exacerbate the effects of oversaturation, heightening the risk of shallow failures.

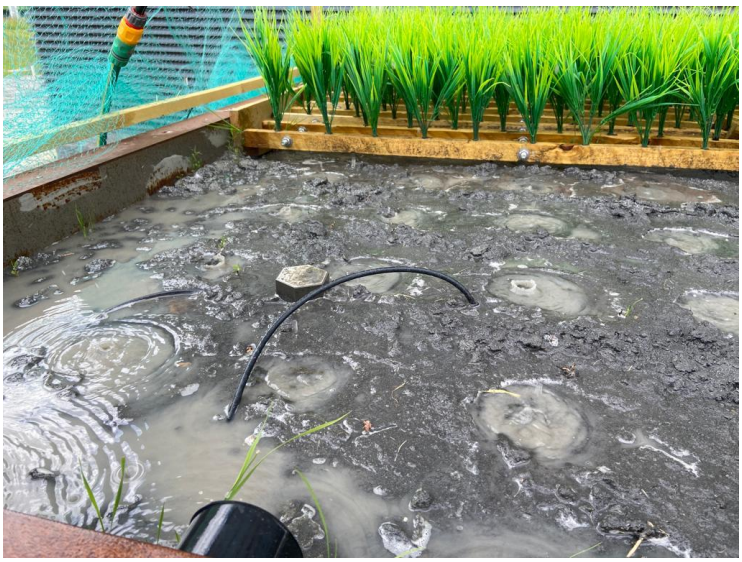

Figure 4.26: Image demonstrating the substantial ponding of rainwater in the crest (Side A photographed here) during E6 application due to its saturated state.

Between E5 and E6, and after RS2 was complete, the shallow desiccation crack network promptly reopened without any suction generation (see A26/B26 – A28/B28 and A30/B30 in Figures 4.24 and 4.25). This consistent pattern of behaviour observed here during RS2's rainfall events is a critical example of how cyclic weather-driven deterioration can manifest within infrastructure embankments at the shallow surface level. In the months following RS2, the consequences of an increased period of intense saturation across the spring-to-summer transition zone became evident in the monitoring results. The wetter-than-average summer which followed RS2's events also amplified its impact. Drying remained confined to the upper 100 mm of the lysimeter slope, resulting in zero accumulation of the high suctions recorded during the summers of 2021 and 2022. Consequently, the shallow crack network observed during RS2 persisted through the summer of 2023. Furthermore, it exhibited the same swift reactions to changes in moisture, amplifying dry-wet cycles in the shallow subsurface.

Figure 4.27A – C demonstrate the progressive formation, deepening and widening of scour channels across E4 – E6 within the bare slope of Side A. Such channels had not been established on Side B beneath the grass canopy, demonstrating its role as an environmental buffer to high-energy surface floodwater. While the absence of deeper desiccation may imply a reduced risk of overall slope failure, these findings speculate a potential shift in vulnerability towards the shallow surface layers. Furthermore, although the risk of deeper-seated instability through significant fluctuations in pore water pressure is less with consistent wet conditions, the observations within Figure 4.27 also suggest a potential transition to erosional or washout failure mechanisms. This shift emphasises the importance of monitoring surface stability and water runoff, as these failure mechanisms could still pose significant safety and operational risks to the transport network. Future research should further delineate how failure mechanisms can evolve with changes in surface desiccation to ensure effective management strategies are developed for infrastructure embankments. It is suggested that links between failures of known modes and the characteristics of desiccation cracking on transport infrastructure embankments be established to determine whether a relationship exists.

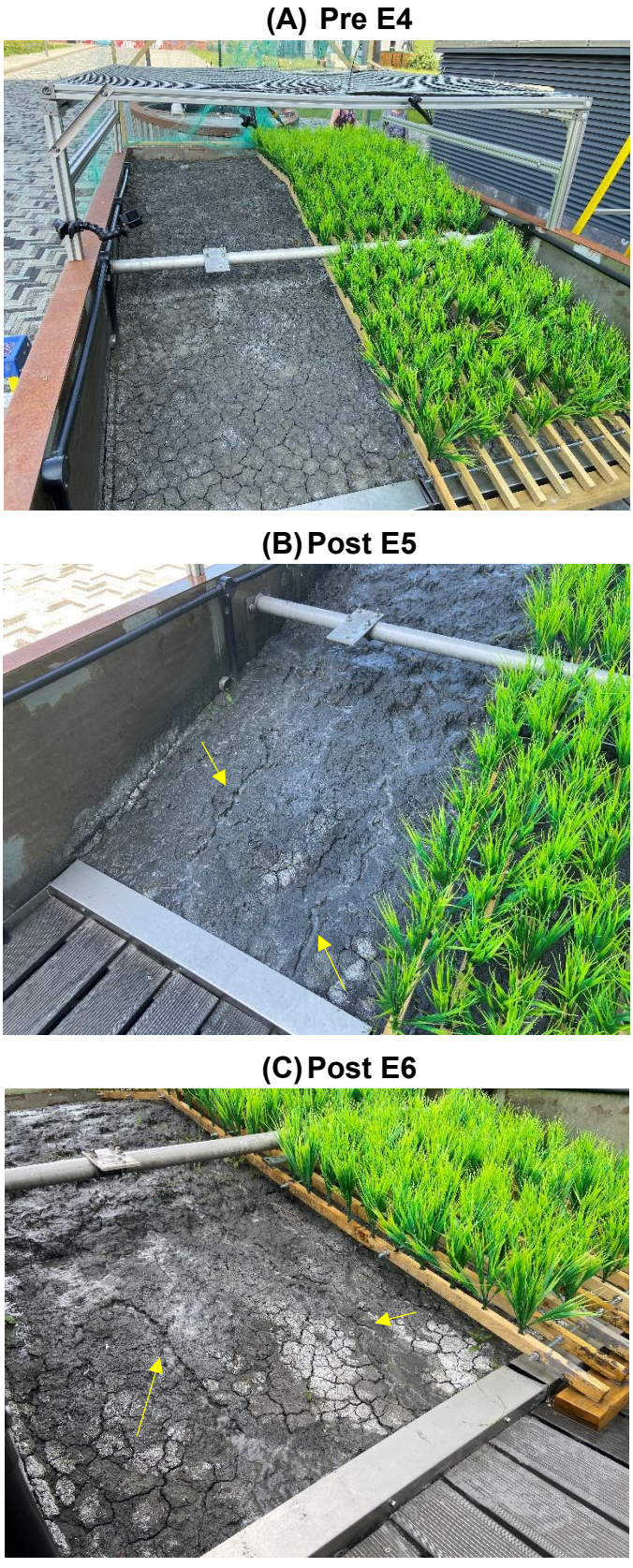

Figure 4.27: Photographs documenting the progressive development of scour channels across RS2 where high surface runoff was generated with (A) pre-E4 with no channel present, (B) post-E5 channels formed, and (C) channels widened post-E6.

4.4 Sheltering Effects of Vegetation Canopies

Given that the lysimeter slope is bare, it does not replicate the complex soil–atmosphere–vegetation interactions typical of live infrastructure embankments and their influence on desiccation cracking. These interactions remain poorly understood, primarily due to the difficulty in isolating the individual and combined effects of vegetation and environmental factors on soil drying processes. Vegetation affects soil moisture both directly, through water uptake and transpiration, and indirectly, by altering exposure to environmental conditions via canopy formation. Canopies act as physical boundary layers, intercepting rainfall and moderating surface exposure to solar radiation, temperature, and wind. Understanding canopy effects is therefore crucial for improving insight into vegetation's role in soil desiccation cracking.

However, establishing a live vegetative canopy on the lysimeter slope would introduce significant complexity, making it difficult to distinguish between hydrological changes driven by physiological plant processes and those caused by physical canopy structure. A faux grass canopy was installed on a wooden frame suspended above Side B of the lysimeter slope to circumvent this, avoiding direct soil contact. This setup was designed not to replicate the full physiological functions of vegetation, but to modify key physical drivers of evaporation as per the Penman-Monteith (1965) Equation (Equation 2.2) – namely, solar radiation (energy) and near-surface air turbulence (aerodynamic resistance and conductance). The experiment aimed to compare soil moisture evolution and desiccation cracking between the faux grass-covered Side B and the bare Side A under natural weathering conditions. This approach enables controlled investigation into how canopy-like boundary conditions influence environmental exposure and soil drying dynamics, serving as a primitive step toward better understanding vegetation's impact on desiccation cracking.

4.4.1 Surface and Sub-surface Temperature Evolution

Figure 4.28A illustrates the surface temperature profiles of Side A (bare) and Side B (canopy), alongside the air temperature data collected from an on-site weather station. Additionally, Figure 4.28B presents the average daily solar radiation and relative humidity values recorded throughout the monitoring period by the same weather station. Surface temperature was measured using a thermal camera, the methodology of which is given in Section 3.3.2. The points selected for analysis encompassed areas of soil in Sides A and B, with careful consideration not to extract values from the faux grass canopy or cracks. Some small gaps are evident in the data and are associated

with the temporary malfunction of the automated image-storing software. The black dashed line in Figure 4.28A and 4.28B indicates the installation date of the faux grass canopy on 20/04/2023.

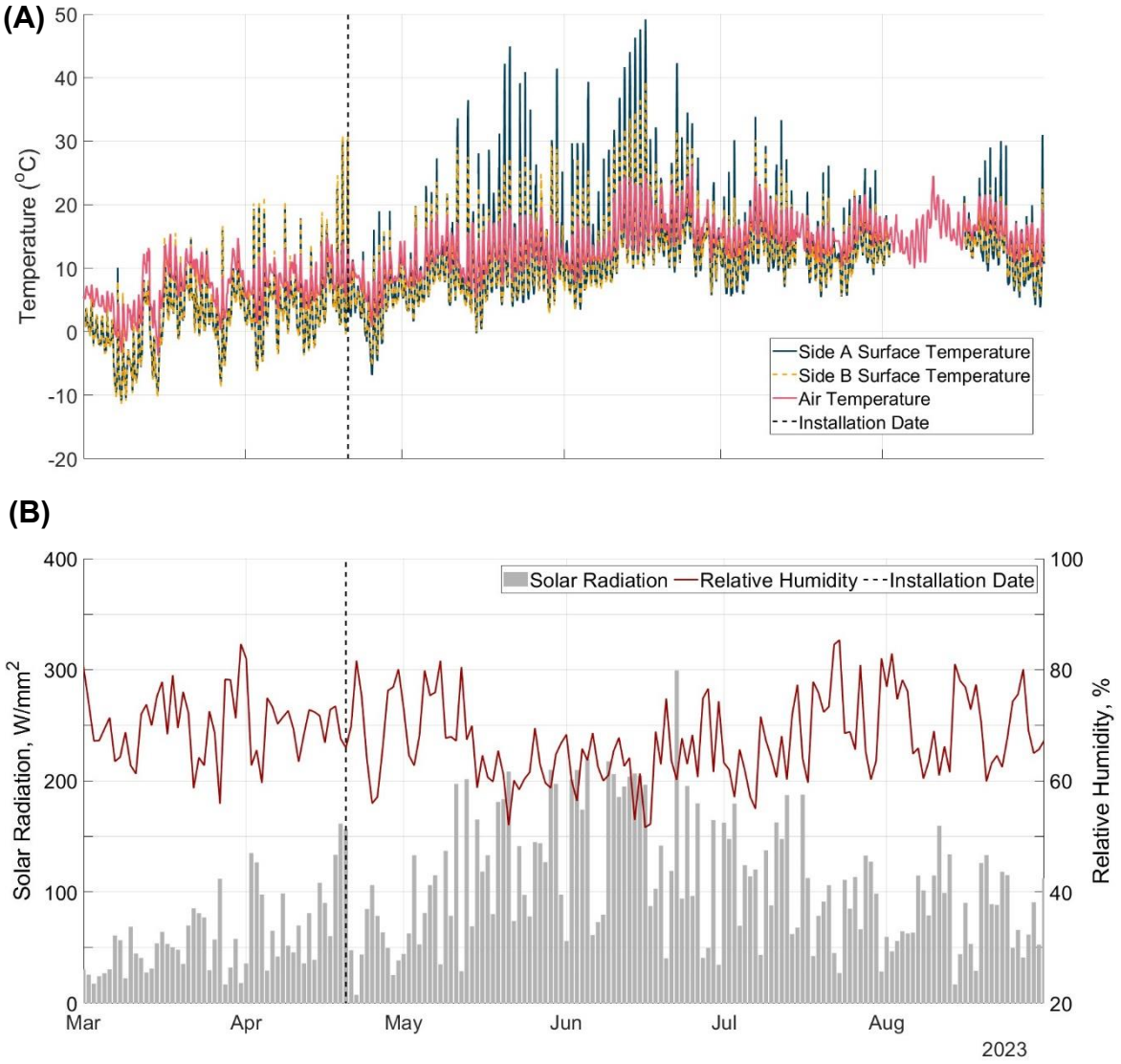

Figure 4.28: (A) Plot of surface temperature (°C) evolution on Sides A (blue) and Side B (yellow) on the lysimeter slope compared to that of air temperature (pink), and (B) average daily solar radiation (W/m^2) and relative humidity (%) for the monitoring period obtained from an on-site weather station. The black dashed line indicates the installation date for the faux grass canopy.

After the canopy is installed, Figure 4.28A shows an apparent deviation in the surface temperature behaviour of Sides A and B. Comparatively, Side A's surface temperature appears highly variable, exhibiting greater peaks and lows, suggesting a heightened sensitivity to the recorded changes in air temperature and solar radiation. In contrast, Side B shows that surface temperature is moderated in both directions, suggesting a more suppressed response to variations in air temperature and solar radiation. Figure 4.28A illustrates that Side B moderates peak temperatures more efficiently than

temperature lows. The findings suggest that the canopy serves principally as a cooling shade mechanism for Side B, effectively mitigating rapid heat gain. Additionally, it exerts a secondary insulating effect that reduces heat loss, thereby contributing to a more stable thermal environment. The lack of these moderating influences on Side A elucidates the severity of direct environmental exposure, likely causing pronounced fluctuations in surface temperature. Furthermore, these thermal extremes tend to promote higher evaporation and desiccation rates, as confirmed by lysimeter data (Section 4.2.3). This aligns with prior findings (Tang et al., 2008, 2010) that associate intense drying with increased evaporation rates and desiccation crack severity.

While Side A and B's surface temperature and the prevailing environmental conditions appear correlated, this relationship is more complex than a direct causal link. It reflects the intricate dynamics of surface energy balance, encompassing net radiation, soil heat flux, and energy exchanged through sensible and latent heat fluxes (Penman, 1948; Monteith, 1965). Furthermore, the response of these factors is modulated by the thermal-moisture properties of the soil, including texture, structure and water content. The faux grass canopy likely modifies energy partitioning by decreasing direct solar radiation, which affects net radiation levels, and by increasing surface shading, which reduces sensible heat flux. Additionally, it could influence surface moisture dynamics, thereby impacting latent heat flux. As a result, the cooling effect observed under the canopy may stem from a greater emphasis on latent heat dissipation and a corresponding reduction in ground heat storage. However, the effects outlined herein are hypothesised; measuring and confirming these effects falls outside the scope of this research and is a recommended area of future study.

As summer approaches, Figures 4.28A and 4.28B show a notable increase in air temperature accompanied by a rise in average solar radiation, while relative humidity lowers. Therefore, during this period, the baseline surface temperatures for Sides A and B gradually increase as these environmental conditions deliver greater net radiation to the soil surface, influencing the surface energy balance and the partitioning of available energy. As the faux canopy evidently suppresses environmental exposure, net radiation reaching Side B will continue to be lower than that experienced by Side A. This significantly reduces the overall temperature increase on Side B compared to Side A.

Additionally, under conditions of greater environmental exposure, Side A experienced a more substantial loss of moisture at an accelerated rate, leading to a faster transition toward unsaturated soil conditions (see Section 4.4.2 for further evidence). This drying of the soil restricts latent heat flux (evaporation), consequently allocating more energy to increase surface temperatures, which accumulated to exceed air temperature readily (see Figure 4.28A). In comparison, Side B exhibits only a few instances where surface temperatures surpass air temperatures. This is due to the slower, steady rate of evaporation sustaining higher moisture levels and the latent heat flux for longer durations. This, in turn, limits the amount of energy available for heating the soil, dampening temperature increases in the process. Notably, bare soil generally exhibits a lower albedo effect than vegetated surfaces, which may enhance the canopy's sheltering effect to Side B.

With the seasonal transition into late summer and early autumn (late July – August), the overall magnitude and rate of air temperature and solar radiation fluctuation begin to decrease. In response, the differences in surface temperature between Sides A and B become less pronounced, yet they remain noticeable due to residual contrasts in surface properties and energy partitioning. This overall decrease in net radiation reduces the energy available to create significant temperature differences between Sides A and B. Air temperatures once again surpassing the soil surface temperature further suggests an overall reduction in net radiation. These results indicate that the beneficial effects of a vegetative canopy are greater during summer months when the supply of net radiation by the prevailing environmental conditions is higher. This notably coincides with the most intense periods of desiccation cracking on infrastructure embankments, illustrating its potential as a protective measure against weather-driven deterioration.

It is also crucial to analyse how these variations in environmental exposure, energy partitioning and subsequent deviations in surface temperature established post-canopy installation affect soil at depth. Changes in subsurface temperature can serve as a proxy for the transfer of heat energy within soil, dictating the propagation rate of evaporation fronts through an embankment by influencing soil moisture and thermal gradients. Fundamentally, the rate and magnitude of heat transfer govern the severity of volume change and the extent of subsurface desiccation. Therefore, Figures 4.29 – 4.31 continue the analysis of soil temperature behaviour in Sides A and B in the subsurface of the lysimeter pre- and post-installation of the canopy, the division of

which is marked by the black dashed line. Graphs of the temporal evolution of soil temperature at depths of (A) 50 mm, (B) 100 mm, (C) 200 mm, (D) 300 mm, (E) 400 mm, and (F) 500 mm within the crest of the lysimeter slope are provided in Figure 4.29. Figures 4.30 and 4.31 present the same variables at 200 mm and 400 mm depths within the upper and lower slope regions, respectively. The locations of the crest, upper and lower slope regions can be viewed in Figure 3.8 within Section 3.3.1.

Figures 4.29 to 4.31 illustrate subsurface temperature profiles that exhibit trends paralleling the surface temperature behaviours observed on Sides A and B. However, these subsurface profiles display a slight temporal lag and exhibit dampened fluctuations. These observations reinforce the notion that the thermal-moisture properties of soil play a pivotal role in regulating temperature fluctuations, both at the surface and in the subsurface layers. All depths and slope regions presented in Figures 4.29 – 4.31 evidence the same deviation in soil temperature behaviour between Sides A and B as was recorded at the surface, post-installation of the canopy. However, this deviation is considerably less defined in the lower slope region (Figure 4.31). This may be due to its lower prominence, which offers shelter from prevailing weather conditions, and a result of increased moisture accumulation at the slope toe under gravitational forces. The increased soil moisture raises the soil's thermal capacity, buffering this region against extreme temperature fluctuations. In the crest and upper slope regions, Side A remains more sensitive to variations in environmental conditions through the subsurface. The bare slope consistently exhibits a greater magnitude of change than Side B, visible to the maximum sensor depths of 500 mm in the crest and 400 mm in the upper slope, shown in Figures 4.29 and 4.30, respectively.

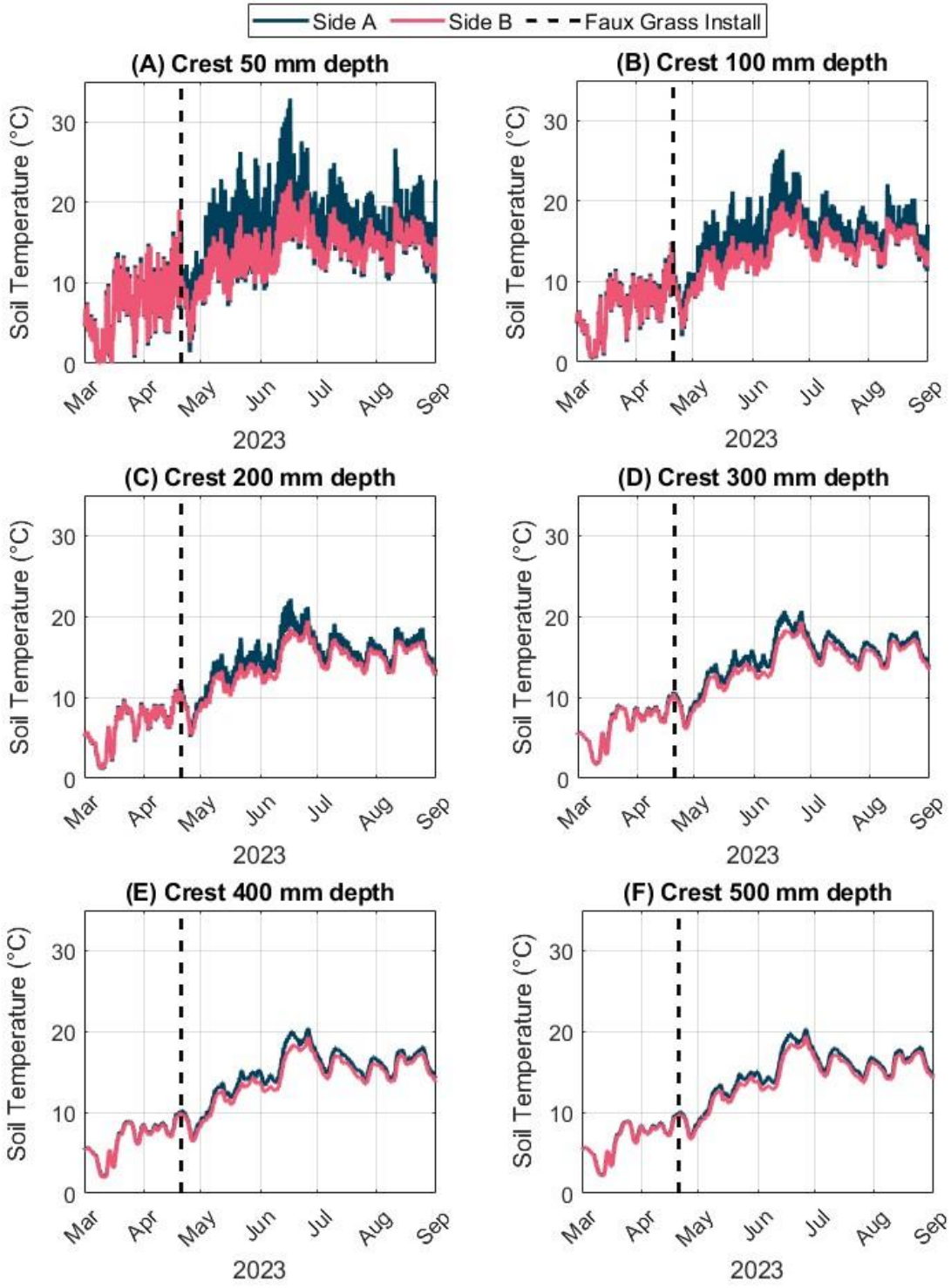

Figure 4.29: Sub-surface temperature (°C) profiles through the lysimeter slope crest at depths of (A) 50 mm, (B) 100 mm, (C) 200 mm, (D) 300 mm, (E) 400 mm, and (F) 500 mm. Sides A and B measurements are plotted in blue and pink, respectively. The black dashed line marks the installation date for the faux grass canopy.

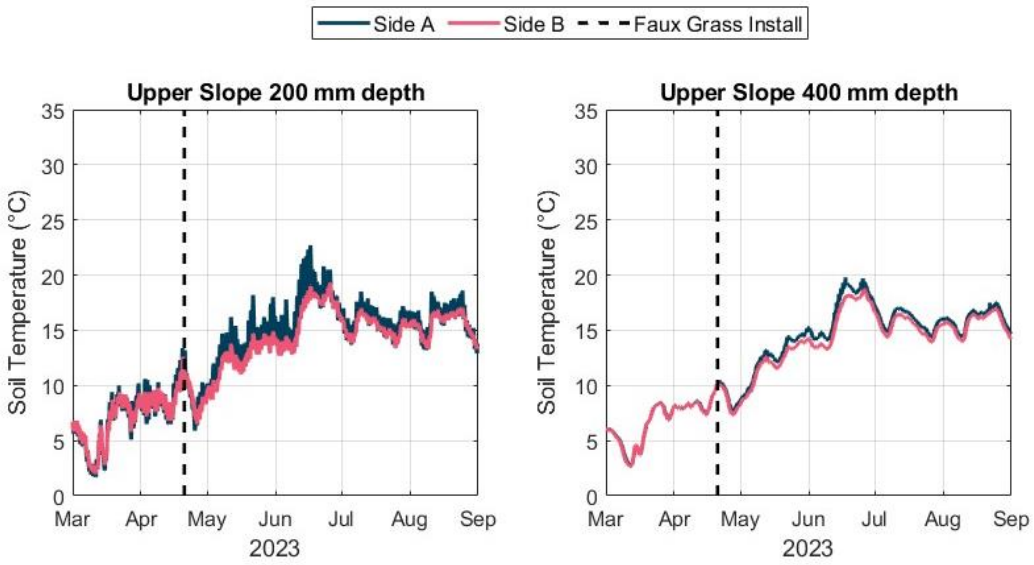

Figure 4.30: Sub-surface temperature profiles through the upper slope region of lysimeter slope at depths of (A) 200 mm and (B) 400 mm. Sides A and B measurements are plotted in blue and pink, respectively. The black dashed line marks the installation date for the faux grass canopy.

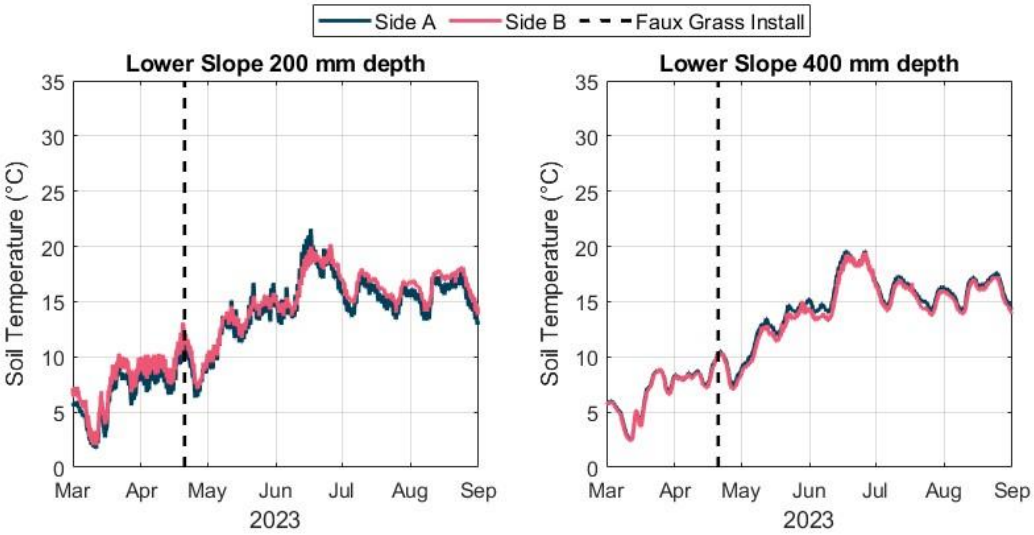

Figure 4.31: Sub-surface temperature profiles through the lower slope region of lysimeter slope at depths of (A) 200 mm and (B) 400 mm. Sides A and B measurements are plotted in blue and pink, respectively. The black dashed line marks the installation date for the faux grass canopy.

This difference remains particularly pronounced during the summer, as observed with surface temperature in Figure 4.28A. However, the divergence in behaviour between the two sides decreases with depth, being most significant in the upper 200 mm of the crest and upper slope. These findings indicate that the physical cover provided by a vegetative canopy can effectively lower soil temperature to a considerable depth by influencing the surface energy balance (primarily through shading), which reduces net radiation reaching Side B. Notably, this moderating effect is most pronounced within

the upper 200 mm of soil, where the prevailing environmental boundary conditions more readily impact the thermal dynamics. Regulating temperature change in the shallow subsurface of embankments is fundamental in reducing the rate of soil drying and, consequently, the propensity for desiccation cracking.

4.4.2 Comparison of Volumetric Water Content Profiles

Following the installation of the faux grass canopy, Section 4.4.1 discussed the disparity in temperature profiles between Sides A and B, which resulted from the changes the canopy imposed on the physical boundary conditions. It is crucial to investigate whether these variations in thermal energy have influenced the strength and rate of propagation of evaporation fronts within the lysimeter slope. The rate and magnitude of evaporation significantly influence the accumulation of tensile stress, thereby increasing the susceptibility of slopes to desiccation crack formation. Therefore, Figure 4.32 presents the evolution of volumetric water content (%) during the monitoring period for depths of (A) 50 mm, (B) 100mm, (C) 200 mm, (D) 300 mm, (E) 400 mm, and (F) 500 mm within the crest of the lysimeter slope. The same plot has also been generated for depths of 200 mm and 400 mm within the upper and lower slope regions in Figure 4.33 and 4.34, respectively.

Figure 4.32 demonstrates that a disparity in the hydrological response of Sides A and B also occurs due to the faux grass canopy installation. However, it is only evident within the upper 100 mm of the crest (Figure 4.32A – B) within the lysimeter slope. The shallowest sensor deployed in both the upper and lower slope regions was positioned at a depth of 200 mm. Consequently, no disparity is observed in these plots, but its potential occurrence within the upper 100 mm should not be discounted. From 200 mm within the slope crest, Figure 4.32 shows minimal fluctuation in volumetric water content, remaining consistently around 60%. Similar behaviour is observed from 200 mm in the upper (Figure 4.33) and lower (Figure 4.34) slope regions, however around a lower volumetric water content of 40 – 45%.

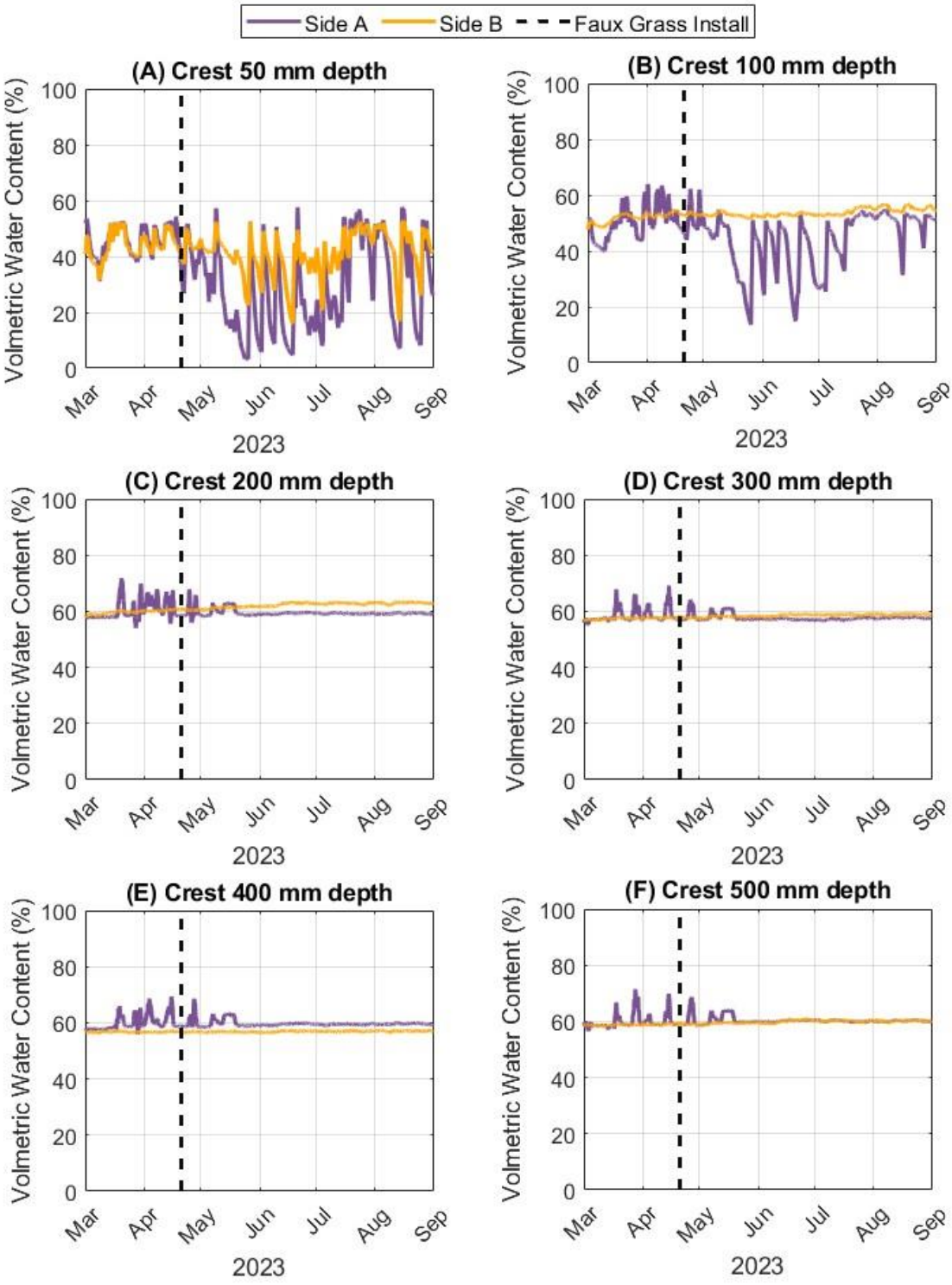

Figure 4.32: Volumetric water content (%) profiles through the lysimeter slope crest at depths of (A) 50 mm, (B) 100 mm, (C) 200 mm, (D) 300 mm, (E) 400 mm, and (F) 500 mm. Sides A and B measurements are plotted in purple and orange, respectively. The black dashed line marks the installation date for the faux grass canopy.

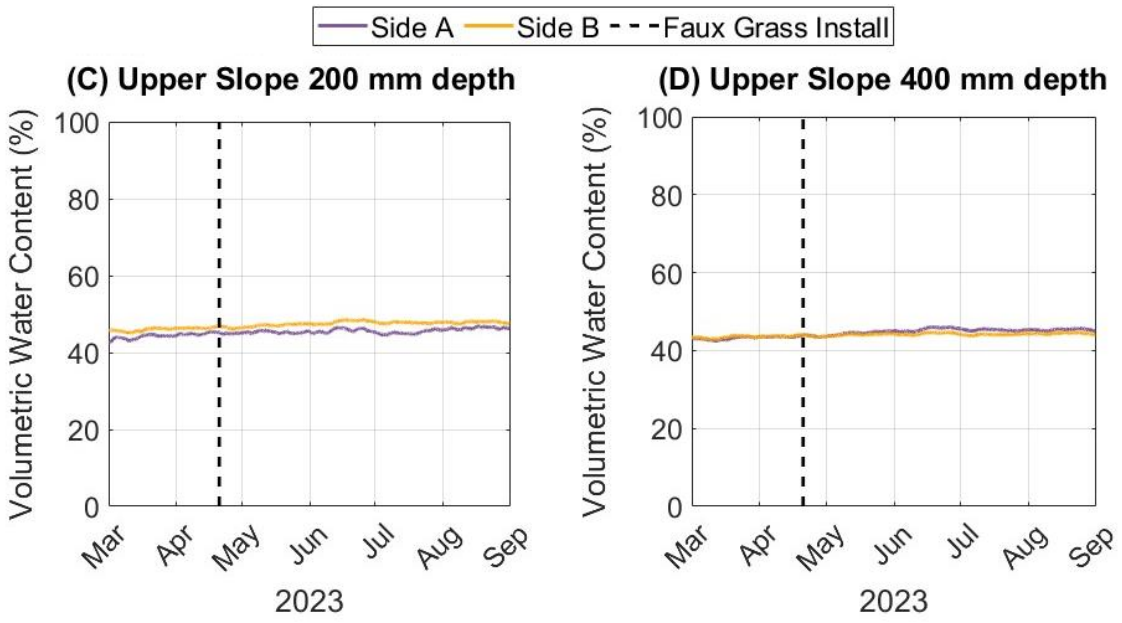

Figure 4.33: Volumetric water content profiles through the upper slope region of the lysimeter slope at depths of (A) 200 mm and (B) 400 mm. Sides A and B measurements are plotted in purple and orange, respectively. The black dashed line marks the installation date for the faux grass canopy.

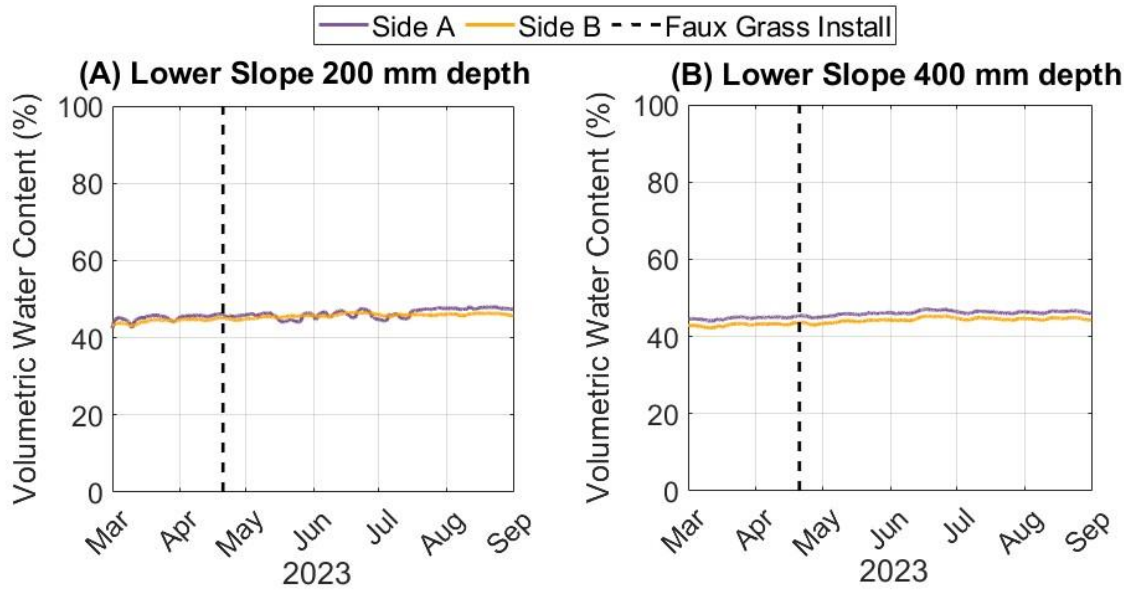

Figure 4.34*:* Volumetric water content profiles through the lower slope region of the lysimeter slope at depths of (A) 200 mm and (B) 400 mm. Sides A and B measurements are plotted in purple and orange, respectively. The black dashed line marks the installation date for the faux grass canopy.

The difference in volumetric water content between these regions could be attributable to the use of different sensors in the crest area. However, the consistent trend in volumetric water content response at depths greater than 200 mm suggests that regional differences may be attributed to inherent variation in water retention and movement. The accumulation of surface water and the reduction of runoff in the flat crest region facilitate enhanced infiltration, which may elevate the volumetric water content in this area relative to the upper and lower slope regions. In contrast, the

steeper gradients in the slope regions promote more efficient drainage. These results indicate that, despite the temperature fluctuations recorded at depths greater than 100 mm in Figure 4.29 to 4.31, the changes were not significant enough to cause any notable evaporation that would affect the volumetric moisture content.

In contrast, after the faux grass canopy installation, moderation of volumetric water content within Side B in both directions is recorded within the upper 100 mm of the slope crest (see Figure 4.32A – B). At 50 mm depth (Figure 4.32A), cyclic fluctuation in Side B's volumetric water content remains notable yet lesser in magnitude compared to Side A. Within the dry-wet cycles evident in Figure 4.32A, the temporal differences in the response of Sides A and B are evident. Side A quickly desaturates and re-saturates, reaching more extreme moisture content in both directions than Side B, particularly in mid-June during cycles of high temperatures and convective summer storms. Conversely, Side B responds more slowly to changes in environmental conditions toward less severe highs and lows of volumetric water content. An example of a varying response to drying in Figure 4.32A is evident mid to late May, whilst the last large dry-to-wet cycle in mid-June displays the differential patterns of re-wetting. These results suggest that, combined with the shading effect that slows evaporation (as per the Penman-Monteith framework), the canopy moderates the volume of rainwater reaching and infiltrating through Side A's surface. In natural vegetated canopies, such interception effects are further enhanced by physiological processes, including evaporation from leaves and water uptake by roots – mechanisms that are not simulated by the faux grass.

The volumetric water content records at 100 mm depth in the crest highlight a key impact of the faux grass canopy installation. While Side A exhibits pronounced cyclic fluctuations in moisture content between approximately 45% and 18%, Side B shows minimal variation, maintaining values near 45% throughout the monitoring period. This suggests that the reduced energy input for evaporation at the surface beneath the faux grass—primarily through shading and reduced near-surface turbulence—limits the penetration of evaporative drying into deeper soil layers. Consequently, moisture levels at depth remain more stable, as illustrated in Figure 4.32B. Additionally, the lack of increased moisture in Side B following rainfall may indicate canopy interception effects reducing infiltration; however, low evaporation rates combined with sustained high saturation could also promote runoff rather than soil absorption.

These findings imply that a physical canopy, such as the faux grass, can act as an environmental buffer by moderating surface energy fluxes and rainfall impact, thereby dampening the magnitude of dry–wet cycling within the soil. This reduction in fluctuation is important because it can limit shrink–swell behaviour and desiccation crack propagation, processes that contribute to irreversible microstructural degradation and potentially compromise the long-term stability of infrastructure embankments under cyclic loading. Although the faux grass does not reproduce physiological vegetation processes like transpiration or root water uptake, its ability to modify key boundary conditions offers valuable insight into the environmental controls affecting soil desiccation.

4.4.3 Disparities in Dry-Wet Cycles and the Impact on Desiccation Cracking

The observed disparities in hydrological and thermal responses between Sides A and B are significant, particularly given that Side B is influenced by a faux grass canopy which modifies critical boundary conditions, such as shading and near-surface airflow. These alterations are essential in evaluating the respective patterns of desiccation crack development on each side. These modifications affect soil temperature and moisture dynamics by reducing surface energy inputs and evaporation rates as per Penman-Monteith (1965), which are fundamental controls on the rate and extent of desiccation cracking within an embankment. While Sections 4.4.1 and 4.4.2 provide comparative insights into overall soil temperature and moisture trends for both sides, a more detailed examination of individual dry–wet cycles is necessary. This will clarify how the differences induced by physical boundary modifications influence the timing, initiation, propagation, and closure of desiccation cracks, independent of physiological vegetation processes.

It is important to note that an extensive surface network of desiccation cracks was present on the lysimeter slope when the canopy was installed over Side B. Furthermore, the slope had been exposed to cyclic environmental loading for 22 months, during which time the deteriorating effects had become visually and quantitatively measurable. Therefore, the pre-existing cracks and weakened zones of tensile strength are likely to dictate much of the desiccation behaviour, making it difficult for the faux grass canopy to develop significant changes in desiccation behaviour. However, evidence suggests the faux grass canopy still has some moderating effect, specifically in the rate and degree of crack opening and closure, which will be discussed. If the canopy had been installed synchronously with slope construction or

the monitoring period had been extended, a greater disparity in desiccation crack behaviour may have been established. This is a recommended area for future study to delineate further the impacts of a vegetative canopy on desiccation cracking.

Figure 4.35 compares the evolution of (A) slope crest volumetric water content (%) profiles in the upper 200 mm, (B) slope crest soil temperature (°C) profiles in the upper 200 mm, (C) air temperature (°C) and rainfall (mm), and (D) surface runoff within Sides A and B across two consecutive dry-wet cycles. These cycles spanned 24 days of monitoring during August 2023. Air and soil temperatures were plotted as a 24-hour moving average to eliminate the variation caused by diurnal cycles. Transposed onto each plot in Figure 4.35 is the temporal occurrence of the surface crack images provided in Figure 4.36. These crack images provide a comparison of the desiccation behaviour within Sides A and B at different stages across the two dry-wet cycles.

Drying Cycle 1

The first drying cycle occurred from August 5th to August 13th, 2023. Figure 4.35 shows three distinct behavioural phases of volumetric water content. Phase 1 occurred between the 5th and 9th of August, with Figure 4.35C showing a gradual increase in air temperature from 13°C to 15°C, during which rainfall was minimal. Soil temperature records in Figure 4.35B demonstrate that Side A responded first to this warming. A gradual increase from 13°C to 14°C is recorded initially in the upper 100 mm, followed by 200 mm after a slight delay. Conversely, Side B's soil temperature remained relatively stable at 14°C across all depths, as documented in Figure 4.35B. For volumetric water content, only measurements at 50 mm depth evidence a response to this soil and air temperature increase. At this depth, Figure 4.35A shows Side A reacting first and displaying a higher rate and volume of moisture loss, decreasing from 52% to 20% in Phase 1. In comparison, Side B's response exhibited a 12-hour delay, from which volumetric water content only reduced from 52% to 43%.

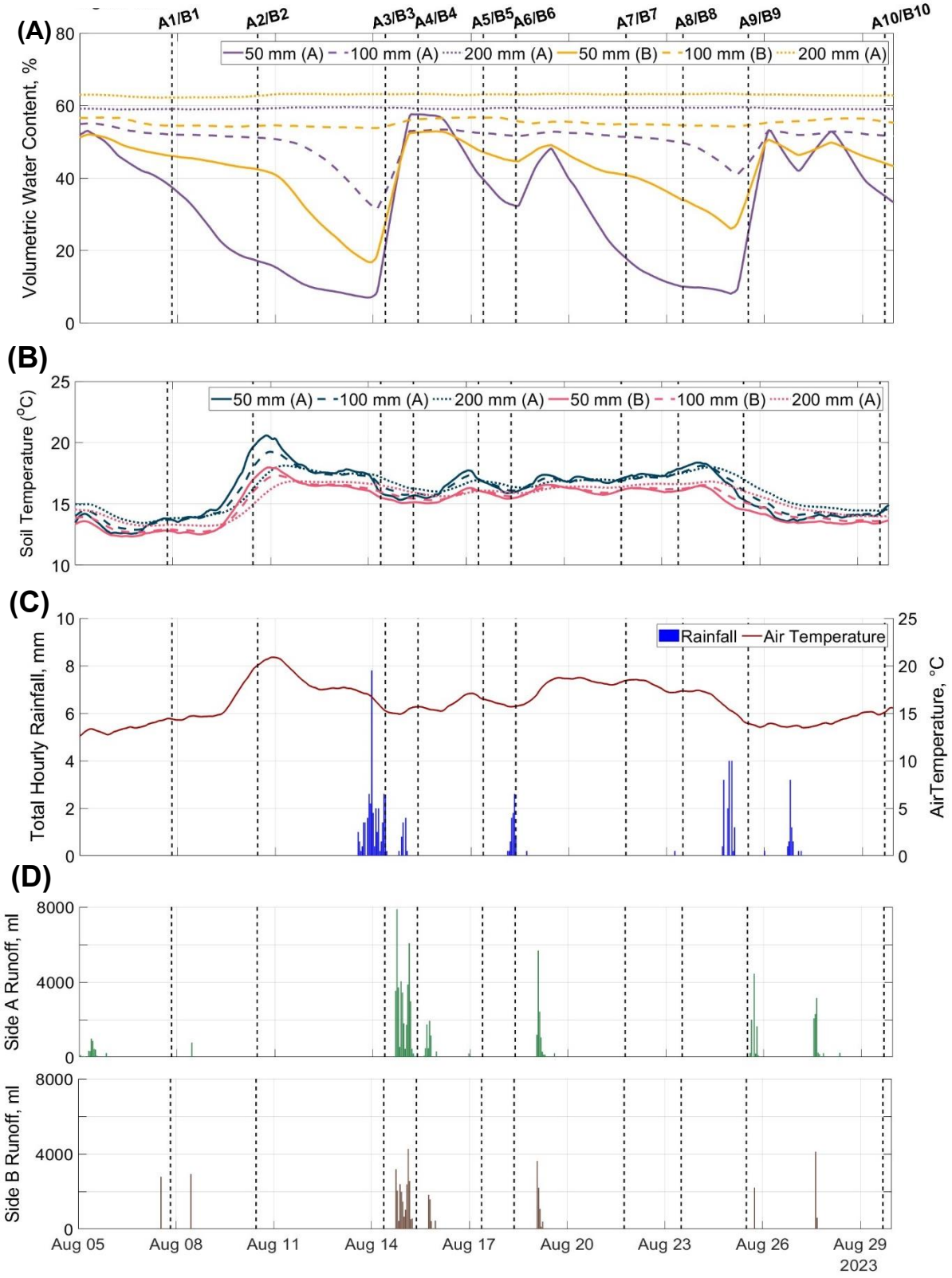

Figure 4.35: Plots of (A) volumetric water content (%) and (B) soil temperature through the slope crest at 50, 100 and 200 mm in Sides A and B, (C) total hourly rainfall (mm) and average air temperature (°C), (D) surface runoff recorded in Sides A and B. Air and soil temperature are plotted as a 24 hour moving average to eliminate diurnal variations. The black dashed lines represent the time occurrence of the crack images provided in Figure 4.12.

	1	2	3	4	5
	07/08/2024	10/08/2024	14/08/2024	15/08/2024	17/08/2024
Side A					
Side B					

	6	7	8	9	10
	18/08/2024	21/08/2024	23/08/2024	25/08/2024	29/08/2024
Side A		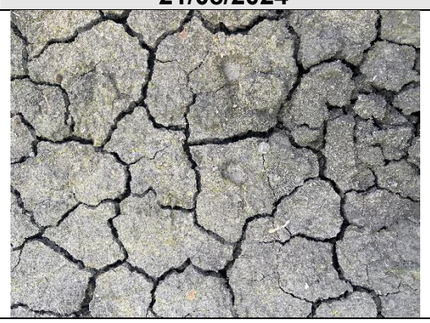	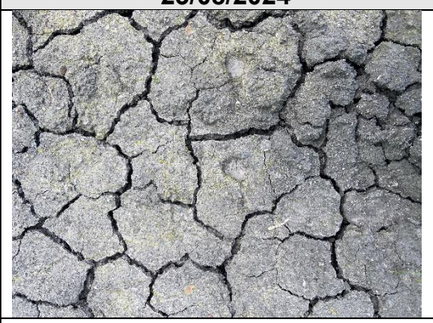	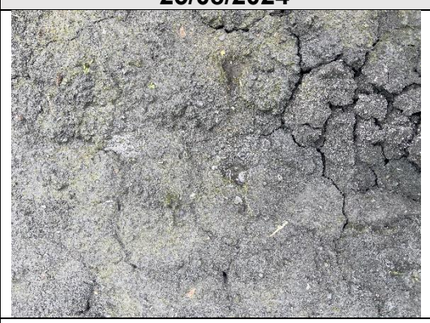	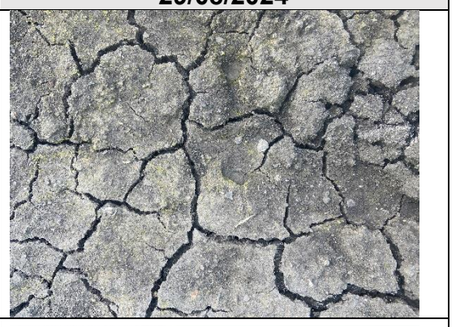
Side B		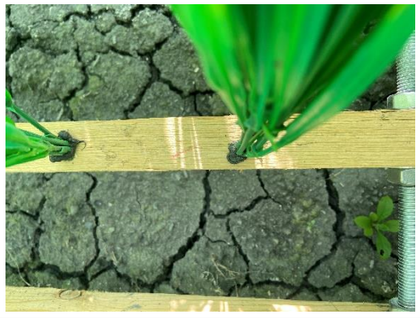			

Figure 4.36: Qualitative comparison of surface crack evolution in Sides A and B across the two dry-wet cycles defined in Figure 4.12. The temporal occurrence of these crack images is annotated in Figure 4.12 by the black dashed lines. The crack images highlight a disparity in the initiation and healing behaviour of desiccation crack behaviour in Sides A and B, with Side B moderating the frequency and rate of these changes across the dry-wet cycles compared to Side A.

Figure 4.36 illustrates the surface crack network in Sides A (A1) and B (B1) at the midpoint of Phase 1 on August 7th. By comparing the two sides, Side A reveals a wider, more established crack network than Side B. Placed in the context of Figure 4.36, Side B is recording lower soil temperatures and a slower evaporation rate around August 7th, effects attributable to the faux grass canopy's modification of physical boundary conditions (shading and near-surface airflow). Consequently, the fill beneath the canopy in Side B is at a higher degree of saturation. It is likely that this higher saturation, coupled with reduced exposure to environmental stress (evaporation), is restricting the rate of crack growth relative to Side A. The runoff measurements during this period also allude to differing crack characteristics between the two sides. A sequence of small rainfall events across August 5th to 8th generated greater runoff from Side B than Side A, as shown in Figure 4.35D. The more open crack network in Side A is likely to have accepted greater infiltrating rainfall relative to Side B's finer network, resulting in less runoff. However, the interception effect of the canopy would further reduce the volume of water reaching the slope surface, decreasing infiltration and thus impacting runoff generation. Therefore, these observations suggest that the faux grass canopy, while not replicating biological and physiological vegetation processes, acts as a simplified physical boundary modifier that initiates a disparity in crack growth rates through its influence on evaporation and infiltration dynamics.

Between the 9th and 11th of August, Phase 2 was identified, which coincides with a rapid increase in air temperature toward its August peak of 22°C, as shown in Figure 4.35C. Subsequently, soil temperature increased in both Sides A and B down to 200 mm under greater net radiation, with the impact magnitude rising and the response time lengthening with depth. Additionally, Side A showed a greater soil temperature increase than Side B at all measurement depths, reflecting the shading effect and reduced near-surface airflow provided by the faux grass canopy. Figure 4.35B documents this, with peak soil temperature on August 11th being 3°C, 2°C, and 2°C higher than Side A at 50 mm, 100 mm, and 200 mm, respectively. Despite significant changes in air and soil temperature, moisture loss in Side B at 50 mm continues along the same trajectory as Phase 1, decreasing volumetric moisture content by only 3%. Similarly, the moisture loss rate of Side A at 50 mm slows, only decreasing by a further 5%. Evidence of evaporation initiating within Side A and B at depths greater than 50 mm is also not yet visible in the results of Figure 4.35A. These results suggest a thermal lag delaying the downward progression of drying fronts, consistent with the

canopy's modification of key energy balance components – reduced net radiation and aerodynamic conductance – that govern soil evaporation rates as per Penman-Monteith (1965).

The disparity in the magnitude of evaporation between Sides A and B by the end of Phase 2 reflects the effect of the faux grass canopy modifying incoming solar radiation and near-surface air turbulence. Reducing solar radiation decreases the net radiation reaching the soil surface, whilst lesser wind exposure may locally increase the relative humidity above the soil surface, both suppressing evaporation according to Penman-Monteith (1965). Further investigation would be required to delineate whether microclimate characteristics differ above the soil due to the physical canopy effects. The slowing of evaporation at 50 mm within Side A and during Phase 2 could indicate the exhaustion of mobile moisture in the shallow subsurface or the provision of insufficient thermal energy at the surface level to trigger evaporation.

A capture of the surface crack network in Sides A and B during Phase 2 is shown by images A2/B2 in Figure 4.36. The widening of Side B's crack network is apparent when comparing images B1 and B2, confirming that Side B's network had yet to stabilise in B1 and that it had exhibited gradual growth in response to the lower yet sustained rate of moisture loss under the faux grass canopy's moderation of physical boundary conditions. In contrast, Side A's network (A2) reveals minimal change from A1, suggesting early stabilisation of surface desiccation under the previous faster and higher evaporation rates.

Phase 3 spans from August 11th until the end of the 13th, which marks the termination of the first drying cycle. During this period, the air temperature drops by 4.5^{o}C over the first 24 hours and stabilises over the remaining 48 hours. Soil temperature in the upper 100 mm mirrors changes in air temperature, with Sides A and B decreasing from their peaks in Phase 2 and stabilising between August 12th and August 14th. This decline in soil temperature is maximum for Side A at 50 mm (3^{o}C) and 100 mm (2^{o}C) and considerably lower for Side B at 50 mm (1.5^{o}C) and 100 mm (0.6^{o}C). This highlights the greater sensitivity of the bare soil surface to fluctuations in environmental energy inputs, consistent with its higher exposure to net radiation and aerodynamic conductance (via wind). However, soil temperature for both Sides A and B at 200 mm depth exhibited no decrease, stabilising at its peak value recorded at the end of Phase 2. These results indicate a thermal lag caused by the soil's heat capacity and delayed energy transfer. This lag reflects the gradual dissipation of stored thermal energy from

prior heating, underscoring the dynamic balance between energy input, conduction, and soil moisture evaporation in controlling subsurface thermal regimes.

Importantly, despite the reduction in soil temperature, the gradient of mass loss in Sides A and B increases at 50 mm depth. These results evidence a lag between peak air temperatures in Phase 2, temporal accumulation of sufficient heat energy and the actual initiation point of sustained evaporation. The increase in moisture loss is more pronounced in Side B, where volumetric water content decreased from 40% to 17% over three days. In contrast, Side A's moisture loss only slightly increased, with volumetric water content declining from 15% to 8%. This suggests that Side B retained a larger moisture reservoir capable of supporting sustained but gradual evaporation, whereas Side A had already undergone significant desaturation due to prior extensive evaporation during Phases 1 and 2. Furthermore, the residual moisture in Side B is held more tightly by capillary forces, requiring a higher energy input for evaporation to proceed, reflecting the complex interplay between soil moisture availability and energy balance.

The initiation of rapid moisture loss in Side B and the reactivation of the moisture loss gradient in Side A at 50 mm highlight the critical role of energy balance, as described by the Penman-Monteith (1965) equation, in governing evaporation potential and soil drying dynamics. The canopy's boundary effect reduces key drivers of evaporation—namely net radiation and aerodynamic conductance—thereby limiting environmental exposure and effectively increasing the energy input required for the same substantial evaporation to occur in Side B. Despite the peak temperatures reached during Phase 2, the overall magnitude of mass loss in Side B remained lower than in Side A, reflecting the canopy's role in reducing net radiation and aerodynamic conductance and thus limiting evaporation**.**

Moreover, evaporation below 50 mm was not initiated in Side B, contrasting with Side A where moisture loss began at 100 mm during Phase 3, with volumetric water content decreasing from 50% to 31%. The absence of rainfall during this Phase 3 likely allowed desiccation crack networks to persist on both sides. Side A's earlier and more extensive crack development, combined with increased energy input, likely promoted deeper drying front propagation. This is consistent with Penman-Monteith principles, as open cracks enhance evaporation by increasing exposed surface area and facilitating both temperature- and wind-driven drying. Therefore, the delayed crack growth and shading

effect provided by the canopy, which reduces the energy available for evaporation from the soil surface, explain the limited depth of moisture loss in Side B.

These results demonstrate that the structural effects of the faux grass canopy can mitigate the influence of temperature extremes on evaporation at depth by reducing solar radiation exposure and slowing the crack propagation rate. Consequently, the potential for severe shrinkage and intense desiccation cracking may also decrease. Conversely, the reactivation of the moisture loss gradient at 50 mm and the deepening of evaporation to 100 mm within Side A present the alternative scenario with a higher consequence for the rate of infrastructure embankment deterioration.

Wetting Cycle 1

The first wetting cycle occurred from August 14th to the end of August 15th. It was initiated by significant cumulative rainfall, starting small at midday on August 13th, reaching a peak of 8 mm per hour at midnight, and ceasing by midday on August 14th. A small drop in soil temperature is recorded at all depths during this period. This was largest in the upper 100 mm of Side A, reducing by 1.5 – 2^{o}C, while the upper 100 of Side A decreased by a maximum of 1^{o}C. Compared to the previous drying cycle, the wetting cycle produces a comparatively instantaneous response in volumetric water content. Figure 4.35A shows rapid increases in volumetric water content coinciding with peak rainfall at depths of 50 mm (Side A and B) and 100 mm (Side A only). Furthermore, the re-saturation at these depths appears to have occurred in a fraction of the time desaturation took, returning to their pre-drying cycle 1 moisture levels within 24 hours. However, a deviation in the response between sides is visible, with Side A gaining more moisture during the same period as Side B due to a faster rate of re-saturation. Due to an infiltration lag, a slightly slower response is recorded at 100 mm (Side B) compared to 50 mm in Sides A and B. At a depth of 100 mm within Side B, the volumetric water content remained unresponsive to changes in environmental conditions.

Images A3/B3 (August 14th) and A4/B4 (August 15th) in Figure 4.36 allow visualisation of how the surface crack networks in Sides A and B respond during this wetting event. Comparing A3 with B3, cracks appear in a more advanced state of healing in Side A than B. By August 15th, cracks in Side A (A4) had healed when peak saturation was reached, with a few cracks of reduced aperture remaining open in Side B (B4). Coupling these observations with the lower rate and magnitude of volumetric water

content increase recorded in Side B (Figure 4.35A), it appears the faux grass canopy physically intercepts or attenuates rainfall before it reaches the soil surface. This interception is purely a structural effect of the canopy and does not involve biological processes such as water uptake or diversion by real vegetation. However, such behaviour would slow the rate of crack closure and may explain the lower volume of surface runoff recorded in Side B by Figure 4.35D. Conversely, substantial runoff is recorded in Side A within Figure 4.35D, suggesting faster crack healing and re-saturation of the fill.

Drying Cycle 2

The second drying cycle commences on August 16th and terminates at the end of the 24th. This cycle can also be divided into three phases. The first occurs between August 15th and 18th, when air temperature fluctuates around 16±1^{o}C and low rainfall occurs. Soil temperatures in the upper 100 mm of Side B follow these small fluctuations more closely, with a comparatively more muted response in Side A at these depths, as seen in Figure 4.35B. This thermal behaviour aligns with the canopy's shading effect, reducing net radiation and, consequently, the energy available for evaporation as described by the Penman-Monteith (1965) equation. The relatively stable, moderate soil temperatures in Side B limited moisture loss, reflected in a smaller decrease in volumetric water content (52% to 44%) at 50 mm compared to Side A (56% to 32%), where greater surface energy promoted stronger evaporation. This highlights how the canopy's modification of surface energy inputs and aerodynamic conditions influences the soil water balance by limiting evaporative demand and sustaining higher moisture retention.

Following Phase 1, a brief 6-hour period of rainfall on August 18th interrupts drying to 50 mm in Sides A and B for 24 hours before evaporation resumes at the previously observed rate. This period is defined as Phase 2, instigating a 16% volumetric water content increase in Side A at 50 mm. However, the same depth in Side B recorded only a 5% increase, suggesting less rainfall reached the surface, possibly due to physical interception by the faux grass canopy. Images A5/B5 and A6/B6 in Figure 4.36 were taken on August 17th and 18th, respectively, and demonstrate that despite shallow subsurface evaporation, the surface crack network has not yet reopened due to the rainfall event on August 18th. However, the fine cracks identified in B4 are still visible, further suggesting continued sheltering of Side B from rain by the canopy. This is

further supported by the larger volume of runoff recorded in Side A relative to Side B within Figure 4.35D.

Phase 3 begins when evaporation restarts at 50 mm within Sides A and B, which occurs at midday on the 19th of August. During this phase, air temperature is constant at 18ºC and rainfall low, with heat accumulation by the end of the drying cycle (August 24th) visibly greater in Side A, forming a 2ºC soil temperature difference with each corresponding depth in Side B. Figure 4.35A illustrates that the 50 mm moisture loss gradient in Side A is greater during the second drying cycle compared to the first. This increase is likely due to the higher sustained soil temperatures during this current drying cycle. The next available crack images (Figure 4.36) were taken on August 21st (A7/B7) and 23rd (A8/B8), illustrating that similar intensity crack networks were sustained during this period on Sides A and B. Without higher temporal resolution crack images from August 18th to 21st, it is not possible to assess the relative rate of crack opening on each side. However, it is important to note that the presence of an established network on August 21st does not imply that the canopy is ineffective at suppressing desiccation. As previously mentioned, a memory of desiccation and weaknesses was established prior to the canopy installation, which would likely have greater control over the resulting crack pattern.

Side B experiences less moisture loss at 100 mm depth, likely because lower air temperatures reduced heat energy reaching this soil layer, limiting evaporation. Additionally, the moisture loss rate in Side A remains relatively constant in the absence of these peak temperatures, leading to a total volumetric water content reduction that is 9% less than in the first drying cycle. These results demonstrate how extreme air temperatures enhance the energy available for evaporation by elevating net radiation at the soil surface and enhancing the vapour pressure deficit between the soil and atmosphere. This process intensifies the latent heat flux and thereby promotes higher evaporation rates, provided soil moisture and aerodynamic conditions are not limiting. Consequently, these extreme temperatures are often associated with a heightened risk of desiccation cracking within infrastructure embankments.

Wetting Cycle 2

The final wetting cycle included in Figure 4.35 starts early on August 25th and is sustained by a sequence of rainfall events until August 28th, when the beginning stages of a third drying cycle are established. During this period air temperature drops by

approximately 4°C, closing the aforementioned 2°C gap between soil temperatures in Side A and B. During periods of lower temperature, this is a notable trend, suggesting the beneficial effects of a vegetated canopy are greater under environmental conditions more conducive to rapid drying. A less pronounced decline in soil temperature on Side B supports the hypothesis that the canopy attenuates near-surface airflow. This attenuation facilitates an increase in relative humidity, which in turn mitigates heat loss and stabilises soil temperature variations by decreasing evaporation rates. These observations are consistent with the principles articulated in the Penman-Monteith (1965) equation.

The resultant volumetric water content response to this wetting event is similar to the first cycle, with the rate and magnitude of re-saturation visibly greater in Side A than in Side B. Therefore, the findings have proven consistent over two wetting cycles, evidencing a clear deviation in hydrological behaviour due to the physical boundary conditions imposed by the canopy installation. The more extreme fluctuations between wet and dry states observed in Side A during these cycles have been presented by other researchers as a key driver of weather-driven deterioration of infrastructure embankments. The process induces microstructural degradation, increasing the fill's propensity to desiccation cracking, and placing the asset at a heightened risk of failure. Images A9/B9 in Figure 4.36 illustrate the surface cracks behave similarly to the first wetting cycle, with cracks healing in Side A but remaining open in Side B due to the canopy's interception of rainfall. Transitioning out of this wetting cycle, images A10/B10 show extensive surface desiccation re-establishing on Side A whilst Side B remains unchanged. These findings are significant, as faster establishment of desiccation can amplify the impact of drying cycles by increasing the evaporative surface area. However, it also extends the period during which an embankment remains vulnerable to failure by preferential flow through cracks, which can rapidly increase pore water pressures to depth. Therefore, the dry-wet cycle and desiccation moderation provided by the structural aspects of a vegetated canopy are significant, particularly from an asset management perspective. Introducing physical boundary conditions that reduce net radiation and near surface air flow can potentially slow the temporal evolution of weather-driven deterioration within infrastructure embankments.

It is important to note that although the grass canopy evidently moderates evaporation, real vegetation could introduce additional complexities to the observed soil moisture dynamics. Vegetation influences the rate of moisture removal from the soil, potentially

amplifying drying cycles and, in turn, increasing the likelihood of volume changes and desiccation. Therefore, further investigation into the complete range of soil-vegetation-atmosphere interactions and their impact on desiccation cracking is required. Nevertheless, the results presented here demonstrate the wider applicability of moderating environmental exposure on infrastructure embankments, whether that is with vegetation or by other interventions.

4.5 Soil-water Retention Characteristics as a Deterioration Indicator

Stirling et al. (2021) proposed an evidence-based conceptual model for how weather-driven deterioration can manifest within infrastructure embankments composed of compacted clay fill. The model demonstrates how deterioration in soil water retention behaviour, material strength, and resistance to macro-scale deformation can result from irreversible microstructural changes that develop through systematic exposure to cyclic wetting and drying. These microstructural changes refer to alterations in the fill's pore-size distribution, primarily caused by the development of interconnected networks of microcracks and the progressive weakening of clay particle bonding. This cumulative damage compromises the fill’s integrity, loosening its compacted structure and increasing the potential for deformation, such as extensive macro-scale desiccation cracking, and its vulnerability to water infiltration.

To track microstructural degradation, the temporal evolution of a fill's soil water retention behaviour can be analysed for changes indicative of pore size redistribution, as demonstrated by Stirling et al. (2021). Soil water retention behaviour can be visualised using a Soil Water Retention Curve (SWRC). The SWRC plots the relationship between soil moisture content and matric suction, which measures the pore-water’s energy state and resistance to evaporation. Finer pore networks are more effective at generating and sustaining high suctions and retaining moisture than coarser networks due to stronger capillary forces, which increase with decreasing pore diameter. Therefore, the geometry of the SWRC is strongly linked to a soil’s pore-size distribution, with any changes in the trajectory of the curve through time suggesting a change of microstructure.

Thus, to determine whether the lysimeter slope exhibits evidence of microstructural degradation, suction and volumetric water content sensors were co-located 200 mm apart at the same depth within the lysimeter slope to produce in-situ SWRCs. Installations were made at 200 mm and 400 mm depths in the upper and lower slope areas and at 200 mm within the crest, as shown in Figure 3.8 in Section 3.3.1. Sensor

locations were selected to compare the evolution of soil-water retention behaviour across different slope regions and to assess whether evolution of deterioration through the slope profile could be captured. Only drying curves were produced, as wetting events resulted in a near-instantaneous suction loss, preventing the acquisition of a sufficient measurement range to construct reliable wetting curves.

4.5.1 Drying Event Definition and SWRC Construction

Long-term datasets of volumetric water content (%) and suction (kPa) from the lysimeter slope are provided in Figure 4.37A for Side A and Figure 4.37B for Side B for depths of 200 mm (all regions), and 400 mm (upper and lower slope only). Due to a sensor malfunction, no suction data at 400 mm within Side A's upper slope could be attained and is consequently absent from Figure 4.37A. Some measurement gaps are also visible and were associated with data logger issues. The sensors installed in the crest region (Tensiomark and SoilVUE^{TM}10) differed from those within the upper and lower slope areas (TEROS-11 and TEROS-21). Consequently, some variations in the magnitude of suction and volumetric content measurements are visible, yet the relative amplitude of change is comparable.

The start of a major drying period was defined as where sustained periods of suction increase occurred above the sensor's baseline value of 0 kPa. Subsequently, the termination of the event corresponded with the peak volumetric water content observed during this prolonged suction increase before any notable decrease. This criterion was selected due to volumetric water content exhibiting a higher sensitivity to daily environmental changes, leading to greater moisture oscillations than the seasonally trending and stable suction data. These minor fluctuations within an overall drying trend produced noise in the soil water retention curve (SWRC), disrupting any observable relationship between volumetric water content and suction. Therefore, the drying event may terminate before the maximum suction shown in Figures 4.37A and 4.37B was reached, particularly if it was synchronous with highly fluctuating moisture content.

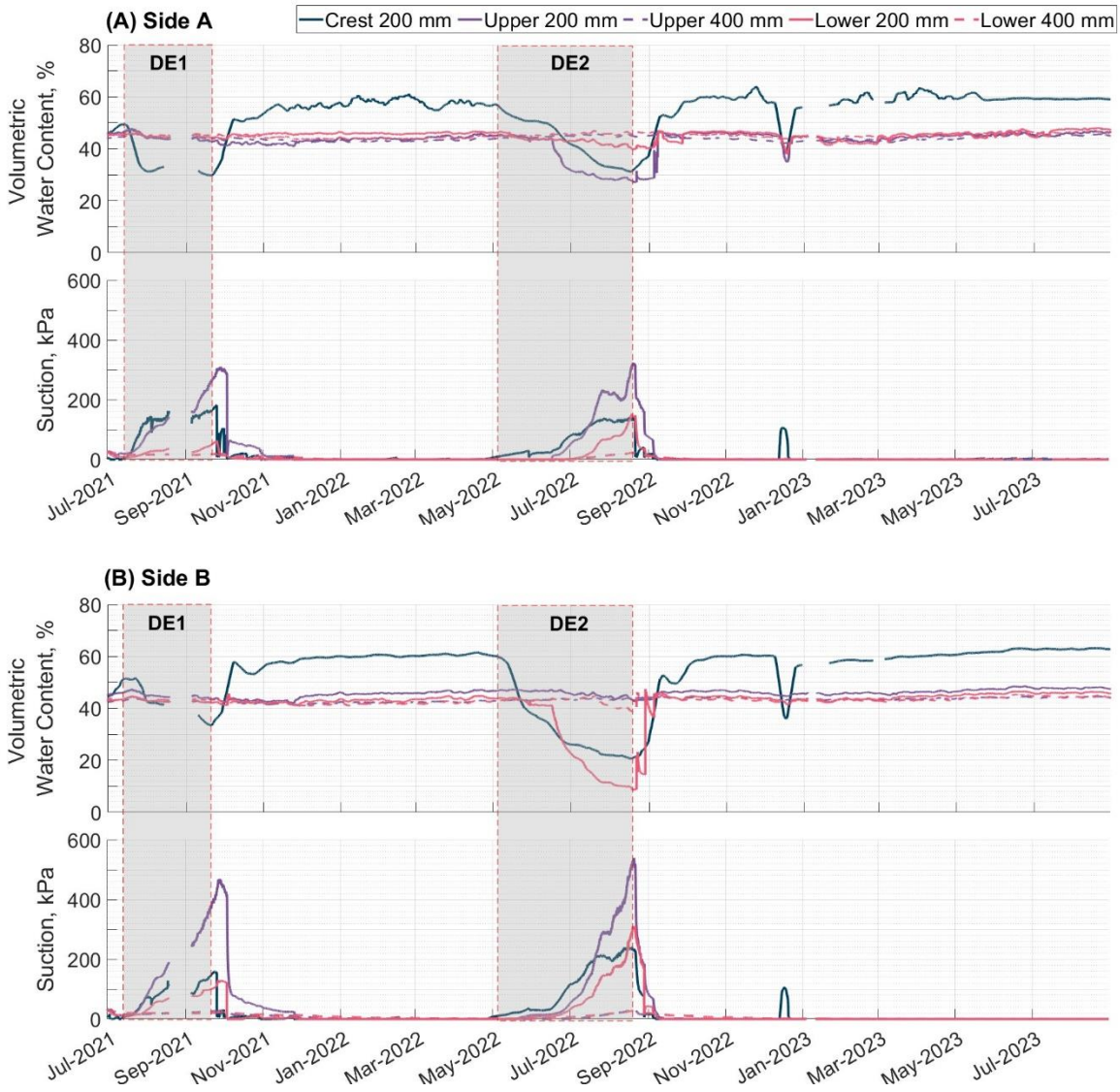

Figure 4.37: Long-term volumetric water content (%) and suction (kPa) datasets which were obtained from (A) Side A and (B) Side B of the lysimeter slope. The occurrences of Drying Event 1 (DE1) and Drying Event 2 (DE2) are highlighted on the graphs.

Figure 4.37 illustrates the complete monitoring dataset for the lysimeter slope from July 2021 to August 2023, with two notable major drying events annotated – DE1 and DE2. The first event (DE1) materialised soon after its construction in the summer of 2021, spanning July 16th to September 20th. During DE1, significant reductions in volumetric water content were observed exclusively at the slope crest, specifically at a depth of 200 mm within Sides A and B. This moisture reduction was matched by a substantial increase in suction to peak values of 180 kPa (Side A) and 160 kPa (Side B). However, despite volumetric moisture content remaining constant at around 45%, the upper and lower slope region sensors at 200 mm depth also record an increase in suction. For 200 mm in the upper slope, suction peaks at 310 kPa (Side A) and 460 kPa (Side B),

and for 200 mm in the lower slope the maximum values attained were 60 kPa (Side A) and 130 kPa (Side B).

An increase in suction without a significant change in volumetric moisture content in the upper and lower slopes indicates that the drying curves for these regions are not aligned with the crest, leading to different moisture loss rates during DE1. This implies that their soil water retention behaviour is inherently distinct, which could be attributed to two factors. Firstly, variation in compaction effort during construction could generate such disparities. Greater compaction generates finer pore sizes, increasing the air-entry value (AEV) and enabling the soil to generate significant suction before desaturation, as seen in the upper and lower slope regions at 200 mm. However, this behaviour may also stem from a more rapid propagation rate of microstructural degradation occurring within the crest, likely associated with its heightened sensitivity to change during dry-wet cycles. This potential accelerated degradation could exacerbate the differences in soil water retention characteristics between slope regions over time, further intensifying the local variations in drying and suction responses. Additionally, the increased compaction resulting from greater overburden pressure and reduced environmental exposure is likely to further contribute to the consistently muted response of the 400 mm sensors to dry-wet cycles. A greater likelihood of air gaps around the crest volumetric water content sensors, given their different installation method, could also be driving the disparities.

To verify the above, core sampling and laboratory testing to generate a complete SWRC for each depth and slope region would be necessary, making this a recommended area for further research. From this current dataset, SWRCs could only be generated for the crest region of Sides A and B at 200 mm depth during DE1, where a clear causal relationship between suction and volumetric water content has been measured. The moisture-suction data obtained from the remaining localities exhibited a limited range, which hindered the development of a SWRC that accurately depicts the critical characteristics of the fill's microstructural properties.

Transitioning into summer from spring the following year initiated the second major drying event (DE2) shown in Figure 4.37. This occurred between the 5th May and 20th August 2022. Within Side A, a reduction in volumetric water content is now noted at 200 mm within the crest and upper slope region, with corresponding peak suction values of 140 kPa and 230 kPa, respectively. DE2 at 200 mm in the upper slope was terminated early on July 29th before the temporary interruption in drying, where suction

decreased and moisture content increased. Within Side B, the crest and lower slope regions at 200 mm lose substantial moisture, with suction peaking at 240 kPa and 310 kPa, respectively. The upper slope at 200 mm in Side B generates the highest suction during DE2 at 540 kPa despite recording no change in moisture content. This finding relates back to prior discussions regarding possible higher compaction and lower deterioration locally in the sensor region, which may significantly influence soil water retention properties that control the SWRC's drying path. From this dataset, the upper and lower slope regions do not consistently yield reliable SWRC curves covering both DE1 and DE2, limiting the ability to assess deterioration across these events. Therefore, SWRCs for the crest at 200 mm (Sides A and B), which provide sufficient data to cover both drying events, will be solely utilised to assess microstructural degradation.

4.5.2 Evidence of Microstructural Degradation

Figure 4.38 contains the SWRCs for the crest at 200 mm during DE1 and DE2 within Sides A and B. Furthermore, the components of the SWRC derived from laboratory measurements (HYPROP and WP4C) have also been illustrated. The markers represent measured data, and the fitting curves, plotted as lines, were derived using the Fredlund and Xing (1994) equation within the HYPROP-FIT software.

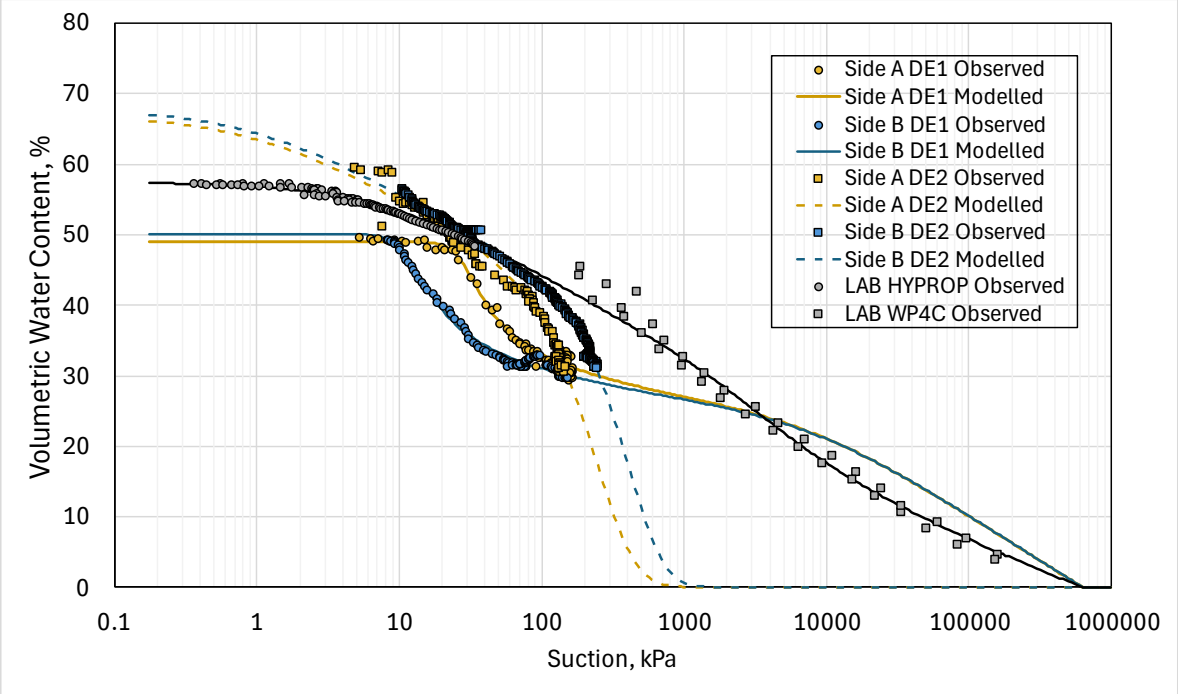

Figure 4.38: Plot of the SWRCs at 200 mm in the slope crest for Sides A and B during DE1 and DE2. This was measured using two methods – HYPROP and WP4C. The markers indicate the observed data from the lysimeter, and the Fredlund-Xing (1994) fitted model curves are plotted as lines.

For Sides A and B, a notable shift in soil water retention behaviour from DE1 to DE2 is observed. It is hypothesised that this phenomenon suggests the occurrence of microstructural deterioration at these localities after one year of environmental exposure. Firstly, given the projection of the SWRCs into the saturated range, the AEV exhibits a decrease in Sides A and B between DE1 and DE2. This decrease in the AEV suggests the fill at this locality has become more susceptible to desaturation at lower suction values. Such behaviour is linked to coarser pore structures exhibiting weaker capillary forces. As a result, these structures are less capable of generating and maintaining high suction, rendering them less effective at resisting drainage during the initial drying stages. Therefore, higher AEVs have significant implications for the frequency and severity of dry-wet cycles, as they facilitate faster desaturation and re-saturation. This can intensify the clay fill's shrink-swell behaviour, accelerating the microstructural degradation rate through micro-cracking and weakening clay particle bonding.

Figure 4.37 illustrates that the 200 mm sensors within the crest have exhibited considerable responsiveness to both drying and wetting cycles since slope construction in July 2021, in contrast to other regions with less sensitivity. However, the reliability of sensors in terms of their interaction with desiccation cracks and contact issues should be considered when interpreting results in this manner. If reliable, these continual, high-magnitude fluctuations in moisture content can indicate an inherently higher vulnerability to weather-driven deterioration in this region, either due to an initially poorer state of compaction, greater environmental exposure, or a combination of both. This compares to finer pore networks with greater water retention, which were suggested to be present in the upper and lower slopes, as they recorded significant suction without changing moisture content. Such behaviour may indicate lesser interaction with desiccation cracks or explain the limited evidence of deterioration in these regions, which is likely to develop at a slower rate.

The apparent change in the gradient of the SWRCs in Figure 4.38 further suggests the development of a coarser pore network between DE1 and DE2. After air entry, DE1’s curves delineate desaturation into two distinct stages, characterised by an inflection point at 1000 kPa. Such behaviour can be linked to compartmentalisation of the soil water retention behaviour into that contributed by micro and macro pore structures, which function independently in response to drying. Pre-inflexion, the DE1’s SWRCs in Figure 4.38 (Side A and B) exhibit rapid drainage at low suction, which is indicative

of the behaviour of large macropores. This rapid drainage at low suctions is likely associated with the increased macro-porosity contributed by desiccation crack formation, which reached a maximum depth of 300 mm during DE1. Post-inflexion, the desaturation process exhibits a more gradual decline in moisture content across a wider range of high suction values. This phenomenon suggests the additional presence of a finer micro-pore network, commonly associated with clay fill, and elucidates remaining intact clay areas. Other researchers have observed this biphasic soil water retention behaviour in SWRCs and have demonstrated it characterises a soil with micro- and macro-cracks encompassing an intact clay matrix (Abbaszadeh et al., 2011; Zhang & Fredlund, 2006; Li et al., 2017; Qian et al., 2022; Liu et al., 2024). Therefore, these results help quantify the hydrological changes that desiccation crack formation can have on clay soil, specifically the vulnerabilities it creates by locally enhancing infiltration and desaturation.

This dual-phase SWRC behaviour is no longer present during DE2 in both Sides A and B, further supporting the suggestive shift in the fill's water retention behaviour during this event. As illustrated by Figure 4.38, DE2's SWRCs exhibit a continual steep desaturation over a much narrower and lower range of suction compared to DE1's curve and the laboratory sample. This shift in the SWRCs' gradient likely points toward the formation of a more uniform yet coarser network of well-connected pores that facilitate rapid desaturation. This pore geometry and connectivity change is characteristic of microstructural degradation (Stirling et al., 2021; Briggs et al., 2023; Liu et al., 2024), likely forming under the crest's inherent sensitivity to environmental cycling, which first became evident during DE1.

Therefore, it is suggested that increased dry-wet cycling accumulating through time causes irrecoverable disaggregation of the Ampthill Clay through micro- and macro-cracking, removing the finer micro-pores and their influence on DE2's soil water retention behaviour. These results agree with similar studies conducted in both the laboratory (Liu et al., 2020; Stirling et al., 2021) and field (Glendinning et al., 2014; Stirling et al., 2021) which unanimously show key shifts in the soil-water retention behaviour with time and environmental exposure. The development of higher macro-porosity is further supported by DE2 curves' trajectory into the saturated range, projecting a substantial increase in saturated water content from DE1. This increase indicates the greater capacity macropores have for accepting infiltrating water, particularly for Side B. Open surface cracks can also accelerate the propagation of

drying and wetting fronts to depth within inherent impermeable materials such as Ampthill Clay. However, increasing this capacity through time and a declining ability to retain moisture may intensify the magnitude and frequency of dry-wet cycling as deterioration progresses. This, in turn, poses serious risks for both microstructural degradation and the stability of infrastructure embankments.

The slight differences in Side A and B's SWRCs highlight that deterioration varying over short distances should be considered. Differences in environmental exposure, cyclic wetting and drying, volume change and desiccation cracking can drive such spatial disparities. Although a detailed analysis of deterioration using SWRCs for the upper slope at 200 mm depth was not possible, Figure 4.37A for Side A indicates potential microstructural degradation, with significant desaturation observed during DE2 at suction levels similar to DE1, where moisture content was stable at 45%. This suggests a decline in the soil's capacity to sustain high suction levels, indicating macro-pore formation and microstructural degradation. In contrast, Side B's upper slope maintains static moisture content under substantial suctions, implying a distinct drying path, possibly due to enhanced compaction or lesser degradation. However, the reliability of sensors in terms of their interaction with desiccation cracks and contact issues should be considered when interpreting such results.

A final observation is that there was no volumetric water content reduction or suction generation during the summer of 2023. Other literature has reported this occurrence (Smethurst et al., 2012; Stirling et al., 2021), particularly during summers with above-average rainfall, which prevents significant drying and impacts the magnitude of suction generation within infrastructure embankments. However, it is important to note that a more superficial, yet surface-extensive network of desiccation cracks was still present during the summer of 2023 under these largely saturated conditions. These cracks were limited to the upper 100 mm of the slope profile, potentially shifting the focal point of microstructural deterioration to shallower depths. However, further core sampling and testing for microstructural analysis would be required to test this hypothesis. These open cracks at the onset of summer convective rainstorms in Summer 2023 provided an increased infiltration capacity in the shallow subsurface of the slope. However, crack healing occurred quickly, generating substantial runoff, which deposited a considerable mass of fines in the runoff channels, as illustrated in Figure 4.39. The loosening of the soil structure may have facilitated this mobilisation, which is likely to deteriorate soil water retention behaviour further.

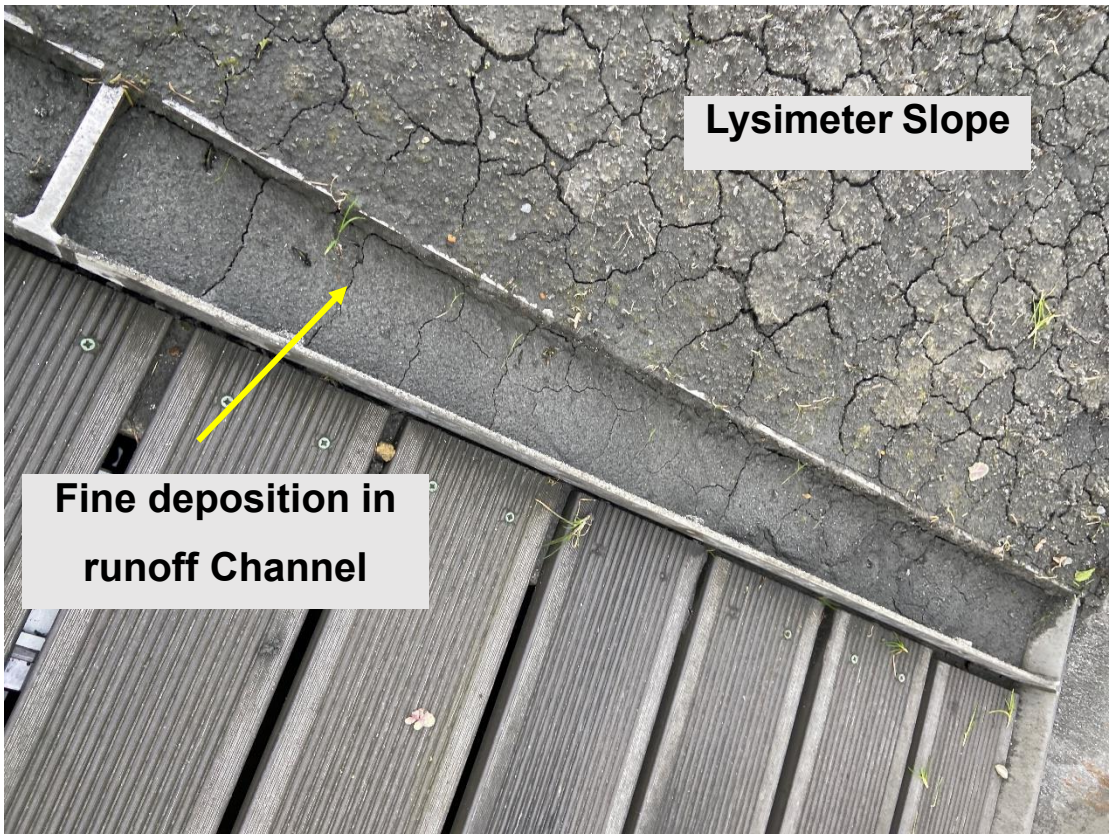

Figure 4.39: Photograph illustrating the significant mass of fines deposited in the runoff channels during Summer 2023 under higher summer rainfall.

Another possible interpretation is that the DE1 curves for Side A and B represent scanning curves that fall between the unmeasured primary wetting curve and the observed main drying curve obtained from laboratory measurements. The field measurements presented here begin from a lower, non-saturated moisture state (~50%) than recorded in the laboratory (~58%). This results in the observation of scanning curves, characteristic of natural soil behaviour, where soil saturation fluctuates between the primary drying and wetting SWRCs. However, before the onset of drying, DE1's soil moisture content remained constant at high saturation for an extended period (see Figure 4.37), indicating a stable condition consistent with field capacity. Therefore, more heterogeneous, manual soil compaction in the field, compared to the greater uniformity achieved in laboratory samples, likely contributed to DE1's lower apparent moisture content at saturation. Furthermore, the DE1 curve intersects the laboratory curve at low saturation, which contradicts the geometry of scanning curves, which should rejoin the main laboratory drying curve. The DE2 curve intersects both the laboratory and DE1 curves, indicating that it also does not represent an intermediate scanning state. This highlights a limitation of laboratory approaches,

which do not account for the greater compaction heterogeneity and field-specific drainage dynamics which influence in-situ soil water retention.

Additionally, the field curves exhibit a significant divergence from the laboratory's main drying curve, especially at lower suction levels. This discrepancy is plausible due to the aforementioned compaction heterogeneity and the unprocessed nature of the fill material used. Both factors can significantly influence the initial soil conditions, structure, and porosity. Importantly, this divergence in the drying curve is characteristic of a dual-porosity fill during drying, where moisture redistribution occurs across distinct micro- and macro-pore domains. Such multi-scale flow processes lead to temporally evolving retention characteristics that differ from classical soil water retention theory and complicate the straightforward identification of scanning curves. While the scanning curve hypothesis for the DE1 curves remains plausible, it cannot be conclusively validated without additional wetting data or advanced dual-permeability modelling approaches that explicitly account for these multi-scale and structural complexities.

Fundamentally, these results have demonstrated that early indicators of microstructural degradation can appear within SWRCs during the early years post-construction. However, detailed microstructural analysis would be needed to accurately confirm and quantify such deterioration. The rate and magnitude of deterioration can vary between different slope regions depending on the inherent soil properties and their degree of environmental exposure. Considering many railway infrastructure embankments are over 100 years old and were constructed without the fundamentals of modern geomechanics (Perry, 2003), deterioration is likely well-established and highly heterogeneous between and within assets. This adds to the complexities in developing methods that predict the severity and consequences of weather-driven deterioration. However, these results provide valuable indicators of potential deterioration and demonstrate how such monitoring setups can be used to analyse the interactions between soil properties, environmental exposure, and desiccation processes. They offer a first approximation of the timescales over which changes in soil water retention behaviour and the associated impacts on embankment stability can develop, although further validation is required to confirm these interpretations, primarily through microstructural analysis and an extended duration of field monitoring.

4.5.3 Field versus Laboratory SWRCs

The laboratory soil water retention curve (SWRC), tested under controlled conditions and compacted to the same initial moisture content and average dry density as the field, exhibited fundamentally different retention behaviour. Unlike the field SWRC, which demonstrated a biphasic distribution, the laboratory curve suggested a well-graded material. This is demonstrated by the gradual gain in suction across a larger range of moisture contents, shown in Figure 4.40. Such divergence highlights the limitations of laboratory testing in examining and explaining moisture dynamics at the field scale. This is particularly true for desiccated soils, where the hydrological changes caused by macro-desiccation would not be accurately represented by small-scale laboratory samples. These findings highlight the critical importance of using empirical field testing, such as the lysimeter study, to capture how these processes manifest at the field scale. This data is critical to inform predictive models that accurately forecast weather-driven deterioration of infrastructure embankments.

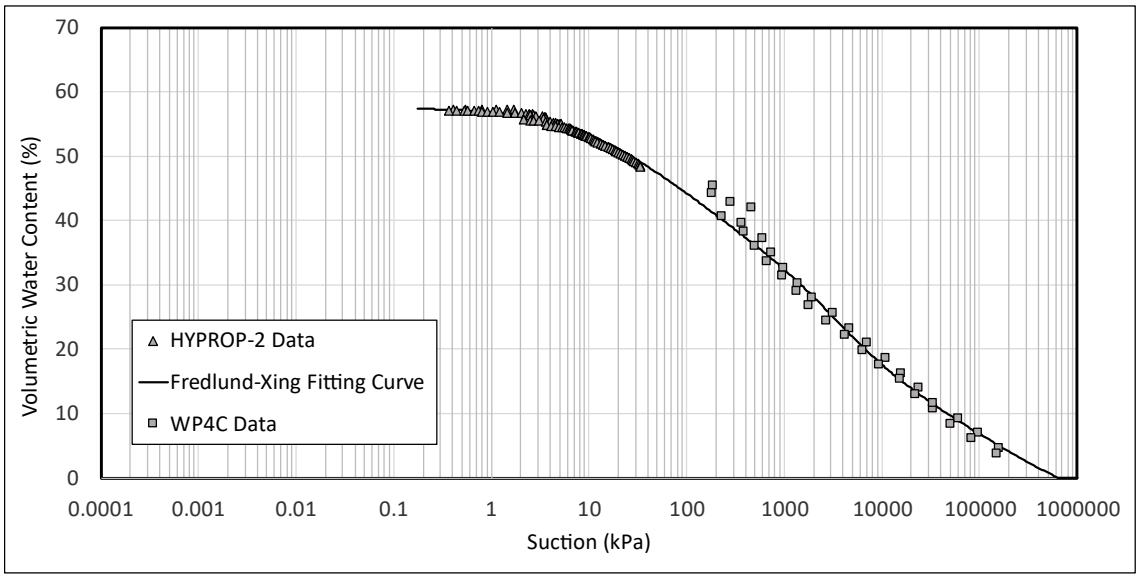

Figure 4.40: The laboratory-derived data for the Ampthill Clay compacted at the average moisture content and dry density of the lysimeter slope post-construction are also provided. This was measured using two methods: HYPROP and WP4C. The markers indicate the observed data from the laboratory testing, and the Fredlund-Xing (1994) fitted model curves are plotted as lines.

4.6 Concluding Remarks

The lysimeter study conducted in this thesis has demonstrated a novel approach to investigating the initiation and manifestation of desiccation-induced deterioration in a compacted clay slope. By employing continuous hydrological monitoring alongside a comprehensive two-year photographic record of the daily desiccation state, this research has facilitated an advanced analysis of the critical factors contributing to

desiccation cracking. Such analysis revealed that desiccation cracking occurred consistently throughout the monitoring period, irrespective of the season. This emphasises the role of wind in Penman-Monteith's (1965) framework as an important drying agent in winter without high temperatures. However, the intensity of desiccation cracking displayed a marked seasonality, which was contingent on the presence of distinct seasonal variations in weather patterns and soil hydrology.

Weather conditions at the spring-to-summer boundary proved fundamental for establishing drying regimes and deep summer desiccation networks, while the intensity of autumnal rainfall patterns dictated their termination. As autumn transitioned into winter, the lack of extensive surface and subsurface drying altered the crack pattern, resulting in a shallower network. This network's more frequent cyclic changes in aperture demonstrated an increased sensitivity to small changes in moisture. However, a fundamental finding of this analysis was the absence of such seasonality in desiccation when distinct drying seasons were absent. This occurred in 2023, when persistent high rainfall from spring to summer and lower temperatures inhibited soil drying and suction generation. As a result, the typical seasonal shift to deeper desiccation observed in the previous two summers did not occur, and shallow crack networks prevailed. Predicting such evolutionary desiccation behaviour will become increasingly challenging as climate change leads to more unpredictable weather patterns.

Empirical studies investigating the effects of weather extremes on infrastructure embankments are notably scarce in the current literature. This significantly hinders comprehension of the negative effects of desiccation in light of future climate change projections. However, the lysimeter methodology provided a step forward towards classifying such effects. This study revealed and quantified the detrimental effects of deep desiccation networks under extreme natural heatwave conditions and during the simulation of storms with a volume uplift applied for climate change. In both instances, significant desiccation facilitated the deeper and near-instantaneous penetration of drying and wetting fronts, resulting in rapid fluctuations in soil suction. The increased storage capacity of a deep desiccation slope was also evident, as it successfully accommodated the entire storm volume without closing cracks and generating surface runoff. Such behaviour has critical implications for short- and long-term embankment stability, especially considering that the frequency of summer convective storms is

projected to increase during hotter and drier summers. Therefore, the likelihood of failures through desiccation-related mechanisms may also increase.

The adaptable nature of the lysimeter methodology enabled a more comprehensive exploration of the physical parameter space affecting desiccation cracking, such as the physical barrier effects introduced by the structural aspects of vegetated canopies. This was examined from an exposure perspective, using faux grass to demonstrate that vegetation canopies can significantly moderate the rate and magnitude of changes in soil moisture and desiccation cracking. Such moderation was attributable to the canopy's sheltering effects, both by intercepting rainfall and reducing solar radiation and wind exposure, fundamental parameters controlling evaporation as per Penman-Monteith (1965). Further delineation of the soil-atmosphere-vegetation interactions and their combined effects on desiccation is a necessity in this field of study. Understanding whether such vegetation will aid the sheltering effects of canopies is crucial to determining their useability in assessment management strategies.

Monitoring in-situ soil suction and moisture content with high spatial and temporal resolution over three consecutive summers effectively captured the emergence of deterioration in soil water retention behaviour. This analysis provided a holistic view of how the cumulative effects of the desiccation behaviour observed throughout the monitoring period impacted the soil's microstructural integrity. Long-term perspectives on desiccation-induced deterioration and its impacts are rarely considered or captured, despite their heightening importance in driving embankment instability. A shift in soil water retention behaviour between Summer 2021 and 2022 evidenced the formation of a coarser and more interconnected pore network, likely attributed to the continual cyclic exposure to wetting and drying and the associated crack formation. Crucially, no suction was generated under the severely saturated conditions of 2023. However, the increased rate of infiltration and evaporation in Summer 2023 further evidences a degraded pore structure, coupled with a reduced ability to generate and main suction. If deterioration can manifest within these comparatively short timeframes, it raises important concerns about the condition of much older assets. As the likelihood and severity of desiccation are projected to rise due to future climate change, the increased risk to embankment stability demands careful consideration in asset management practices.

Chapter 5. Role of Environmental and Construction Parameters in Desiccation Crack Development

5.1 Introduction

Desiccation cracking within infrastructure embankments is a transient process, strongly influenced by near-surface fluctuations in soil moisture (Yu et al., 2021; Stirling et al., 2021, 2018). Temporal and spatial variations in physical and environmental boundary conditions govern these fluctuations. As discussed in Sections 4.2.5 and 4.4, the physical boundary conditions play a crucial role in shaping the formation of the environmental boundary conditions applied to the lysimeter slope. These included features of the slope morphology, vegetation canopies, lysimeter casing, and surrounding built environment. Together, these features regulated environmental exposure, evaporation, and the subsequent locations of crack initiation within the Ampthill Clay fill.

However, quantifying the individual effects of these physical and environmental boundary conditions on desiccation cracking within the lysimeter slope is highly complex. This is due to the uncontrollable nature of the outdoor experiment. However, the strong interdependency of environmental boundary conditions on the physical features of the surrounding environment also makes it difficult to uncouple their individual effects on desiccation cracking. Therefore, a series of small-scale laboratory tests were designed to isolate specific environmental and physical factors that may promote or reduce the occurrence of desiccation cracking by quantitatively modifying the inputs to Penman-Monteith's (1965) equation. Factors were chosen based on observations made while monitoring the lysimeter slope to complement its findings.

In Section 4.4, the structural effects of a vegetated canopy on slope hydrology and desiccation were explored in detail. A faux grass canopy was constructed and extended above the surface to minimise the introduction of complex soil-atmosphere-vegetation interactions that are difficult to uncouple (Tang et al., 2018a; Bordoloi et al., 2020). This study provided valuable insight into a canopy's control on solar radiation, wind and rainfall attenuation in terms of regulating moisture fluxes and suction (stress) gradients that instigate desiccation cracking. However, vegetation is typically established within topsoil layers added above the fill within real infrastructure embankments. This topsoil's composition, organic content, thickness, and permeability can significantly influence evaporation from the underlying fill by regulating moisture retention and migration within the embankment (Reeves et al.,

2006; Hughes et al., 2009; Mair, 2021). Therefore, Section 5.2 investigates how the presence and variation of topsoil properties can affect desiccation cracking within compacted clay fill. This is intended as a next step in understanding these complex soil-atmosphere-vegetation interactions, which largely govern moisture movement in the upper active zone of infrastructure embankments where desiccation is most prominent (Ridley, 2012; Tang et al., 2018; Powrie & Smethurst, 2019; Bordoloi et al., 2020; Yu et al., 2021).

Prevailing weather conditions, including temperature, humidity, solar radiation, wind speed, and precipitation, were also integral to forming and evolving environmental boundary conditions on the lysimeter slope, per Penman-Monteith's (1965) equation. These environmental variables significantly influence soil moisture dynamics and thermal regimes in the shallow active zone of infrastructure embankments, where desiccation cracking occurs (Glendinning et al., 2014; Eminue et al., 2018; Stirling et al., 2018; Powrie & Smethurst, 2019; Yu et al., 2021; Zeng et al., 2024). Understanding these environmental parameters' individual and combined effects on evaporation from compacted clay fill is essential for accurately predicting desiccation crack behaviour in embankments. The lysimeter observations noted the prevalence of desiccation cracking on the slope during winter when high temperatures and solar radiation were absent. Consequently, this confirmed Penman's (1948) hypothesis that wind-driven drying is significant for evaporation under such conditions. Therefore, Section 5.3 explores the isolated effect of wind speed on desiccation cracking using smaller-scale laboratory tests. Compacted layers of Ampthill Clay were used, and for comparison, their properties matched those of the lysimeter slope fill. These experiments intend to determine the capabilities of different wind speeds in driving desiccation in the absence of any other drying medium.

The lysimeter study in Chapter 4 could only assess surface desiccation cracking as an indicator of cracking severity. However, continuous hydrological monitoring through different patterns of surface desiccation revealed the significance of the subsurface depth and volume dimensions of desiccation cracks in controlling the overall slope hydrology. Non-intrusive methods that provide a multidimensional characterisation of desiccation cracking are emerging within the literature (e.g., Yesiller et al., 2000; Levatti et al., 2017; Julina & Thyagaraj, 2019; Zhuo et al., 2022). However, the sample preparation methods in these research projects rarely represent the highly heterogeneous nature of infrastructure embankment fill (Leonard et al., 2003; Sanchez

et al., 2013; Tang et al., 2019). To address this gap and understand how the compacted lysimeter fill could influence subsurface desiccation, Section 5.4 details how resin was utilised in the wind speed samples from Section 5.3 to highlight their subsurface desiccation patterns. Cross-sections were then taken to visualise whether features of the compacted clay fill and wind speed influence the subsurface desiccation pattern.

5.2 Impact of Topsoil Characteristics on Evaporation from Clay Fill

The topsoiling of UK infrastructure embankments is a multifaceted and standard approach for reducing the deterioration rate and ensuring the long-term stability of these key assets (Hughes et al., 2009). Topsoil promotes vegetation growth, with well-established root networks and plant canopies protecting embankment fill from weather-driven erosional processes (Reeves et al., 2006; Mair, 2021). Additionally, the topsoil acts as a buffer layer, preventing direct exposure to environmental conditions. Therefore, acting with vegetation, topsoil can regulate the rate and magnitude of evaporation from the underlying fill (Tang et al., 2018a; Bordoloi et al., 2020). The rate and magnitude of evaporation are fundamental controls of drying-induced shrinkage within plastic clay fills (Dyer et al., 2009; Eminue et al., 2018; Stirling et al., 2018). Differential shrinkage under spatially and temporally variable evaporation results in the accumulation of shear and tensile stresses and strains, which can form desiccation cracks if they exceed the overall soil tensile strength (Tang et al., 2008; Kodikara & Costa, 2013; Tang et al., 2021).

Within BS3882:2015, the range of allowable compositions for multipurpose topsoil is defined based on limits placed on the following parameters – soil texture, particle size, pH, plant nutrient content, organic matter, carbon-to-nitrogen ratio, electrical conductivity, potential phytotoxic element content, visible contaminants, and sharps (e.g., glass) content. Figure 5.1, extracted from BS3882:2015, illustrates the acceptable textural classifications that can be used, mainly excluding pure sands due to washout and compressible clay- or silt-dominant topsoil that loses structural integrity upon handling (British Standards, 2015). A broad range of topsoil compositions remain within these specifications, and suitability is often assessed on site-specific requirements such as drainage and vegetation type.

However, water retention behaviour varies with changes in soil properties. Topsoil dominated by clay minerals has higher water retention capabilities stemming from their high specific surface area, cation exchange capacity, capillary action in the fine pores and propensity for hydration and swelling (Bowles, 1979; Holtz & Kovacs, 1989;

Reeves et al., 2006). This allows clay-dominant soils to remain saturated over a greater range of suction values, i.e., over a longer drying duration (Tarantino & Di Donna, 2019). Additionally, clay-dominant topsoil often contains a higher organic content, further enhancing water adsorption (Bowles, 1979; Holtz & Kovacs, 1989; Reeves et al., 2006). Conversely, larger and interconnected pores within sand-dominant topsoil facilitate faster drainage when exposed to the same drying rate as clay-dominant topsoil (Tarantino & Di Donna, 2019). Consequently, different topsoil compositions will respond uniquely to shifts in environmental conditions.

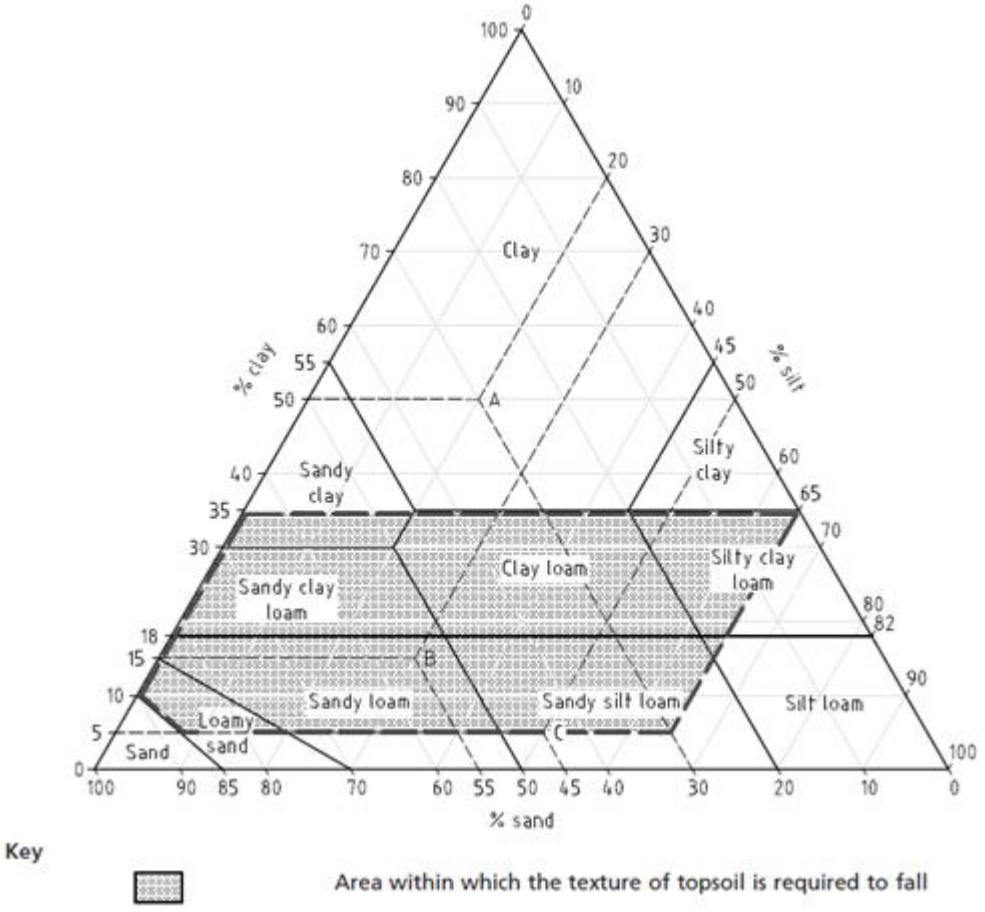

Figure 5.1: Plot illustrating the acceptable textural classifications that can be used in general infrastructure topsoiling as extracted from BS3882:2015.

Despite the above knowledge, there has been limited research into topsoil design on infrastructure embankments from the perspective of managing the deteriorating effects of shrinkage and desiccation of high-plasticity clay fills (Bordoloi et al., 2020; Jamalinia et al., 2020). This research gap within the literature can be mainly attributed to the significant complexities in studying the changes in soil-atmosphere-vegetation processes upon introducing desiccation cracks (Bordoloi et al., 2020). However, examining topsoil as a standalone entity without vegetation could be an initial approach

to improve understanding of these complex relationships between topsoil application, evaporation, shrinkage, and cracking. Insights gained from such studies can help inform the design of effective construction and management strategies that ensure the longevity of infrastructure embankments.

Thus, a series of laboratory experiments were conducted to investigate the impact of topsoil presence, composition, thickness, and initial moisture content on the evaporation rate, total shrinkage, and propensity for desiccation crack formation within the high-plasticity Ampthill Clay fill. Table 5.1 outlines the compositions of the two simplified topsoil varieties utilised during these tests. As mentioned previously, their compositions were not chosen to reflect the full structural or biological complexity of field-matured topsoil. A topsoil mainly composed of sand (TS1) and another with a higher clay content (TS2) were chosen to decipher whether variation in water retention behaviour impacts clay fill evaporation. Despite the initial intention to analyse desiccation crack formation, no cracks were observed in any of the test specimens, which will be discussed in greater detail in Section 5.2.4. Consequently, the focus shifted to examining moisture loss and volume change, which are closely linked as precursors to, and drivers of, crack formation.

Table 5.1: Compositions of TS1 (sandy topsoil) and TS2 (clayey topsoil) utilised in Test 1 and 2.

	% Gravel	% Sand	% Silt and Clay
TS1 (Sandy Topsoil)	15	83	2
TS2 (Clayey Topsoil)	0.4	60	40

Each test comprised four boxes (dimensions 400 x 300 x 170 mm) – labelled A1 to D1 for Test 1 and A2 to D2 in Test 2 –filled with 90mm of compacted Ampthill Clay. Varying compositions and thicknesses of topsoil with different initial moisture contents were placed above the Ampthill Clay; specimen-specific setup details are provided in Table 5.2. All specimens were allowed to dry within an environmental chamber set at 14^{o}C and 80% relative humidity. These conditions were chosen to represent average summer conditions in Newcastle upon Tyne, UK and therefore, are not conducive to rapid drying. The testing schedule in Table 5.2 was designed to quantify the relative contributions of these various topsoil parameters to changes in evaporation, shrinkage, and desiccation within the underlying Ampthill Clay fill.

Table 5.2: Experiment schedule for Tests 1 (A1-D1) and 2 (A2-D2), detailing the composition, thickness and initial moisture content of the topsoil and fill material used in each specimen.

		Test 1				Test 2			
Box ID		**A1**	**B1**	**C1**	**D1**	**A2**	**B2**	**C2**	**D2**
Topsoil	**Composition**	-	TS1	TS1	TS2	-	TS1	TS1	TS2
	Thickness (mm)	-	20	20	40	-	20	40	40
	Initial Moisture Content (%)	-	2	2	2	-	20.2	20.2	18.6
Fill	**Composition**	Ampthill Clay							
	Thickness (mm)	90							
	Initial Moisture Content (%)	40							

5.2.1 Changes in Topsoil Thickness and Subsequent Evaporation Patterns

The British Standard guidance for topsoiling (BS 3882:2015) quotes 300 mm as the maximum allowable depth of topsoil to be applied for landscaping infrastructure embankments. Chosen depths are project-specific and depend on various factors, including design requirements, self-drainage, rooting zones, and nutrient availability for vegetation growth (British Standards, 2015). However, advice on how topsoil thickness can be adapted to benefit the performance of the clay fills they overlay is outside the scope of this standard. This omission is significant as topsoil can potentially modify the hydrological response of clay fill to environmental conditions Reeves et al., 2006; Tang et al., 2018; Bordoloi et al., 2020). The hydrological response significantly controls the overall stability of an embankment, influencing weather-driven deterioration processes such as shrink-swell cycles, desiccation cracking, and flood erosion (Glendinning et al., 2014; Mukhlisin & Khiyon, 2018; Stirling et al., 2021; Briggs et al., 2023). Therefore, recommendations on suitable topsoil thicknesses that help mitigate risks associated with fill deterioration would help optimise embankment performance and long-term resilience to environmental stressors.

To investigate whether topsoil presence and thickness alter the hydrological response of underlying fill, a 90 mm layer of Ampthill Clay was overlain with 20 mm (B1) and 40 mm (C1) of TS1 (sandy) topsoil and compared to a control sample (A1) without topsoil. Changes in the rate and magnitude of evaporation can be observed in Figure 5.2, which plots cumulative mass loss for A1-C1 (Test 1) as a percentage of the initial starting mass for the 24-week monitoring period. The graph illustrates that the

evaporation rate and total mass loss are visibly greater in the absence of topsoil (A1), stabilising after losing 21% of its initial mass within eight weeks of drying. Without topsoil, the surface of the Ampthill Clay layer is directly exposed to the environmental conditions within the chamber, allowing faster evaporation and penetration of drying fronts. Free shrinkage from the container edges further aided the mass loss rate by exposing a greater evaporative surface area. Therefore, the case of no topsoil represents a worst-case scenario for rapid and voluminous evaporation.

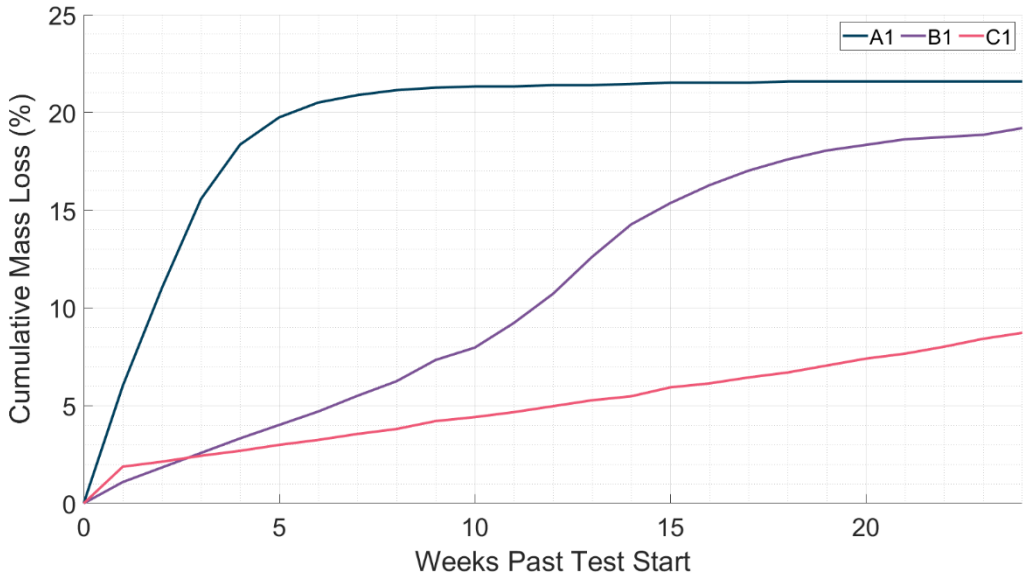

Figure 5.2: Graph illustrating the cumulative mass loss of specimens A1, B1, C1 and D1 expressed as a percentage of the total initial mass.

With the application of TS1 in B1 and C1, the mass loss rate was near linear. Both curves progressed considerably slower than that of A1 (no topsoil), the reduction in rate becoming more pronounced as topsoil thickness increases. Evaporation begins to plateau in B1 (20 mm) after 20 weeks of monitoring, 12 weeks later than no topsoil (A1). This slower evaporation rate generated a total mass loss of 19%, slightly lower than that of A1 at 21%. A slight steepening of B1's gradient is noted at Week 10 before shallowing again at Week 14. The collapse of the loose, sandy topsoil layer into the shrinkage gap between the soil sample and container increased the evaporative surface area of the Ampthill Clay within B1. Notably, a plateau was not reached in C1 (40 mm), with the mass loss rate maintaining the same trajectory through to the end of the test. This specimen demonstrated the slowest evaporation rate, attaining a total mass loss of 8%.

The reduced evaporation rate and delayed onset of the plateau phase in the mass loss curves of B1 and C1 indicate the presence of a capillary barrier effect imposed on the underlying Ampthill Clay by the coarser sandy topsoil (TS1). When two unsaturated soils with different water retention characteristics (i.e., sandy topsoil and clay fill) are placed in contact, their initial suctions are in a state of disequilibrium. Due to its lower initial water content, TS1 demonstrates a higher matric suction than the underlying clay fill, establishing a suction gradient that facilitates upward water movement through capillary flow. Water redistributes until a common suction is reached at the material interface, which is intermediate between the initial suctions of the two materials. During this equilibration process, the water contents of the soils adjust according to their respective SWRCs. The sandy topsoil (TS1), characterised by a steeper SWRC, exhibits a pronounced increase in water content close to the material interface in response to minimal changes in soil suction. In contrast, with its flatter soil water retention curve, the clayey soil demonstrates a comparatively minor decrease in water content for equivalent increases in suction.

However, due to TS1's weak water retention capacity and the development of a suction gradient between the base and surface of the topsoil layer, the migrated moisture is rapidly lost under continued evaporative demand. As the sandy layer becomes increasingly dry, its unsaturated hydraulic conductivity drops significantly, forming a capillary barrier that restricts further upward moisture movement from the underlying clay. In Figure 5.2, the capillary barrier effect is notably more pronounced in C1 than in B1, which can be attributed to the increased thickness of the sandy topsoil applied in the former sample.

Thicker sandy topsoil layers (C1) enhance the efficacy of the capillary barrier effect owing to several factors: the greater water storage capacity of the layer, the more gradual establishment of suction gradients, and the slower equilibration of suction with the underlying clay layer. The increased storage capacity delays drying at the base of the topsoil, allowing suction gradients between the surface and the clay interface to develop more gradually. As a result, the transmission of suction (i.e., the drying front) from the surface toward the material interface progresses more slowly, leaving the clay fill less affected by surface evaporation for a longer period. Consequently, the bottom of the sandy layer remains wetter for longer, delaying suction equilibrium with the clay and preserving a more persistent barrier to capillary flow. As the sandy topsoil dries from the surface downward, its unsaturated hydraulic conductivity decreases sharply.

The capillary barrier effect becomes fully established once the unsaturated hydraulic conductivity becomes too low to support upward moisture migration from the wetter clay. This alters near-surface hydrological dynamics by limiting further evaporation from the underlying clay and thereby reducing its overall total moisture loss.

The mass loss curve in Figure 5.2 demonstrates that thinner sandy topsoil layers (B1) are less effective than thicker ones (C1) at maintaining a capillary barrier. Thin topsoil layers with limited water storage capacity dry quickly, creating suction gradients that are rapidly transmitted to the clay-topsoil material interface. This process accelerates suction equilibration between the two layers, allowing moisture to be drawn upward from the clay. However, the sandy topsoil's low retention capacity means this water is quickly lost to evaporation, undermining the persistence of the capillary barrier. As a result, although B1 shows reduced moisture loss within the topsoil compared to A1, it is less capable than C1 of sustaining a hydraulic barrier over time. When evaporation is intense or the sandy layer remains thin or dry, suction equilibrium is rapidly attained, and hydraulic connectivity is maintained. This facilitates continued upward flow from the underlying clay fill, which evaporates at the topsoil layer's surface.

In addition to hydraulic effects, increased topsoil thickness influences the material interface's thermal regime. Thicker topsoil acts as a thermal buffer, reducing heat transfer to the Ampthill Clay by several mechanisms: i) forming a more robust physical barrier to environmental fluxes, ii) adsorbing incoming heat and preventing its rapid transmission to the clay fill, iii) imposing a more gradual temperature change onto the clay fill. Such thermal moderation limits the energy available to drive evaporation, further contributing to the lower mass loss in C1 compared to A1 and B1.

Overall, these results demonstrate that the thickness of topsoil can significantly influence moisture dynamics in underlying clay fills by controlling suction gradients, hydraulic conductivity and evaporation rates. Thicker sandy topsoil layers (C1) are more efficient at regulating the rate and magnitude of evaporation from the underlying clay fill by forming effective capillary barriers and regulating the thermal regime at the material interface. Thinner topsoil layers (B1) also reduce evaporation rates compared to bare clay (A1). However, their limited storage capacity and poor moisture retention lead to the rapid development of suction gradients at the material interface, which quickly undermines the effectiveness of the capillary barrier, allowing for greater moisture loss from the underlying clay. With topsoil regulating the rate and magnitude of moisture loss within embankment fill, rapid shrinkage and swelling of clay under

direct exposure to environmental conditions could be reduced. This is important for minimising the accumulation of weather-driven and desiccation crack-induced deterioration of infrastructure embankments composed of plastic clay.

5.2.2 Evaporation Patterns under Various Topsoil Compositions

As introduced in Section 5.1, topsoil's water retention behaviour varies greatly with composition. Additional complexities emerge when considering interlayer moisture movement across the fill-topsoil transition zone, where contrasting compositions will impact the efficiency of capillary rise (Tarantino & Di Donna, 2019). Both factors will affect the rate and magnitude of moisture transfer from the clay fill to the topsoil surface for evaporation. Furthermore, heat transfer efficiency will also vary with composition, affecting the propagation rate of drying fronts through the topsoil into the clay fill. Therefore, understanding the impact of different topsoil compositions on moisture loss from underlying clay fill is crucial for effectively managing shrink-swell and desiccation-induced deterioration processes within infrastructure embankments. With this understanding, informed recommendations on topsoil composition, layering and maintenance can be provided to ensure the long-term resilience of these assets to weather-driven deterioration.

To investigate the effect of topsoil composition on evaporation from underlying clay fill, 90 mm layers of Ampthill Clay were overlain with a 40 mm layer of TS1 (C1) and TS2 (D1) topsoil. The results for C1 and D1 are presented in Figure 5.3 as the cumulative mass loss as a percentage of the initial specimen mass. A1 (no topsoil) and B1 (20 mm TS1) have also been compared.

During the initial six weeks of the experiment, C1 (TS1) attains a higher cumulative mass loss than D1 (TS2) at any given monitoring point. At week two, an inflection in the mass loss rate for C1 is observed, from which the evaporation rate continues to increase, however, at a considerably slower rate than previously recorded. Conversely, the mass loss rate of D1 remains consistent and eventually surpasses that of C1 by week six, growing and sustaining a gap in the cumulative mass loss until the end of the test.

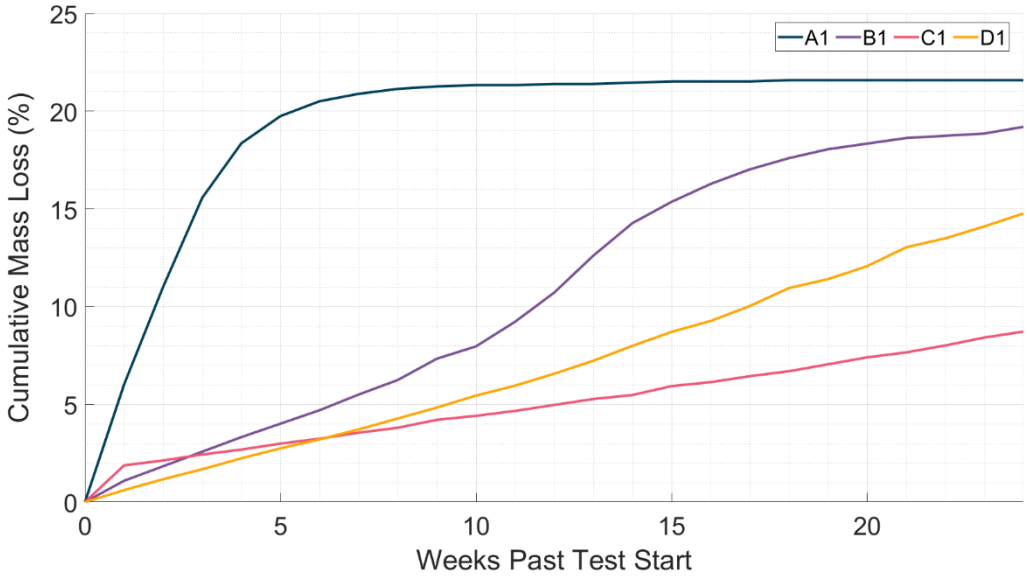

Figure 5.3: Graph illustrating the cumulative mass loss of specimens A1, B1, C1 and D1 expressed as a percentage of the total initial mass.

With environmental conditions held constant, the mass loss gradients reported reflect the evolving availability of surface water for evaporation through time. For C1, the initial phase of rapid evaporation reflects TS1's lower water retention and high responsiveness to surface evaporative demand compared to TS2 in D1. However, given the TS1's initial moisture content (2%), this early drying phase is completed quickly, as evidenced by C1's steep mass loss curve during the first week of monitoring (see Figure 5.3). As C1 dries, its role as a capillary barrier (see Section 5.2.1) becomes increasingly effective, thereby restricting the moisture transfer rate and magnitude from the underlying clay to the topsoil surface for evaporation. This phenomenon is illustrated in Figure 5.3 by the inflection point in C1's mass loss curve after one week of monitoring. Subsequently, while mass loss continues, it does so at a diminished rate.

In contrast, D1 – featuring the clayey topsoil (TS2) – exhibited a consistent evaporation rate throughout the experiment. However, by the conclusion of the test, it had lost a greater proportion of its initial mass, specifically 14%, compared to C1, which lost only 8%. This difference can be attributed to the hydraulic properties of TS2 and its interaction with the underlying Ampthill Clay. The clayey topsoil (TS2) shares a closer compositional and hydraulic similarity with the underlying Ampthill Clay than TS1 (sandy topsoil) used in C1. This similarity, shown in comparable pore structures and flatter SWRCs, indicates that equilibrium will be easier to reach despite TS2's low initial moisture content (2%). However, the rate of water movement is slower than C1 due to the overall lower hydraulic conductivity of clay material. The resultant diminished

suction gradient restricts the rate and extent of moisture transfer from the clay to the topsoil layer during the early drying stages, as illustrated in Figure 5.3.

Following the initial equilibrium phase, the high water retention capacity and low hydraulic conductivity of TS2 play essential roles in moderating the evaporation rate. These intrinsic properties facilitate prolonged moisture retention within the topsoil layer, thereby moderating the development of suction gradients and diminishing the driving force for moisture migration from the underlying Ampthill clay. As a result, the capillary barrier effect recorded in C1, featuring sandy topsoil (TS1), is either weakened or entirely absent. Instead, moisture exchange remains relatively continuous, sustaining a steady evaporation rate as seen in Figure 5.3. This continuity results in a greater overall moisture loss within D1 compared to C1, where the formation of the capillary barrier effectively restricted long-term moisture loss from the Ampthill Clay.

It is important to note that the above is only the case when comparing different compositions of the same thickness. As discussed in Section 5.2.2, decreasing the thickness of the sandy topsoil layer (B1) makes it less efficient than C1 and D1 (40 mm topsoil layers) at suppressing evaporation. Furthermore, the wider gap in total mass loss when changing only topsoil thickness (B1 to C1) versus changing only composition (B1 to D1) suggests that increasing the topsoil thickness has a more significant barrier effect than altering the composition. These findings also highlight that contrasts in water retention behaviour and formation of capillary barriers at the material interface have a greater impact on evaporation than the rate of heat transfer to the clay fill. Sandy topsoil characteristically has a higher thermal diffusivity compared to clayey topsoil due to its greater air-filled porosity and lower water retention capacity. This effect may also be sustaining the steady evaporation rate in D1. However, the lesser influence of this effect is evident in the more efficient mass loss in Test 1 with clayey topsoil (TS2) than in Test 2 with the same thickness of sandy topsoil (TS1). These observations may change depending on the composition of the topsoil that is being investigated. Future research should expand the range of topsoil compositions and thicknesses studied to develop a further understanding of this interactive behaviour.

Overall, in this experiment, thicker layers of TS1's sandy topsoil (C1) are the most effective at suppressing the rate and magnitude of evaporation from the underlying clay fill by acting as capillary barriers. Therefore, sandy topsoil (TS1) is a more efficient buffer to evaporation than clayey topsoil (TS2), suggesting it would provide greater suppression of shrink-swell and desiccation cracking by implementing a slower and

lower rate of moisture change. This is followed by thick layers of TS2 (D1), with thin layers of TS1 (B1) and no topsoil (A1) providing the least protection to the underlying clay fill. However, despite TS1 being the most efficient evaporation barrier, sandy topsoil has a higher erosion and washout potential than clayey topsoil. Therefore, erosion susceptibility should also be considered when choosing a topsoil composition. The mixed composition topsoil in the loamy sand/sandy loam/sandy clay loam divisions of Figure 5.1 will likely be more resilient than pure sand.

5.2.3 Evaporation Patterns Under Changing Topsoil Initial Moisture Content

Environmental exposure, stockpiling before placement, and in-situ wetting post-installation naturally elevate the moisture content of topsoil. Therefore, topsoil is rarely spread onto embankments in an air-dried state, with the low moisture content of 2% adopted in Test 1 (Table 5.2) being only relevant to extremely dry conditions. The moisture content of the soil, or its degree of saturation, significantly impacts its water retention behaviour and hydraulic conductivity, pivotal factors controlling water availability for evaporation. It is, therefore, important to understand how the antecedent conditions at the onset of drying can affect the topsoil's effectiveness as a protective barrier. This will assist in designing construction and maintenance standards that ensure the long-term resilience of infrastructure embankments.

To alter the antecedent conditions of the topsoil, Test 2 (A2 – D2) was carried out (Table 5.2), where the initial topsoil moisture content was increased, and mass loss results were compared to Test 1 (A1 – D1). Specimen preparation and topsoil thicknesses remained identical between Tests 1 and 2, the only change being an increase in the topsoil moisture contents from 2% to 20.4% and 18.6% for the TS1 and TS2 compositions, respectively. A 12-week comparison of cumulative mass loss expressed as a percentage of the initial mass of each specimen for Tests 1 and 2 is presented in Figure 5.4. Both A1 and A2 were used as control samples without topsoil and prepared identically, reflected in the near-indistinguishable evaporation behaviour displayed by the mass loss curves.

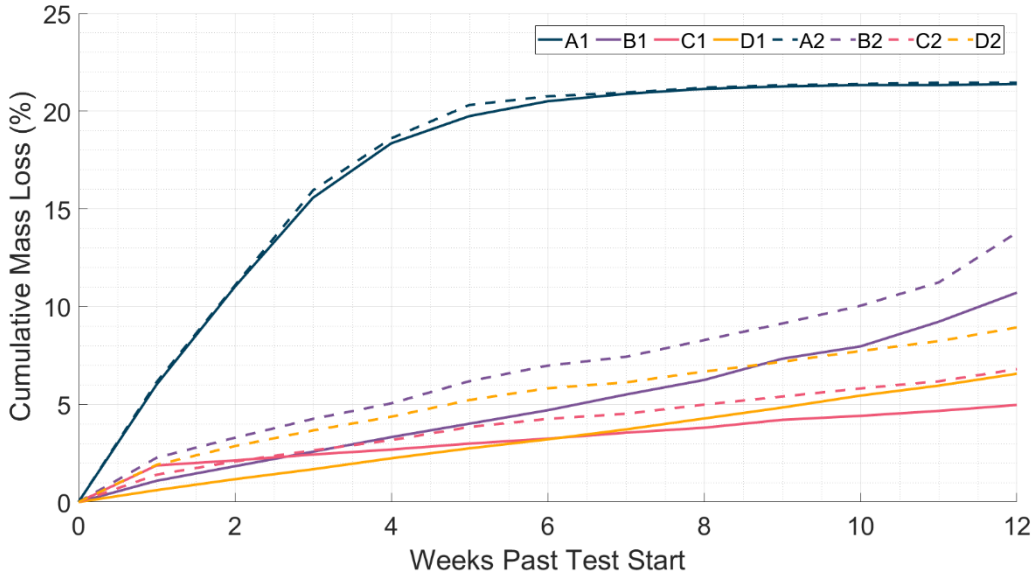

Figure 5.4: Cumulative mass loss for Test 1 (A1-D1) and Test 2 (A2-D2) specimens that are compared over a 12-week monitoring duration and expressed as a percentage relative to the initial specimen mass.

For boxes with topsoil, the cumulative mass loss is greater at any given moisture content during Test 2 than in Test 1. Overall, the total mass loss in B2 was approximately 3% higher than in B1 and 2% higher between C1/D1 and C2/D2. Given that the environmental conditions were consistent between Tests 1 and 2, the observed increase can be attributed to the greater moisture availability at the surface, which enhanced the rate and magnitude of early-stage evaporation. This is supported by the steeper mass loss gradients recorded for B2–D2 during the first week of monitoring (see Figure 5.4), where the wetter topsoil created a stronger moisture gradient with the surrounding air, facilitating more rapid evaporation.

While the initial mass loss gradients were steep due to elevated surface moisture availability, this rapid evaporation phase did not persist. An inflection point in the mass loss curve was observed after approximately one week (see Figure 5.4), likely corresponding to depletion of readily available surface moisture, after which the rate followed a more gradual upward trajectory. The higher initial moisture content reduced the suction within the topsoil, diminishing the suction differential across the interface with the Ampthill Clay. This weakened gradient would impede moisture redistribution and delay the onset of suction equilibrium in B2 – D2. Consequently, the slower upward flux of moisture from the Ampthill Clay could not keep pace with the initial evaporative demand, resulting in a flattening of the mass loss curve during the latter drying stages. For C1, this effect would also increase the time taken to establish an effective capillary barrier.

The impact of these two opposing processes – an initial increase in evaporation driven by higher surface moisture availability, and a delayed contribution from the Ampthill Clay due to slower suction equilibration – partially offset one another. As a result, although cumulative moisture loss was greater across the duration of the test, the overall shape and gradient of the mass loss curves remain broadly consistent with those observed in Test 1. Furthermore, the hierarchy of cumulative mass loss remains consistent with that observed in Test 1, despite variations in initial moisture content. The ranking was as follows: 1) A2 – no topsoil, 2) B2 – 20 mm TS1, 3) 40 mm TS2, and 4) 40 mm TS1. This consistency underscores that the evaporation dynamics continue to be governed not only by the physical and hydraulic properties of the topsoil layer, such as thickness, texture, and water retention behaviour, but also critically by the hydraulic contrast across the clay-topsoil material interface. While increased initial moisture content contributes to higher total evaporation by sustaining early-stage near-surface losses, it does not alter the longer-term dominance of capillary barrier effects and hydraulic connectivity patterns in regulating moisture movement.

While providing a macroscopic view of the evaporation process, Figure 5.4 does not delineate the individual contributions of the topsoil and Ampthill Clay layers to the total recorded mass loss. Using an average mass loss to monitor evaporation within a specimen comprising two different soils masks the gradual progression of drying gradients through the topsoil and fill layers. As a result, the primary source of evaporating water (i.e. topsoil or fill) at any given point during the test cannot be accurately identified. Moreover, it does not clarify whether the increase in total mass loss from Test 1 to Test 2 translates to any discernible shifts in evaporation mechanics from the underlying Ampthill Clay. Given the overarching aim of these experiments, a breakdown of mass loss by layer is essential to comprehensively understand the impact of varied topsoil characteristics on the temporal evolution of evaporation from the underlying clay fill.

To determine their respective roles in the overall evaporation process, moisture content samples were taken in both the topsoil and Ampthill Clay layers at the start and end of each test. The percentage change in moisture content for each specimen is provided in Figure 5.5 (Test 1) and Figure 5.6 (Test 2). Positive and negative changes represent relative increases and decreases in moisture, respectively. Direct comparisons of total moisture content cannot be made between tests as Test 1 was sampled after 24 weeks of drying, whilst Test 2 was terminated and tested after 12 weeks. Despite this,

variations in moisture movement mechanisms are visible and can be compared between the two tests.

The sampled initial and final moisture content values were utilised to estimate the final mass of the topsoil and Ampthill Clay layers individually. Relative contributions of each layer to the total mass loss were then determined using these calculated values. The details and results of this process are presented in Table 5.3. While soil sampling may capture moisture content gradients, the results are typically presented as an average, similar to the readings obtained from a balance in Figure 5.4. However, balance readings represent the overall average without the risk of selectively sampling drier areas. As a result, differences in the moisture content values were recorded between the two methods despite both measuring the same material. Nevertheless, the essential trends and approximate relative layer contributions to the recorded total mass loss remain evident.

Figure 5.5 demonstrates the dynamic moisture exchange between the Ampthill Clay and the overlying topsoil layers during Test 1. Samples A1 (no topsoil), B1 (20 mm TS1) and D1 (40 mm TS2) exhibit similar percentage decreases in Ampthill Clay moisture content – 77%, 75% and 74%, respectively. This observation indicates that, across extended drying periods, Ampthill Clay moisture loss in these topsoil samples can reach comparable levels to those of bare soil. Consequently, this finding suggests that B1 and D1's topsoil configurations offer limited long-term suppression of moisture loss from underlying clay fill.

This outcome reinforces earlier observations that thin layers of TS1 (sandy topsoil) functioned poorly as a capillary barrier in B1. Their low water retention and limited storage capacity allowed rapid upward moisture transfer from the underlying Ampthill Clay, offering little evaporation resistance and contributing to the fill's accelerated desaturation. Similarly, the thick clayey topsoil in D1 also demonstrated limited effectiveness as a capillary barrier. Despite its high water retention capacity, its physical and hydraulic continuity with the underlying Ampthill Clay enabled persistent yet slower moisture transfer across the interface. This sustained hydraulic connection allows the clay fill to progressively lose moisture, with TS2 offering limited resistance to long-term evaporation.

Table 5.3: The calculations conducted to determine the individual contributions of all topsoil and Ampthill Clay layers to the total specimen mass loss recorded in A1-A2 in Test 1 and A2-D2 in Test 2.

		Units	Test 1				Test 2			
			A1	B1	C1	D1	A2	B2	C2	D2
Ampthill Clay Fill	Mass Initial	kg	15.8	15.8	15.8	15.8	15.8	15.8	15.8	15.8
	Moisture Content Initial	%	40	40	40	40	40	40	40	40
	Dry Mass	kg	11.3	11.3	11.3	11.3	11.3	11.3	11.3	11.3
	Moisture Content Final	%	9.2	9.9	25.2	0.3	9.7	20.8	30.8	27.4
	Mass End	kg	12.3	12.4	14.2	12.5	12.4	13.7	14.8	14.4
	Change in Mass	kg	-3.5	-3.4	-1.6	-3.3	-3.4	-2.1	-1	-1.4
Topsoil	Mass Initial	kg	-	1.65	3.92	3.84	-	1.82	3.46	4.12
	Moisture Content Initial	%	-	0.02	0.02	0.02	-	0.204	0.204	0.186
	Dry Mass	kg	-	1.62	3.84	3.76	-	1.51	2.87	3.47
	Moisture Content Final	%	-	3.2	4.1	4.1	-	0.05	0.067	0.068
	Mass End	kg	-	1.67	3.99	3.91	-	1.59	3.06	3.71
	Change in Mass	kg	-	+0.02	+0.07	+0.07	-	-0.23	-0.4	-0.41
Totals	Total Specimen Mass Loss	kg	-3.5	-3.38	-1.53	-3.23	-3.4	-2.33	-1.4	-1.81
	Ampthill Clay Contribution to Total Mass Loss	%	ND	ND	ND	ND	**100**	**90**	**71**	**77**
	Topsoil Contribution to Total Mass Loss	%	ND	ND	ND	ND	**-**	**10**	**29**	**23**

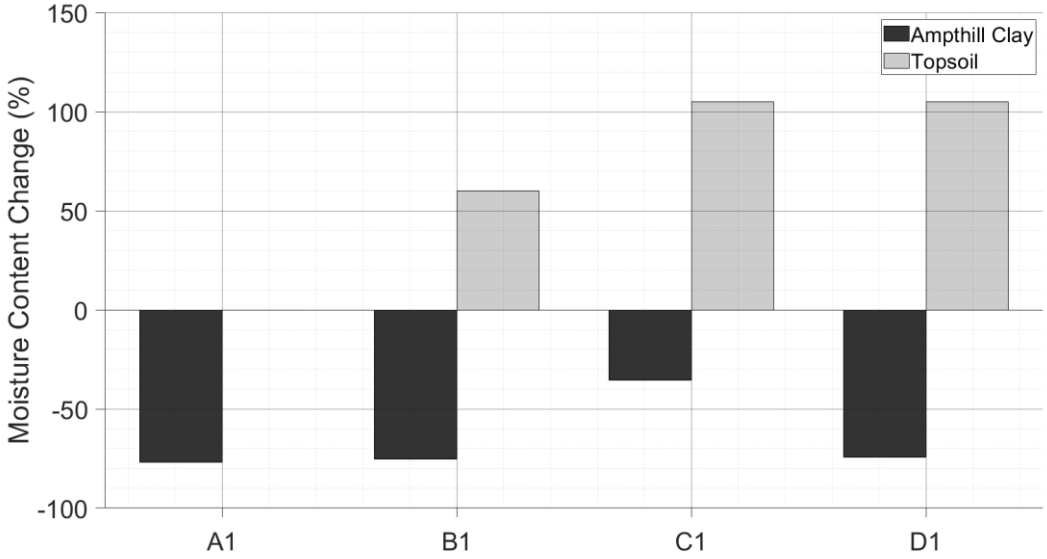

Figure 5.5: Graph illustrating the percentage change relative to the initial moisture content for both topsoil and Ampthill Clay layers within Test 1 specimens (A1-D1).

In contrast, C1 (40 mm TS1) exhibited a considerably smaller reduction in Ampthill Clay moisture content (36%). This reinforces the earlier interpretation that C1's thick sandy (TS1) topsoil layer functions as an effective capillary barrier. The coarse texture and low water retention of TS1 facilitated the rapid development of a persistent unsaturated zone of low hydraulic conductivity at the material interface. As a result, upward moisture flux from the underlying Ampthill clay became impeded, significantly limiting its moisture loss over the remaining test duration.

In Table 5.3, the gain in mass of the topsoil (highlighted blue) contradicts the overall loss in mass recorded for the specimen (highlighted red). Therefore, determining the individual roles of topsoil and Ampthill Clay in the overall mass loss becomes too complex for the data gathered. However, the higher mass loss in the Ampthill Clay layer (highlighted orange) and the initial air-dried state of the topsoil at application (2%) support the hypothesis that the Ampthill Clay functioned as the main moisture reservoir. The Ampthill Clay's moisture loss was directly dependent on the efficiency of moisture redistribution across the material interface. Table 5.3 quantitatively demonstrates that this transfer was less efficient in C1, due to the capillary barrier formation, with less overall moisture reaching the topsoil surface and evaporating. In contrast, the other systems facilitated more direct and sustained upward movement, reflected in the higher total specimen mass loss values.

All topsoil layers showed a gain in moisture content, further confirming the net upward migration of water. These gains varied with topsoil thickness, with thinner sandy topsoil (B1) displaying a lower moisture increase, consistent with its limited storage capacity and high evaporative flux. Conversely, the thicker topsoil layers (C1 and D1) absorbed more moisture, reflecting their larger storage volumes. However, the mechanisms behind their moisture gain differ. In D1, the high water retention capacity of the TS2 enables it to effectively retain moisture. In contrast, in C1, the capillary barrier restricted upward moisture resupply, while a dry surface layer suppressed evaporation, likely trapping moisture within the sandy topsoil.

These results emphasise the importance of considering the inherent moisture retention characteristics of the applied topsoil and its performance as an evaporation buffer across extended drying cycles. Assessing topsoil design and application characteristics could help mitigate deterioration driven by volume change and desiccation crack formation in infrastructure embankments.

It is recognised that the moisture contents attained in Test 1 represent final states after 24 weeks of drying and do not capture the temporal evolution of moisture redistribution. However, Figure 5.6 demonstrates the percentage change in moisture content in Test 2 for the Ampthill Clay and topsoil layers within specimens A2–D2 after 12 monitoring weeks. Therefore, this plot may provide insight into the influence of topsoil characteristics on the shorter-term evaporation dynamics of the Ampthill Clay.

Although the absolute values of moisture content change are not comparable between Tests 1 and 2 due to differing monitoring durations, similarities between trends can still be discussed. In contrast to the convergence observed for A2, B2 and D2 in Test 1, Test 2 shows distinct differences in the Ampthill Clay moisture content for these samples at 12 weeks of drying. As expected, A2 (bare soil) records the greatest reduction in Ampthill Clay moisture content (75%), reflecting the absence of any physical, thermal or hydrological buffering effects. Sample B2 shows the next highest clay moisture loss (48%), reinforcing earlier observations that thin sandy topsoil layers offer limited evaporative suppression due to low water retention and storage capacity, and poor capillary barrier performance. The reduction in moisture content of Ampthill Clay in D2 was measured at 32%. This aligns with the slower evaporation dynamics inherent to the clayey topsoil. As discussed previously, although the topsoil maintains hydraulic connectivity, its elevated moisture retention and diminished conductivity significantly attenuate the surface transfer and loss of Ampthill Clay moisture. Finally,

C2 continues to demonstrate the least moisture reduction in the Ampthill Clay, consistent with the effective capillary barrier created by the thick sandy topsoil, which restricts upward water flux due to the formation of a persistent low conductivity, unsaturated zone at the material interface. Finally, C2 continues to exhibit the least reduction in Ampthill Clay moisture content, consistent with the hypothesis that it forms an effective capillary barrier irrespective of initial moisture content.

In Test 1, conducting sampling after a 12-week monitoring duration, rather than Test 1's 24 weeks, provides further clarity on the significance of topsoil characteristics and interface dynamics in influencing short-term evaporation behaviour. At this drying stage, differences in Ampthill Clay desaturation are more pronounced, underscoring how factors such as topsoil thickness, texture, water retention capacity, and capillary barrier effectiveness critically influence early moisture loss. The clearer separation between A2, B2, and D2 highlights the extent to which evaporative fluxes are modulated by the ability of the overlying topsoil to buffer, retain, or restrict moisture transfer in the initial drying period. Importantly, these short-term disparities emerging in records of mass loss are significant for shrinkage and desiccation cracking, with the onset and development likely to be faster for embankments with thinner, sandier topsoil (B2) than thicker sandy (C2) or clayey topsoil (D2).

Within Test 2, the topsoil's initial moisture content was increased from 2% in Test 1 to 20.4% and 18.6% for TS1 (B2 – C2) and TS2 (D2) compositions, respectively. As shown in Figure 5.6, all topsoil layers experienced a net decrease in moisture, driven by enhanced near-surface evaporation enabled by the greater moisture availability. Specimen B2 exhibited the greatest percentage decrease in topsoil moisture (76%), reflecting the limited water retention capacity of the thin sandy topsoil (TS1), which promotes rapid evaporation. In contrast, D2 showed the smallest reduction (63%), consistent with the higher water retention of the clayey topsoil (TS2), which slows moisture transfer and helps retain moisture under drying conditions. Specimen C2, with a thicker sandy topsoil layer, displayed an intermediate reduction (67%). This is likely attributed to developing a dry surface layer and capillary barrier at the top and base of the topsoil layer, respectively. These conditions restricted both downward and upward moisture movement, effectively isolating the remaining moisture within the profile and reducing its exposure to evaporative loss.

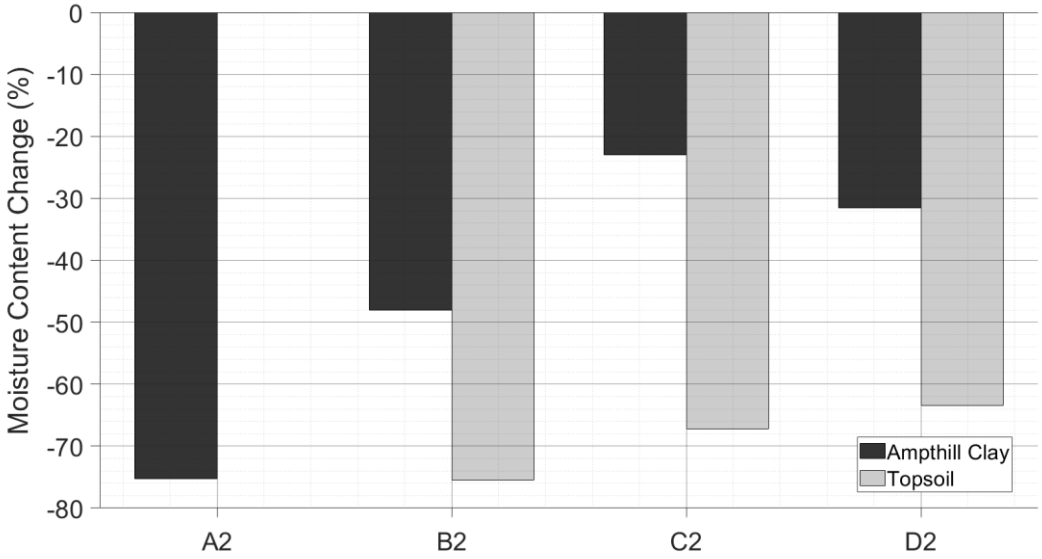

Figure 5.6: Graph illustrating the percentage change in moisture content relative to the initial moisture content for both topsoil and Ampthill Clay layers within Test 2 specimens (A2-D2).

In contrast to Test 1, all Test 2 layers experienced a mass reduction, allowing individual layer contributions to the overall mass loss to be calculated and recorded within Table 5.3. This differs from Test 1, where it was assumed that moisture migration from the underlying Ampthill Clay into the overlying topsoil contributed approximately 100% to the total mass loss due to the moisture gain recorded in all initially dry topsoil layers. These contributions were then compared across the different specimens to further investigate the evaporation dynamics of Ampthill Clay under different topsoil thicknesses, compositions, and initial moisture contents.

As expected, the results in Table 5.3 illustrate that the contribution of Ampthill Clay to the overall mass loss varied depending on the topsoil layer composition and thickness. For A2 without topsoil, Ampthill Clay accounted for 100% of the total mass loss, acting as the sole evaporative source. However, with an overlying thin layer of partially saturated topsoil (B2), this contribution decreased to 90% and was reduced further under greater thicknesses of clayey (D2) and sandy topsoil (C2) to 77% and 71%, respectively. The relative percentage splits of Ampthill Clay to topsoil contributions were as follows: B2 – 90:10 (20 mm TS1), C2 – 71:29 (40 mm TS1) and D2 – 77:23 (40 mm TS2).

The observed Ampthill Clay contributions are consistent with prior discussions on the capacity of each topsoil configuration to either facilitate or hinder upward moisture flux, depending on differences in hydraulic and retention characteristics across the material

interface. Despite the initial higher topsoil moisture content, B2 continued to provide little resistance to evaporation, promoting rapid desaturation of the underlying clay. In D2, the thicker clayey topsoil allowed consistent yet steadily sustained moisture transfer due to textural and hydraulic similarity with the Ampthill Clay, but slowed the evaporation rate due clay's higher water retention capacity. Specimen C2's much lower contribution reaffirmed the role of the thick sandy topsoil as an effective capillary barrier, limiting vertical moisture flux and reducing clay desaturation.

The distribution of topsoil contributions to total mass loss in Test 2 clearly affirms the behavioural mechanisms previously inferred in Test 1. Under elevated initial topsoil moisture conditions, these patterns more distinctly reveal the roles of topsoil composition and thickness in controlling evaporative dynamics and moisture redistribution. Specifically, B2 exhibited the highest topsoil contribution (10%), consistent with its limited storage and retention capacity. Rapid desaturation of this thin sandy layer maintained steep suction gradients across the material interface, enabling the greater moisture extraction from the underlying Ampthill Clay recorded in Figures 5.5 and 5.6. Specimen C2, with a thicker sandy topsoil, showed a higher topsoil contribution (29%), due to its larger initial moisture store. However, it restricted Ampthill Clay's contribution by lowering its hydraulic conductivity as it desaturated, forming a capillary barrier above the material interface. The clayey topsoil in D2 recorded the lowest topsoil contribution to total mass loss, reflecting its high water retention and low hydraulic conductivity. The similar retention behaviour of both the Ampthill Clay and TS2 meant suction equilibrium was easier to reach, but the inherently slow movement and release of water in both layers limited evaporation. Given its higher retention capacity, migrated moisture is more likely to be retained within the topsoil, reducing its net contribution to mass loss over the test duration.

Notably, despite exhibiting greater percentage reductions in moisture content (Figure 5.6), the topsoil layers contributed less to total mass loss (Table 5.3) due to their lower overall moisture stores relative to the Ampthill Clay. However, Test 2's results evidenced the critical role a higher initial topsoil moisture content played in moderating the evaporation rate from the underlying Ampthill Clay compared to Test 1. By reducing the suction contrast at the material interface, the hydraulic gradient driving upward moisture transfer was weakened. This slowed the rate of suction equilibration between the clay and topsoil, thereby limiting moisture transfer to the surface and slowing the evaporation rate. Additionally, it should be noted that since evaporation had not

stabilised in Test 2, some upward flux from the Ampthill Clay may still be occurring and temporarily retained in the topsoil, partially masking the ongoing contributions of each layer. This underlines the transient and interdependent nature of moisture movement in layered systems, shaped by capillary barrier effects, hydraulic properties, and evolving suction equilibrium across material interfaces.

From these results, the importance of topsoil characteristics on the evaporation dynamics of clay fill is highlighted. Specifically, thicker layers of sandy topsoil with a higher initial degree of saturation are the most efficient capillary barriers, suppressing evaporation from the underlying fill material. Considerations of suitable topsoil compositions and thicknesses should be incorporated into the design of infrastructure embankments to prevent rapid changes in moisture and initiation of shrinkage and desiccation. Furthermore, maintenance plans to ensure the benefits of topsoil remain effective should be outlined to ensure the long-term stability of these assets.

5.2.4 Topsoil Effect on Shrinkage and Desiccation Cracking

Shrink-swell behaviour and desiccation cracking are weather-driven deterioration processes that affect high-plasticity clay fills (Stirling et al., 2021; Briggs et al., 2023). Under drying regimes, shrinkage and compaction of the soil skeleton can induce differential settlement across an embankment. This is problematic as multiple transportation and utility infrastructure components rely on the structural integrity of embankments to remain serviceable. In addition, drying, and therefore shrinkage, are rarely uniform, leading to localised development of tensile stresses. Desiccation cracks can form if these tensile stresses exceed the overall soil tensile strength, creating pathways for rapid infiltration and inducing further asset instability through swelling and suction loss.

The severity of desiccation is often associated with the rate and magnitude of drying the clay fill experiences. As the degree of shrinkage and desiccation is projected to increase under climate change (Kilsby et al., 2009; Loveridge et al., 2010; Toll et al., 2012; Tang et al., 2018; Huang et al., 2023), the development of design and management procedures that can reduce the rate and magnitude of evaporation is needed. Therefore, this research investigated topsoil application as a potential aid for moderating evaporation by analysing its impact on shrinkage and desiccation after drying events. Attaining such insight will assist in developing topsoil design and management procedures that provide infrastructure embankments with long-term resilience to deterioration.

Photographs of the surface of the Ampthill Clay were taken after drying to confirm or exclude the presence of desiccation cracking. It is important to note that no desiccation cracking occurred within any specimen used within Tests 1 and 2, including those without topsoil. Conversely, Ampthill Clay is known as a very high plasticity clay readily subject to desiccation cracking in the field and other experiments conducted in this research (see Section 4.2 and 5.3.2). There are several reasons why this may have occurred, mainly relating to the environmental conditions imposed by the chamber and the equipment used for the experiment. Experimental setups, including specimen size and container type, have been shown by other researchers to influence desiccation (Li & Zhang, 2011; Zeng et al., 2020). The chosen setup encourages free rather than restrictive shrinkage, which is less likely to create desiccation cracks due to lower tensile stress development (Lakshmikantha et al., 2018; Zeng et al., 2020). This highlights the uncertainties in small-scale laboratory-based investigations and the importance of reproducing comparable field embankment parameters.

Replicating realistic environmental conditions and climate cycling are crucial factors in desiccation crack formation. The air temperature and relative humidity values selected for this experiment, which are average summer conditions for Newcastle upon Tyne, were held constant for the test duration. Although not conducive to rapid drying, these values were chosen to enforce low environmental stress on the soil through a slow and gradual evaporation rate. This approach lowers the risk of desiccation crack formation. However, it's important to note that the environmental chamber did not replicate wind and solar radiation – two key initiators of drying, as per Penman-Monteith's (1965) equation, and desiccation. This underscores the need for comprehensive inclusion of environmental parameters to accurately replicate field drying gradients that induce desiccation, ensuring the reliability of research results.

Natural or manmade-induced heterogeneity in infrastructure embankments can serve as areas of weakness, which become focal points of tensile stress accumulation and desiccation crack formation (Wang et al., 2018; Tang et al., 2021; Yu et al., 2021). This heterogeneity can be inherently linked to the physical soil properties or construction methods used to form the embankment (Perry et al., 2003; Briggs et al., 2017). However, it can be introduced and manifest through time by various processes, such as weather-driven deterioration, biological activity, root growth, erosion, and adding new material during maintenance. These processes can also lead to layer mixing or topsoil washout, obscuring the boundary between the topsoil and clay-fill layers in field

embankments over time. As a result, the reliability of the topsoil layer as a protective barrier against rapid evaporation, shrinkage and desiccation may be compromised. Therefore, the absence of desiccation within these experiments could be attributed to the primitive and homogeneous nature of the soil. These results underscore the importance of considering and managing heterogeneity in infrastructure design and maintenance, which can significantly impact the long-term resilience of embankments. Regularly maintaining the quality and thickness of topsoil on infrastructure embankments is a proactive maintenance method.

For all specimens within Tests 1 and 2, the initial dimensions of the Ampthill Clay layer were compared to those at the end of the experiment to determine the amount of volumetric shrinkage that occurred. Results between tests are not comparable as shrinkage was measured in Test 1 after 24 weeks of drying, whereas Test 2 was only subject to 12 weeks. Although desiccation cracks were not observed, volume loss for each specimen was analysed with the perspective of shrinkage being a precursor to desiccation. Greater shrinkage suggests a higher potential for desiccation if the soil and environmental conditions are conducive to those discussed above. Figure 5.7 and Figure 5.8 assess the percentage loss in volume due to shrinkage relative to Ampthill Clay's initial dimensions for Test 1 (A1 – D1) and Test 2 (A2 – D2), respectively.

The results in Figure 5.7 and Figure 5.8 demonstrate a correlation between the degree of volumetric shrinkage and moisture reduction within the Ampthill Clay. In Test 1, specimens A1, B1 and D1 exhibited similar reductions in moisture content after 24 weeks of monitoring (Figure 5.6), ranging between 74–77%, and a narrow range of volumetric loss at 25–28% (Figure 5.7). While these final values suggest a common evaporative equilibrium, they mask important differences in the rate and control of moisture loss, which ultimately influence desiccation behaviour. The diverging mass loss trajectories in Figure 5.4 indicate that A1 experienced the most rapid moisture loss, followed by B1 and then D1 – an order reflecting the absence, thickness, and composition of the overlying topsoil layers.

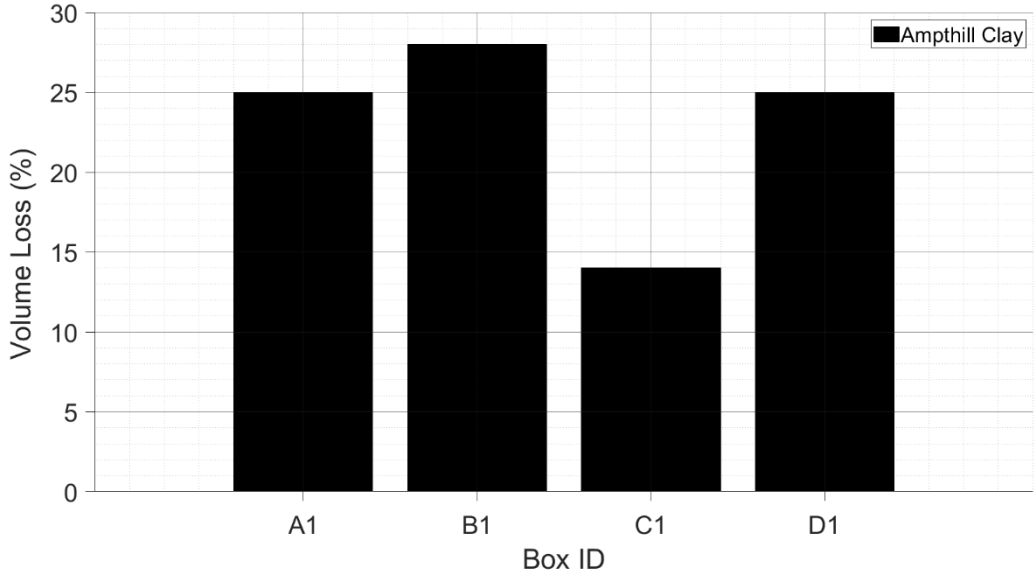

Figure 5.7: Graph demonstrating the percentage loss in volume due to shrinkage relative to Ampthill Clay's initial dimensions for Test 1 specimens (A1-D1).

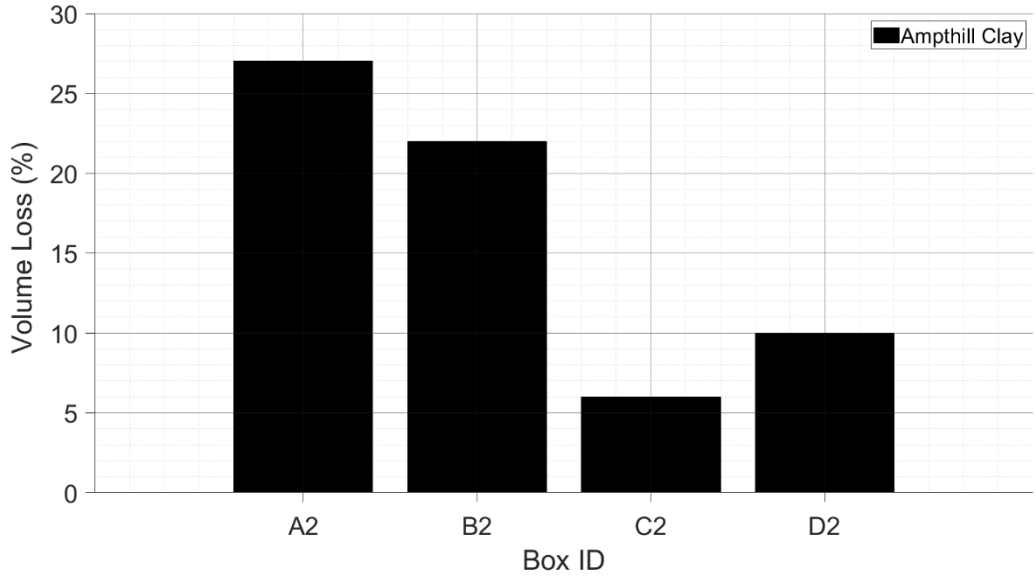

Figure 5.8: Graph demonstrating the percentage loss in volume due to shrinkage relative to Ampthill Clay's initial dimensions for Test 2 specimens (A2-D2).

In association with a lesser reduction in moisture content of 36% in C1, the volume loss was also considerably lower at 14%. These results suggest that when unsaturated, the topsoil characteristics of C1 are the only effective means of suppressing shrinkage in the Ampthill Clay under long drying durations. As a result, the potential for desiccation would be lowest for this specimen. This is directly attributable to the substantial thickness of sandy topsoil (TS1), which barriers upward capillary movement and prevents rapid changes in moisture that drive shrinkage within clay fill.

These differences are closely linked to the varied water retention characteristics of each topsoil. Specimen A1, lacking any topsoil cover, allowed immediate surface exposure and rapid, unimpeded evaporation. This accelerated moisture loss led to a swift increase in suction within the Ampthill Clay, driving significant shrinkage and likely stress accumulation, thereby elevating the potential for desiccation cracking. Similarly, B1's thin sandy topsoil offered a limited evaporative resistance due to low water retention and high suction gradients, also encouraging faster volumetric shrinkage and heightening desiccation crack potential.

Specimen D1, featuring thicker clayey topsoil was characterised by a higher water retention and lower hydraulic conductivity. These intrinsic properties imposed a greater resistance to upward moisture flux. This moderation of suction gradients resulted in slower accumulation of volumetric change, thereby lowering the potential for desiccation-induced stress despite achieving similar total shrinkage to A1 and B1 under long-term drying. In contrast, specimen C1's thick sandy topsoil established a pronounced capillary barrier, significantly restricting moisture movement and suction development, which in turn limited volumetric shrinkage to 14% and minimised the desiccation cracking risk. These results demonstrate the timing and distribution of water loss, influenced by the textural and hydraulic properties at the material interface (i.e., contrast between SWRCs), ultimately governing the rate of suction development, volumetric shrinkage and desiccation cracking potential. This highlights the importance of both water retention capacity and evaporation pathway resistance in controlling desiccation risk.

In contrast to Test 1, greater differences in moisture content reduction were recorded between specimens in Test 2 (see Figure 5.6), which were ordered from highest to lowest as follows: A2 (75%), B2 (48%), D2 (32%) and C2 (23%). Similar patterns of disparity are observed in Figure 5.8 for percentage volumetric loss, with the greatest shrinkage occurring in A2 (27%), followed by B2 (22%), D2 (10%) and lastly, C2 (6%). Therefore, these results support the hypothesis that the rate of shrinkage and desiccation potential is inherently controlled by the contrasting water retention behaviour across the fill-topsoil material interface, which differs with topsoil composition and thickness.

Terminating Test 2 after 12 weeks was strategic to determine if different topsoil characteristics led to varied shrinkage paths. From this, deeper insights into the evolving relationships between topsoil characteristics, moisture loss, and shrinkage

during the early stages of evaporation were attained. These relationships were less clear during the extended monitoring period of Test 1, where moisture and volume loss calculations indicated a stage where evaporation and shrinkage within A1, B1, and D1 had reached a common equilibrium. Understanding the impact of topsoil on the moisture and volume loss rate is crucial, as these parameters significantly influence stress accumulation and crack initiation within high plasticity fills.

Figure 5.8 shows that specimen B2 continued to exhibit the highest shrinkage and desiccation potential; however, earlier sampling provided additional insight into how the thin sandy topsoil layer slightly suppressed the rate of shrinkage accumulation compared to the exposed clay in A2. Specimen C2 showed the lowest shrinkage, again attributed to the formation of a capillary barrier and low unsaturated hydraulic conductivity in the sandy topsoil, both of which restricted upward moisture flux from the Ampthill Clay. The elevated initial moisture content of the topsoil further suppressed shrinkage by lowering the suction differential and moisture transfer across the material interface, reducing the clay fill's contribution in the initial evaporation stage. Specimen D2 allowed easier moisture redistribution due to similarity in the clay-topsoil physical and hydraulic properties, but these materials' high water retention and low hydraulic conductivity slowed evaporation. Furthermore, the same reduction in suction differential at the material interface would have also suppressed the drive for evaporation. Consequently, these processes lowered suction gradients and limited upward moisture fluxes, instead retaining greater moisture and reducing shrinkage relative to A2 and B2.

These results clearly demonstrate how topsoil (type, thickness, and water retention) and material interface properties influence underlying clay's evaporation dynamics and shrinkage behaviour. It supports the concept that capillary barriers (C2) and high retention topsoil (D2) are more effective in reducing desiccation risk, while minimal (B2) or no topsoil (A2) exacerbates shrinkage due to unimpeded moisture loss and high suction gradients.

5.3 Isolated Effects of Wind Speed on the Desiccation Cracking Process

While the impacts of temperature (e.g., Tang et al., 2010; Song et al., 2016; Cheng et al., 2021), humidity, and precipitation (e.g. Cheng et al., 2021; Tian et al., 2023) have been thoroughly researched in existing literature using mainly laboratory testing, there is a significant research gap in the impact of solar radiation and wind on desiccation, with limited studies available (Eminue et al., 2018; Stirling et al., 2018; Poulsen et al., 2020; Cordero et al., 2021; Yu et al., 2021; Poulsen, 2022; Zeng et al., 2024). This is due to the ease of replicating the former within a laboratory environment, where each parameter's effect on evaporation and desiccation can be measured directly. Conversely, accurately replicating and isolating the contribution of solar radiation and wind in a laboratory, which captures the scale of these parameters' variability, is notably challenging. According to the principles established by Penman (1948) and Monteith (1965), the intensity of wind speed and solar radiation, both key drivers of evaporation, can vary significantly over short durations and distances due to weather fluctuations, surface resistances and their interaction with local boundary conditions. Additional complexities arise from wind analysis if the directional component, turbidity, and coupling effect of air temperature and relative humidity during evaporation are considered (Poulsen et al., 2020; Poulsen, 2022; Zeng et al., 2024). Furthermore, different sources (i.e. direct and diffuse) and spectral compositions of solar radiation affect soil temperature and evaporation differently.

It is also important to consider that existing laboratory studies rarely account for natural variations in environmental conditions. Common analysis methods involve applying extreme temperatures (Tang et al., 2010; Estabragh et al., 2015; Wang et al., 2017; Louati et al., 2021; Tian et al., 2022) to induce drying cycles and fully submerge samples for re-wetting (Basma et al., 1996; Kalkan, 2011; Al-Yaqoub et al., 2017; Tang et al., 2020; Zaidi et al., 2021). Natural weather cycles are much more complex, and applying extremes is not representative of desiccation in milder, temperate climates with changeable weather. Depending on the season, different environmental factors alter the relative influence of the radiative and aerodynamic components in the Penman-Monteith equation, thereby shifting the dominant drivers of drying and desiccation in temperate climates (Penman, 1948; Monteith, 1965; Poulsen et al., 2020; Poulsen, 2022). An example of this is the occurrence of desiccation cracking in the lysimeter slope (Chapter 4) during winter, where despite low temperatures and reduced solar radiation, sustained drying likely occurred due to elevated wind speeds

driving the aerodynamic component of the evaporation process, in line with the Penman (1948) and Penman-Monteith (1965) formulations.

Consequently, conducting research that encompasses the comprehensive array of environmental factors influencing evaporation, as delineated in the Penman-Monteith (1965) equation, which includes variables such as net radiation, wind speed, humidity, and temperature, provides a more nuanced and accurate framework for understanding and predicting desiccation cracking. This approach enables the development of more effective predictive models and mitigation strategies for managing desiccation cracking in various soil environments. An initial study on the role of solar radiation exposure in desiccation crack formation was explored within Section 4.5. Therefore, a complimentary series of laboratory tests have been designed to help quantify the effects of wind speed on desiccation crack formation.

For the experiment, four boxes (dimensions 400 x 300 x 170 mm) – labelled W1 to W4 – were filled with 90 mm of compacted Ampthill Clay and placed within a Perspex chamber. Figure 5.9 demonstrates the experimental setup, where the wind was simulated across the specimen surface by blowing air through an inflow pipe connected to an electric fan. An outlet on the opposite side of the chamber provided an exit route for the wind. A different wind speed was applied to each specimen to capture their individual effects on desiccation crack formation: (W1) 0 m/s representing calm conditions with no wind; (W2) 1.5 m/s representing a gentle breeze; (W3) 4.5 m/s representing a moderate breeze; (4) 18 m/s representing high winds usually experienced during gusty storm conditions. The continuous application of these wind speeds over extended periods does not accurately reflect the true natural variation of the parameter. However, it offers an initial opportunity to closely observe the evolution of evaporation and desiccation under different wind speeds, which vary the aerodynamic forcing (Penman, 1948; Monteith, 1965) under otherwise controlled conditions. Continuous measurement of relative humidity and temperature within the chamber and photographic documentation of surface crack evolution were also carried out. The testing schedule followed is outlined in Table 5.4.

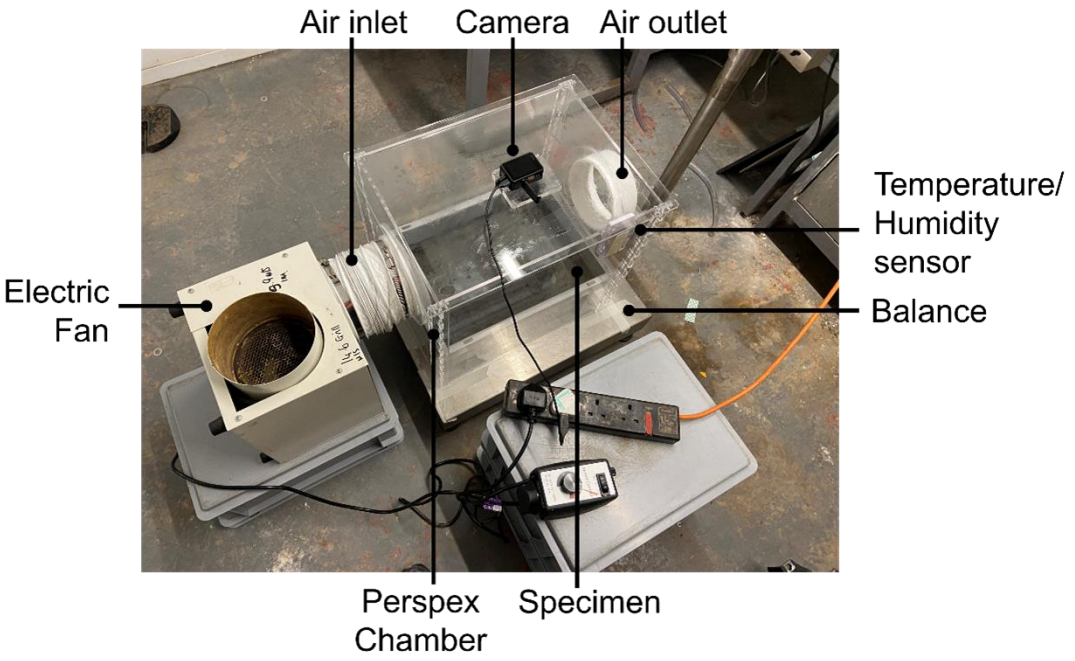

Figure 5.9: The experimental setup illustrates the specimen within a Perspex Chamber. The wind is supplied to the chamber via an inlet connected to an electric fan and escapes through an outlet on the opposite side. A camera for surface crack imaging was used, and specimen mass loss was recorded using a balance.

Table 5.4: Details of the testing schedule for W1 (0 m/s), W2 (1.5 m/s), W3 (4.5 m/s) and W4 (18 m/s).

Test ID	W1	W2	W3	W4
Wind Speed (m/s)	0	1.5	4.5	18
Fill Composition	Ampthill Clay			
Fill Thickness (mm)	90			
Fill Initial Moisture Content (mm)	40			

5.3.1 Microclimate and Evaporation Evolution under Various Wind Speeds

In Figure 5.10, the temporal evolution of cumulative mass loss is provided for W1 (0 m/s), W2 (1.5 m/s), W3 (4.5 m/s) and W4 (18 m/s). Each test was concluded when there was no further change in mass loss with time. The exception is W1, whose results were adversely affected by a malfunction in the temperature-controlled room housing the experiment. This triggered a rapid increase in air temperature, which, by altering the net energy available at the surface and increasing the vapour pressure deficit, enhanced the potential evaporation rate in accordance with the Penman-Monteith (1965) equation. Consequently, results after this malfunction were considered invalid and excluded from Figure 5.10. Furthermore, dashed lines in the mass loss curve of W4 represent data loss intervals that resulted from an issue with the mass logger

software. This issue was resolved for subsequent tests (W1 to W3). Therefore, interpolations between known results were calculated and plotted using a 10-point moving average to connect results across these data loss intervals.

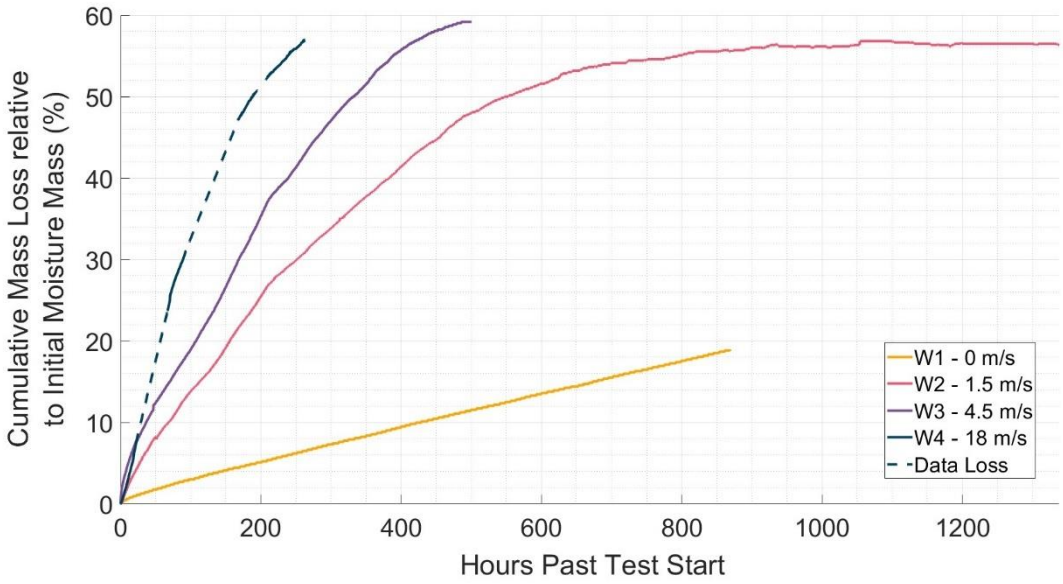

Figure 5.10: A plot of the evolution of cumulative mass loss relative to initial moisture mass (%) against hours past test start for W1 (0 m/s), W2 (1.5 m/s), W3 (4.5 m/s), and W4 (18 m/s).

A comparative analysis of the mass loss curves in Figure 5.10 illustrates that increasing the wind speed enhances aerodynamic conductance (i.e., reducing the aerodynamic resistance to vapour movement), thereby elevating the energy available for evaporation and significantly increasing the mass loss rate, consistent with the Penman-Monteith (1965) equation. This effect was enhanced under higher wind speeds, where increased aerodynamic conductance accelerated moisture depletion and led to earlier plateauing of evaporation in W4, followed by W3 and W2. The absence of a plateau in the mass loss curve of W1 is due to the previously discussed invalid results, which led to a misconception about when this plateau occurred. However, the mass loss rate is increasing linearly at a notably slower rate, with evaporation projecting to plateau significantly later in the absence of wind compared to W2 – W4. These findings quantitatively demonstrate the established role of wind-driven drying in accelerating evaporation, consistent with the Penman-Monteith (1965) framework, where evaporation efficiency increases with wind velocity. Rapid drying has major implications for the rate and severity of shrinkage and desiccation cracking for highly sensitive plastic clay embankment fills. Increased evaporation rates lead to higher suction gradients, greater shear strains and stresses, and intensified cracking, which accelerates soil deterioration.

However, to fully understand the driving mechanisms of these variations in mass loss, investigation into the impact of wind speed on microclimate evolution during evaporation is required. The microclimate develops locally above the soil's surface, encompassing important gradients in air pressure, temperature, relative humidity, and wind speed. These variables directly influence the energy balance at the soil surface and are fundamental components of the Penman-Monteith (1965) equation, which governs evaporation by quantifying the combined effects of radiation, aerodynamic, and surface resistances. Therefore, to investigate and compare microclimate evolution during W1 – W4, a sensor measuring temperature and humidity was installed within the chamber, 280 mm above the Ampthill Clay's surface. This placement enabled temperature and humidity to be continuously monitored and correlated with changes in the rate and magnitude of evaporation under the specified wind speeds.

Figure 5.11A – D presents the temporal evolution of cumulative mass loss (%) in relation to air temperature (°C) and relative humidity (%) for wind treatments W1 through W4. The data indicate that increasing wind speed induces greater fluctuations in relative humidity while attenuating variability in air temperature within the soil microclimate. Consistent with Penman-Monteith's (1965) equation, evaporation is regulated by net radiation, aerodynamic conductance (enhanced by wind speed), and surface resistance, all modulated by microclimatic gradients in temperature, humidity, and wind velocity. Figure 5.11B and Figure 5.11C show relatively stable air temperatures near 14°C during W2 and W3, with a 1.8°C increase at the end of W3 corresponding to the cessation of evaporative cooling as the latent heat flux declines. The absence of this thermal increase at higher wind velocities (W3 and W4) implies a critical wind speed threshold beyond which convective heat transfer effectively balances the energy budget by enhancing turbulent mixing and suppressing post-evaporation warming. This interpretation is corroborated by the pronounced temperature oscillations under no-wind conditions in W1 (Figure 5.11A), where the lack of forced convection permits greater sensitivity to ambient thermal fluctuations. These results emphasise the pivotal role of wind-driven aerodynamic conductance in

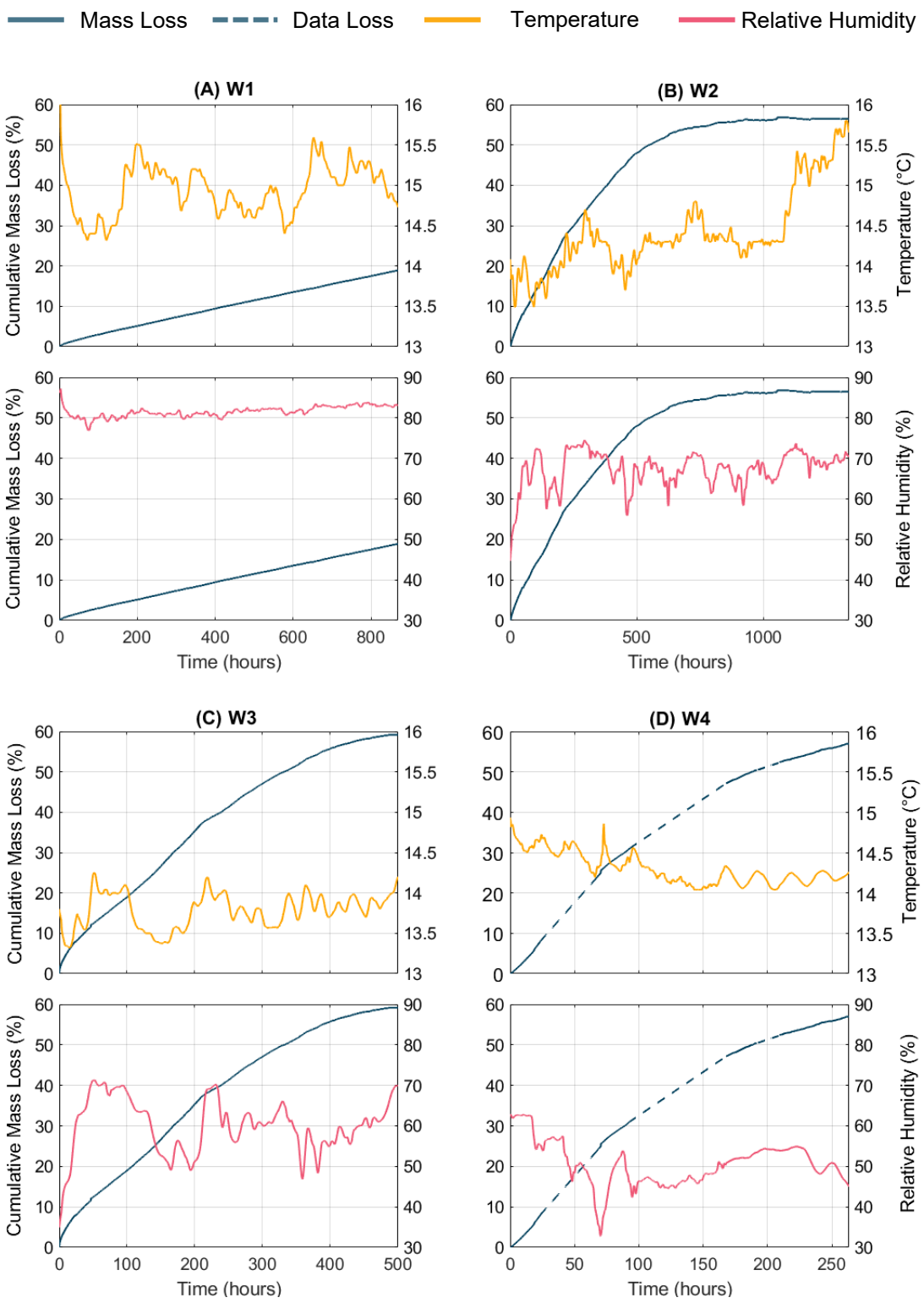

Figure 5.11:Comparison of Cumulative Mass Loss (%) (navy line) with the evolution of air temperature (°C) (yellow line) and relative humidity (%) (pink line) within the chamber through time (hours) for (A) W1 - 0 m/s, (B) W2 - 1.5 m/s, (C) W3 - 4.5 m/s, and (D) 18 m/s. Cumulative Mass Loss (%) is expressed as a percentage relative to each specimen's total initial moisture mass. The dashed navy line indicates areas of data loss.

stabilising the microclimate thermal regime and accelerating evaporative fluxes, as articulated by the Penman-Monteith (1965) framework. The enhanced evaporation rates under increased wind conditions bear significant implications for desiccation cracking and soil shrinkage processes within engineered embankment materials, particularly during transient drying episodes.

While temperature variations were suppressed under increased wind speeds, relative humidity exhibited more pronounced fluctuations, reflecting the complex microclimatic response to aerodynamic changes. These variations in relative humidity are critical for characterising vapour pressure deficits and atmospheric demand, key drivers of evaporation as first described by Penman (1948). Understanding these fluctuations provides deeper insight into the coupled soil-atmosphere exchanges influenced by wind-driven turbulent transfer. Therefore, the following analysis examines the modulation of relative humidity and overall microclimate evolution across W1 to W4, emphasising their role in controlling the energy balance and evaporation dynamics.

During the initial 70 hours of monitoring in W4 (Figure 5.11D), relative humidity reduced from 60% to 35% under the highest applied wind speed of 18 m/s. This period coincided with the peak phase of mass loss in the Ampthill Clay, again highlighting the role of wind-driven aerodynamic conductance in enhancing evaporation (Penman, 1948; Monteith, 1965). Consequently, the documented reduction in relative humidity highlights the role of strong winds in promoting turbulent mixing. This process effectively dissipates moisture-laden air and replaces it with drier air, thus maintaining a significant vapour pressure deficit. This mechanism is particularly efficient where steep temperature and humidity gradients exist, as during W4's rapid evaporation phase. Within the initial 70-hour period, this enhanced aerodynamic conductance established a self-perpetuating cycle, sustaining elevated evaporation rates by continuously renewing the air's capacity to hold moisture and preserving steep vapour pressure gradients at the soil–atmosphere interface**.** Due to the wind's suppression of local moisture accumulation, relative humidity remained persistently low, as depicted in Figure 5.11D, which shows a decline from pre-test equilibrium levels**.**

After the initial 70-hour monitoring period, relative humidity in W4 rapidly increased from 35% to 50% within a 15-hour window. Figure 5.11D illustrates that the initiation of this increase coincided with a deceleration in Ampthill Clay's mass loss rate. At 170 hours of monitoring, the mass loss curve deflected further toward a plateau, with relative humidity subsequently stabilising at 50%, with some minor fluctuations. These

results illustrate that the impact of wind-driven aerodynamic conductance on microclimate evolution significantly diminished as soil moisture reserves were depleted and evaporation rates declined. With reduced moisture flux from the Ampthill Clay, the local vapour pressure deficit decreased, attenuating the driving force for turbulent mixing. Consequently, the moisture gradient between the soil surface and the incoming dry air lessened, reducing convective moisture removal. As a result, moisture released during this later evaporation phase accumulated locally, leading to the observed increase and subsequent stabilisation of relative humidity.

Whilst high wind speeds (W4) have demonstrated a significant, yet evaporation stage-dependent, impact on microclimate evolution, low (W2 - Figure 5.11B) and moderate (W3 - Figure 5.11C) wind speeds exhibit a directly less pronounced and more gradual effect. Lower wind speeds generate reduced turbulent and aerodynamic conductance, thereby diminishing air mixing efficiency and displacement of moisture-saturated air near the soil surface. The attenuation in convective transfer is evident in Figure 5.10, where mass loss rates decline progressively as wind speed is lowered from W4 to W1. The reduced evaporative flux under lower wind speeds results in a weaker vapour pressure gradient between the soil surface and surrounding atmosphere, limiting the driving force for air replacement. Therefore, moisture accumulates in the microclimate, causing a gradual increase in relative humidity, contrasting with the significant decrease observed under high winds speeds in W4. Relative humidity in W2 increases from 50% to 70% in the initial 100 hours of monitoring and W3 from 40% to 70% by 60 hours, as illustrated in Figure 5.11B and Figure 5.11C, respectively.

After this initial increase, relative humidity fluctuates substantially and irregularly between high and low values. This differs from W1's relative humidity behaviour, where no wind speed is applied. The absence of such fluctuations in W1 confirms that even lower wind velocities (W2–W3) maintain a measurable influence on microclimate dynamics by enhancing aerodynamic conductance. This is further supported by the overall humidity being at least 20% lower in tests where wind was applied (W2 – W4). These patterns reflect the progressive development of vapour pressure gradients as evaporation proceeds, which intermittently intensify to drive transient wind-induced air mixing events, temporarily lowering relative humidity. The irregularity in these fluctuations indicates that evaporation within the Ampthill Clay and convective exchange with the microclimate are less spatially and temporally uniform under lower

wind speeds, consistent with the aerodynamic resistance component described in the Penman-Monteith (1965) framework.

The findings of this initial analysis of the relationship between wind speed and microclimate evolution are significant in the context of wind-driven drying of real infrastructure embankments. Under the influence of wind, evaporative fluxes – governed by aerodynamic conductance as articulated in the Penman-Monteith equation – are substantially elevated. This leads to both an increased rate and a greater cumulative magnitude of moisture loss relative to no-wind conditions. Elevated wind velocities amplify this effect, particularly in the early stages of evaporation, by creating a self-sustaining process. The continuous replacement of moisture-saturated air with drier ambient air maintains steep vapour pressure deficits across the soil-atmosphere interface. This process intensifies latent heat flux and reinforces soil moisture gradients, promoting accelerated drying independent of high air temperatures or solar radiation inputs as per the Penman-Monteith (1965) equation. These findings underscore the critical role of wind-driven convective transport in modulating evaporative dynamics and highlight its potential to significantly influence desiccation processes within engineered embankments.

This self-sustaining process was most efficient in the early stages of the drying cycle, when soil moisture content was near saturation, facilitating sustained latent heat flux due to abundant surface moisture availability. As moisture decreased, the reduction in surface water limited evaporative flux. This diminished the vapour pressure gradient that drives mass transfer, thereby decreasing the effectiveness of wind-induced evaporation enhancement. However, the presence of wind in W2 – W4 continued to sustain an overall lower humidity in the chamber compared to the high levels (~90%) recorded within W1. Even though a constant wind speed of 18 m/s is unrealistic, it demonstrates the capacity of increased wind-driven aerodynamic conductance to accelerate drying rates and magnitudes within embankment fill. Furthermore, these results demonstrate the ease and speed of transition between a wet and dry state under high winds, which could amplify cyclic deterioration of embankment fill through more frequent volume change and desiccation.

However, it is important to note that many railway infrastructure embankments are already in an advanced state of tensile strength deterioration (Perry et al., 2003; Briggs et al., 2017; Spink, 2020; Briggs et al., 2023) particularly compared to these test specimens, which have only experienced one drying cycle. Consequently, lower wind

speeds may have an equally adverse effect on the rate of cyclic and desiccation-induced deterioration of the embankment fill. The subsequent section will provide a more detailed exploration of the observed relationships between wind speed and desiccation cracking.

5.3.2 The Evolution of Wind-driven Desiccation Cracking

The above analysis of microclimate evolution demonstrated that drying patterns within the Ampthill Clay exhibited temporal and spatial variability influenced by wind speed, consistent with established aerodynamic and energy balance principles (Penman, 1948; Monteith, 1965). Rapid and heterogeneous drying is the key factor in desiccation crack initiation, producing substantial suction gradients that elevate shear and tensile stresses. This intensifies cracking and compromises the overall integrity of embankment fill (Stirling et al., 2018; Wang et al., 2018; Hun et al., 2021; Tang et al., 2021). In W1 (no wind) and W2 (1.5 m/s), no desiccation cracking occurred, only volumetric shrinkage. Conversely, desiccation cracking was initiated in W3 (4.5 m/s) and W4 (18 m/s), with crack severity correlating positively to wind speed, reflecting the enhanced evaporative demand predicted by the Penman-Monteith (1965) framework. The absence of desiccation cracking within W1 highlights the limited drying potential without wind-driven aerodynamic conductance under low air temperature and solar radiation. However, the lack of crack formation in W2 (1.5 m/s) supports the earlier hypothesis of a critical wind speed threshold required to sufficiently augment evaporation rates and induce differential stress accumulation necessary for crack initiation and propagation

To provide a more detailed analysis of crack formation under different wind speeds, evaporation and microclimate evolution phases were compared with the Crack Intensity Factor (CIF) trajectory. The CIF is a quantitative measure of cracking severity and was calculated at one-minute intervals using photographs taken of the Ampthill Clay's surface, a detailed methodology is provided in Section 3.4.4. Figure 5.12 plots the cumulative mass loss (%) and CIF development during W4 where a constant wind speed of 18 m/s was applied.

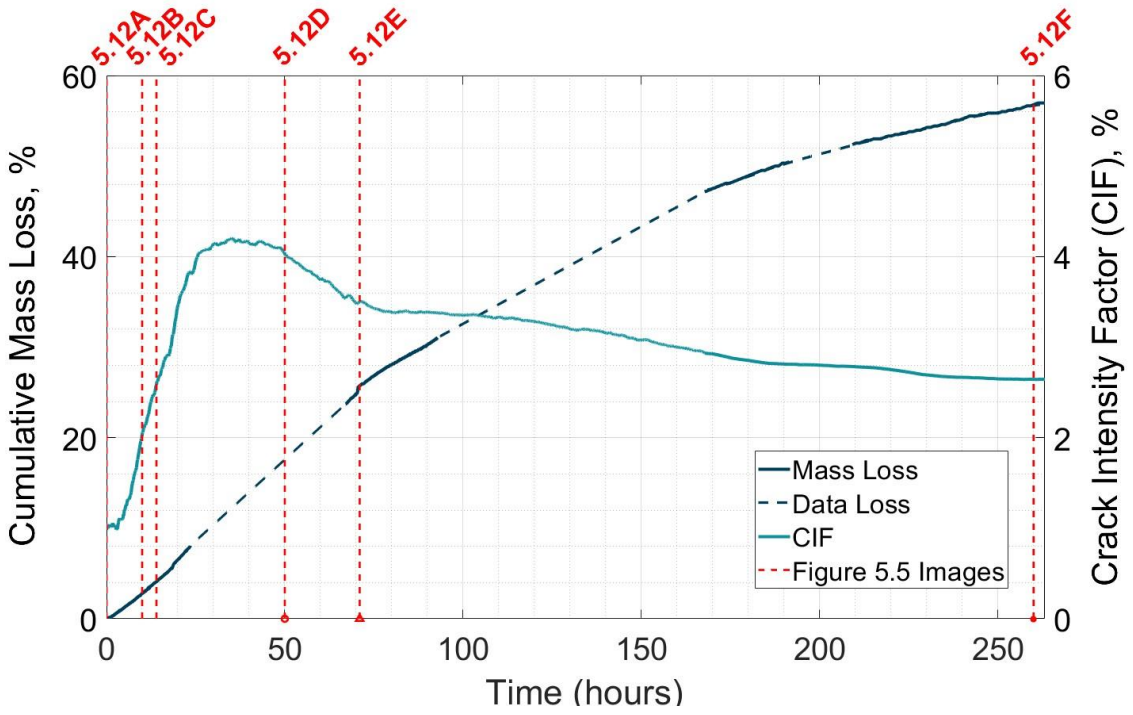

Figure 5.12: Comparison of Cumulative Mass Loss (%) with the evolution of the Crack Intensity Factor (CIF, %) with time for W4 (18 m/s). Data loss is the mass loss curve is indicated by the dashed line, calculated using a moving average. The temporal occurrence of Figures 5.13A - F are indicated by the red dashed lines.

Accompanying the CIF curve in Figure 5.12 is Figure 5.13A – F, which visually depicts the evolution of desiccation cracks during W4. The temporal occurrence of each cracked state within Figure 5.13A – F has been annotated on the CIF curve in Figure 5.12. The onset of desiccation in W4 is shown to be near instantaneous upon exposure to the high (18 m/s) wind speed. A comparison of the CIF and mass loss curves in Figure 5.12 demonstrates that cracking commenced before any significant loss in moisture was established. For reference, the Ampthill Clay was compacted at 40% moisture content, achieving a bulk density of 1.78 Mg/m3 and an approximate degree of saturation of 76%. From this, cracking began in W4 while the specimen was partially saturated and retained significant moisture.

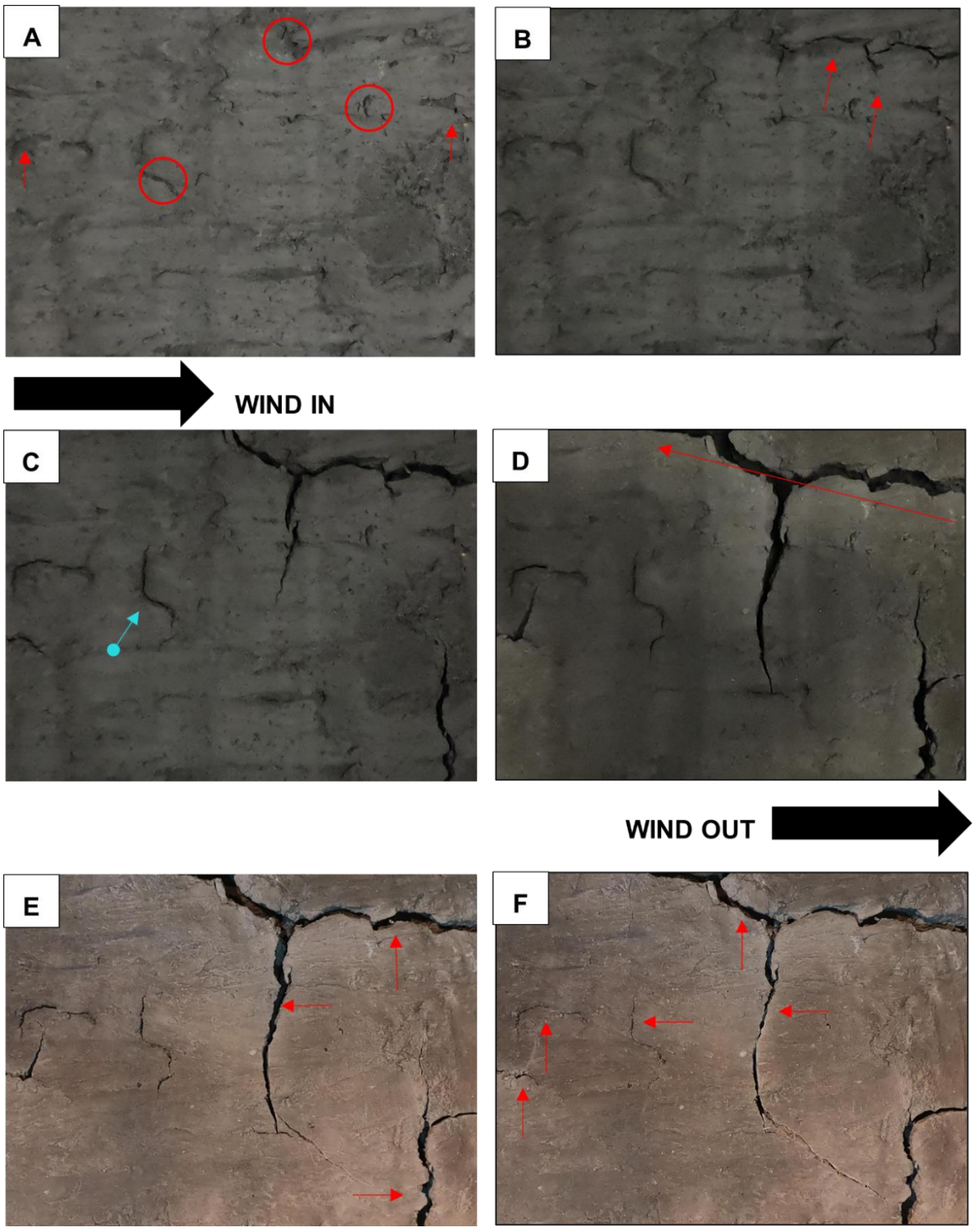

Figure 5.13: Photographs showing the evolution of desiccation cracking within W4 (18 m/s) where (A) crack initiation at container walls and at heterogeneities, (B) Propagation of cracks in length and depth, (C) Widening of cracks, (D) Maturing of crack network, (E) Compression of crack apertures indicated by red arrows, (F) Stabilising of aperture reduction with red arrows indicating areas of compression. The direction of wind flow is indicated on the figure. The temporal occurrences of A – F are annotated within Figure 5.12.

Crack initiation in saturated soils is well-documented (Tang et al., 2011; Tollenaar et al., 2017; Cordero et al., 2021) and closely tied to the transition from saturated to unsaturated states along the SWRC. In high-plasticity clays like Ampthill Clay, significant suction develops before air entry while saturation remains near unity (Tarantino & Di Donna, 2019). This suction generates strong capillary forces that induce tensile stresses, causing cracks. As evaporation reduces water content, suction and effective stress rise, leading to a sharp decline in void ratio within the saturated range, which typically triggers cracking.

The process discussed is often non-uniform due to spatial heterogeneity in soil physical and chemical properties, which affects soil hydraulic conductivity and surface resistance parameters within the Penman-Monteith (1965) framework. This variability influences moisture fluxes between the soil and the atmosphere. Additionally, factors such as slope angle, topography, aspect, and physical obstructions modulate essential microclimatic variables—net radiation, wind speed, temperature, and humidity—essential for the energy balance and aerodynamic conductance components of the Penman-Monteith equation. In railway embankments, for instance, fill heterogeneity has established over their 100-plus years of service (Skempton, 1995; Perry et al., 2003; Mair, 2021), which results in variable evaporation rates and moisture gradients across the fill materials. Consequently, the interplay between soil property variability and localised microclimatic conditions leads to distinctly non-uniform evaporation patterns, as anticipated by coupled soil-atmosphere energy and mass exchange models.

Accurately measuring localised changes in moisture flux is challenging, and using a single representative moisture content measurement, as shown in Figure 5.10, is often considered the only feasible solution. However, in the crucial early stages of evaporation, the resolution of results obtained via this approach often obscures the emergence of these important evaporation, moisture content, suction and stress gradients. This is where the value of high-temporal resolution surface photography becomes evident, as it has proven invaluable in these experiments for documenting the emergence of localised desaturation zones and the resultant crack initiation within them.

From the high-temporal resolution images, crack initiation was observed in areas of the sample associated with greater heterogeneity in mechanical soil properties. Other researchers have shown that inconsistencies in soil mechanical properties create

weakened zones of low tensile strength, which are then at greater risk of desiccation (Wang et al., 2018; Tang et al., 2020, 2021). The relationship between cracking and points of soil heterogeneity is especially important in real infrastructure embankments. As infrastructure ages and is exposed to weather-related deterioration, the degree of heterogeneity in soil properties increases over time (Perry et al., 2003). Consequently, an embankment's vulnerability to desiccation cracking can also heighten over time. Figure 5.13A illustrates that desiccation cracks in W4 were initiated either closely parallel or at the specimen-container interface (see red arrows) or internally within the specimen (see red circles). Compaction close to the container is poorer, and the mixed material interface (clay and plastic) does not exhibit the same strong interparticle friction as exists between clay particles. This may have generated a weakened tensile strength boundary zone that desiccation cracking exploited.

Other studies have shown internal crack localities originating due to various factors, including heterogeneous soil compositions, structure, and compaction quality, which ultimately cause cracking by encouraging differential evaporation patterns, water loss, and suction (stress) accumulation (Weinberger, 2001; Costa et al., 2013; Wang et al, 2018). Due to the unprocessed and manually compacted nature of the Ampthill Clay fill, a combination of these processes was likely responsible for crack initiation. Notably in W4, some internal cracks were observed to initiate from larger, surface-exposed pores in the compacted clay matrix. These can disrupt the continuity and cohesion of the finer clay matrix, locally reducing tensile strength. Furthermore, the lower water retention capacity and higher exposed surface area of larger pores can exacerbate evaporation. Therefore, larger pores can become focal points for tensile stress accumulation, and their propensity to desiccation increases as the locally lower tensile strength is more readily exceeded. Figure 5.13A evidences the drying around these pores during W4, with desaturated thinner surface layers first detaching from the more saturated deeper layers. This detachment generated a tensile pull from which cracks then propagated to release the accumulated tensile stress.

After initiation, the cracks entered a rapid growth phase, lengthening and deepening (Figure 5.13B) before considerably widening until a maximum aperture was reached (Figure 5.13C). Figure 5.12 demonstrates this phase, where the CIF sharply increases towards its peak value of 4.3% within the initial 35 hours of monitoring. Figure 5.13A – D demonstrate that most cracks opened and widened parallel and then propagated perpendicularly to the longer container edge. At the same time, a smaller number

opened and widened parallel and then propagated perpendicularly to the shorter container edge. Previous research using similar small-scale laboratory testing has shown that the orientation of the principal tensile stress mainly governs the pattern of crack evolution (Costa et al., 2013; Wang et al., 2018; Zeng et al., 2020). Desiccation cracks tend to open parallel to the maximum tensile pull and propagate perpendicular to it, following the path of least resistance. These observations suggest the principal tensile stress in W4 could initially be oriented perpendicular to the long container edge, with a smaller secondary tensile stress component acting toward the short edge.

However, the tensile stress distribution is often more complex than a simple biaxial case, evolving temporally and spatially as changes in internal and external constraints to shrinkage are encountered. For laboratory tests, external constraints are largely provided by the boundary conditions imposed on the specimen from environmental conditions or frictional resistance with the sample container (Wang et al., 2018; Zeng et al., 2020). Although container boundary effects are not representative of the field embankments, contact with other materials, such as utilities or other soil compositions and interlayer boundaries, would impose differing levels of restraint and impact desiccation crack evolution. Conversely, internal restraints evolve from heterogeneity in the inherent properties of the fill, such as stiffness, structure, compaction degree, moisture content, suction, and cohesion. Due to the age and construction methods used in infrastructure embankments, heterogeneity is widely present yet challenging to quantify, making the stress field complex and the cracking behaviour difficult to predict. Furthermore, desiccation cracks' formation and growth can reshape a fill's stress field as it attempts to equilibrate the accumulation of differential stresses. Later observations of non-uniform shrinkage over time within both W4 and W3 specimens suggest the alternative operation of a dynamic, complex stress field, which will be discussed in further detail later in this section.

The cracks gained their length by propagating from the crack tip, driven by the desire to resolve the tensile stresses accumulated at this location. Propagation continued until the tensile stresses were equilibrated in space or at an intersection with another crack that occurred at a 90-degree angle. The former was mostly observed in cracks orientated perpendicular to the longer container edge, stabilising quicker after propagating considerably shorter lengths (see blue arrows in Figure 5.13C). Conversely, the latter process was more efficient within cracks orientated parallel to the longer container edge. From Figure 5.13B (red arrows), these cracks were notably

concentrated along the specimen's top edge or within the right corner. As drying continued, they progressively joined to form a large crack extending the length of the long edge, as shown by the red arrow in Figure 5.13D. These observations suggest a stronger tensile stress component acting perpendicular to the longer container edge, facilitating more significant crack growth in the parallel direction. However, further detailed analysis of tensile stress and strain development using this experimental setup would be required to support this hypothesis.

During crack evolution and once equilibrium was reached (Figure 5.13D), a discernible division in crack characteristics was observed between the left and right sides of specimen W4. Crack initiation was significantly more active on the right side, displaying greater propagation distances, widths, and durations of sustained growth. However, fewer cracks appeared on the left side, and their growth was notably brief, forming shorter and thinner cracks which became isolated in space. This spatial asymmetry in crack development is consistent with the generation of non-uniform evaporation, driven by variable soil properties and aerodynamic conductance (Penman, 1948; Monteith, 1965). Variations in exposure to, and complexities in the flow dynamics of, the supplied wind occurred. The wind was supplied to the specimen through an inlet at the left side of the chamber, and its escape outlet was on the right (Figure 5.9). Consequently, the left side was inherently more sheltered as the flow accelerated across the specimen to the outlet on the right to satisfy emerging pressure gradients. The observed progressive increase in local wind velocity from left to right would have enhanced the aerodynamic conductance within the Penman-Monteith (1965) model. This enhancement would facilitate stronger evaporative fluxes and result in more pronounced moisture gradients directed toward the outlet. Consequently, the localised shear and tensile stresses, along with strain accumulation, became concentrated on the right side, where the wind-driven vapour pressure deficit was at its maximum.

Furthermore, supplying a high-velocity wind (18 m/s) into this confined space would generate significant turbidity as most airflow would impact the right-side wall and rebound. Due to the small size of the outlet relative to the chamber's holding volume, the air outflow rate was restricted, further intensifying the concentration of turbulent air on the right side. This increase in turbulence enhanced aerodynamic conductance, thereby accelerating the rate of vapour transfer across the soil–atmosphere interface. As a result, the right side experienced greater environmental forcing, which facilitated increased evaporation, moisture loss and differential accumulation of shear and tensile

stresses. The elevated aerodynamic conductance promoted rapid propagation of drying fronts to depth by accelerating surface moisture removal and steepening subsurface moisture gradients. This sustained high evaporation maintained greater moisture and suction differentials, promoting stress accumulation and more frequent and intense crack initiation and propagation.

These findings align with the principles embedded in Penman-Monteith and related coupled energy-mass transfer models, which account for spatial variability in aerodynamic conductance and microclimate conditions. They illustrate how localised differences in wind exposure and turbulence influence evaporation and crack evolution. Such observations are fundamental to understanding and predicting desiccation on real infrastructure embankments, where highly complex spatial and temporal variations in wind exposure operate. This fundamentally results from their inherent features (e.g. alignment to prevailing wind) and physical obstacles in the surrounding environment (e.g. shading or channelling by other infrastructure and vegetation). Yu et al. (2020) observed this effect at the BIONICS test embankment site, where desiccation was greater in the aspect most exposed to the prevailing wind direction.

After reaching its peak value, the CIF decreased moderately to 3.5% over the following 25 hours. The CIF continued to decrease for the remaining test duration but at a progressively slower rate, finally stabilising at 2.6%. The moderate decrease was likely due to a change in the stress field, as compressive shrinkage replaced the previous opposing tensile forces that had stabilised as the cracking peaked (see Figure 5.13E – F). As the evaporation front advanced deeper into the specimen, consistent with Penman–Monteith–based expectations of diminishing surface flux under declining moisture availability, moisture gradients became more homogenised. This resulted in volumetric shrinkage of the bulk soil, leading to partial closure of desiccation cracks under the resultant compressive stresses, shown by the reduced crack apertures in Figure 5.13E. At first, the shrinkage was fast as the specimen detached from the container walls, providing a greater surface area for evaporation. This mechanical boundary change enhanced vapour transfer and supported further drying, leading to the moderate decrease in CIF recorded in Figure 5.12. As soil moisture depletes, reduced hydraulic conductivity limits water transport to the surface, while declining surface vapour pressure lowers the vapour pressure gradient. This reduces latent heat flux and suppresses evaporation rates, as the Penman–Monteith (1965) equation

predicted. The associated homogenisation of suction (stress) gradients within the clay slowed shrinkage, stabilising the CIF. Cracks with a notable reduction in aperture are highlighted by the red arrows in Figure 5.13E – F.

Importantly, the growth, stabilisation, and moderate reduction in CIF occurred during the initial 70 hours of the test, coinciding with W4's most rapid phase of evaporation, as recorded in Figure 5.12. As previously discussed, this rapid evaporation phase was driven by wind-enhanced aerodynamic conductance, which continually replaced moisture-saturated air with dry air. According to the Penman–Monteith framework, this process maintained a high vapour pressure deficit across the soil-atmosphere interface, sustaining latent heat flux and accelerating evaporation rates. This sustained evaporative demand was critical in promoting the elevated crack initiation and propagation observed. Figure 5.12 illustrates that the growth of these desiccation cracks stabilised halfway through this rapid evaporation phase, where only 16% of W4's moisture resources had been evaporated. Although the wind initially acted alone, a fully established, intense network of cracks this early in the drying cycle likely acted as an additional influence on the subsequent evolution of evaporation and shrinkage within W4.

Relating mass loss measurements with microclimate evolution and surface imaging confirms a critical interdependency between wind speed and desiccation cracking, consistent with Penman-Monteith (1965) principles. Initially, wind-driven evaporation maintained a strong vapour pressure deficit, promoting rapid moisture loss. The development of open cracks increased the effective soil surface area and enhanced aerodynamic conductance and latent heat flux. This facilitated accelerated vapour transfer and deeper penetration of drying fronts into the saturated sample interior, sustaining elevated evaporation rates throughout the test duration. The increase in evaporation due to open cracks has been widely quantified in the literature (Tang et al, 2018; Poulsen et al, 2020; Song et al, 2020; Zeng et al, 2020; Poulsen et al, 2021). For instance, Poulsen (2021) observed a 65% rise in total evaporation when comparing non-cracked and cracked soil exposed to the same wind speed.

Visual analysis of evolving surface conditions at high temporal resolution allowed this influence of cracks on the resultant drying patterns to be observed. This is detailed in Figure 5.14A – D, where the yellow contours demonstrate the progressive extension of drying fronts away from the crack walls, observable due to the light-to-dark contrast between the dry and saturated Ampthill Clay, respectively. Poulsen et al. (2020) found

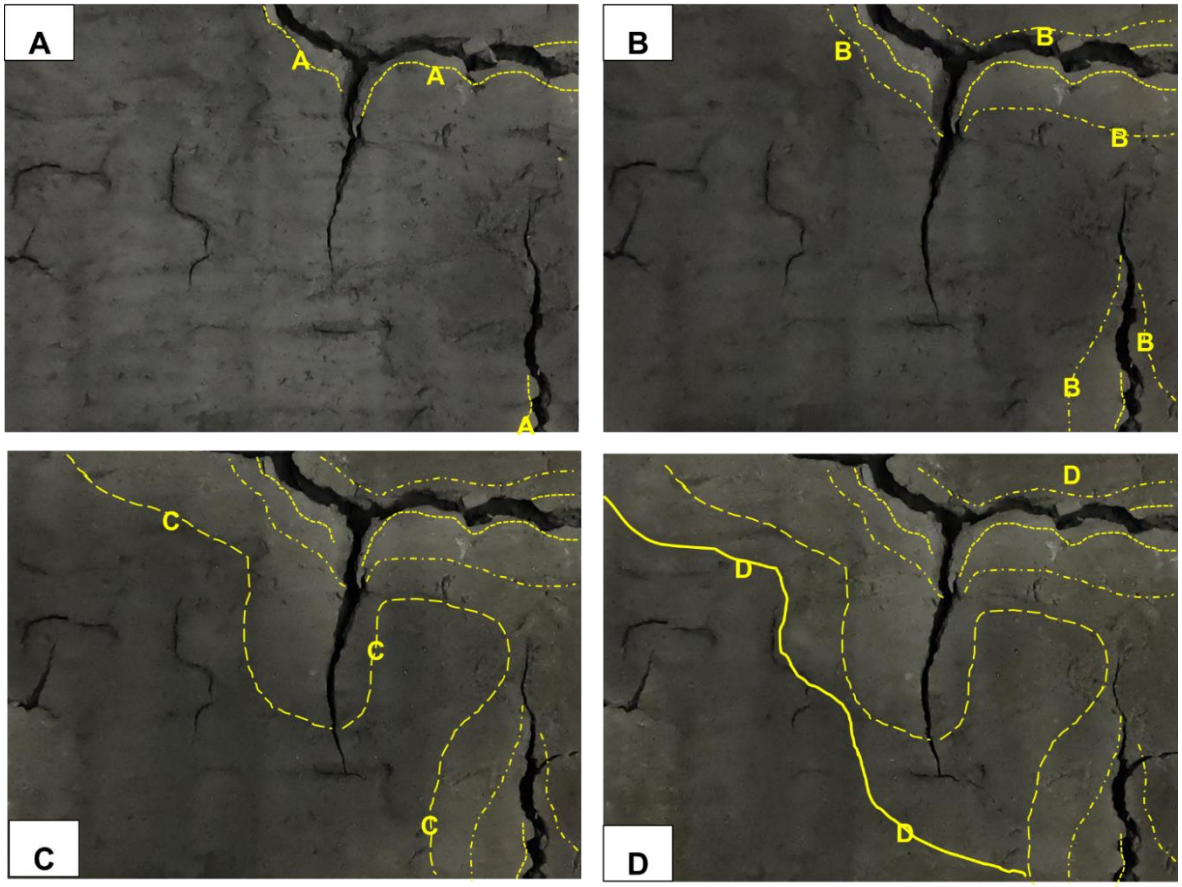

Figure 5.14 :Photographs with annotated contours of drying fronts progressing outward from the crack walls in W4, beginning with Contour A and finishing at Contour D.

that near-surface wind speed increases locally above cracks oriented parallel to the prevailing wind direction, greatly enhancing crack ventilation and evaporation by increasing the aerodynamic conductance. Figure 5.14A – D support these findings, which illustrate drying first appearing and propagating more extensively from the wider cracks located in the top right and oriented parallel to the wind direction. Comparison of the less propagated drying fronts formed around cracks perpendicular to the wind direction further stresses the importance of crack orientation in wind-driven drying.

Figure 5.14A – D illustrates drying fronts progressing through the W4 from the top left toward the bottom right. As discussed earlier, greater crack initiation and propagation occurred in the top right of W4, correlating to locally higher wind turbulence, aerodynamic conductance and vapour exchange with the atmosphere. These results suggest that wind-driven drying could have played a more dominant role in W4's crack evolution, potentially outweighing the role of the internal stress field. The uneven distribution of wind-driven drying and its subsequent interaction with open cracks could create a complex shear and tensile stress field by facilitating heterogeneous

evaporation and shrinkage. Future research should consider mapping stress distribution during wind-driven drying to identify whether such relationships are measurable.

Enhanced moisture flux from open cracks intensified vapour transfer into atmosphere, elevating relative humidity by increasing water vapour concentration in the local microclimate. Figure 5.15 compares CIF evolution with temperature (yellow line) and relative humidity (pink line) during W4. Following the CIF peak, relative humidity continues to substantially decrease, reflecting the sustained efficiency of wind-driven aerodynamic conductance that rapidly replaces humid air with drier air, supported by increased moisture flux from open cracks. The enhanced vapour transfer maintains a high vapour pressure gradient across the soil-atmosphere interface, promoting continued latent heat flux and evaporation. Sustained evaporation seems to have facilitated the transition from a largely tensile stress field to compressible shrinkage during the second half of the rapid mass loss phase. As the specimen detached from the container edges, the evaporative surface area increased, further accelerating moisture loss. The associated volumetric shrinkage generated a moderate reduction in crack aperture until the 70-hour mark. Beyond this point, the reduction in crack width reduced aerodynamic conductance, reducing evaporative flux despite continued energy availability, as evidenced by the slowing of the mass loss rate. Correspondingly, Figure 5.15 demonstrated relative humidity increased as the evaporative energy declined. These observations demonstrate a dynamic coupling between wind-induced aerodynamic conductance and desiccation cracking that collectively governs evaporation rates and microclimate evolution, consistent with the coupled energy and mass transfer processes described by Penman-Monteith theory.

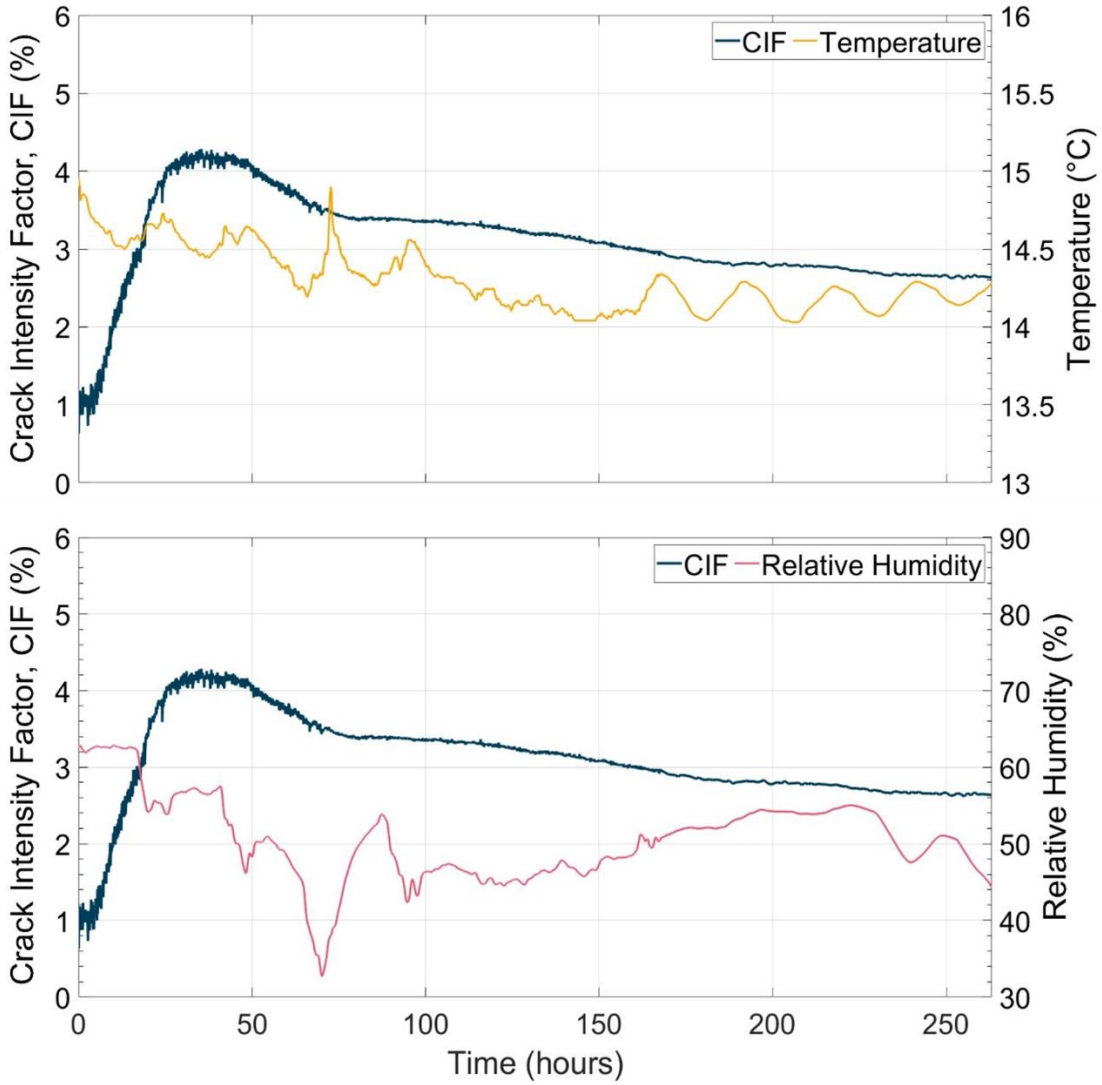

Figure 5.15: Comparison of Crack Intensity Factor (CIF) (%) evolution with air temperature (°C) and relative humidity (%) within the chamber of W4.

A comparison of the CIF evolution within W4 (18 m/s) with that of W3 (4.5 m/s) confirms that wind speed plays a controlling role in the initiation, intensity, and density of the resultant crack network by affecting the aerodynamic conductance. Figure 5.16 plots the cumulative mass loss and CIF development in W3 (4.5 m/s), with annotations referring to the timings of Figure 5.17A – F, which provide photographs of the desiccation crack evolution during W3. The dashed line indicates a period of CIF data loss, resulting from a memory card failure. To connect the data across this interval, a 10-point moving average was calculated and plotted. A comparison of air temperature (°C) and relative humidity (%) evolution within the chamber with CIF development during W3 is provided in Figure 5.18

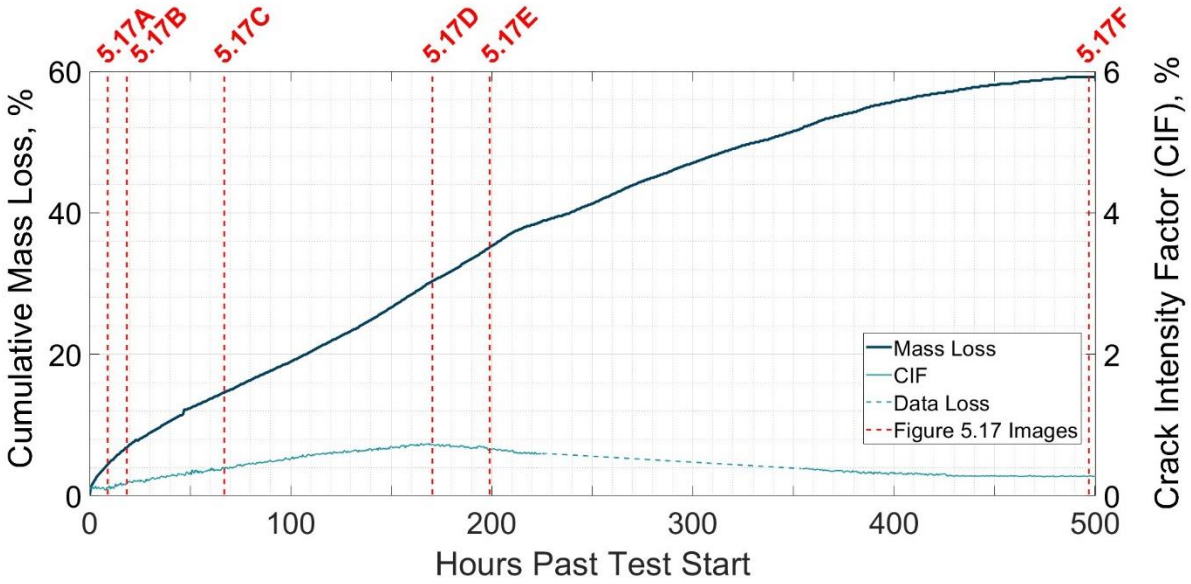

Figure 5.16: Comparison of Cumulative Mass Loss (%) with the evolution of the Crack Intensity Factor (CIF, %) with time for W3 (4.5 m/s). The dashed line represents an area of data loss in CIF data. The temporal occurrence of Figures 5.17A - F are indicated by the red dashed lines.

A wind speed of 4.5 m/s notably increased the mass loss rate, as demonstrated in Figure 5.10. However, it did not reach the critical wind speed threshold previously discussed, which was necessary to sustain the continuous decrease in local relative humidity and maintain the elevated evaporation rates observed in W4. Conversely, evaporation under this wind speed increased relative humidity, reducing vapour pressure gradients and thus lowering aerodynamic conductance and turbulent mass transfer. Desiccation cracks opened parallel and propagated perpendicular to the longer specimen edge after 5 hours of wind exposure, as depicted in Figure 5.17A – C. The CIF reached its peak of 0.75% after 170 hours of monitoring, compared to W4's 4.3% peak achieved after 35 hours. These results align with the diminished evaporative demand in W3, which limited latent heat loss, stabilising the soil's energy balance. The slower removal of moisture reduced the development of suction gradients, which in turn slowed the initiation and propagation of desiccation cracks by decreasing the generation of tensile and shear stresses and strains in W3. As shown in Figure 5.17F, only one primary crack formed in the top right corner of the specimen. The location of this crack further emphasises the importance of increased aerodynamic conductance from concentrated and turbulent airflow in this region, causing localised increases in environmental stress on the specimen as the wind attempts to exit the outlet.

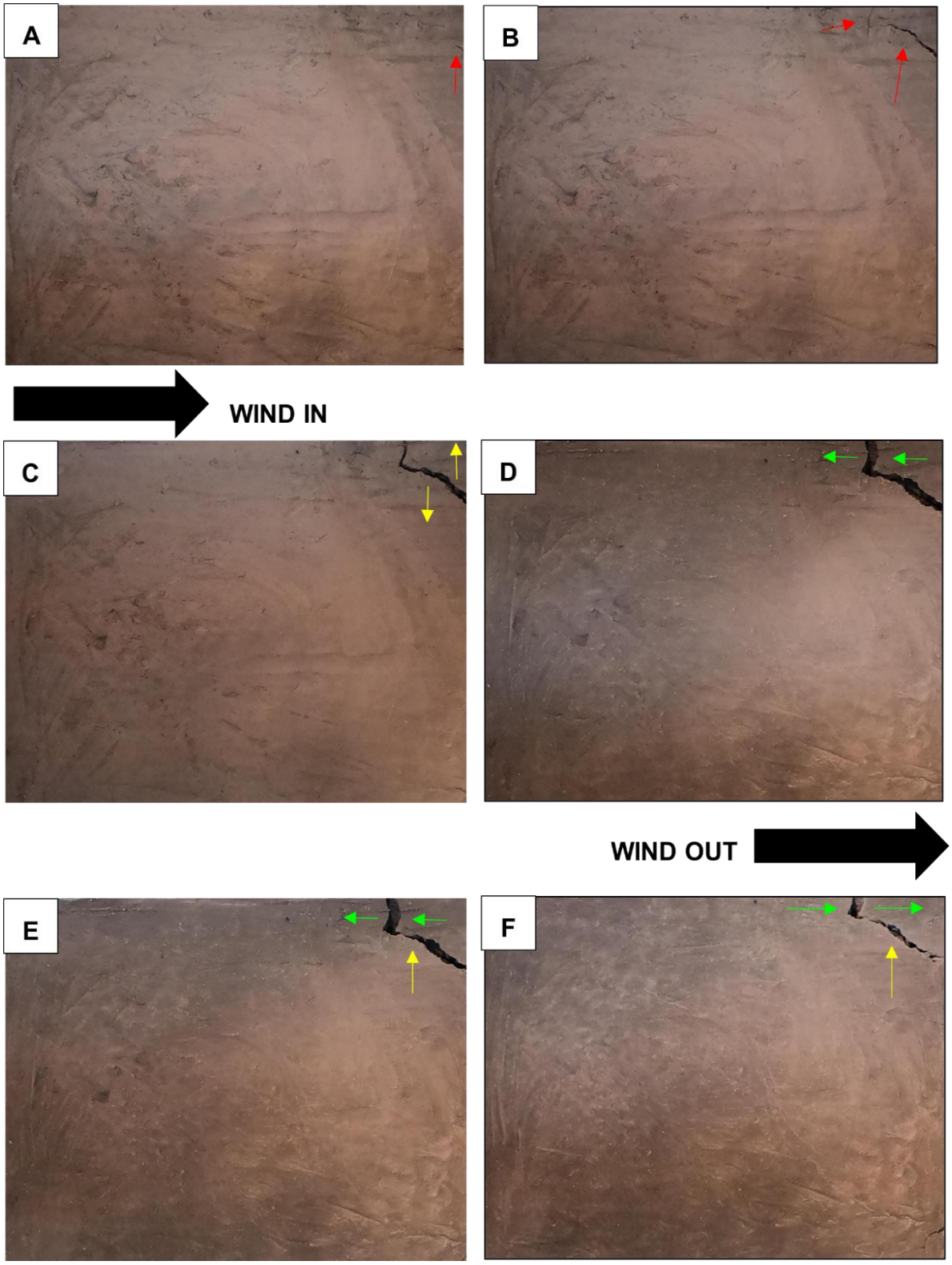

Figure 5.17: Photographs showing the evolution of desiccation cracking within W3 (4.5 m/s) where (A) crack initiation at heterogeneities, (B) Propagation of cracks in length and depth, (C) Widening of cracks parallel to long-edge, (D) Widening parallel to short-edge, (E) Reduction in crack aperture perpendicular to long edge due to shrinkage (F) Reduction in crack aperture perpendicular to short-edge due to shrinkage. The direction of wind flow is indicated on the figure. The temporal occurrences of A – F are annotated within Figure 5.16.

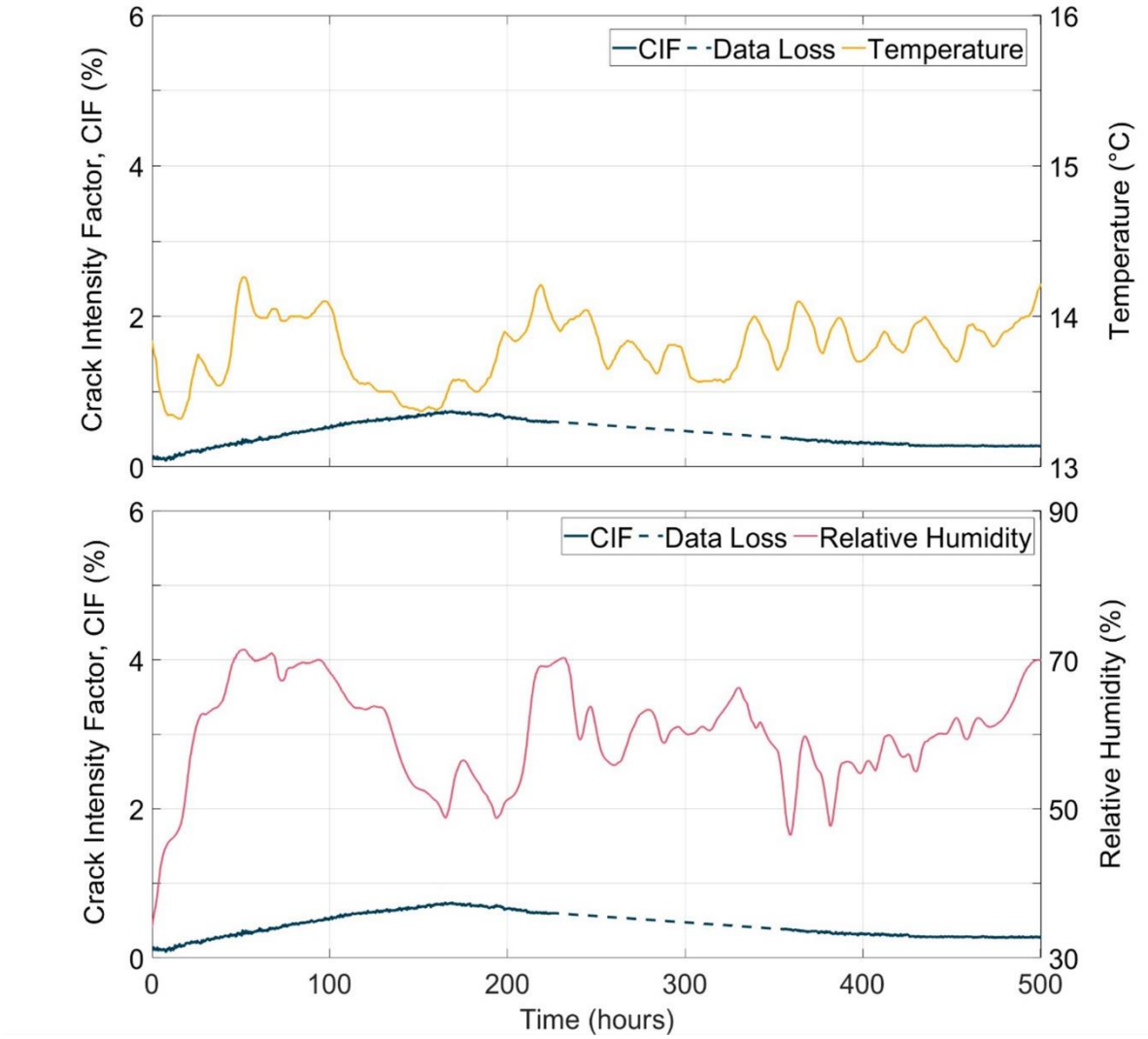

Figure 5.18: Comparison of Crack Intensity Factor (CIF) (%) evolution with air temperature (°C) and relative humidity (%) within the chamber of W3. Dashed lines represent areas of data loss within the CIF records.

After reaching its peak Figure 5.16 illustrates a consistent, gradual decline in CIF toward a plateau of 0.25%. As shown in Figure 5.18, relative humidity and air temperature were lowest during this likely transition between stress regimes, demonstrating where the synergistic relationship between open cracks and wind speed was most efficient in W3. However, this relationship is considerably less effective in W3 due to the comparatively lower crack intensity, which reduces the effective evaporative surface area and limits moisture loss. The absence of W4's elevated period of shrinkage in W3 demonstrates this, with lower suction gradients reducing stress accumulation, likely facilitating a more gradual transition from a largely tensile to a compressive stress field. Therefore, this suggests that the open crack did not have as significant an impact or contribution to the overall mass loss as W4.

Figure 5.18 subsequently demonstrates that both relative humidity and air temperature increase as the crack aperture reduces under volumetric shrinkage. The recorded changes in microclimate conditions demonstrate the addition of moisture from the newly exposed specimen edges during volumetric shrinkage. This initiates a new cycle in which the activation of wind-driven evaporation will not occur until a high enough vapour pressure gradient has been generated across the soil-atmosphere interface. This cyclic pattern of evaporative flux and moisture replenishment persists until mass loss and shrinkage plateau, stabilising the microclimate. This differs greatly from the evaporation behaviour of W4, where continuous removal of humid air prevented such cyclicity. Consequently, these observations further underscore that the efficiency of wind-driven drying is intrinsically controlled by crack intensity and the resultant moisture availability, influencing the soil–atmosphere energy and mass exchange.

Nevertheless, the singular open crack still affected the evolution of drying fronts, with accelerated penetration to depth being localised in the vicinity of the open crack. This was shown to strongly influence W3's pattern of volumetric shrinkage and direction of crack aperture reduction by localising moisture loss and suction (stress) accumulation. Shrinkage initially occurred on the right boundary adjacent to the crack, where drying was most pronounced. This compression seemed to occur concurrently with a possible tensile pull toward the left side, which overall widened the crack aperture on the section perpendicular to the longer specimen edge (Figure 5.17D). As drying continued, shrinkage initiated from the top and bottom of the specimen, resulting in a significant reduction in crack aperture on the crack section parallel to the longer specimen edge (Figure 5.17E). Subsequently, shrinkage from the left side then occurred as this specimen edge detached from the container surface, which partially closed the crack section oriented parallel to the longer specimen edge (Figure 5.17F).

This variable and temporally changing shrinkage behaviour further suggests the development of a complex stress field. This complexity is likely exacerbated by exposure to differing wind characteristics, which locally alter aerodynamic conductance and, consequently, the evaporation rate. Overall, greater shrinkage occurred in W3 than in W4, confirming the influence of wind-driven microclimate dynamics, as described by Penman-Monteith (1965) principles, on the spatial and temporal evolution of the stress field within embankment fill. This supports the understanding that exposure to high winds can significantly exacerbate desiccation cracking processes in infrastructure embankments.

Despite the reduced effect on evaporation and desiccation within the Ampthill Clay, the wind speed used in W3 is a more accurate representation of the average monthly wind speed in Newcastle upon Tyne, UK. Therefore, the moderate elevation in evaporation and crack initiation recorded at 4.5 m/s remains significant for accelerating drying cycles within infrastructure embankments. It is also important to consider how evaporation and desiccation could be amplified within infrastructure embankments at a more advanced stage of deterioration. Unlike these relatively intact specimens exposed to a single drying cycle, aged embankments exhibit reduced capacity to maintain saturation due to accumulated microstructural deterioration, leading to faster suction generation and earlier crack initiation under lower drying intensities. This diminished hydraulic resilience likely accelerates desiccation initiation, exacerbating degradation beyond what is observed in the controlled experiments.

Overall, the results presented here demonstrate how increasing aerodynamic conductance through adjusting wind speed impacts desiccation cracking and their subsequent synergistic relationship sustains rapid evaporation. These observed relationships are fundamental to the understanding of weather-driven deterioration processes within infrastructure embankments. The context of these results is of particular relevance upon considering UKCP18's projections of an increased frequency of windstorms occurring with climate change (Met Office, 2023). Emphasising the emerging importance and relevance of studies on wind-driven drying and desiccation of infrastructure embankments as an area of consideration in the long-term management of these key assets.

5.4 Subsurface Characterisation of Desiccation Cracking in Compacted Fill

The Crack Intensity Factor (CIF) is one-dimensional, solely assessing the surface expression of desiccation cracks and neglecting the subsurface components that play critical roles in developing weather-driven deterioration within infrastructure embankments. Long-term monitoring of this cyclic deterioration process within the lysimeter slope (Section 4.2) demonstrated the limitations of the CIF as a measure of cracking severity. Greater CIF values were attained for (A) a surface-extensive, superficial winter crack network (Figure 5.19A), compared to (B) a sparsely distributed yet substantially wider and deeper summer crack network (Figure 5.19B). Therefore, without considering the subsurface component, these results suggest that the cracking severity in (A) was greater than that of (B).

However, the long-term hydrological monitoring that accompanied the CIF indicated that (B) had more pronounced short- and long-term impacts on the deterioration of the lysimeter slope's hydromechanical properties. Therefore, importantly absent from a CIF evaluation is the consideration that cracks with greater volume, depth, and connectivity in the subsurface greatly enhance infiltration and evaporation, intensifying dry-wet cycles and the extent of microstructural degradation. Over time, a progressive extension of the active, weathered zone occurs within an embankment. This is characterised as a zone of weakened mechanical strength, exhibiting a greater likelihood of developing shallow or deep-seated failures. With cracking severity projected to increase under climate change extremes (Loveridge et al., 2010; Bordoloi et al., 2020; Stirling et al., 2021), a transition into two- (2D) or ideally three-dimensional (3D) characterisation of crack propagation mechanisms is required. From this, a more comprehensive assessment of how weather-driven deterioration develops within infrastructure embankments could be achieved.

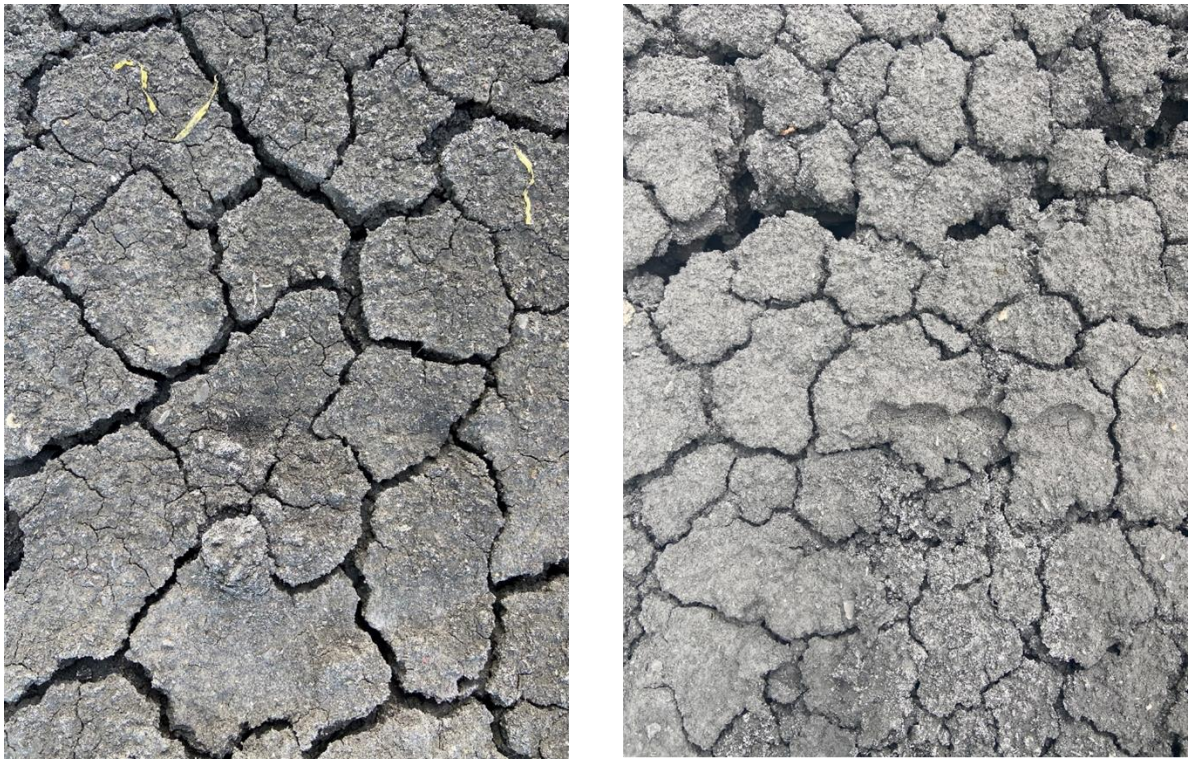

Figure 5.19: Photographs illustrating the (A) surface extensive yet superficial winter crack network and (B) sparsely distributed yet substantially wider and deeper summer crack network. Similar Crack Intensity Factors (CIF) were attained for these images despite suspected differences in subsurface crack depth and volume.

Existing literature has explored various destructive and non-destructive techniques to quantify desiccation cracking in 2D or 3D. Destructive techniques are usually in 2D,

involving visual observation of sample cross-sections (Yesiller et al., 2000; Leonard et al., 2003) or excavation of trenches in the field (Konrad & Alanazi, 2011). However, laser devices have also obtained a 2D profile (Sanchez et al., 2013). Non-destructive techniques that allow 3D characterisation include Ground Penetrating Radar (GPR) (Levatti et al., 2017), X-ray computed tomography (X-ray CT) (Julina & Thyagaraj, 2019; Tang et al., 2019), structured light scanning (Zhuo et al., 2022) and 3D laser scanning (Hirmas et al., 2016). While these techniques have provided valuable insights into subsurface desiccation processes, their application to samples representative of infrastructure embankment fill is limited (Julina & Thyagaraj, 2019; Zhuo et al., 2022). Typically, these methods are applied to smaller-scale, homogeneous slurry specimens (Leonard et al., 2003; Sanchez et al., 2013; Levatti et al., 2017; Tang et al., 2019) which exhibit different desiccation behaviour than compacted, inherently heterogeneous embankment fill.

Therefore, to gain insight into the 2D development of subsurface cracks within compacted, heterogeneous fill material, a resin was poured into the Ampthill Clay samples used in Section 5.3 during the investigation of wind-driven desiccation. Cross sections were then taken, and image processing of the subsurface crack networks was conducted. Utilising these samples also provided additional insights, enabling the effect of varying wind speed on subsurface desiccation to be determined. Furthermore, the penetration depth and pattern of the resin could help determine the potential preferential flow pathways that desiccated soil with surface cracks may provide. Although this method is limited in application due to its destructive nature, it presents a first-step approach to improving the characterisation of crack development within soil conditions comparable to real infrastructure embankments composed of compacted fill.

5.4.1 Subsurface Desiccation Under High Wind Speeds

Figure 5.20 illustrates the approximate locations of the cross-sections CS4.1 – CS4.8 taken through W4 (18 m/s wind speed) at 45 mm intervals to analyse the spatial distribution of subsurface desiccation cracking. Photographs of the corresponding cross-sections are provided in Figure 5.21, demonstrating the resin's effectiveness in highlighting the sub-surface crack network. The significant finding of these cross-sections is the presence of an extensive crack network of high connectivity within the subsurface region of W4. The connectivity of the cracks, highlighted by the reach of resin infiltration, underscores the importance of understanding subsurface desiccation

from a hydrological perspective. If the resin represented infiltrating rainwater, this crack network would significantly promote preferential flow, potentially accelerating weather-driven deterioration in infrastructure embankments.

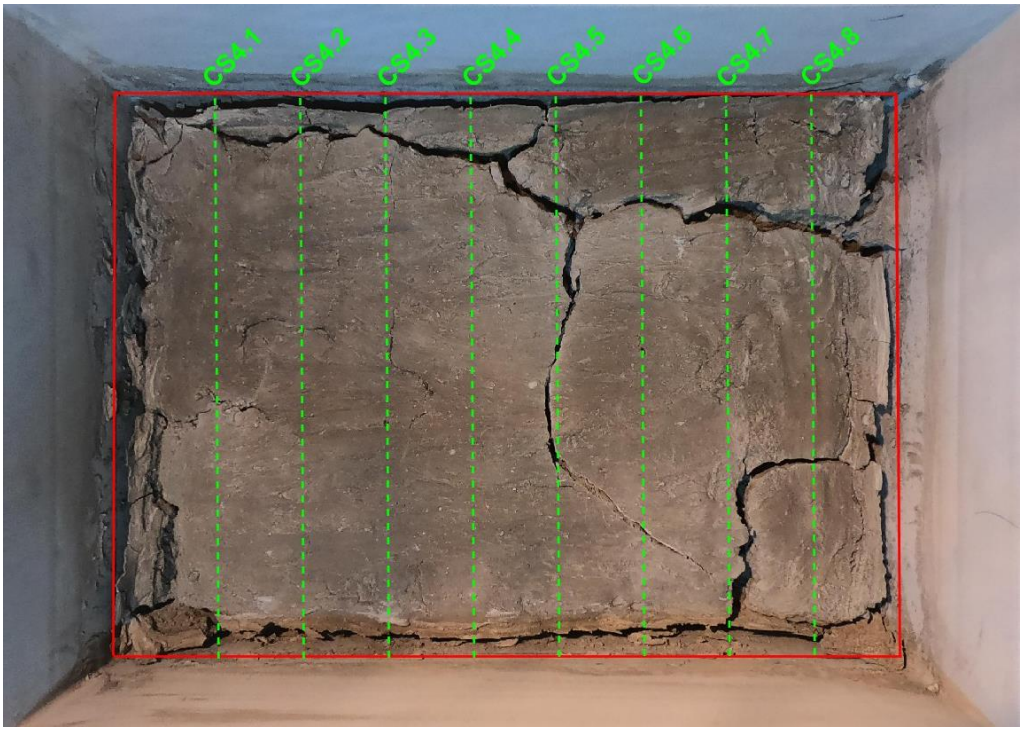

Figure 5.20: Approximate locations of cross sections CS4.1 to CS4.8 taken at 40 mm intervals through sample W4 after it was exposed to an 18 m/s wind speed. The photograph demonstrates the end state of surface desiccation at the termination of test W4, and cross-sections were taken post-curing of the resin.

Figure 5.21 provides a qualitative measure of the complexity that sub-surface desiccation crack networks can exhibit. Desiccation cracks that daylight on the surface of W4 are initially oriented perpendicular to the surface in the upper layer. Further examination of these cracks deeper within the sample shows they transition to an almost parallel alignment relative to the specimen surface. Each sample comprises four 22.5 mm layers with three distinct boundary interfaces with characteristically lower cohesion and mechanical strength. As cracks tend to propagate along the path of least resistance, the weakened boundaries between the compacted layers can provide such criteria. Therefore, it is suggested that these layer boundaries may influence the crack propagation direction of all samples used in this experiment and may lead to the observed shifts in orientation during crack formation. Furthermore, sub-parallel or oblique cracks could represent displacement or distortion of these layers by the simultaneous formation of shear and tensile stresses (Zeng et al., 2020). These stresses form as the sample undergoes heterogeneous shrinkage in response to

spatially and temporally variable moisture loss and suction (stress) generation during evaporation. However, confirming both suggested hypotheses would require further investigation into post-drying changes in soil structure.

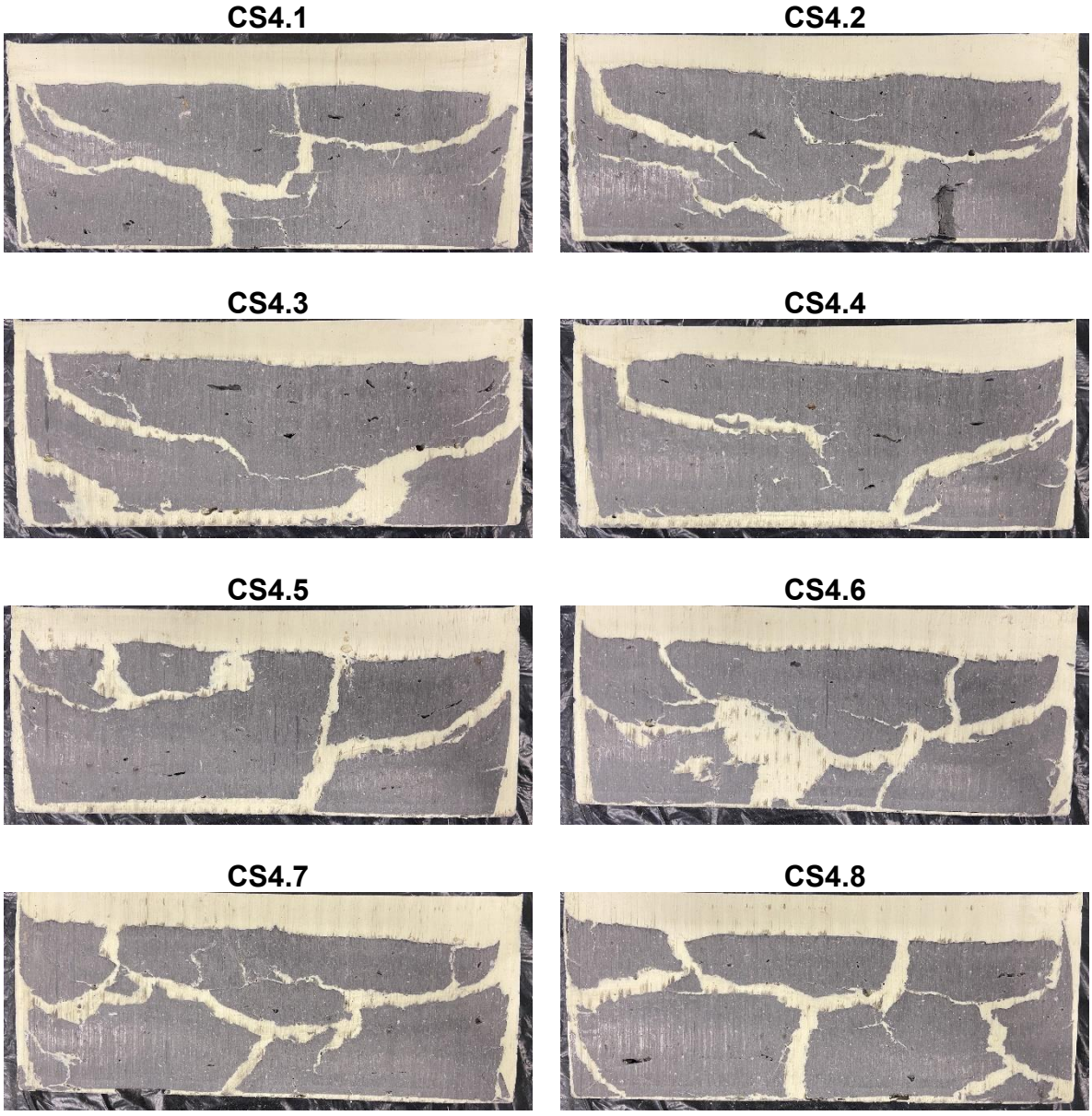

Figure 5.21: Photographs of cross-sections CS4.1 - CS4.8 taken through W4 post-resin-curing, highlighting the distribution of subsurface desiccation. Zones of resin can be distinguished by their yellow colour.

Importantly, desiccation cracks are additionally initiated either within the sample interior or from the base of the specimen. However, distinguishing between these modes is impossible without a temporal record of crack formation. Nevertheless, these results highlight the inadequacy of the CIF in representing the sub-surface complexities of desiccation crack formation within compacted fill. Although container effects are not directly relatable to real infrastructure embankments, the concept of a change in

mechanical strength, either at the boundaries between compacted layers or other buried infrastructure, is relevant. Consequently, if the rate of drying, suction gradients and magnitude of tensile stress accumulation are sufficiently high, sub-surface initiation of desiccation could occur within infrastructure embankments.

Intersection angles between subsurface desiccation cracks appear to deviate from the 90 degrees recorded at the surface. Both 90-degree (e.g. CS4.1 in Figure 5.21) and oblique (e.g. CS4.4 in Figure 5.21) interactions are visible within the subsurface crack network. These results support the earlier suggestion that a complex and highly dynamic stress field with both tensile and shear components may be operating in W4 under exposure to heterogeneous wind characteristics, which vary aerodynamic conductance as per the Penman-Monteith (1965) framework. This effect would be particularly pronounced in the depth dimension, where gradual propagation of drying fronts enhances suction gradients, generating higher shear stresses and strains which intensify cracking. Additionally, the distribution of open cracks and their orientation relative to the prevailing wind direction was shown in Section 5.3.2 to exacerbate aerodynamic conductance and enhance subsurface evaporation.

To quantify subsurface desiccation, the cross-section images in Figure 5.21 were processed using MATLAB to calculate the Crack Intensity Factor (CIF), following the method described in Section 3.4.4. The CIF results for each cross-section taken through W4 are provided in Figure 5.22. Reviewing the graph, a notable decrease in CIF occurs with increasing distance from the short container edges, with the lowest values recorded within cross sections CS4.4 and CS4.5. The higher CIF values in exterior cross-sections (CS4.1 – 4.3 and CS4.6 – 4.7) could be attributed to poorer cohesion at the container-fill interface, resulting in lower tensile strength and higher desiccation susceptibility. Difficulty compacting fill near the container edges could further exacerbate this susceptibility, creating heterogeneous distributions of mechanical strength and porosity. Heterogeneity in these properties increases the likelihood of uneven drying and shrinkage, accumulating tensile stress and initiating desiccation. However, this spatial contrast in subsurface desiccation could also result from slower propagation of drying fronts to the sample interior compared to an exterior zone, which is more exposed as the edges detach from the container as the sample shrinks. This would lead to a more gradual and uniform moisture loss, reducing suction gradients and stress accumulation that drive desiccation crack initiation.

Further spatial distributions in CIF are observed in Figure 5.22, with overall higher values recorded within cross-sections on the specimen's right side (CS4.5 – S4.8) compared to the left (CS4.1 – 4.4). Cross-sections CS4.1 (left) and CS.4.8 (right) in Figure 5.21 visually depict this contrasting behaviour, with the right-side cross-sections displaying a more extensive and interconnected subsurface network of desiccation cracks. These results are consistent with the surface CIF findings presented in Figure 5.13, where a greater intensity and density of desiccation cracks were recorded on the specimen's right side. This further demonstrates that increased wind turbulence enhances aerodynamic conductance (Penman, 1948; Monteith, 1965), facilitating more efficient vapour transfer across the soil–atmosphere interface. As a result, evaporation is accelerated and desiccation cracking intensified. Furthermore, this higher surface CIF, and parallel orientation of cracks to the wind direction encouraged crack ventilation, promoting faster propagation of drying fronts through the subsurface on the right. Theoretically, both these processes would generate high differential tensile and shear stress through enhanced suction gradients through the subsurface, fuelling greater initiation and propagation of desiccation cracks.

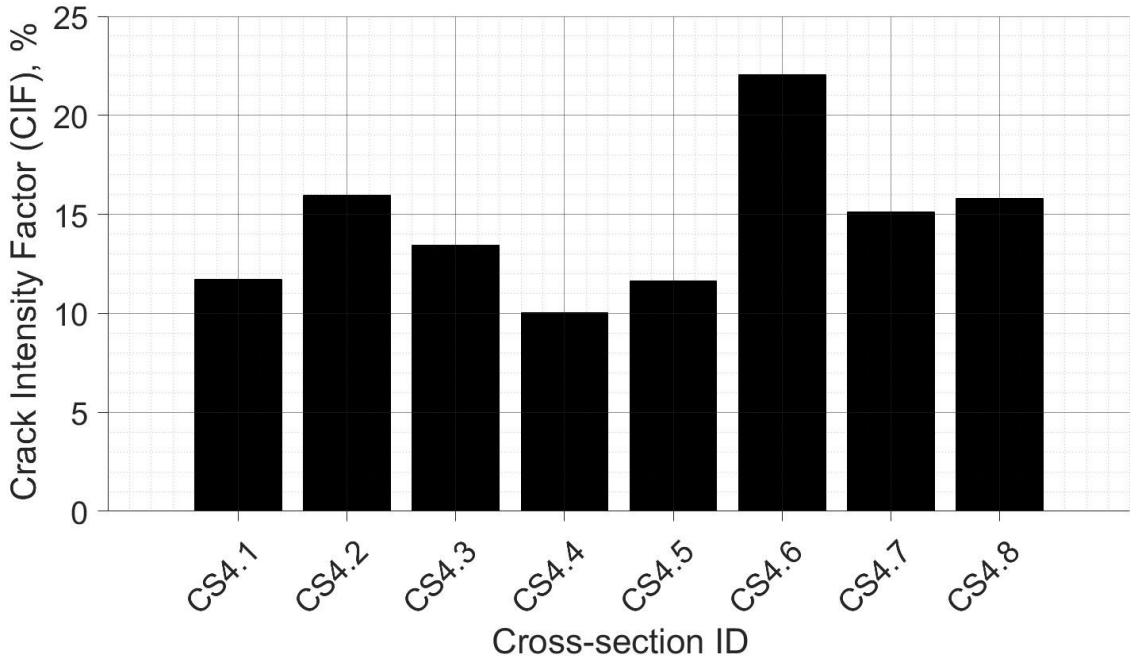

Figure 5.22: Plot of Crack Intensity Factor (CIF) (%) for cross sections CS4.1 to CS4.8 taken in W4. CIF was calculated through image processing of the photographs displayed in Figure 5.21 using the technique outlined in Section 3.4.4. A right-left side and interior-exterior divide in CIF is visible.

5.4.2 Subsurface Cracking Under Low to Moderate Wind Speeds

To compare the sub-surface development of desiccation cracks under the different wind speeds, the resin was also poured into W3 (4.5 m/s) and W2 (1.5 m/s) and cross sections were taken at the same 45 mm interval as W4. Figure 5.23 illustrates the locations of the cross sections taken in W3 and, importantly, demonstrates the occurrence of only one surface crack in the upper right corner of the specimen. Figure 5.24 provides the corresponding photographs illustrating the network of subsurface desiccation for each cross-section taken through W3.

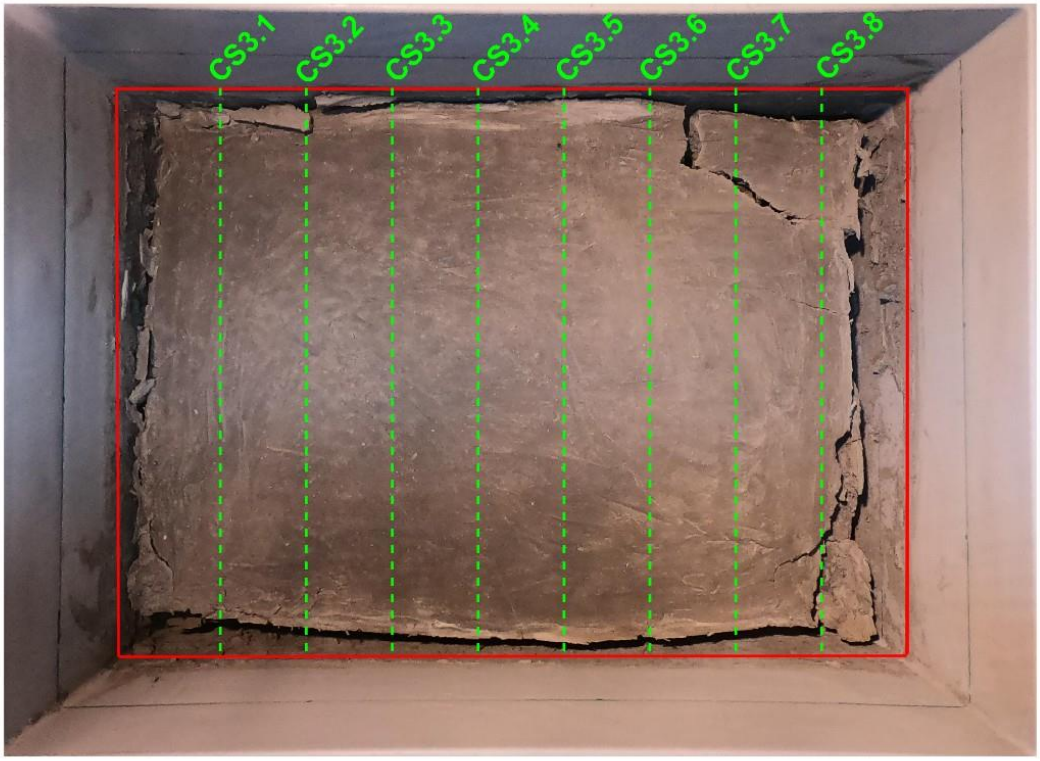

Figure 5.23: Approximate locations of cross sections CS3.1 to CS3.8 taken at 40 mm intervals through sample W3 after exposure to a 4.5 m/s wind speed. The photograph demonstrates the end state of surface desiccation at the termination of test W3, and cross-sections were taken post-curing of the resin.

These images evidence the presence of subsurface cracking throughout the sample, not isolated to the far-right cross-section as the surface expression of cracking would suggest. The subsurface crack network of W3 shares similarities with W4 in that cracks have propagated parallel, perpendicular, and obliquely to the specimen surface. Furthermore, variation in crack intersection angles is also evident, with both these features supporting the prevalence of a complex stress field. The overall distribution of cracking severity is also comparable, with more cracks in the exterior (CS3.1 – 3.2 and CS3.7 – 3.8) cross sections than those in the interior (CS3.3). The specimen's

right side exhibits a more extensive network of cracks compared to the left, consistent with surface desiccation distribution. This disparity underscores the persistent effects of wind intensity and turbidity on aerodynamic conductance. These elements, in turn, influence the subsurface moisture content and suction gradients, which are responsible for initiating desiccation.

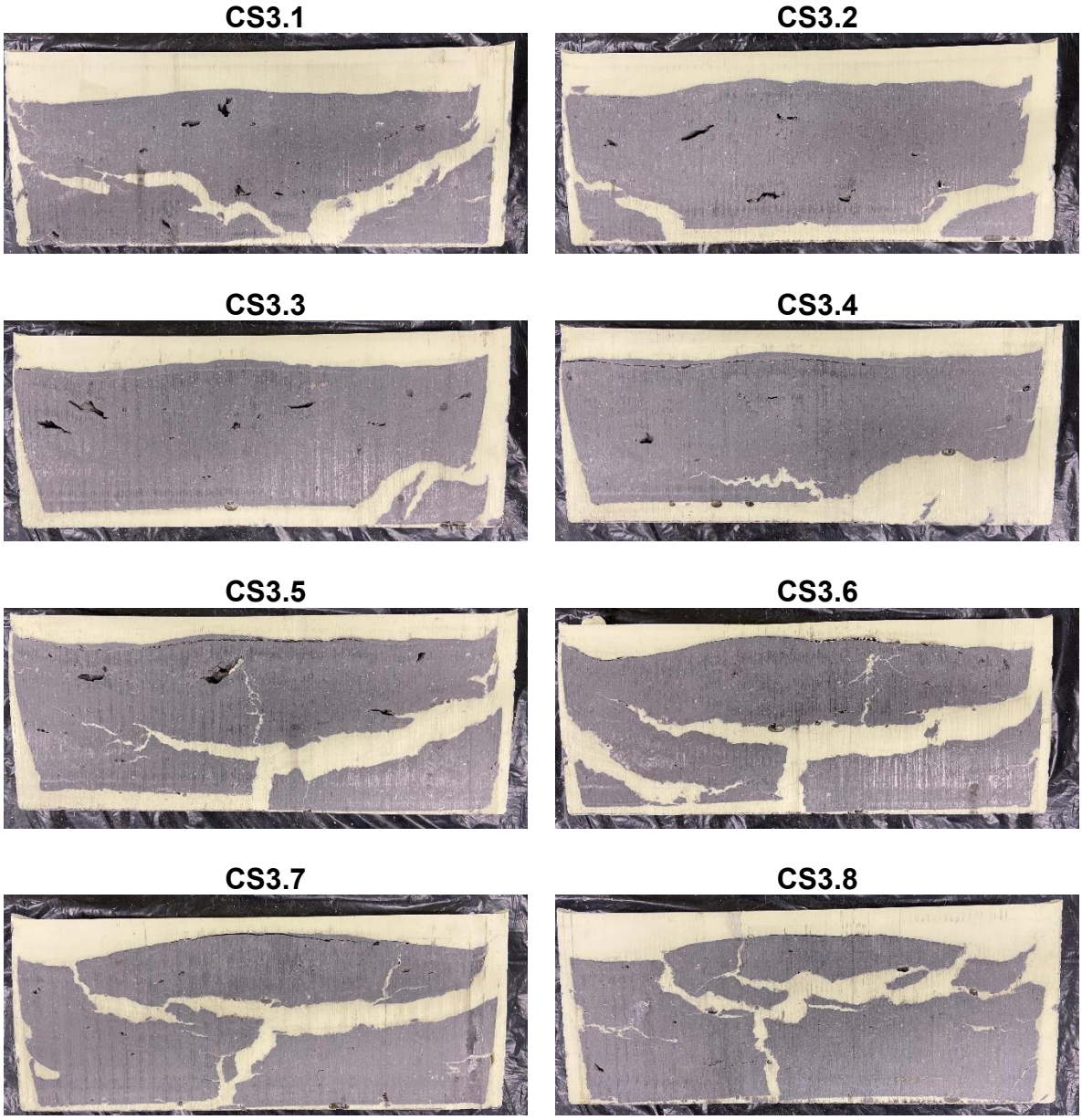

Figure 5.24: Photographs of cross-sections CS3.1 – CS3.8 taken through W3 post-resin-curing, highlighting the distribution of subsurface desiccation. Zones of resin can be distinguished by their yellow colour.

However, distinct differences in the number and nature of cracks in W3's subsurface are observed compared with W4. The CIF results for each cross-section taken through W3 are presented in Figure 5.25, with the right-left side divide in CIF appearing more pronounced compared to W4 (see Figure 5.22). This can be attributed to two factors.

First, the severity of desiccation cracking on W4's left side is considerably greater than in W3, and the CIF contrast with the right side is less notable. Therefore, higher wind speeds enhance aerodynamic conductance and latent heat flux, increasing evaporation efficiency across the soil-atmosphere interface as the Penman-Monteith (1965) equation predicted. This accelerates moisture loss and suction generation, steepening suction gradients, and induces higher tensile and shear stress differentials, thereby promoting greater strain and more widespread desiccation cracking. Secondly, W4's network contains numerous well-connected cracks, whereas W3's has a few large cracks that extend through the subsurface and appear wider. However, their greater apparent width may be due to the angle at which the cross-section intersects the sub-parallel crack, causing an overestimation of the CIF values and a greater right-left side contrast in W3. This is most likely the case for the expanse of resin visible in CS3.4 within Figure 5.24 and, therefore, should be considered a limitation of this technique requiring further investigation.

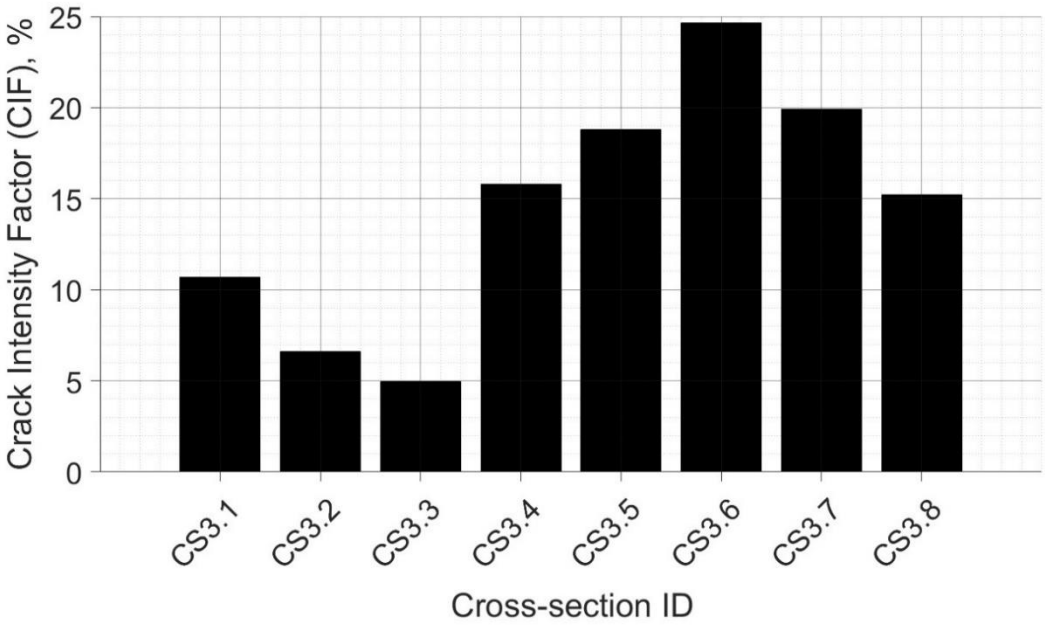

Figure 5.25: Plot of Crack Intensity Factor (CIF) (%) for cross sections CS3.1 to CS3.8 taken in W3. CIF was calculated through image processing of the photographs displayed in Figure 5.24 using the technique outlined in Section 3.4.4. A right-left and exterior-interior divide in the CIF results is visible.

The locations of the cross-sections taken through W2 (1.5 m/s) are shown in Figure 5.26, illustrating the absence of surface desiccation cracks. Corresponding photographs of W2's cross-sections (CS2.1 – CS2.8) are provided in Figure 5.27, which conversely reveal the presence of a subsurface desiccation crack network. The nature of desiccation cracks is similar to W3, displaying a few larger cracks that expand

the breadth of the specimen. Additionally, the range of propagation orientations and intersection angles are similar, and the right-side crack within CS2.1 shows potential evidence of crack deflection along compacted layer boundaries.

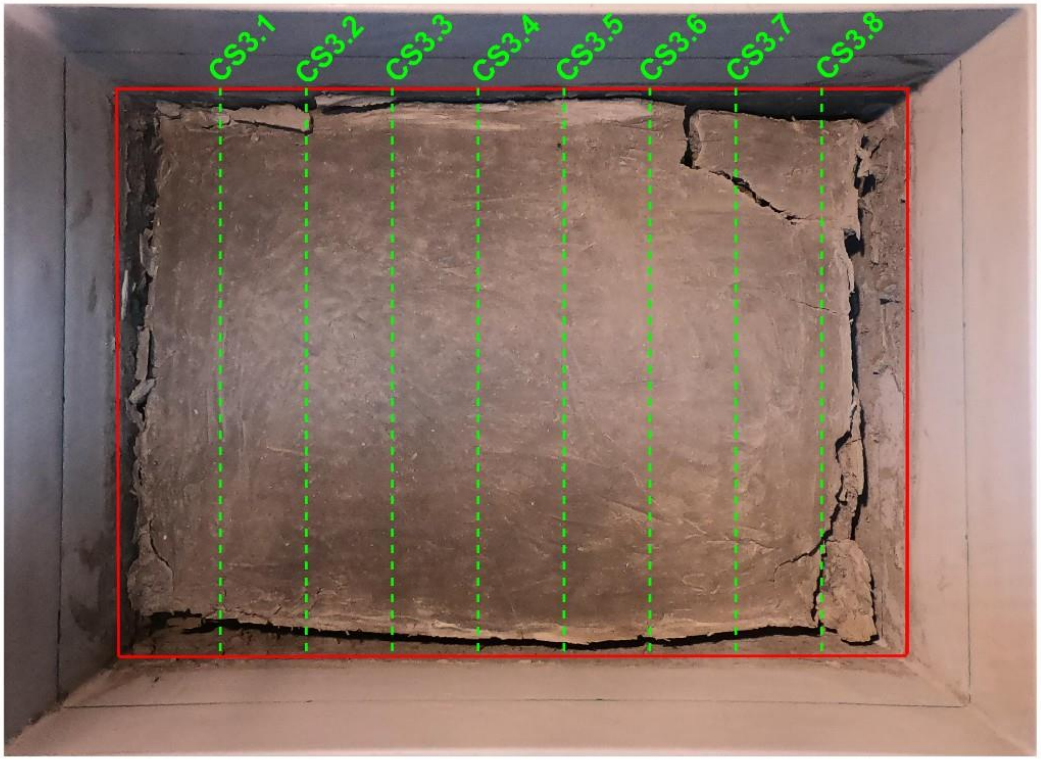

Figure 5.26: Approximate locations of cross sections CS3.1 to CS3.8 taken at 40 mm intervals through sample W3 after exposure to a 4.5 m/s wind speed. The photograph demonstrates the end state of surface desiccation at the termination of test W3, and cross-sections were taken post-curing of the resin.

Variations in resin fill thickness at the cross-section edges also may insinuate that shrinkage was not uniform. These observations suggest that heterogeneity plays a crucial role in generating and shaping the evolution of a complex stress field during evaporation. The diverse cracking patterns are likely influenced by varying material properties, which affect the fill's water retention behaviour and thereby regulate the onset and progression of soil shrinkage and crack propagation

The nature of external environmental stressors can amplify this heterogeneity's baseline effect on desiccation cracking. Illustrating this, W2's crack network is less extensive than observed at higher wind speeds (W3 and W4), confirming that the aerodynamic conductance component of evaporation is a key control of cracking severity at the surface and subsurface level. Features recorded in W3 and W4, including greater desiccation in exterior cross sections and a left-right side divide in

cracking severity, remain consistent in W2's subsurface. The distribution of CIF values in Figure 5.28 for W2's cross-sections supports this, with the expansion of the interior low CIF zone (CS2.3 – 2.5) and the highest CIFs within the far-right cross-sections (CS2.7 – 2.8).

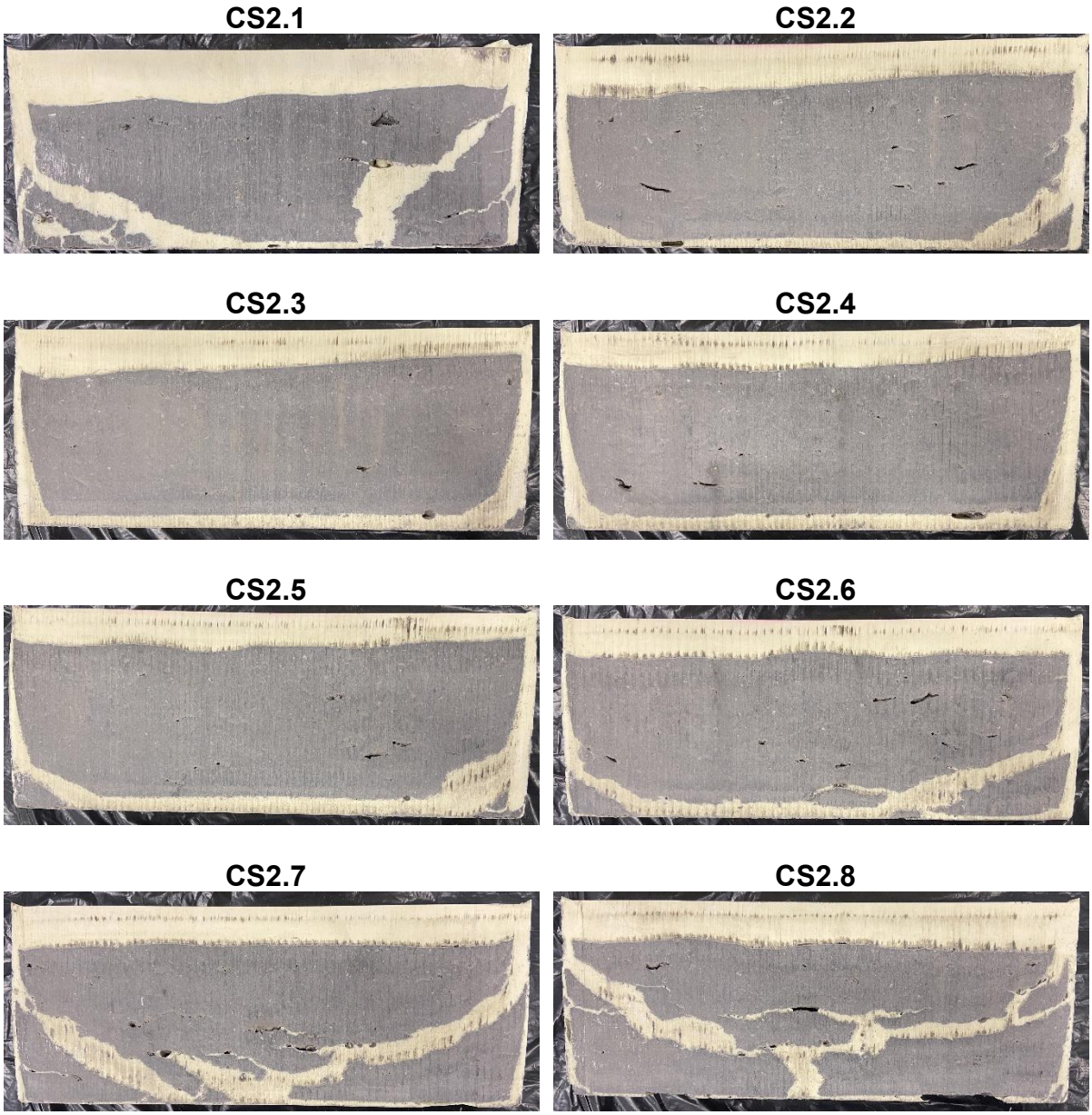

Figure 5.27: Photographs of cross-sections CS2.1 – CS2.8 taken through W2 post-resin-curing, highlighting the distribution of subsurface desiccation. Zones of resin can be distinguished by their yellow colour.

Therefore, the effects of greater right-side aerodynamic conductance under higher wind intensity and turbidity on sub-surface desiccation remain persistent, even though overall moisture fluxes and suction gradients are lower. For infrastructure embankments, subsurface desiccation occurring at low wind speeds and without surface cracks is significant, as it obscures the soil structural deterioration manifesting

at depth. Therefore, without a multi-dimensional analysis of embankment desiccation cracking, a full assessment of the integrity and stability is not accurately achievable.

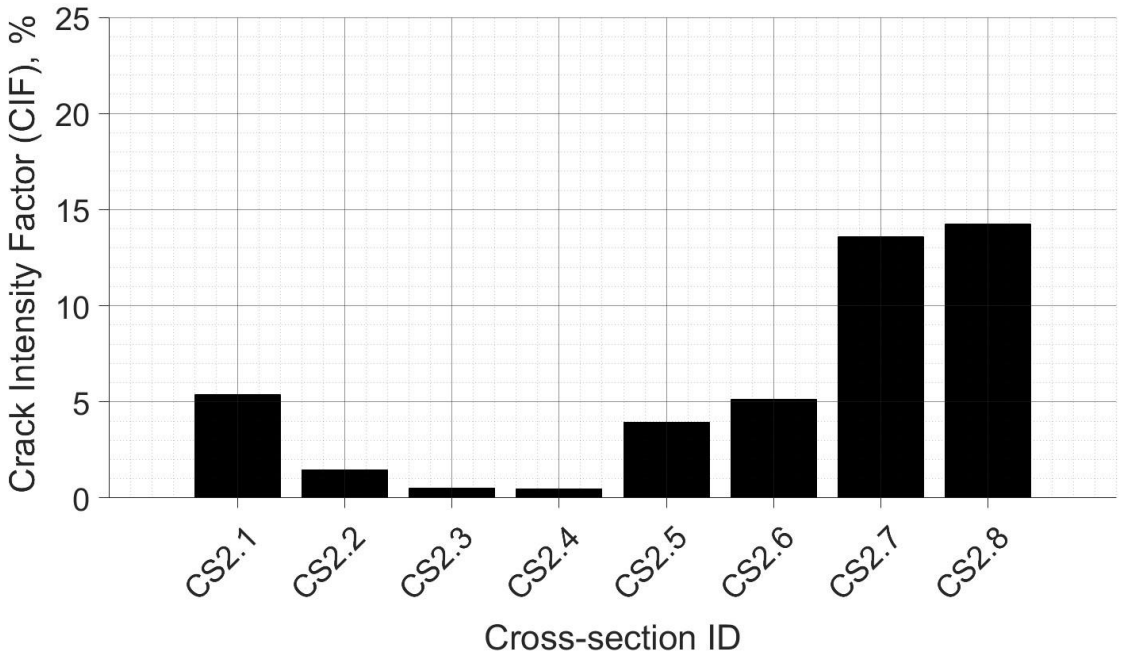

Figure 5.28: Plot of Crack Intensity Factor (CIF) (%) for cross sections CS2.1 to CS2.8 taken in W2. CIF was calculated through image processing of the photographs displayed in Figure 5.26 using the technique outlined in Section 3.4.4. A right-left and exterior-interior divide in the CIF results is visible.

5.4.3 Subsurface Desiccation Under No Wind

Figure 5.29 shows the surface state at the end of W1 (no wind) and highlights the locations where cross sections CS1.1 – CS1.8 were taken. Visual depictions of CS11 – CS1.8 are also provided in Figure 2 to allow for a qualitative assessment of subsurface desiccation. It is important to highlight that the subsurface conditions captured by the cross-sections represent specimen W1 post-malfunction of the temperature-controlled room. Therefore, exposure to higher temperatures during drying likely intensified subsurface desiccation by increasing the evaporative demand and enhancing vapour pressure gradients. The specific contribution of this temperature increase cannot be isolated from other interacting variables when interpreting the results. Nevertheless, distinct differences in subsurface desiccation are recorded without wind exposure and will be discussed.

Surface desiccation did not occur during W1, only substantial volumetric shrinkage, as illustrated in Figure 5.28. In the cross-section images (Figure 5.30), greater volumetric

shrinkage in W1 compared to W2 – W4 (see Figures 5.21, 5.24 and 5.27) is supported by a larger resin thickness at the specimen edges. The thickness of this resin infill increases toward the exterior cross sections (CS1.1 – 1.2 and CS 1.7 – 1.8), representing the extent of volume loss due to shrinkage. Within the cross-sections of W2 (Figure 5.27), W3 (Figure 5.24) and W4 (Figure 5.21), greater edge shrinkage is associated with cross-sections with no or limited desiccation and are primarily located in the specimen interior. This suggests that lower exposure to evaporative forcing, reduced temperature and vapour pressure gradients, or more uniform initial compaction in the specimen interior slowed the advance of drying fronts. As a result, lower suction gradients and more homogeneous shrinkage occurred, limiting differential stress accumulation and reducing the likelihood of crack formation. These observations are consistent with coupled energy–mass transfer and stress–strain response principles in unsaturated soils.

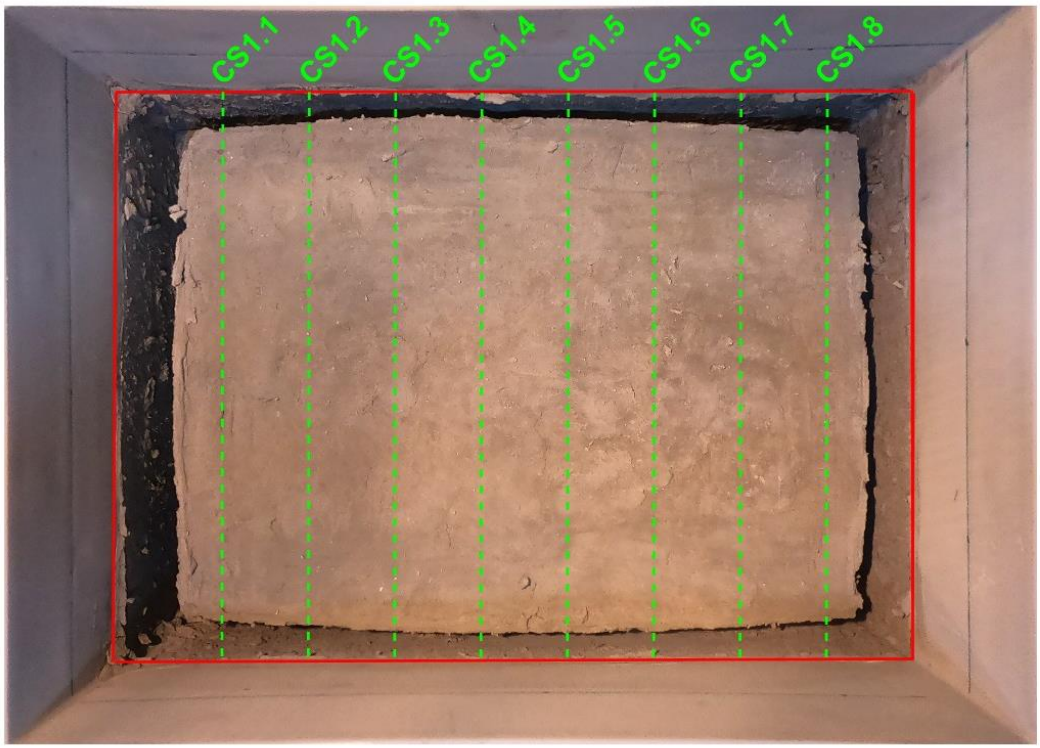

Figure 5.29: Approximate locations of cross sections CS1.1 to CS1.8 taken at 40 mm intervals through sample W1. This sample was exposed to no wind. The photograph demonstrates the end state of surface desiccation at the termination of test W1, and cross-sections were taken post-curing of the resin.

Importantly, similar to W2, W1's cross sections reveal that desiccation cracking occurred in the subsurface despite its absence on the specimen's surface. The temporal formation of these cracks, in terms of pre- or post-malfunction of the

temperature-controlled room, is unknown. However, the intensity of subsurface cracking remains considerably lower than in W2–W4, consistent with predictions from the Penman–Monteith (1965) framework. The reduced aerodynamic conductance and lower moisture flux rates result in weaker evaporative driving forces, leading to more gradual development of suction and hydraulic gradients. Consequently, tensile and shear stress and strain accumulation are slower and less intense, limiting the extent and severity of crack propagation.

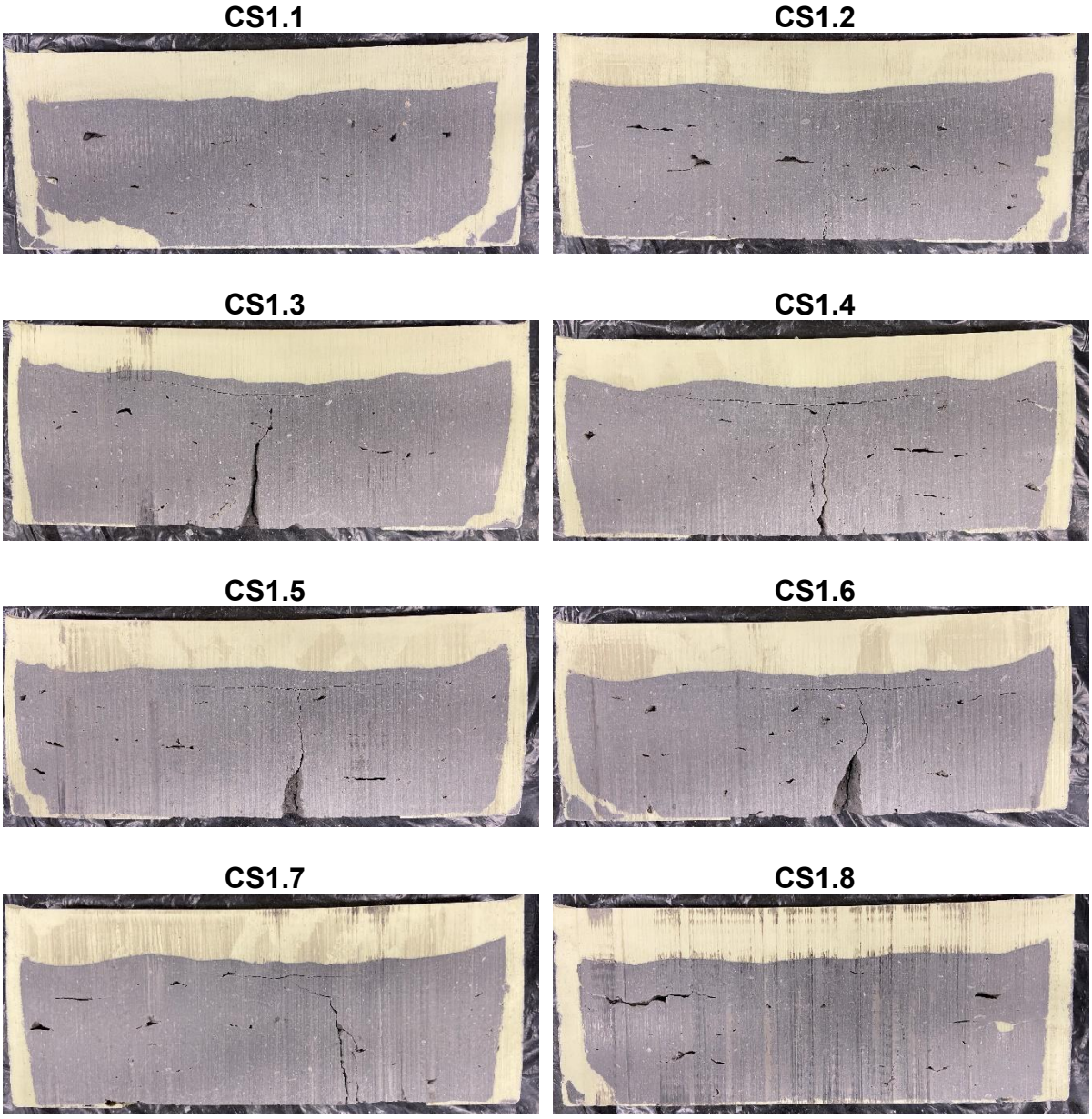

Figure 5.30: Photographs of cross-sections CS1.1 – CS1.8 taken through W1 post-resin-curing, highlighting the distribution of subsurface desiccation. Zones of resin can be distinguished by their yellow colour.

Cracks highlighted by the resin are mainly concentrated at the base corners of the specimen, cutting across at oblique angles, as seen in CS1.1 – 1.2 and CS1.5 – 1.8 of Figure 5.30. Other researchers have observed similar subsurface crack patterns (Zeng et al., 2020), attributing their formation to the simultaneous production of tensile and shear stresses under heterogeneous drying and shrinkage. Therefore, these results support the suggested hypothesis that a complex and continuously evolving stress field operates in compacted fills irrespective of the level of environmental stress. Small cracks originating from and propagating perpendicular to the short container edge are also present. The prevalence of desiccation cracks appears to increase as cross-sections approach the sample exterior. This is supported by Figure 5.31, which presents a quantitative measure of subsurface desiccation, showing a higher CIF in cross-sections closer to the container edges (e.g., CS1.1 and CS1.8). The graph in Figure 5.31 also highlights the absence of the left-right side divide in CIF recorded in W2 – W3. These results further elucidate the significance of spatial variation in wind magnitude and turbidity in driving increases in aerodynamic conductance, differential stress accumulation and therefore, surface and subsurface variation in desiccation cracking severity. This cause-and-effect relationship was not present in W1 due to the absence of wind.

In contrast to tests exposed to wind (W2 – W4), subsurface crack connectivity in W1 under no wind appears significantly lower. In the central region of cross sections CS1.3 – 1.8 in Figure 5.30, suspected cracks have not been infilled with resin, suggesting they do not form a continuous network in the sample, as the tensile stresses driving propagation of the crack tip were not sufficiently high. It is important to note that the cross-section sampling process has artificially widened the larger vertical crack in the centre of CS1.3 – 1.7. These observations underscore how wind-driven drying can significantly enhance the formation of preferential flow channels in the subsurface, a critical factor that drives infrastructure embankment instability. However, further multi-dimensional analysis is needed to assess the extent of crack connectivity fully and accurately.

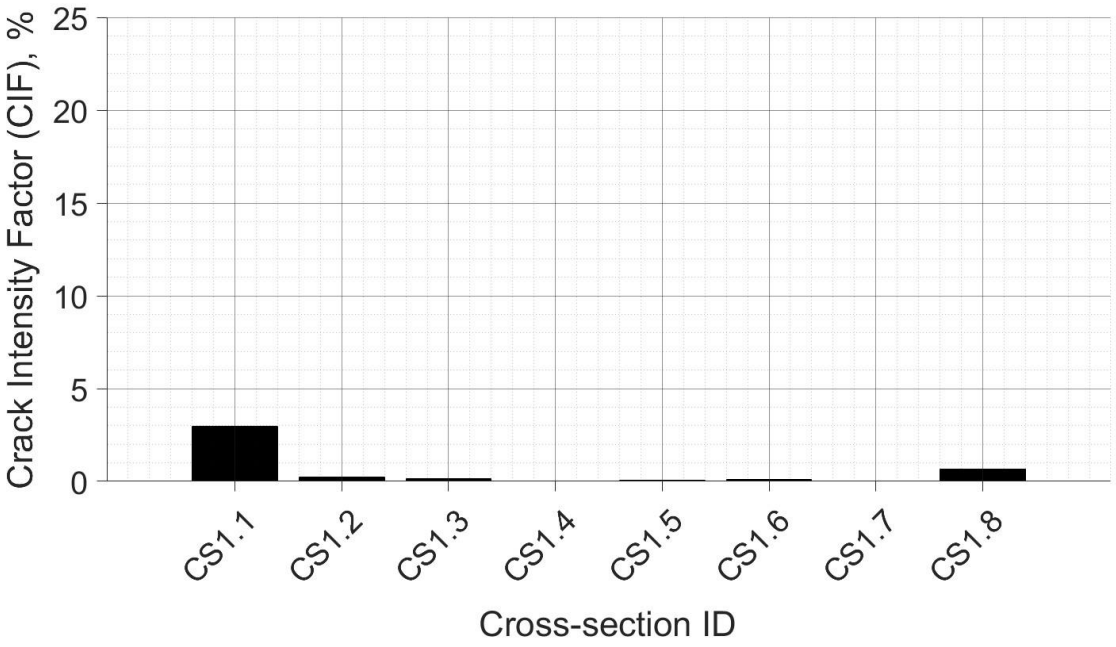

Figure 5.31: Plot of Crack Intensity Factor (CIF) (%) for cross sections CS1.1 to CS1.8 taken in W1. CIF was calculated through image processing of the photographs displayed in Figure 5.29 using the technique outlined in Section 3.4.4. An exterior-interior divide in the CIF results is visible, but no left-right side divide.

5.5 Concluding Remarks

The small-scale laboratory tests in Chapter provided insight into how altering the physical and environmental boundary conditions through modifying parameters in the Penman-Monteith (1965) equation can influence moisture transfer dynamics and desiccation behaviour within Ampthill Clay fill. Section 5.2 outlined how topsoil can be engineered to improve the long-term hydraulic and mechanical stability of infrastructure embankments exposed to weather-driven deterioration processes, such as climatic cycling, shrink-swell and desiccation cracking. The results demonstrated that variations in topsoil thickness, composition, and initial moisture content significantly affected evaporation rates, suction gradients, and the onset and extent of volumetric change in Ampthill Clay. This relative impact was primarily controlled by the level of the contrast between the fill and the topsoil's soil water retention behaviour, as this governed the rate and magnitude of evaporative fluxes.

From the characteristics tested, thick layers (40 mm) of sandy (TS1) topsoil (i.e. C1 and C2) proved most efficient at suppressing rapid evaporation and shrinkage, particularly under higher initial moisture contents (C2). This effectiveness is attributed to the combined effects of low unsaturated hydraulic conductivity, capillary barrier

formation at the material interface, increased storage capacity and dampened thermal gradients, all of which limited moisture flux and delayed drying front propagation into the underlying clay. This measurable impact of topsoil composition and thickness on the soil moisture dynamics within embankment fill introduces an additional consideration when analysing soil-atmosphere-vegetation interactions and their combined effect on desiccation cracking.

Notably, desiccation cracking was absent from all topsoil experiment specimens, attributed to setup-related limitations and the absence of pervasive environmental stressors, such as the wind utilised in Section 5.3. However, greater shrinkage occurred in fill when topsoil was either i) absent, ii) initially unsaturated, or iii) a thin layer, increasing the likelihood of desiccation cracking. It is crucial to recognise that other forms of deterioration must be considered when selecting a suitable topsoil for infrastructure embankments. While purely sandy compositions may be effective capillary barriers, they are more susceptible to physical weathering via erosional washout. Therefore, implementing mixed composition topsoil with higher sand contents, such as loamy sand/sandy loam/sandy clay loam divisions of Figure 5.1, could offer more resilient options. However, further research is required, including using matured topsoil that more accurately represents the structural, biological and compositional characteristics found in the field.

The wind speed experiments conducted in Section 5.3 demonstrated a strong coupling between airflow dynamics and desiccation processes in compacted clay specimens, consistent with the governing principles of the Penman–Monteith (1965) equation and coupled energy–mass transfer theory. Higher wind speeds enhanced aerodynamic conductance and sustained vapour pressure gradients at the soil–atmosphere interface, accelerating evaporation rates and intensifying suction gradients. These conditions promoted earlier and more severe tensile and shear stress and strain accumulation, resulting in more rapid crack initiation and extensive crack propagation, most significantly in W4. Moderate (W3) and low (W2) wind speeds produced significantly reduced or absent desiccation cracking, confirming the existence of a critical wind speed threshold required to sustain high aerodynamic conductance and evaporative flux.

Furthermore, open desiccation cracks amplified evaporation by increasing the effective surface area and facilitating deeper moisture loss, reinforcing a self-sustaining feedback loop between cracking and evaporation. The spatial heterogeneity of drying,

driven by chamber airflow geometry and turbulence, led to asymmetric desiccation patterns and complex stress field development across specimens. The interaction between wind speed, crack evolution, and microclimate feedbacks emphasises the importance of aerodynamic forcing in controlling the spatial and temporal development of desiccation cracking within infrastructure-relevant geomaterials.

The investigations carried out in Section 5.4 using resin revealed that the impact of the synergetic relationship extended into the subsurface, with crack intensity and connectivity also increasing under higher winds and in areas of greater exposure. Soil heterogeneity and layer boundaries were exploited by desiccation, which are integral features in live assets. Cracks showed evidence of propagation under tensile, compressive and shear components, further suggesting that wind-driven drying produces a complex stress field. However, the results also demonstrated subsurface desiccation where surface cracking was absent, demonstrating the importance of multi-dimensional characterisation to fully assess weather-driven deterioration in infrastructure embankments.

The 2D limitations of these experiments were noted, with further multi-dimensional analysis needed to assess subsurface desiccation in compacted clay fill fully. Furthermore, it is important to consider that the fill used in these experiments is primitive in comparison to ageing infrastructure embankments exposed to many cycles of physical and environmental loading. Therefore, this acceleration of evaporation and desiccation under wind-driven drying could be more significant in deteriorated infrastructure assets, and the relationship should be explored over a greater number of environmental cycles.

The Penman-Monteith (1965) framework demonstrates here that factors beyond commonly explored air temperature are critical to desiccation, particularly in climates where seasonal weather patterns prevail and extremes in temperature or high solar radiation are less common. This was illustrated by the prevalence of desiccation cracks on the lysimeter slope during winter (Chapter 4). Moreover, solely linking weather records to desiccation is inadequate, as a complex interaction of physical boundary conditions shapes the true environmental boundary conditions on slopes. Therefore, these findings emphasise the importance of further research into the broad range of parameters accounted for in Penman-Monteith's (1965) equation, which may influence the rate and magnitude of evaporation and desiccation within infrastructure embankments.

Chapter 6. Conclusions and Future Recommendations

6.1 Introduction

The primary aim of this thesis was to investigate the coupled interaction of desiccation cracking and hydrological processes within an embankment slope across varying temporal and spatial scales. This research arose from the increasing concern over the detrimental effects of desiccation-induced deterioration on the structural integrity of infrastructure embankments. These assets play a vital role in ensuring the efficient and safe operation of the transport network. However, managing and forecasting their future performance is increasingly challenging due to the rising unpredictability and extremes of weather patterns, which will likely impact both the rate and extent of deterioration observed in the field.

The literature review identified a notable gap in the empirical characterisation of desiccation crack formation and the related deterioration processes under conditions that closely mimic field-scale processes. As weather-driven deterioration processes, such as desiccation cracking, increasingly threaten infrastructure assets, accurate forecasting of future stability using predictive models becomes critical. This necessitates robust input measurements that can effectively characterise and quantify deterioration's spatial and temporal evolution. Therefore, this thesis demonstrates the efficacy of a multi-scale approach to address this significant research gap, incorporating characteristics of field-scale behaviour throughout.

This approach employed an intermediate-scale slope built within an outdoor lysimeter, generating a novel two-year, high-resolution dataset that captures compacted clay's desiccation crack and hydrological evolution under varying antecedent and extreme weather conditions. The dataset and an accompanying detailed laboratory study offered valuable insights into the parameters that govern desiccation. However, it also fundamentally illustrated how the severity of desiccation governs the slope’s hydrological response to changes in environmental conditions. Additionally, it highlighted how this vulnerability evolved with time in response to varying weather conditions and the advancement of desiccation-induced deterioration.

The conclusions drawn from this methodological approach are classified into distinct subsections, each aligned with the specific high-level research objectives outlined in Chapter 1. This structured categorisation facilitates a comprehensive understanding of the findings and their relevance to the overarching research aim. Recommendations

on further study directions and key avenues that would progress further toward understanding the fundamental threat desiccation-induced deterioration poses to the UK's infrastructure assets are also provided.

6.2 Moisture Flux Dynamics Relative to Desiccation State

By presenting a detailed examination of the lysimeter study's results, this thesis has effectively demonstrated its capability of capturing the intricacies of moisture flux dynamics within a compacted clay slope affected by desiccation cracking. The findings provide evidence that aligns with previously documented behaviours observed in field-scale assets. Specifically, they agree that slope hydrology and desiccation are seasonally dependent (Eminue et al., 2018; Yu et al., 202) as well as demonstrate the hydrological implications associated with exposure to unseasonably high rainfall events (Smethurst et al., 2012; Stirling et al., 2021). This demonstrates its ability to capture the processes operating within live infrastructure embankments. However, it has also created a novel scale dataset with an almost complete two-year record of daily cracking status. Daily crack status was then cross-referenced with continuous measurements of the slope's hydrological behaviour and local weather to generate a holistic view of moisture flux dynamics within a desiccated slope. This section outlines the key findings from this dataset on how desiccation drives variation in moisture flux dynamics under different magnitudes of drying and wetting.

Two distinct types of cracking networks were identified on the lysimeter slope, and their differing impacts on moisture flux dynamics were discussed. Results illustrated how these behaviours varied greatly from the hydrological response of the slope under an intact state, mostly related to the added moisture storage capacity that the cracks provide. Deeper crack networks were associated with warm and dry summer conditions, which assisted evaporation by increasing net radiation and prevented crack closure by minimising rainfall. This was particularly amplified under heatwave conditions. Through the summer, these deep networks accommodated the rainfall volume from low to medium-intensity events without generating runoff or a significant change in aperture, slope moisture content, or soil suction.

The extent to which these deep crack networks influenced infiltration capacity remained unclear until extreme storm events were studied. It was demonstrated that the desiccated slope critically absorbed each storm's rainfall volume. Results indicated evidence of rapid preferential flow to crack depths, showing the shallowing of the crack network with each storm event, yet no runoff was generated. A rapid loss of suction,

followed by a gradual gain, was observed after each storm, reducing the maximum recorded suction further with each applied event. Runoff was not recorded until two days past the last event, after exposure to a high-intensity natural rainfall event. These results effectively show the significant ramifications of deep desiccation on moisture flux dynamics. The risk of infiltration-induced stability within a highly desiccated embankment is expected to heighten under future climate change projections, illustrating the importance of expanding on such studies and understanding the threat posed to the stability of these key assets.

The second crack network type was comparatively superficial, demonstrated by the shallower fluctuations in volumetric moisture content. This network prevailed during the winter seasons and Summer 2023 and was associated with the generation of zero soil suction. The results demonstrated this network's more frequent cyclic changes in aperture, related to rapidly fluctuating moisture content in the shallow subsurface from 0 to 100% over short timescales. From this, the failure locations may shift from deep to shallow slips. The findings presented in this research underscore the substantial and highly evolving changes that desiccation cracks create in the moisture dynamics of an embankment. Therefore, empirical field characterisation of the additional permeability of embankments in their desiccated state must be incorporated into predictive behavioural models. Such methods are essential for accurately forecasting the resilience of these structures in response to climate change projections.

6.3 Behavioural Evolution Under Cyclic Exposure to Weather and Desiccation

Monitoring in-situ soil suction and moisture content with high spatial and temporal resolution over three consecutive summers captured the potential development of weather-driven deterioration within the lysimeter slope. In-situ SWRCs were generated, first capturing a biphasic distribution of pore sizes in the summer post-construction, then showing how open cracks markedly affect the soil water retention behaviour within an intact clay matrix. Within a year, evidence indicative of deterioration was evident in the SWRCs. The SWRCs suggested the development of a coarser network of interconnected pores, which were less able to generate and sustain high suction. Higher saturated water contents support this increased storage capacity. The absence of suction in Summer 2023 may have suggested further deterioration of soil water retention behaviour. However, it could also be a function of the persistently saturated slope conditions. Further microstructural analysis is needed to confirm these findings.

Despite being unable to generate a SWRC, Summer 2023 illustrated deterioration through its increased sensitivity to prevailing weather. The rapid cyclic variation between fully saturated and unsaturated states evidences an increased rate of infiltration and evaporation. Such behaviour indicates a degraded and coarser pore structure, which is less likely to resist moisture movement to and from its pores. Within each drying cycle, superficial desiccation cracks open and closed rapidly, which will have major implications for the rate at which microstructural degradation manifests in the shallow subsurface.

Other indirect indicators of deterioration were observed on the lysimeter slope. These included an increased washout and cumulation of fine particles within the runoff channels, resulting from the more frequent and intense runoff formed under the shallow crack networks. The loss of the fine fraction of the soil is a permanent form of deterioration that significantly impacts its suction generation capacity. Additionally, scour channels formed from intense surface runoff were observed, underscoring the need to consider a shift in the predominant failure mechanism of an embankment exhibiting a shallower crack network.

6.4 Influencing Parameters in Desiccation Crack Formation

The lysimeter and laboratory studies advanced the understanding of desiccation control parameters. This was achieved by moving beyond the conventional focus on temperature extremes to consider additional environmental factors influencing evaporation. These include net radiation, vapour pressure deficit, and aerodynamic resistance, as defined by the Penman-Monteith equation. This approach offered a more comprehensive perspective on the interplay of factors influencing the formation and severity of desiccation cracking in the field. Key findings demonstrating the knowledge advances made by this research are discussed below.

Desiccation cracking severity showed a clear seasonal dependence, evident only when weather patterns aligned with seasonal norms. Illustrating this, a greater net radiation supply through warm and dry weather during the spring-to-summer transition was crucial for deep summer desiccation. At the same time, the intensity of autumn rainfall initiated the closure of these networks and the formation of shallower winter networks. In the years this seasonality was displayed, summers with heatwave conditions facilitated the more rapid growth of deep desiccation by further increasing net radiation, the vapour pressure deficit, latent heat flux and rapid moisture loss to depth. Conversely, only shallower networks were supported under unseasonably high

spring-to-summer rainfall due to no reprieve from saturated slope conditions. These results highlighted the evolutionary nature of desiccation cracking, demonstrating that predictability will become increasingly challenging as climate change leads to more unpredictable weather patterns and hydrological responses.

Another insight gained from this research is the importance of considering other environmental factors contributing to drying and soil desiccation. During the lysimeter study, desiccation cracking was displayed across all seasons. For winter, this corroborated Penman's (1948) hypothesis that wind is equally important in evaporation, becoming a vital desiccation driver in the absence of high temperatures. The laboratory studies confirmed that surface and subsurface cracking initiation rate, intensity, and connectivity increased under greater aerodynamic conductance as per Penman-Monteith's (1965) equation. Furthermore, wind and desiccation cracking demonstrated a synergistic relationship. This behaviour facilitated faster and deeper propagation of drying fronts, likely facilitating the growth of subsurface desiccation networks. Consequently, failure to consider all environmental variables may grossly underestimate a slope's vulnerability to desiccation, stressing the need to transition away from solely investigating temperature effects.

The important role of spatial and temporal variation in environmental exposure for desiccation crack formation was highlighted throughout this research using various aspects of the methodology. Shading effects created by interactions between environmental and physical boundary conditions generated spatial variation in desiccation cracking on the lysimeter slope. The structural characteristics of the faux grass canopy influenced soil moisture dynamics and desiccation cracking by altering key components of the surface energy balance. Specifically, it reduced net radiation and increased aerodynamic resistance by physically shielding the surface from direct solar radiation and wind. Additionally, it moderated rainfall flux to the soil, attenuating shrink–swell cycles. These combined effects led to more minor fluctuations in soil moisture and suction, reducing the crack opening and closure rate. In laboratory conditions, the enhanced aerodynamic resistance also promoted the development of more dispersed and less concentrated desiccation cracking patterns by increasing wind turbulence near the surface. Such results demonstrate how spatial variation in environmental exposure can lead to significant disparities in soil responses, even across relatively small distances.

These small spatial scales over which environmental exposure can occur exemplify one of the many complexities inherent to embankments, where heterogeneity is a fundamental characteristic influencing processes such as desiccation cracking. The physical properties of soil can also vary significantly across different spatial scales, influenced by factors like compaction and structural degradation over time. This variability can be exacerbated by greater environmental exposure or facilitate the differing responses observed to the prevailing weather. This was demonstrated by the changing suction and volumetric water content responses observed across various regions of the lysimeter slope. Some of these variations can be attributed to greater exposure in areas like the crest region, while others suggest a stronger local influence of desiccation-induced deterioration. Heterogeneity is inherently difficult to predict, but studies like this highlight the magnitude of its variability, thereby enhancing the understanding of the diverse responses an embankment may exhibit in the field.

6.5 Recommendations for Further Study

The experimental work on the model slope has provided a novel dataset and critical insights into the mechanisms of desiccation, the hydrological response of slopes, and the challenges associated with monitoring and replicating real-world conditions. Reflecting on these findings, this section outlines the key lessons learned and sets a clear direction for future research. For clarity and practical application, the content is divided into three distinct parts:

1. **Lessons Learned from the Model Slope Experiment** – outlining what should be adopted for future similar experiment iterations and addressing what would be done differently if starting from scratch, based on experimental limitations and observed behaviour.
2. **Field-Scale Monitoring Recommendations** – translating the lessons learned from the experimental findings into actionable strategies for real-world embankment monitoring and risk management.
3. **Recommendations for Laboratory-Scale Experiments** – outlining how future laboratory-scale tests can better replicate natural conditions while maintaining experimental control.

6.5.1 Lessons Learned from the Model Slope Experiment

Recommendations for further study would be to continue investigating this phenomenon at the scale presented in this research, expanding on the interesting questions the study raised. Specific aspects of the model slope experiments have contributed significantly to the overall understanding of desiccation and hydrological behaviour in a compacted clay slope, particularly in relation to behaviour changes under climate change. These aspects should be incorporated into any future experiment iterations, and are as follows:

1. Longer-term monitoring, inclusive of a broader scale of weather extremes forecasted by climate change. Examining and quantifying the recovery process from such events provides greater knowledge of material resilience.
2. Tracking changes in soil-water retention behaviour provides a non-intrusive analysis method and valuable insight into the real-time development of microstructural degradation. Incorporating a sensor setup which allows this is recommended in future research.
3. Analysing results from the perspective of how desiccation cracking and soil hydrology could affect the failure mode within infrastructure embankments. This is essentially how asset owners characterise the stability of their infrastructure earthworks.
4. Developing upon empirical measurements of solar radiation, wind, relative humidity and changes in physical boundary conditions impacting desiccation cracking. This gives a better perspective of local environmental boundary conditions and potential effects on evaporation.
5. Developing a systematic and consistent imaging method to generate a high-resolution dataset of surface desiccation across the duration of any experiment. This dataset was invaluable to understanding the slope's hydrological behaviour and the real-time response of desiccation to changes in environmental conditions.

The lysimeter slope has provided several key insights into designing experiments for monitoring desiccation-prone slopes. Reflecting on the process, the following lessons emerged, which would inform a redesigned approach if starting anew:

- **Surface Crack Analysis**: A more fixed and systematic method for surface crack monitoring should be implemented. This would involve imaging multiple regions of the slope (upper, lower and crest), allowing for spatial comparisons and

correlations with subsurface hydrological conditions. A greater temporal resolution would also be utilised.

- **Minimising Boundary Effects**: Improvements in the physical setup are necessary to reduce artificial boundary conditions. Enhancing air circulation within the lysimeter and closely monitoring these external physical controls on environmental boundary conditions would help quantify and minimise edge effects that are not representative of field embankments.
- **Site-Specific Weather Data**: Localised weather monitoring – especially near-surface wind speeds, temperature, and humidity – should be introduced better to understand their influence on evaporation rates and desiccation patterns. This would help decouple microclimatic variability from general weather station data. Installing sensors closer to the slope surface would help achieve this.
- **Weighing Lysimeter**: Implementing a weighing mechanism within the lysimeter would significantly improve understanding of the water balance. This would strengthen interpretations related to storage capacity changes in the desiccated slope.
- **Progressive Complexity Towards Real Embankments**: A more phased approach to mimic field conditions would be beneficial – introducing vegetation, scaling up dimensions, and progressively isolating environmental variables in a controlled manner would provide more field-representative results.
- **Extended Monitoring and Subsurface Characterisation**: Longer-term monitoring, followed by detailed subsurface sampling and investigations (e.g. with resin injection to map desiccation), would allow correlations between microstructural degradation and hydrological behaviour over time. This would supplement and/or confirm the accuracy of in-situ field measurements.
- **Geophysical Monitoring**: Employing non-intrusive geophysical techniques such as electrical resistivity tomography (ERT) or ground penetrating radar (GPR) would provide temporal insight into subsurface desiccation and its evolution, which is often masked in surface-only assessments.
- **Climate-Relevant Rainfall Simulations**: Simulated rainfall events should replicate expected patterns under climate change – applying realistic storm

profiles during summer periods would help assess how future climatic conditions influence slope desiccation and hydrological response.

- **Vegetation impact:** further delineating the effects of vegetation is complex, but a crucial next step to fully understand the problem.
- **Slope design:** introducing a more concrete divide of sides within the slope to provide more accurate control and variant setups would be better for comparing and contrasting the roles of different physical and environmental variables.

6.5.2 Field-Scale Monitoring Recommendations

Translating findings from controlled experiments to real-world embankments presents unique challenges. The following considerations are critical for effective field monitoring and understanding of desiccation processes:

- **Subsurface Characterisation**: Advanced characterisation methods must be employed to understand spatial variability. Testing and comparing the efficacy of multiple geophysical and direct sampling techniques is essential. However, it is appreciated that the latter is difficult to conduct on live assets.
- **Microstructural Analysis**: Regular sampling should be conducted to investigate the extent and progression of microstructural deterioration within the embankment materials. This can be done through e.g., window sampling, which is commonly used on assets to install other monitoring equipment.
- **Sensor Networks**: Deploying a dense network of suction and moisture sensors across slope profiles will allow for detailed tracking of the soil water retention curve (SWRC) evolution through time. Involving these in the construction of new embankments would provide invaluable insight.
- **Surface Crack Documentation**: Improved visual logging methods for surface cracking—ranging from CCTV integration to remote sensing—can supplement manual inspections. Education and standardisation of logging protocols of desiccation cracks will enhance consistency, although vegetation cover may still obscure visibility.
- **Indicators of Desiccation**: Monitoring for specific signatures, such as changes in SWRC behaviour or evidence of dual porosity, could provide early indicators of desiccation-driven deterioration.

- **Cover Testing**: Trials with different surface covers (vegetative, geosynthetics, plastic sheets, etc.) should be carried out to evaluate their effects on desiccation processes, particularly on known susceptible slopes.
- **Local Climate Context**: Localised environmental monitoring should be prioritised over reliance on distant weather stations. Understanding microclimatic variability – especially in slopes with differing orientations or shading – will improve the predictive capacity of desiccation models.
- **In-situ permeability tests:** conducting infiltration tests (e.g., Guelph Permeameter) can highlight areas of increased micro and macro deterioration, allowing surface and subsurface identification of desiccation vulnerable areas and allow interventions to be targeted accordingly.

6.5.3 Recommendations for Laboratory-Scale Experiments

The design of laboratory-scale tests needs to evolve to be more representative of field-scale conditions. Based on lessons from the lysimeter and laboratory experiments in this thesis, the following strategies are proposed:

- **Realistic Soil Representation**: Laboratory testing must transition from over-processed, fine soils and exaggerated drying to tests using actual embankment fills at various stages of degradation. This enables more realistic assessments of field behaviour.
- **Integrated Environmental Modelling**: All variables within the Penman-Monteith framework – radiation, temperature, wind speed, humidity – should be varied in controlled tests to assess their collective and individual impacts on desiccation and evapotranspiration. Efforts to use methods which accurately represent naturally varying environmental conditions are also recommended.
- **Vegetation Effects in Laboratory Settings**: Introducing vegetation into lab tests would help replicate natural embankment surface conditions. This allows quantification of evapotranspiration, shading effects, wind attenuation, and rainfall interception. All of which could be imposed in the laboratory.
- **Comparative Analysis of Topsoil Treatments**: Using vegetated versus non-vegetated topsoil, with and without organic matter, will provide better insight into the added complexity introduced by biological processes and their influence on hydrological and structural behaviour.

References

Abbaszadeh, M.M., Houston, S., Zapata, C., Houston, W., Welfert, B. & Walsh, K. (2011) 'Laboratory determination of Soil-Water Characteristic Curves for cracked soil', Unsaturated Soils - Proceedings of the 5th International Conference on Unsaturated Soils, 1pp. 409–415.

Albrecht, B.A. & Benson, C.H. (2001) 'Effect of Desiccation on Compacted Natural Clays', Journal of Geotechnical and Geoenvironmental Engineering, 127(1), pp. 67–75.

Alexsander, S., Mochtar, I.B. & Utama, W. (2017) 'The Measurements of Water Intrusion through Cracks Propagation Inside Slopes to Explain the Cause of Slope Failure-Case Study of Embankment in the Sanggu-Buntok Airport, Central Kalimantan, Indonesia', Journal Soils and Foundations, 22(14), pp. 5347–5362.

Allen, R.G., Pereira, L.S., Raes, D. and Smith, M., 1998. FAO Irrigation and drainage paper No. 56. *Rome: food and agriculture organization of the United Nations*, *56*(97), p.e156.

Al-Yaqoub, T.H., Parol, J. & Znidarcic, D. (2017) 'Experimental investigation of volume change behavior of swelling soil', Applied Clay Science, 137pp. 22–29.

Auvray, R., Rosin-Paumier, S., Abdallah, A. & Masrouri, F. (2014) 'Quantification of soft soil cracking during suction cycles by image processing', European Journal of Environmental and Civil Engineering, 18(1), pp. 11–32.

Baninajarian, L., Ghassemi, A., Sangiuliano, T., Desira, A. & Bashir, R. (2019) Effect of climate change on soil embankment stability, in [Online]. 2019

Basma, A.A., Al-Homoud, A.S., Husein Malkawi, A.I. & Al-Bashabsheh, M.A. (1996) 'Swelling-shrinkage behavior of natural expansive clays', Applied Clay Science, 11(2), pp. 211–227.

Boley, C. & Herzog, F. (2015) 'Experimental investigation of frost induced suction stresses in fine grained materials', in Geotechnical Engineering for Infrastructure and Development. [Online]. pp. 553–558.

Booth, A. 2014. Impacts ofdesiccation cracking and climate change on highway cutting hydrology. PhD thesis, Loughborough University.

Bordoloi, S., Hussain, R., Gadi, V.K., Bora, H., Sahoo, L., Karangat, R., Garg, A. & Sreedeep, S. (2018) ‘Monitoring soil cracking and plant parameters for a mixed grass species’, Geotechnique Letters, 8(1), pp. 49–55.

Bordoloi, S., Leung, A.K., Gadi, V.K., Hussain, R., Garg, A. & Sekharan, S. (2019) ‘Water Retention and Desiccation Potential of Lignocellulose-Based Fiber-Reinforced Soil’, Journal of Geotechnical and Geoenvironmental Engineering, 145(11), .

Bordoloi, S., Ni, J. & Ng, C.W.W. (2020) ‘Soil desiccation cracking and its characterization in vegetated soil: A perspective review’, Science of The Total Environment, 729p. 138760.

Bouma, J. (1980) ‘Field measurement of soil hydraulic properties characterizing water movement through swelling clay soils’, Journal of Hydrology, 45(1), pp. 149–158.

Bowles, J.E. (1979a) Physical and geotechnical properties of soils. Second Edi. New York: McGraw-Hill Book Company.

Briggs, K.M., Dijkstra, T.A. & Glendinning, S. (2019) ‘Evaluating the deterioration of geotechnical infrastructure assets using performance curves’, in International Conference on Smart Infrastructure and Construction 2019, ICSIC 2019: Driving Data-Informed Decision-Making. [Online]. pp. 429–435.

Briggs, K.M., Helm, P.R., Smethurst, J.A., Smith, A., Stirling, R., Svalova, A., Trinidad González, Y., Loveridge, F.A. & Glendinning, S. (2023) ‘Evidence for the weather-driven deterioration of ageing transportation earthworks in the UK’, Transportation Geotechnics, 43p. 101130.

Briggs, K.M., Loveridge, F.A. & Glendinning, S. (2017) ‘Failures in transport infrastructure embankments’, Engineering Geology, 219pp. 107–117.

Brinker, C.J. and Scherer, G.W., 2013. Sol-gel science: the physics and chemistry of sol-gel processing. Academic press.

British Standards, 1990. Methods of test for Soils for civil engineering purposes 1377-Part 2: Classification tests. London: British Standards Institution.

British Standards, 1990. Methods of test for Soils for civil engineering purposes 1377-Part 4: Compaction related tests. London: British Standards Institution.

British Standards Institution (BSI) (2015) BS 3882:2015 – Specification for topsoil and requirements for use. London: BSI.

Centre for Environmental Data Analysis (CEDA) (2018) HadUK-Grid: A collection of gridded climate observations for the UK. Available at: https://catalogue.ceda.ac.uk/uuid/4dc8450d889a491ebb20e724debe2dfb/ (Accessed: 27 November 2024).

Charkley, F.N., Zhang, K. & Mei, G. (2019) 'Shear Strength of Compacted Clays as Affected by Mineral Content and Wet-Dry Cycles', Advances in Civil Engineering, 2019(1), p. 8217029.

Chen, R., Lindqwister, W., Wu, F., Mielniczuk, B., Hueckel, T. & Veveakis, M. (2023) 'The physics of desiccation cracks 1: Ductile fracturing and dependence on relative humidity', Geomechanics for Energy and the Environment, 35p. 100488.

Chen, R. & Ng, C.W.W. (2013) 'Impact of wetting–drying cycles on hydro-mechanical behavior of an unsaturated compacted clay', Applied Clay Science, 86pp. 38–46.

Cheng, Q., Tang, C.-S., Xu, D., Zeng, H. & Shi, B. (2021) 'Water infiltration in a cracked soil considering effect of drying-wetting cycles', Journal of Hydrology, 593p. 125640.

Clarke, D. & Smethurst, J.A. (2010) 'Effects of climate change on cycles of wetting and drying in engineered clay slopes in England', Quarterly Journal of Engineering Geology and Hydrogeology, 43(4), pp. 473–486.

Cordero Arias, J., Najdi, A., Encalada, D., Prat, P. & Ledesma, A. (2020) 'Experimental and numerical analysis of soil desiccating cracks in compacted and non-compacted specimens', E3S Web of Conferences, 195p. 3021.

Cordero, J.A., Prat, P.C. & Ledesma, A. (2021) 'Experimental analysis of desiccation cracks on a clayey silt from a large-scale test in natural conditions', Engineering Geology, 292p. 106256.

Costa, S., Kodikara, J. & Shannon, B. (2013) 'Salient factors controlling desiccation cracking of clay in laboratory experiments', Géotechnique, 63(1), pp. 18–29.

Cui, Y.-J., Tang, C.-S., Tang, A.M. & Ta, A.N. (2014) 'Investigation of soil desiccation cracking using an environmental chamber', Rivista Italiana di Geotecnica, 48(1), pp. 9 – 20.

Davies, O., Rouainia, M., Glendinning, S. & Birkinshaw, S. (2008) ‘Assessing The Influence Of Climate Change On The Progressive Failure Of A Railway Embankment’, 12th International Conference on Computer Methods and Advances in Geomechanics 2008, 6.

Dias, A.S., Hughes, P. & Toll, D. (2023) ‘Irreversible effects of drying-wetting cycles on shrinkage and water retention of compacted London clay’, E3S Web of Conferences, 382pp. 0–5.

Dijkstra, T. & Dixon, N. (2010) ‘Climate change and slope stability in the UK: Challenges and approaches’, Quarterly Journal of Engineering Geology and Hydrogeology, 43pp. 371–385.

Dixon, N., Crosby, C.J., Stirling, R., Hughes, P.N., Smethurst, J., Briggs, K., Hughes, D., Gunn, D., Hobbs, P., Loveridge, F., Glendinning, S., Dijkstra, T. & Hudson, A. (2019) ‘In situ measurements of near-surface hydraulic conductivity in engineered clay slopes’, Quarterly Journal of Engineering Geology and Hydrogeology, 52(1), pp. 123–135.

Durner, W. & Iden, S.C. (2021) ‘The improved integral suspension pressure method (ISP+) for precise particle size analysis of soil and sedimentary materials’, Soil and Tillage Research, 213.

Dyer, M., Utili, S. & Zielinski, M. (2009) ‘Field survey of desiccation fissuring of flood embankments’, Proceedings of the Institution of Civil Engineers - Water Management, 162(3), pp. 221–232.

EA (2014) Flood risk assessment for planning applications. Available at: https://www.gov.uk/guidance/flood-risk-assessment-for-planning-applications (Accessed: 27 November 2024).

EA (2016) Flood risk assessments: climate change allowances. Available at: https://www.gov.uk/guidance/flood-risk-assessments-climate-change-allowances (Accessed: 27 November 2024).

El-Zein, A., Airey, D., Yu, B., Esgandani, G.A., Proust, G., Dias-da-Costa, D., Gao, Y., Gan, Y. & Chen, S. (2021) ‘Self-repair of cracks and defects in clay: a review of evidence, mechanisms, theories and nomenclature’, Acta Geotechnica, 16(12), pp. 3741–3760.

Eminue, O., Davie, C. & Stirling, R. (2018) Moisture Movement and Mechanisms of Desiccation Crack Development in Engineered Clay Fills Desiccation Cracking in Geotechnical Infrastructure Conclusions.

Estabragh, A.R., Parsaei, B. & Javadi, A.A. (2015) 'Laboratory investigation of the effect of cyclic wetting and drying on the behaviour of an expansive soil', Soils and Foundations, 55(2), pp. 304–314.

Faulkner, D. (1999) Flood estimation handbook 2: Rainfall frequency estimation. Available at: https://www.ceh.ac.uk/sites/default/files/2021-11/Flood-Estimation-Handbook-2-Rainfall-Frequency-Estimation-Duncan%20Faulkner_2-9-21.pdf (Accessed: 27 November 2024).

Fredlund, D.G., Rahardjo, H. & Fredlund, M.D. (2012) 'Unsaturated Soil Mechanics in Engineering Practice', Unsaturated Soil Mechanics in Engineering Practice, 132(March), pp. 286–321.

Fredlund, D.G. & Xing, A. (1994) 'Equations for the soil-water characteristic curve', Canadian Geotechnical Journal, 31(4), pp. 521–532.

Glendinning, S., Hall, J. & Manning, L. (2009) 'Asset-management strategies for infrastructure embankments', Proceedings of the Institution of Civil Engineers - Engineering Sustainability, 162(2), pp. 111–120.

Glendinning, S., Hughes, P., Helm, P., Chambers, J., Mendes, J., Gunn, D., Wilkinson, P. & Uhlemann, S. (2014) 'Construction, management and maintenance of embankments used for road and rail infrastructure: implications of weather induced pore water pressures', Acta Geotechnica, 9(5), pp. 799–816.

Greve, A., Andersen, M.S. & Acworth, R.I. (2010) 'Investigations of soil cracking and preferential flow in a weighing lysimeter filled with cracking clay soil', Journal of Hydrology, 393(1), pp. 105–113.

Griffifth, A.A. (1924) 'The theory of rupture', International Congress for Applied Mechanics,

Hallett, P.D. & Newson, T.A. (2005) 'Describing soil crack formation using elastic–plastic fracture mechanics', European Journal of Soil Science, 56(1), pp. 31–38.

Herrera, M.C., Lizcano, A. & Santamarina, J.C. (2007) ‘Colombian volcanic ash soils’, in Characterisation and Engineering Properties of Natural Soils. [Online]. 2007 pp. 2385 – 2409.

Hirmas, D.R., Giménez, D., Mome Filho, E.A., Patterson, M., Drager, K., Platt, B.F. & Eck, D. V (2016) ‘Quantifying Soil Structure and Porosity Using Three-Dimensional Laser Scanning’, in Alfred E Hartemink & Budiman Minasny (eds.) Digital Soil Morphometrics. [Online]. Cham: Springer International Publishing. pp. 19–35.

Holmes, D.M., Vasant Kumar, R. & Clegg, W.J. (2006) ‘Cracking During Lateral Drying of Alumina Suspensions’, Journal of the American Ceramic Society, 89(6), pp. 1908–1913.

Holtz, R.D. & Kovacs, W.D. (1981) An introduction to geotechnical engineering. New Jersey: Prentice-Hall Inc.

Huang, W., Loveridge, F.A., Briggs, K.M., Smethurst, J.A., Saffari, N. & Thomson, F. (2024) ‘Forecast climate change impact on porewater pressure regimes for the design and assessment of clay earthworks’, Quarterly Journal of Engineering Geology and Hydrogeology, 57(1), pp. qjegh2023-015.

Hughes Paul N, Hen-Jones Rosalind, Stirling Ross A, Glendinning Stephanie, Gunn David A, Chambers Jonathon E, Dijkstra Tom A, Smethurst Joel & Flesjo Kristine (2016) ‘Challenges in monitoring and managing engineered slopes in a changing climate’, E3S Web Conf., 9p. 4009.

Hughes, P.N., Glendinning, S., Mendes, J., Parkin, G., Toll, D.G., Gallipoli, D. & Miller, P.E. (2009) ‘Full-scale testing to assess climate effects on embankments’, Proceedings of the Institution of Civil Engineers - Engineering Sustainability, 162(2), pp. 67–79.

Hun, D.-A., Yvonnet, J., Guilleminot, J., Dadda, A., Tang, A.-M. & Bornert, M. (2021) ‘Desiccation cracking of heterogeneous clayey soil: Experiments, modeling and simulations’, Engineering Fracture Mechanics, 258p. 108065.

Ighil Ameur, L. (2023) ‘Analysis of climate change impacts on the shrinkage-swelling phenomenon of clayey soils to adapt infrastructures’, E3S Web of Conf., 382p. 1003.

Jamalinia, E., Vardon, P.J. & Steele-Dunne, S.C. (2020) ‘The impact of evaporation induced cracks and precipitation on temporal slope stability’, Computers and Geotechnics, 122p. 103506.

Jones, L., Banks, V. & Jefferson, I. (2020) ‘Chapter 8 Swelling and shrinking soils’, Geological Society, London, Engineering Geology Special Publications, 29(1), pp. 223–242.

Julina, M. & Thyagaraj, T. (2019) ‘Quantification of desiccation cracks using X-ray tomography for tracing shrinkage path of compacted expansive soil’, Acta Geotechnica, 14(1), pp. 35–56.

Kalkan, E. (2011) ‘Impact of wetting–drying cycles on swelling behavior of clayey soils modified by silica fume’, Applied Clay Science, 52(4), pp. 345–352.

Kandalai, S., John, N.J. & Patel, A. (2023) ‘Effects of Climate Change on Geotechnical Infrastructures — state of the art’, Environmental Science and Pollution Research, 30(7), pp. 16878–16904.

Khan, M., Hossain, M., Khan, S., Samir, S. & Aramoon, A. (2017) Impact of Wet-Dry Cycles on the Shear Strength of High Plastic Clay Based on Direct Shear Testing, in [Online]. 2017 pp. 615–622.

Kilsby, C., Glendinning, S., Hughes, P.N., Parkin, G. & Bransby, M.F. (2009) ‘Climate-change impacts on long-term performance of slopes’, Proceedings of the Institution of Civil Engineers - Engineering Sustainability, 162(2), pp. 59–66.

Kodikara, J. & Costa, S. (2013) ‘Desiccation Cracking in Clayey Soils: Mechanisms and Modelling’, in Lyesse Laloui & Alessio Ferrari (eds.) Multiphysical Testing of Soils and Shales. [Online]. 2013 Berlin, Heidelberg: Springer Berlin Heidelberg. pp. 21–32.

Konrad, J.-M. & Alanazi, R. (2011) ‘Desiccation of a sensitive clay: Field experimental observations’, Canadian Geotechnical Journal, 34pp. 929–942.

Konrad, J.-M. & Ayad, R. (1997) ‘An idealized framework for the analysis of cohesive soils undergoing desiccation’, Canadian Geotechnical Journal, 34(4), pp. 477 – 488.

Laboratory, R.R. (1952) ‘Soil Mechanics for Road Engineers’. HSMO

Lakshmikantha, M.R., Prat, P. & Ledesma, A. (2012) ‘Experimental evidence of size effect in soil cracking’, Canadian Geotechnical Journal, 49pp. 264–284.

Lakshmikantha, M.R., Prat, P. & Ledesma, A. (2009) ‘Image Analysis for the Quantification of a Developing Crack Network on a Drying Soil’, Geotechnical Testing Journal - GEOTECH TESTING J, 32.

Lakshmikantha, M.R., Prat, P.C. & Ledesma, A. (2018) ‘Boundary Effects in the Desiccation of Soil Layers with Controlled Environmental Conditions’, Geotechnical Testing Journal, 41(4), pp. 675–697.

Lakshmikantha, M.R., Prat, P.C., Tapia, J. & Ledesma, A. (2008) ‘Effect of moisture content on tensile strength and fracture toughness of a silty soil’, in Unsaturated Soils: Advances in Geo-Engineering - Proceedings of the 1st European Conference on Unsaturated Soils, E-UNSAT 2008. [Online]. 2008 pp. 405 – 409.

Lakshmikantha, M.R., Reig, R., Prat, P.C. & Ledesma, A. (2013) ‘Origin and Mechanism of Cracks Seen at the Bottom of a Desiccating Soil Specimen’, in Geo-Congress 2013. [Online]. pp. 790–799.

Leonard, A., Blacher, S., Marchot, P., Pirard, J.P. & Crine, M. (2003) ‘Image analysis of X-ray microtomograms of soft materials during convective drying’, Journal of Microscopy, 212(2), pp. 197 – 204.

Levatti, H. (2023) ‘Review of Methods to Solve Desiccation Cracks in Clayey Soils’, Geotechnics, 3pp. 808–828.

Levatti, H.U., Prat, P.C., Ledesma, A., Cuadrado, A. & Cordero, J.A. (2017) ‘Experimental Analysis of 3D Cracking in Drying Soils Using Ground-Penetrating Radar’, Geotechnical Testing Journal, 40(2), pp. 221–243.

Li, J.H., Lu, Z., Guo, L.B. & Zhang, L.M. (2017) ‘Experimental study on soil-water characteristic curve for silty clay with desiccation cracks’, Engineering Geology, 218pp. 70–76.

Li, J.H. & Zhang, L.M. (2011) ‘Study of desiccation crack initiation and development at ground surface’, Engineering Geology, 123(4), pp. 347–358.

Liu, C., Tang, C.-S., Shi, B. & Suo, W.-B. (2013) ‘Automatic quantification of crack patterns by image processing’, Computers & Geosciences, 57pp. 77–80.

Liu, G., Toll, D., Kong, L.-W. & Asquith, J. (2020) ‘Matric Suction and Volume Characteristics of Compacted Clay Soil under Drying and Wetting Cycles’, Geotechnical Testing Journal, 43p. 20170310.

Liu, P., Xia, Y. & Shang, M. (2020) ‘A bench-scale assessment of the effect of soil temperature on bare soil evaporation in winter’, Hydrology Research, 51(6), pp. 1349–1357.

Liu, Y., Zhao, Y., Vanapalli, S.K. & Mehmood, M. (2024) ‘Soil-water characteristic curve of expansive soils considering cumulative damage effects of wetting and drying cycles’, Engineering Geology, 339p. 107642.

Louati, F., Trabelsi, H., Jamei, M. & Taibi, S. (2021) ‘Impact of wetting-drying cycles and cracks on the permeability of compacted clayey soil’, European Journal of Environmental and Civil Engineering, 25(4), pp. 696–721.

Loveridge, F.A., Spink, T.W., O’Brien, A.S., Briggs, K.M. & Butcher, D. (2010) ‘The impact of climate and climate change on infrastructure slopes, with particular reference to southern England’, Quarterly Journal of Engineering Geology and Hydrogeology, 43(4), pp. 461–472.

Luo, Y., Zhang, J., Zhou, Z., Shen, Z., Chong, L. & Victor, C. (2021) ‘Investigation and prediction of water infiltration process in cracked soils based on a full-scale model test’, Geoderma, 400p. 115111.

Luo, Y., Zhang, J., Zhou, Z. & Victor, C. (2023) ‘Modelling preferential flow induced by dynamic changes of desiccation cracks: A comparative numerical study’, Geoderma, 433p. 116471.

Luo, Z., Wang, S., Ou, Q., Hamka, M.Q., Li, X., Xu, C. & Ding, X. (2023) ‘Multi-effect investigation on desiccation crack evolution and mechanical behavior of swelling clay’, Acta Geotechnica,

Ma, T., Wei, C., Yao, C. & Yi, P. (2020) ‘Microstructural evolution of expansive clay during drying–wetting cycle’, Acta Geotechnica, 15(8), pp. 2355–2366.

McBrayer, M.C., Mauldon, M., Drumm, E.C. & , G. V (1997) ‘Infiltration Tests on Fractured Compacted Clay’, Journal of Geotechnical and Geoenvironmental Engineering, 123(5), pp. 469–473.

Met Office (2018) UKCP18 headline findings v4. Available at: https://www.metoffice.gov.uk/binaries/content/assets/metofficegovuk/pdf/research/ukcp/ukcp18_headline_findings_v4_aug22.pdf (Accessed: 27 November 2024).

Meter Group (2021) ‘PARIO Automated Soil Particle Size Analyzer: User Manual. Version 1.2. Munich, Germany: Meter Group. Available at: https://metergroup.com/products/pario/pario-support/ (Accessed: 27 November 2024).

Miller, C. J., Mi, H. & Yesiller, N., 1998. Experimental analysis of desiccation crack propagation in clay liners. Journal of the American Water Resources Association 34(3), 677-686.

Miller, G., Hassanikhah, A. & Varsei, M. (2015) Desiccation crack depth and tensile strength in compacted soil, in [Online]. 2015

Monteith, J.L., 1965. Evaporation and environment. In *Symposia of the society for experimental biology* (Vol. 19, pp. 205-234). Cambridge University Press (CUP) Cambridge.

Morris, P.H., Graham, J. & Williams, D.J. (1992) 'Cracking in drying soils', Canadian Geotechnical Journal, 29(2), pp. 263–277.

Morsy, A.M., Helm, P.R., El-Hamalawi, A., Smith, A., Hughes, P.N., Stirling, R.A., Dijkstra, T.A., Dixon, N. & Glendinning, S. (2023) 'Development of a Multiphase Numerical Modeling Approach for Hydromechanical Behavior of Clay Embankments Subject to Weather-Driven Deterioration', Journal of Geotechnical and Geoenvironmental Engineering, 149(8), p. 4023062.

Muddle, D.M. & Briggs, K.M. (2019) 'Macropore structure and permeability of clay fill samples from a historic clay fill earthwork', Transportation Geotechnics, 19pp. 96–109.

Mukhlisin, M. & Khiyon, K.N. (2018) 'The Effects of Cracking on Slope Stability', Journal of the Geological Society of India, 91(6), pp. 704–710.

Nachshon, U., Dragila, M. & Weisbrod, N. (2012) 'From atmospheric winds to fracture ventilation: Cause and effect', Journal of Geophysical Research: Biogeosciences, 117(G2), .

Nahlawi, H. & Kodikara, J.K. (2006) 'Laboratory experiments on desiccation cracking of thin soil layers', Geotechnical & Geological Engineering, 24(6), pp. 1641–1664.

Network Rail (2018) 'Earthworks Technical Strategy'. Network Rail, United Kingdom (June).

Ng, C.W.W., Wang, Y., Zhang, S. & Zhang, Q. (2024) 'Effects of climate change on soil embankments for transport infrastructure', Transportation Geotechnics, 48p. 101324.

Nicholls, R.A. (1994) ‘M40 Oxford–Birmingham: geology and geotechnics of the Waterstock–Banbury section’, Proceedings of the Institution of Civil Engineers - Transport, 105(4), pp. 283–295.

Novák, V., Šimåunek, J. & van Genuchten, M.Th. (2000) ‘Infiltration of Water into Soil with Cracks’, Journal of Irrigation and Drainage Engineering, 126(1), pp. 41–47.

Nowamooz, H. & Masrouri, F. (2010) ‘Relationships between soil fabric and suction cycles in compacted swelling soils’, Engineering Geology, 114(3), pp. 444–455.

ORR (2024) Annual report of health and safety on Britain’s railways 2023 to 2024.

ORR (2021) Earthworks and Drainage Weather Resilience - Targeted Assurance Review. (May).

Penman, H.L., 1948. Natural evaporation from open water, bare soil and grass. *Proceedings of the Royal Society of London. Series A. Mathematical and Physical Sciences*, *193*(1032), pp.120-145.

Peron, H., Hueckel, T., Laloui, L. & Hu, L.B. (2009) ‘Fundamentals of desiccation cracking of fine-grained soils: experimental characterisation and mechanisms identification’, Canadian Geotechnical Journal, 46(10), pp. 1177–1201.

Perry, J., Pedley, M. & Reid, M. (2003) ‘Infrastructure embankments: condition appraisal and remedial treatment’, Ciria, pp. 174–180.

Pires, L.F., Cooper, M., Cássaro, F.A.M., Reichardt, K., Bacchi, O.O.S. & Dias, N.M.P. (2008) ‘Micromorphological analysis to characterize structure modifications of soil samples submitted to wetting and drying cycles’, CATENA, 72(2), pp. 297–304.

Poulsen, T.G. (2022) ‘Predicting evaporation from moist, cracked soil, based on near-surface wind speed, crack width and crack distance’, European Journal of Soil Science, 73(1), p. e13215.

Poulsen, T.G., Cai, W. & Garg, A. (2020) ‘Water evaporation from cracked soil under moist conditions as related to crack properties and near-surface wind speed’, European Journal of Soil Science, 71(4), pp. 627–640.

Power, C., Mian, J., Spink, T., Abbott, S. & Edwards, M. (2016) ‘Development of an Evidence-based Geotechnical Asset Management Policy for Network Rail, Great Britain’, Procedia Engineering, 143pp. 726–733.

Powrie, W. & Smethurst, J. (2019) ‘Climate and Vegetation Impacts on Infrastructure Cuttings and Embankments’, in Liangtong Zhan, Yunmin Chen, & Abdelmalek Bouazza (eds.) Proceedings of the 8th International Congress on Environmental Geotechnics Volume 1. [Online]. 2019 Singapore: Springer Singapore. pp. 128–144.

Proctor, R.R. (1993) ‘Fundamental Principles of Soil Compaction’, Enginering News Record,

Qi, W., Zhang, Zhan-yu, Wang, C., Chen, Y. & Zhang, Ze-min (2020) ‘Crack closure and flow regimes in cracked clay loam subjected to different irrigation methods’, Geoderma, 358p. 113978.

Qian, J., Lin, Z. & Shi, Z. (2022) ‘Experimental and modeling study of water-retention behavior of fine-grained soils with dual-porosity structures’, Acta Geotechnica, 17(8), pp. 3245–3258.

Reeves, G.M., Sims, I. & Cripps, J.C. (2006) Clay Materials Used in Construction. Geological Society of London.

Reid, J.M. & Clark, G.T. (2000) ‘A whole life cost model for earthworks slopes’. TRL430

Ridley, A., McGinnity, B. & Vaughan, P. (2004) ‘Role of pore water pressures in embankment stability’, Proceedings of the Institution of Civil Engineers - Geotechnical Engineering, 157(4), pp. 193–198.

Ridley, A.M. (2012) Relationships between climate, vegetation, pore water pressures and the serviceability of clay slopes, in [Online]. 2012

Ritchie, J.T. & Adams, J.E. (1974) ‘Field Measurement of Evaporation from Soil Shrinkage Cracks’, Soil Science Society of America Journal, 38(1), pp. 131–134.

Robert Mair, Lord (2021) ‘A Review of Earthworks Management’, Network Rail, (February), .

Römkens, M.J.M. & Prasad, S.N. (2006) ‘Rain Infiltration into swelling/shrinking/cracking soils’, Agricultural Water Management, 86(1), pp. 196–205.

Rouainia, M., Helm, P., Davies, O. and Glendinning, S. 2020. Deterioration of an infrastructure cutting subjected to climate change. Acta Geotechnica, 15, 2997–3016.

Sanchez, M., Atique, A., Kim, S., Romero, E. & Zielinski, M. (2013) ‘Exploring desiccation cracks in soils using a 2D profile laser device’, Acta Geotechnica, 8(6), pp. 583–596.

Sawada, M., Sumi, Y. & Mimura, M. (2021) ‘Measuring desiccation-induced tensile stress during cracking process’, Soils and Foundations, 61.

Scherer, G.W. (1990) ‘Theory of Drying’, Journal of the American Ceramic Society, 73(1), pp. 3–14.

Seto, J.T.C. & Konrad, J.-M. (1994) ‘Pore pressure measurements during freezing of an overconsolidated clayey silt’, Cold Regions Science and Technology, 22(4), pp. 319–338.

Shin, H. & Santamarina, J.C. (2011) ‘Desiccation cracks in saturated fine-grained soils: Particle-level phenomena and effective-stress analysis’, Geotechnique, 61(11), pp. 961 – 972.

Sivakumar, V., Zaini, J., Gallipoli, D. & Solan, B. (2015) ‘Wetting of compacted clays under laterally restrained conditions: initial state, overburden pressure and mineralogy’, Géotechnique, 65(2), pp. 111–125.

Skempton, A.W. (1995) ‘Embankments and Cuttings on the early Railways’, Construction History, 11pp. 33–49.

Slingo, J.M., Davies, P. and Fowler, H.J. 2020. Weather Advisory Task Force (WATF) Final Report, February 2021.

Smethurst, J.A., Clarke, D. & Powrie, W. (2012) ‘Factors controlling the seasonal variation in soil water content and pore water pressures within a lightly vegetated clay slope’, Géotechnique, 62(5), pp. 429–446.

Smethurst, J.A., Smith, A., Uhlemann, S., Wooff, C., Chambers, J., Hughes, P., Lenart, S., Saroglou, H., Springman, S.M., Löfroth, H. & Hughes, D. (2017) ‘Current and future role of instrumentation and monitoring in the performance of transport infrastructure slopes’, Quarterly Journal of Engineering Geology and Hydrogeology, 50(3), pp. 271–286.

Song, W., Cui, Y.-J., Tang, A.-M. & Ding, W.-Q. (2013) ‘Development of a Large-Scale Environmental Chamber for Investigating Soil Water Evaporation’, Geotechnical Testing Journal, 36p. 20120142.

Song, W.-K., Cui, Y.-J., Tang, A.M., Ding, W.-Q. & Wang, Q. (2016) ‘Experimental study on water evaporation from compacted clay using environmental chamber’, Canadian Geotechnical Journal, 53(8), pp. 1293–1304.

Spink, T. (2020) ‘Strategic geotechnical asset management’, Quarterly Journal of Engineering Geology and Hydrogeology, 53(2), pp. 304–320.

Stirling, R., Davie, C. & Glendinning, S. (2013) ‘Numerical modelling of desiccation crack induced permeability’, Proceedings of the 18th International Conference on Soil Mechanics and Geotechnical Engineering, Paris, pp. 813–816.

Stirling, R., Glendinning, S., Davie, C., Hen-Jones, R. & Hughes, P. (2018) The Behaviour and Influence of Desiccation Cracking on a Full-Scale, Vegetated Infrastructure Embankment, in [Online]. September 2018

Stirling, R.A., Hughes, P., Davie, C.T. & Glendinning, S. (2015) ‘Tensile behaviour of unsaturated compacted clay soils — A direct assessment method’, Applied Clay Science, 112–113pp. 123–133.

Stirling, R.A., Toll, D.G., Glendinning, S., Helm, P.R., Yildiz, A., Hughes, P.N. & Asquith, J.D. (2021) ‘Weather-driven deterioration processes affecting the performance of embankment slopes’, Géotechnique, 71(11), pp. 957–969.

Sun, C., Tang, C.-S. & Cheng, Q. (2024) ‘Coupling Effect of Climate Change and Soil Cracks on the Stability of Soil Slopes’, in Sijing Wang, Runqiu Huang, Rafig Azzam, & Vassilis P Marinos (eds.) Engineering Geology for a Habitable Earth: IAEG XIV Congress 2023 Proceedings, Chengdu, China. [Online]. 2024 Singapore: Springer Nature Singapore. pp. 171–186.

Tang, A.M., Hughes, P.N., Dijkstra, T.A., Askarinejad, A., Brenčič, M., Cui, Y.J., Diez, J.J., Firgi, T., Gajewska, B., Gentile, F., Grossi, G., Jommi, C., Kehagia, F., Koda, E., ter Maat, H.W., Lenart, S., Lourenco, S., Oliveira, M., Osinski, P., et al. (2018) ‘Atmosphere–vegetation–soil interactions in a climate change context; impact of changing conditions on engineered transport infrastructure slopes in Europe’, Quarterly Journal of Engineering Geology and Hydrogeology, 51(2), pp. 156–168.

Tang, C., Shi, B., Gao, W., Chen, F. & Cai, Y. (2007) ‘Strength and mechanical behavior of short polypropylene fiber reinforced and cement stabilized clayey soil’, Geotextiles and Geomembranes, 25(3), pp. 194–202.

Tang, C., Shi, B., Liu, C., Zhao, L. & Wang, B. (2008) ‘Influencing factors of geometrical structure of surface shrinkage cracks in clayey soils’, Engineering Geology, 101(3), pp. 204–217.

Tang, C., Shi, B., Liu, C., Zhao, L. & Wang, B. (2008c) ‘Influencing factors of geometrical structure of surface shrinkage cracks in clayey soils’, Engineering Geology, 101(3), pp. 204–217.

Tang, C.-S., Cheng, Q., Leng, T., Shi, B., Zeng, H. & Inyang, H.I. (2020) ‘Effects of wetting-drying cycles and desiccation cracks on mechanical behavior of an unsaturated soil’, CATENA, 194p. 104721.

Tang, C.-S., Cui, Y.-J., Shi, B., Tang, A.-M. & Liu, C. (2011) ‘Desiccation and cracking behaviour of clay layer from slurry state under wetting–drying cycles’, Geoderma, 166(1), pp. 111–118.

Tang, C.-S., Cui, Y.-J., Tang, A.-M. & Shi, B. (2010) ‘Experiment evidence on the temperature dependence of desiccation cracking behavior of clayey soils’, Engineering Geology, 114(3), pp. 261–266.

Tang, C.-S., Shi, B., Liu, C., Gao, L. & Inyang, H. (2010) ‘Experimental Investigation of the Desiccation Cracking Behavior of Soil Layers during Drying’, Journal of Materials in Civil Engineering, 23(6), pp. 873–878.

Tang, C.-S., Shi, B., Liu, C., Suo, W.-B. & Gao, L. (2011) ‘Experimental characterization of shrinkage and desiccation cracking in thin clay layer’, Applied Clay Science, 52(1), pp. 69–77.

Tang, C.-S., Zhu, C., Cheng, Q., Zeng, H., Xu, J.-J., Tian, B.-G. & Shi, B. (2021) ‘Desiccation cracking of soils: A review of investigation approaches, underlying mechanisms, and influencing factors’, Earth-Science Reviews, 216p. 103586.

Tang, C.-S., Zhu, C., Leng, T., Shi, B., Cheng, Q. & Zeng, H. (2019) ‘Three-dimensional characterization of desiccation cracking behavior of compacted clayey soil using X-ray computed tomography’, Engineering Geology, 255pp. 1–10.

Tarantino, A. & Di Donna, A. (2019) ‘Mechanics of unsaturated soils: Simple approaches for routine engineering practice’, Rivista Italiana di Geotecnica, 44(4), pp. 5–46.

Tian, B.G., Cheng, Q., Tang, C.S. & Shi, B. (2023) ‘Healing behaviour of desiccation cracks in a clayey soil subjected to different wetting rates’, Engineering Geology, 313p. 106973.

Tian, B.-G., Cheng, Q., Tang, C.-S., Zeng, H., Xu, J. & Shi, B. (2022) ‘Effects of compaction state on desiccation cracking behaviour of a clayey soil subjected to wetting-drying cycles’, Engineering Geology, 302p. 106650.

Toll, D.G., Mendes, J., Gallipoli, D., Glendinning, S. & Hughes, P.N. (2012) ‘Investigating the impacts of climate change on slopes: field measurements’, Geological Society, London, Engineering Geology Special Publications, 26(1), pp. 151–161.

Tollenaar, R.N., van Paassen, L.A. & Jommi, C. (2017) ‘Observations on the desiccation and cracking of clay layers’, Engineering Geology, 230pp. 23–31.

Trabelsi, H., Louati, F., Jamei, M. & Taibi, S. (2018) Wet- dry cycles effect on the saturated hydraulic conductivity, in [Online]. September 2018

Ullah, S., Khan, M.U. & Rehman, G. (2020) ‘A Brief Review of the Slope Stability Analysis Methods’, Geological Behavior, 4pp. 73–77.

Vallejo, L.E. (2009) ‘Fractal analysis of temperature-induced cracking in clays and rocks’, Géotechnique, 59(3), pp. 283–286.

Wang, C., Zhang, Z., Liu, Y. & Fan, S. (2017) ‘Geometric and fractal analysis of dynamic cracking patterns subjected to wetting-drying cycles’, Soil and Tillage Research, 170pp. 1–13.

Wang, C., Zhang, Z., Qi, W. & Fan, S. (2018) ‘Morphological Approach to Quantifying Soil Cracks: Application to Dynamic Crack Patterns during Wetting-Drying Cycles’, Soil Science Society of America Journal, 82(4), pp. 757–771.

Wang, L.-L., Tang, C.-S., Shi, B., Cui, Y.-J., Zhang, G.-Q. & Hilary, I. (2018) ‘Nucleation and propagation mechanisms of soil desiccation cracks’, Engineering Geology, 238pp. 27–35.

Wei, X., Hattab, M., Bompard, P. & Fleureau, J.-M. (2016) ‘Highlighting some mechanisms of crack formation and propagation in clays on drying path’, Géotechnique, 66(4), pp. 287–300.

Weinberger, R. (2001) ‘Evolution of polygonal patterns in stratified mud during desiccation: The role of flaw distribution and layer boundaries’, GSA Bulletin, 113(1), pp. 20–31.

Weinberger, R. (1999) ‘Initiation and growth of cracks during desiccation of stratified muddy sediments’, Journal of Structural Geology, 21(4), pp. 379–386.

Wells, R.R., DiCarlo, D.A., Steenhuis, T.S., Parlange, J.-Y., Römkens, M.J.M. & Prasad, S.N. (2003) ‘Infiltration and Surface Geometry Features of a Swelling Soil following Successive Simulated Rainstorms’, Soil Science Society of America Journal, 67(5), pp. 1344–1351.

White A, Chambers J, Whiteley J, Wilkinson P, Boyd J, Briggs K, Blake A, Smethurst J, Glendinning S, Stirling R, Uhlemann S.(2024) ‘Rapid Condition Assessment of Earthwork Assets’, Ground Engineering, pp. 28–32.

Xiao, G., Ye, Z., Xu, G., Zeng, J. & Zhang, L. (2021) ‘Temperature Effect on Crack Evolution of Red Clay in Guilin’, Water, 13(21), .

Xu, Xu-tang, Shao, L., Huang, J., Xu, Xiang, Liu, D., Xian, Z. & Jian, W. (2021) ‘Effect of wet-dry cycles on shear strength of residual soil’, Soils and Foundations, 61(3), pp. 782–797.

Yesiller, N., Miller, C.J., Inci, G. & Yaldo, K. (2000) ‘Desiccation and cracking behavior of three compacted landfill liner soils’, Engineering Geology, 57(1), pp. 105–121.

Yu, Z., Eminue, O.O., Stirling, R., Davie, C. & Glendinning, S. (2021) ‘Desiccation cracking at field scale on a vegetated infrastructure embankment’, Géotechnique Letters, 11(1), pp. 88–95.

Zaidi, M., Ahfir, N.-D., Alem, A., Taibi, S., El Mansouri, B., Zhang, Y. & Wang, H. (2021) ‘Use of X-ray computed tomography for studying the desiccation cracking and self-healing of fine soil during drying–wetting paths’, Engineering Geology, 292p. 106255.

Zarzycki, J., Prassas, M. & Phalippou, J. (1982) ‘Synthesis of glasses from gels: the problem of monolithic gels’, Journal of Materials Science, 17(11), pp. 3371 – 3379.

Zeng, H., Tang, C.-S., Cheng, Q., Zhu, C., Yin, L.-Y. & Shi, B. (2020) ‘Drought-Induced Soil Desiccation Cracking Behavior With Consideration of Basal Friction and Layer Thickness’, Water Resources Research, 56(7), p. e2019WR026948.

Zeng, H., Tang, C.-S., Zhu, C., Vahedifard, F., Cheng, Q. & Shi, B. (2022) ‘Desiccation cracking of soil subjected to different environmental relative humidity conditions’, Engineering Geology, 297p. 106536.

Zeng, L., Liu, J., Zhang, J., Bian, H. & Lu, W. (2018) ‘Effect of Colluvial Soil Slope Fracture’s Anisotropy Characteristics on Rainwater Infiltration Process’ Annan Zhou (ed.), Advances in Civil Engineering, 2018p. 7351628.

Zeng, Z.-J., Tang, C.-S., Zhu, C., Cheng, Q., Luo, Z.-Q., Yang, Z.-M. & Shi, B. (2024) ‘An improved cracked soil evaporation model accounting for solar radiation and wind effect’, Computers and Geotechnics, 174p. 106598.

Zhang, J., Zhu, D. & Zhang, S. (2020) ‘Shallow slope stability evolution during rainwater infiltration considering soil cracking state’, Computers and Geotechnics, 117p. 103285.

Zhang, L. & Fredlund, D. (2006) Characteristics of water retention curves for unsaturated fractured rocks, in [Online]. 2006

Zhao, G., Han, Z., Zou, W. & Wang, X. (2021a) ‘Evolution of mechanical behaviours of an expansive soil during drying-wetting, freeze–thaw, and drying-wetting-freeze–thaw cycles’, Bulletin of Engineering Geology and the Environment, 80(10), pp. 8109–8121.

Zhao, G., Han, Z., Zou, W. & Wang, X. (2021b) ‘Evolution of mechanical behaviours of an expansive soil during drying-wetting, freeze–thaw, and drying-wetting-freeze–thaw cycles’, Bulletin of Engineering Geology and the Environment, 80(10), pp. 8109–8121.

Zhong, H., Wang, Y., Zhang, S., Zhang, Q. & Ng, C.W.W. (2024) ‘Effects of extreme drought–rainfall on slope failure mechanisms: centrifuge modelling’, Canadian Geotechnical Journal, 61(4), pp. 820–826.

Zhuo, Z., Zhu, C., Tang, C.-S., Xu, H., Shi, X. & Mark, V. (2022) ‘3D characterization of desiccation cracking in clayey soils using a structured light scanner’, Engineering Geology, 299p. 106566.

Appendix A

Appendix A details the MATLAB code designed for the analysis of images captured from both surface and subsurface desiccation cracks generated during the wind speed tests (refer to Section 5.3). Furthermore, Tables X to X present the findings from a comprehensive sensitivity analysis aimed at refining several key components of this code, including the adaptive threshold sensitivity value, structuring element size and width, as well as the colour space threshold type. This thorough analysis plays a crucial role in enhancing the accuracy and reliability of the image processing methodology employed in this study.

Surface Crack Image Analysis MATLAB Code

```
%% This code was used to obtain the surface Crack Intensity Factor for the images taken during the wind speed experiment

% Specify input and output folders

    inputFolder = 'path_to_input_folder'; Replace 'path_to_input_folder' with actual path to folder where images are stored

    outputFolder = 'path_to_output_folder'; Replace 'path_to_output_folder' with actual path to folder where images are stored

% Get a list of all surface crack image files within the input folder

    imageFiles = dir(fullfile(inputFolder, '*.jpg')); % Update the extension if your images have a different format

% Initialise arrays to store pixel counts

    numZerosAll = zeros(length(imageFiles), 1);

    numOnesAll = zeros(length(imageFiles), 1);

% Create output directory for masks created during the binarisation of the surface crack images

    maskFolder = fullfile(outputFolder, 'masks');

    if ~exist(maskFolder, 'dir')

        mkdir(maskFolder);

    end

% Loop through each surface crack image file in the input folder and apply the image processing techniques to output the number of cracked and non-cracked pixels to an excel file

    for i = 1:length(imageFiles)

        % Load the image

        imagePath = fullfile(inputFolder, imageFiles(i).name);

        X = imread(imagePath);
```

```
        % Convert the image to grayscale
        imgray = im2gray(X);

        % Apply an adaptive threshold to convert the surface crack image to binary
        BW = imbinarize(imgray, 'adaptive', 'Sensitivity', 0.9, 'ForegroundPolarity', 'bright');

        % Apply open and close morphological operators to reduce noise in the binarised image
        width = 4;
        se = strel('square', width);
        BW_opened = imopen(BW, se);

        % Close mask with square
        width = 4;
        se = strel('square', width);
        BW_closed = imclose(BW_opened, se);

        % Save the binary mask image to a specified folder within your specified output path
        maskImagePath = fullfile(maskFolder, ['mask_' imageFiles(i).name]);
        imwrite(BW_closed, maskImagePath);

        % Calculate the number of 0 and 1 pixels
        numZeros = sum(BW_closed(:) == 0);
        numOnes = sum(BW_closed(:) == 1);

        % Store pixel counts
        numZerosAll(i) = numZeros;
        numOnesAll(i) = numOnes;
    end

% Create a table to store pixel count results
    results = table({imageFiles.name}', numZerosAll, numOnesAll, 'VariableNames', {'Image_Name',
    'Num_Zeros', 'Num_Ones'});

% Save the results to your output folder as an Excel file called 'CIF_results.xlsx' and display a message
once successful
    writetable(results, fullfile(outputFolder, 'CIF_results.xlsx'));
    disp('Pixel count results saved to Excel file successfully.');
```

Subsurface Crack Image Analysis MATLAB Code

Step 1 – Create a Function for Colour Thresholding Crack Image

```
function [BW, maskedRGBImage] = createMask(RGB)
    %createMask  Threshold RGB image using auto-generated code from the colorThresholder app.
    %  [BW, MASKEDRGBIMAGE] = createMask(RGB) thresholds image RGB using
    %  auto-generated code from the colorThresholder app. The colorspace and
    %  range for each channel of the colorspace were set within the app.
    %  The segmentation mask is returned in BW, and a composite of the mask and
    %  original RGB images is returned in maskedRGBImage.

    % Convert RGB image to chosen color space
    I = rgb2hsv(RGB);

    % Define thresholds for channel 1 based on histogram settings
    channel1Min = 0.086;
    channel1Max = 0.208;


    % Define thresholds for channel 2 based on histogram settings
    channel2Min = 0.000;
    channel2Max = 1.000;

    % Define thresholds for channel 3 based on histogram settings
    channel3Min = 0.000;
    channel3Max = 1.000;

    % Create mask based on chosen histogram thresholds
    sliderBW = (I(:,:,1) >= channel1Min ) & (I(:,:,1) <= channel1Max) & ...
            (I(:,:,2) >= channel2Min ) & (I(:,:,2) <= channel2Max) & ...
            (I(:,:,3) >= channel3Min ) & (I(:,:,3) <= channel3Max);
    BW = sliderBW

    % Morphological operations for refinement
    se = strel('disk', 10);
    BW = imopen(BW, se);
    BW = imclose(BW, se);

    % Initialise output masked image based on input image
    maskedRGBImage = RGB;

    % Set background pixels where BW is false to zero
```

```
    maskedRGBImage(repmat(~BW, [1 1 3])) = 0;

end
```

Step 2 – Output Binary Masks and Conduct CIF Calculation

```
%%% Function to output binary masks and count pixel values

% Define input and output folder paths

addpath('path_to_mask_function');  % Replace with the actual path where createMask.m function is located

inputFolder = 'path_to_input_folder'; Replace 'path_to_input_folder' with actual path to folder where images are stored

outputFolder = 'path_to_output_folder'; Replace 'path_to_input_folder' with actual path to folder where images are stored

excelFilePath = 'path_to_excel_file'; % Path to save the Excel file

% Create the output folder if it does not exist

if ~exist(outputFolder, 'dir')

    mkdir(outputFolder);

end

% Get a list of all images in the input folder (assuming JPG format)

imageFiles = dir(fullfile(inputFolder, '*.jpg')); % Adjust file extension if needed

% Initialize a cell array to store pixel counts

pixelCounts = cell(length(imageFiles), 3); % Each row will contain the filename, black count, and white count

pixelCounts(1, :) = {'Filename', 'Black Pixel Count', 'White Pixel Count'}; % Header row

% Loop over each image in the folder

for k = 1:length(imageFiles)

    % Read the current image

    imagePath = fullfile(inputFolder, imageFiles(k).name);

    RGB = imread(imagePath);

    % Apply the color thresholding mask to get binary image

    [BW, ~] = createMask1(RGB); % Call your createMask function (Step 1)

    % Create output path for the binary image

    [~, name, ~] = fileparts(imageFiles(k).name); % Get file name without extension

    outputImagePath = fullfile(outputFolder, [name '_BW.jpg']);

    % Save the binary mask image (BW)
```

```
    imwrite(BW, outputImagePath, 'jpg'); % Save as jpg binary image

    % Count the number of black and white pixels
    blackPixelCount = sum(BW(:) == 0); % Count of black pixels
    whitePixelCount = sum(BW(:) == 1); % Count of white pixels

    % Store the counts in the pixelCounts array
    pixelCounts(k + 1, :) = {name, blackPixelCount, whitePixelCount}; % Store filename, black, and white counts

    % Display progress in the command window
    disp(['Processed and saved: ', name, '_BW.jpg']);
end

% Write the pixel counts to an Excel file
writecell(pixelCounts, excelFilePath); % Write the cell array to an Excel file
disp(['Pixel counts saved to: ', excelFilePath]);
disp('Processing complete. Binary images saved to the output folder.');
```

Table A.1: Sensitivity analysis on the impact of the adaptive threshold sensitivity values 0.4, 0.9 and 1.0 on the resultant CIF. This analysis was conducted on four images sampled from the 4.5 m/s wind speed dataset. The chosen option is highlighted in green, which for this study was a sensitivity threshold of 0.9, as it was most efficient at removing background noise whilst preserving the crack area.

W3 – 4.5 m/s wind speed			
IMG1 – Original Image	IMG2 – Original Image	IMG3 – Original Image	IMG4 – Original Image
			
IMG1 – Sensitivity 0.4 (CIF = 99.82%)	IMG2 – Sensitivity 0.4 (CIF = 99.84%)	IMG3 – Sensitivity 0.4 (CIF = 98.56%)	IMG4 – Sensitivity 0.4 (CIF = 98.47%)
			
IMG1 – Sensitivity 0.9 (CIF = 0.38%)	IMG2 – Sensitivity 0.9 (CIF = 0.43%)	IMG3 – Sensitivity 0.9 (CIF = 0.72%)	IMG4 – Sensitivity 0.9 (CIF = 0.47%)
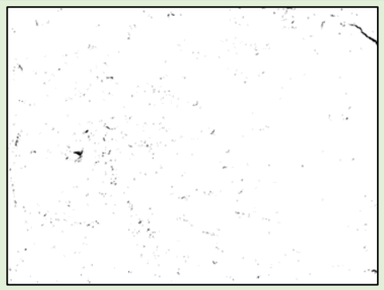	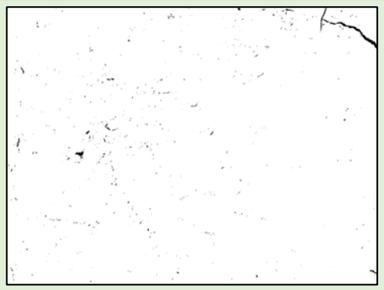		
IMG1 – Sensitivity 1.0 (CIF = 0.15%)	IMG2 – Sensitivity 1.0 (CIF = 0.23%)	IMG3 – Sensitivity 1.0 (CIF = 0.57%)	IMG4 – Sensitivity 1.0 (CIF = 0.35%)
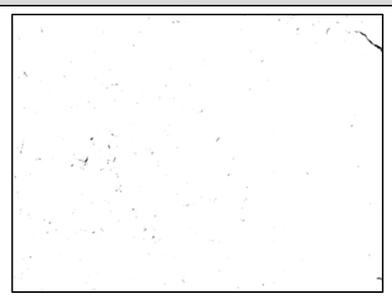	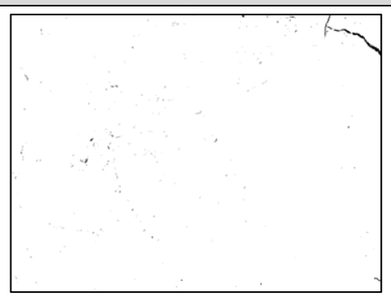	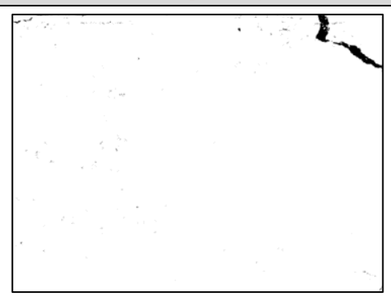	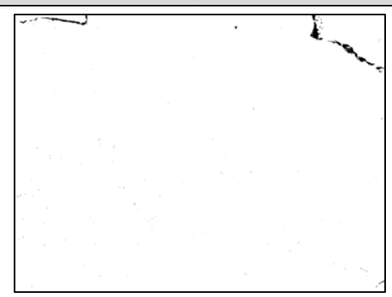

Table A.2: Sensitivity analysis on the impact of disk, diamond and square structuring element shapes used for noise removal on the resultant CIF. The structuring element width was held constant at 4 x 4 pixels. This analysis was conducted on four images sampled from the 4.5 m/s wind speed dataset. The chosen option is highlighted in green, which for this study was the square structuring element, as it was most efficient at removing background noise whilst preserving the crack area.

W3 – 4.5 m/s wind speed			
IMG1 – Original Image	IMG2 – Original Image	IMG3 – Original Image	IMG4 – Original Image
			
IMG1 – SE Shape Disk (CIF = 0.13%)	IMG2– SE Shape Disk (CIF = 0.19%)	IMG3 – SE Shape Disk (CIF = 0.58%)	IMG4 – SE Shape Disk (CIF = 0.38%)
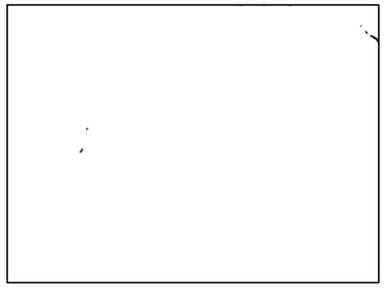	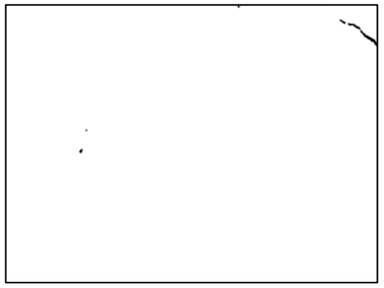	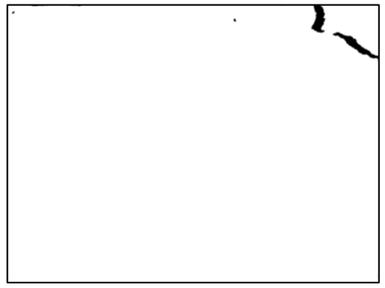	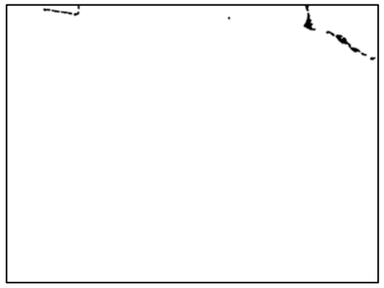
IMG1 – SE Shape Diamond (CIF = 0.12%)	IMG2– SE Shape Diamond (CIF = 0.18%)	IMG3 – SE Shape Diamond (CIF = 0.58%)	IMG4 – SE Shape Diamond (CIF = 0.38%)
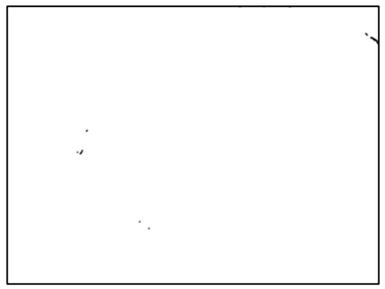	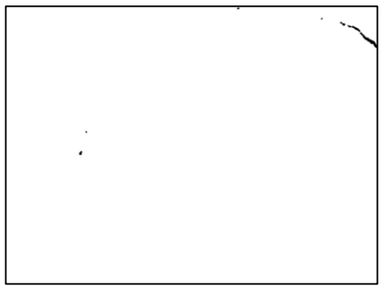	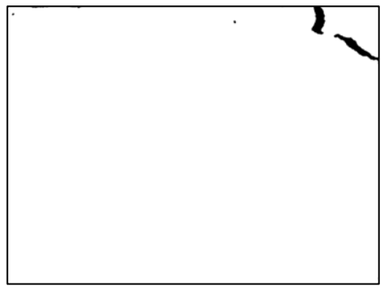	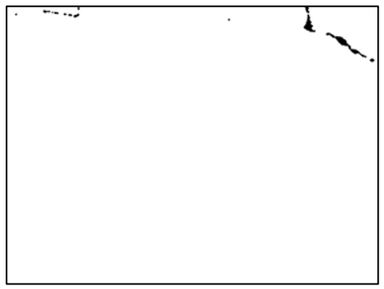
IMG1 – SE Shape Square (CIF = 0.16%)	IMG2– SE Shape Square (CIF = 0.24%)	IMG3 – SE Shape Square (CIF = 0.60%)	IMG4 – SE Shape Square (CIF = 0.39%)
			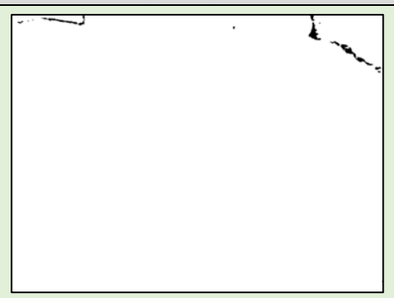

Table A.3: Sensitivity analysis on the impact of a square structuring element of width 1x1 pixels, 4x4 pixels and 8x8 pixels on the resultant CIF. This analysis was conducted on four images sampled from the 4.5 m/s wind speed dataset. The chosen option is highlighted in green, which for this study was the 4x4 structuring element, as it was most efficient at removing background noise whilst preserving the crack area.

W3 – 4.5 m/s wind speed			
IMG1 – Original Image	IMG2 – Original Image	IMG3 – Original Image	IMG4 – Original Image
			
IMG1 – SE Width 1 x 1 pixels (CIF = 0.38%)	IMG2– SE Width 1 x 1 pixels (CIF = 0.43%)	IMG3 – SE Width 1 x 1 pixels (CIF = 0.72%)	IMG4 – SE Width 1 x 1 pixels (CIF = 0.47%)
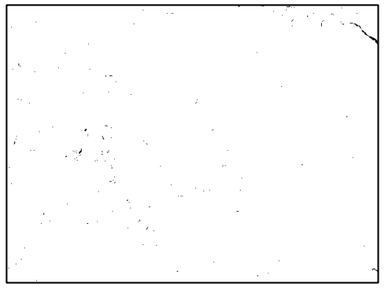	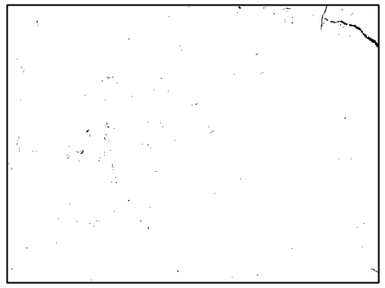	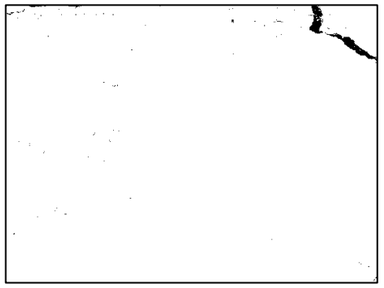	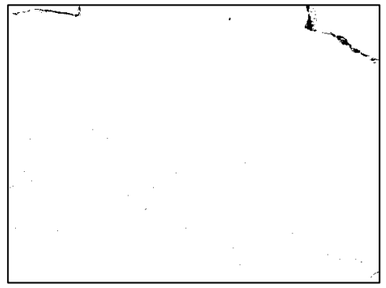
IMG1 – SE Width 4 x 4 pixels (CIF = 0.16%)	IMG2– SE Width 4 x 4 pixels (CIF = 0.24%)	IMG3 – SE Width 4 x 4 pixels (CIF = 0.60%)	IMG4 – SE Width 4 x 4 pixels (CIF = 0.39%)
			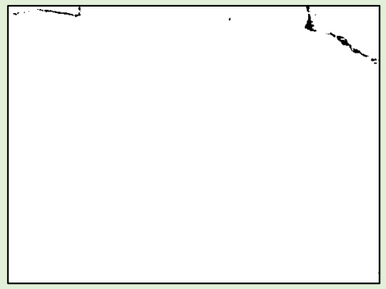
IMG1 – SE Width 8 x 8 pixels (CIF = 0.09%)	IMG2– SE Width 8 x 8 pixels (CIF = 0.16%)	IMG3 – SE Width 8 x 8 pixels (CIF = 0.58%)	IMG4 – SE Width 8 x 8 pixels (CIF = 0.38%)
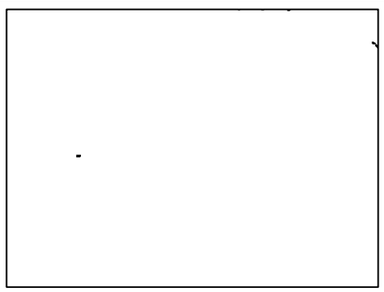	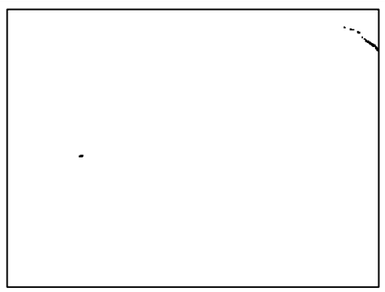	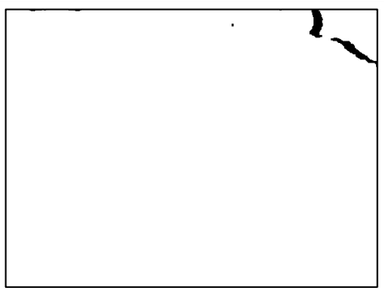	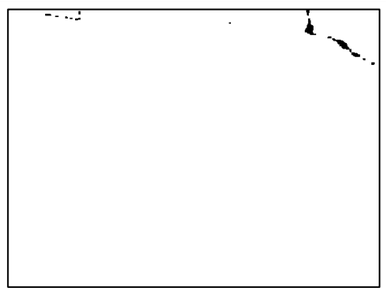

Table A.4: Sensitivity analysis on the impact of the adaptive threshold sensitivity values 0.4, 0.9 and 1.0 on the resultant CIF. This analysis was conducted on four images sampled from the 18 m/s wind speed dataset. The chosen option is highlighted in green, which for this study was a sensitivity threshold of 0.9, as it was most efficient at removing background noise whilst preserving the crack area.

W4 – 18 m/s wind speed			
IMG1 – Original Image	IMG2 – Original Image	IMG3 – Original Image	IMG4 – Original Image
			
IMG1 – Sensitivity 0.4 (CIF = 98.21%)	IMG2 – Sensitivity 0.4 (CIF = 95.05%)	IMG3 – Sensitivity 0.4 (CIF = 91.92%)	IMG4 – Sensitivity 0.4 (CIF = 92.68%)
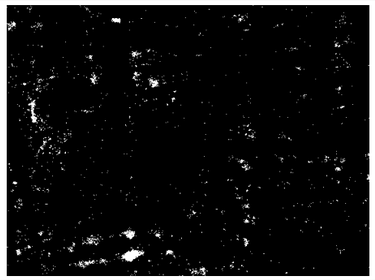	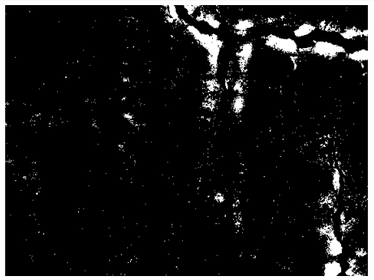	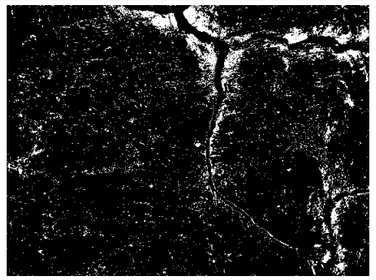	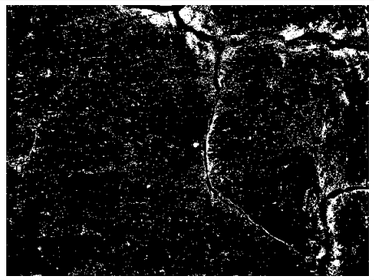
IMG1 – Sensitivity 0.9 (CIF = 2.15%)	IMG2 – Sensitivity 0.9 (CIF = 4.68%)	IMG3 – Sensitivity 0.9 (CIF = 3.98%)	IMG4 – Sensitivity 0.9 (CIF = 3.31%)
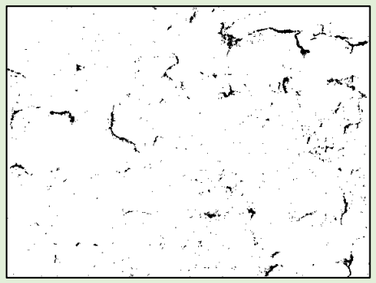	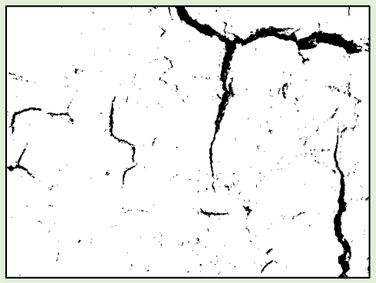	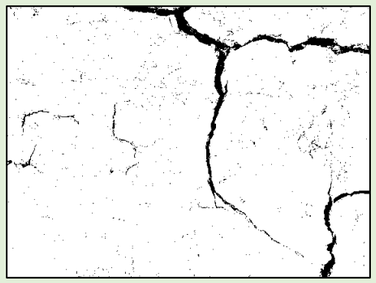	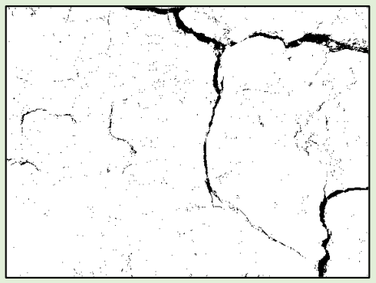
IMG1 – Sensitivity 1.0 (CIF = 0.93%)	IMG2 – Sensitivity 1.0 (CIF = 3.65%)	IMG3 – Sensitivity 1.0 (CIF = 3.22%)	IMG4 – Sensitivity 1.0 (CIF = 2.57%)
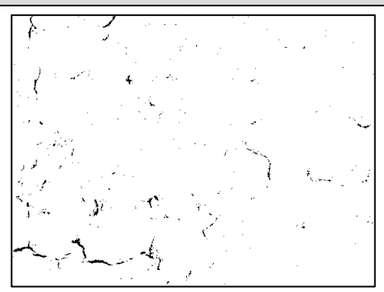	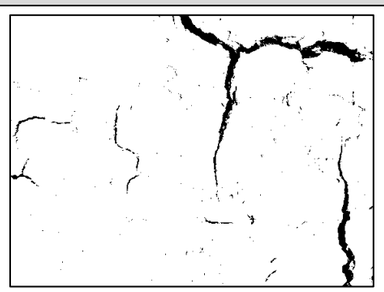	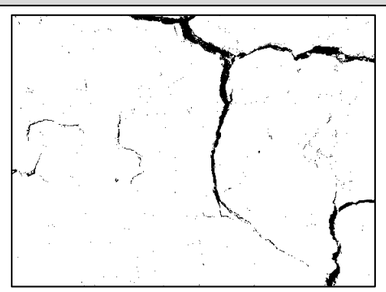	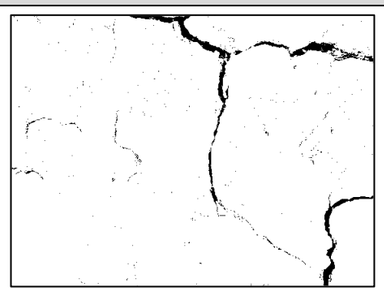

Table A.5: Sensitivity analysis on the impact of disk, diamond and square structuring element shapes used for noise removal on the resultant CIF. The structuring element width was held constant at 4 x 4 pixels. This analysis was conducted on four images sampled from the 18 m/s wind speed dataset. The chosen option is highlighted in green, which for this study was the square structuring element, as it was most efficient at removing background noise whilst preserving the crack area.

W4 – 18 m/s wind speed			
IMG1 – Original Image	IMG2 – Original Image	IMG3 – Original Image	IMG4 – Original Image
			
IMG1 – SE Shape Disk (CIF = 1.73%)	IMG2 – SE Shape Disk (CIF = 4.38%)	IMG3 – SE Shape Disk (CIF = 3.48%)	IMG4 – SE Shape Disk (CIF = 2.73%)
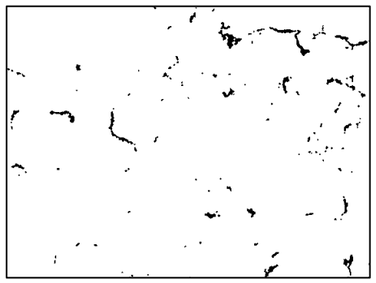	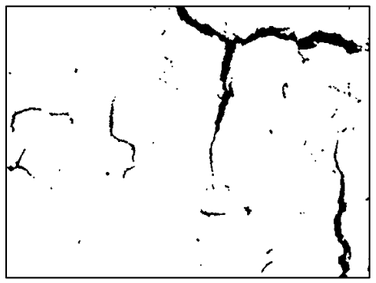		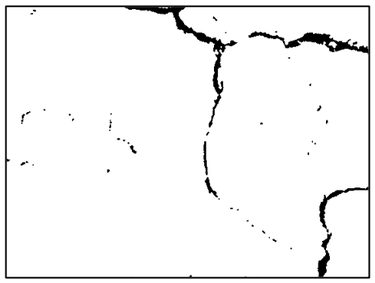
IMG1 – SE Shape Diamond (CIF = 1.66%)	IMG2 – SE Shape Diamond (CIF = 4.36%)	IMG3 – SE Shape Diamond (CIF = 3.53%)	IMG4 – SE Shape Diamond (CIF = 2.79%)
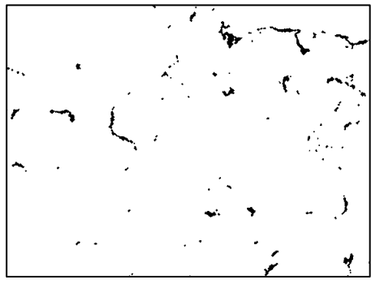	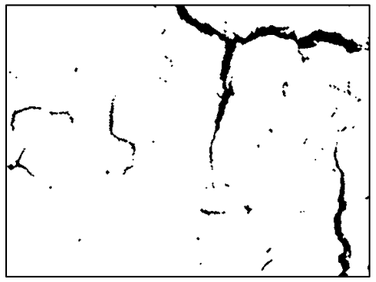		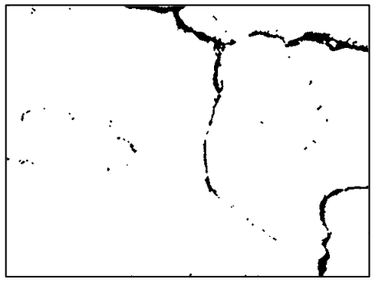
IMG1 – SE Shape Square (CIF = 1.89%)	IMG2 – SE Shape Square (CIF = 4.52 %)	IMG3 – SE Shape Square (CIF = 3.48%)	IMG4 – SE Shape Square (CIF = 2.75%)
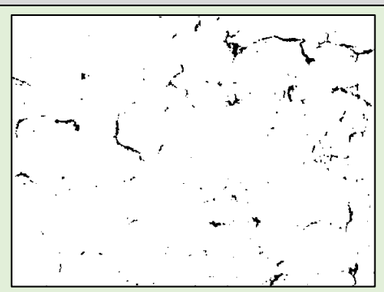	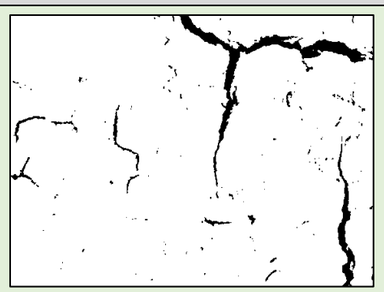		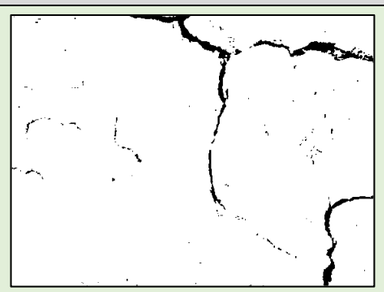

Table A.6: Sensitivity analysis on the impact of a square structuring element of width 1x1 pixels, 4x4 pixels and 8x8 pixels on the resultant CIF. This analysis was conducted on four images sampled from the 18 m/s wind speed dataset. The chosen option is highlighted in green, which for this study was the 4x4 structuring element, as it was most efficient at removing background noise whilst preserving the crack area.

W4 – 18 m/s wind speed			
IMG1 – Original Image	IMG2 – Original Image	IMG3 – Original Image	IMG4 – Original Image
			
IMG1 – SE Width 1 x 1 pixels (CIF = 2.15%)	IMG2 – SE Width 1 x 1 pixels (CIF = 4.68%)	IMG3 – SE Width 1 x 1 pixels (CIF = 3.98%)	IMG4 – SE Width 1 x 1 pixels (CIF = 3.31%)
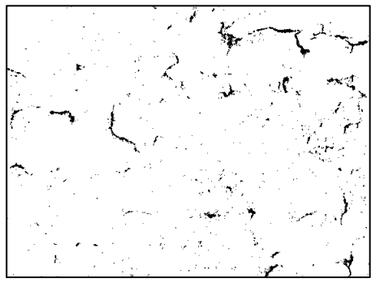	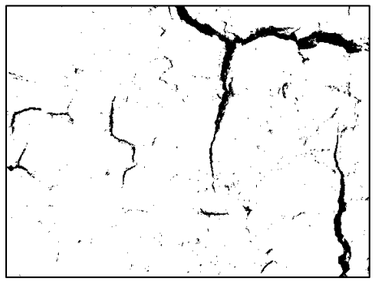	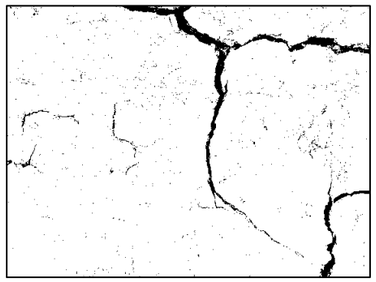	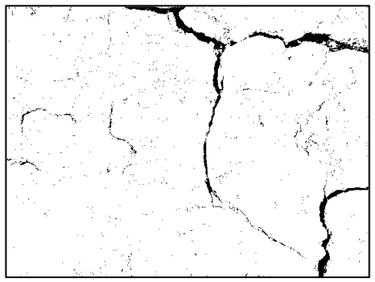
IMG1 – SE Width 4 x 4 pixels (CIF = 1.98%)	IMG2 – SE Width 4 x 4 pixels (CIF = 4.52%)	IMG3 – SE Width 4 x 4 pixels (CIF = 3.48%)	IMG4 – SE Width 4 x 4 pixels (CIF = 2.75%)
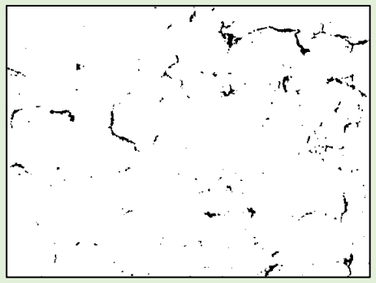	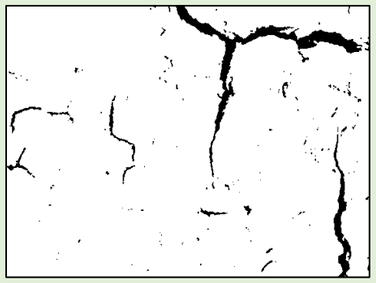		
IMG1 – SE Width 8 x 8 pixels (CIF = 1.61%)	IMG2 – SE Width 8 x 8 pixels (CIF = 4.29%)	IMG3 – SE Width 8 x 8 pixels (CIF = 3.56%)	IMG4 – SE Width 8 x 8 pixels (CIF = 2.87%)
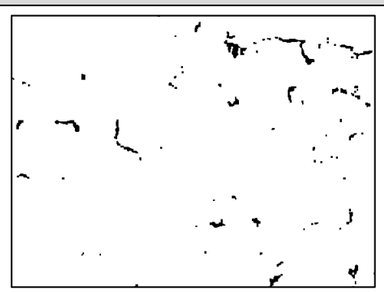	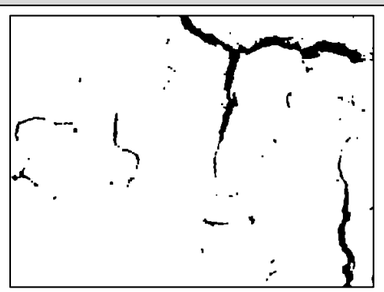	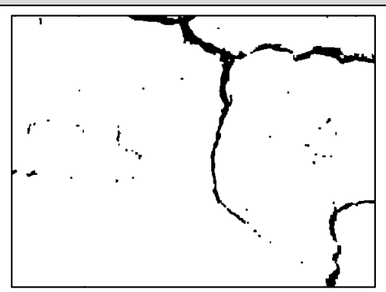	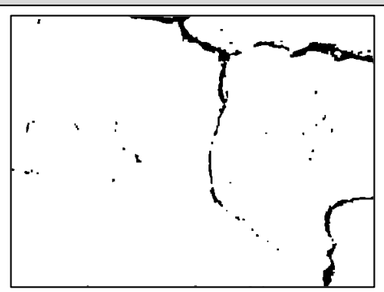

Table A.7: Colour space sensitivity analysis conducted using MATLAB's *colorThresholder* app to observe the impact of RGB, HSV, Lab* and YCbCr colour spaces on the resultant CIF. One sample RGB image from each of the four wind speed tests (W1 – W4) was used in the analysis. Except for the RGB colour space, performance was similar. HSV was chosen as crack segmentation was easier, and it was slightly more efficient at removing background noise whilst preserving the crack area.

Sample ID	Original Image	Colour Space Sensitivity Analysis	
W1 0 m/s wind speed test		**HSV (CIF = 3.38%)** 	**Lab* (CIF = 3.61%)** 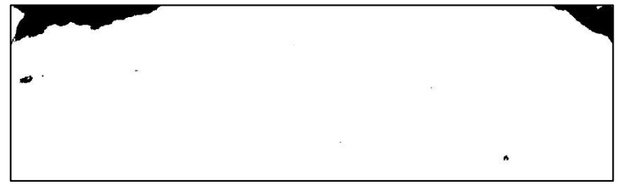
		RGB (CIF = 4.29%) 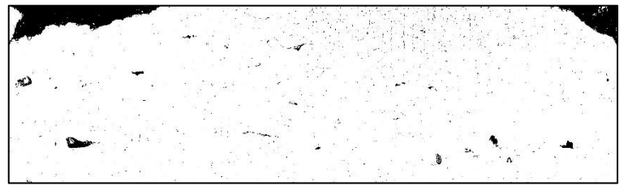	**YCbCr (CIF = 3.44%)** 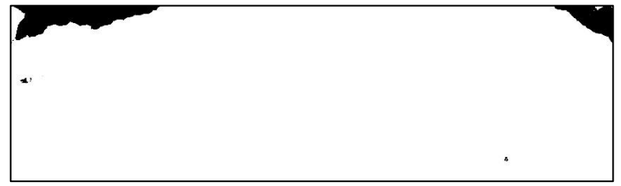
W2 1.5 m/s wind speed test		**HSV (CIF = 18.26%)** 	**Lab* (CIF = 21.37%)** 
		RGB (CIF = (15.06%) 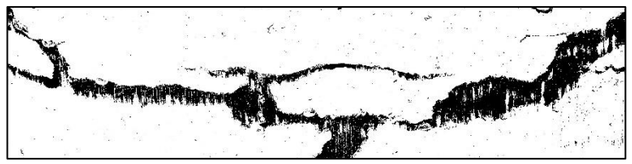	**YCbCr (CIF = 17.40%)** 

Table A.7 (continued): Colour space sensitivity analysis conducted using MATLAB's *colorThresholder* app to observe the impact of RGB, HSV, Lab* and YCbCr colour spaces on the resultant CIF. One sample RGB image from each of the four wind speed tests (W1 – W4) was used in the analysis. Except for the RGB colour space, performance was similar. HSV was chosen as crack segmentation was easier, and it was slightly more efficient at removing background noise whilst preserving the crack area.

Sample ID	Original Image	Colour Space Sensitivity Analysis	
		HSV (CIF = 15.79%)	**Lab* (CIF = 17.01%)**
W3 4.5 m/s wind speed test			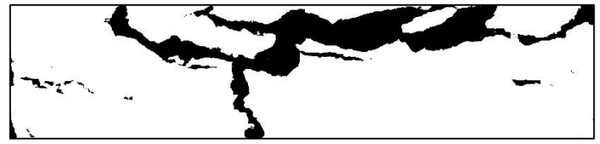
		RGB (CIF = (15.20%)	**YCbCr (CIF = 14.83%)**
			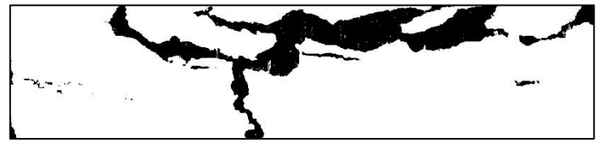
		HSV (CIF = 15.23%)	**Lab* (CIF = 17.25%)**
W4 18 m/s wind speed test			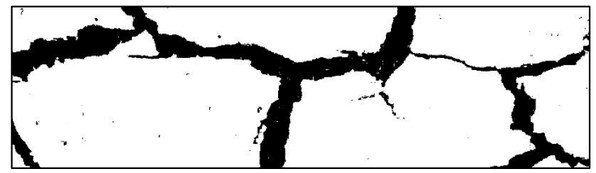
		RGB (CIF = (13.93%)	**YCbCr (CIF = 15.46%)**
			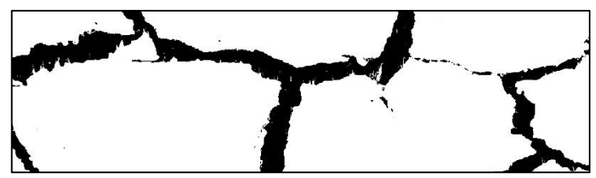

Table A.8: Sensitivity analysis on the impact of disk, diamond and square structuring element shapes (4 x 4 pixel width) used for noise removal on the resultant CIF. This analysis was conducted on four images sampled from the subsurface crack dataset, one for each wind speed (W1 – W4). This study's most efficient option (highlighted in green) was the disk structuring element, as it was most efficient at removing background noise while preserving the crack area.

Subsurface Crack Analysis			
W1 – RGB Image	W2 – RGB Image	W3 – RGB Image	W4 – RGB Image
			
W1 – SE Shape Disk (CIF = 3.33%)	W2 – SE Shape Disk (CIF = 17.14%)	W3– SE Shape Disk (CIF = 15.06%)	W4– SE Shape Disk (CIF = 14.46%)
			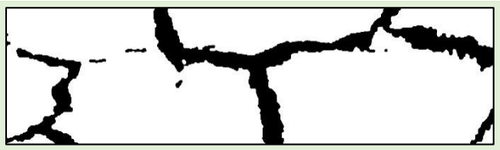
W1 – SE Shape Diamond (CIF = 3.33%)	W2 – SE Shape Diamond (CIF = 17.11%)	W3– SE Shape Diamond (CIF = 14.97%)	W4– SE Shape Diamond (CIF = 14.48%)
		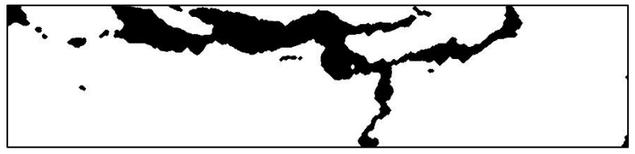	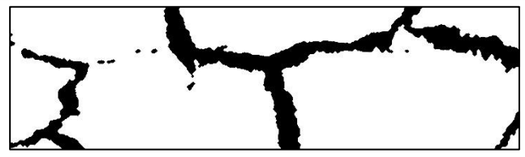
W1 – SE Shape Square (CIF = 3.36%)	W2 – SE Shape Square (CIF = 17.52%)	W3– SE Shape Square (CIF = 15.43%)	W4– SE Shape Square (CIF = 14.90%)
			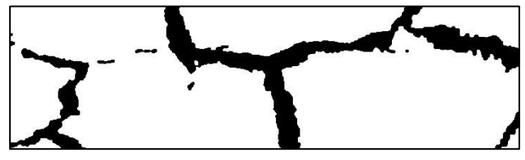

Table A.9: Sensitivity analysis on the impact of 5x5, 10x10 and 15x15 pixel element grid widths (disk-shaped structuring element) on the resultant CIF. This analysis was conducted on four images sampled from the subsurface crack dataset, one for each wind speed (W1 – W4). This study's most efficient option (highlighted in green) was the 10x10 pixel grid width, as it was most efficient at removing background noise while preserving the crack area.

Subsurface Crack Analysis			
W1 – RGB Image	W2 – RGB Image	W3 – RGB Image	W4 – RGB Image
			
W1 – SE Width 5 x 5 pixels (CIF = 3.36%)	W2 – SE Width 5 x 5 pixels (CIF = 17.55%)	W3– SE Width 5 x 5 pixels (CIF = 15.49%)	W4– SE Width 5 x 5 pixels (CIF = 14.97%)
			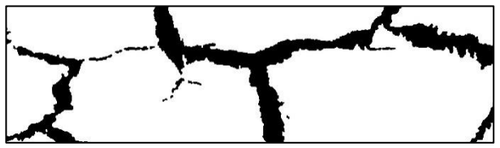
W1 – SE Width 10 x 10 pixels (CIF = 3.33%)	W2 – SE Width 10 x 10 pixels (CIF = 17.14%)	W3– SE Width 10 x 10 pixels (CIF = 15.06%)	W4 – SE Width 10 x 10 pixels (CIF = 14.46%)
			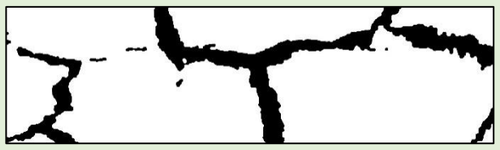
W1 – SE Width 15 x 15 pixels (CIF = 3.33%)	W2 – SE Width 15 x 15 pixels (CIF = 16.30%)	W3– SE Width 15 x 15 pixels (CIF = 14.55%)	W4 – SE Width 15 x 15 pixels (CIF = 14.00%)
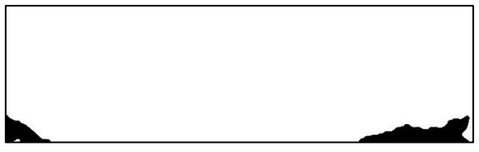	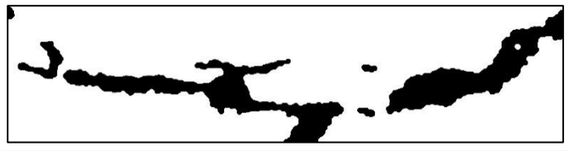	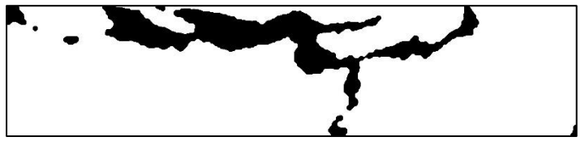	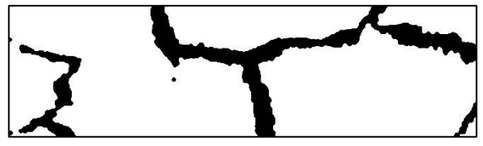

Appendix B

This appendix contains the complete RAW dataset for volumetric water content and suction through the crest, upper and lower slope regions.

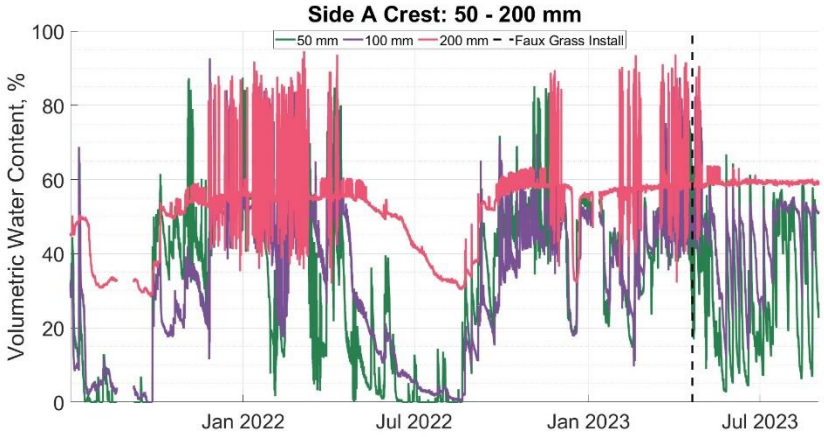

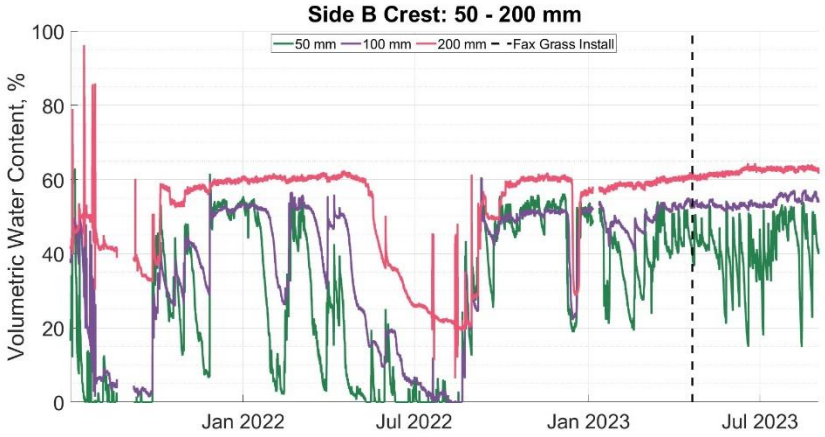

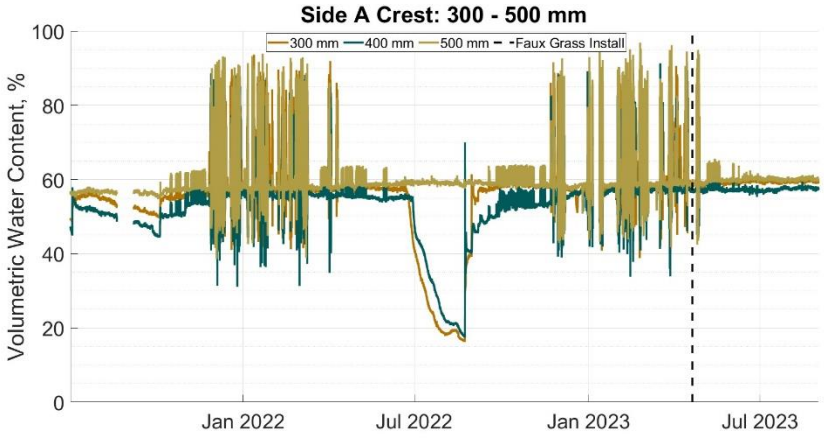

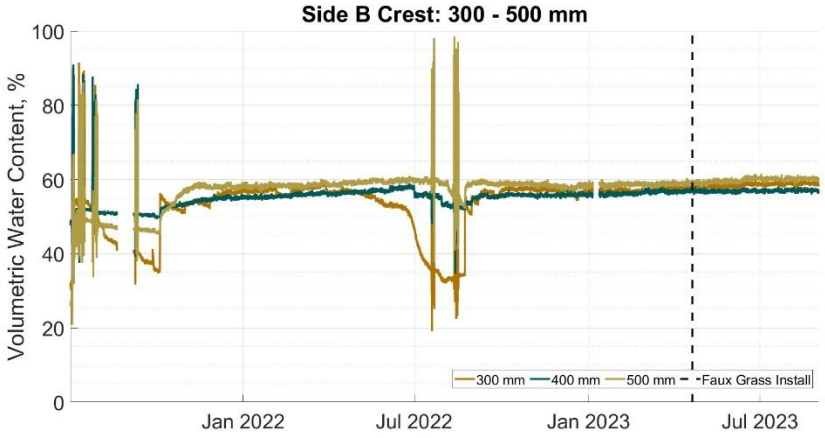

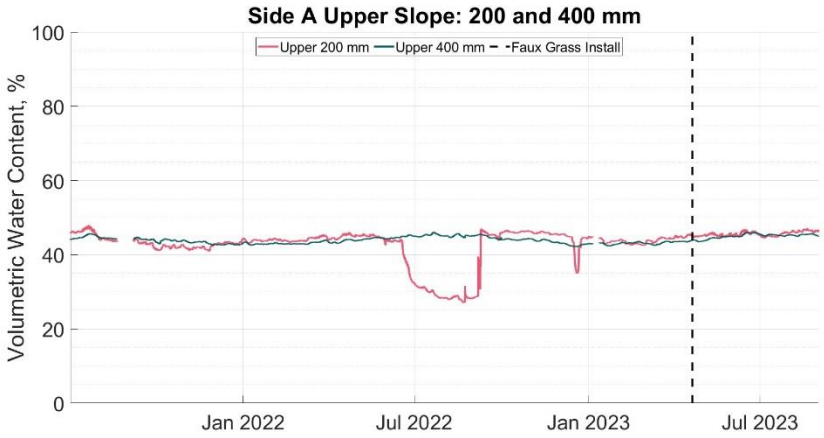
Side A Upper Slope: 200 and 400 mm
Upper 200 mm
Upper 400 mm
Faux Grass Install
Volumetric Water Content, %
100
80
60
40
20
0
Jan 2022
Jul 2022
Jan 2023
Jul 2023

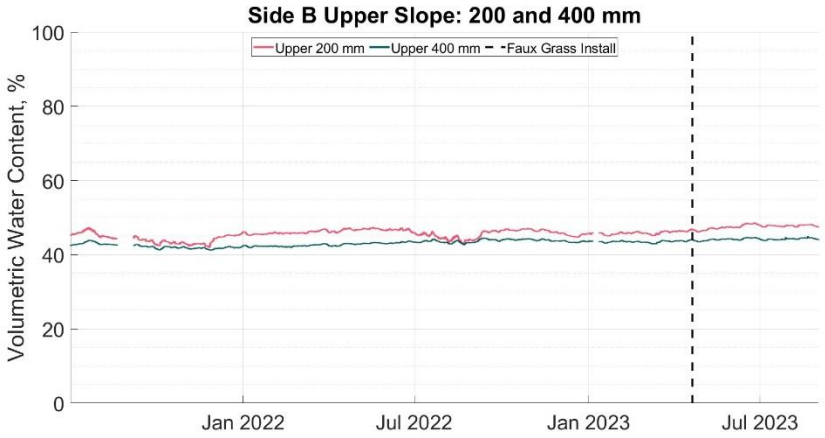
Side B Upper Slope: 200 and 400 mm
Upper 200 mm
Upper 400 mm
Faux Grass Install
Volumetric Water Content, %
100
80
60
40
20
0
Jan 2022
Jul 2022
Jan 2023
Jul 2023

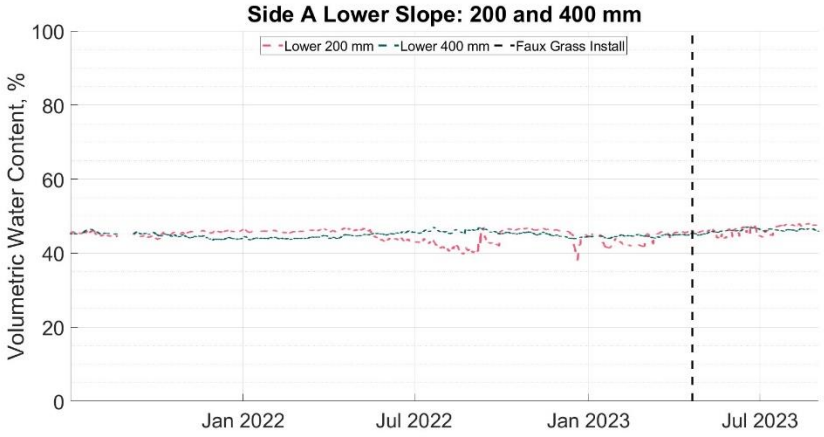
Side A Lower Slope: 200 and 400 mm
Lower 200 mm
Lower 400 mm
Faux Grass Install
Volumetric Water Content, %
100
80
60
40
20
0
Jan 2022
Jul 2022
Jan 2023
Jul 2023

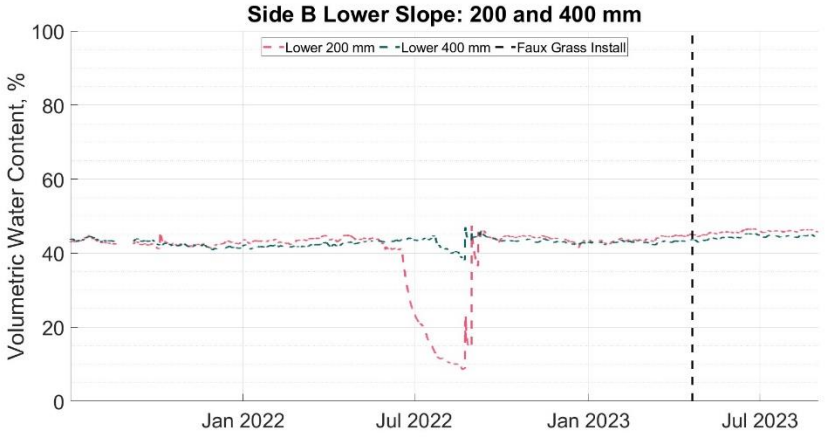
Side B Lower Slope: 200 and 400 mm
Lower 200 mm
Lower 400 mm
Faux Grass Install
Volumetric Water Content, %
100
80
60
40
20
0
Jan 2022
Jul 2022
Jan 2023
Jul 2023

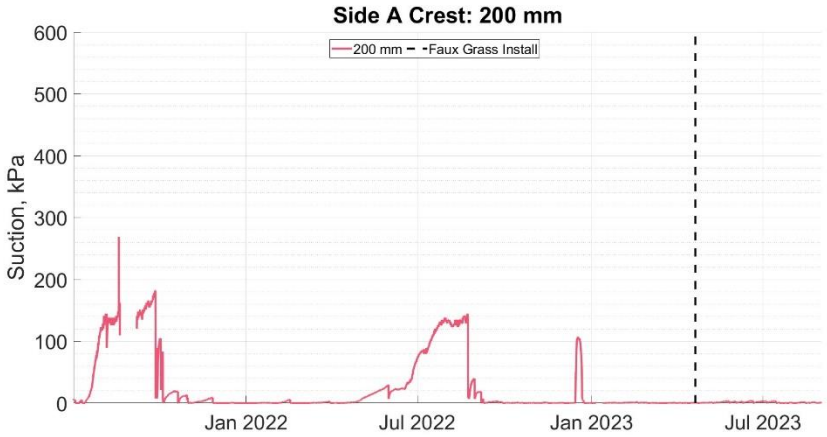
Side A Crest: 200 mm
200 mm
Faux Grass Install
Suction, kPa
600
500
400
300
200
100
0
Jan 2022
Jul 2022
Jan 2023
Jul 2023

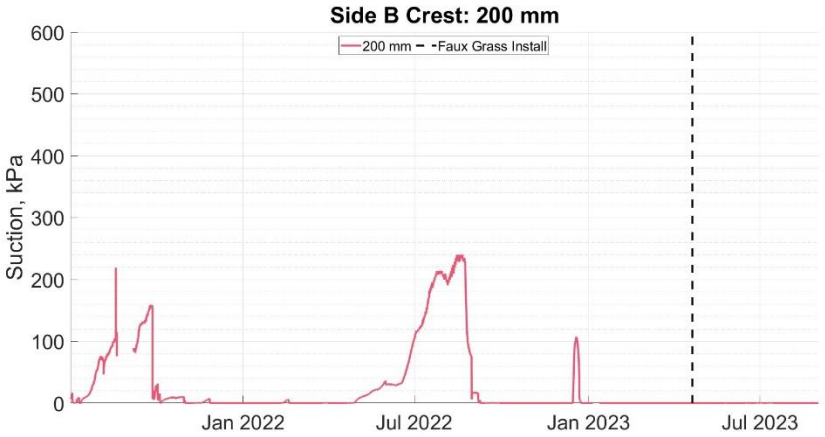
Side B Crest: 200 mm
200 mm
Faux Grass Install
Suction, kPa
600
500
400
300
200
100
0
Jan 2022
Jul 2022
Jan 2023
Jul 2023


Side A Upper Slope - 200 mm
Upper 200 mm
Faux Grass Install
Suction, kPa
600
500
400
300
200
100
0
Jan 2022
Jul 2022
Jan 2023
Jul 2023

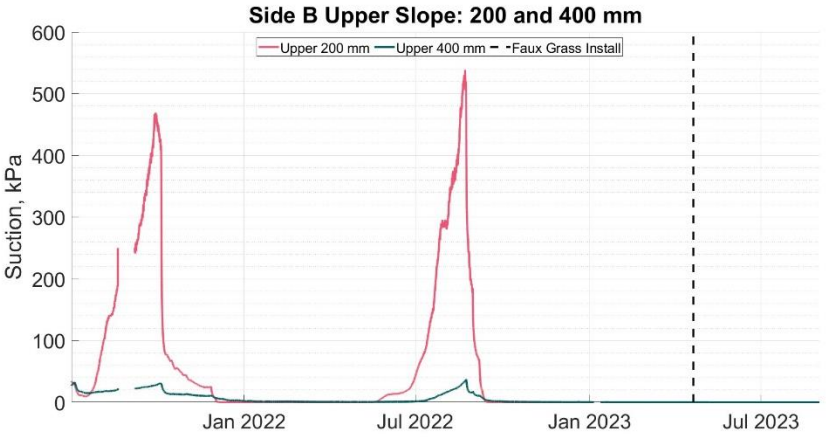
Side B Upper Slope: 200 and 400 mm
Upper 200 mm
Upper 400 mm
Faux Grass Install
Suction, kPa
600
500
400
300
200
100
0
Jan 2022
Jul 2022
Jan 2023
Jul 2023

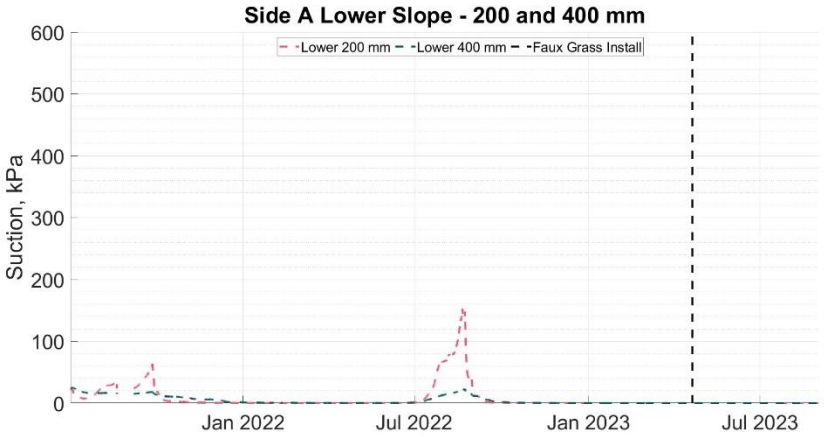
Side A Lower Slope - 200 and 400 mm
Lower 200 mm
Lower 400 mm
Faux Grass Install
Suction, kPa
600
500
400
300
200
100
0
Jan 2022
Jul 2022
Jan 2023
Jul 2023

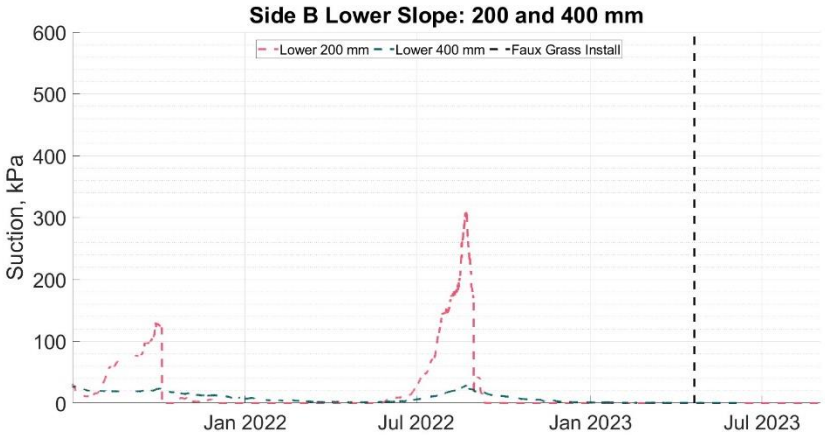
Side B Lower Slope: 200 and 400 mm
Lower 200 mm
Lower 400 mm
Faux Grass Install
Suction, kPa
600
500
400
300
200
100
0
Jan 2022
Jul 2022
Jan 2023
Jul 2023